Journal of NUCLEAR SCIENCE and TECHNOLOGY, Supplement 5, p. 139–142 (June 2008)

Production Cross-Sections of ^{186}Re Radionuclide from the Proton Bombardment on Natural Tungsten

Mayeen U. KHANDAKER[1], Md. S. UDDIN[1,2], Kwangsoo KIM[1], Manwoo LEE[1], Kyung-Sook KIM[1], Youngseok LEE [3], Young-Sik CHO[4], Young-Ouk LEE[4], and Guinyun KIM[*1]

[1] *Department of Physics, Kyungpook National University,1370 Sankyok-dong, Buk-gu, Daegu 702-701, Korea*
[2] *Institute of Nuclear Science and Technology, Atomic Energy Research Establishment, Savar, GPO Box No.3787, Dhaka-1000, Bangladesh.*
[3] *Material Team, R & D Division, National Fusion Research Center, Daejeon 305-333, Korea.*
[4] *Nuclear Data Evaluation Lab., Korea Atomic Energy Research Institute, Daejeon 305-600, Korea*

The excitation function of the ^{nat}W(p,xn)^{186}Re nuclear reaction was measured as a function of the proton energy in the range of 6 - 40 MeV by using a stacked-foil activation technique combined with high-purity germanium gamma-ray spectroscopy at the MC50 cyclotron of the Korea Institute of Radiological and Medical Sciences. The present results are in good agreement with the earlier reported experimental data and the theoretical calculation based on the TALYS code. The thick target integral yield was also deduced from the measured excitation function and stopping power of ^{nat}W over the energy range from threshold up to 40 MeV.

KEYWORDS: excitation function, ^{nat}W(p,xn)^{186}Re reactions, 42 MeV proton, stacked-foil activation technique, integral yield

I. Introduction

The cyclotrons with energy ranges from few tens to few hundreds MeV were applied to the nuclear medicine especially in technologically advanced countries. The radionuclide produced at cyclotron with neutron deficient and decay mainly by an electron capture (EC) or a β^+ emission is especially suitable for diagnostic studies. Rhenium (Re) has varieties of applications in nuclear medicine including radioimmunotherapy, radionuclide synovectomy, and bone pain palliation.[1)] The most widely used rhenium radioisotopes ^{186}Re and ^{188}Re have suitable properties for radiotheraphy. In principle, neutron rich radionuclide ^{186}Re can be produced in different ways, the dominant routes are; by nuclear reactor through (n,γ) process and by cyclotron through ^{186}W(p,n)^{186}Re process. The principal drawback of the former process is that the radionuclide ^{186}Re is produced as carrier added form with low specific activity, whereas the later is better due its carrier-free nature and also for high specific activity. High specific activity is generally required for radiolabeling of tumor-specific antibodies.[2)] Moreover, an additional advantage is that sufficient amount of ^{186}Re can be produced by using a compact cyclotron.[3)] Recent survey[4-6)] has shown that the radionuclide ^{186}Re is an ideal candidate for radioimmunotherapy, especially in bone pain palliation. This is due its short range β^- emission (<2mm in tissue) with energies at 1.07 and 0.933 MeV, low-abundance (9%) γ-ray emission at 137 keV, which allows for in-vivo tracking of the radiolabeled biomolecules and the estimation of dosimetry calculation. The suitable 3.7-day half-life allows sufficient time for the synthesis and shipment of potential radiopharmaceuticals.

Only a few earlier investigations[7-9)] were carried out for the production of high specific activity ^{186}Re radionuclide in no carrier added (NCA) form by the proton bombardment on enriched tungsten targets using cyclotron but discrepancies are found among these data set. These inconsistencies severely limit the reliability of data evaluations. However, an accurate knowledge of excitation function is critically needed for the optimization of production condition. The aim of this work was to measure the production cross-section and estimate the integral yields of ^{186}Re radionuclide from the proton bombardment on natural tungsten target using the MC-50 cyclotron at the Korea Institute of Radiological and Medical Sciences (KIRAMS) in order to enrich, as well as increase the reliability of the existing data set.

II. Experimental Procedure

The production cross-sections of ^{186}Re were measured as a function of proton energy in the energy range of 6-40 MeV using a stacked-foil activation technique combined with high purity germanium (HPGe) γ-ray spectrometry. The irradiation technique, the activity determination, and the data evaluation were described in elsewhere.[10)] High purity metallic form of tungsten (>99.99%) with a thickness of 200 μm, 50 μm thick copper (>99.98%) and 100 μm thick aluminum (99.999%) foils with natural isotopic compositions were assembled in two separate stacks. The aluminum and the copper foils were used to monitor the beam intensity and to degrade the beam energy, as respectively. Two stacked-samples were separately irradiated for 0.5 hour with 42 MeV proton beam of 10 mm diameter and a beam current of about 100 nA in the external beam line

*Corresponding author, E-mail: gnkim@knu.ac.kr

of the MC50 cyclotron at the KIRAMS. The beam intensity was kept constant during irradiation. The activity measurements of the irradiated samples of both the stacks were started about 15 hours after the end of the irradiation. The HPGe-detector (EG&G Ortec.) was coupled with a 4096 multichannel analyzer (MCA) with the associated electronics to determine the photo peak area of the γ-ray spectrum. The spectrum analysis was done using the program Gamma Vision 5.0 (EG&G Ortec.). Each sample was recounted 3~4 times to avoid disturbance by overlapping gamma-lines from undesired sources and in order to more accurately evaluate the longer-lived radionuclide. All samples were measured at 15 cm and 25 cm distances between the sample and the detector to keep dead time within 10% and to suppress the sum-coincidence effect caused by the coincidental detection of two or more γ-rays in cascade. The efficiency of the HPGe-detector was determined using the standard radiation sources.

III. Data Analysis

Cross-sections for the independent and cumulative formation of ^{186}Re in proton-induced activation on natural tungsten were determined from the decay rates of the ^{186}Re and the measured proton beam intensity. The proton beam intensity was determined from the measured activities induced in aluminum and copper monitor foils at the front position of each stack using the reactions, ^{27}Al(p,x)^{22,24}Na and ^{nat}Cu(p,x)^{62}Zn, respectively. The use of the multiple monitor foils decreases the probability of introducing unknown systematic errors in activity determination. The beam intensity was considered constant to deduce cross-sections for each foil of the stack. The loss of proton energy along the stacked was calculated by the computer program SRIM-2003.[11] In order to calculate the cross-sections, the decay data of the ^{186}Re were taken from the NUDAT database[12], and the threshold energy of the contributing reaction was taken from T-2 Nuclear Information Service [13]. The standard cross-section data for the monitors were taken from internet service[14].

The thick target integral yield can be determined by using the measured excitation function. On the basis of excitation functions, the production yield under ideal conditions can be determined as the upper limit of the direct experimental value.

In the present experiment, we have tried to make the reasonable effort to minimize or eliminate systematic errors. However, the combined uncertainty in each cross-section was estimated by considering the following uncertainties; statistical uncertainty of γ-ray counting (0.5-10%), uncertainty in the monitor flux (~7%), and uncertainty in the efficiency calibration of the detector (~4%). The overall uncertainties of the cross-section measurements were in the range of 8-13%. The uncertainty of proton energy was calculated from the uncertainties of the incident beam energy, the target thickness and homogeneity, and the beam struggling. The calculated uncertainty of a representing point in the excitation function ranges from ±0.3 to ±0.9 MeV.

IV. Results and Discussion

The cross-sections for the formation of 186Re in the interactions of protons with natural tungsten, measured in this work, are presented in **Table 1**. The obtained cross-section data and deduced yield are shown in **Fig. 1-3** together with the literature values and the calculated values of the theoretical model code TALYS.

Table 1 Measured production cross-sections of ^{186}Re

E_p(MeV)	σ (mb)	E_p(MeV)	σ (mb)	E_p(MeV)	σ (mb)
39.9	6.59±0.71	30.0	7.79±0.82	15.9	10.31±1.07
38.3	7.26±0.65	28.0	9.27±0.85	13.0	11.31±0.97
37.0	7.83±0.87	25.8	7.81±0.82	10.8	16.87±1.66
35.2	7.32±0.93	23.4	7.99±0.72	6.6	2.39±0.32
33.4	7.79±0.86	21.6	9.13±0.98		
31.5	7.38±0.68	19.0	9.16±0.86		

1. Production cross-sections of the monitor reaction

The use of monitor reactions in monitor foils with same area with the target foils of interaction is a very simple, convenient and a cheap method for energy and intensity measurements of charged particle beams used for radioisotope production. This process has especially a great importance when the deduced beam parameters are used in the determination of new experimental data such as cross sections or yields. The use of monitor reaction means performing relative measurement.

To avoid any mistake in determination of the effective bombarding energy of the target foils in the stack, the excitation function of the monitor reaction, ^{nat}Cu(p,xn)^{62}Zn was measured simultaneously with desired targets and compared to the recommended values over the investigated energy region. As shown in **Fig. 1**, the measured values are in well consistent with the recommendation[14] and that fact confirms the reliability of the incident beam energy degradation calculation, effective beam current and the measured cross-sections for the investigated nuclides.

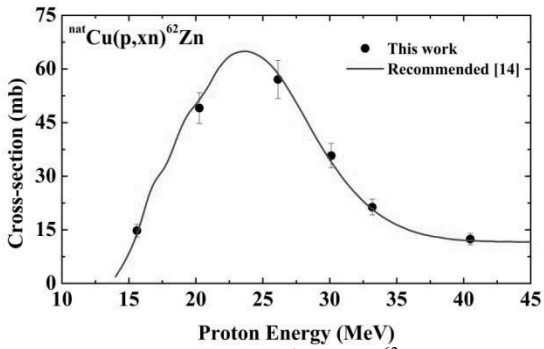

Fig. 1 Excitation function of the ^{nat}Cu(p,xn)^{62}Zn monitor reaction.

2. Production cross-sections of ^{186}Re

The most suitable reaction path for the production of ^{186}Re from the proton bombardment on natural tungsten is ^{186}W(p, n)^{186}Re (Q= -1.069 MeV). The cross-section of the

direct formation of ^{186}Re from the ^{nat}W+p process was measured up to 40 MeV. The present measurements are compared in **Fig. 2** with the available experimental values[8,15-18] and the theoretical calculations using the code TALYS. TALYS is a nuclear-reaction computer program which simulates basically all types of nuclear reactions, in the energy range of 1 keV - 200 MeV. With a few exceptions, the database of this code is based on the Reference Input Parameter Library[19]. As shown in **Fig. 2**, the excitation function of ^{186}W(p,n)^{186}Re reaction has a peak at around 9 MeV. Unfortunately, we could not measure the cross-sections in the range of 6.6 - 10 MeV due to the thick target samples. The present results are in general good agreement with the data reported by Lapi *et al.*[15], Tarkanyi *et al.*[17], and Szelecsenyi *et al.*[18]. The theoretical calculations by TALYS are consistent with the present results in our investigated energy region. Shigeta *et al.*,[8] measured the production cross-sections of ^{186}Re by using an isotopically enriched sample ^{186}W, and hence their data showed higher values than any other measurements. The data reported by Zhang *et al.*[16] are very low compared with other measurements.

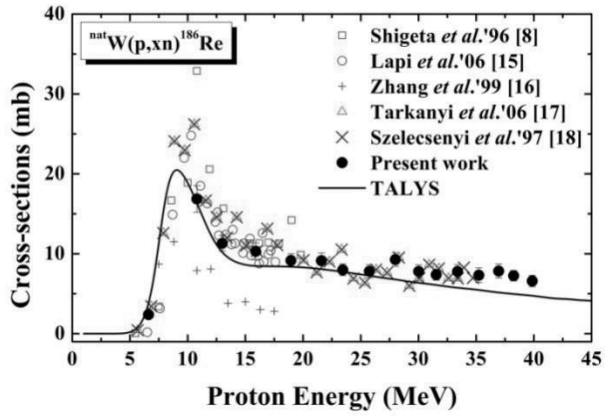

Fig. 2 Excitation function of the ^{nat}W(p,xn)^{186}Re reaction.

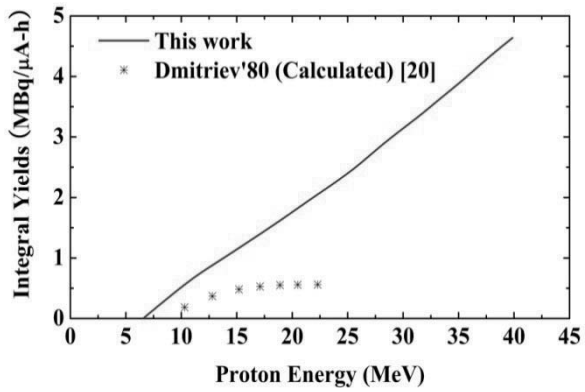

Fig. 3 Integral yields of ^{186}Re from a natural tungsten target as a function of proton energy

3. Integral yield

The integral yield of a radionuclide from a nuclear process was deduced using the measured cross-sections of ^{186}Re and stopping power of ^{nat}W over the energy range from threshold up to 40 MeV. It is expressed as MBq μA^{-1} h^{-1}, i.e. for an irradiation at beam current of 1 μA for 1 hour. The obtained result is shown in **Fig. 3** with the calculated yield by Dmitriev[20] as a function of proton energy. The calculated values of Dimitriev, where they did not use their measurement, were different from the present result. The optimum production range of ^{186}Re radionuclide was found for proton energy at 7-14 MeV. The integral yield of ^{186}Re at 15.9 MeV is 1.25 MBq μA^{-1} h^{-1}. For application purposes by using enriched ^{186}W-target (99%), the yield of ^{186}Re may be increased up to 4.32 MBq μA^{-1} h^{-1}.

V. Conclusions

The new independent and cumulative excitation function of the ^{nat}W(p,xn)^{186}Re reaction was measured in the energy range of 6.6 - 40 MeV by using a stacked-foil activation technique with an overall uncertainty of about 13%. In general the present measured data agreed with other measurements except the data reported by Zhang *et al.*[16]. The ^{186}Re is one of the most useful radionuclide for internal radiotherapy in nuclear medicine. The measured excitation function of this radionuclide will help effectively to optimize the production conditions. The optimum production of this radionuclide was found in the energy range 7-14 MeV whereas at 15.9 MeV the integral yield was obtained as 1.25 MBq μA^{-1} h^{-1}, which could be increased up to 4.32 MBq μA^{-1} h^{-1} using 99% enriched ^{186}W-target. Although nowadays, ^{186}Re is produced commercially by using nuclear reactors, the cyclotron offers the alternative production route of this isotope in no carrier added form. In the last decade, the rapid installations of hospital based cyclotrons in the world were driven by the advent of advances in various imaging techniques. However, the present measured cross-sections data from ^{186}W(p,n)^{186}Re process will be very helpful to prepare a recommended data base leading to the practical applications.

Acknowledgement

The author would like to express their sincere thanks to the staffs of the MC50 Cyclotron Laboratories for their cordial help in performing the experiment. This work is partly supported through the Ministry of Science and Technology (Project No. M20702000008-07B0200-00810, M20704000011-7M0400-01110) and by the user program of the Proton Engineering Frontier Project (Project No. M2 02AK010014-07A1101-01419).

References

1) L. F. Mausner, S. C. Srivastava, "Selection of radionuclides for radioimmunotherapy," Med. Phys. **20**, 503 (1993).
2) W. A. Volkert, W. F. Goeckeler, G. J. Ehrhardt, et al., "Therapeutic radionuclides: production and decay property considerations," J. Nucl. Med. **32**, 174 (1991).
3) L. Solin, V. A. Jakovlev, I. E. Alekseev et al., "Cyclotron Yields of Rhenium-186," Proc. 5th Int. Conf. on Isotopes, Brussels, Belgium, April 25-29, p. 131 (2005).

4) S. Kinuya, K. Yokoyama, M. Izumo et al., "Locoreginal radioimmunotherapy with 186Re-labeled monoclonal antibody in treating small peritoneal carcinomatosis of colon cancer in mice in comparison with 131I-counterpart," Cancer Lett. **219**, 41 (2005).
5) S. Kinuya, K. Yokoyama, M. Izumo et al., "Feasibility of 186Re-radioimmunotherapy for treatment in an adjuvant setting of colon cancer," J. Cancer Res. Clin. Oncol. **129**, 392 (2003).
6) E. J. Postema, P. K. Borjesson, W. C. Buijs et al., "Dosimetric Analysis of Radioimmunotherapy with 186Re-Labeled Bivatuzumab in Patients with Head and Neck Cancer," J. Nucl. Med. **44**, 1690 (2003).
7) N. C. Schoen, G. Orlov, R. J. McDonald, "Excitation functions for radioactive isotopes produced by proton bombardment of Fe, Co, and W in the energy range from 10 to 60 MeV," Phys. Rev., **C 20**, 88 (1979).
8) N. Shigeta, H. Matsuoka, A. Osa et al., "Production Method of No-Carrier-Added 186Re," J. Radioanal. Nucl. Chem. **85**, 205 (1996).
9) E. M. Moustapha, G. J. Ehrhardt, C. J. Smith et al., "Preparation of cyclotron-produced 186Re and comparison with reactor-produced 186Re and generator-produced 188Re for the labeling of bombesin," J. Nucl. Med. Biol. **33**, 81 (2006).
10) M. S. Uddin et al., "Excitation functions of the proton induced nuclear reactions on natZn up to 40 MeV," Nucl. Instr. and Meth. **B 258**, 313 (2007).
11) J. F. Ziegler, J. P. Biersack, U. Littmark, SRIM-2003 code, "The stopping and range of ions in solids," Pergamon, New York (2003), Available at <http://www.srim.org/>.
12) National Nuclear Data Center, the NuDat database, available at <http://www.nndc.bnl.gov/nudat2>.
13) Reaction Q-values and thresholds, Los Alamos National Laboratory, T-2 Nuclear Information Service, Available at < http://t2.lanl.gov/data/qtool.html>.
14) F. Tarkanyi et al., IAEA-TECDOC-1211, "Beam monitor reactions, Charged Particle Cross-Section Database for Medical Radioisotope Production: Diagnostic Radioisotopes and Monitor Reactions, Co-ordinated Research Project (1995-1999)," IAEA, Vienna. Austria, May 2001. Available from <http://www-nds.iaea.org/ medical/>.
15) S. Lapi, W. J. Mills, J. Wilson et al., "Production cross-sections of 181–186Re isotopes from proton bombardment of natural tungsten," App. Radiat. Isot. **65**, 345 (2007).
16) X. Zhang, W. Li, K. Fang et al., "Excitation functions for natW(p,xn)181-186Re reactions and production of no-carrier-added 186Re via 186W(p,n)186Re reaction," Radiochim. Acta **86**, 11 (1999).
17) F. Tarkanyi, S. Takacs, F. Szelecsenyi et al., "Excitation functions of proton induced nuclear reactions on natural tungsten up to 34 MeV," Nucl. Instr. and Meth. **B 252**, 160 (2006).
18) F. Szelecsenyi, S. Takacs, F. Tarkanyi et al., in: J.R. Heys, D.G. Mellilo, Chichester, et al. (Eds.), "Study of production possibility of no-carrier-added 186Re via proton induced reaction on tungsten for use in radiotherapy," Proc. 6th Int. Symp. on Synthesis and Appl. of Isotopically Labelled Compounds, Philadelphia, USA, Sept. 14–18, 1997, John Wiley and Sons, p. 701 (1998).
19) Reference Input Parameter Library. Available at <http://www-nds. iaea.org/RIPL-2/>.
20) P. P. Dmitriev, G. A. Molin, "Yields of rhenium-181, rhenium-182m, rhenium-182, rhenium-183, rhenium-184m, rhenium-184, and rhenium-186 when irradiating tungsten with protons and deuterons and tantalum with α–particles," Atom. Energy. **48**, 122 (1980).

Journal of NUCLEAR SCIENCE and TECHNOLOGY, Supplement 5, p. 143–146 (June 2008)

Performance Evaluation of a Beam-shaping Assembly for Accelerated-BNCT Using the Neutron Generation Experiment of $^{7}Li(p,n)^{7}Be$ Reaction

Kyung-O KIM[1], Sang Hoon JUNG[2], Soon Young KIM[2], Gi-Dong KIM[3], and Jong Kyung KIM[1*]

[1]*Department of Nuclear Engineering, Hanyang University, Seoul, Korea*
[2]*Innovative Technology Center for Radiation Safety, Hanyang University, Seoul, Korea*
[3]*Korea Institute of Geoscience and Mineral Resource, Daejeon, Korea*

An experiment for performance evaluation of a beam-shaping assembly to generate therapeutic neutrons has been carried out for accelerator-based boron neutron capture therapy (BNCT). Neutron beams are produced by using $^{7}Li(p,n)^{7}Be$ reaction, which has a high neutron yield for low energy neutrons comparing with other reactions. The manufactured assembly is composed of two moderators, AlF_3 and Al, and a surrounding graphite reflector in order to focus the generated neutrons from the Li-target on the epithermal energy range with high intensity and quality. The target neutrons from $^{7}Li(p,n)^{7}Be$ reaction and epithermal neutrons generated from the assembly were measured by He-3 detector. It was convinced from the experiment that the beam-shaping assembly, designed in this study, can shape the source neutron beam into the effective neutron beam for BNCT of which epithermal neutrons occupy the 87.4 %. The experimental result was verified through the use of Monte Carlo simulation using MCNPX code. Appropriate agreement was found between the calculated and measured results in a wide energy range from 0 to 800 keV.

KEY WORDS: BNCT, neutron source, beam-shaping assembly, epithermal neutron, proton accelerator

I. Introduction

Boron neutron capture therapy (BNCT) is a binary radiation treatment method for cancer that uses specially combined compounds to deliver Boron-10 to tumor cells, which will be irradiated with thermal neutrons. BNCT studies and a clinical treatment have been developed by using nuclear reactors that are easily used to generate the neutrons. In the case of using reactors, however, it is difficult to install them into the hospitals. In addition, patient treatments can be carried out only during the operation of the reactor.

In recent years, there have been several advanced studies on accelerator-based BNCT. In particular, $^{7}Li(p,n)^{7}Be$ reactions, that are commonly used in BNCT, have a high yield of low energy neutrons compared to other reactions.

For efficient BNCT, neutron beams with a proper energy spectrum should be provided such that most of the neutrons could be irradiated in the tumor after being slowed down to thermal energy ranges. Therefore, a good spectrum shaping to epithermal energy ranges is an essential requirement for BNCT. Also, it was widely recognized that neutrons in the epithermal range (4 eV – 40 keV) are suitable for treating deep-seated cancer without a high skin dose[1)]. For this reason, epithermal neutrons would be generated with an accelerator-based BNCT system composed of a neutron source and beam-shaping assembly.

In a previous study, the target system and a beam-shaping assembly design, with good neutron beam quality and high intensity for BNCT, were researched at Hanyang University[2)]. In the study, neutrons were generated from the lithium target through $^{7}Li(p,n)^{7}Be$ reaction, and moderated to a suitable energy spectrum for BNCT.

To evaluate the performance of the beam-shaping assembly, two experiments were performed in this study, measurements of neutron beams from the lithium target and the neutron beams moderated by the beam-shaping assembly using a 2.5 MeV proton accelerator. The experiment results were normalized by an induced beam current, and compared to each other. Also, the accuracy of the experiment was assessed through the comparison of measured results and calculated ones by the MCNPX code.

II. Methods and Materials

1. Beam-shaping Assembly

With the aim of producing epithermal neutrons, a beam-shaping assembly was designed in previous researches[1), 2)]. That assembly was composed of two moderators with a surrounding reflector as shown in **Fig. 1**. The moderators were respectively filled with aluminum fluoride (ρ=2.78 g/cm^3) and aluminum (ρ=2.78 g/cm^3), and the reflector was made of graphite (ρ=1.85 g/cm^3).

Beam qualities produced from the beam-shaping assembly had been evaluated by using a MCNPX simulation with reference to the parameters recommended by IAEA[3)], and the results are presented in **Table 1**. It was recognized that all the recommendations were satisfied except the neutron current-to-flux ratio. Especially, it was found that unnecessary radiations (thermal and fast neutrons, gamma-ray) to be deposited in the normal tissue were significantly reduced by the beam-shaping assembly, and 87.4 % of the neutrons moderated by the assembly

*Corresponding Author, Tel: +82-2-2220-0464, Fax: +82-2-2294-4800, E-Mail: jkkim1@hanyang.ac.kr

were focused in the epithermal energy range (4 eV - 40 keV). Even though the current-to-flux ratio did not satisfy the recommendation, it was comparable to that of the beam-shaping assemblies designed by other research works[4), 5), 6)].

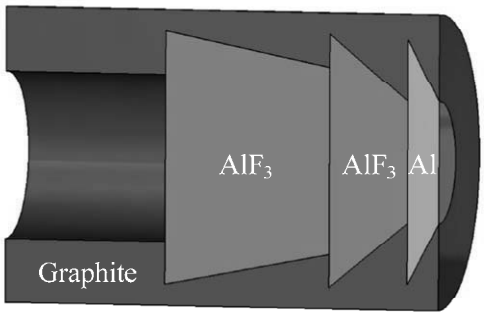

Fig. 1 Beam shaping assembly for generating epithermal neutron beam is consisted of two moderators of AlF_3 and Al. These are about 35 cm thick axially and 15 cm in diameter. Moderators are surrounded by graphite reflectors each of which is about 9 cm thick.

Table 1 Comparison of beam quality parameters between the neutron beams designed in this study and the IAEA recommendations

	IAEA Recommendations	This work
D_n/Φ_{epi} [Gy-cm^2/n_{epi}]	$< 2.0\times10^{-13}$	7.12×10^{-14}
D_γ/Φ_{epi} [Gy-cm^2/n_{epi}]	$< 2.0\times10^{-13}$	2.48×10^{-14}
Φ_{th}/Φ_{epi}	< 0.05	0.04
J_{total}/Φ_{total}	> 0.7	0.62
Φ_{th} [%]	3.5	
Φ_{epi} [%]	87.4	
Φ_{fast} [%]	9.1	

- D_n: Fast Neutron Dose, D_γ: Gamma Dose, J_{total}: Neutron Current
- Φ_{th}, Φ_{epi}, Φ_{total}: Thermal, Epithermal, and Total Neutrons

2. Experiment for Measuring Epithermal Neutrons

The 1.7 MV tandem accelerator at the Korea Institute of Geoscience and Mineral Resource (KIGAMS) was used to produce relatively low energy neutrons of mean energy less than 350 keV by bombarding 2.5 MeV protons on a thick lithium target. A target thickness of 100 μm was employed in this experiment to cause significant loss of proton energy. The diameter of the proton beam was about 1 cm, and the average beam current of the proton accelerator was 0.53 μA. A He-3 proportional counter was used to measure the neutrons generated from the Li-target and moderated by the assembly as a neutron spectrometer.

In the experiments, the He-3 counter was arranged to be paralleled with the assembly and covered by a 1 mm-thick cadmium sheet used to reduce significantly the thermal neutrons scattered from surrounding structures. In order to increase the reliability of the detection signal, which might be decreased due to a pile-up effect when the moderated neutrons were measured, the assembly was located 300 cm away from the Li-target for the purpose of moderating only the neutrons emitted from the target through the angle ranges of 0 to 4^o. The He-3 counter was located just behind the assembly.

Experiments were carried out twice to measure the neutrons directly from the lithium target and moderated neutrons through the assembly. These experiments were performed with enough time in order to detect sufficient neutrons. Two experiment setups were presented and are shown in **Fig. 2**.

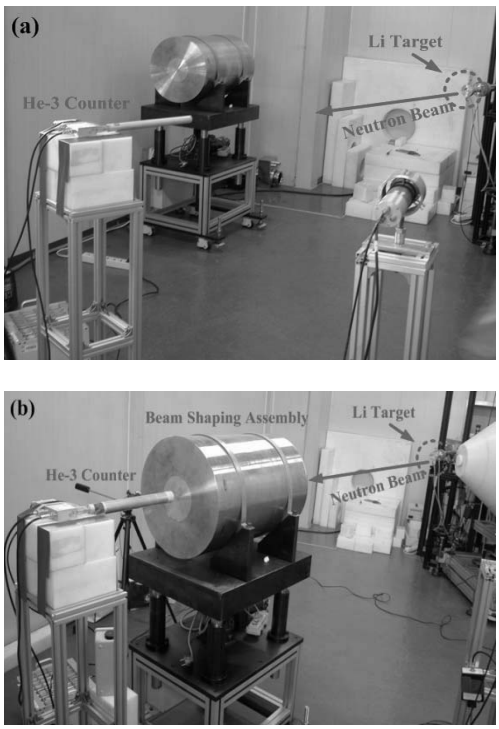

Fig. 2 Experiment configurations for measuring (a) target neutrons and (b) moderated neutrons from the beam-shaping assembly

III. Results and Discussions

1. Measurement Results

The pulse height distributions of the neutron beam from the beam-shaping assembly and the lithium target are presented in **Fig. 3**. In this figure, the neutron spectrum is calibrated with the three peaks such as triton (25 % of Q-Value), proton (75 % of Q-Value), and the epithermal peak (= Q-value, 764 keV) [7), 8)], and these results are normalized by the proton beam current. It was recognized that the measured counts in all energy ranges were reduced by the beam-shaping assembly. Especially, the decreasing ratio of

the high energy neutrons above 40 keV is more significant than that of the low energy neutrons below 40 keV.

In order to confirm the efficiency of the beam-shaping assembly, the total neutron energy range was divided into 21 ranges including the epithermal energy range. The measured counts in each energy range were compared with those in the highest neutron energy range (748.89 – 785.13 keV) in separate experiments. The ratios of measured counts in each energy bin to those in the highest energy range are reflected with neutron detection efficiency, and presented in **Fig. 4,** for both the source and moderated spectra. From the result, it was confirmed that the epithermal neutrons generated by the assembly are more than about 950 times with reference to those in the highest energy range. On the other hand, this ratio for the source spectrum is about 210 times. It was, therefore, found that the beam shaping assembly for the accelerator-based BNCT was well designed to get significant epithermal neutrons.

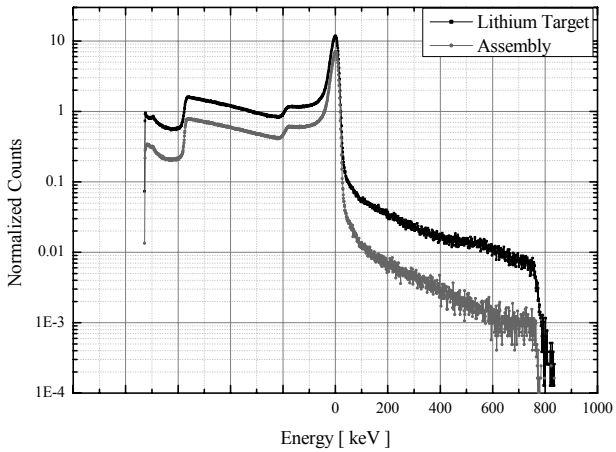

Fig. 3 Comparison of the measured results between target neutrons and moderated ones through the beam-shaping assembly using a He-3 counter

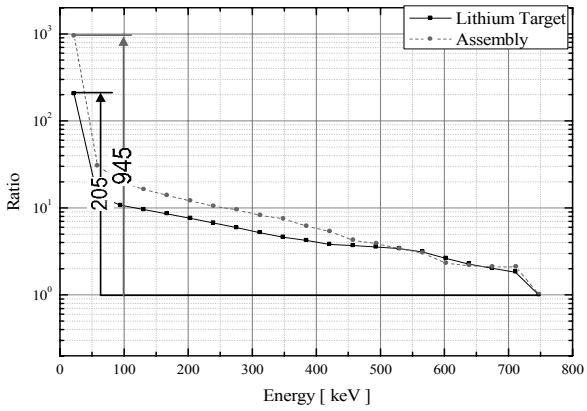

Fig. 4 Comparison of the count ratios with reference to those in the highest energy bin (748.89 – 785.13 keV), between the source and moderated neutrons from the assembly

2. Comparison with Simulation Result

The efficiency of the He-3 detector was determined by MCNPX[9] in order to compare the experimental result with the simulation one. The He-3 detector was simulated in the same condition, and a pencil beam of mono-energy neutrons was incident to the detector surface at 1 m distance away, with the energy interval of 25 keV from 0 to 1 MeV. The calculated efficiency shown in **Fig. 5** was reflected in the comparison results.

The calculated epithermal neutron spectrum from the beam-shaping assembly is shown together with the experimental result in **Fig. 6**. Appropriate agreement in this comparison was found in a wide energy range from 0 – 800 keV. The moderated neutrons were well focused in the thermal and epithermal energy ranges (0 eV – 40 keV).

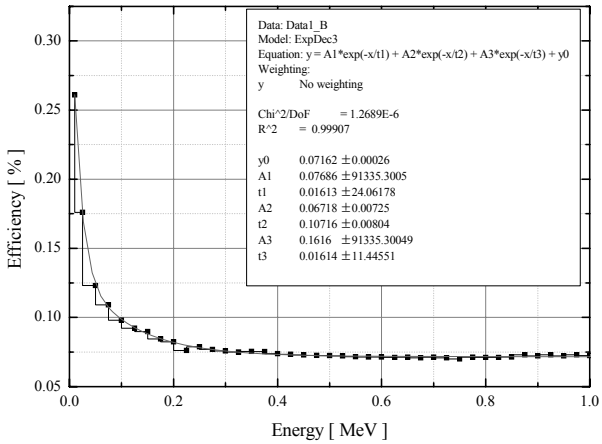

Fig. 5 Calculated He-3 detector efficiency as a function of neutron energy

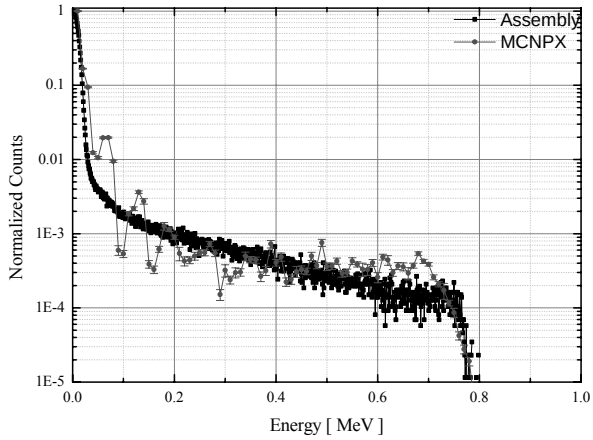

Fig. 6 Comparison of the neutron spectrum from the experiment with the calculated one using MCNPX at the port of beam-shaping assembly

IV. Conclusions

The performance of the beam-shaping assembly was evaluated by using $^{7}Li(p,n)^{7}Be$ neutrons[10]. It was

confirmed that the moderated neutrons through the assembly were well focused into the epithermal energy range at about 88 %. Also, good agreement was obtained between the calculated and experimental results in all energy ranges (0 – 800 keV).

Through the experiment performed in this study, the design technology of therapeutic neutron beams for accelerator-based BNCT is expected to be elevated and progressed to the realization of clinical treatment for the cancer patients. The beam-shaping assembly proposed in this study is well-suited for installation into the hospital environment.

Acknowledgement

This study was performed under the long-term nuclear research and development program sponsored by the Ministry of Science and Technology of Korea (M20505050003-05A0905-00310), and supported by the Innovative Technology Center for Radiation Safety (R11-2000-067-01001-0).

References

1) Deok-jae Lee, Chi Young Han, Jong Kyung Kim, and Byung-Chan Na, "Spectrum Shaping of Epithermal Neutron Beam for Accelerator-Based BNCT and Dosimetric Evaluation Using a Brain Phantom," Journal of Nuclear Science and Technology, Supplement **4**, 180-183 (2004).
2) M. Y. Paek, C. Y. Han, and J. K. Kim, "A Characteristic Analysis of an Accelerator-Based Epithermal Neutron Beam for Boron Neutron Capture Therapy," Proceedings of the First iTRS International Symposium on Radiation Safety and Detection Technology (ISORD-1), Seoul, Korea, July 18-19, 292-296 (2001).
3) IAEA, Current Status of Neutron Capture Therapy, IAEA-TECDOC-1223, IAEA, (2001).
4) E. Durisi, A. Zanini, C. Manfredotti, F. Palamara, M. Sarotto, L. Visca, and U. Nastasi, "Design of an Epithermal Column for BNCT based on D-D Fusion Neutron Facility," Nuclear Instruments and Methods in Physics Research A, **574**, 363-369 (2007).
5) O. E. Kononov, V. N. Kononov, M. V. Bokhovko, V. V. Korobeynikov, A. N. Soloviev, A. S. Sysoev, I. A. Gulidov, W. T. Chu, and D. W. Nigg, "Optimization of an Accelerator-Based Epithermal Neutron Source for Neutron Capture Therapy," Applied Radiation and Isotopes, **61**, 1009-1013 (2004).
6) N. Cerullo, J. Esposito, and G. G. Daquino, "Spectrum Shaping Assessment of Accelerator-Based Fusion Neutron Sources to be used in BNCT Treatment," Nuclear Instruments and Methods in Physics Research B, **213**, 641-645 (2004).
7) J. B. Marion, and J. L. Fowler, "Fast Neutron Physics," Interscience Publisher INC., 413-439 (1960).
8) Esam M. A. Hussein, "Handbook on Radiation Probing, Gauging, Imaging, and Analysis," Kluwer Academic Publishers, 194-204 (2002).
9) D. Pelowitz, Ed., "MCNPX User's Manual Version 2.5.0," LA-CP-05-0369, Los Alamos National Laboratory, (2005).
10) X. L. Zhou and C. Lee, "Lithium Compounds as Targets for (p,n) Reactions," Applied Radiation Isotopes, **48**, 1493-1496 (1997)

Journal of NUCLEAR SCIENCE and TECHNOLOGY, Supplement 5, p. 147–150 (June 2008)

Retrospective Dosimetry Using Violet Thermoluminescence from Natural Quartz in Soil

Hiroki Fujita*

Japan Atomic Energy Agency, 4-33 Muramatsu, Tokai-mura, Naka-gun, Ibaraki 319-1194, Japan

The violet thermoluminescence (VTL)-retrospective dosimetry was developed and was then confirmed to be effectual method in emergency situation using quartz extracts from surface soil collected around tokai, Ibaraki, Japan. All of the measurements were undertaken by VTL measurement condition using modified single aliquot regenerative-dose protocol.

An on-line automatic spectrometric system installed with a small spectrometer and a CCD camera unit was developed for weak and changeable TL-spectrum measurement with rising temperature for application to natural quartz. From spectrometry of the TL, two emission peaks, consisting of 400 nm and 620 nm, were revealed. In this paper, 400 nm were only investigated.

The accumulated γ-doses of quartz extracts from surface soils which were 10 m from radiation source at gamma field at the Institution of Radiation Breeding (IRB), National Institute of Agrobiological Sciences (NIAS), were evaluated to be 0.8~0.9 Gy using VTL measurement, concordant with the value measured by the commercial pocket dosimeter. In addition, the dose of quartz extracted from surface soils set at 20 m was evaluated to be 0.2 Gy, agreeable to the value calculated from the pocket dosimeter's value. Conclusively, the VTL-retrospective dosimetry was recommended for the quartz extracts from surface soils in the emergency situation.

KEYWORDS: violet thermoluminescence, quartz, single-aliquot regenerative-dose protocol, retrospective dosimetry

I. Introduction

Thermoluminescence (TL) and optically stimulated luminescence (OSL) have been observed from dielectric materials such as quartz and feldspar after heated up to 450 °C and stimulated with light, respectively. The luminescence is emitted, depending on irradiation dose of minerals. These TL and OSL phenomena are known to be effective in widespread use for archeological and quaternary geological dating using sediment layers and burnt materials (Kaul et al., 1966; Fleming, 1970, 1972; Aitken, 1985, 1992, 1998; Wintle, 1997).

Several studies have demonstrated that luminescence techniques applied to ceramics can be successfully used for retrospective assessment of the cumulative absorbed dose due to the gamma radiation arising from radioactive fall-out (Bailiff, 1995; Bailiff et al., 2004; Bougrov et al., 1998; Haskell et al., 1994;). The assessment of the total dose accumulated in a sample makes use of a mineral such as quartz exposed to an unknown dose (natural or accidental signal). The luminescence intensity emitted by the sample can be compared with the resulting from a calibration dose (regenerated signal) given after the measurement of the as-received one (Murray and Wintle, 2002). In order to assess the accidental dose correctly, the contribution due to radiation of natural sources should be subtracted from the total dose measured from the TL or OSL signals. Therefore, this contribution must be evaluated on the basis of the environmental dose rate measured by means of complementary techniques such as measurements of naturally occurring radioactivity for dried-soil material following to the correction of water content in the as-received soil (Aitken, 1985).

Violet TL (VTL) from natural quartz was found to possess merits on the assessment of accidental radiation dose in the previous paper (Fujita and Hashimoto, 2007). The VTL has three advantages over other luminescence measuring techniques: (1) the absence of natural dose accumulated over geological period, (2) the ability to retain a record of accident exposure with negligible fading over the time interval within some years until measurement and (3) the detection limit to determine accidental doses of tens of mGy.

In this study, two samples of natural quartz extracted from surface soils have been used for the optimization of the VTL measurement conditions and for the validation of the retrospective dosimetry technique developed by the previous paper (Fujita and Hashimoto, 2007). The samples were irradiated at gamma field which would be similar to a real environment in an emergency situation. In advance, TL spectrometric system using CCD camera had been developed to measure TL spectrum.

II. Experimental

1. Sample preparation

Two kinds of surface soils (~5 cm) were collected from different points around tokai, Ibaraki, Japan. Each of the samples was packed in plastic container in the laboratory

*Corresponding Author, Tel No: +81-29-282-111, E-mail: fujita.hiroki@jaea.go.jp

under red light conditions without special treatment, separately. The containers were covered by aluminum foil to avoid bleaching effect of sun light on the samples after artificial irradiation, respectively. The samples were then exposed to γ-ray for 8 hours in the gamma field of the Institution of Radiation Breeding (http://www.irb.affrc.go.jp/index-E.html) after buried in underground of the depth between 0 and 5 cm at two points of 10 m and 20 m from the source. As a result, four packed samples were simultaneously set in the gamma field. The samples set at 10 m were deposited with the pocket dosimeter (Aloka, AMD-112) which was packed with the same way as surface soils. The dosimeter provides dose rate linearity of ±10 % (~0.1 Sv h^{-1}) together with an excellent energy dependent response of ±30 % between 50 keV and 3.0 MeV.

The radiation in the gamma field is obtained from a point source with 88.8 TBq ^{60}Co (January, 2005) that is built into the irradiation device kept on irradiation tower. The tower is placed in the center of a circular field of 100 m radius. The irradiation is basically repeated every day for eight hours from 0:00 p. m. to 8:00 p. m.: therefore, the dose rate measured in Gy day^{-1} at 10 m distant from the source is approximately 2 Gy day^{-1} (January, 2007). The field is surrounded by a shielding dike of 8 m in height.

After the irradiation, the samples were withdrawn from the field. The samples were prepared under faint red light not to affect the accumulated signals in quartz. The quartz grains were extracted from the soil samples, using the procedure described in the previous paper (Fujita and Hashimoto, 2007). Each sample was not annealed at 450 ºC to hold TL signals accumulated by both natural and artificial irradiations in order to simulate real accident situation.

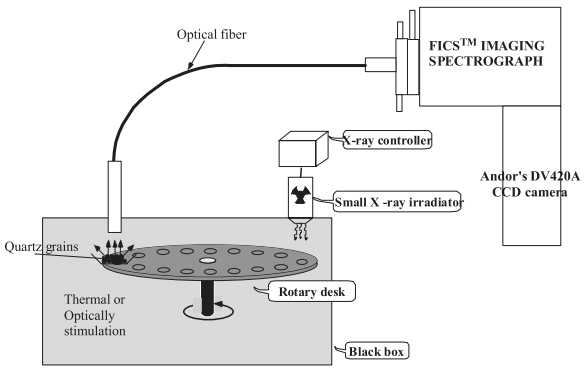

Fig. 1 Schematic diagram showing the luminescence spectrometry system.

2. TL measurements

A TL spectrometry has been applied for the quartz grain samples by the on-line CCD camera (Andor Technology, DV 420A-OE) and spectroscope (Oriel instruments, FICS 77441) combined with an automated TL / OSL-reader system (Japan Radiation Engineering Company, JREC) with a small X-ray irradiator (Varian, VF-50J tube) as demonstrated in **Fig. 1**. It is modified to measure spectra in the wavelength range of 200-650 nm, in order to avoid the black body radiation from sample and heater. The wavelength calibration of spectroscopic instrument was conducted by mercury lamp. Measurements are fully automated, allowing up to 16 samples to be measured in any one experimental run. The system was controlled at a linear heating rate of 1 °C sec^{-1}.

VTL glowcurves were measured by the automated TL / OSL-reader system installed with a small X-ray irradiator (Varian, VF-50J tube), which has been developed for a single aliquot regeneration (SAR) method (Hashimoto et al., 2002; Nakagawa et al., 2003). For the detection of VTL, a violet (Schott, UG-11) and an infrared cut (Kenko, IRC-65L) filters were installed between the photomultiplier tube (PMT, Hamamatsu, R585S) and the sample heating site as described in the previous paper (Fujita and Hashimoto, 2007). All samples examined were about 5 mg in weight.

The irradiation dose rate of X-ray occurred by the system was calibrated using TL intensity from quartz irradiated by standard 137Cs source at the Radioisotopes Center in Niigata University.

III. Results and Discussion

1. TL spectrometry using CCD camera

Fig. 2 shows a typical TL spectrum in contour expression from natural quartz grains irradiated to about 2 kGy of X-ray. The red TL (RTL) peak ranging from 550-650 nm in wavelength and around 330 °C could be recognized in the contour map. However, the quartz sample was known to emit violet TL (VTL, 350-450nm) described in the previous paper (Fujita and Hashimoto, 2007), but could not be recognized in **Fig. 2**. Thus, the TL intensity integrated in the region of 50-400 °C was measured. As a result, two broad TL emission bands are recognized at 400 nm (violet) and 630 nm (red), although **Fig. 2** shows the RTL emission alone in the whole region of temperatures. This observation accords completely with the previous result (Fujita and

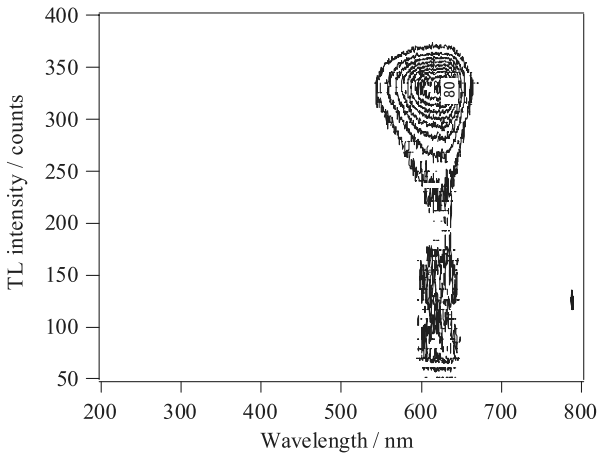

Fig. 2 TL emission spectrum for quartz extracted from surface soil around tokai. The sample temperature was controlled to be heated at a linear heating rate of 1°C sec^{-1}.

Hashimoto, 2007). In the reliable luminescence spectrometry, wavelength shift with the repeat of measurement cycles is a very important factor. TL wavelength variations were checked by repeating TL spectrum measurements for same quartz grain sample. The wavelength of maximum intensity was determined to be at 630±1.9 nm for 620-630 nm in RTL region (Hashimoto et al, 1993; Scholefield and Prescott, 1999) and indicates good reproducibility. Consequently, it was confirmed that this system gives good reproducibility in TL spectrometry.

2. VTL measurements

Soil samples were exposed at the positions of 10 m and 20 m from the gamma-ray source in the field, additionally pocket dosimeter was buried in the 10 m point together. Thereafter, the samples remained stable for a period of at least one week because of extracting procedure of quartz grains.

In the reliable TL measurements, a SAR method is necessary. In the SAR-method, all procedures should be done using the same aliquot. The SAR-method is consisting of repeated cycles of two following steps; (1) TL measurement to construct glowcurve and (2) artificial irradiations of known doses. Then, TL-values integrated in the fixed range were plotted against the additive doses to obtain a dose response curve. The accumulated dose is a dose estimated by inserting the integrated luminescence intensity from the glowcurve in the sample irradiated in the field into the dose response curve. Originally, its usefulness has been limited in some TL applications due to the heat-induced sensitivity changes (the predose effect) in the dosimeter material. However, quartz grain samples extracted from surface soils collected around tokai appeared no sensitivity variation of VTL peaks higher than 200 °C as described in the previous paper (Fujita and Hashimoto, 2007). Therefore, it may be suitable for determining equivalent dose (Deq) using higher temperature VTL peaks.

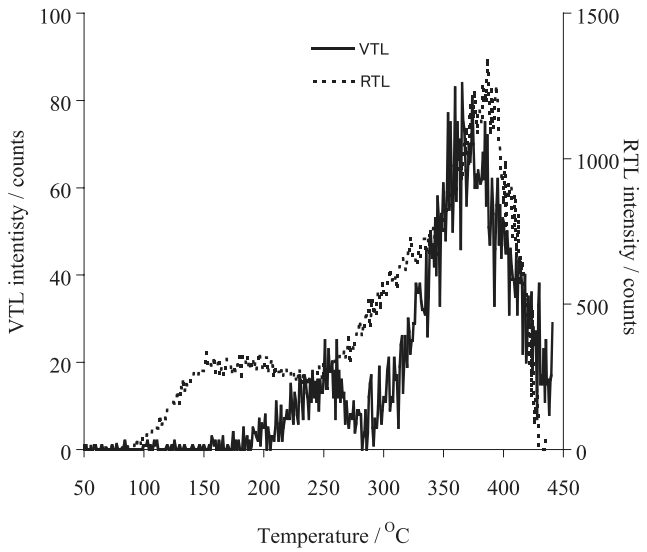

Fig. 3 VTL and RTL glowcurves of quartz grains from the surface soils collected around tokai.

As shown in **Fig. 3**, VTL glowcurve from as-receiveed quartz grains without artificial irradiation had no peaks lower than 200 °C, compared with RTL one. The result also suggests the advantage of VTL-retrospective dosimetry because the VTL peaks as the retsospective dosimetry <250 °C could exclude the interference from a naturally accumulated dose as described in the previous paper (Fujita and Hashimoto, 2007).

A dose reponse curve was constructed by applying 1-5 Gy X-ray doses as shown in **Fig. 4**. Several VTL peaks at 80-250 °C were observed during heating, after X-ray irradiation. The heating rate was 1 °C sec^{-1}. The curves obtained by all VTL measurements were not shown supralinearity shape.

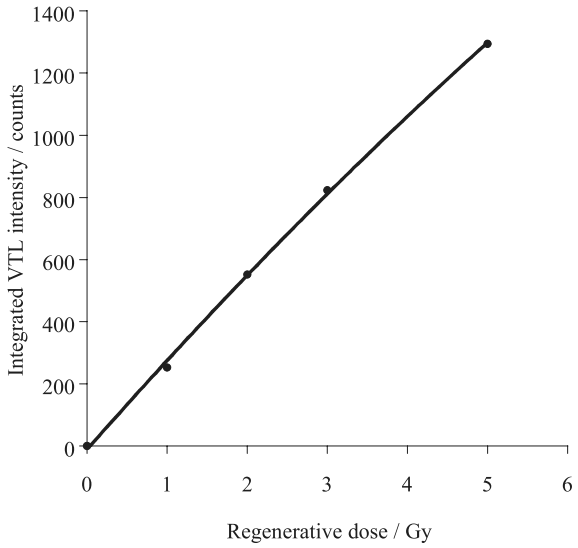

Fig. 4 VTL response curve as a function of regenerative doses.

An artificial irradiated dose was deduced for each aliquot by fitting the luminescence value obtained during the first thermal stimulation cycle to a least-squares linear regression calculated from the regeneration growth curves. **Table 1** presents the resulting averages of each VTL peak from each sample. The experimental errors of equivalent doses are standard deviation derived from three to five aliquot analyses. Absorbed doses (Ds) of the samples irradiated at 10 m were 0.8-0.9 Gy, using VTL peaks at 200 °C. These results were in good agreement with a dose obtained from the pocket dosimeter, which yielded a D=0.79 Gy. Ds of the samples irradiated at 20 m were 0.2 Gy, using the VTL peaks at same temperature of 10 m. These results were also in good agreement with a dose calculated from the dose at 10 m, which yielded a D=0.20 Gy. In the case of calculations using 250 °C VTL peaks, all of the D was overestimated. The reason may be that the obtained D include natural accumulated dose not to erase natural components prior to VTL glowcurve measurements.

The doses evaluated from quartz grains were similar values in various storage durations of one week to three months between irradiation and measurement cycles, as predicted in the previous paper (Fujita and Hashimoto, 2007)

Table 1 Comparison of accumulated doses from measurements of VTL at peaks of 200 °C of quartz extracts.

Quartz grain sample	VTL / Gy (10 m)	VTL / Gy (20 m)
	200 °C peak	200 °C peak
Tokai	0.79±0.065	0.16±0.029
Hitachinaka	0.86±0.16	0.19±0.036
Pocket dosimeter	0.79	(0.20)

IV. Conclusions

Our results indicate that dosimetry based on the technique of VTL measurement can apply for the retrospective one. In an emergency situation, it is feasible to detect radiation doses on the order of 1 Gy if the VTL dosimetry is performed within one week to three months following the event. Further work is necessary to determine whether longer delays would also allow accurate excess dose detection, although the mean life times at VTL traps at both of 200 and 250°C were long enough to obtain dose for few years as shown in the previous paper (Fujita and Hashimoto, 2007).

Acknowledgements

Author wishes to expresses his sincere thanks to Dr. Nishimura, National Institute of Agrobiological Sciences for his help in this work. He would like to express his gratitude to Professors emeritus Tetsuo Hashimoto, Niigata University, Japan, for valuable discussion.

References

1) Aitken, M. J. Thermoluminescence dating.Academic Press Inc., London. (1985).
2) Aitken, M. J. Optical dating. Quat. Sci. Rev. 11, 127-131 (1992).
3) Aitken, M. J. An introduction to optical dating. Oxford Universtiy Press, Oxford. (1998).
4) Bailiff, I. K. The use of ceramics for retrospective dosimetry in the Chernobyl exclusion zone. Radiat. Meas. 24, 507-511 (1995).
5) Bailiff, I. K., Stepanenko, V. F., Göksu, H. Y., Jungner, H., Balmukanov, S. B., Balmukanov, T. S., Khamidova, L. G., Kisilev, V. I., Kolyadao, I. B., Kolizshenkov, T. V.
6) and Shoikhet, Y. N. The application of retrospective luminescence dosimetry in areas affected by fallout from the Semipalatinsk Nuclear Test Site: am evaluation of potential. Health Phys. 87, 625-641 (2004).
7) Bougrov, N. G., Göksu, H. Y.,Haskell, E. H., Degteva, M. O., Meckbach, R. and Jacob, P. Issues in the reconstruction of the environmental doses on the basis of thermoluminescence measurements in the Techa riversides. Health Phys. 75, 574-583 (1998).
8) Fleming, S. J. Thermoluminescence dating: Refinement of the quartz inclusion method. Archaeometry 12, 133-147 (1970).
9) Fleming, S. J. Thermoluminescence authenticity testing of ancient ceramics using radiation-sensitivity changes in quartz. Naturwissenschaften 59,145-151 (1972).
10) Fujita, H. and Hashimoto, T. Usability of VTL from natural quartz grains for retrospective dosimetry. Radiat. Prot. Dosim. 123, 143-147 (2007).
11) Hashimoto, T., Kojima, M., Shirai, N. and Ichino, M. Activation energies from blue- and red-thermoluminescence (TL) of quartz grains and mean lives of trapped electrons related to natural red-TL. Nucl. Tracks Radiat. Meas. 21, 217-223 (1993).
12) Hashimoto, T., Nakagawa, T., Hong, D. G. and Takano, M. An automated system for both red/blue thermoluminescence and optically stimulated luminescence measurements. J. Nucl. Sci. Technol. 39, 108-109 (2002).
13) Haskell, E. H., Bailiff, I. K., Kenner, G. H., Kaipa, P. L. Wrenn, M. E. Thermoluminescence measurements of gamma-ray doses attributable to fallout from Nevada test site using bricks as natural dosimeters. Health Phys. 66, 380-991 (1994).
14) Kaul, I. K., Bhattacharya, P. K. and Tolpadi, S. Age determination by study of the thermoluminescence of smoky quartz. Journal Geophys. Res. 71 (4), 1275-1282 (1966).
15) Murray, A. S. and Wintle, A. G. Retrospective dose assessment: the measurement of the dose in quartz in dating and accidental dosimetry. Radiat. Prot. Dosim. 101, 301-308 (2002).
16) Nakagawa, T., Usuda, H. and Hashimoto, T. Optically stimulated luminescence (OSL) and thermoluminescence (TL) measurements on red TL (RTL) quartz samples using a new automated OSL/TL measuring system. J. Radioanal. Nucl. Chem. 255(2), 355-358 (2003).
17) Scholefield, R. B. and Prescott, J. R. The red thermoluminescence of quartz: 3-D spectral measurements. Radiat. Meas. **30**, 83-95 (1999).
18) Wintle, A. G. Luminescence dating: laboratory procedures and protocols. Radiat. Meas. **27**, 385-393 (1997).

Journal of NUCLEAR SCIENCE and TECHNOLOGY, Supplement 5, p. 151–154 (June 2008)

Application of Estimating Effective Dose from External Radiation using Two Dosimeters during Maintenance Periods at KNPPS

Hee Geun Kim* and Tae Young Kong

Korea Electric Power Research Institute, Daejeon, Korea

The application of a two-dosimeter and its algorithm and a test of its use in an inhomogeneous high radiation field are described. The goal was to develop an improved method for estimating the effective dose during maintenance periods at Korean nuclear power plants (NPPs). The use of the method in domestic and international NPPs including USA, Canada and Japan was also investigated. The algorithms used by the Canadian Ontario Power Generation (OPG) and American ANSI HPS N13.41, Lakshmanan, NCRP, EPRI and Texas A&M University were extensively analyzed as two-dosimeter algorithms. The possibility of their application to NPPs was evaluated using data for each algorithm from two-dosimeter results for an inhomogeneous high radiation field during maintenance periods at Korean NPPs.

KEYWORDS: two additional dosimeters, multidosimetry, two-dosimeter algorithm, effective dose, inhomogeneous high radiation field

I. Introduction

Radiation workers can be exposed to a high-level radiation during the maintenance of reactor coolant pumps, pressurizers, and water chambers of steam generators for overhaul of a NPP in spite of the short working hours since, dose rate gradients are high in these areas. In general, since the radiation dose rate is high and the radiation field is inhomogeneous, if radiation workers use only one thermoluminescent dosimeter (TLD) on their chest, the amount of radiation exposure cannot be monitored exactly. Therefore, additional dosimeters are provided to workers for radiation work in an inhomogeneous radiation field in NPPs. Two dosimeters are usually provided and one is located on the chest and the other is on the head. In this case, the radiation dose to the whole body for radiation workers at NPPs is determined by the high deep dose between two radiation doses from these dosimeters, as a conservative method for evaluating the amount of radiation exposure.

The intent of this paper is to develop a solution of the overestimation and underestimation of the effective dose in an inhomogeneous radiation field. The application of a two-dosimeter algorithm is described, for estimating the exact deep dose to radiation workers in an inhomogeneous radiation field. In addition, situations in which additional dosimeters should be provided, a review of preceding studies on two-dosimeter algorithms, the technical background and results of adopting these algorithms for application at Korean NPPs, and the test results of their use at Korean NPPs are described in detail. In particular, three additional dosimeters are provided to radiation workers who wear them at the head, chest, and back during maintenance periods, and the measured values are analyzed for the purpose of applying an algorithm.

*Corresponding Author, Tel. +82-42-865-5551, Fax. +82-42-865-5504, E-Mail; hkkim@kepri.re.kr

II. Current Issues of Using a Two-dosimeter

In Korean NPPs, additional dosimeters are provided to workers depending on the type of radiation work carried out, for calculation of a deep dose; however, several problems are involved. First, the provision for the conditions of use of additional dosimeters is slightly different. Although Korean NPPs apply the guidelines of the Institute of Nuclear Power Operations (INPO) for providing additional dosimeters, the guidelines for their use are not clear. In addition, the method used to implement their use, including the number of additional dosimeters to be used is slightly different among Korean NPPs. In general, additional dosimeters (two-dosimeters) are placed on the chest and head with regard to the only top and bottom directions of the incident radiation for water chambers of steam generators. If radiation sources exist in front and back of the radiation worker, it is difficult to monitor the exact amount of radiation exposure to workers. The adoption of a maximum deep dose as the effective dose without respect to the average value of radiation doses considering the weighting factors between radiation doses from dosimeters is also conservative, thus creating an overestimation problem.

III. Two-dosimeter Algorithm

The two-dosimeter algorithms, developed thus far, are the algorithms of the Canadian OPG, ANSI, NCRP, EPRI & NRC, and Texas A&M University. In the OPG (formerly

Ontario Hydro) radiation dosimetry program, the radiation protection guidelines of OPG, conditions for using two-dosimeters, application of weighting factors for TLD read-outs and algorithms, and the method for estimating the effective dose are clearly described. According to this program, an additional dosimeter except the regular one on the chest is provided to radiation workers when specific parts of the body are exposed to high radiation and the radiation worker should wear this dosimeter on the head to estimate the amount of radiation exposure. In Canada, the guideline for the use of two-dosimeters applied the ICRP-26 before the legislation of ICRP-60; that is, the two-dosimeter algorithm applied the weighting factors of ICRP-26 before 1989. In this guideline, factors of 0.4 and 0.6 are used for the each dose from the head and chest to calculate the effective dose. On the other hand, the equation for calculating radiation exposure is altered in Eq.1 if the weighting factors of ICRP-60 are used[1].

$$H_E(estimate) = 0.11H_P(10)_{head} + 0.89H_P(10)_{torso} \quad (1)$$

where H_E is the effective dose and H_P is the deep dose.

The guideline for two-dosimeters, developed by the ANSI in 1997, is described in HPS N13.41[2]. This guideline provides that radiation workers wear a dosimeter on their chest and additional multiple dosimeters in the body area where exposure to high radiation would be expected. In this guideline, the compartment factors, calculated by application of the tissue weighting factors are defined for applying the two-dosimeter algorithm. The effective dose for a radiation worker is calculated by the sum of the products of multiple dosimeters read-outs. The equation for the calculation of the effective dose is written by Eq. 2.

$$H_E = \sum_C W_C H_{P,C}(10) \quad (2)$$

where $H_{p,c}(10)$ is the dosimeter read-out for each area of the body and the highest read-out from the adjacent area is used for unmeasured areas of the body.

The NCRP-122 report of NCRP in 1995 (Use of personal monitors to estimate effective dose equivalent and effective dose to workers for external exposure to a low-LET radiation) provided that the effective dose is calculated by giving weight to the dosimeter read-outs. In this report, a PMMA phantom was used and the calculated conversion factor, published in 1987 by the ICRP, for a photon with energies of 30 keV ~ 1 MeV in various radiation fields was utilized as the conversion factor for $H_E/H_p(10)$. In addition, this report recommends giving weight to $H_p(10)$, which is the read-out of two dosimeters on the chest and back, for the calculation of effective dose if the energy of incident photons is unknown. These two methods are described in Eq. 3 and 4[3].

$$H_E(estimate) = 0.70H_P(10)_{front} + 0.30H(10)_{back} \quad (3)$$

In Eq. 3, a 70% weight is given to the dose from the chest (front) and a 30% weight is given to the dose from the back for calculating the effective dose; $(H_E(estimate)-E)/E$ is minimized to close to zero.

$$H_E(estimate) = 0.55H_P(10)_{front} + 0.50H(10)_{back} \quad (4)$$

Eq. 4 describes the method NCRP(55/50) in which a 55% weight is given to the dose from the chest (front) and a 50% weight is given to the dose from the back to calculate the effective dose. NCRP uses this method to avoid a 10% overestimation of the effective dose.

NRC Regulatory Issue Summary 2004-01 published in 2004 by the US NRC provided regulatory guidelines for the calculation of the effective dose equivalent from external radiation exposure using two-dosimeters[4]. This report suggested giving proper weight to the two-dosimeter read-outs to calculate the effective dose and this method originated from the research results of EPRI. The NRC approves only the weighting method among the mean and weighting methods of two-dosimeter algorithm. The NRC method for the calculation of effective dose equivalent from external sources (EDEex) is written by Eq. 5[4].

$$EDE_{ex} = \frac{1}{2}(Hi + Mean) = \frac{3}{4}Hi + \frac{1}{4}Lo \quad (5)$$

where Hi is the highest value and Lo is the lowest value from the dosimeter read-outs on the chest and back. This equation is similar to Eq. 6 derived from Xu's algorithm, published in 1995[5].

$$H_E(estimate) = \frac{[H_p(10)_{\max.of.fornt/back} + H_p(10)_{avg.of.front/back}]}{2} \quad (6)$$

Xu performed experiments using three photons with energies of 80 keV, 300 keV, and 1 MeV in various radiation fields. In particular, the effective dose was calculated from point sources in several locations away from the human body.

Texas A&M University published several papers concerning the calculation of an effective dose by giving weight to the dosimeter read-outs for two-dosimeter use in inhomogeneous radiation fields. Eq. 7 shows Lakshmanan's method, in which the sum of $H_p(10)$ from two personal dosimeters is divided by 1.5[6].

$$H_E(estimate) = \frac{[H_p(10)_{front} + H_p(10)_{back}]}{1.5} \quad (7)$$

In this equation, the effective dose was calculated from the various radiation fields and the energy ranges of the photons were from 30 keV to 1.25 MeV. The calculated effective dose from a hexagonal phantom with the inside filled water is similar to $H_p(10)$ from the front dosimeter.

Kim's algorithm developed in 1998 is expressed as follows, Eq. 8 [7].

$$H_E(estimate) = h(H_E)[0.58H_p(10)_{front} + 0.42H_p(10)_{back}] \quad (8)$$

where $h(H_E) = \dfrac{0.9H_E(AP)}{0.58H_{front}(AP) + 0.42H_{back}(AP)}$

IV. Selection Experiments on the Optimal Two-dosimeter Algorithm

Several two-dosimeter algorithms were compared and analyzed from various points of view for possible application to Korean NPPs. The analyzed algorithms were seven kinds of two-dosimeter algorithms, the algorithm of the Canadian Ontario Power Generation (OPG) used at the Pickering NPPs, the algorithm of American National Standards Institute (ANSI), the two algorithms of the National Council on Radiation Protection (NCRP (70/30) and NCRP (55/50)), the algorithm of Electric Power Research Institute (EPRI (Xu)) approved by the Nuclear Regulatory Commission (NRC), and the two algorithms of Texas A&M University (Lakshmanan and Kim)[1~5].

Three additional dosimeters (TLD) and a supplementary dosimeter (ADR) were provided to radiation workers who wore a TLD at the head, chest, and back simultaneously to analyze the two-dosimeter application to Korean NPPs during a maintenance period at the Yonggwang NPPs No. 2. The algorithms of the OPG and ANSI need TLD read-outs on the head and chest, and the other algorithms require TLD read-outs on the chest and back. The experiments were conducted at the Yonggwang NPPs No. 2 in 2004 for the installation and removal of a nozzle-dam of a steam generator, a penetration test (PT) of the reactor head, and replacing the heater of the pressurizer. Additional experiments which were similar to the above experiments at a Yonggwang NPPs No. 2 were also performed at the Ulchin NPPs No. 2 during a maintenance period in 2005.

A comparison of the estimated effective dose, which showed the highest TLD read-out of two-dosimeters at Younggwang NPPs No. 2, was conducted. As a result, the effective dose calculated by the above 7 two-dosimeter algorithms was lower than the highest TLD read-out, by approximately 10~50%. The effective dose from the experiments at Ulchin NPPs No. 2 was also calculated by the same method used at the Yonggwang NPP and it was found that the comparison results of Ulchin NPPs No. 2 were similar to those of Yonggwang NPPs No. 2.

The effective doses were calculated using each algorithm to analyze the differences among the 7 two-dosimeter algorithms. The results showed that, there were no remarkable differences among the calculated effective doses, except for Lakshmanan's algorithm and no big differences in effective doses according to the position of two-dosimeters worn on the head and chest or the chest and back. These results are illustrated in **Fig. 1~2**. In both figures, the horizontal and longitudinal axises represent the number of TLD wearers and their calculated effective dose equivalent, respectively.

This paper recommends the NCRP algorithm presented by the NCRP-122 report in 1995 as an optimal two-dosimeter algorithm in consideration of the above points. In particular, since most developed algorithms show no big differences in results for practical inhomogeneous radiation fields, it was concluded that the application of the NCRP algorithm to Korean NPPs was acceptable, due to the NCRP's solid technical background. The important issue was that the NCRP suggested two two-dosimeter algorithms (NCRP (70/30) and NCRP (55/50)); however, NCRP recommended only the NCRP (55/50) algorithm for use. The final conclusion of the NCRP was that, if the algorithm of NCRP (55/50) was used as a two-dosimeter algorithm, the possibility of underestimating the effective dose would be reduced[3].

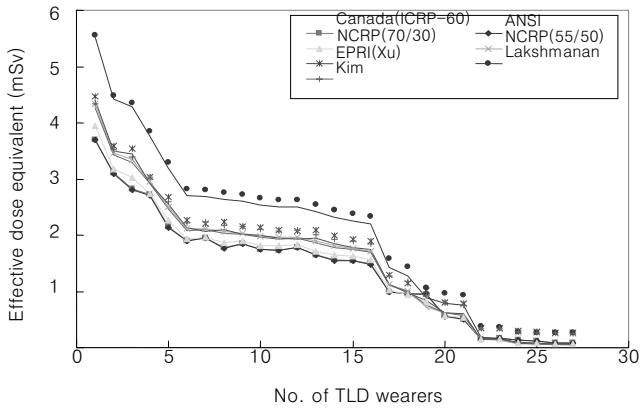

Fig. 1 Application of two-dosimeter algorithm for the installation of steam generator nozzle dam at Yonggwang NPPs No. 2

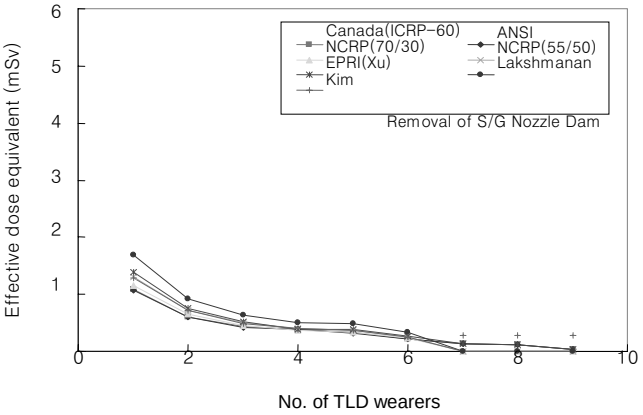

Fig. 2 Application of two-dosimeter algorithm for the removal of steam generator nozzle dam at Yonggwang NPPs No. 2

V. Conclusion

The Korean NPP's procedures for the provision of two-dosimeters follow the INPO guidelines for radiological protection at nuclear power stations; however, each NPP does not have a standardized set of regulations and the INPO guidelines are applied conservatively. Thus, it is necessary to benchmark the INPO guidelines and foreign procedures of two-dosimeters and to standardize the procedures at Korean NPPs. The number of radiation workers who are exposed to over 2 mSv of radiations during a single work period was investigated and reached approximately 20~30% of the total radiation workers. Since, in Korean nuclear regulations, rigid radiation management is performed for over 2 mSv of radiation exposure, providing additional dosimeters to radiation workers who are expected to be exposed to over 2 mSv of radiations is reasonable. In addition, it is concluded that the optimal number of additional dosimeters provided is two.

The application of 7 two-dosimeter algorithms developed by nuclear regulatory agencies and facilities to Korean NPPs was investigated, to analyze anticipated problems that may arise. Three additional dosimeters (TLD) were provided to radiation workers who wear a TLD at head, chest, and back simultaneously for high radiation work to analyze the two-dosimeter application to Korean NPPs during a maintenance period at the Yonggwang NPPs No. 2 and Ulchin NPPs No. 2. After the radiation work, the 7 two-dosimeter algorithms were applied to two-dosimeter read-outs and the effective doses were calculated; as a result, the calculated effective doses were very similar to one another, except for Lakshmanan's algorithm. Thus, it was concluded that no matter what algorithms are applied to Korean NPPs, the procedure used for estimating radiation exposure will be improved.

In particular, the preceding research showed that wearing two-dosimeters at the chest and back rather than at the chest and head reduces the overestimation or underestimation of the effective dose. In addition, since the NRC or NCRP recommends that a radiation worker wear two-dosimeters at the head and back, it is reasonable that Korean NPPs follow the international standard and the trend toward the use of two-dosimeters. After interview with the radiation workers, it was also found that the workers felt themselves more convenient when they wore two-dosimeters at chest and back rather than at the chest and head. Thus, it was concluded that wearing two-dosimeters at the chest and back is suitable for a radiation worker, because of the above reasons. Finally, the NCRP (55/50) algorithm was regarded as optimal two-dosimeter algorithm in an inhomogeneous radiation field due to no big specificity, no big variation depending the location of the radiation source, and position where two-dosimeters are worn on the chest and back, which reduced the risk of underestimating the effective dose.

Acknowledgement

This research was carried out with the financial support of Korea Hydro & Nuclear Power Corporation.

References

1) Personal Communication with Arif Khan and Dave Whillans of OPG, Summary of Changes to the Method of Assigning Dose from Multiple TLD Badges, (2002).
2) American National Standards Institute (ANSI), An American National Standard Criteria for Performing Multiple Dosimetry, Report No. HPS N13.41, (1997).
3) National Council on Radiation Protection and Measurements (NCRP). Use of Personal Monitors to Estimate Effective Dose Equivalent and Dose to Workers for External Exposure to Low-LET Radiation, NCRP Report No.122, Bethesda, (1995).
4) United States Nuclear Regulatory Commission, NRC Regulatory NRC Regulatory Issue Summary 2004-01, Method for Estimating Effective Dose Equivalent from External Radiation Sources Using Two Dosimeters, Report No. RIS 2004-01, (2004).
5) Xu, X. G., Reece, W. D., and Poston, J. W., "A Study of the Angular Dependence Problem in Effective Dose Equivalent Assessment," Health Physics, 68(2), 214-224, (1995).
6) Lakshmanan, A. R., Kher, R. K., Supe, S. J., "Estimation of Effective Dose Equivalent Using Individual Dosimeters," Radat. Prot. Dosim. 35(4), 247-252, (1991).
7) Kim, C. H., Reece, W. D., and Poston, J. W., "Development of a Two-dosimeter Algorithm for Better Estimation of Effective Dose Equivalent and Effective Dose," Radiation Protection Dosimetry, 81(2), 101-112, (1999).

Journal of NUCLEAR SCIENCE and TECHNOLOGY, Supplement 5, p. 155–158 (June 2008)

Improvement of Internal Dose Measurement Program Using a Whole Body Counter at Nuclear Power Plants

Tae Young Kong* and Hee Geun Kim

Korea Electric Power Research Institute, Daejeon, Korea

A whole body counter (WBC) is used in nuclear power plants (NPPs) to identify and measure the radioactivity in the bodies of human beings. In this study, several experiments were conducted to improve the internal dose measurement procedures using a WBC in NPPs. First, back and forth countings using a WBC were carried out to set up the discrimination program between internal and external radioactive contamination in NPPs. Second, experiments on selecting an optimal geometry of the WBC and locating the contaminated area of radionuclides were performed.

KEY WORDS: whole body counter, internal and external contamination, geometry

I. Introduction

A whole body counter (WBC) is used in nuclear power plants (NPPs) to identify and measure the radioactivity in the bodies of human beings. In most NPPs, several whole body counters are used to monitor internal radioactive contamination of workers. However, it has been found that external contamination is occasionally estimated as internal radioactive contamination in whole body counting. The amount of detected radioactivity can be much higher than that of the actual radioactivity owing to this misclassified contamination, since radioisotopes attached to the skin come into close proximity to the detectors of the WBC. Finally, this leads to not only misjudgment of external contamination as internal contamination, but also excessively conservative estimation of radioactive contamination.

A WBC provides four geometries, which compensate the detector's efficiency depending on the location where radionuclides are deposited in the body, to measure the exact radioactivity inside the worker's body. In most NPPs, efficiency calibrations of the WBC for all geometries, i.e., the whole body, thyroid, lung, and gastrointestine, are conducted every six months. These calibration results are then reported to check the performance and mechanical conditions of the WBC. However, only the whole body geometry is used to detect the internal radioactivity during whole body counting, and the most conservative radioactivity is finally recorded. This is attributed to the absence of information and standard processes to approximately choose and use the geometry of the WBC.

In this study, several experiments were carried out to set up a discrimination program between internal and external radioactive contamination using a humanoid phantom and a WBC. In addition, experiments to select an optimal WBC geometry and to locate the contaminated areas of radionuclides were conducted so that detected radioactivities could be analyzed depending on geometries. Finally, an appropriate procedure for selecting the geometry of a WBC is proposed.

II. Materials

Experiments were conducted using a WBC, phantoms, and radiation sources. The WBC utilized for the experiments is Canberra's vertical linear Fastscan (Model 2250), which is used for in vivo measurements of radionuclides with energies from 300 keV to 1.8 MeV at most NPPs. This WBC system consists of two large sodium iodide detectors, which typically provide an a priori lower limit of detection (LLD) of about 150 Bq for ^{60}Co with a count time of one minute for a normal person containing ^{40}K.

Two kinds of phantoms were used, a humanoid phantom of a typical Korean male, developed by the Radiation Health Research Institute (RHRI) for radiation protection purposes, and a Canberra's Transfer phantom, developed for the calibration of a WBC. The humanoid phantom satisfies the reference Korean physical model (Height: 170.9cm, Weight: 68.1kg, etc.) and is sliced into 2cm sections to facilitate dose mapping[1]. **Fig. 1** shows the front, back, and flank side of the humanoid phantom attached with tags numbered 1 to 14 for the front, 15 to 28 for the backside, and F0 to F3 for the flank in order to position the radioactive source. The Canberra Transfer phantom was designed for efficiency calibration with the Canberra linear geometry of a WBC. This phantom can simulate four geometries: the whole body, thyroid, lung, and gastrointestine (GI), and thus can provide more accurate and reliable measurement results using compensation for the detector's efficiency depending on the deposited area of radionuclides in the body (**Fig. 2**). In addition, these two phantoms satisfy the performance criteria for in vivo measurements of ANSI N13.30, which describes the phantom standards to obtain validated internal exposure activity.

*Corresponding Author, Tel. +82-42-865-5552, Fax. +82-42-865-5504, E-Mail: eagertae@kepri.re.kr

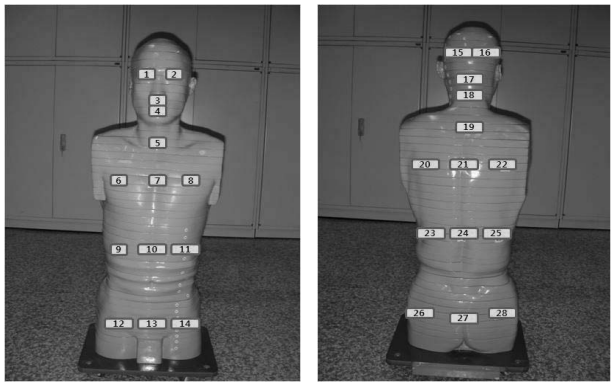

Fig. 1 Humanoid of typical Korean male

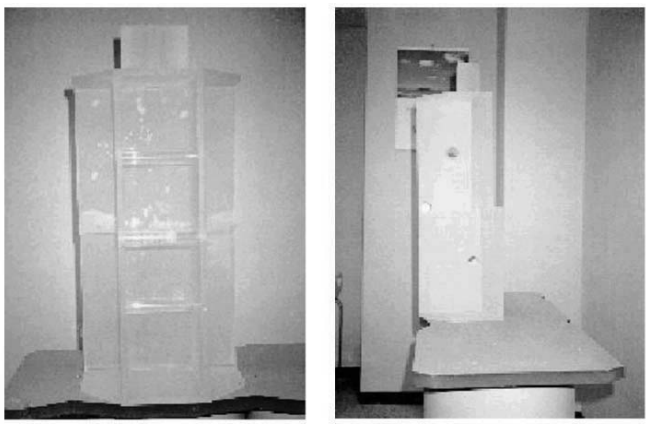

Fig. 2 Canberra Transfer Phantom

In the experiments, a mixed gamma source of ^{137}Cs and ^{60}Co, used in the WBC daily quality assurance assessment, was attached to the humanoid phantom surface. In addition, respective point sources of ^{137}Cs and ^{60}Co, manufactured by the Korea Research Institute of Standards and Science, were inserted into the humanoid phantom. These two radionuclide sources were used for the experiments because they are the most important and common internal dose contributors for pressurized water reactors (PWR). For the Canberra Transfer phantom, a liquid mixed gamma source was inserted into four efficiency calibration holes of the phantom.

III. Method

In this study, three detailed experiments were conducted to set up the discrimination program between the internal and external radioactive contamination and two detailed experiments were performed to suggest a program to select an optimal geometry of WBC. First, back and forth counting for the humanoid phantom using a WBC was conducted to differentiate external contamination from internal contamination. It is assumed that the difference in the detected radioactivities between the front and backside counts is higher than that of the internal contamination when the radionuclides are attached on the surface of the skin[2]. Since the body of the phantom shields the radiation from the source to the detectors and the distance from the source to the detectors are changed when the phantom is turned around in the WBC, the measurement ratios of back and forth counting would be high in the case of external contamination. On the contrary, in the case of internal contamination, there is no significant change in the distance between the body of the phantom and the detectors. Furthermore, the radiation shielding is not a consequential factor, since it is located inside the phantom; thus, the difference between the front and backside counts is not distinguishable.

In the WBC geometry experiment, two detailed experiments were performed. First, an experiment to select an optimal WBC geometry was carried out to compare the detected radioactivities depending on the WBC geometries[3]. The radionuclide source was placed on each of four efficiency calibration locations of the phantom, assuming that the radionuclide was deposited on whole body, thyroid, lung, and GI area. The radioactivity was then measured using four geometries for each deposition area. This makes it possible to compare and analyze the detected activities between the cases of using a suitable WBC geometry for deposition area and using an inappropriate WBC geometry for the deposition area. Second, an experiment to locate the contaminated area of radionuclides was conducted. Here, the locations of deposited nuclides were determined using count rates of the upper and lower detectors of the WBC. In this experiment, the radionuclide sources were placed between slices, from the top to bottom in sequence, of the humanoid phantom and countings were subsequently performed for each location. Since the count rates of the upper and lower detectors of the WBC would change with the locations of deposited nuclides, it is possible to approximately position the contaminated area of radionuclides using the detected count rates. The counting time was three minutes for all experiments.

IV. Experiments and Results

1. Experiments on external or internal contamination

a. External contamination

The first result was obtained from the experiment that the external radioactive contamination happens on either

front or backside of workers. The average ratios of front and backside counts were shown to be 8.8 for ^{60}Co and 14.2 for ^{137}Cs for the attachment of a mixture source to front side of the phantom. For a source positioned on the backside of the phantom, similar results were also obtained; the average ratios of the front and backside counts were 7.0 for ^{60}Co and 11.4 for ^{137}Cs (**Fig. 3**).

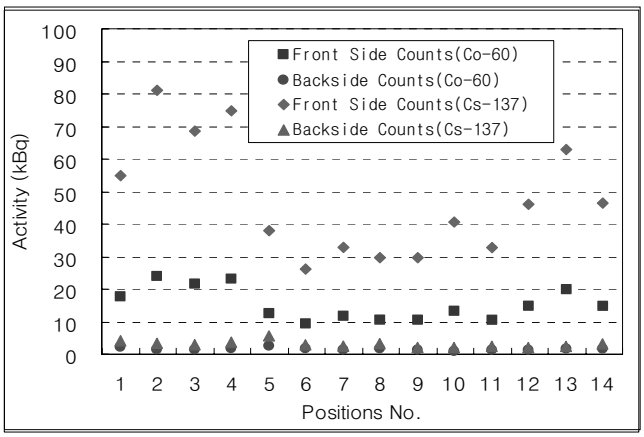

(a) Position of a source on front side of the phantom

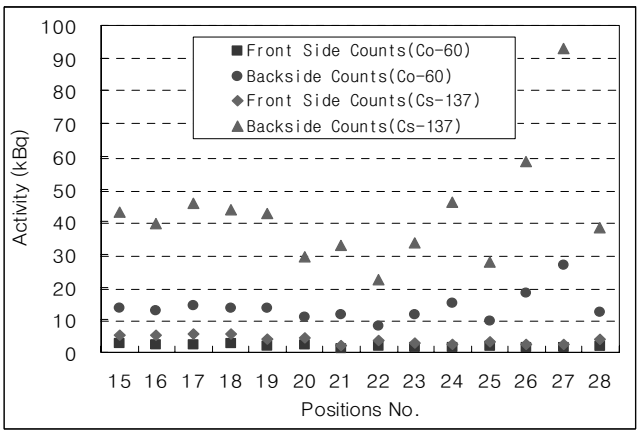

(b) Position of a source on backside of the phantom

Fig. 3 The detected activities of experiments on front or backside radioactive contamination using a whole body geometry

In **Fig. 3**, the front side counts of ^{137}Cs and ^{60}Co at Nos. 2~4 and 12~14 and backside counts at Nos. 26~27 were relatively high. Since the radiation sources were attached to the nose and jaws of the phantom, the source was relatively close to the detector. This resulted in high counts at Nos. 2~4. In addition, the phantom head is relatively thin compared to the thickness of the chest and abdomen. Thus, the attenuation of radioactivity was less at the head than at the chest and abdomen; this also resulted in high counts at Nos. 2~4. For the high counts at the bottom of the phantom (Nos. 12~14 and Nos. 26~27), it was determined that these positions were located at the right front of the lower detector in the WBC and the radiation from the source was detected to be relatively high.

The second result was obtained from the experiment in which the external radioactive contamination happens on both sides of worker flank. Two point sources of ^{60}Co and ^{137}Cs were attached to the humanoid phantom flank: ^{137}Cs for the left flank and ^{60}Co for the right flank. Back and forth counting was then carried out as the phantom was turned around in the WBC. There was no distinguishable difference between the back and forth counts. The average ratios of front and backside counts were shown to be 1.2 for both ^{60}Co and ^{137}Cs using all geometries.

The third one was intended for the case of simultaneous contamination of front and backside of workers. Four point sources of ^{60}Co and ^{137}Cs were attached to both the front and backside of the humanoid phantom surface. In the first case, two point sources of ^{60}Co and ^{137}Cs were fixed on the backside of the phantom (position No. 21) while two other point sources of ^{60}Co and ^{137}Cs were positioned on the front side of the phantom from locations No. 1 to No. 14 in sequence. For the second case, two point sources of ^{60}Co and ^{137}Cs were fixed on the front side of the phantom (position No. 7) while two other point sources of ^{60}Co and ^{137}Cs were positioned on the backside of the phantom from locations No. 15 to No. 28 in sequence. It was demonstrated that the average ratios of front and backside counts were 0.6 for ^{60}Co and 1.5 for ^{137}Cs for the first case and 0.9 for ^{60}Co and 2.0 for ^{137}Cs for the second case using all geometries.

b. Internal contamination

For the case of internal radioactive contamination, an experiment where radiation sources were located inside the phantom was conducted. Two point sources of ^{137}Cs and ^{60}Co were placed on the phantom slice and back and forth counting was subsequently carried out while the phantom was turned around in the WBC. As a result, it was found that the average ratios of the front and backside counts were 1.4 for ^{60}Co and 1.5 for ^{137}Cs; thus, there was not a significant difference between the front and backside counts.

c. Simultaneous contamination of both internal and external phantom body

Two sets of experiments were carried out: the first entails experiments of front and backside contamination, respectively. Four point sources of ^{137}Cs and ^{60}Co were used; two sources of ^{137}Cs and ^{60}Co were placed inside the phantom and the other two sources were attached to either the front or backside of the phantom surface. Back and forth counting was then carried out while the phantom was turned around in the WBC. The experimental results indicated that the average ratios of the front and backside counts were 2.7 for ^{60}Co and 2.0 for ^{137}Cs for the attachment of external sources to the front side of the phantom. For the positioning of sources on the backside of the phantom, the average ratios of the front and backside counts were 3.1 for ^{60}Co and 2.4 for ^{137}Cs. It, thus, was assumed that there was no big difference in the case of simultaneous contamination of both internal and external body.

The second experiment entails simultaneous contamination of both the internal body and flank region. Similar to previous experiments, two point sources of ^{137}Cs and ^{60}Co were located inside the phantom and two sources were attached to the phantom's flank. From the results, there was no conspicuous difference between the front and backside counts; the average ratios of the front and backside counts were 0.9 for ^{60}Co and 0.9 for ^{137}Cs, respectively.

2. Experiments on WBC geometry

a. Selecting an optimal WBC geometry

Experiments to select an optimal WBC geometry were conducted so that detected radioactivities could be analyzed depending on geometries. In the first experiment, point sources of ^{60}Co and ^{137}Cs were respectively placed on four locations, for efficiency calibration, inside the humanoid phantom, where it was assumed that the radionuclides were deposited on the whole body, thyroid, lung, and gastrointestine (GI) area. Countings were, then, performed under all geometries for each location. In order to compare the results depending on the phantom used in the experiments, the experiment used Canberra's Transfer phantom and a mixed gamma liquid source instead of the humanoid phantom and point sources were also assessed. These two experiments produced almost similar results regardless of the type of phantom and radiation source. Both sets of results indicated that the detected activity under a whole body geometry was higher than those of any other geometries. Thus, if only the whole body geometry is used for whole body counting without regard to the locations where radionuclides are deposited, the results will always be more conservative than the real internal radioactivity.

b. Positioning the contaminated area of radionuclides

An experiment to locate the area contaminated by radionuclides was conducted to find the locations of deposited nuclides using the count rates of the upper and lower detectors of the WBC. Point sources of ^{60}Co and ^{137}Cs were placed between slices of the humanoid phantom, from the top to bottom in sequence. Countings were then performed for each location. The experimental results demonstrated that the count rate of the upper and lower detectors of the WBC varied according to the locations of radiation sources. The count rate of the upper and lower detectors was approximately 90:10 at the top slice of the phantom (head). The count rate of the upper detector decreased and the count rate of the lower detector increased as the locations of radiation sources were moved downward. The count rate of the upper and lower detectors was about 85:15 for the thyroid, 75:25 for the lung, 60:40 for the whole body, and 35:65 for the gastrointestine, respectively. It is, therefore, possible to find the contaminated area of radionuclides using the count rate of the upper and lower detectors if radioactivity is detected during whole body counting.

V. Conclusions

In this study, several experiments involving back and forth counting using a WBC and a phantom were performed to set up a discrimination program between the internal and external radioactive contamination. From the results, it was found that the use of front and backside counts can be applied to distinguish between internal and external radioactive contamination. The ratio of detected radioactivities between front and backside counts was more than approximately a factor of 2 for external contamination. It is, however, necessary to carry out further steps to discriminate external contamination from internal contamination in the case of a ratio of less than factor 2. In this case, several re-counts at regular intervals should be performed within a fixed period of time. Finally, a method to determine whether internal contamination has occurred was employed, based on a comparison between re-counting results and the intake retention function graphs of corresponding nuclides. It is recommended that this counting method be used only radioactivity is detected in normal counting.

In addition, several experiments were carried out to analyze the detected radioactivities depending on the geometries of the WBC and to locate the area of radionuclide contamination. From the results of the experiments, it was found that the detected activity under a whole body geometry is always more conservative than that of any other geometries, and the count rate of the upper and lower detectors of the WBC varies according to the locations of deposited radiation sources. It is thus possible to select the optimal geometry for detected radionuclides to measure the exact internal radioactivity under consideration of physical and biological characteristics of radionuclides, including the deposited locations using the count rates of the upper and lower detectors of the WBC.

Acknowledgement

This research was carried out with the financial support of the Korea Hydro & Nuclear Power Corporation.

References

1) Kim, J. I., Choi, H., Lee, B. I., Lim, Y. K., Kim, C. S., Lee, J. K., and Lee, C. Physical Phantom of Typical Korean Male for Radiation Protection Purpose, Radiation Protection Dosimetry Advance Access, doi:10.1093/rpd/nci338, (2006).
2) Kong, T. Y., and Kim, H. G. The Establishment of Geometry and General Outlines of Operation for Whole Body Counter, Korea Electric Power Research Institute, TM.I05NJ14.2006. 73, pp. 28-32, (2006).
3) Kong, T. Y., and Kim, H. G. The Experimental Report for the Selection of WBC Geometry and Position of Deposited Radionuclides, Korea Electric Power Research Institute, TM.I05NJ14.P2006.462, pp. 13-32, (2006).

Journal of NUCLEAR SCIENCE and TECHNOLOGY, Supplement 5, p. 159–162 (June 2008)

Evaluation of the Effectiveness of the Lead Aprons and Thyroid Shields Worn by Cardiologists in Angiography Departments of Two Main General Hospitals in Mashhad, Iran

M. T. Bahreyni Toossi[1*], H. Zare[1], Sh. Bayani[1], and S. Esmaili[2]

[1]*Medical Physics Research Center, Medical Dosimetry Laboratory, Mashad University of Medical Sciences, Mashad-Iran*
[2] *Faculty of Medicine, Azad University of Sanandaj-Iran*

In recent years coronary artery angiography and angioplasty procedures have become very popular. Consequently radiation protection of the cardiologists, their assistants and technicians working in the vicinity of the x-ray tube is essential. Although in recent years in developed countries, high dose x-ray examinations such as coronary angiography have attracted the attention of health physicists but in developing countries it may take some years before it would receive any attention. In Iran generally film badge is the most common personal radiation monitoring device used for this purpose; it is placed beneath the lead apron. The shielding effect of different lead aprons and thyroid shields have been evaluated. TL dosimeters, suitably calibrated, were placed over and under lead shields corresponding to the thyroid and gonad positions of the personnel. 233 angiography examinations by femoral route were included in this work. Four types of aprons and three types of thyroid shields were examined. They were different in shape and lead equivalent thickness. Our results have revealed that apron with 0.35 mmPb, one piece and front closed has maximum shielding effect. Also thyroid shield with 0.5 mmPb and very large edge provide a better protection against radiation than other types.

KEYWORDS: cardiovascular, angiography, TLD, lead apron, thyroid shield.

I. Introduction

Now days x-ray fluoroscopy machines of different designs are widely used in different branches of clinical medicine for diagnosis and treatments. These procedures are carried out by radiologists and non radiologists e.g. urologists, internists, neurosurgeons, cardiologists and so on. Although these procedures are considering minimally invasive, but significantly improve medical care of patients, on the other hand they create new risks for interventionalists. Scattered radiation from the patient represents the major source of exposure during these procedures. Although radiation dose of this kind does not cause an acute effect to the interventionalist but it may influence stochastic effects such as carcinogenesis [1)].

Cardiovascular diseases are among three major causes of death in many developed and developing countries e.g. Iran, on the other hand the number of cardiovascular angiography departments are fewer than needed. The combinations of these two factors impose a heavy load of CA (Coronary Angiography) and PTCA (Percutaneous Transluminal Coronary Angioplasty) examinations on the existing centers. These centers are fully booked all the year round, many cardiologists and technicians work two shifts a day. The over all condition in terms of radiation protection is not optimistic. In many countries the regulatory authorities are not practically vigilant. In such countries the most common personal radiation monitoring device is film badge. It is worn on beneath the lead apron. In this circumstances film badge is not an appropriate dosimeter. Dose reduction property of lead shielding depends on several factors. Lead equivalent thickness of shielding, and kVp used during the procedure are two major parameters. There is also different opinion, in regards to where the dosimeter should be placed, out side or beneath the apron. Although proper selection and use of aprons and other shielding are playing an important role to avoid unnecessary exposure but very few studies have been carried out in this area.[1-3)] A very useful work has been carried out in Netherlands to demonstrate the protection efficiency of lead aprons[2)]. Some workers have tried to estimate radiation dose received by interventionalist by placing humanoid phantom on fluoroscopy bed and measuring radiation dose at the approximate location where in real operation the interventionalist would stand during the procedure[1)]. In another study staff dose has been estimated by electronic personal dosimeters. In Iran, for the first time we performed a comprehensive study to assess organ and effective dose of patients, cardiologists and their assistants, also the effect of wearing on different type and style of aprons and thyroid shields in two teaching hospitals in Mashad-Iran. In this article the latter part of this work is reported.

II. Materials and Methods

General speaking dosimetry of either patients or personnels are much easier and less time consuming by modeling or utilization of humanoid phantom, but real data are produced when dose estimation is carried out in real conditions. In this work measurements were carried out for

*Corresponding Author, Tel. +98 511 8828576, Fax. +98 511 8002320, E-mail: bahreynimt@mums.ac.ir

115 CA and 30 PTCA procedures by the femoral rout at two teaching hospitals in Mashhad/Iran. Five and seven cardiologists were involved at hospitals A and B respectively. All cardiologists used a standard procedure for CA and PTCA examinations. At both hospitals x-ray systems used were Siemens Angioscop (COROSKOP T.O.P) with an under couch tube. The fluoroscopy mode routinely used is 12.5 pulses per second for adult patients. The tube voltage for fluoroscopy was automatically adjusted and ranged from 65 to 85 kV. Total filtration was equal to 4.5 mmAl. In this study mean fluoroscopy time for CA and PTCA were equal to 3.4 and 7.8 min respectively. This work was carried out over a period of months. Cardiologists and their assistants were asked to wear on two TLD badge each holding two TLD-100 chips, one over the lead apron and the other under the apron corresponding to their gonads and thyroids. Special attention was paid to carefully position the TLD holders on aprons according to the anatomy of the person wearing it. TLD holders (3.5 cm × 4.5 cm) were designed and made from PMMA specially for this study. TLD-100 chips were firmly held in the recesses provided in the holders. PMMA holders also protected TLD chips from chemical damage, humidity and physical wear and tears. As our center is a few kilometers far from the two hospitals, each batch of TLD holders taken to angiography departments included two holders, which were kept in an appropriate place within the department but out side the examination room. They were returned to our laboratory on the same day. The latter TLDs were used to estimate the effect of environmental radiation and other physical parameters. TLD chips were annealed at 400°c in an electric muffled furnace for one hour, then they were transferred (on an Aluminum planchet) to a specially designed and made cooling block of brass to be cooled down to room temperature for 15 minutes. Finally dosimeters were heated again at 100°c in a microprocessor controlled low temperature electric furnace for two hours. This protocol is necessary to clean up every residual dose from previous exposures TL dosimeters were exposed to a known dose of γ-rays from a standard source incorporated in the irradiator 2210 manufactured by Thermo Electron Corporation. This process accomplishes calibration of TLDs. Dosimeters were individually marked before transferring to hospitals. After exposure they were read by manual Harshaw 3500 model reader.

Mean dose of every two TLDs (in a single holder) was taken as representative entrance surface dose of the corresponding organ.

Various types (lead equivalency and style) of lead aprons and thyroid shields examined in this study are as follows.

a) Aprons

Type 1: old, one piece, front opened and 0.5 mmPb.

Type 2: old, one piece, front closed and 0.5 mmPb

Type 3: new, one piece, front closed and 0.35 mmPb.

Type 4: two pieces, front closed and 0.35 mmPb.

b) Thyroid shields

Type 1: new model, very brief and 0.5 mmPb.

Type 2: old model, with extended edge, 0.5 mmPb.

Type 3: old model, with very large edge, 0.5 mmPb.

The number of different type of lead aprons and thyroid shields worn by cardiologists were not equal, and they chose it according to their convenience.

Fig. 1 and **Fig. 2** show the different types of apron and thyroid shields.

Fig. 1 Different types of lead apron

Fig. 2 Different types of thyroid shields

III. Results:

Average dose absorbed by eight groups of TLDs worn under and over four different types of aprons (corresponding to gonad position) are presented in **Table 1**.

Table 2 is also providing the average absorbed dose by six groups of TLDs worn over and under three different types of thyroid shields (corresponding to thyroid position).

Table 1 Average absorbed dose of TLDs worn on over and under the different lead aprons

Type of apron	Number of examinations	Average absorbed dose (μGy)	
		Over apron	Under apron
Type 1	27	134.9	23.4
Type 2	56	127.2	36.9
Type 3	97	99	15.9
Type 4	53	107	52.1

Table 2 Average absorbed dose of TLDs worn on over and under the different thyroid shields

Type of apron	Number of examinations	Average absorbed dose (μGy)	
		Over apron	Under apron
Type 1	72	80.4	44.4
Type 2	46	86.2	37
Type 3	21	40.5	11.2

Fig. 3 and **Fig. 4** show percentage of absorbed radiation by different types of aprons and thyroid shields respectively.

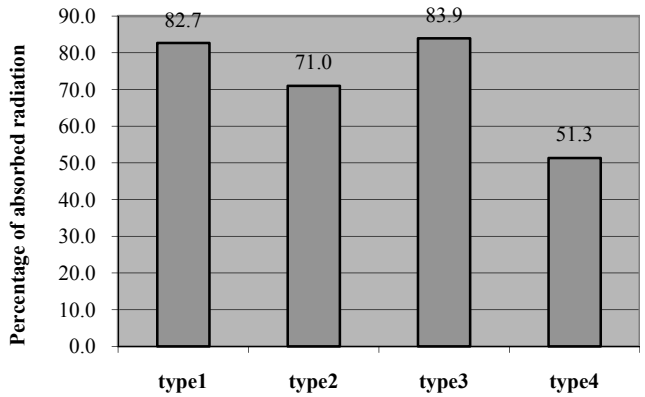

Fig. 3 Percentage of absorbed radiation by different lead aprons

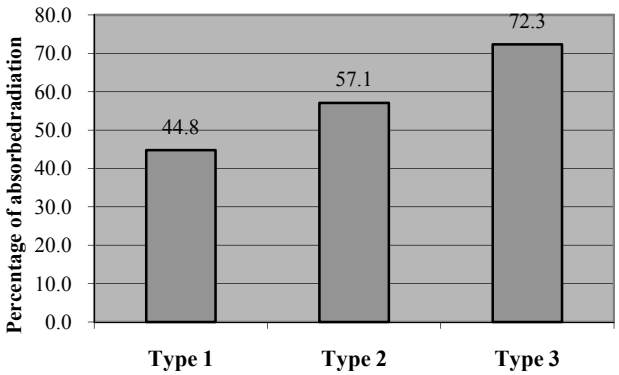

Fig. 4 Percentage of absorbed radiation from different thyroid shields

Our results have revealed that aprons type 1 and 3 have maximum shielding effect and absorb 82.7% and 83.9 % of incident photons respectively, in case of thyroid shields type 3 is more efficient (absorbs 72.3% of incident radiation).

IV. Discussion and conclusion

Interventional procedure performed by x-rays e.g. cardiovascular angiography are a major source of radiation exposure to operators.[4,5] Radiation exposure arising from these procedures is affected by multiple factors such as: distance from the patient, proximity to the primary radiation field, fluoroscopy time, fluoroscopy technique, pulse frequency settings, x-ray tube filters, collimation, operator experience and procedure type.[6-8] Currently there are several radiation protection methods available which can significantly reduce radiation exposure of personnel in cardiovascular fluoroscopy. One of the easily available methods is wearing of proper shielding e.g. lead aprons, thyroid shields, lead glasses and very flexible lead gloves. Effective utilization of all these factors results in significant reduction in radiation exposure. However in many cases some of these factors may get out of operator's control due to unexpected condition arising during the fluoroscopy.

But a proper shielding is always accessible. In our study this issue is fairly obvious, from **Fig. 3** it is clearly evident that lead aprons generally reduce radiation exposure to operator's gonad, but the reduction factor varies from 2 to 6.2 and depends on the style and thickness (lead equivalent) of the apron. In this study it became evident that the apron marked as type 3 provides the most effective shielding to operators organs. Type 1 apron has the second best protective feature; indicating that apron style does affect its shielding strength, however its lead content is the same as type 2. Apron type 1 when worn and fastened properly, right and left sides are over lapped more than 10 cm, consequently type 1 apron provides a thicker and more effective shielding. In practice heavier aprons are not convenient for extended procedures. Protective ability of thyroid shields are not identical, type 3 is twice as effective as type 1. Although lead equivalency of all 3 types are equal, but very large extended edge of type 3 makes it more protective.

In another study performed in Netherlands researchers have assessed the efficiency of lead aprons in reducing radiation exposure to uterus, they have concluded that frontal aprons in predominantly AP orientation and wrap round apron in a mixed geometry will have a protective factor above 5 (for 0.25 mmPb) even for very high kVp.

Acknowledgement:

The authors would like to thank research council and the office of vice president for research affairs of Mashhad University of medical sciences for their financial support of this works.

Reference:

1) J.S. Luchs, A. Rosioreanu, D. Gregorius, et al., 'Radiation safety during spine interventions.' J. Vasc. Interv. Radiolo., 16, 107 (2003).
2) D. Zweers, J. Geleijins, N.J.M. Aarts, et al., 'Patient and staff radiation dose in flouroscopy-guided TIPs procedures and dose reduction, using dedicated flouroscopy exposure settings.' Br. J. Radiol., 71, 672 (1998).
3) H. Von Boellicher, K. Links der waser, 'Optimization of

radiation protection in cardiology and radiology: Thyroid protection collors significantly reduce the effective dose.' Biomedizinische Technik, Vol. 50, Supplementary Vol. 1, Part 2, 1299 (2005).
4) American College of Radiology. Radiation risk: a primer, Reston, VA: ACR (1996).
5) L. Berlin, 'Radiation-induced skin in juries and fluoroscopy.' AJR Am. J. Roentgenol, 177, 21 (2001).
6) A.T. Young, R.L Morin, D.W. Hunter, et al., 'Surface shield: device to reduce personnel radiation exposure.' Radiology, 159, 801 (1986).
7) WH. Bush, D. Jones, GE. Brannen. 'Radiation dose to personnel during percutaneous renal calculus removal.' AJR Am. J. Roentgenol, 145, 1261 (1985).
8) WH. Bush, D Jones, RP. Gibbons. 'Radiation dose to patient and personnel during extracorporeal shock wave lithotripsy.' J. Urol., 138, 716 (1987).

Journal of NUCLEAR SCIENCE and TECHNOLOGY, Supplement 5, p. 163–166 (June 2008)

Fast Neutron Exposure Evaluation Using the Ex-vessel Neutron Dosimetry System

Choon Sung Yoo[1*] and Jong-Ho Park[2]

[1] *Korea Atomic Energy Research Institute, 150 Dukjin-dong, Yuseung-gu, Daejeon, Korea*
[2] *Chungnam National University, 220 Gung-dong, Yuseung-gu, Daejeon, Korea*

The Code of Federal Regulations, Title 10, Part 50, Appendix H, requires that the neutron dosimetry be present to monitor the reactor vessel throughout its plant life. The Ex-Vessel Neutron Dosimetry Systems which consist of sensor sets, radiometric monitors, gradient chains, and support hardware have been installed for Korean nuclear power plants after a complete withdrawal of all six in-vessel surveillance capsules. The systems have been installed in the reactor cavity annulus in order to characterize the neutron energy spectrum variations axially and azimuthally over the beltline region of the reactor vessel. In addition, stainless steel gradient chains are used in conjunction with the encapsulated dosimeters to complete the mapping of the neutron environment between the discrete locations chosen for spectrum determinations. Cycle specific neutron transport calculations were performed to obtain the energy dependent neutron flux throughout the reactor geometry including the dosimetry positions. Comparisons between the calculations and measurements were performed for the reaction rates of each dosimetry sensor and the results show good agreements.

KEYWORDS: Neutron Dosimetry, Pressure Vessel, Neutron Spectrum, Surveillance Capsule

I. Introduction

In the assessment of the state of embrittlement of light water reactor (LWR) pressure vessels, an accurate evaluation of the neutron exposure of the beltline region of the vessel is required. In Appendix G to 10 CFR 50[1)], the beltline region is defined as "the region of the reactor vessel shell material (including welds, heat affected zones, and plates or forgings) that directly surrounds the effective height of the reactor core and adjacent regions of the reactor vessel that are predicted to experience sufficient neutron radiation damage to be considered in the selection of the most limiting material with regard to radiation damage". Therefore, plant specific exposure assessments must include evaluations as a function of the axial and azimuthal location over the entire beltline region.

Regulatory Guide 1.190, "Calculational and Dosimetry Methods for Determining Pressure Vessel Neutron Fluence"[2)] describes state-of-the-art calculation and measurement procedures that are acceptable to the NRC staff for determining pressure vessel neutron fluence. Also included in Regulatory Guide 1.190 is a discussion on the steps required to qualify and validate the methodology used to determine the neutron exposure of the pressure vessel wall. One important step in the validation process is the comparison of plant specific neutron transport calculations with available measurements.

The Code of Federal Regulations, Title 10, Part 50, Appendix H[3)], requires that the neutron dosimetry be present to monitor the reactor vessel throughout its plant life. In order to satisfy this requirement, all plants have plant specific in-vessel surveillance capsules which include neutron dosimery sensors, and these capsules are typically located on the neutron pad between the core and the reactor vessel in the downcomer region. These six in-vessel capsules are to be withdrawn and analyzed periodically with respect to the surveillance program. If all six in-vessel surveillance capsules have been withdrawn, there is no more neutron dosimetry system to monitor the neutron exposure of the reactor vessel. And thus it is needed to install an alternative neutron dosimetry system to monitor the neutron exposure throughout a plant's life.

The Ex-Vessel Neutron Dosimetry (EVND) program was designed for a continuous monitoring of reactor vessel exposures by fast neutron (E > 1 MeV) for the plants of which all in-vessel surveillance capsules have been withdrawn. Basically total six EVND capsules had been installed at various locations of reactor cavity annulus between the reactor vessel outer wall and the biological shield.

Plant and cycle specific neutron transport calculations were performed in order to obtain the neutron spectra for the entire region of the reactor vessel beltline for Yonggwang Nuclear Unit (YGN) 1&2 and for Kori Nuclear Unit (KNU) 3&4 which have the EVND system and are the typical 3-loop nuclear power plants in Korea. The evaluations of EVNDs for the four plants were performed on the guidance specified in Regulatory Guide 1.190 and presented in this paper.

II. Neutron Transport Calculation

Plant specific forward transport calculations were carried out by using the three-dimensional flux synthesis technique described in Regulatory Guide 1.190 as below:

*Corresponding Author, Tel. +82-42-868-8084, Fax. +82-42-862-2311, E-Mail; csyoo@kaeri.re.kr

$$\phi(r,\theta,z) = \phi(r,\theta) \bullet \frac{\phi(r,z)}{\phi(r)} \quad (1)$$

where $\phi(r,\theta,z)$ is the synthesized three-dimensional neutron flux distribution, $\phi(r,\theta)$ is the transport solution in an R-θ geometry, $\phi(r,z)$ is the two-dimensional solution for a cylindrical reactor model using the actual power distribution, and $\phi(r)$ is the one-dimensional solution for a cylindrical reactor model using the same source per unit height as that used in the R-θ two-dimensional calculation. For the analysis, all transport calculations were carried out by using the DORT 3.1 discrete ordinate code[4] and the BUGLE-96 cross-section library[5]. The BUGLE-96 library provides a 67 group coupled neutron-gamma ray cross-section data set produced specifically for a light water reactor application. In these analyses, anisotropic scattering was treated with a P_5 Legendre expansion and the angular discretization was modeled with an S_{16} order of angular quadrature. The fuel assembly specific enrichment and burnup data were used to generate the spatially dependent neutron source throughout the reactor core. This source description included a spatial variation of the isotopic dependent (^{235}U, ^{238}U, ^{239}Pu, ^{240}Pu, ^{241}Pu, and ^{242}Pu) fission spectra, neutron emission rate per fission, and energy release per fission based on the burnup history of individual fuel assemblies

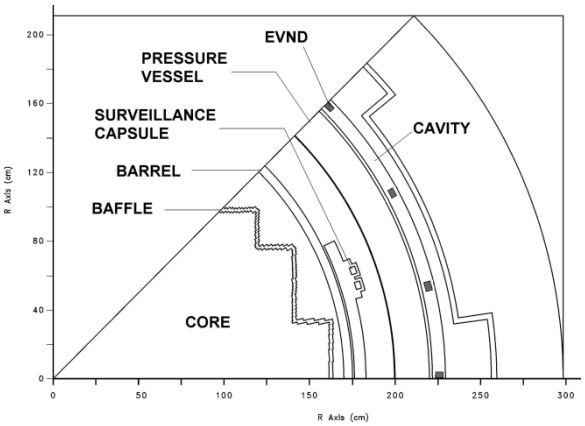

Fig. 1 R-θ Geometry model of neutron transport calculations for the 3-loop reactors

Plain view of the R-θ model of the 3-loop reactor geometry at the core midplane is shown in **Fig. 1**. A single octant is depicted showing the arrangement of the neutron pads and surveillance capsule attachments. In addition to the core, reactor internals, pressure vessel and primary biological shield, the models developed for these octant geometries also included explicit representations of the surveillance capsules, the pressure vessel cladding, the pressure vessel reflective insulation, and the reactor cavity liner plate.

In developing the R-θ analytical models of the reactor geometry shown in **Fig.1**, nominal design dimensions were employed for the various structural components. Water temperatures and, hence, coolant density in the reactor core and downcomer regions of the reactor were taken to be representative of full power operating conditions (2775 MW). The reactor core was treated as a homogeneous mixture of fuel, cladding, water, and miscellaneous core structures such as fuel assembly grids, guide tubes, etc. As shown in this figure EVND sets are installed at the locations of an azimuthal angle of 0º, 15º, 30º, and 45º in the reactor cavity

A sectional view of the R-Z model of the reactor is shown in **Fig. 2**. The model is extended radially from the centerline of the reactor core out to a location interior to the primary biological shield and over a fourteen foot axial span from an elevation one foot below to one foot above the active fuel region. The axial extent of the model was chosen to permit the determination of the maximum exposure of the vessel materials in the beltline region opposite the reactor core.

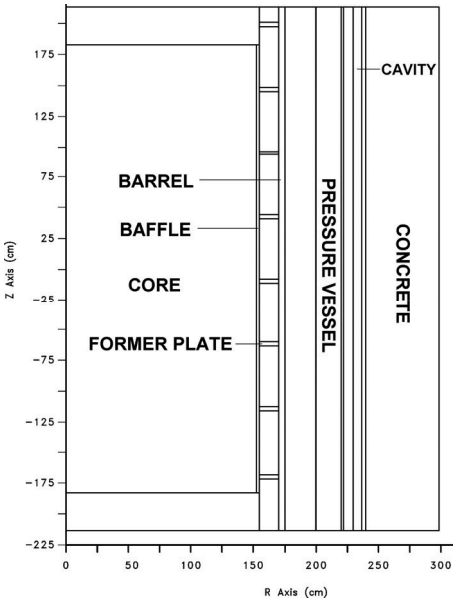

Fig. 2 R-Z Geometry model of neutron transport calculations for the 3-loop reactors

As in the case of the R-θ models, nominal design dimensions and full power coolant densities were employed in the calculations. In this case, the homogenous core region was treated as an equivalent cylinder with a volume equal to that of the active core zone. The stainless steel former plates located between the core baffle and core barrel regions were also explicitly included in the model.

The one-dimensional radial model used in the synthesis procedure consists of the same radial mesh intervals included in the R-Z model. Thus, radial synthesis factors, $\phi(r,z)/\phi(r)$, can be determined on a meshwise basis throughout the entire geometry.

The SORCERY[6] computer code was used to prepare a fixed distributed source for the DORT transport calculations. This code prepares a fixed distributed source in DORT X-Y, R-θ, or R-Z discrete ordinates transport theory code space mesh. Given the initial ^{235}U enrichments

and assembly burnup data, SORCERY properly accounts for the fission of ^{235}U, ^{238}U, ^{239}Pu, ^{240}Pu, ^{241}Pu, and ^{242}Pu. The radial core burnup distributions were taken from the appropriate Nuclear Design Reports for the analyzed operating cycles. And other important nuclear design data such as the fuel assembly specific initial enrichments, and core average axial power distributions were also obtained from the respective design reports.

Cycle specific neutron spectra in all the reactor geometries from the initial cycle to the current operating cycle were determined by using the above three-dimensional flux synthesis technique for the four typical 3-loop pants. The calculated neutron spectrum at the location of EVND can be validated by comparisons of the reaction rates for the various neutron dosimeter sensors with the measurement from the EVND systems. The calculated reaction rates with an uncertainty can be obtained by the following equation[7]:

$$R_i \pm \delta_{R_i} = \sum_g (\sigma_{ig} \pm \delta_{\sigma_{ig}})(\phi_g \pm \delta_{\phi_g}) \tag{2}$$

where R_i is the reaction rate of dosimeter *i*, ϕ_g is the neutron spectrum calculated at the location of dosimeter set, σ_{ig} is an appropriate multi-group dosimeter reaction cross-section, and δ_i is the associated uncertainty of parameter *i*. SAND/FERRET/INTVAL computer code sequence[8] was used to determine the calculated reaction rates for each dosimeter sensor and the dosimeter cross-section, SNLRML[9] , was used for this purpose.

III. Dosimetry Evaluation

Total six EVND capsules containing six fast neutron sensors listed in **Table 1** had been installed at the various locations of the reactor cavity. These locations correspond to azimuthal locations of 0º, 15º, 30º, and 45º relative to the core major axes as shown in **Fig. 1** For the azimuthal 0º where the maximum fast neutron (E > 1.0 MeV) flux of the vessel occurs, three EVND capsules had been positioned at the top, middle, and bottom of the actual core height and the others were located at the middle of the core for each azimuthal angle. Note that the axially maximum fast neutron flux on the vessel is dependent on the axial power distribution of the core and typically found near the core middle. **Fig. 3** shows the axial location of the dosimetry sets installed in the reactor cavity. Stainless steel bead chains containing iron, nickel, and cobalt as radiometric monitors had also been positioned from top to bottom of the reactor core to monitor the axial gradients of the flux distributions at each azimuthal angle of the cavity.

The use of passive neutron sensors does not yield a direct measure of the energy dependent neutron flux at the measurement location. Rather, the activation or fission process is a measure of the integrated effect where the time- and energy- dependent neutron flux irradiates on the target materials during the corresponding reactor operation periods.

Table 1. Ex-vessel Neutron Dosimetry Sensors

Material	Reaction	Half-life of the Product
Copper	^{63}Cu(n,α)^{60}Co	5.271 y
Titanium	^{46}Ti(n,p)^{46}Sc	83.79 d
Iron	^{54}Fe(n,p)^{54}Mn	312.3 d
Nickel	^{58}Ni(n,p)^{58}Co	70.82 d
^{238}U	^{238}U(n,f)^{137}Cs	30.07 y
^{237}Np	^{237}Np(n,f)^{137}Cs	30.07 y

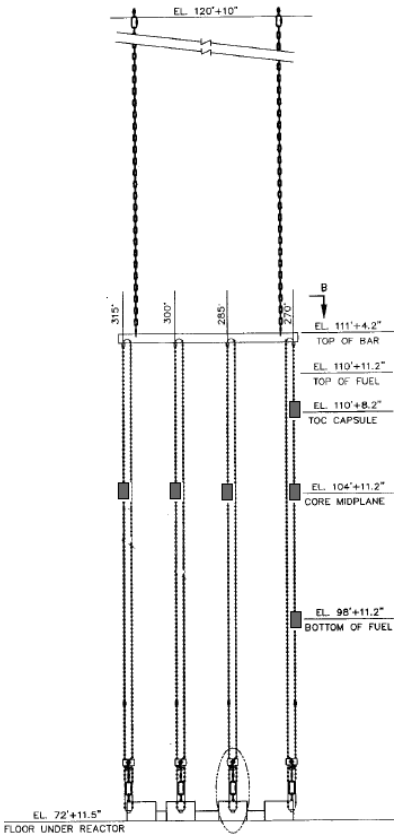

Fig. 3 Axial location of EVNDs

Having the measurement of the specific activities, the operating history of the reactor, and the physical characteristics of the neutron sensors, reaction rates referenced to a full power operation are determined from the following equation

$$R = \frac{A}{N_0 F Y \sum_{j=1}^{n} \frac{P_j}{P_{ref}} C_j [1-e^{-\lambda t_j}][e^{-\lambda t_d}]} \tag{3}$$

where,

R = reaction rate averaged over the irradiation period and referenced to operation at a core power level of P_{ref} (rps/atom),

A = measured specific activity (dps/gm),

N_0 = number of target element atoms per gram of sensor,

F = weight fraction of the target isotope in the sensor material,

Y = number of product atoms produced per reaction,

P_j = average core power level during irradiation period j (MW),

P_{ref} = maximum or reference core power level of the reactor (2775 MW),

C_j = calculated ratio of ϕ(E>1.0 Mev) during irradiation period j to the time weighted average ϕ(E>1.0 Mev) over the entire irradiation period,

λ = decay constant of the product isotope (s^{-1}),

t_j = length of irradiation period j (s),

t_d = decay time following irradiation period j (s).

and the summation is carried out over the total number of monthly intervals comprising the irradiation period.

IV. Results and Conclusions

The EVND sets had been installed during the overhauls after Cycle 14 and 15 for YGN-1&2 and KNU-3&4, respectively. A comparison of the measurement and the calculation results of the reaction rates for each EVNDs were performed.

Table 2. The Reaction Rate Comparison (M/C)

Material	YGN-1	YGN-2	KNU-3	KNU-4
^{63}Cu	0.91	0.91	0.98	0.97
^{46}Ti	0.99	0.96	1.00	0.98
^{54}Fe	0.97	0.96	1.07	0.98
^{58}Ni	0.93	0.89	0.91	0.87
^{238}U	0.98	0.93	1.01	0.95
^{237}Np	1.02	0.98	1.08	0.88
Average	0.97	0.94	1.01	0.94

Table 2 lists the ratio of the measurement to calculation (M/C) of the reaction rate for the EVNDs installed at the middle of an azimuthal angle 0º where the maximum fast neutron flux is expected. As shown in this table the reaction rates of calculation and measurement are very close to each other. **Fig. 4** shows the comparison of reaction rate for ^{54}Fe contained in the stainless steel bead chain of azimuthal angle 0º for KNU-3 and shows a good agreement.

In this study, the ex-vessel neutron dosimetry system was installed and evaluated for the typical 3-loop plants in Korea. The results shows good agreement with calculation for the reaction rates of each sensor. Thus it is expected that this system can be used in the monitoring of the fast neutron exposure for the reactor vessel embrittlement assessments.

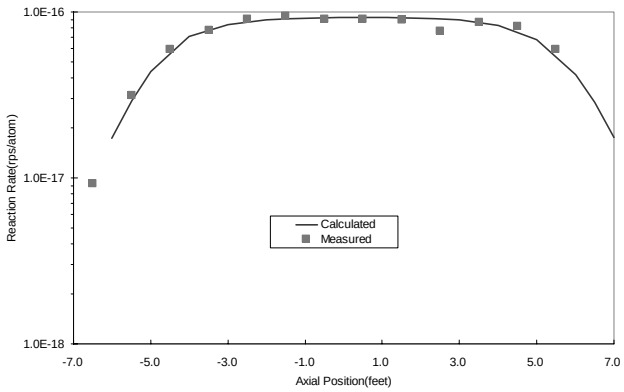

Fig. 4 Reaction rate of ^{54}Fe in the stainless steel bead chain (KNU-3 azimuthal 0º)

References

1) Code of Federal Regulations Title 10 Part 50, "Domestic Licensing of Production and Utilization Facilities," Appendix G, "Fracture Toughness Requirement" and Appendix H, "Reactor Vessel Materials Surveillance Requirements," January 1992.
2) Regulatory Guide 1.190, "Calculational and Dosimetry Methods for Determining Pressure Vessel Neutron Fluence," U. S. Nuclear Regulatory Commission, Office of Nuclear Regulatory Research, March 2001.
3) CFR Part50, Appendix H, "Reactor Vessel Material Surveillance Program Requirements," U.S. NRC, January 1, 1998.
4) RSICC Computer Code Collection CCC-650, "DOORS 3.1, One-, Two, and Three-Dimensional Discrete Ordinates Neutron/Photon Transport Code System," August 1996.
5) RSIC Data Library Collection DLC-185, "BUGLE-96, Coupled 47 Neutron, 20 Gamma-Ray Group Cross Section Library Derived from ENDF/B-VI for LWR Shielding and Pressure Vessel Dosimetry Applications," March 1996.
6) Westinghouse Electric Company LLC, "SORCERY User Manual," December 2001.
7) Westinghouse Electric Company LLC, "Benchmark Testing of the FERRET Code for Least Squares Evaluation of Light Water Reactor Dosimetry," WCAP-16083-NP Rev. 0, May 2004.
8) Westinghouse Electric Company LLC, "SAND/FERRET/INTVAL User Manual," November 1997.
9) RSIC Data Library Collection DLC-178, "SNLRML Recommended Dosimetry Cross-Section Compendium," July 1994

Journal of NUCLEAR SCIENCE and TECHNOLOGY, Supplement 5, p. 167–170 (June 2008)

Improving Radiochromic Film's Sensitivity Limit with an Optical Common-mode Rejection and a Flatbed Color Scanner

OHUCHI Hiroko*

Graduate School of Pharmaceutical Sciences, Tohoku University, 6-3 Aoba, Aramaki, Aoba-ku, Sendai, Miyagi, 980-8578,JAPAN

A novel method, an optical common-mode rejection (CMR), which can greatly improve the dosimetric sensitivity limit of a radiochromic film (RCF) through use of a set of color outputs from an RGB color scanner has been developed. RCFs are known to have microscopic and macroscopic uniformity, which comes from the intrinsic thickness variations in the film's active radiochromic layer and coating. These variations in the response make the optical S/N (signal-to-noise ratio) lower, resulting in lower film sensitivity. The basic principle of the optical CMR is the compensation of RCF film nonuniform response by creating a ratio of the two signals where the factors common to both numerator and denominator cancel out. The scheme was applied to create two types of ratios using two combinations, red /green and red/blue. MD-55-2 type dosimetry films, which were exposed to100 kV X-ray beams in the range from 5 mGy to 8.1 Gy, were scanned with a flatbed color image scanner and the digital data was analyzed. The results obtained with the optical CMR and the conventional analysis method using the only red pixel values were compared. The detection limit can be greatly improved with the optical CMR scheme using the combination of red and green.

KEYWORDS: high sensitivity, non-uniformity, optical common-mode rejection, signal-to-noise ratio, color scanner, film dosimetry, radiochromic, MD-55-2

I. Introduction

Radiochromic film (RCF) is a thin, high resolution, 2D planar dosimeter and broadly applied in dosimetry for radiotherapy such as IMRT (intensity modulated radiation therapy)[1,2] and interventional radiology[3,4]. In radiochromic films, an organic-based dye is used, which causes a change in their optical properties due to polymerization when exposed to ionizing radiation and the change of color intensity/optical density is a measure of energy deposited. The main advantages of radiochromic film dosimeters are near tissue-equivalence, having a flat energy response, the coupling of rapid full planar acquisition, high-spatial resolution, and wide dynamic range of absorbed doses. However, RCFs have large disadvantages as radiation dosimeters, e.g. their low sensitivity to ionizing radiation and non-uniformity of response. These preclude their application to measure lower doses accurately. Various studies have reported that film sensitivity can be improved by layering multiple sheets of film together[5], using a red acetate filter[6], and wrapping the film with UV phosphor screens[7], however further improvements in sensitivity appear to have reach their limit.

Assuming macroscopic and microscopic non-uniformities of film layers, including the thickness variations in the film's active radiochromic layer and coating, were the main causes of light disturbance (noise) against the lights (signal), resulting in lower film sensitivity, we developed an optical common-mode rejection (CMR) that can improve the dosimetric sensitivity limit of a radiochromic film through use of a set of red R and green G color components, by using a spectrophotometer[8]. The two light components are neighboring wavebands about 100 nm apart and suffer a common fate, with the exception of wavelength-dependent events, having passed together along common attenuation paths. The R component is highly sensitive to radiation exposure as two absorption peaks are located at wavelengths of 617 and 675 nm[9], while the G output is less sensitive than the R output due to the absence of a clear absorption peak in the green waveband. The ratio of the two components (R:G) is analogous to the 'common-mode rejection' (CMR) in electronics, where the factors common to both numerator and denominator cancel out. This result indicated that the CMR can compensate the intrinsic variation in the film's layer by using red and green components.

The use of commercially available document scanners instead of the expensive laser densitometers make it possible to measure and obtain each component output at three wavelengths red, green, and blue of the RGB image[10-12]. To our knowledge, no publication has so far been reported using the combination to improve sensitivity described above.

In this paper, the optical CMR scheme was applied to the R, G, and B component outputs from a flatbed color scanner in transmission mode used to scan a MD-55-2 type dosimetry film after irradiation with 100 kV X-rays. The blue component is 200 nm apart from red component and hardly affected by two absorption peaks located in red component. Based on an assumption that the blue component represents the intrinsic variation in the film's coating, a ratio using red and blue components was created and then, the result was compared to that obtained using the R/G ratio and the conventional way using the red pixel values.

*Corresponding Author, Telephone: +81-22-795-6797
Fax: +81-22-795-6797 e-mail: hiroko@mail.pharm.tohoku.ac.jp

II. Materials and methods

1. Radiochromic film and irradiation

A commercially supplied RCF system (model MD-55-2, manufactured by International Specialty Products) was used. Its two 16-μm thick radiation-sensitive layers, each containing di-acetylene monomer crystals, are separated from each other by a 25-μm thick polyester layer sealed by 67-μm thick polyester side layers. This film type is available in sheet sizes of 12.7 x 12.7 cm. The dosimetric characteristics of the MD-55-2 film were determined by cutting sheets of film into small 2 x 2 cm squares. Due to their sensitivity to dust, scratches, the films were handled with great care, tagged by a layer of clear transparency to hold and support them. Standard precautions which apply to radiochromic film handling, such as keeping film temperature controlled as outlined in TG-55[13], were employed. The film pieces were exposed to X-ray beams of 100 kV with a 1.0-mm Al filter from an MBR-1520R unit (Hitachi Medico Co.) in the range from 5 mGy to 8.1 Gy. The tube current of 5 or 20 mA was used. For each exposure, two film samples were irradiated. The amount of radiation was monitored with a thimble ionization chamber, installed inside the unit.

2. Scanning procedure and image processing

The films were scanned before and twenty-four hours after exposure with an Epson ES-10000G flatbed color image scanner with a transparency adapter (SEIKO EPSON Co.) with 600 dpi resolution (42.3 μm/pixel) and 16 bits per color of the digital resolution dpi. The scans were performed in transmission mode with no color correction factors or filters. ES-10000G has CCD line sensors and its light source is white xenon cold cathode fluorescent lamp. For color separation, R, G and B a CCD color filter was used. Image splitting produces three separate 65536 intensity levels of R, G or B images corresponding to each color CCD channel.

A 3 x 3 cm square area with uniform response was identified by performing blank scans with the same condition described above and delimitated in order to use only this area for digitalization. Blank scans (no film), meaning the zero-light transmitted intensity, were repeated 5 times with a white lid closed in transmission mode. The same number outputs such as 0, 2, 4 appeared in the square for each color and each scan. No ununiformity was observed in blank scans for each RGB output and they were negligible. For each film, scanning was repeated five consecutive times and acquired images were averaged. The obtained digital data were evaluated using self-written routines in MATLAB 7.3 software (The Mathworks, Natick, MA). The digital data before exposure was subtracted pixel-by-pixel from the post-exposure image for each film. The serial images obtained by scanning each film before and after exposure were aligned using fiducial marks. After mathematical operations, the averages of the results were taken for 1 x 1 cm square at the center of each film. To obtain spectra of the films, the transmittance of the unexposed and irradiated films over the range of 300 - 800 nm in 1.0-nm steps was obtained by using the spectrophotometer DU-7400 (Beckman Coulter).

3. Optical density and mathematical operation using the optical CMR method

The transmittance is obtained as digitalized output of the R, G, and B component. The relationship between transmittance (T) and optical density (OD) used in film dosimetry can be expressed as follows,

$$OD = \log_{10}(2^{16}/T),$$

$$\text{net } OD = OD - OD_0 = \log_{10} T_0 - \log_{10} T = \log_{10} (T_0/T) \quad (1)$$

where subscripts denote unirradiated background quantities and 'net' stands for the quantities after removing the background.

The conventional analysis way uses only red component, at which net OD_Rd is defined as,

$$\text{net OD\_Rd} = \log_{10} (Rd_0 /Rd) \quad (2)$$

In the optical CMR scheme, in which red and green components are used, T should be replaced by Rd/Gr, where Rd and Gr are each amount of transmittance lights. Thus, net reduced OD (net ROD_Rd_Gr) in the optical CMR scheme is written as,

$$\text{ROD\_Rd\_Gr} = \log_{10} (Rd/Gr),$$

$$\text{net ROD\_Rd\_Gr} = \log_{10} ((Rd_0/Gr_0)/(Rd/Gr)) \quad (3)$$

In another way, the ratio are created by using Rd and B0, which denotes unirradiated background quantities of transmittance lights for blue component. The Bl0 represents the variation in the film coating, since it appears to be nearly independent of radiation exposures. The net reduced OD (net ROD_Rd_Bl) can be obtained by a following equation as,

$$\text{net ROD\_Rd\_Bl} = \log_{10}((Rd_0/Bl_0)/Rd) \quad (4)$$

III. Results and discussion

Fig. 1 shows the absorption spectra for MD-55-2 film unirradiated and exposed to 8.1 Gy of X-ray over the range of 300 - 800 nm in 1.0-nm steps and an example of filter functions for red, green, and blue wavebands on CCD. The vertical is expressed as light transmission in percentage, T (%). The results show the absorption spectra produce two pronounced peaks located at 617 and 675 nm, which are lying in the red region of the light spectra and both responsible for the same R output from the color scanner. It also shows G output is less sensitive than R output is owing to the absence of a clear absorption peak in the green waveband and B output is nearly insensitive.

The three dose-response curves as a function of delivered dose ranging from 8.1 mGy to 8.1 Gy of 100 kV X-ray beams and from films scanned 24 hrs after exposure are plotted in **Fig. 2**. These curves are obtained with each three index of net OD_Rd (■), net ROD_Rd_Gr (○), and net ROD_Rd_Bl (△). These indices represent the net optical density obtained with the conventional analysis using the red pixel values in Eq. (2), that with the optical CMR scheme using R/G ratios in Eq. (3), and using R/B ratios in Eq. (4), respectively. In Fig.2, each linear fit is expressed as solid line for three indices and equations are demonstrated. Error bars show one standard deviation for each index. Two linear fits obtained by net OD_Rd (■) and net ROD_Rd_Bl (△) are plotted almost in the same line. In Fig.2, another curve

expressed by open squares (□) is also plotted, representing a dose-response curve using the green component. The slope of this curve is 0.0034, indicating the G outputs are almost one third less sensitive than the R outputs, in which the slope of net OD_Rd is 0.0090.

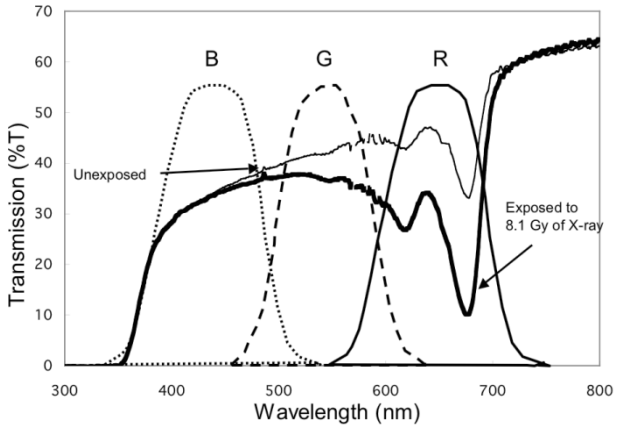

Fig. 1 Absorption spectra for MD-55-2 radiochromic film unirradiated and exposed to 8.1 Gy of X-ray over the range of 300 - 800 nm in 1.0-nm steps and an example of filter functions for red, green, and blue wavebands on CCD.

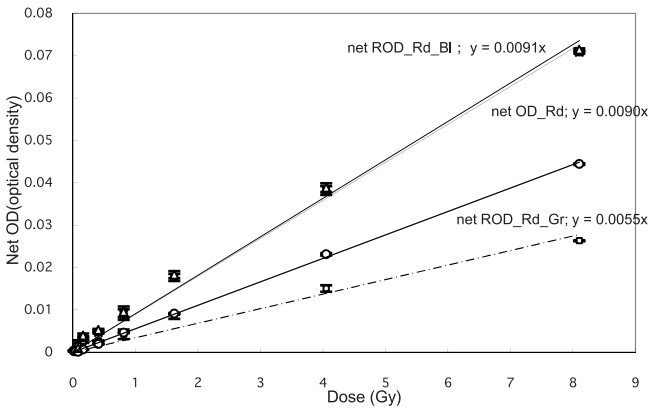

Fig. 2 Closed squares represent the net optical density obtained by using red component in Eq. (2), open circles show the net reduced OD calculated by R and G components in Eq. (3), and open triangles show the net reduced OD calculated by R and B components in Eq. (4), respectively.

The quotients between measured and fitted data by regression equations were obtained by a following equation for three types of indices of net OD_Rd, net ROD_Rd_Gr, and net ROD_Rd_Bl,

$$OD_{quotients} = OD_{meas.} / OD_{calc} \quad (5)$$

The results of quotients as a function of delivered dose in the range from 8.1 mGy to 8.1 Gy for three indices are plotted in **Fig. 3**. Error bars are shown in the figure as one standard deviation. The quotients for three indices remain below 1.0 in the range from 81 mGy to 8.1 Gy. For the delivered dose below 81 mGy, those for two indices of net OD_Rd and net ROD_Rd_Bl become large, while the quotients for an index of ROD_Rd_Gr remain small to 16.2 mGy. The detection limit was greatly improved with the optical CMR method using the combination of R and G components, while much improvement was not observed in the result by using the combination of R and B, compared to the results obtained by the conventional analysis using R values. The optical CMR method improves the detection limit through improving the optical S/N (signal-to-noise ratio). The green component is assumed to represent the variations in the film coating since it is less sensitive than the red component is, as shown in Fig. 1. The non-uniformities of film response come from not only the intrinsic variation in the film coating (base) but also the variation in sensitive material. The ratio of R/G also compensates the nonuniform distribution of sensitive material on the film base, because the signal of each RG channel is linear to both the dose and the film active layer mass as shown in Fig.2. The blue component is assumed to represent only the variations in the film coating.

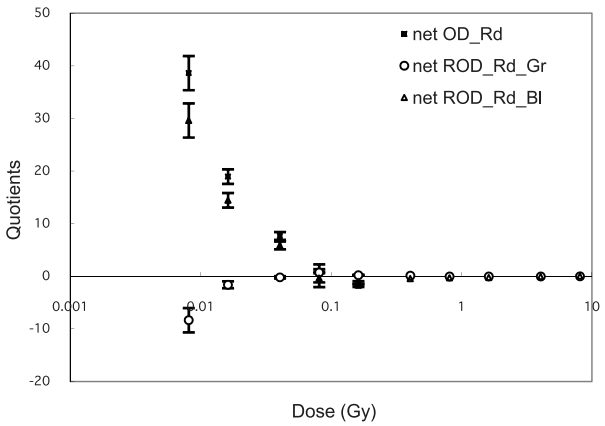

Fig. 3 Quotients between measured and fitted data by regression equations are plotted as a function of delivered dose in the range from 8.1 mGy to 8.1 Gy with three types of net ODs.

Fig. 4 shows the expanded figure of dose-response curves for two indices of OD_Rd (□) and ROD_Rd_Gr (●) in the very low range from 5 mGy to 0.8 Gy. The values obtained from two samples were plotted for each index. The same regression lines and equations appeared in **Fig.2** were demonstrated. Error bars show one standard deviation for each index. Those obtained using net OD_Rd exhibit a large discrepancy in measured optical densities between two samples and does not show a consistency with a linear fit. In contrast, the measured optical densities of two samples obtained with the optical CMR scheme show a good consistency each other and both values show an excellent consistency with a linear fit. These results indicate that the CMR scheme makes it possible to reproduce the measured optical densities and measure the dose until the very low dose of 5 mGy.

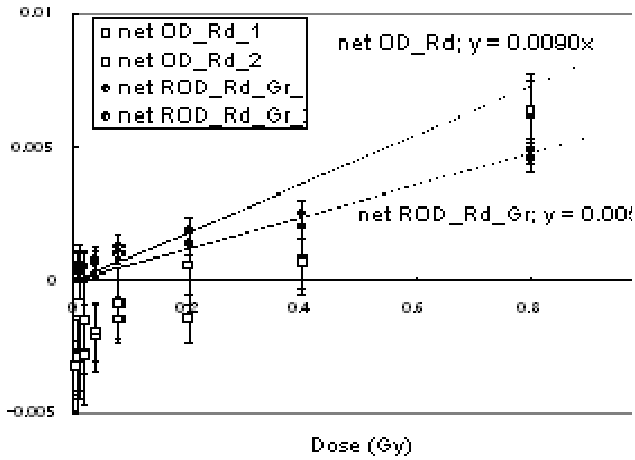

Fig. 4 Expanded figures of dose-response curves for two indices of OD_Rd (□) and ROD_Rd_Gr (●) in the very low range from 5 mGy to 0.8 Gy. The values obtained from two samples were plotted for each index. The measured optical densities of two samples obtained with the optical CMR scheme show a good consistency each other and both values show an excellent consistency with a linear fit.

IV. Summary

Comprehensive results show that the detection limit was greatly improved with the optical CMR method using the combination of Rd and Gr components, while much improvement was not observed in the result by using the combination of Rd and Bl. The optical CMR method improves the detection limit through improving the optical S/N (signal-to-noise ratio). The non-uniformities of film response come from not only the intrinsic variation in the film coating (base) but also the variation in sensitive material. The ratio of R/G is assumed to compensate both variations.

Both optical densities of measured and calculated by a linear fit in the dose-response showed a good consistency across the range from 5 mGy to 8.1 Gy when using the combination of Rd and Gr.

References

1) C. Fiandra, U. Ricardi, R. Ragona, et al., "Clinical use of EBT model GafchromicTM film in radiotherapy," Med. Phys., 33, 4314 (2006).
2) K. N. Morris, M. D. Weil, R. Malzbender, "Radiochromic film dosimetry of contrast-enhanced radiotherapy (CERT)," Phys. Med. Biol., 51, 5915 (2006).
3) M. Amano, H. Nishitani, S. Kohno, et al., "Measurement of patient skin dose in interventional radiology using radiochromic reflecting-type sheet films," Jpn. J. Radiol. Technol., 58, 420 (2002).
4) R. Y. L. Chu, G. Thomas, F. Maqbool, "Skin entrance radiation dose in an interventional radiology procedure," Health Phys., 91, 41 (2006).
5) T. Cheung, M. J. Butson, P. K.N. Yu, "Use of multiple layers of Gafchromic film to increase sensitivity," Phys. Med. Biol., 46, N235-N240 (2001).
6) D. O. Odero, G. R. Gluckman, K. Welsh, et al., "The use of an inexpensive red acetate filter to improve the sensitivity of GAFChromic dosimetry," Med. Phys., 28, 1446 (2001).
7) M. Geso, T. Ackerly, W. Patterson, "Improving radiochromic film's sensitivity by wrapping it with UV phosphor," Med. Phys., 31, 1014 (2004).
8) H. Ohuchi, K. Abe, "An optical common-mode rejection for improving the sensitivity limit of a radiochromic imaging film," Nucl. Instrum. Methods Phys. Res., A 558, 576 (2006).
9) M. J. Butson, P. K. N. Yu, T. Cheung, et al., "Radiochromic film for medical radiation dosimetry," Mater. Sci. Eng., R. 41, 61 (2003).
10) M. Bazioglou and J. Kalef-Ezra, "Dosimetry with radiochromic films: a document scanner technique, neutron response, applications," Appl. Radiat. Isot., 55, 339 (2001).
11) H. Alva, H. Mercado-Uribe, M. Rodriguez-Villafuerte, et al., "The use of a reflective scanner to study radiochromic film response," Phys. Med. Biol., 47, 2925 (2002).
12) O. Hupe, J. Brunzendorf, "A novel method of radiochromic film dosimetry using a color scanner," Med. Phys., 33, 4085 (2006).
13) A. Niroomand-Rad, C. R. Blackwell, B. M. Coursey, et al., "Radiochromic film dosimetry: Recommendations of AAPM Radiation Therapy Committee Task Group 55," Med. Phys., 25, 2093 (1998).

Journal of NUCLEAR SCIENCE and TECHNOLOGY, Supplement 5, p. 171–174 (June 2008)

Tritium Monitor Based on Gas-flow Proportional Counter

Xianguo Tuo, Keliang Mu*, Zhe Li, and Xiangyang Li

Chengdu University of Technology, Chengdu, Sichuan, China, 610059

The tritium surface contamination monitor based on gas-flow proportional counter is introduced in this paper. The detector is very advantageous for detecting low energy beta particles. Its detection efficiency is 84%, higher than the similar type monitors. Besides, Plateau Length is longer than 300V, Plateau slope is less than 1%/100V, Lowest Detection Limit is 0.221 Bq/cm2, the relative expansion uncertainty is 0.56%/h. The capabilities are superiority and steadiness. As a result, it can be well used to monitor tritium contamination in working sites or other places, with great value for usage and wide application fields.

KEY WORDS: tritium, gas-flow proportional counter, surface contamination, in-site

I. Introduction

Tritium may be produced in the upper atmosphere when cosmic rays strike nitrogen molecules in the air, and as a byproduct during nuclear weapons explosions, reactors producing and special production reactors, where the isotope lithium-6 is bombarded to produce tritium.

There are several important applications of tritium. The most significant is as a component in the triggering mechanism in thermonuclear (fusion) weapons. Huge quantities of tritium are required for the maintenance of nuclear weapons capabilities. In addition, there are also many other usages of tritium in daily life, such as, tritium lights, tritium cells, etc.

Tritium has a half-life of 12.33 years and emits a very weak beta particle. Its highest decay energy is about 18.6 keV, and average energy is about 5.7 keV. Tritium is quite similar to hydrogen, flavourless and colorless. People, especially who live near to, or work in nuclear fuel cycle facilities and research laboratories, may contact with tritium and inhale it , or absorb it into their skin. Thus the risk of developing cancer can be increasing, even though tritium is one of the least dangerous radionuclides. So it is necessary to monitor tritium contamination in radioactive labor site or laboratory, etc.

Conventional techniques established are mainly based on utilization of an ionization process and a scintillation process by interactions with β-rays emitted from tritium species. In this paper, a tritium contamination monitor system based on gas-flow proportional counter was developed, which adopts nuclear detection, electron and information process techniques. The whole device, which is motivated by lithium batteries, can be recognized as a tritium surface contamination monitor. The power consumption is low and detection efficiency is high, so it can be well used to monitor tritium contamination in working site or other environment, with high using value and broad application fields.

∗Corresponding Author, Tel. 86-28-8407-7936 Email. mklily@163.com
Supported by 2006JG002500 and 40574059.

II. Principium of Monitor

The activity of tritium surface contamination A_s was obtained by **Eq** (1), **Eq** (2) and **Eq** (3). The counting rate n and the counting rate of background n_B must be collected accurately, which is important for computing A_s and the capability of the monitor.

$$n = \frac{\sum_{1}^{c} N_i}{c \times t} \quad (1);$$

$$\varepsilon_i = \frac{n - n_B}{q_{2\pi.sc} \cdot \varepsilon_g} = \frac{n - n_B}{E_{sc} \cdot \varepsilon_g \cdot W} \quad (2);$$

$$A_s = \frac{n - n_B}{\varepsilon_i \times \varepsilon_s \times W} \quad (3);$$

In the equations, n is the counting rate (s^{-1}), c is the numbers of measurements, t is the time of measuring (s), N_i is the single count value ε_i is the detection efficiency, n_B is the counting rate of background (s^{-1}) $q_{2\pi.sc}$ is the surface emissivity of the standard source in the active area (s^{-1}), W is the active area (cm^2), E_{sc} is the surface emissivity of the standard source in unit area $(s^{-1} \cdot cm^{-2})$, ε_g is the geometrical efficiency, ε_s is the source efficiency.

III. System Structure

The instrument for measuring tritium is mainly made up of radiation detector, amplifier, signal acquisition module, main module and peripheral equipment, etc[6]. The whole structure of the system is shown in **Fig. 1**.

The high voltage for gas-flow proportional counter is supplied by a high voltage module and the gas (CH_4) was supplied by a high air pressure gas-bottle. Beta-ray emitted from tritium is detected by the proportional counter, and transformed into electric signal, which is magnified by amplifiers (preamplifier and main amplifier). Then the signal

is shaped, discriminated and selected by the signal acquisition module. At last, the pollution activity is computed, stored and processed in the main module. At the same time, some technique functions are carried out, such as keyboard operation, LCD display, alarming at low voltage, USB/RS232 interface, which are convenient for usage.

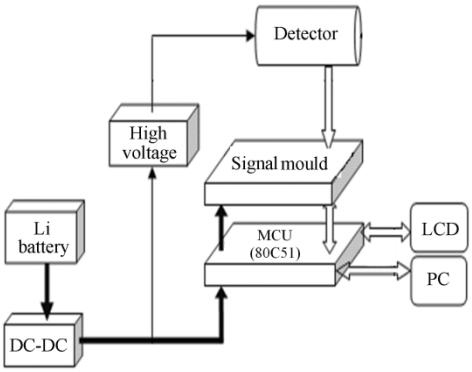

Fig. 1 Structure of tritium measuring instrument

1. Detector Selection

The no-window or thin-window detector with high sensitivity is needed for measuring tritium, because the energy of β particles emitted from tritium is low and the highest energy of beta is about 18keV. Proportional counter was mostly used in the past, while scintillation counter is adopted in recent years. The developed instrument uses the gas-flow proportional counter.

In order to ensure the detection precision and quality, gas-flow proportional counter adopted gold anticathode and it was filled with methane (CH_4) gas. Beta-ray can be effectively detected in the gas under a high voltage field(3700~4500V). The structure of the gas-flow proportional counter is shown in **Fig. 2**.

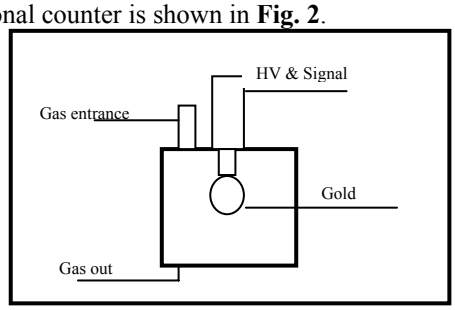

Fig. 2 Gas-flow Proportional Counter

The samples can be placed under the detector, so the particles directly are emitted into the active volume, which is very advantageous for detecting the low energy beta particles. A thin window（1mm，reticulation copper） was added to avoid the contamination of detector (**Fig.3**).

Fig. 3 Gas-flow Proportional Counter

2. Signal Module

Advanced electron-collection techniques are adopted to ensure obtaining the faint signal output from the detector, such as high precision AD chips, vacuum and shield skills, and the technical background A-V (Ampere-Voltage) convector. The precision of faint signal can reach up to $6\sim10\times10^{-13}$A.

With the help of techniques, such as signal magnifying, process shaping, widening etc, the collected signals are changed into impulse signals for processing in the later circuit.

3. Instrument Main Processor

80C51F series microprocessor (CYGNAL, 80C51F24PI) is used as the main processor of instrument with basic frequency 24MHz. There is a Flash memorizer in the chip, which can meet the need of program and data storage.

In addition, the integrated level of the microprocessor is high. It belongs to SOC (system on a chip) and has good periphery interfaces. LCD display for picture and character, keyboard circuit and software programs are developed by periphery pins of this chip. The result can be displayed in time and parameters can be set expediently. Besides, USB/RS232 interface is adopted for communication with PC, which can meet the need for further data processing.

IV. Capability Test

1. Plateau Length

The standard source ^{99}Tc (Radiation Activity: 0.61uCi) was used to test the monitor. The time of measuring t was 5s, the numbers of measurements c was 8, the flux of work gas was 120ml/min, the relative humidity was 81%， the temperature of environment was 18℃.

The result of the test was that the plateau length was 400V from 3700V to 4100V. The Plateau Slope was less than 1%/100V. (Shown in **Fig.4**)

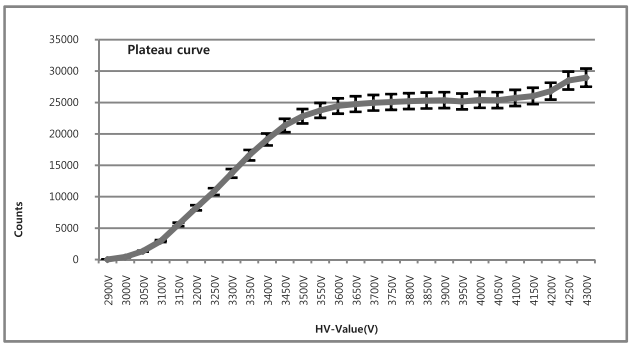

Fig. 4 Plateau Curve of Monitor

2. Counting Test

The standard source ^{99}Tc (Radiation Activity: 0.61uCi) was used to test the monitor. The time of measuring t was 60s, the numbers of measurements c was 50, the flux of work gas was 125ml/min, the high voltage was 3850V, and there was not protected net at the cathode. the relative humidity was 81%, the temperature of environment was 18℃.

The result was that there was about 76％ data in one time variance, 90% in double variance, and 100% in thrice variance. (Shown in **Fig. 5**)

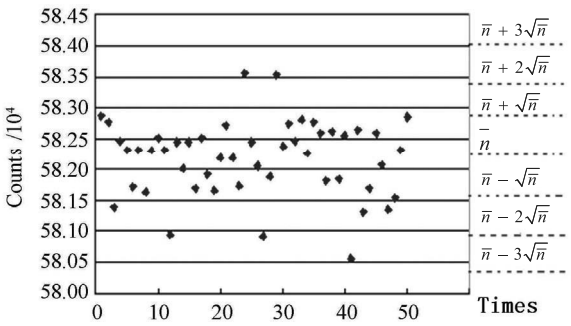

Fig. 5 Scatter plot of ^{99}TC counting data

3. Detection Efficiency

The standard source ^{3}H (surface emissivity: 1308/（2π・min)) was used to test the monitor. The time of measuring t was 60s, the numbers of measurements c was 50, the flux of work gas was 125ml/min, the high voltage was 3950V. The relative humidity was 81%，the temperature of environment was 18℃. The result of measuring was listed in **Table 1**. The detection efficiency was computed by **Eq.(2)**. Because the area of detector was more than source, the geometrical efficiency ε_g was 100% for 2π surface. And the counting rate n was 1194.72 s^{-1}, the counting rate of background n_B was 1.6s^{-1}.

The detection efficiency of this monitor (2π surface, active area of the detector was 37.25 cm^2, 2π surface emissivity was 1308 min^{-1}) was 84% and the relative expansion uncertainty (U_r) of detection efficiency was less than 10%(k=2), which were computed used ^{3}H as the referenced source and verified by the Metrology and Testing Center in China[7].

Table 1 The result of measuring

c	n*60s	c	n*60s	c	n*60s	c	n*60s	c	n*60s
1	1190	**11**	1189	**21**	1193	**31**	1199	**41**	1195
2	1198	**12**	1201	**22**	1198	**32**	1203	**42**	1193
3	1184	**13**	1200	**23**	1196	**33**	1198	**43**	1198
4	1184	**14**	1199	**24**	1194	**34**	1185	**44**	1197
5	1191	**15**	1196	**25**	1195	**35**	1182	**45**	1200
6	1197	**16**	1200	**26**	1190	**36**	1195	**46**	1196
7	1188	**17**	1195	**27**	1191	**37**	1194	**47**	1201
8	1203	**18**	1197	**28**	1186	**38**	1196	**48**	1201
9	1203	**19**	1191	**29**	1200	**39**	1192	**49**	1198
10	1181	**20**	1194	**30**	1201	**40**	1192	**50**	1196

4. Lowest Detection Limit

$$LD = \frac{2\sqrt{2}K \cdot \sqrt{n_B}}{t \cdot \varepsilon_i \cdot W} \qquad (4);$$

Lowest Detection Limit LD was computed by **Eq** (4). K was the confidence coefficient corresponding with confidence level(if K=1.645, confidence was 95％). Lowest Detection Limit LD was 0.221Bq/cm^2（t=600 s）.

Then the activity of the tritium surface contamination, A_s, was computed by **Eq** (3). After finishing development of the monitor, many capabilities were tested and the results of testing were listed[7] in the **Table 2**.

Table 2 Capability of the Monitor

Capability	**Result**
Plateau Length	>300V
Plateau Slope	＜1%/100V
Lowest Detection Limit	0.221 Bq/cm^2
Stability	0.56%/h
Variance Coefficient	2.88%
Weigh	~1.5 Kg
Power Supply	>20 h

V. Conclusion

The tritium surface contamination monitor with the gas-flow proportional counter is feasible. The detector adopted gold anticathode and gas methane (CH4) in the paper can detect effectively β-ray. It is not easy polluted by β-ray, which can reduce the background. So the detection efficiency is higher in the similar type monitors. Small volume, long time of power supply, and low background are fitted for in-site using. The monitor is able to be used in the lab or in the location, workroom of tritium lights and tritium cells produced, and nuclear power plant, et al.

But the monitor is designed only for the surface contamination, so the question of self-absorption in thick

samples is not solved. Another methods or technologies will be researched deeply, such as radioactivity relatively measure, etc.

References

1) NCRP. 'Tritium in the environment'. USA, Washington, DC: NCRP, 1979.
2) CHEN Mingxiu, et al. 'Design of YTH model of liquid scintillation tritium measuring instrument,' Nucl Electron Detect Technol, 2004, 24(6).
3) REN Tianshan, et al. 'Concentration and change of tritium in environmental water in China'. Chinese Journal of Radiological Medicine and Protection, 2001, 21(5).
4) CHEN Zhuzhou et al. 'Environment Radioactivity Survey and Estimate,' Beijing Atomic Energy Press, 1991.
5) YANG Huaiyuan et al. 'The Report of Environment Radio survey in Tianwan NPP (Nuclear Power Plant),' China Institute for Radiation Protection, 2003.
6) MU Keliang et al. 'Development of portable tritium surface contamination survey meter,' Nucl Electron Detect Technol, 2006, 26(4).
7) TUO Xianguo et al. 'A tritium measuring instrument with high detection efficiency,' Nuclear Technology, 2007, 30(4).
8) Shmayda, C.R. Shmayda, W.T.Monitoring 'tritium activity on surfaces: Recent developments.' Fusion Science and Technology, 2002, 41(3).
9) Hochel, R.C. Clark, E.A. 'Tritium characterization in cement and concrete.' Radioactive Waste Management and Environmental Restoration, 2000, 22(3).
10) Surette,R.A. Wood,M.J. 'Evaluation of instruments and techniques for monitoring of tritium-contaminated surfaces.'Fusion Technology, 1995, 28(3)

Journal of NUCLEAR SCIENCE and TECHNOLOGY, Supplement 5, p. 175–178 (June 2008)

Development of new Generation-type Multi-functional Electronic Personal Dosemeters

Tomoya Nunomiya[1*], Shigeru Abe[1], Iwao Matsumoto[1],
Tsuyoshi Sakamaki[1], Kei Aoyama[1], Takashi Nakamura[1,2]

[1]*Tokyo Factory, Fuji Electric Systems Co. Ltd.*
Fuji-machi 1, Hino, Tokyo 191-8502, Japan
[2]*Cyclotron and Radioisotope Center, Tohoku University*
Aramaki, Aoba, Aoba-ku, Sendai 980-8578, Japan

We have developed advanced new-generation-type small, light, multi-functional electronic personal dosemeters (NRF3 series) using silicon semiconductor radiation detectors for dose management of workers at nuclear power plants and accelerator facilities. These dosemeters are 60 x 78 x 27 mm^3 in size and approximately 103 to 115 g in weight, which are capable of measuring personal gamma-ray dose equivalent (NRF30), gamma-ray and neutron dose equivalents (NRF31) and gamma-ray and beta-ray dose equivalents (NRF34). These dosemeters are driven by a lithium battery, CR123A, continuously for about 2000 hours in normal use and can read out the time sequential dose equivalent data via infrared (IR) communication. In addition to IR communication method, NRF31 can read out the dose equivalent data via radio communication using an exclusive radio communication unit.

KEYWORDS: silicon semiconductor detector, personal dosemeter, NRF3 series, energy response

I. Introduction

The nuclear and accelerator facilities are now increasingly used, especially high-energy accelerators for various purposes such as nuclear physics, medical science, and engineering research. It is very important to monitor the personal dose equivalent of workers in such facilities by using a real-time personal dosemeter. As real-time personal dosemeter, the silicon semiconductor detectors are world-widely used in nuclear and accelerator facilities. We had already developed the real-time personal dosemeters using silicon detectors about ten years ago and they have been on sale as the NRN and NRY series from Fuji Electric Systems Co. Ltd. (FES). Here in this study, we have developed advanced new-generation-type real-time personal dosemeters using four-type silicon semiconductor detectors. The performance tests of the new type dosemeters have been performed using gamma rays and X rays of various energies at the Facility of Radiation Standard (FRS) of the Japan Atomic Energy Agency (JAEA), and monoenergetic neutrons of various energies at Fast Neutron Laboratory (FNL) of Tohoku University in Japan and using neutron sources at FRS of JAEA and FES.

II. Dosemeter Description

The new generation-type small, light, multi-functional electronic personal dosemeters (NRF3 series) have been developed, which are capable of measuring personal gamma-ray dose equivalent (NRF30), gamma-ray and neutron dose equivalents (NRF31) and gamma-ray and beta-ray dose equivalents (NRF34). The external appearance of the dosemeter, NRF31, is shown in **Fig. 1**. This dosemeter, NRF31, is 60 x 78 x 27 mm^3 in size and approximately 115 g in weight and is driven by a lithium battery, CR123A, continuously for about 2000 hours in normal use and can read out the time sequential dose equivalent data via infrared (IR) communication. It can read out each dose equivalent data using an exclusive radio communication unit.

Fig.1 Gamma-ray and neutron dosemeter, NRF31.

The personal dose equivalents, Hp(10), can be obtained using four types of silicon semiconductors; a gamma-ray sensor (detection energy from 35 keV to 6 MeV), a beta-ray sensor (from 300 keV to 2.2 MeV)[1)], a slow-neutron sensor (from thermal to 1 MeV) and a fast-neutron sensor (above 1 MeV)[1-4)]. The gamma-ray sensor is a 2 x 2 mm^2 photo diode and the beta-ray sensor is 3 x 3 mm^2 p-type amorphous silicon as shown in **Fig. 2**. The slow neutron sensor is 10 x 10 mm^2 p-type amorphous silicon on which a natural boron layer is deposited around an aluminum electrode to produce

∗Corresponding author : TEL +81-42-585-6171, FAX +81-42-581-9412, E-mail nunomiya-tomoya@fesys.co.jp

$^{10}B(n, \alpha)$ reaction as shown in **Fig. 3**. It is masked with 1.1-mm-thick B_4C compound (density; 1.17 g cm^{-3}, chemical composition; ^{nat}B: 40.0 wt%, Si: 48.9 wt%) for thermal neutron absorber. The fast neutron sensor is also a 10 x 10 mm^2 p-type amorphous silicon on which a polyethylene radiator of about 0.1 mm thickness is attached to produce recoil protons through the H(n, n) reaction. Low-resistivity silicon is used for neutron sensors to reduce the gamma-ray sensitivity by reducing the thickness of the depletion layer.

III. Performance Tests

The performance tests of the dosemeter were carried out complying with the IEC Standard IEC 61526 (1998)[5] and JIS Standard JIS Z 4312 (2003). The performance tests for gamma rays and X rays with various energies have been done at the FRS of the JAEA and tests for neutrons with various energy spectra have been done in the monoenergetic neutron field at FNL of Tohoku University in Japan[6] and using neutron sources at FRS of JAEA and FES. Test for beta rays is in preparation.

The X-ray and gamma-ray energies using in this work were from 32 keV to 158 keV (QI:0.8), 662 keV of ^{137}Cs, 1.25 MeV (average energy) of ^{60}Co and 6.12 MeV of ^{16}N. The dosemeter was put on a 40 x 40 x 15 cm^3 thick acrylic phantom and the source to dosemeter distance was fixed at 100 cm for X-ray, ^{137}Cs and ^{60}Co irradiation and 40 cm for ^{16}N irradiations.

The monoenergetic neutrons of 250, 550 keV, 1, 2, 5 and 15MeV were produced at FNL and the graphite-moderated thermal neutron field and a bare ^{252}Cf (average energy 2.3 MeV) source at JAEA and a bare ^{241}Am-Be (average energy 4.4 MeV) neutron source at FES were also used in this test. Experimental arrangement at FNL is shown in **Fig. 4**. These monoenergetic neutrons were produced by the $^7Li(p,n)$, T(p,n), D(d,n) and T(p,n) reactions from Li, D and T targets respectively by bombarding proton and deuteron. Absolute neutron fluence of the monoenergetic peak were measured by using a ^{235}U fission chamber just about 3-cm down-stream from the target at 0 degree to the incident beam direction, and as a relative fluence monitor, a H_2 proportional counter, was fixed at 45 degree about 200-cm distant from the target, where all equipments were fixed at 150-cm high from the floor level. In advance to the experiment, the counts of relative fluence monitor were characterized to the absolute neutron fluence given by the fission chamber. The distance between the target and the dosemeter was 40 cm. The dosemeter attached on an acrylic phantom of 40 x 40 x 15 cm^3 was irradiated to neutrons. The error of neutron fluence monitoring was estimated to be less than 10% and the room scattering component was evaluated within 5% as given in Ref. 6.

Irradiation tests at JAEA and FES were performed using neutron sources at 40 cm or 100 cm distance. Absolute values of neutron fluence were obtained from their neutron-emission rates. The errors of neutron fluence monitoring and the room scattering component were both estimated within 5%.

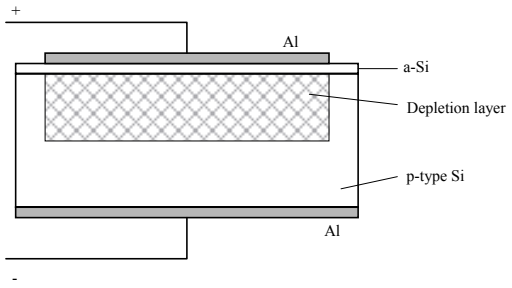

Fig. 2 Cross-sectional view of the beta-ray sensor

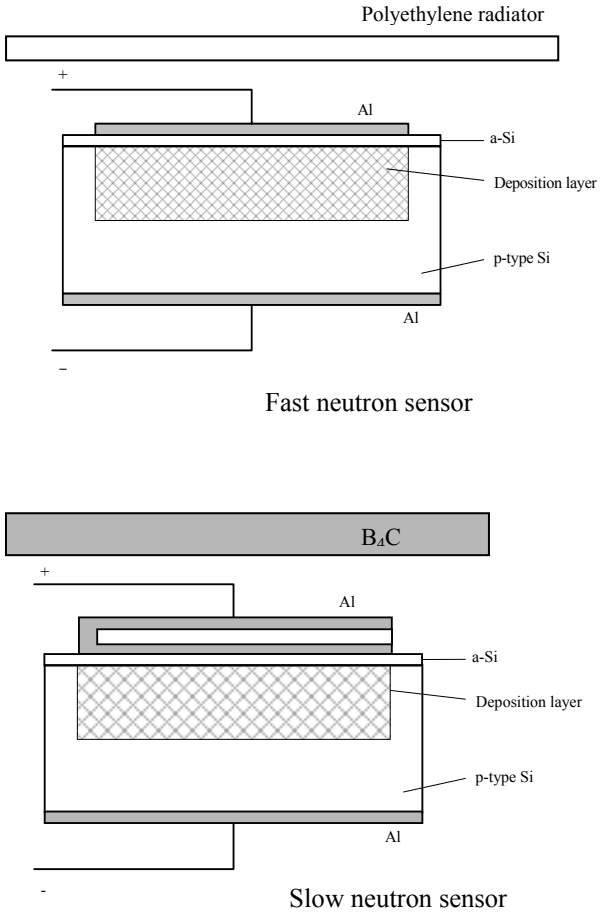

Fig. 3 Cross-sectional view of the fast and slow neutron sensors.

IV. Results and discussion

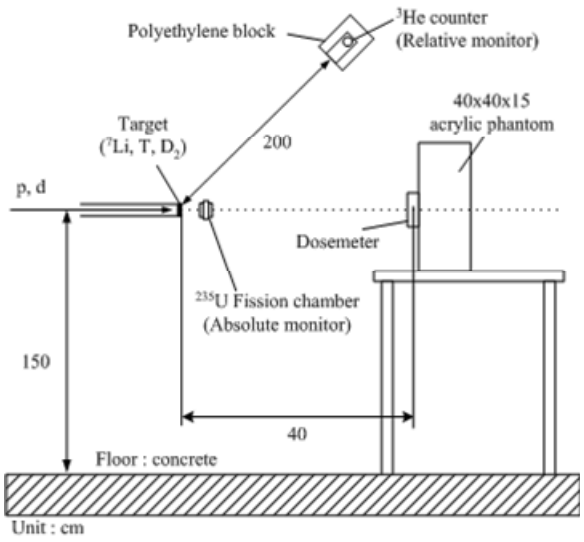

Fig. 4 Experimental arrangement at FNL.

The relative value of detection efficiencies, relative energy responses, normalized to ^{137}Cs gamma rays (662 keV) are shown in **Fig. 5. Fig. 5** indicates that these types of dosemeters, NRF30, NRF31 and NRF34, can evaluate the gamma-ray dose equivalent, Hp(10), within 15% deviation in the energy range from 50 keV to 6 MeV. Previous types of gamma-ray dosemeter, NRY2 series, can evaluate the Hp(10) within 20% deviation in the energy range from 60 keV to 6 MeV. The lower limit of gamma-ray and X-ray detection energy is 32 keV. Because the lower limit was 50 keV in the previous types of dosemeter, this 18 keV-reduced lower limit in these new dosemeters brought much improved result. We are improving this lower detection limit down below 20 keV.

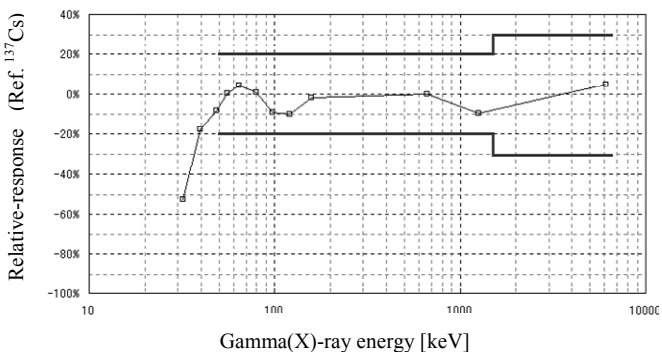

Fig. 5 Relative response of the NRF30 to gamma-ray energies from 32 keV to 6 MeV. Solid line is the energy response specification of NRF3 series.

The relative response to neutron energy normalized to ^{241}Am-Be source (4.4 MeV average energy) is shown in **Fig. 6** together with the first results[4]. It is found that this dosemeter, NRF31, has good response for neutron energy from about 100 keV to 4.4 MeV (^{241}Am-Be neutron source) within 50% difference to the Hp(10). Thermal neutron response and high-energy neutron response of 5 MeV, on the other hand, give overestimated values of about 30 times and about 2 times, respectively to Hp(10). The B_4C compound including ^{nat}B of 40 wt% (^{10}B of about 8 wt%) was placed in front of the thermal neutron sensor to decrease its sensitivity, but it is still much higher than expected. In order to further decrease this sensitivity, it is necessary to increase the B_4C thickness or to use the ^{10}B-enriched boron in the absorber. The higher response of 5 MeV is caused by charged particles of protons and alpha particles through the direct silicon reactions such as Si(n, p) and Si(n, α) reactions. It is necessary to investigate the optimized discrimination level for high-energy charged particles for better fitting to the Hp(10). We are now going to improve these responses in this energy range.

While on the other hand, this dosemeter using two silicon sensors has a great advantage having two optionally changeable parameters[1,2,4]. The actual neutron fields in various nuclear and accelerator facilities have different continuous energy spectra, therefore, this dosemeter can give Hp(10) within factor of 2 accuracy in these fields by adjusting these parameters, as already given in Ref. 3. This unique optional function in the NRF series dosemeters is quite useful to fit any facilities having different neutron spectra.

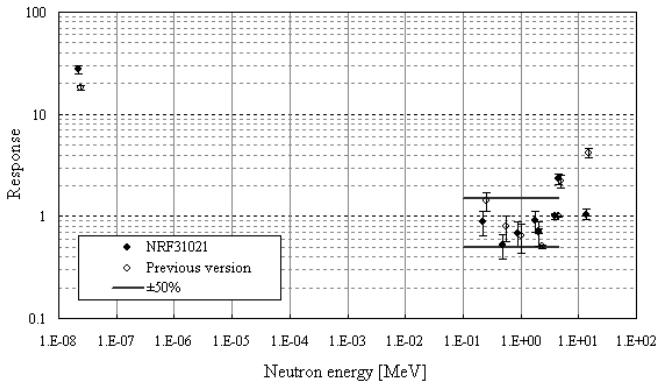

Fig. 6 Relative response of neutron dosemeter, NRF31 to neutron energies from thermal to 15 MeV together with the response of the previous version of NRF31 [4].

V. Conclusion

The NRF3 series have good responses for gamma-ray and X-ray from 50 keV to 6 MeV, which is within 20% difference to Hp(10). We are improving this 20% difference energy range between 20 keV and 6 MeV.

The NRF31 have good response for neutron energy from 100 keV to 4.4 MeV (^{241}Am-Be neutron source), which is within 50% difference to Hp(10). Thermal neutron response and high-energy neutron response of 5 MeV give overestimated values of about 30 times and about 2 times, respectively, to Hp(10).

This gamma-ray and neutron dosemeter, NRF31, can read out each dose equivalent data using an exclusive radio communication unit. This dosemeter can also be used as a

small and light-weighted area monitor of gamma rays and neutrons by characterizing it to ambient dose equivalent, H*(10). This dosemeters are useful equipments as area monitors in the facility where a large area monitor system can not be placed or in the accelerator facility where a number of radiation-producing spots exist from vending magnets, collimators/slits or other structures.

Acknowledgments

The authors wish to thank the staffs of JAEA and of Prof. Baba's Laboratory of Tohoku University for their great help during the testing, and wish to thank the staffs of the FNL for operating the Dynamitron accelerator.

Reference

1) M. Sasaki, T. Nakamura, N. Tsujimura, O. Ueda, T. Suzuki, Development and characterization of real-time personal dosemeter with two silicons, Nucl. Instr. and Meth. A. 418, pp.465-475 (1998).
2) T. Nunomiya1, T. Ishikura1, O. Ueda1, N. Tsujimura, M. Sasaki, T. Nakamura, Energy response for high-energy neutrons of multi-functional electronic personal dosemeter, Proceedings of 11th International Congress of the International Radiation Protection Association, Madrid, Spain, 23-28 May 2004.
3) N. Tsujimura, Characteristic evaluation and standard calibration of Si-type real-time personal dosemeter, Master's thesis of Tohoku University, Feb. 1993 [in Japanese].
4) T.Nunomiya, S.Abe, K.Aoyama, Development of advanced-type multi-functional electronic personal dosemeter, Proceedings of Tenth Symposium on Neutron Dosimetry, Progress in dosimetry of neutrons and light nuclei, Uppsala, Sweden, June 12-16 2006
5) International Standard, IEC 61526 first edition (1998).
6) M. Baba, M. Takada, T. Iwasaki, S. Matsuyama, T. Nakamura, H. Ohguchi, T. Nakao, T. Sanami and N. Hirakawa, Development of monoenergetic neutron calibration fields between 8 keV and 15 MeV, Nucl. Instr. and Meth. A. 376, pp.115-123 (1996).

Journal of NUCLEAR SCIENCE and TECHNOLOGY, Supplement 5, p. 179–182 (June 2008)

Construction of a High-quality Voxel Model VKH-Man Using Serially Sectioned Images from Visible Korean Human Project in Korea

Sang Hyoun CHOI[1], Jong Hwi JEONG[2], Sungkoo CHO[2], Min Suk CHUNG[3], Hyun Do HUH[1], Woo Chul KIM[1], Kun-Woo CHO[4], and Chan Hyeong KIM[2*]

[1]*Department of Radiation Oncology, College of Medicine, Inha University, Incheon, Korea*
[2]*Department of Nuclear Engineering, Hanyang University, Seoul, Korea*
[3]*Department of Anatomy, Ajou University School of Medicine, Suwon, Korea*
[4]*Korea Institute of Nuclear Safety, Daejeon, Korea*

In this study, a high-quality voxel model of a Korean adult male was constructed using the Visible Korean Human (VKH) project's serially sectioned anatomical images. The VKH images are transverse color photographs obtained from the serial sectioning of an adult Korean male cadaver (164 cm, 55 kg) at 0.2 mm intervals. A total of 28 organs and tissues were segmented with the color photographic images. The height and weight of the constructed voxel model, VKH-Man, is 164 cm and 59.6 kg, respectively. The voxel resolution of the model is 1.875 mm x 1.875 mm x 2 mm. The developed model was implemented into a Monte Carlo particle transport simulation code, MCNPX, to calculate the organ and tissue doses and, thereby, the effective doses, and the calculated values were compared with the values obtained from other computational models (KTMAN-2, VIP-Man, and ICRP-74).

KEYWORDS: dosimetry, effective dose, organ dose, voxel model, Monte Carlo

I. Introduction

The tomographic model, also known as the voxel model, was first reported by Gibbs *et al.* in the middle 1980s and used for the calculation of effective doses for dental radiology examinations[1)]. Since then, most voxel models have been constructed using CT and MR images[2-4)].

In general, CT and MR images provide fairly good information for accurate delineation of organs and tissues, but it is very difficult to distinguish some organs and tissues that share similar properties with neighboring tissues or that are in continuous movement (e.g., ovaries, pancreas, oesophagus, adrenals, thymus, small intestine, heart) [5-6)]. Consequently, subjective decisions are made in the process of delineation, which can impair the integrity of the developed voxel model. Recently, Xu *et al.*[7)] constructed a high-quality voxel model, VIP-Man, based on serially sectioned anatomical images of a male cadaver, but the model represents a very large person (186 cm and 103 kg), and thus cannot be used to represent a Korean male.

In the present study, a high-quality voxel model was constructed using the Visible Korean Human (VKH) project's[8)] serially sectioned anatomical images. The VKH images are high-resolution transverse color photographs obtained from the serial sectioning of an adult Korean male cadaver (164 cm, 55 kg) at 0.2 mm intervals. The developed model was implemented into a Monte Carlo particle transport simulation code, MCNPX[9)], to calculate the organ and tissue doses and, thereby, effective doses, and the calculated values were compared with the values obtained from other computational models (KTMAN-2, VIP-Man, and ICRP-74) [4, 7, 10)].

II. Methods

1. VKH anatomical images

The VKH anatomical images were obtained from the cadaver of a 33-years-old Korean male (164 cm, 55 kg), who showed no significant pathological findings apart from pneumonia and leukemia. The cadaver, which was embedded and frozen, was serially sectioned at 0.2 mm intervals with a cryomacrotome and photographed with a high-resolution digital camera (DSC560, Kodak; resolution: 3,040 x 2,008). A total of 8,590 photographic images were obtained for the whole body of the cadaver. The images were color images of very high resolution (0.1875 mm x 0.1875 mm), making it possible to delineate organs and tissues, including very small anatomical structures such as blood vessels and intestinal walls, very accurately.

2. Segmentation of organs and tissues

In this study, the color anatomical images were selected for every 2 mm interval, so that 850 images were selected out of the total of 8,590. The organs and tissues were segmented using both automatic and manual processes, as necessary. The organs and tissues distributed through the whole body or clearly distinguished by the RGB values were segmented automatically with Photoshop 7.0™ and Interactive Data Language (IDL 5.6). The eyes, lenses, bones, skin, muscle, colon, small intestine, ET region, red bone marrow, and gall bladder were automatically segmented. The organs that could not be segmented automatically were segmented manually using a screen digitizer (Model:

*Corresponding Author,Tel. +82-2-2220-0513; Fax. +82-2-2220-4057;E-mail: chkim@hanyang.ac.kr

CINTIQ 15X, WACOM Co., Ltd) and Photoshop 7.0™'s Magnetic Lasso tool. This tool marks the region of selection by identifying differences of color. Manual segmentation was employed for the thyroid, bladder, prostate, salivary glands, adrenals, esophagus, spleen, stomach, lungs, brain, liver, thymus, pancreas, gonads, kidneys, heart, oral mucosa, and blood vessels.

The red bone marrow was segmented using both the CT images and color anatomical images. First, the entire skeletal system was segmented with the CT images. Then, the red bone marrow was separately segmented according to the RGB values of the color anatomical images within the region of the skeletal system. The skeletal system was divided into nine sub-regions, and the red bone marrow was segmented considering its distribution in those skeletal-system sub-regions (ICRP-70[11]).

The thickness of skin is known to be 1.47 – 2.45 mm (ICRP 89[12]), and cannot be accurately defined in a voxel model unless the voxel resolution is unacceptably high. In this study, the skin was represented simply by adding one layer of voxels to the surface of the whole body.

A total of 28 organs and tissues were segmented with the color anatomical images. After the segmentation, the resolution of the serially sectioned images was reduced down to 1.875 mm x 1.875 mm considering the computing speed and memory of the computers in use. Consequently, the voxel resolution of the final model is 1.875 mm x 1.875 mm x 2 mm, which is adequate for accurate calculation of organ and tissue doses.

3. Monte Carlo simulations

The developed voxel model was implemented in a Monte Carlo particle transport simulation code, MCNPX [9], for the calculation of the organ and tissue doses and, thereby, effective doses. The three-dimensional array of the voxel model was converted into a format appropriate to MCNPX. The organ- and tissue-averaged absorbed doses and effective doses were calculated per unit air kerma. The considered irradiation geometries were broad parallel photon beams of anterior-posterior (AP), left lateral (LLAT) and posterior-anterior (PA) with photon energies of 0.015 - 10 MeV. The energy deposition tally of track-length estimation, *F6, was used to calculate the organ and tissue doses. The statistical errors in the organ and tissue doses were less than 5% for all of the cases considered in this study, except for 0.015 MeV, for which the statistical errors were as large as 100%.

III. Results and Discussion

Fig. 1 shows the developed model, VKH-Man. The height and weight of the model are 164 cm and 57.6 kg, respectively. The voxel resolution is 1.875 mm x 1.875 mm x 2 mm. The model is composed of 247 x 141 x 850 voxels (= 29,602,950 voxels), which corresponds to 489.307, 279.321, and 1,772.59 cm in the x, y and z directions, respectively. The developed model contains a total of 28 organs and tissues, the masses of which are shown in **Table 1**. The dose conversion coefficients, that is, the organ- or tissue-averaged absorbed dose per unit air kerma free-in-air (D_T/K_a), were calculated using VKH-Man, and the calculated values were compared with the values from a Caucasian adult male model, VIP-Man, and a Korean adult male model, KTMAN-2. The calculated values were also compared with the values from ICRP-74[10], in which the dose conversion coefficients were calculated with a set of MIRD-type computational models[13]. **Fig. 2** shows the dose conversion coefficients for some of the selected organs and effective doses.

Fig. 1 The voxel model VKH-Man developed in this study

Table. 1 Mass of organs and tissues segmented in VKH-Man

Organ	Mass (g)	Organ	Mass (g)
Thyroid	18.8	Bladder	39.2
Lens	0.9	Thymus	28.7
Prostate	13.0	Muscle	19934.3
Salivary glands	75.8	Pancreas	108.5
Adrenal	8.5	Gonads	24.3
Oesophagus	34.0	Small intestine	253.1
Spleen	980.4	Colon	352.2
Stomach	164.8	Eyes	19.2
Lung	1476.9	Kidney	384.2
Red bone marrow	929.9	Extrathoracic tissue	63.0
Bone	7293.7	Gall bladder	104.4
Skin	3656.9	Heart wall	513.1
Brain	1701.6	Oral mucosa	19.1
Liver	1931.3	Blood	220.3

The calculated values of the organ and tissue doses and effective doses were very reasonable when compared with the values from the other models. In general, the differences among the organ and tissue doses were very small for the AP irradiation geometry. For the LLAT geometry, the differences were somewhat larger, and VKH-Man showed higher doses than the other models in most of the cases, seemingly due to the fact that the arms of VKH-Man are shifted backward, meaning that the internal organs in the trunk are less shielded by the arms for the LLAT geometry.

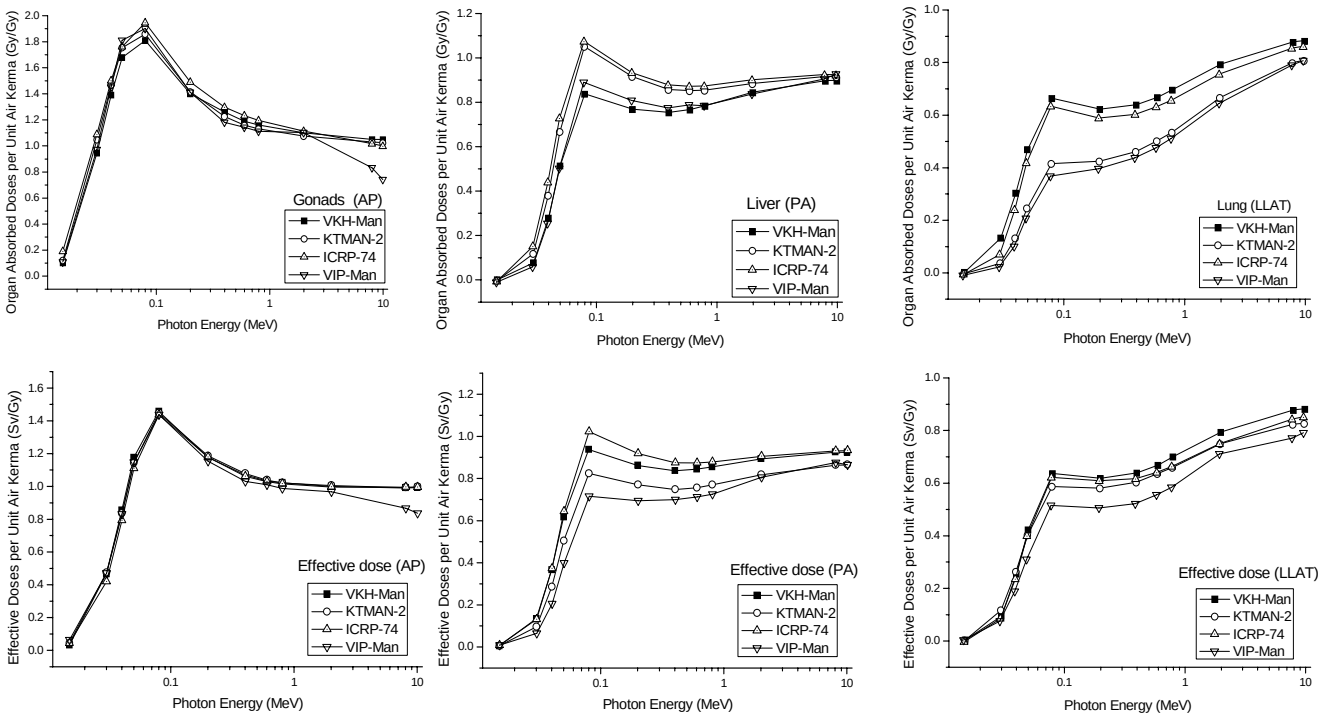

Fig. 2 The calculated values of organ-averaged absorbed doses and effective dose for VKH-Man, KTMAN-2, VIP-Man, and ICRP-74

The calculated values of the effective doses were also in good agreement for all of the models considered in this study. The difference was less than 10% for the AP and LLAT geometries and less than 30% for the PA geometry, for photon energies greater than 0.03 MeV. VIP-Man always showed the smallest values for the effective dose, mainly due to the fact that VIP-Man is much larger (186 cm, 104 kg) than the other models employed in this study.

IV. Conclusions

In this study, a high-quality voxel model of a Korean adult male was constructed using the Visible Korean Human (VKH) project's serially sectioned color anatomical images. The height and weight of the developed voxel model are 164 cm and 59.6 kg, respectively. The voxel resolution of the current model is 1.875 mm x 1.875 mm x 2 mm, but the resolution can be improved to 0.1875 mm x 0.1875 mm x 0.2 mm as necessary for any region of interest.

Acknowledgement

This study was supported by the Korean Ministry of Science and Technology through ERC (RII-2000-067-03002-0), BAERI (M20508050003-05B0805-00310), and Korea Institute for Nuclear Safety (KINS).

References

1) S. J. Gibbs, A. Pujol, T. S. Chen and A. W. Malcolm, "Computer-Simulation of Patient Dose from Dental Radiography," J. Dental Research, 63, 209 (1984).
2) G. Zubal, C. R. Smith, E. O. Smith, Z. Rattner, G. Gindi, P. B. Hoffer, "Computerized three-dimensional segmented human anatomy," Med. Phys. 21[2] (1994).
3) Kramer, J. W. Vieira, H. J. Khoury, F. R. A. Lima, and D. Fuelle, "All about MAX: a male adult voxel phantom for Monte Carlo calculations in radiation protection dosimetry," Phys. Med. Biol. 48, 1239-1262 (2003).
4) C. Lee, C. Lee, S. Park, J. Lee, "Development of the two korean adult tomographic computational phantoms for organ dosimetry," Med. Phys. 33[2] (2006).
5) M. Zankl, A. Wittmann, "The adult male voxel model "Golem" segmented from whole-body CT patient data," Radiat. Environ. Biophys. 40:153−62 (2001).
6) M. Caon, "Voxel-based computational models of real human anatomy: a review," Radiat. Environ. Biophys. 42:229–.235 (2004).
7) T. C. Chao, A. Bozkurt, X.G. Xu, "Conversion Coefficient based on the VIP-Man anatomical model and EGS4-VLSI code for external monoenergetic photons from 10 keV to 10 MeV," Health Phys., 81[2]:163-183 (2000).
8) J. S. Park, M. S. Chung, J. Y. Kim, H. S. Park, "Visible Korean Human: Another trial for making serially sectioned images," Medical Imaging Vol.4681[3] : 171-183 (2002).
9) D. B. Pelowitz, MCNPX User's Manual Version 2.5.0, NM: Los Alamos National Laboratory, Los Alamos, LA-CP-05-0369 (2005).
10) International Commission on Radiological Protection, Conversion Coefficient for use in Radiological Protection against External Radiation, ICRP Publication 74, Pergamon Press, Oxford (1996).
11) International Commission on Radiological Protection, Basic Anatomical and physiological Data for use in Radiological Protection: The Skeleton, ICRP Publication 70, Pergamon Press, Oxford (1994).
12) International Commission on Radiological Protection, Basic

Anatomical and physiological Data for use in Radiological Protection: Reference Values, ICRP Publication 89, Pergamon Press, Oxford (2003).
13) R. Kramer, M. Zankl, G. Williams and G. Drexler, "The calculation of dose from external photon exposures using reference human phantoms and Monte-Carlo methods, Part 1: The male (ADAM) and female (EVA) adult mathematical phantoms," GSF Bericht S-885, GSF-National Research Center for Health and Environment (1982).

Journal of NUCLEAR SCIENCE and TECHNOLOGY, Supplement 5, p. 183–186 (June 2008)

Dependence of the Glass Badge response on the different calibration phantoms

Daisuke MAKI*, Tatsuya SAKAI, Yasuhiro KOGUCHI, Hiroyuki OHGUCHI,
Wakako SINOZAKI, and Norimichi JUTO

Oarai Research Center, Chiyoda Technol Corporation, 3681, Narita-cho, Oarai-machi, Higashi-ibaraki-gun, Ibaraki 311-1313, Japan

Chiyoda Technol Corporation provides a glass badge including the GD-450 for photon dosimetry and the WNP composed of a poly-allyldiglycol carbonate, the CR39, for neutron dosimetry. For maintenance of quality on monitoring service, it is very important to establish the dose estimation formula for a calibration phantom. In this study, we evaluated the GD-450 response for photon energy range from 10 keV to 1250 keV and the WNP response for neutron energy range from thermal to 15 MeV, both by experiment and Monte Carlo calculation. The dependence of the Glass Badge response was clarified on three different calibration phantoms.

KEYWORDS: Glass Badge, Dosimetry, Phantom, Monte Carlo calculation

I. Introduction

The Radiophoto-Luminescence Glass dosemeter (GD-450) using a silver activated phosphate glass was commercially supplied by our company in October 2000.We have provided as glass badges by including the GD-450 for photon dosimetry and the Wide Range Neupit (WNP) composed of poly-allyldiglycol carbonate, the CR39, for neutron dosimetry. In order to establish the dose equivalent calculation formula for calibration of personal dosemeters, the Polymethyl Methacrylate (PMMA) phantoms have ever been used, but the ISO water slab phantom was added in Japan under the revision of Japanese Industrial Standards (JIS) in December 2005[1]. Furthermore, it was prescribed that the response of personal dosemeters to photons and neutrons should be calibrated with a water phantom, although it is possible to use a PMMA phantom in energetic gamma-ray calibration such as 662 keV. Therefore, we have been providing dose equivalent data with the dose equivalent calculating formula evaluated from the dosemeter responses which were made from the irradiation data using the water phantom since October 2006.

Here in this study, we evaluated the GD-450 response for photon energy range from 10 keV to 1250 keV and the WNP response for neutron energy ranges from thermal to 15 MeV, both by experiment and Monte Carlo calculation.

II. Glass Badge

1. Structure of Glass Badge

GD-450 is a Radio-Photoluminescence (RPL) glass dosemeter having five filters made of two plastic (called as E1 and E2), an aluminum (called as E3), a copper (called us E4) and a tin (called as E5) as shown in **Fig. 1**. Metallic filters are ring-shaped for improving the directional dependence. GD-450 can give the dose equivalent by measuring the amount of RPL which is excited by ultraviolet rays from an N_2 gas laser for photons of energies from 10 keV to 10 MeV and beta rays of energies from 300 keV to 3 MeV. WNP is composed of a poly-allyldiglycol carbonate, the CR39, attached by Boron-Nitride (BN) sheet as an alpha-particle converter and Polyethylene (PE) sheet as a recoil proton radiator as shown in **Fig. 2**. Etch-pits generated by charged particles produced by the $^{10}B(n,\alpha)$ reaction and H(n,p) reaction appear by etching the irradiated CR39 with alkaline solution. The dose equivalent is obtained by counting the number of etch-pits per unit area (etch-pit density) with a microscope.

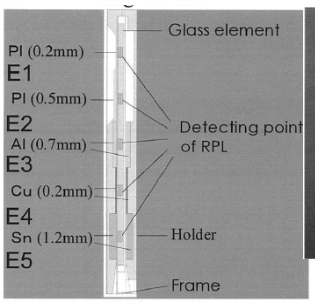

Fig. 1 Cross-sectional view of GD450

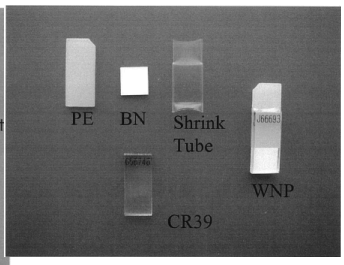

Fig. 2 WNP and its compositions

2. Dose Calculation by Glass Badge

Glass Badge is irradiated on the calibration phantoms for evaluating the correction factors because they are dependent on the phantom type due to a change of the amount of RPL or etch-pit density.

In Japan, three types of calibration phantom are used, that is, the PW (ISO water slab phantom, 30×30×15 cm^3), the P30 (PMMA, 30×30×15 cm^3) and the P40 (PMMA,40×40×15 cm^3) phantoms[1]. Thus, the irradiation was done using these phantoms.

III. Experiments

1. GD-450

For GD-450, the correction factors are evaluated from "Filter Sensitivity (FS)". FS value is estimated according to the following processes, 1) Calculating net amount of RPL of five elements of GD-450, E1 to E5, for each energy, 2)

*Corresponding Authors, Tel: +81-29-266-3113, FAX: +81-29-264-9031, E-mail: maki-d@c-technol.co.jp

Dividing 1) by air kerma to obtain net amount of RPL per air kerma (called as response) and 3) Dividing the responses of five elements for each energy by the response of E5 to an energy of a ^{137}Cs source (called as FS).

We irradiated GD-450 attached on the P40 and the PW phantoms by using X-ray beams of effective energies from 12 keV to 200 keV from a X-ray generating machine, 662 keV gamma rays from a ^{137}Cs source and 1250 keV gamma rays from a ^{60}Co source. Irradiations of free air kerma were done from 0.88 to 4.39 mGy with the P40 phantom and from 1.56 to 6.06 mGy with the PW phantom. Irradiation distance between a source and GD-450 was set at more than 2 m enough to maintain a charged particle equilibrium (CPE) and X-ray beams were to be considered as parallel. However, in gamma ray irradiation, two build-up plates (made of 2 mm and 4 mm thick PMMA for a ^{137}Cs and a ^{60}Co sources, respectively)[2] were used for the condition of CPE. The followings were done with FS values.

2. WNP

We irradiated WNP attached on the P30 and the PW phantoms by using thermal neutrons generated from a graphite pile at JAERI (Japan Atomic Energy Research Institute, now JAEA) and mono-energetic neutrons of 144, 565 keV and 5, 15 MeV generated by accelerators at AIST (Advanced Institute of Industrial Science and Technology). Neutron fluence was 2.8×10^7 (cm^{-2}) for thermal neutrons and 1.0×10^7 (cm^{-2}) for mono-energetic neutrons. The followings were done with etch-pit density of CR39 only attached on the BN converter to observe the effect of low energy neutrons backscattered from a phantom.

Ⅳ. Monte Carlo Calculations

1. GD-450

Fig. 3 is the schematic diagram for Monte-carlo simulation to calculate the responses of GD-450 and WNP. In the calculation, GD-450 was simplified as a glass detector with filters. We assumed a parallel beam irradiation on the phantom and the distance between a source plane and phantom surface was set at 2 m. In this study, we calculated the FS value and backscattered fraction, that is albedo, each from the P30, P40 and PW phantoms by using the PHITS code developed by Iwase et al.[3] and the photon cross section library, MCNPLIB02[4].The calculations were done for mono-energetic photons from 10 keV to 1250 keV. We first calculated the energy deposition in each element using the T-Heat tally which is equivalent to the F6:P tally in the MCNP4C2 code using the kerma approximation methods[5]. Then, we calculated the air absorbed dose in a spherical monitoring volume of 1 cm radius as shown in **Fig. 3**. This volume was set at a position behind the build-up plate and had a negligibly small contribution of photons backscattered from the phantom. Assuming that the CPE could be achieved and air absorbed dose was equal to the air kerma in the calculated energy ranges, we obtained the FS values from the T-Heat tally. The backscattered fraction from a phantom, that is albedo, was obtained from the current tally on a phantom surface behind E1 as follows.

$$f = \frac{y}{x}$$

where, x is the current of incident photons and y is the current of photons backscattered from a phantom.

2. WNP

In the calculation, the WNP was simplified as the CR39 with a BN converter and a PE radiator. We assumed a parallel beam irradiation on the P30 and the PW phantoms and the irradiation distance was set at 50 cm. Thermal neutron spectrum of the Maxwell distribution having mean energy of 0.025 eV and mono-energetic neutron spectra of 144, 565 keV and 5, 15 MeV were used in the calculations. We used the MCNP4C2 code[5], neutron cross section library ENDF-60[4] and S(α,β) library[4] to do precise transport for thermal neutrons in water or PMMA. The S(α,β) data for polyethylene was used instead of that for the PMMA phantom[6].

In order to compare between experimental and calculation values, we calculated neutron fluence at a surface of CR39 on the BN converter and the alpha-particle yields from ^{10}B(n,α) reactions using microscopic cross section based on JENDL3.3[7], as follows

$$R(E) = N_B \frac{\sum_{i=1} \sigma_a(E_i)\phi(E_i)}{\Phi_0(E)}$$

where, $R(E)$ is ^{10}B(n,α) reaction yields per incident neutron fluence, N_B is the number of ^{10}B in BN converter, $\phi(E_i)$ is neutron fluence in ith energy bin, $\sigma_a(E_i)$ is microscopic cross section of ^{10}B(n,α) reaction according to $\phi(E_i)$ and $\Phi_0(E)$ is incident neutron fluence.

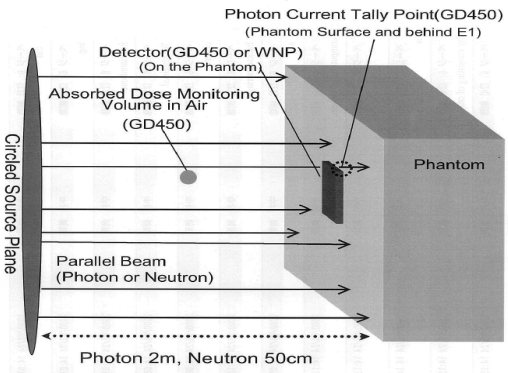

Fig. 3 Schematic diagram for calculation

V. Results and Discussions

1. GD-450

Fig. 4 shows the ratio of backscattered fractions of the P30 and PW to that of the P40 phantom. In **Fig. 4**, the amount of backscattered photons slightly decreases with those size of the P30 and the P40 phantom, while that is larger in the PMMA than in the PW phantom. **Table 1** shows the density of atoms and electrons in PMMA and PW

phantom. **Table 1** shows that the density of electrons is smaller for the PW than for the PMMA phantom. The main reaction occurred in these phantoms is Compton scattering in this energy range. Because the cross section of the Compton scattering is proportional to the number of electrons, the amount of backscattered photons is larger in the PMMA than in the PW phantom.

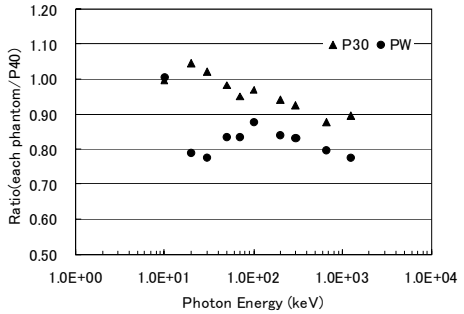

Fig. 4 Ratio of the backscattered fractions of the P30 and PW to that of the P40 phantom

Table 1 Atom and electron density of phantoms

Compounds	PMMA		PW	
	Atom density (n/cm^3)	Electron density (n/cm^3)	Atom density (n/cm^3)	Electron density (n/cm^3)
C	3.58×10^{22}	2.15×10^{23}	-	-
H	5.73×10^{22}	5.73×10^{22}	6.69×10^{22}	6.69×10^{22}
O	1.43×10^{22}	1.15×10^{23}	3.34×10^{22}	2.68×10^{23}
Total	1.07×10^{23}	3.87×10^{23}	1.00×10^{23}	3.34×10^{23}

Fig. 5 shows the experimental and calculated FS values of five elements. The experimental FS values are greater in the PMMA than those in the PW phantom. This is because the energy deposition to element decreases due to the decrease of the photons backscattered from the PW phantom. While, the calculated FS values of E1 and E2 are greater in the PMMA phantoms than in the PW phantom, no differences of the FS values for E3, E4 and E5 are seen between the PMMA and the PW phantoms. This may be due to the following two reasons.

1) Unlike ring-shaped metallic filter, for E1 and E2, photons backscattered from a phantom are absorbed directly by a glass detector (**Fig. 1**). Therefore, E1 and E2 might be influenced strongly by photons backscattered from a phantom and 2) Calculated air kerma contains photons backscattered from a phantom and strictly saying it is not a free air kerma. Thus, calculated air kerma might be larger than free air kerma. Therefore, the dependence of energy deposition in five elements might be canceled out by 1) and 2) in the FS calculation and FS values of E1 and E2 strongly depend on the phantom type.

In **Fig. 5**, the calculated FS values show better agreement with the experimental values, as the atomic number of filter becomes large. This may be due to the following two reasons. 1) In case of low atomic number filter i.e. E1 and E2, weakly penetrating photons backscattered from a phantom are absorbed directly by a glass detector without photoelectric absorption in the filter and will produce inhomogeneous distribution of color center in the element volume due to too short ranges of secondary electrons. While, in case of filters of high atomic number i.e. E3, E4 and E5, the number of weakly penetrating photon will decrease due to the effective photoelectric absorption in those filters. As the results, relative ratio of strongly penetrating photons will increase and strongly penetrating photons will produce color center uniformly in the element volume and 2) The RPL detection was done around a center of glass elements, while on the contrary, energy deposition in glass elements were calculated in all element volume by using the kerma approximation method, therefore, the amount of energy deposition evaluated by above two methods might not be agree due to color center distribution in the element volume. In other words, filter dependency of the degree of agreement between experimental and calculated FS values can be understood with color center distribution in the element volume.

2. WNP

Fig. 6 shows the ratio of experimental and calculated alpha-particle yields of the PW to those of the P30 phantom. The experimental and calculated values show good agreement with 95 % confidence level. **Fig. 6** also shows that no difference of alpha-particle yields can be seen between these two phantoms.

Ⅵ. Conclusion

We evaluated the Glass Badge response for three types of phantoms, the PW (ISO water slab phantom, $30\times30\times15$ cm^3), the P30 (PMMA, $30\times30\times15$ cm^3) and the P40 (PMMA ,$40\times40\times15$ cm^3) with experiment and Monte Carlo calculation. FS values of GD-450 changed with phantom material and its size due to the change of photons backscattered from a phantom. In case of WNP, no difference of alpha-particle yields can be observed for the P30 and the PW phantom.

Acknowledgement

The authors wish to thank AIST and JAEA for irradiations of WNP. The authors wish to thank Dr. Koji Niita of Research Organization for Information Science & Technology (RIST) for teaching us how to use the PHITS code and Prof. Emeritus Takashi Nakamura for giving us many advices to complete this paper.

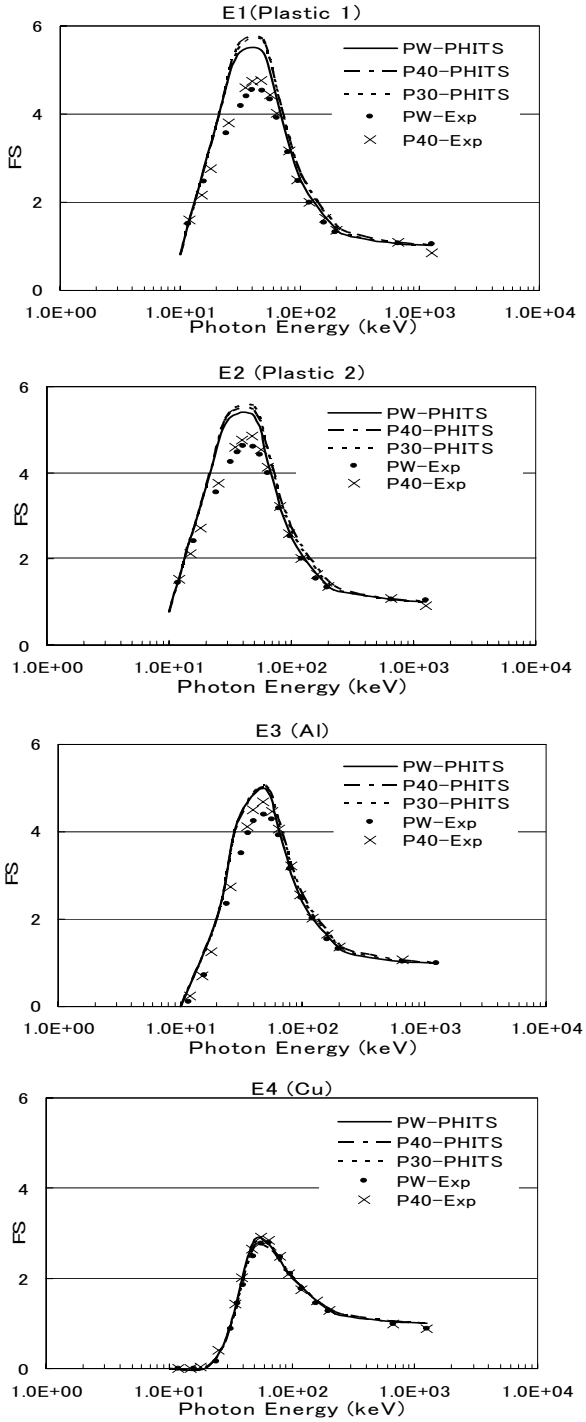

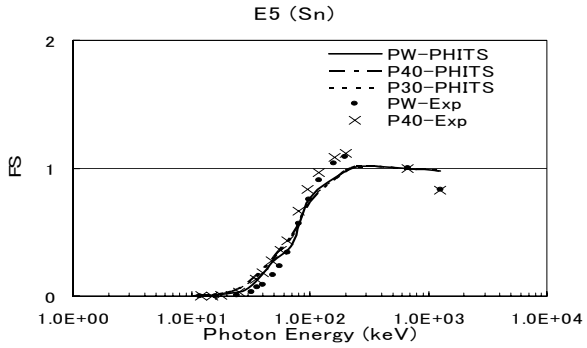

Fig. 5 Experimental and calculation FS values for E1, E2, E3, E4 and E5 filters

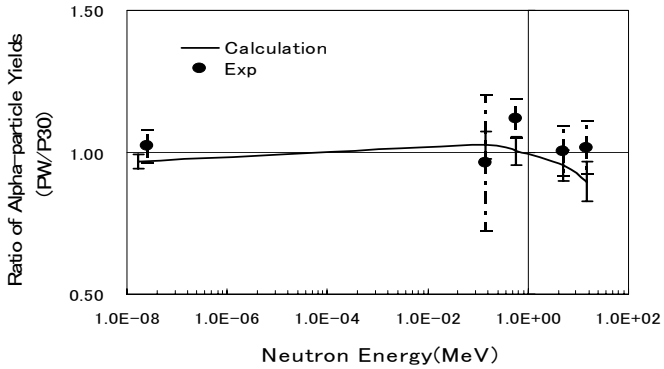

Fig. 6 Ratio of experimental and calculated alpha-particle yields of the PW to those of the P30 phantom

References

1) Japanese Industrial Standards: calibration phantom for personal dosemeters, JIS Z4331, Japanese Standards Association (2005), [in Japanese].
2) International Standard: X and gamma reference radiation for calibrating dosemeters and doserate meters and for determining their response as a function of photon energy-Part3, ISO4037-3(first edition), International Organization for Standardization (1999).
3) H.Iwase, K.Niita, T.Nakamura, "Development of General-Purpose Particle and Heavy Ion Transport Monte Carlo Code," *J.Nucl. Sci. Technol.*,**39,** 1142 (2002).
4) *RSICC DATA LIBRARY COLLECTION MCNPDATA*, DLC-200, Los Alamos National Laboratory (2001).
5) J.F.Briesmeister(Ed), *MCNP-A General Monte Carlo N-Particle Transport Code Version 4C-Manual*, LA-13709-M, Los Alamos National Laboratory (2000).
6) N.E.Hertel, J.C.McDonald, "Calibration of neutron personnel dosemeters in terms of the ICRU operational quantities, "*Radiat.Prot.Dosim.,* **37**[3] ,149-156 (1991).
7) K. Shibata, T. Kawano, T. Nakagawa et al., "Japanese Evaluated Nuclear Data Library Version 3 Revision-3: JENDL-3.3," *J. Nucl. Sci. Technol.*, **39**, 1125 (2002)

Journal of NUCLEAR SCIENCE and TECHNOLOGY, Supplement 5, p. 187–190 (June 2008)

Development of Wide-energy Range X/γ-ray Survey-meter

Seini YAMAMURA[1*], Takashi NAKAMURA[1,2], Katsuhito ITOU[1], Osamu HATAKEYAMA[1], and Kaoru MASUI[1]

[1]*Tokyo Factory, Fuji Electric Systems Co. Ltd. Fuji-machi 1, Hino, Tokyo 191-8502, Japan*
[2]*Cyclotron and Radioisotope Center, Tohoku University, Aramaki, Aoba, Aoba-ku, Sendai 980-8578, Japan*

The X-ray radiation produced from various X-ray generating machines has energies between 8 keV to 300 keV and for monitoring environmental gamma rays, the energy range to be measured is from 40 keV up to 1500 keV. We developed a wide-energy range X/γ-ray survey-meter , which can measure ambient dose equivalent H*(10), covering the energy range of 8 keV to 1500 keV by dividing the two energy ranges, from 8 to 300keV for X-ray mode and from 40 to 1500keV for γ-ray mode, both energy responses are within 25% from 10keV up to 300keV and from 50keV up to 1500keV using a 12.7mm diameter by 12.7mm thick NaI(Tl) scintillator.

KEYWORDS: NaI(Tl), energy compensation, G-Function, H*(10)

I. Introduction

The X-ray radiation produced from various X-ray generating machines, which are widely used in medical purposes such as X-ray CT, mammography, X-ray radiographs of chest, teeth, stomach and so on, has energies between 8 keV to 300 keV. For measuring the stray X-ray radiation leaked from these machines, the conventional ionization-chamber type survey-meter has been world-widely used. But, this type of survey-meter has poor accuracy coming from low sensitivity, especially almost no sensitivity to X-rays of energy below 25 keV.

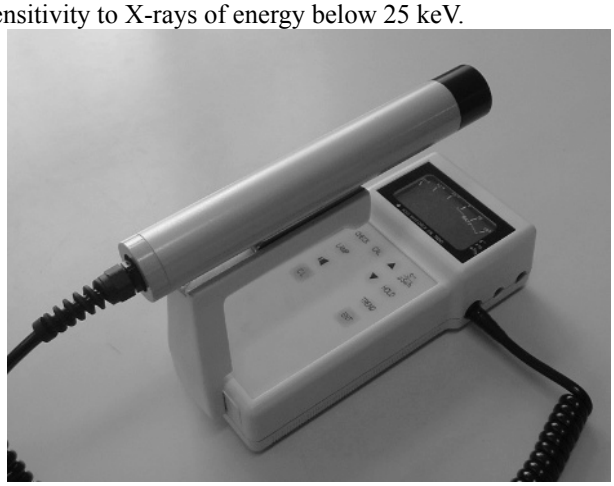

Fig. 1 Outlook of wide-energy range X/γ-ray survey-meter

We have already developed a NaI(Tl) scintillation-type survey-meter, NHC4, which can measure ambient dose equivalent H*(10) with high sensitivity for X-rays in the energy range of 10 keV to 200 keV up to 4 μSv/h[1)].

Here in this work, we further developed a wide-energy range X/γ-ray survey-meter, which can measure ambient dose equivalent H*(10), covering the energy range of 8 keV to 1500 keV by dividing the two energy ranges, from 8 to 300keV for X-ray mode and from 40 to 1500keV for γ-ray mode, using a 12.7mm diameter by 12.7mm thick NaI(Tl) scintillator with thin aluminum window. **Fig. 1** gives the outlook of the wide-energy range X/γ-ray survey-meter.

II. Materials and Methods

1. Detector Probe

Fig. 2 shows the outlook of the detector probe and the inner structure. The NaI(Tl) scintillator has 12.7mm diameter and 12.7mm thick cylinder of which the surface is covered with a aluminum case to shut off visible light.

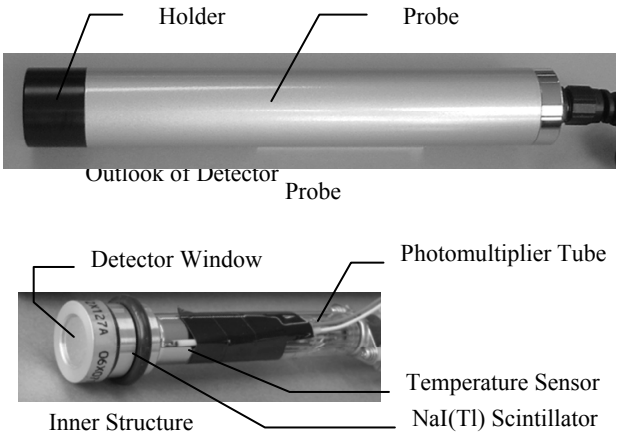

Fig. 2 Outlook of detector probe and the inner structure

This detector size was selected to have higher sensitivity for photons up to 1500 keV energy and better directional dependence. In order to measure low energy X rays down to 8 keV, a thin aluminum window was attached to the top of the aluminum case, considering high transmission efficiency for low energy photons. The outside surface of the scintillation detector is covered additionally with a holder made of plastic resin to protect the detector window. The scintillator coupled with the photomultiplier, R647 (Hamamatsu Photonics K.K.), are encapsulated with a temperature sensor into a probe made of aluminum.

*Corresponding Author, Tel: +81-42-585-6171, Fax +81-42-581-9412, E-mail: yamamura-seini@fesys.co.jp

2. Block Diagram and Oeration

Fig. 3 shows the block diagram of the wide-energy range X/γ-ray survey-meter.

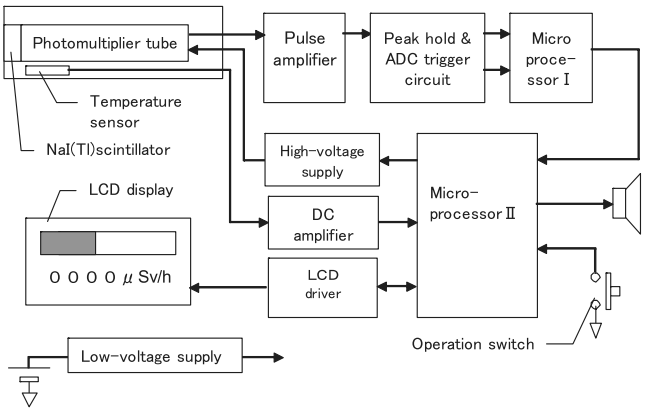

Fig. 3 Block diagram of the wide-energy range X/γ-ray survey-meter

The output pulses from the scintillator are fed into the amplifier and the output pulse heights from the amplifier are adjusted to those suited the ADC input specification of the Micro-processor I according to the mode of operation, by changing the high voltage bias of the photo-multiplier (PMT). This bias voltage is controlled by the Micro-processor II. The Peak-hold & ADC trigger circuit holds the peak height of output pulses from the amplifier and outputs the peak-detected signal (start signal of pulse height analysis) to the Micro-processor I. When this signal is detected, the pulse height peak corresponding to photon energy is converted into digital signals with the ADC in the Micro-processor I. Then, the ambient dose equivalent can be estimated from the table of spectrum-weight G-function corresponding to photon energy as described later and the summed-up dose value is transferred to the Micro-processor II when the measured dose value becomes over the pre-determined value. The dose rate is finally shown in the LCD display.

In order to compensate the temperature dependence of the detector, the temperature sensor was installed in the probe. The sensor signal is amplified with the direct current amplifier and the amplified direct current voltage is fed to the ADC of the Micro-processor II in order to convert it to the digital data. The digital data is used to compensate the temperature dependence by changing the bias voltage of PMT through the bias voltage control data based on the temperature compensation function.

III. Estimation of Spectrum-Weight G-Function

Based on the EGS-4 calculation[2], the response functions of the detector probe which was modeled as shown in **Fig.4 ,** were calculated in the energy range of 6 keV to 1500 keV, and the spectrum-weight function, so-called G-function, was obtained in the following process.

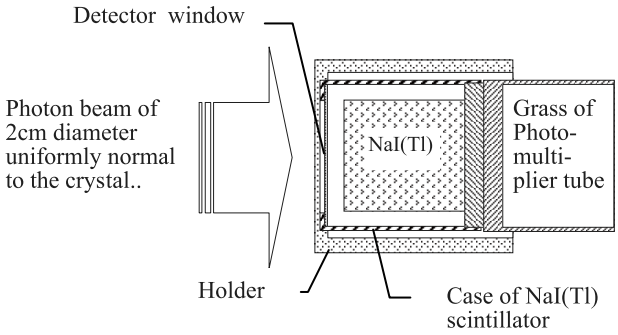

Fig. 4 Geometry in the EGS-4 calculation.

The measured pulse height distribution, $P(E_R)$, is given by

$$P(E_R) = \int R(E, E_R)\, \Phi(E)\, dE, \quad (1)$$

where $R(E, E_R)$ is the response function per photon (count $cm^2\gamma^{-1}$) and $\Phi(E)$ is the energy spectrum ($\gamma\ cm^{-2}$).

The ambient dose equivalent, H*(10) (Sv) is given by

$$H^*(10) = \int \Phi(E)\, h(E)\, dE, \quad (2)$$

where h(E) is the fluence-to-ambient-dose-equivalent conversion coefficient in Sv $cm^2\gamma^{-1}$ which is given by ICRP74 [3] . Then, G function is introduced,

$$h(E) = \int R(E, E_R)\, G(E_R)\, dE_R, \quad (3)$$

By combining Eq. (2) and Eq. (3), we can get

$$H = \int P(E_R)\, G(E_R)\, dE_R. \quad (4)$$

The G-function is given by solving Eq. (3) inversely using the unfolding calculation program based on the successive iteration method by Kim et al.[4].

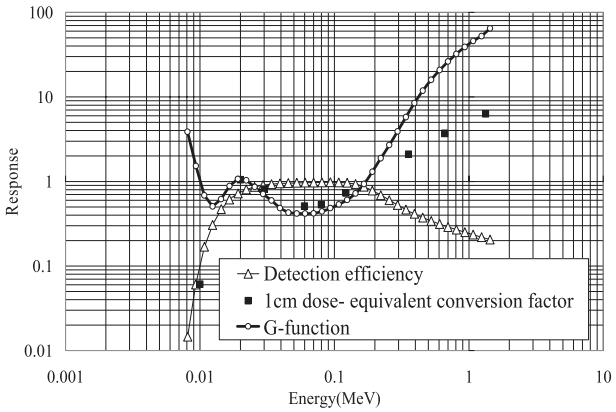

Fig.5 Calculated spectrum-weight G-function (pSv/count) as a function of photon energy, compared with the detection efficiency (count cm^2/γ) and the fluence-to-ambient-dose-equivalent conversion coefficient (pSv cm^2/γ) for the NaI(Tl) scintillator (12.7mm diameter and 12.7mm thick cylinder)

The thus-obtained G-functions for the NaI(Tl) detector, 12.7 mm diameter by 12.7 mm thickness one for wide-energy range survey-meter are shown in **Fig. 5**, together with the detection efficiency d(E) (counts cm^2/γ) and the h(E) values for comparison. The h(E) value decreases around 10 keV and keeps rather constant value between 20 keV to 150 keV, which means that the ratio of h(E)/d(E) (pSv cm^2/counts) divided by the detector surface in cm^2 gives rather constant value of pSv/counts in the energy range of 10 keV to 150 keV. The G-function curve is close to the h(E) curve below 150 keV, but increases with increasing photon energy due to decrease of detection efficiency. A steep increase of the G-function below 10 keV is due to the low energy X-ray absorption through the window and the blocking of signals lower than the lower discrimination level.

IV. Fabrication of Wide-energy Range X/γ-ray Survey-meter

Based on the above consideration, a new wide-energy range X/γ-ray survey-meter was fabricated. This survey-meter has both the dose rate indicator in analog mode and the dose indicator integrated during certain time interval in digital mode, for use in the burst radiation field actually occurred in X-ray generating machines.

The energy response of the survey-meter to the ambient dose equivalent, H*(10), was determined as a function of photon energy in the following way. First, the energy spectra were measured both in the X-ray mode (8 keV to 300 keV) and in the γ-ray mode (40 keV to 1500 keV) using the reference X-ray beams of 10 to 200 keV energies at Japan Quality Assurance Organization (JQA) and γ rays of 59.5 keV ^{241}Am, 122 keV ^{57}Co, 340 keV ^{133}Ba and 662 keV ^{137}Cs, 1250 keV ^{60}Co reference sources at Fuji Electric Systems Co. Ltd. Each output pulse height was multiplied with the spectrum-weight G-function shown in **Fig. 5**, and the thus-adjusted pulse heights were all summed up to get the H*(10) value indicated by the survey-meter, that is the indicated value.

Fig. 6 and **7** show the obtained energy responses to H*(10), respectively, normalized to 100 keV energy for X-ray mode and 662 keV energy for γ-ray mode. These graphs clearly indicate that the energy responses to H*(10) both in the X-ray and the γ-ray modes are within 25% deviation.

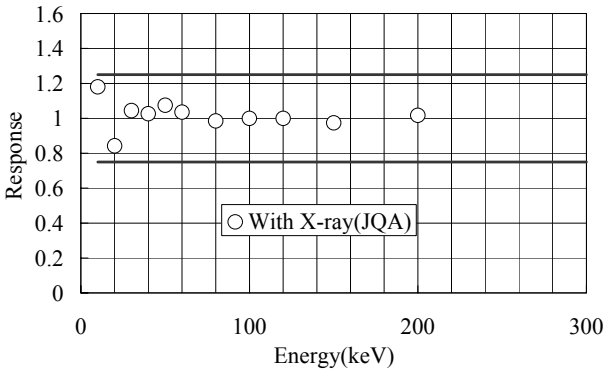

Fig. 6 Energy response of survey-meter to H*(10) normalized at 100 keV in the X-ray mode

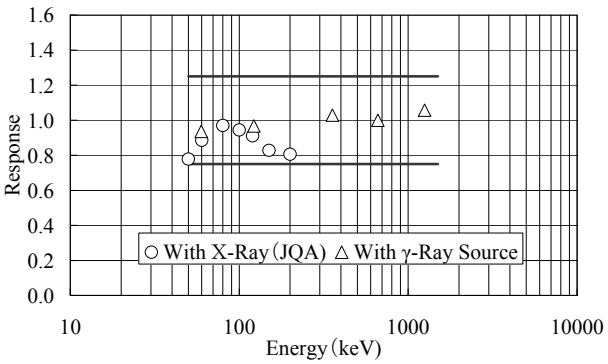

Fig. 7 Energy response of survey-meter to H*(10) normalized at 662 keV in the γ-ray mode

The linearity of the indicated value to the ambient dose equivalent rate was investigated by 59.5 keV photons of ^{241}Am sources of 3.7 MBq and 3.7 GBq for the X-ray mode, and by 662 keV photons of ^{137}Cs source of 0.37 to 370 GBq for the γ-ray mode.

The results are shown in **Fig. 8** for the X-ray mode and in **Fig.9** for the γ-ray mode.

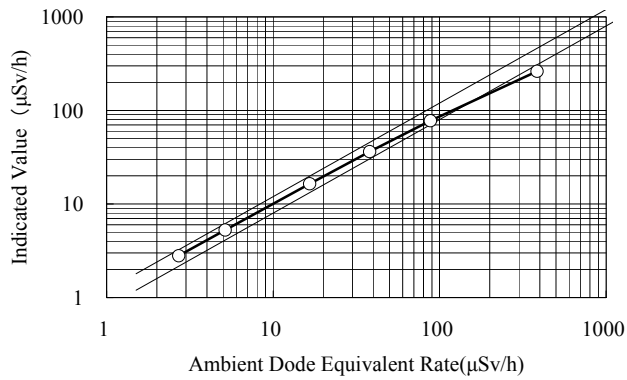

Fig. 8 Linearity of the survey-meter indicator with X-ray mode to ambient dose equivalent rate for ^{241}Am 59.5 keV gamma rays

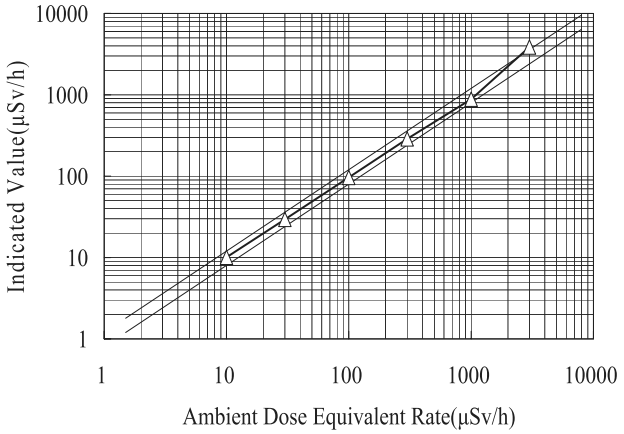

Fig. 9 Linearity of the survey-meter indicator with γ-ray mode to ambient dose equivalent rate for 137Cs 662 keV gamma rays

These figures indicate that the deviation from the linearity is within 20 % in the dose rate region lower than 100 μSv/h for the X-ray mode and is within 20 % in the dose rate region lower than 2 mSv/h for the γ-ray mode.

V. Conclusion

Following the low-energy X-ray scintillation survey-meter, we could further develop a new wide-energy range X/γ-ray scintillation survey-meter which can measure X and γ-rays of energy from 8 keV up to 1500 keV with high detection efficiency, as expected. This survey-meter will be a high-quality radiation instrument for radiation management in various facilities using X-ray generating machines and any radiological installations, and for environmental monitoring around nuclear facilities.

Table 1 summarizes the characteristics of newly-developed wide-energy range X/γ-ray survey-meter.

Table 1 Physical characteristics of the wide energy range X/γ -ray survey-meter

Item	Characteristics		
Energy renge	8keV ~ 1500keV/H*(10) Responce		
Energy response	X-ray mode		+25 ~ -25% (10 ~ 300keV)
	γ-ray mode		+25 ~ -25% (50 ~ 1500keV)
Range of indication	X-ray mode	Dose rate	BG ~ 100 μSv/h
		Dose	0.001 ~ 9.999μSv
	γ-ray mode	Dose rate	BG ~ 2mSv/h
		Dose	0.001 ~ 9.999μSv
Error of indicated value	±20%		

Acknowledgements

The authors wish to thank Dr. S. Takagi of Mitsubishi Research Institute Co. Ltd. for using the EGS-4 code, Dr. E. Kim of National Institute of Radiological Sciences for using the G-function calculation program.

References

1) K. Aoyama, K. Masui, S. Yamamura, T. Nakamura, T. Yabutani, Y. Namito, Development of Low-Energy X-ray Survey-Meter, Radiation Detectors and Their uses, KEK Proceedings 2006-7 November.57-67 (2006).
2) W.R. Nelson, H. Hirayama, D.W.O. Rogers, The EGS4 Code System, SLAC-Report-265, Stanford Linear Accelerator Center (1985).
3) International Commission on Radiological protection, Conversion Coefficients for Use in Radiological Protection Against External Radiation, ICRP Publ. 74 (1995).
4) E. Kim, A. Endo, Y. Yamaguchi et al., Development of Detector for Neutron Monitor of Wide Energy Range, JAERI-Tech 2002-041, March (2002).

Journal of NUCLEAR SCIENCE and TECHNOLOGY, Supplement 5, p. 191–193 (June 2008)

Basic Study on the Estimation of Medical Exposure Dose Using Monte Carlo Simulation

Yoichi YAMAGUCHI[1*], Takashi SASAKI[1], Seiki ONISHI[2], and Mamoru BABA[1]

[1]*Cyclotron and Radioisotope Center, Tohoku University, Sendai, Japan*
[2]*National Maritime Research Institute, Mitaka, Japan*

In order to make dose estimation in FDG-PET which is a very useful technique for whole-body cancer screening, we developed a computation system by employing a Monte Calro photon transport program UCBEAM based on the EGS4 code and the voxel phantom OTOKO. The code simulates the dose in each organ on the basis of source (FDG) distribution using the Monte Carlo simulation of annihilation photons transport.

By using the experimental data for the distribution of cumulative activity by H M Deloar et al which was obtained using TLD during PET, the present approach provides dose distribution generally consistent with measurement. It is promising for estimation of exposure rate in each organ during medical screening.

KEYWORDS: FDG-PET, dosimetry organs, EGS, voxel phantom, internal dose exposure

I. Introduction

FDG-PET is a useful technique for whole-body cancer screening owing to its functional imaging of cancer. In Japan, it is used in around two hundred medical facilities.

PET is based on the detection of a pair of annihilation gamma-rays emitted from positron emitting nuclides like ^{18}F, ^{11}C, ^{13}N, ^{15}O and so on absorbed in human body. In the screening using PET, therefore, a large amount of radioactivity from ~ several ten's to a few hundred of MBq is administrated for examinee, although the life of the radioactivity is generally very short.

The technique, therefore, may cause a significant dose exposure to organs during the screening due to positron itself and also annihilation gamma-rays. In addition, it is well known that annual exposure of Japanese due to medical diagnostics is very high compared with the world averaged values. It is important, therefore, to estimate quantitatively the exposure dose during the PET screening technique. It should be noted that, PET causes exposure from internal sources by administrated activities and may induce local exposure by positrons and annihilation gamma-rays in contrast to those in X-ray CTs. For the above mentioned reasons, we have to know more accurately the exposure in PET-CT procedure to confirm the safety of cancer screening using radiation. However, until now, only very few studies have been reported on the quantitative estimation of exposure dose during PET-CT screening.

Generally, internal dose is difficult to measure and thereby should be evaluated through calculation using an appropriate technique. For that purpose, the Monte Carlo simulation will be most useful because detailed modeling is required both for radiation transport and organs arrangement in human bodies.

The present study, therefore, aims at the development of numerical dose evaluation system using a Monte-Carlo technique and an appropriate voxel phantom.

II. Methods

In order to fulfill the requirement above mentioned, the present study adopts a combination of Monte Carlo code UCBEAM and a voxel phantom for detailed simulation of photon transport and the absorbed dose in human body adopting a realistic modeling of human body.

1. UCBEAM

The UCBEAM code[1)] has been developed by one of the author (S.O) on the basis of the extended version of the EGS4 code[6)]. It is designed to enable detailed dose estimation in organs for external irradiation of human body in a combination with the OTOKO phantom[2)] or MIRD phantom.

Originally, it is designed to simulate the irradiation of the human body from outside, and could not simulate the cases with internal source in PET. For the reason, we modified the UCBEAM code to enable the simulation in the case of internal distributed sources like in PET.

The information on the source distribution which is necessary as the source term in the calculation was taken from experimental measurement of cumulative activity. In the present case, the source distribution data was taken from the experimental data by H M Deloar et al. [3)], which was obtained from a combination of measurement using TLD during PET scanning with model calculations.

By using the combination, we simulated internal and local exposure during an FDG-PET screening for an adult healthy body based on the information about positron source distributions.

*Corresponding Author, Tel. +81-22-241-795-7806, E-Mail; gucci@cyric.tohoku.ac.jp

2. OTOKO Phantom

The OTOKO phantom[2] has been developed by Saito et al., on the basis of segmented CT images. It represents a human body's geometry of a Japanese male adult with a standard size, 175 cm in height and 65 kg in weight, and consists of voxels, 1 mm x 1 mm x 1cm. These voxels were configured to correspond to the composition of actual human body and tissue/organ region. Therefore, the OTOKO phantom enables us to estimate the local exposure dose in each tissue in detail using a realistic model of human body

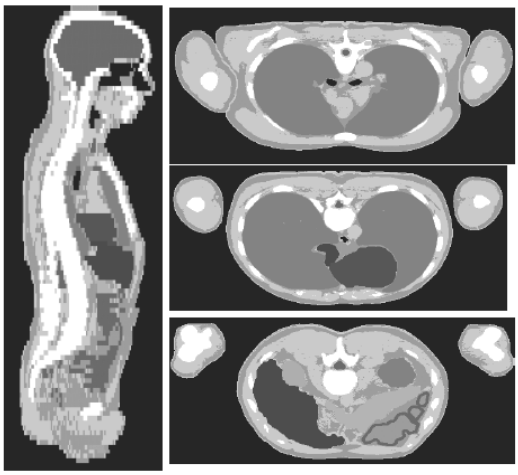

Fig.1 OTOKO phantom

3. Source parameters

(1) Source geometry

In the simulation, the source distribution which is indispensable for simulation was obtained from cumulative activities of positron emitting nuclides estimated on the basis of dose measurement in several data point on the outside surface of the body. The cumulative activities means the bulk of decays happened in the body during the FDG-PET screening processes. The source distribution adopted in the present calculation is that measured by Deloar et al, for healthy adult male. **Table1** shows the cumulative activities of each organ and tissues.

Table 1 Cumulated activity of each organ [3]

Organ	Cumulated activity[Bq*h/MBq]
Brain	260
Heart	65
Lungs	52
Liver	88
Kidneys	32
Spleen	8.4
Pancreas	7.5
Bladder	156
Others	1966
Total	2634.9

(2) Source energy spectrum

For simulation, the energy distribution of positron is required as well as gamma-source distribution. Positrons emitted from ^{18}F are generated after the beta-decay. Since beta-decay is multi-body decay, emitted positrons have a continuous energy spectrum up to 633 keV. In this study, for simplicity, we assumed the positron energy spectrum of ^{18}F to be a monochromatic on the basis of the following equation[4]:

$$E = E_{\max} / 3, \qquad E_{\max} = 633 \ keV \tag{1}$$

III. Result and Discussion

1. Organ and tissue absorbed doses

The results of the present calculation for the absorbed dose in organ and tissue are shown in **Table 2**. The present positron source simulation gave results on almost all of tissues and could be compared with experimental data by Delor et al.

The present result on the positron dose simulation follows the general trend of organ dependence of experimental data, and shows general agreement with the experimental values for almost of tissues and organs. However, in detail, the agreement between the present results and experimental values show different feature for each organ. The present results are larger than measurements significantly for spleen, adrenal and small intestine but smaller inversely for bladder, liver and lung. The reasons for those fluctuations are discussed below.

First, we assumed the positron energy spectrum from ^{18}F to be a monochromatic. It is possible that the assumption affects the result. Positron especially affects the results for organs with high concentration of ^{18}F like bladder. It is desirable, therefore, to make calculation with realistic positron energy spectrum.

Second, experimental dose by H M Deloar et al used the S value in estimation of dose for each organ. It is based on the MIRD phantom data. The MIRD phantom is modeled corresponding to the body of western male adult, but the OTOKO phantom represents the body of a Japanese male adult. It means that there are some different positional relations between the OTOKO and the MIRD phantoms. Therefore, their difference may affect the gamma-ray flux estimation in organs of the abdomen.

Third, voxels were too large to accurately describe an organ. Some organs had millimeter scale structure, but voxels in the OTOKO phantom had 1cm height. It means that oversized organs caused larger movement distance in organ and dose overestimation. It has great effects in a short-range radiation, like electrons and positrons.

IV. Summary and Conclusion

In this study, we developed a Monte Carlo simulation system for the assessment of absorbed dose in each organ during cancer scanning employing PET. We employed a Monte Carlo code UCBEAM based on the EGS4 code and a voxel phantom OTOKO with modifying the UCBEAM to treat internal radiation sources to apply to PET.

Table 2 Calculated absorbed dose and reference values (mGy / MBq)

Target Organs	UCBEAM	TLD method	UCBEAM/TLD	ICRP
Adrenal	**1.89E-02 ± 2.52E-04**	**1.40E-02 ± 2.00E-03**	**1.35**	**1.40E-02**
Bladder	**9.06E-02 ± 7.24E-04**	**3.70E-01 ± 3.20E-01**	**0.24**	**1.70E-01**
Stomach	**1.83E-02 ± 2.00E-04**	**1.40E-02 ± 1.80E-03**	**1.31**	**1.20E-02**
Small intestine	**1.88E-02 ± 4.88E-05**	**1.40E-02 ± 1.90E-03**	**1.34**	**1.30E-02**
Kidney	**3.12E-02 ± 1.07E-04**	**2.60E-02 ± 2.60E-03**	**1.20**	**2.10E-02**
Liver	**2.34E-02 ± 4.79E-05**	**1.90E-02 ± 3.70E-03**	**1.23**	**1.20E-02**
Lung	**1.32E-02 ± 2.63E-05**	**1.90E-02 ± 4.30E-03**	**0.69**	**1.10E-02**
Pancreas	**2.30E-02 ± 1.34E-04**	**3.60E-02 ± 1.80E-02**	**0.64**	**1.20E-02**
Spleen	**2.75E-02 ± 1.83E-04**	**1.60E-02 ± 3.80E-03**	**1.72**	**1.20E-02**
Testes	**1.52E-02 ± 2.06E-04**	**1.40E-02 ± 1.90E-03**	**1.08**	**1.50E-02**
Thyroid	**1.31E-02 ± 3.09E-04**	**1.30E-02 ± 1.60E-03**	**1.01**	**9.70E-03**
Brain	**4.33E-02 ± 6.64E-05**	**4.10E-02 ± 6.10E-03**	**1.06**	**2.60E-02**
Heart Wall	**3.47E-02 ± 9.21E-05**	**3.20E-02 ± 1.10E-02**	**1.09**	**6.50E-02**
Effective dose (mSv/MBq)	**1.73E-02 ± 5.93E-05**	**2.70E-02 ± 1.70E-02**	**0.64**	**2.70E-02**

The results of the simulations were compared favorably with cited reference based on measurement.

The present model will be useful for detailed evaluation of medical dose exposure of each organ in PET and also CT, which will be more popular in the near future.

Acknowledgement

The author would like to thank Dr. M.Hagiwara for his useful comment on EGS and so on.

References

1) S.Ohnishi, N.Odano, N.Nariyama and K.Saito, "Analysis of localized dose distribution in human body by Monte Carlo code system for photon irradiation," *Radiation Protection Dosimetry*, **Vol. 111** No.1:65-71 (2004).
2) K.Saito, A.Wittmann, S.Koga, Y.Ida, T.Kamei, J.Fhunabiki, M.Zankl, "Construction of a computed tomographic phantom for a Japanese male adult and dose calculation system.".
3) Deloar M Hossian "Internal absorbed dose estimation by TLD method for 18F-FDG and comparison with the dose estimates from whole body PET," *Phys. Med. Biol*, **44**, 595-606 (1999).
4) N. Tsoulfanidis, "Measurement and Detection of Radiation, " 1983.
5) ICRP, "Radiation Dose to Patients from Radiopharmaceuticals," ICRP PUBLICATION, No.53 (1993).
6) W R. Nelson, H Hirayama, D W. O. Rogers, "THE EGS4 SYSTEM, " SLAC-265 (1985).

Journal of NUCLEAR SCIENCE and TECHNOLOGY, Supplement 5, p. 194–196 (June 2008)

The Intakes and Committed Effective Dose from Internally Deposited Iodine-131 due to an Internal Contamination Event of Ulchin Nuclear Power Plant in Korea – Experiences and Lessons Learnt

Hee Geun Kim* and Tae Young Kong

Korea Electric Power Research Institute, Daejeon, Korea

This paper describes the lessons learned after ^{131}I(iodine-131) contamination at Korean nuclear power plnats during the refueling period, including whole body counting measurement systems, the estimation of intake, and the calculation of committed effective dose. In particular, various internal dose calculations and computer programs were applied with the revised biokinetic models and a new dosimetric model for the human respiratory tract of ICRP. Finally, the estimated intake and committed effective dose were reviewed and intercompared based on the intake retention fraction of the ICRP.

KEY WORDS: Committed Effective Dose, ^{131}I, Internal Dose Assessment, Intake Retention Fraction

I. Introduction

In general, the occupational exposure to radioiodine is a rare occurrence in the nuclear industry. In case of exposure to radioiodine, ^{131}I is the most common contributor in nuclear power plants (NPPs). In ^{131}I contamination, on-site workers are most likely to be exposed through inhalation to potentially hazardous airborne particles or vapors. Iodine is rapidly absorbed into the circulation via inhalation, is concentrated in the thyroid, and then is excreted in the urine. ^{131}I in the body is normally monitored directly by measuring whole body activity using a whole body counter with a NaI(Tl) detector. All of the common forms of iodine are readily taken up the body. For the inhalation of a particular form of iodine, the lung absorption type F for ICRP-66 and ICRP-78 publications or class D for ICRP-30 and ICRP-54 publications is assumed, while elemental iodine vapor is assigned to class SR-1 (soluble or reactive) with the absorption type F for ICRP-66 and ICRP-78 publications.

During the refueling period of Ulchin NPPs in Korea at the end of 2002, a number of workers inside the reactor building were contaminated by the inhalation of ^{131}I from the primary system opening. Almost all the workers were internally contaminated with ^{131}I and a few were also internally contaminated by ^{58}Co and ^{60}Co. All the workers were requested to check the activity deposited in the body using a portal monitor. If portal monitoring indicated that they were contaminated, they were also requested to a second monitoring for activity using a whole body counter with two NaI(Tl) scintillation detectors. According to the iodine biokinetic model, whole body counting was carried out two times after work (within 24hr) and again after 3 days to 10 days. It was found that the maximum intake and committed effective doses (CED) were approximately 3% of the annual limits for intake.

*Corresponding Authors, Tel. +82-42-865-5551, Fax. +82-42-865-5504, E-Mail; hkkim@kepri.re.kr

This paper describes the lessons learned after ^{131}I contamination at Korean NPPs during the refueling period, including whole body counting measurement systems, the estimation of intake, and the calculation of CED. In particular, various internal dose calculations and computer programs were applied with the revised biokinetic models and a new dosimetric model for the human respiratory tract of ICRP. Finally, the estimated intake and CED were reviewed and intercompared based on the intake retention fraction of the ICRP.

II. Internal Contamination Event

Ulchin NPPs, which are located at the east coast in Kyungsangpukdo province, have 6 reactors in operation currently. Ulchin reactors of unit #3 and #4, the Korean standard nuclear power plant (KSNP) generating 1,000MWe, has reached the first critical state in December 1997 and has been in commercial operation since August 1998.

To inspect the U-tube of steam generator, the drainage of coolant and the manway opening at Ulchin unit #3 were conducted after the shutdown of reactor during the fourth maintenance period at the end of 2002. The first day of maintenance period, most radiation workers who accessed the reactor building were contaminated internally by ^{131}I. Most internal contamination was occurred at the first day during the three-day access period. It was also found that the total number of radiation workers who had internal contamination by ^{131}I was approximately one hundred. The reason of the occurrence of internal contamination for many radiation workers was that the manway opening was carried out before the full removal of ^{131}I, so the iodine in coolant was volatilized and then finally the radiation workers inhaled the gaseous iodine. In addition, it was recognized that the radioactivity of ^{131}I was increased by the volatilization during the manway opening, but the volatilization velocity of iodine in the reactor coolant system was faster than expected and the withdrawal of radiation workers from the reactor

building was delayed since it took a time for iodine sampling and nuclide analysis in the air of reactor building.

III. Whole Body Counting

All radiation workers, who are supposed to enter the reactor building for the radiation works during the maintenance period, should take a radiation work permit (RWP). After radiation works, they have to take a portal monitoring at the access gate of reactor building to check whether they have radioactive contamination or not. If the radioactivity is detected, the workers who are contaminated by radionuclide should take a whole body counting to measure the radioactivity and to identify the nuclide in the body of workers more precisely.

The whole body counter (WBC) utilized for the detection of ^{131}I in radiation workers was Canberra's vertical linear Fastscan (Model 2250)[1]. This WBC system consists of two large NaI(Tl) scintillation detectors (7.6x12.7x40.6cm) that typically provide a priori lower limit of detection (LLD) of approximately 150 Bq for ^{60}Co with a count time of one minute for a normal person containing K-40. In addition, it is possible to process approximately 30 ~ 50 workers in an hour. Canberra's Fastscan is displayed in **Fig. 1**.

Fig. 1 Whole body counter (Canberra's Fastscan)

As a result of whole body counting for the radiation workers who were contaminated by ^{131}I, it was found that the deviation of detected activity for some workers was high in spite of same work and work place. In addition, the deviation of tendency, which the activity of ^{131}I was decreasing, was high individually after daily whole body counting for these workers. It was considered that these phenomena were attributed by the dynamic metabolism due to the intake of iodine. For some workers, the radioactivity of ^{131}I was not detected by the whole body counting which was conducted on the next day or after shower although their activity was remarkable at the initial whole body counting. In this case, it was concluded that this contamination was not internal but external contamination.

The whole body counting was, thus, performed again after 3 ~ 10 days from the intake of ^{131}I for all contaminated workers in consideration of the deviation of detected activity, decreasing tendency, and the characteristics of dynamic metabolism by ^{131}I. This made possible to avoid of misjudgment of external contamination as internal contamination for the case that radionuclide was attached to the skin of workers and to reduce the uncertainty of internal dose calculation by the dynamic metabolism for ^{131}I. The biokinetic model for iodine metabolism is displayed in **Fig. 2**[2].

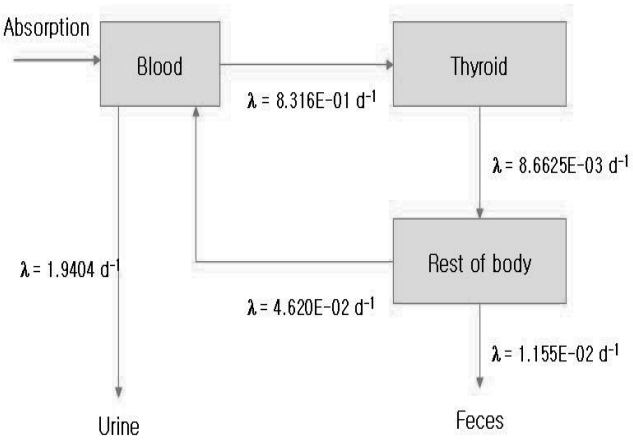

Fig. 2 Biokinetic model for iodine metabolism (ICRP-78)

The calculation of intake and CED were carried out using various computer codes for internal dose assessment with the information of measured nuclide and its activity from the process of whole body counting for the contaminated workers. The computer codes used for the calculation of CED were CINDY based on the ICRP-30's model, LUDEP based on the ICRP-66/78's model, and KIDAC, based on the ICRP-66/78's model, developed in Korea. In addition, to verify the calculation process of intake and CED, MONDAL code developed by NIRS of Japan was used and the hand calculation using intake retention fraction (IRF) of ICRP-78 publication was performed[3,4].

In the process of internal dose assessment, it was assumed that the radioactive contamination was occurred by the inhalation of ^{131}I in the air inside the reactor building and there was only one single intake. For the inhalation of a particular form of iodine, both the lung absorption type F and elemental for ICRP-66/78 publications and the class D for ICRP-30/54 publications were applied to the calculation. In case of type F and elemental, there were approximately two times of difference for the intake estimation, but CED was similar to each other due to two times of offset to committed effective dose equivalent coefficient. The time interval from the intake to measurement was calculated on the basis of radiation work schedule and the record of access to reactor building. In this process, IRF of ICRP was used and the intake estimation was carried out through dividing the detected activity by IRF.

As a result of internal dose assessment using ICRP-30/54's model, it was found that the maximum exposure dose was 0.76mSv and the number of radiation workers whose dose was over 0.1mSv was 58. However, there was a difference of the intake estimation and the calculation of CED between ICRP-30/54 and ICRP-66/78 publications in consideration of the time interval from the intake to the whole body counting. This was attributed by the change of metabolism for ^{131}I in ICRP-30/54 publication to offset faster than that of ICRP-66/78 publication and the increase of committed effective dose equivalent coefficient approximately 25% in ICRP-30/54 publication. In addition, to prevent the error of intake estimation and to verify the calculation process, the intake was calculated based on the radioactivity concentration of ^{131}I in the air of work place and the respiration rate of radiation worker, and then the result was compared with that of whole body counting. In this process, the result of whole body counting was used for the official intake estimation. To consider radiation worker' susceptibility to internal radiation exposure, the consultation with the foreign specialist was also conducted to check the result again[3].

IV. Conclusion

The internal radiation exposure by ^{131}I occurred at the end of 2002 at Ulchin NPPs was not only a big controversial issue in Korea, but also an opportunity for the improvement of dose assessment. Before the application of ICRP-60 publication to Korean NPPs, this gave us the opportunity to enhance the level of technology for internal dose assessment and to improve the points at issue of measurement and calculation of internal dose.

In particular, a lot of technical training courses for internal dose assessment have opened and performed several times. In addition, the NPP procedure to reduce the radioactivity in the reactor system before the shutdown of reactor was improved and the procedures of measurement and assessment of internal radiation exposure were unified. In relation to this incident, the technical report including the technical guide and procedures was written to suggest a systemic approach to the internal dose assessment. Finally, this made possible to prepare the quality assurance program to improve the reliability of measurement and assessment of internal radiation exposure.

Acknowledgement

This research was carried out with the financial support of Korea Hydro & Nuclear Power Corporation.

References

1) Korea Hydro & Nuclear Power Co., Procedure of Korean Nuclear Power Plants, Estimation and Management of Internal Dose, (2002/2004).
2) International Commission on Radiological Protection (ICRP), Individual Monitoring for Intake Exposure of Workers/ Replacement of ICRP Publication 54, ICRP Publication 78, Pergamon press, (1998).
3) Private Communication with Dr. Nobuhito Ishigure of National Institute of Radiological Science (NIRS), Japan, (http://www.nirs.go.jp).
4) National Institute of Radiological Science (NIRS), The Support System for Internal Dosimetry, Monitoring to Dose Calculation (MONDAL), (http://www.nirs.go.jp), (2003). A Feasibility Study on a Dual-beam Port Assembly for Accelerator-Based

Journal of NUCLEAR SCIENCE and TECHNOLOGY, Supplement 5, p. 197–200 (June 2008)

A Feasibility study on a Dual-beam Port Assembly for Accelerator-Based Boron Neutron Capture Therapy

Kyung-O KIM[1], Soon Young KIM[2], and Jong Kyung KIM[1*]

[1]*Department of Nuclear Engineering, Hanyang University, Seoul, Korea*
[2]*Innovative Technology Center for Radiation Safety, Hanyang University, Seoul, Korea*

A new type of beam shaping assembly, named dual-beam port assembly, was designed, which provides high epithermal neutron flux for the accelerator-based boron neutron capture therapy (BNCT). Neutron beams were produced by using a ^{7}Li(p,n)^{7}Be reaction, and the neutrons emitted to the solid angle bin of 50 – 150^{o} to the direction of incoming 2.5 MeV protons were targeted to the beam shaping for using the neutron source beam with relatively low mean energy. The solid angle range was determined by the analysis of neutron spectrum and angle distribution generated from the ^{7}Li(p,n)^{7}Be reaction. In this study, many sensitivity calculations using MCNPX were carried out to find good moderators and reflectors for developing the therapeutic beams of high epithermal neutron flux. As a result, heavy water and Fluental^{TM} were employed as the moderator, and graphite for reflector. Therapeutic neutrons generated from each beam port were compared with IAEA recommendations to evaluate the performance of the dual-beam port assembly. It was realized that the dual-beam port assembly provides high epithermal neutron flux of 1.01×10^{9} (#/cm^{2}-s-mA) at each side beam port as well as satisfies the beam quality standards recommended by IAEA. Hence, it is feasible to apply this dual-beam port assembly design to the accelerator-based BNCT.

KEY WORDS: BNCT, neutron source, beam shaping assembly, epithermal neutron, proton accelerator

I. Introduction

Thermal and epithermal neutrons have an essential role in the efficiency of BNCT. While thermal neutrons are suitable for the direct treatment of superficial cancers, epithermal neutrons are preferred to deep-seated tumors due to their deep penetration compared to thermal neutrons[1)].

In order to improve the effectiveness of BNCT, it is important to change the shape of the neutron spectrum from the target into the shape focused into epithermal neutron. Therefore, many researchers have studied the effective design of a beam shaping assembly that was required to moderate fast neutrons for obtaining the therapeutic neutron beams. In general, most of the assemblies were composed of some components such as moderator, reflector, gamma shielding, and delimiter.

By this time, all the studies on the accelerator-based BNCT beams have assumed a forward facing geometry in which the epithermal neutron beams to be emitted are collinear with the incoming proton beam[2), 3), 4), 5)]. This is a reasonable approach to get a high quantity of fast neutrons, since the forward neutron yields to the direction of the proton beam are markedly high among the produced neutrons. However, a high quantity of epithermal neutrons at a beam port could not be easily achieved through the moderation of fast neutrons, since the neutrons emitted in a forward direction with a proton beam have a high mean energy of about 400 keV. Therefore, many collisions including absorption reaction are expected during the slowing down process, which is not effective to change the original neutron spectrum into the desired one focused into the epithermal neutrons[6)].

In order to enhance neutron economics, a beam shaping assembly having a dual-beam port was first designed by using MCNPX code. This assembly design was focused on the production of suitable epithermal neutron beam for the accelerator-based BNCT. The neutron beam qualities have been validated with some IAEA recommended values of the fast neutron dose, gamma dose, and ratio of thermal flux to epithermal flux.

II. Perpendicular Neutron Source

Currently, it is well known that the ^{7}Li(p,n)^{7}Be reaction is the most promising reaction for the accelerator-based BNCT neutron sources, due to the high neutron yield among other reactions and relatively low energy neutrons to be produced.

The optimized proton energy was determined to obtain the high quantity of relatively low energy neutrons from the source. Neutron yield from the proton energy range below 2.5 MeV is relatively low for effective BNCT treatment, whereas longer moderation length, in an opposite case (E_p > 2.5 MeV), is needed to get same epithermal neutrons due to high mean neutron energies[5), 6)]. In this study, therefore, the neutron source for BNCT was assumed to be produced from a 2.5 MeV proton beam with a 100 μm lithium target which is sufficient to cause the significant energy loss of impinged proton energy. Both the energy spectrum and angular distribution of the neutrons produced by proton beams were investigated by MCNPX calculation[7)]. The calculated neutron yield as a function of its energy and angle is shown in **Fig. 1**. This figure shows those neutrons produced in each solid angle bin of 30^{o}. The neutrons produced by 2.5 MeV protons impinging on a Li-7 target

*Corresponding Author, Tel: +82-2-2220-0464, Fax: +82-2-2294-4800, E-mail: jkkim1@hanyang.ac.kr

have a maximum energy of approximately 800 keV, and most of the neutrons are emitted into the solid angle ranges from 30° to 60° with regard to the direction of proton beam.

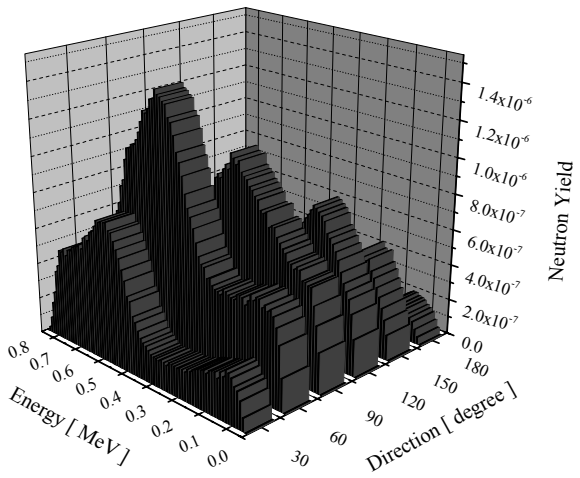

Fig. 1 Neutron Yield for the $^{7}Li(p,n)^{7}Be$ Reaction as a Function of Neutron Energy and Angles with Regard to the Incident Proton Energy of 2.5 MeV

In order to determine the direction of the assembly beam port, the neutron energy spectrum was divided into two cases depending on the neutron emission angle. In the first case, 1) Forward neutrons: sum of energy spectrum in the solid angle bin of 0–40° to the direction of the proton beam, in the second case, 2) Perpendicular neutrons: sum of energy spectrum in the solid angle bin of 50–150° to the direction of the proton beam. The solid angle bin of 0–40° was based on the solid angle of the emitted neutrons mainly used to moderate in the previous studies on the beam shaping assembly design. The perpendicular solid angle range was determined to obtain a high quantity of relatively low energy neutrons from the source through many simulation trials. It was found that relatively low energy neutrons were emitted into the solid angle bin of 50–150° to the direction of proton beam.

The compared results between forward and orthogonal neutrons are shown in **Fig. 2**. It is recognized that the neutrons emitted in the orthogonal direction have a maximum energy of approximately 650 keV. In particular, the number of neutrons in the energy range of 100–300 keV is about 2 times higher than that of the forward neutrons because neutron flux decrease is found above 400 keV as the neutron emission angle moves away from the normal vector on the target surface. That is, the mean energy of the emitted neutrons also decreases with increasing angle, so that less moderation is required[8].

Therefore, by examining the characteristics of the neutron source, it is noted that the orthogonal neutrons generated from the $^{7}Li(p,n)^{7}Be$ reaction are more efficient to produce epithermal ones for the accelerator-based BNCT.

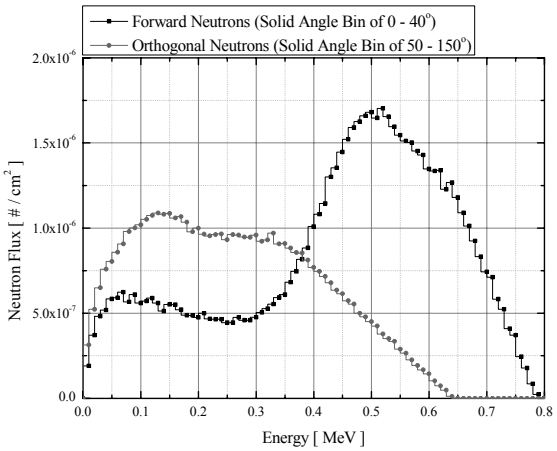

Fig. 2 Calculated Neutron Energy Spectrums Depending on the Neutron Emission Angle (Forward and Orthogonal Directions)

III. Design of a Dual-beam Port Assembly

Based on the investigation of the neutrons from $^{7}Li(p,n)^{7}Be$ reaction, a dual-beam port assembly was designed to enhance neutron economics and to obtain a suitable neutron energy spectrum. Several different types of materials were investigated to moderate the neutrons to epithermal energies: light water, heavy water, and graphite. Another popular type of BNCT moderator, Fluental™ (47.25 % Al, 52.25 % F, and 0.5 % Li), was also considered[9].

In particular, based on the cross-section data, it is known that one of the major components of Fluental™, aluminum, has the highest scattering and lowest absorption cross-sections of the fast neutrons among the other elements. One of the benefits of using Fluental™ as a moderator is that the scattering cross-sections of fluorine and aluminum have series of resonances at high energies that provide good neutron moderation to epithermal energies, where the absorption cross-section is much smaller.

In this study, two moderators, heavy water and Fluental™, were selected based on simulation results. Heavy water was also employed as a moderator since it has the highest moderating ratio. **Fig. 3** shows the cross-sectional geometry of the beam shaping assembly used in the calculations. Two moderators are respectively filled with Fluental™ (ρ=2.9 g/cm^3) and heavy water (ρ=1.1056 g/cm^3), and reflector is made of graphite (ρ=1.85 g/cm^3). Also, cadmium filter was included to reduce the fast neutrons at each beam port. This assembly has two same size beam ports of left and right sides. The thickness of the primary moderator is 3 cm, and the secondary one is 8.99 cm, with a 0.01-cm-thick cadmium filter.

In **Fig. 4**, neutron energy spectra calculated by running MCNPX with ENDF VI data are shown at each beam port. The proton beam of 1 cm in diameter was employed in this calculation, and the tallies used were based on the track length estimate of neutrons at each beam port. From the calculation result, most of the neutrons moderated were focused into the epithermal energy region (4 eV – 40 keV),

in particular, the maximum peak was shown in the energy range from 10 to 20 keV. Therefore, the dual-beam port assembly can generate similar neutron spectra at each beam port with good quality of epithermal neutrons.

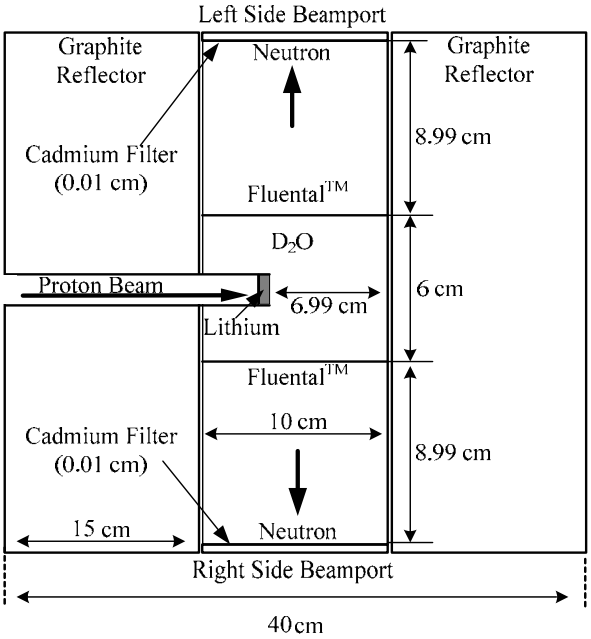

Fig. 3 Configuration of a Dual-beam Port Assembly to Produce Epithermal Neutrons

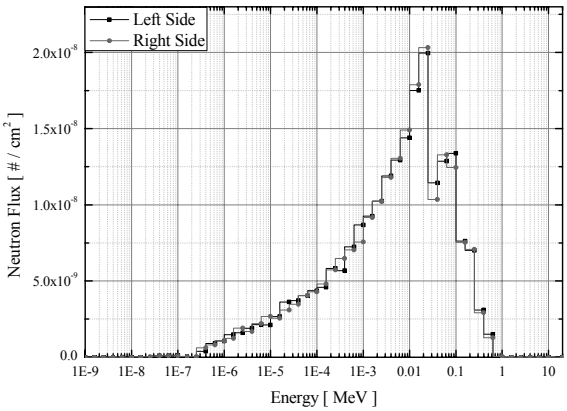

Fig. 4 Comparison of the Neutron Energy Spectrum at Dual-beam Port

IV. Beam Quality Parameters

The radiobiology of BNCT is more complicated than other radiation modalities, because the radiation field in BNCT consists of several separate radiation dose components (fast and thermal neutron doses, boron dose, and gamma dose), in which these radiations have different physical properties and biological effectiveness. **Table 1** shows some recommended values for thermal to epithermal neutron flux ratio (Φ_{th}/Φ_{epi}) and fast neutron and gamma doses at the beam port of a BNCT facility except current-to-flux ratio[10]. The current-to-flux ratio is not considered in this dual-beam port assembly, since this ratio provides a measure of the fraction of neutrons that are moving in the forward beam direction.

To evaluate the qualities of the neutron beams from each beam port, the comparison between calculation results and IAEA recommendations was made in **Table 1**[11]. It was recognized that the neutron beams produced at each beam port satisfy the recommendations for all parameters. Especially, the most important value of epithermal neutron flux was completely satisfied at each side beam port. It is, therefore, found that the dual-beam port assembly for the accelerator-based BNCT was sufficiently satisfied to get significant epithermal neutrons.

Table 1 Comparison of Beam Quality Parameters between the Neutron Beams Designed in this Study and the IAEA Recommended Values

	IAEA Recommendation	Left Side	Right Side
D_n/Φ_{epi} [Gy-cm^2/n$_{epi}$]	$< 2.0\times10^{-13}$	1.99×10^{-13}	1.95×10^{-13}
D_γ/Φ_{epi} [Gy-cm^2/n$_{epi}$]	$< 2.0\times10^{-13}$	8.93×10^{-15}	9.01×10^{-15}
Φ_{th}/Φ_{epi}	< 0.05	0.048	0.048
Φ_{th} [#/cm^2-s-mA]	-	4.94×10^{7}	4.84×10^{7}
Φ_{epi} [#/cm^2-s-mA]	$> 1.0\times10^{9}$	1.01×10^{9}	1.01×10^{9}
Φ_{fast} [#/cm^2-s-mA]	-	2.83×10^{8}	2.78×10^{8}

- D_n: Fast Neutron Dose, D_γ: Gamma Dose, J_{total}: Neutron Current
- Φ_{th}, Φ_{epi}, Φ_{total}: Thermal, Epithermal and Total Neutron Fluxes

V. Conclusions

The feasibility of a new design of beam shaping assembly, named dual-beam port assembly, was investigated, in order to produce a suitable epithermal neutron beam for the accelerator-based BNCT. As the results of this study, it is noted that the neutrons emitted into the solid angle bin of 50–150^o to the direction of the proton beam from ^{7}Li(p,n)^{7}Be reactions were well focused into the epithermal region compared with forward ones. This is because the mean energy of the perpendicular neutrons is lower than that of the forward ones, so that the probability of survival to epithermal region comes to high. It is, therefore, possible to reduce the size of the neutron moderating system, because it requires less moderation for producing therapeutic neutrons.

It is also recognized that the performance of the dual-beam port assembly is enhanced because epithermal neutrons for treating cancers are generated from two directions at the same time. In addition, by comparing the results of beam quality parameters obtained from the perpendicular direction neutrons with the recommended values of IAEA, it is realized that the new dual-beam port assembly for the accelerator-based BNCT was well designed.

It is also expected that the installation of a small-sized, beam shaping assembly will be possible to install into hospitals for practical use in the near future.

Acknowledgement

This study was performed under the long-term nuclear research and development program sponsored by the Ministry of Science and Technology of Korea (M20505050003-05A0905-00310), and supported by the Innovative Technology Center for Radiation Safety (R11-2000-067-01001-0).

References

1) Deok-jae Lee, Chi Young Han, Jong Kyung Kim, and Byung-Chan Na, "Spectrum Shaping of Epithermal Neutron Beam for Accelerator-Based BNCT and Dosimetric Evaluation Using a Brain Phantom," Journal of Nuclear Science and Technology, Supplement **4**, 180-183 (2004).
2) A. A. Burlon, A. J. Kreiner, A. A. Valda, D. M. Minsky, H. R. Somacal, M. E. Debray, and P. Stoliar, "Optimization of a Neutron Production Target and a Beam Shaping Assembly Based on th ^{7}Li(p,n)^{7}Be Reaction for BNCT," Nuclear Instruments and Methods in Physics Research B, **229**, 144-156 (2005).
3) O. E. Kononov, V. N. Kononov, M. V. Bokhovko, V. V. Korobeynikov, A. N. Soloviev, A. S. Sysoev, I. A. Gulidov, W. T. Chu, and D. W. Nigg, "Optimization of an Accelerator-Based Epithermal Neutron Source for Neutron Capture Therapy," Applied Radiation and Isotopes, **61**, 1009-1013 (2004).
4) A. E. Hawk, T. E. Blue, and J. E. Woollard, "A Shielding Design for an Accelerator-Based Neutron Source for Boron Neutron Capture Therapy," Applied Radiation and Isotopes, **61**, 1027-1031 (2004).
5) Hitoshi Yokobori, Makoto Sasaki, and Toshiyuki Yamanaka, "Design Study on an Accelerator-Based Facility for BNCT and Low Energy Neutron Source," Progress in Nuclear Energy, **37**, 321-326 (2000).
6) C. Lee and X. L. Zhou, "Thick Target Neutron Yields for the ^{7}Li(p,n)^{7}Be Reaction near Threshold," Nuclear Instruments and Methods in Physics B, **152**, 1-11 (1999).
7) D. Pelowitz (Ed.), MCNPX User's Manual Version 2.5.0, Los Alamos National Laboratory, (2005).
8) S. Green, D. A. Allen and T. D. Beynon, "Design for an Accelerator-based Orthogonal Epithermal Neutron Beam for Boron Neutron Capture Therapy," Med. Phys., **26**, 71-76 (1999).
9) Thomas E. Blue, and Jacquelyn C. Yanch, "Accelerator-Based Epithermal Neutron Sources for Boron Neutron Capture Therapy of Brain Tumors," Journal of Neuro-Oncology, **62**, 19-31 (2003).
10) IAEA, Current Status of Neutron Capture Therapy, IAEA-TECDOC-1223, IAEA, (2001).
11) N. Cerullo, J. Esposito, and G. G. Daquino, "Spectrum Shaping Assessment of Accelerator-Based Fusion Neutron Sources to be used in BNCT Treatment," Nuclear Instruments and Methods in Physics B, **213**, 641-645 (2004).

Journal of NUCLEAR SCIENCE and TECHNOLOGY, Supplement 5, p. 201–204 (June 2008)

A New GUI Based Patient-Specific Treatment Planning System for Boron Neutron Capture Therapy

Sang Hoon JUNG[1], Ik Soo CHOI[2], Sung Ho PARK[3], Kyung-O KIM[4], and Jong Kyung KIM[4*]

[1]*Innovative Technology Center for Radiation Safety, Hanyang University, Seoul, Korea*
[2]*Medical Information Team, Asan Medical Center, Seoul, Korea*
[3]*Department of Radiation Oncology, Asan Medical Center, Ulsan University, Seoul, Korea*
[4]*Department of Nuclear Engineering, Hanyang University, Seoul, Korea*

A new patient-specific treatment planning system, called BTPS, was developed for Boron Neutron Capture Therapy (BNCT). To facilitate planning BNCT, the BTPS was designed through overall planning procedures based on a user-friendly graphical user interface (GUI). A dose calculation engine based on MCNPX was embedded in the BTPS. An accelerated tally technique in MCNP and a parallel computing system to significantly reduce the computation time are also employed. To investigate the performance of the BTPS, computation times for calculating the absorbed dose in a voxel head phantom were evaluated according to the number of computers. To assess the results from the BTPS, thermal neutron fluxes and absorbed doses in a rectangular phantom were calculated and compared with those obtained by using the SERA. The differences in the thermal neutron fluxes and absorbed doses calculated by using BTPS and SERA were 4.3% and 3.8%, respectively, in root mean square. The BTPS facilitates planning of patient-specific BNCT treatments with easy manipulation, and the absorbed dose in the phantom can be calculated with the efficient computation time and good accuracy comparable to that of SERA. Therefore, it is noted that the BTPS is clinically superior to treatment planning systems of BNCT, and allows non-MCNP users to plan easily optimized BNCT treatment.

KEYWORDS: BNCT, 3D dosimetry computation, treatment planning system, MCNP

I. Introduction

Boron neutron capture therapy (BNCT) is a highly targeted binary cancer treatment involving a selective accumulation of ^{10}B compound in a tumor and subsequent neutron irradiation. The neutron capture reaction of ^{10}B emits high linear energy transfer particles (LET), i.e. α and $^{7}Li^{+}$, and their energies are deposited at the cell level with high relative biological effectiveness. Moreover, various interactions of the incident neutron with soft tissues or bone elements deliver doses to normal tissues and tumors[1)].

To estimate absorbed doses delivered by the complicated interactions of incident neutrons, 3D Monte Carlo (MC) dose calculations, which simulate heterogeneous patient's geometries and solve the radiation transport without any approximations, are required in contrast to the conventional radiotherapy based on semi-empirical or analytic methods[2)]. Several treatment planning systems for BNCT have been developed based on MC dose calculations, such as the Simulation Environment for Radiotherapy Applications (SERA, INEEL)[3)], NCT_Plan (Havard-MIT)[4)], Boron Distribution Treatment Planning System (BDTPS, University of Pisa)[5)], and JAERI Computational Dosimetry System (JCDS, JAERI)[6)].

A general purpose radiation transport code, MCNP[7)], has been embedded in the dose calculation engine of these treatment planning systems with the exception of SERA, which has a unique dose calculation engine based on rtt_MC, called seraMC3).

In previous studies, a treatment planning system for BNCT[8)], which can generate a voxel phantom from patients' images and analyze the absorbed dose based on dose calculation using MCNP, had been carried out through inclusive research on accelerator-based BNCT at Hanyang University[9)]. For planning treatment of BNCT, the system requires distinct pre/post-processing programs to generate a MCNP input for whole treatment environments and to import the results from a MCNP run. For routine clinical processes, the distinct procedures should be automated and systematically linked with MCNP.

A new patient-specific treatment planning system based on a graphical user interface to facilitate planning of BNCT, BTPS (BNCT Treatment Planning System), was developed in this work. Major characteristics of the BTPS were introduced with a treatment plan for glioblastoma multiforme (GBM). Performance of the BTPS was investigated by evaluating computation time for absorbed dose calculation in a voxel phantom using the BTPS. To assess the results, thermal neutron fluxes and absorbed doses in a simple geometry were calculated by using the BTPS, and compared with those obtained by using SERA, which has been most widely used for treatment planning in BNCT.

II. Methods and Materials

The BTPS has a dose calculation engine which consists of MCNP and various tools systematically linking with MCNP.

**Corresponding Author, Tel. +82-2-2220-0464, Fax. +82-2-2294-4800, E-mail: jkkim1@hanyang.ac.kr

MCNP can easily reconstruct voxel phantoms from a patient's images by using a repeated lattice structure and can freely configure information on the irradiation field including its energy spectrum, angular distribution, and source position[7]. However, given the computation time to obtain the results with reasonable statistical certainty, MC dose calculation would be relatively poor as a dose calculation engine in a treatment planning system[2].

To enhance the performance of the computational dosimetry, a specially accelerated tally technique for lattice geometry, or 'mesh tally' in MCNPX and MCNP5[10], is embedded into the dose calculation engine of the BTPS.

The absorbed dose in BNCT has been conventionally calculated by combining four dose components which mainly contribute to the absorbed dose in BNCT, i.e., gamma dose (D_γ), neutron dose (D_n), proton dose (D_p), and boron dose (D_B)[1]. The dose components have been calculated by converting tallied neutron and photon fluxes with fluence-to-kerma values[11] based on ICRU 46[12] and 63[13].

A GUI-based BTPS was built with C++ Builder and works on the Windows® platform. All approaches for the development of the BTPS were matched to BNCT clinical treatments, as shown in **Fig. 1**, and customized for clinicians and researchers' use, to facilitate the treatment plan and dosimetric evaluation in BNCT.

The BTPS includes three common modules, i.e. image, plan, and analysis modules, and a dose calculation engine, as shown in **Fig. 1**.

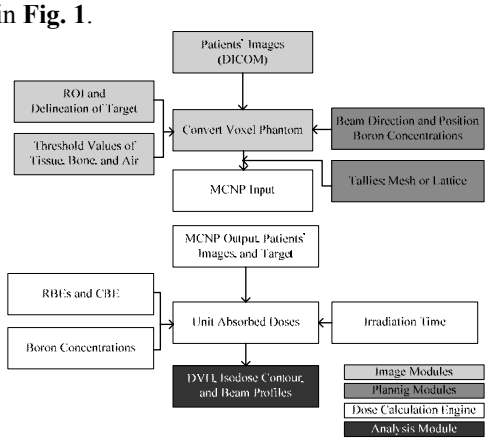

Fig. 1 A Brief Flow of the Treatment Plan by Using the BTPS

III. Results

1. BTPS Structure

Major characteristics of the BTPS are described with a clinical treatment plan for glioblastoma multiforme (GBM).

(1) Image Module

The image module visualizes all procedures of a treatment plan using the BTPS. Before the personalized treatment planning of BNCT, 3D patient-specific voxel phantoms, which were reconstructed from the patient's images, are constructed. Because the image module supports DICOM, the standard medical imaging format, the images from any diagnostic imaging technologies, CT, MRI, and PET, can be reconstructed.

The target volume is easily delineated, as shown in **Fig. 2-(a)**, and the region-of-interest (ROI) and the voxel size, which will be used to construct voxel phantoms, are easily defined. For defining the three primary materials (i.e., air, normal tissue, and bone) in each voxel, averaged CT numbers for each voxel are automatically classified according to the density ranges which depend on the primary tissues types[15], and the density ranges are adjustable by using a conventional editing program.

(2) Plan Module

The plan module simulates all treatment environments for BNCT. The details of an irradiation field including source position and direction can be created with easy manipulation, as shown in **Fig. 2-(b)**. Because the energy spectrum and radial/angular distribution of the field depends on BNCT facilities, the information on the irradiation field can be easily adjusted. Boron concentrations, assumed to be homogeneously distributed in tumor or normal tissue, are included for a dose calculation.

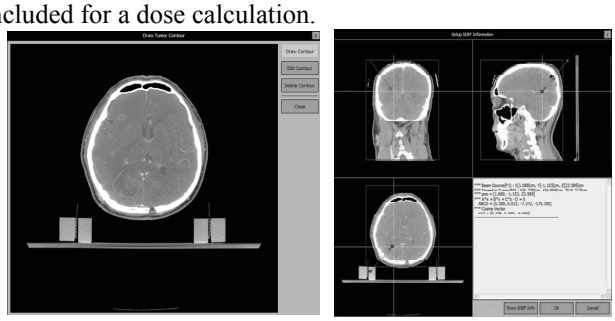

(a) (b)

Fig. 2 Screenshots of (a) Delineating Target Volume and (b) Positioning Irradiation Field

Tally types of dose components or neutron fluxes are selected for dose calculations using MCNP. The three essential dose components (i.e., boron, total neutron, and gamma doses) are chosen, and neutron dose, proton dose, or neutron fluxes also can be optionally calculated. Mesh tallies or lattice tallies are selectively used for the absorbed dose calculation.

(3) Dose Calculation Engine

The dose calculation engine contains several methods for automatically generating MCNP inputs and analyzing results from the MCNP run. The 3D voxel phantoms from the Image module, as shown in **Fig. 3-(a)**, and the treatment environments from the plan module are consolidated and converted to the MCNP input, as shown in **Fig. 3-(b)**. Selected dose components are calculated using kerma values corresponding to each dose component. The kerma values are also adjustable.

The dose calculation engine imports the results from the MCNP run, and calculates the dose rates of dose components with irradiated neutron flux, RBE values and CBE values corresponding to each dose component. The absorbed dose rate is calculated with boron concentrations by combining all dose rates of the dose components.

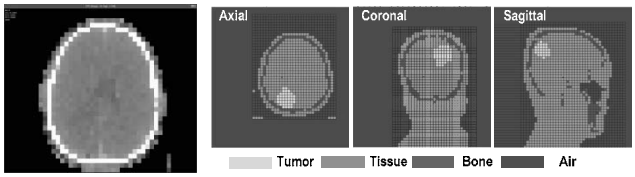

(a) (b)

Fig. 3 A Generated Voxel Head Phantom: Viewing on (a) BTPS and (b) MCNP

(4) Analysis Module

The analysis module reports and analyzes the dose calculation results in order to evaluate a treatment plan. The Analysis module imports all the dose rates, including the absorbed dose rate, or fluxes from the dose calculation engine. Total doses or neutron fluences are calculated with an irradiation time for BNCT.

To evaluate the dose distribution and therapeutic effect of a treatment plan, total doses or neutron fluences are converted and displayed as isodose contours and a dose volume histogram (DVH), as shown in **Fig. 4** and **5**. Dose profiles, as shown in **Fig. 6**, are very useful for evaluating dosimetric characteristics of neutron production from the targets and beam shaping assemblies developed for BNCT.

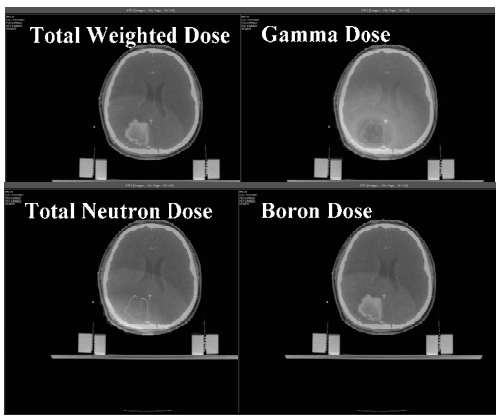

Fig. 4 Isodose Contours for Each Dose

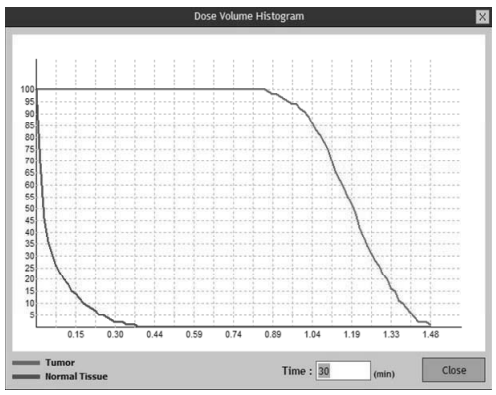

Fig. 5 Dose Volume Histogram and Irradiation Time

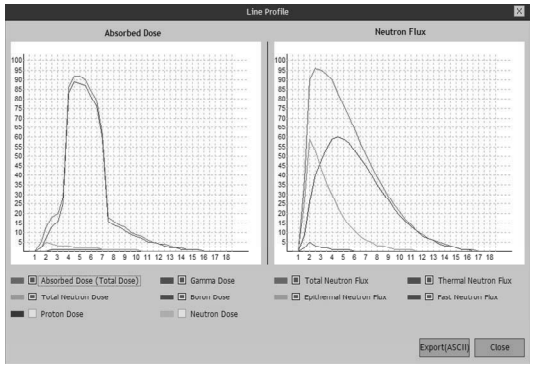

Fig. 6 Profiles of Doses and Neutron Fluences according to Depth: (Left) Percentage Depth Doses for Dose Components and (Right) Neutron Fluxes

2. Performance of the BTPS

In order to evaluate the performance of the BTPS, computation times for calculating absorbed dose in the same phantom were investigated according to the number of computers. The phantom, which was reconstructed from images of a patient with GBM by using the BTPS, consists of 17×18×23 of 1 cm^3 voxels. In this work, the epithermal neutron beam for accelerator-based BNCT developed at Hanyang University[14] was used as a neutron beam. These calculations were performed by using a mesh tally with the same computers (Pentium IV, 3.2 GHz) and the same history of 10^7.

Fig. 7 shows the computation times according to the number of computers. Since the computation time for the BTPS's calculating the absorbed dose for the phantom was less than 5 minutes, as shown in **Fig. 7**, the BTPS can allow immediately re-calculating the absorbed dose with neutron fluxes and boron concentrations measured by monitoring systems.

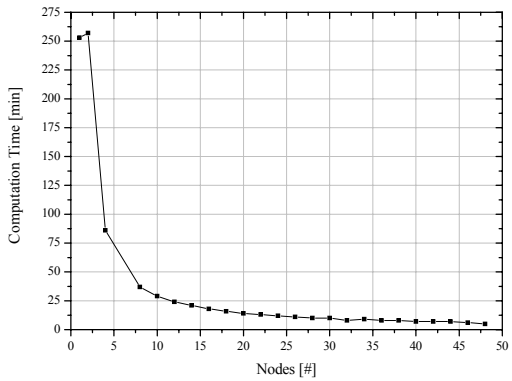

Fig. 7 Variation of Computation Time according to Number of Computers

To assess the results from the BTPS, neutron fluxes and absorbed doses in a rectangular phantom (14×14×14 cm^3) were calculated by using the BTPS, and compared with those by using SERA[16]. The phantom was filled with brain materials of ICRU 46[12] and 10 ppm of ^{10}B, and the same neutron beam in the manual of SERA was used as the neutron source[16].

Fig. 8 shows normalized neutron fluxes and absorbed doses along the central axis of the irradiating beam. The thermal neutron fluxes and absorbed doses were good agreement with differences of about 4.3% and 3.8%, respectively, in the root mean square.

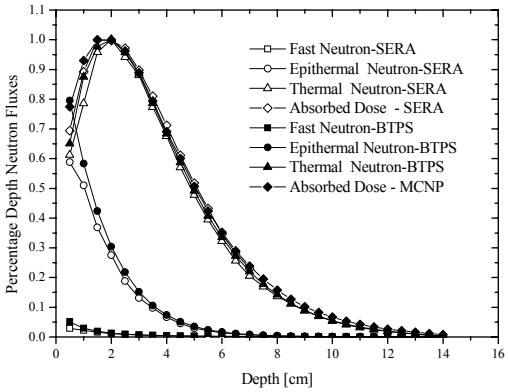

Fig. 8. Normalized Neutron Fluxes and Absorbed Doses along the Beam Centerline

IV. Conclusions

The BTPS, a patient-specific treatment planning system for BNCT, was developed in this work. The BTPS enables planning clinical treatments of BNCT with easy manipulation through a user-friendly GUI. Also, the BTPS provides various indicators, such as isodose contours, DVH, and dose profiles, which are suitable to clinical treatments with or studies of BNCT. The performance of the BTPS was investigated through evaluation of computation times according to the number of computers. BTPS can calculate the absorbed dose in the voxel head phantom within a few minutes. Moreover, the accuracy of the BTPS results was evaluated to be comparable to that of SERA.

The BTPS facilitates planning of patient-specific BNCT treatments with efficient computation time and good accuracy. BTPS also includes routine clinical procedures for planning BNCT with a friendly GUI. It is noted that BTPS is clinically superior to the treatment planning systems of BNCT, and allows non-MCNP users to plan easily optimized BNCT treatment.

Acknowledgement

This work was supported by the SRC/ERC program (R11-2000-067-01001-0) and the long-term research and development program (M20505050003-05A0905-00310) of Ministry of Science & Technology/Korea Science and Engineering Foundation.

References

1) IAEA, Current Status of Neutron Capture Therapy, IAEA-TECHDOC-1223, IAEA, 2001.
2) Jacob Van Dyk, Ed., "The Modern Technology of Radiation Oncology Volume 2," Medical Physics Publishing, 91-131 (2007).
3) Nigg, D.W., Wemple, C.A., Wessol, D.E., and Wheeler, F.J., "SERA, An Advanced Treatment Planning System for Neutron Therapy and BNCT," *Transactions of the American Nuclear Society*, **80**, 66-68 (1999).
4) Gonzalez, S.J., Santa Cruz, G.A., Kiger III, W.S., Palmer, M.R., Busse, P.M., and Zamenhof, R.G., "NCTPlan, the New PC version of MacNCTPlan: Improvements and Verification of a BNCT Treatment Planning System," Research and Development in Neutron Capture Therapy, Monduzzi Editore, Bologna, Italy, 557-561 (2002).
5) N. Cerullo, G.G. Daquino, L. Muzi, and J. Esposito, "Development of a Treatment Planning System for BNCT Based on Positron Emission Tomography Data: Preliminary Results," *Nuclear Instruments and Methods in Physics Research Section B,* **213**, 637-640 (2004).
6) Kumada H., Yamamoto K., Torii Y., Matsumura A., Yamamoto T., Nose T., Nakagawa Y., Kageji Y., Uchiyama, J., "Development of the JAERI Computational Dosimetry System (JCDS) for Boron Neutron Capture Therapy," JAERI-Tech 2003-002, 2003.
7) D.B. Pelowitz, Ed., "MCNPX User's Manual Version 2.5.0," LA-CP-05-0369, Los Alamos National Laboratory, 2005.
8) S. H. Park, C. Y. Han, S. Y. Kim, and J. K. Kim, Use of the CT Images for BNCT Calculation: Development of BNCT Treatment Planning System and Its Applications to Dose Calculation for VOXEL Phantoms, *Radiation Protection Dosimetry*, **110**, 661-667 (2004).
9) Deok-jae Lee, Chi Young Han, Sung Ho PARK, and Jong Kyung KIM, "An Acceleartor-based Epithermal Neutron Beam Design for BNCT and Dosimetric Evaluation Using a Voxel Head Phantom," *Radiation Protection and Dosimetry*, **110**, 655-660 (2004).
10) W.S. Kiger, III, A.G. Hochberg, J.R. Albritton, and Tim Goorley, "Performance Enhancements of MCNP4B, MCNP5, and MCNPX for Monte Carlo Radiotherapy Planning Calculations in Lattice Geometries," LA-UR-04-4751, Los Alamos National Laboratory, 2005.
11) J.T. Goorley, W.S. Kiger, and R.G. Zamenhof, "Reference Dosimetry Calculations for Neutron Capture Therapy with Comparison of Analytical and Voxel Models," *Medical Physics*, **29**, 145-156 (2002).
12) ICRU 46, ''Photon, Electron, Proton, and Neutron Interaction Data for Body Tissues,'' International Commission on Radiation Units and Measurements, Bethesda, MD, 1992.
13) ICRU 63, ''Nuclear Data for Neutron and Proton Radiotherapy and for Radiation Protection,'' International Commission on Radiation Units and Measurements, Bethesda, MD, 2000.
14) Kyung-O KIM, Sang Hoon JUNG, Soon Young KIM, and Jong Kyung KIM, "Evaluation of a Neutron Beam Generation Facility for the Accelerator-Based BNCT," *Proceedings of the Korea Nuclear Society 2006 Autumn Meeting*, November 2-3, 2006.
15) J.J. DeMarco, T.D. Solberg, and J.B. Smathers, "A CT-Based Monte Carlo Simulation Tool for Dosimetry Planning and Analysis," *Medical Physics*, **25**, 1-11 (1998).
16) Wessol D.E, Wemple C.A., Wheeler F.J., Harkin G.J., Frandsen M.W., Albright C.L., Cohen M.T., Rossmeier M.B., and Cogliati J.J., "SERA-Simulation Environment for Radiotherapy Applications, User's Manual-Version 1C0," INEEL-EXT-02-00698, 2002.

Journal of NUCLEAR SCIENCE and TECHNOLOGY, Supplement 5, p. 205–208 (June 2008)

Uncertainty in Committed Effective Doses Caused by Assuming a Single Intake Pathway in the Interpretation of Bioassay Results

Jong-Il LEE[1,2,*] and Jai-Ki LEE[2]

[1]*Korea Atomic Energy Research Institute, P.O. Box 105, Yuseong-gu, Daejeon 305-600, Republic of Korea*
[2]*Hanyang University, 17 Haengdang-dong, Seongdong-gu, Seoul 133-791, Republic of Korea*

Intakes of radionuclides through both inhalation and ingestion pathways may occur during an incident involving unsealed radionuclides. If one assumes only one intake pathway in this case, which is usual in a routine monitoring, a significant error in the evaluated committed effective dose (E_{50}) may result. In order to quantify this potential error, variations of resultant committed effective doses were analyzed for different fractions of the inhaled activities to the total intake of some selected radionuclides: $^{57, 58, 60}$Co, $^{134, 137}$Cs, $^{89, 90}$Sr and ^{32}P. Simulated bioassay measurements for the whole body, urine and feces at 1 day after the intakes were generated based on the biokinetic models and data of the radionuclides. For the inhalation intake, AMAD of 5 μm was assumed and the different absorption Types were considered. Given that the intake happened via both pathways, the ratios of E_{50} with assumption of a single intake pathway to the true E_{50} were in the range of 0.01~ 72.59 for ^{90}Sr (Type S) and of 0.06 ~ 16.70 for ^{60}Co (Type S), which are unacceptably wide ranges. Generally larger errors are expected when the feces assay and Type S are applied. A strategy which employs two methods of bioassay or two successive measurements is proposed to reduce the potential error caused by a misjudgment of the intake pathway.

KEY WORDS: bioassay, intake pathway, committed effective dose, potential error, error reduction strategy

I. Introduction

A committed effective dose (E_{50}) by an internal radiation exposure due to an intake of a radionuclide is evaluated as a product of the intake (in Bq) and the committed effective dose coefficient[1)] (in Sv/Bq) by the following equation.

$$E_{50} = \sum_p I^p e_{50}^p \quad (1)$$

where I^p is the intake of a radionuclide through an intake pathway p, and $\mathbf{e_{50}^p}$ is the effective dose coefficient as an intake pathway p. The intake is calculated by dividing the activity of the body content, organ content or daily excretion measured at time t days after an inhalation or ingestion of a radionuclide by the predicted value of a body retention fraction or a daily excretion rate at time t days after an inhalation or ingestion of a radionuclide. If the intake through each intake pathway is known, the total committed effective dose is calculated by a sum of the committed effective doses due to both intake pathways.

The body retention fraction or the daily excretion rate at time t days after an intake of a radionuclide varies with several conditions including the intake pathway (inhalation, ingestion, injection), the assay subject (whole body, lung, thyroid, urine, feces), AMAD (activity median aerodynamic diameter) and absorption type (Type F, M, S) of inhaled particles, fractional uptake of element from the GI tract (f_1 value) and the intake mode (acute, chronic).[2)] Especially the effective dose coefficient is depended on the intake pathway, AMAD, absorption Type and f_1 value. As a result, selection of the intake pathway affects the evaluated committed effective dose.

Intakes of radionuclides through both inhalation and ingestion pathways may particularly occur during an incident involving unsealed radionuclides. If one assumes only one intake pathway as usual in the routine monitoring while there are intakes through both pathways, a significant error in the evaluated E_{50} may result. In order to demonstrate this potential error, variations of resultant E_{50} were analyzed for different fractions of the inhaled activities to the total intake for some selected nuclides: $^{57, 58, 60}$Co, $^{134, 137}$Cs, $^{89, 90}$Sr and ^{32}P. Based on the analysis, a strategy which employs two methods of bioassay or two successive measurements was proposed to reduce the error caused by a misjudgment of an intake pathway.

II. Evaluation of the potential error in E_{50}

In this paper, $^{57, 58, 60}$Co (Type M, S), $^{134, 137}$Cs (Type F), $^{89, 90}$Sr (Type F, S) and ^{32}P (Type F, M) were considered. These radionuclides are of high potential of internal exposure in the work environment of either a nuclear power plant or nuclear medicine department in hospitals. **Table 1** shows the effective dose coefficients for the intake pathway and the whole body retention fraction or the daily excretion rate at 1 day after a single inhalation or ingestion of these radionuclides. These values were obtained from the ICRP-78[2)] or by using the IMBA computer code[3)] assessing the behavior of radionuclides in the body according to the respiratory tract model[4)], the GI tract model[5)] and the biokinetic models[5-7)].

The relation between the bioassay measurements by two methods of bioassay and the body retention fraction or the

*Corresponding Author, Tel: +82-42-868-8409, Fax: +82-42-868-8609, E-Mail: jilee2@kaeri.re.kr

daily excretion rate at time t days after a single inhalation and ingestion of a radionuclide is given as follows.

$$M_A(t) = I^{inh} \times F_A^{inh}(t) + I^{ing} \times F_A^{ing}(t) \quad (2)$$

$$M_B(t) = I^{inh} \times F_B^{inh}(t) + I^{ing} \times F_B^{ing}(t) \quad (3)$$

where $M_A(t)$ and $M_B(t)$ are the bioassay measurements by an A or B type bioassay, I^{inh} and I^{ing} are intakes through an inhalation or ingestion respectively. $F_A{}^{inh}(t)$, $F_A{}^{ing}(t)$, $F_B{}^{inh}(t)$ and $F_B{}^{ing}(t)$ are the body retention fraction or the daily excretion rate for an A or B type bioassay at time t days after a single inhalation or ingestion.

The simulated bioassay measurements for the whole body, urine and feces at 1 day after a single inhalation and ingestion were generated by using equations (2) or (3) based on a biokinetic model and data of $^{57, 58, 60}$Co (Type M, S), $^{134, 137}$Cs (Type F), $^{89, 90}$Sr (Type F, S) and ^{32}P (Type F, M) for various inhalation fractions (0 ~ 100%). For inhalation, AMAD of 5 μm was assumed. Calculations were carried out by a spreadsheet program developed in this study. **Table 2** shows, as an example, the simulated bioassay measurements when 100 Bq of ^{60}Co (Type S for inhalation) was inhaled or ingested with different inhalation fractions and the true committed effective doses corresponding to the given inhalation fraction. Similar calculations were made for other radionuclides and the potential deviations of the evaluated E_{50} based on assumption of a single intake pathway from the true E_{50} were estimated.

Table 1 Effective dose coefficient and intake retention fraction of the whole body or the daily excretion rate at 1 day after an inhalation or ingestion of a radionuclide

Radionuclide	Inhalation				Ingestion			
	e_{50}^{inh}	$F_{wb}^{inh}(1)$	$F_{u}^{inh}(1)$	$F_{f}^{inh}(1)$	e_{50}^{ing}	$F_{wb}^{ing}(1)$	$F_{u}^{ing}(1)$	$F_{f}^{ing}(1)$
^{57}Co (Type M)	3.9×10^{-10}	4.8×10^{-1}	2.0×10^{-2}	1.0×10^{-1}	2.1×10^{-10}	7.1×10^{-1}	2.8×10^{-2}	2.6×10^{-1}
^{57}Co (Type S)	6.0×10^{-10}	4.9×10^{-1}	5.7×10^{-3}	1.1×10^{-1}	1.9×10^{-10}	7.1×10^{-1}	1.4×10^{-2}	2.7×10^{-1}
^{58}Co (Type M)	1.4×10^{-9}	4.8×10^{-1}	2.0×10^{-2}	1.0×10^{-1}	7.4×10^{-10}	7.0×10^{-1}	2.7×10^{-2}	2.6×10^{-1}
^{58}Co (Type S)	1.7×10^{-9}	4.9×10^{-1}	5.6×10^{-3}	1.1×10^{-1}	7.0×10^{-10}	7.1×10^{-1}	1.4×10^{-2}	2.7×10^{-1}
^{60}Co (Type M)	7.1×10^{-9}	4.9×10^{-1}	2.0×10^{-2}	1.0×10^{-1}	3.4×10^{-9}	7.1×10^{-1}	2.8×10^{-2}	2.6×10^{-1}
^{60}Co (Type S)	1.7×10^{-8}	4.9×10^{-1}	5.7×10^{-3}	1.1×10^{-1}	2.5×10^{-9}	7.1×10^{-1}	1.4×10^{-2}	2.7×10^{-1}
^{134}Cs (Type F)	9.6×10^{-9}	6.0×10^{-1}	7.9×10^{-3}	2.2×10^{-4}	1.9×10^{-8}	9.8×10^{-1}	1.6×10^{-2}	3.1×10^{-4}
^{137}Cs (Type F)	6.7×10^{-9}	6.0×10^{-1}	7.9×10^{-3}	2.2×10^{-4}	1.3×10^{-8}	9.8×10^{-1}	1.6×10^{-2}	3.1×10^{-4}
^{89}Sr (Type F)	1.4×10^{-9}	-	6.7×10^{-2}	4.7×10^{-2}	2.6×10^{-9}	-	5.6×10^{-2}	2.1×10^{-1}
^{89}Sr (Type S)	5.6×10^{-9}	-	8.0×10^{-4}	1.1×10^{-1}	2.3×10^{-9}	-	1.8×10^{-3}	2.8×10^{-1}
^{90}Sr (Type F)	3.0×10^{-8}	-	6.8×10^{-2}	4.8×10^{-2}	2.8×10^{-8}	-	5.6×10^{-2}	2.2×10^{-1}
^{90}Sr (Type S)	7.7×10^{-8}	-	8.1×10^{-4}	1.1×10^{-1}	2.7×10^{-9}	-	1.8×10^{-3}	2.8×10^{-1}
^{32}P (Type F)	1.1×10^{-9}	-	4.9×10^{-2}	1.4×10^{-2}	2.4×10^{-9}	-	8.5×10^{-2}	6.7×10^{-2}
^{32}P (Type M)	2.9×10^{-9}	-	3.6×10^{-2}	2.6×10^{-2}	2.4×10^{-9}	-	8.5×10^{-2}	6.7×10^{-2}

e_{50}^{inh} : the effective dose coefficient for inhaled radionuclide (Sv/Bq), e_{50}^{ing} : the effective dose coefficient for ingested radionuclide (Sv/Bq).
$F_{wb}^{inh}(1)$: the whole body retention fraction at 1 day after an inhalation, $F_{wb}^{ing}(1)$: the whole body retention fraction at 1 day after an ingestion.
$F_{u}^{inh}(1)$: the daily urinary excretion rate at 1 day after an inhalation, $F_{u}^{ing}(1)$: the daily urinary excretion rate at 1 day after an ingestion.
$F_{f}^{inh}(1)$: the daily fecal excretion rate at 1 day after an inhalation, $F_{f}^{ing}(1)$: the daily fecal excretion rate at 1 day after an ingestion.

Table 2 Simulated bioassay measurements at 1 day after any inhalation and ingestion of ^{60}Co (Type S, 5 μm AMAD) by using the intake retention fraction or daily excretion rate

Intake (Bq)		True E_{50}	Activity in whole body	Urinary Excretion	Fecal Excretion
Inhalation	Ingestion	(Sv)	(Bq)	(Bq/d)	(Bq/d)
0	100	2.50×10^{-7}	71.0	1.40	27.0
10	90	3.95×10^{-7}	68.8	1.32	25.4
20	80	5.40×10^{-7}	66.6	1.23	23.8
30	70	6.85×10^{-7}	64.4	1.15	22.2
40	60	8.30×10^{-7}	62.2	1.07	20.6
50	50	9.75×10^{-7}	60.0	0.985	19.0
60	40	1.12×10^{-6}	57.8	0.902	17.4
70	30	1.27×10^{-6}	55.6	0.819	15.8
80	20	1.41×10^{-6}	53.4	0.736	14.2
90	10	1.56×10^{-6}	51.2	0.653	12.6
100	0	1.70×10^{-6}	49.0	0.570	11.0

III. Results And Discussion

Table 3 shows the ratios of the evaluated E_{50} based on the assumption of a single intake pathway, either inhalation or ingestion, to the true E_{50} corresponding to the actual intake pathway when the simulated bioassay measurements of ^{60}Co given in **Table 2** were used. It was assumed that the absorption Type S and AMAD of 5 μm be known. Since dose coefficient for inhalation intake is larger than that for ingestion intake, the assumption of sole inhalation intake results overestimates of the committed effective dose and vice versa. The ratios were in the range of 0.06 ~ 16.7.

The whole results for $^{57, 58, 60}$Co (Type M, S), $^{134, 137}$Cs (Type F), $^{89, 90}$Sr (Type F, S) and ^{32}P (Type F, M) are summarized in **Table 4** as a range of ratios of the evaluated E_{50} to the true E_{50} calculated by the same method when different monitoring methods, e.g. whole body counting, urine or feces bioassay, are employed. **Fig. 1** shows the range of the ratios of the evaluated E_{50} by assuming one intake pathway to the true E_{50}, which encompassing the three different bioassay methods.

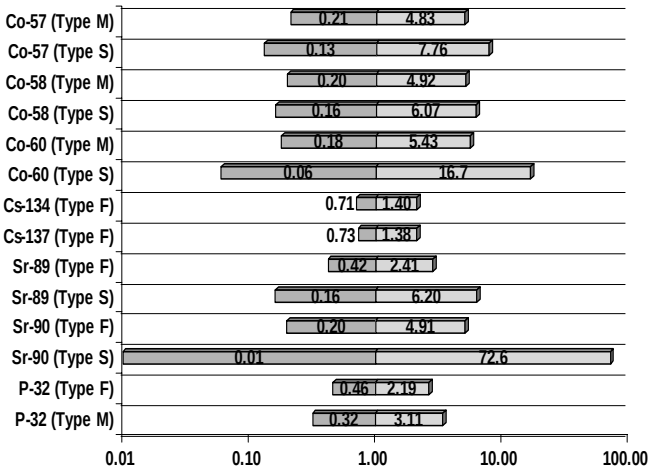

Fig. 1 Range of the ratios of the evaluated committed effective dose (E_{50}) with assumption of a single intake pathway to the true E_{50} from actual inhalation and ingestion of radionuclides (5 μm AMAD)

Table 3 Ratios of the evaluated committed effective dose (E_{50}) with assumption of a single intake pathway to the true E_{50} from actual intake pathways of ^{60}Co (Type S, 5 μm AMAD)

Intake fraction (%)		Whole body bioassay		Urine bioassay		Feces bioassay	
Inhalation	Ingestion	Inhalation assumption	Ingestion assumption	Inhalation assumption	Ingestion assumption	Inhalation assumption	Ingestion assumption
0	100	9.89	1.00	16.70	1.00	16.69	1.00
10	90	6.04	0.61	9.94	0.60	9.94	0.60
20	80	4.28	0.43	6.82	0.41	6.81	0.41
30	70	3.26	0.33	5.01	0.30	5.01	0.30
40	60	2.60	0.26	3.84	0.23	3.84	0.23
50	50	2.14	0.22	3.01	0.18	3.01	0.18
60	40	1.79	0.18	2.40	0.14	2.40	0.14
70	30	1.52	0.15	1.93	0.12	1.93	0.12
80	20	1.31	0.13	1.56	0.09	1.56	0.09
90	10	1.14	0.12	1.25	0.07	1.25	0.08
100	0	1.00	0.10	1.00	0.06	1.00	0.06

Table 4 Range of the ratios of the evaluated committed effective dose (E_{50}) with assumption of a single intake pathway to the true E_{50} from actual intake pathways

Radionuclide	Whole body bioassay		Urine bioassay		Feces bioassay	
	Inhalation assumption	Ingestion assumption	Inhalation assumption	Ingestion assumption	Inhalation assumption	Ingestion assumption
^{57}Co (Type M)	1.00 ~ 2.75	0.36 ~ 1.00	1.00 ~ 2.60	0.38 ~ 1.00	1.00 ~ 4.83	0.21 ~ 1.00
^{57}Co (Type S)	1.00 ~ 4.58	0.22 ~ 1.00	1.00 ~ 7.76	0.13 ~ 1.00	1.00 ~ 7.75	0.13 ~ 1.00
^{58}Co (Type M)	1.00 ~ 2.76	0.36 ~ 1.00	1.00 ~ 2.55	0.39 ~ 1.00	1.00 ~ 4.92	0.20 ~ 1.00
^{58}Co (Type S)	1.00 ~ 3.52	0.28 ~ 1.00	1.00 ~ 6.07	0.16 ~ 1.00	1.00 ~ 5.96	0.17 ~ 1.00
^{60}Co (Type M)	1.00 ~ 3.03	0.33 ~ 1.00	1.00 ~ 2.92	0.34 ~ 1.00	1.00 ~ 5.43	0.18 ~ 1.00
^{60}Co (Type S)	1.00 ~ 9.85	0.10 ~ 1.00	1.00 ~ 16.70	0.06 ~ 1.00	1.00 ~ 16.69	0.06 ~ 1.00
^{134}Cs (Type F)	0.83 ~ 1.00	1.00 ~ 1.21	1.00 ~ 1.02	0.98 ~ 1.00	0.71 ~ 1.00	1.00 ~ 1.40
^{137}Cs (Type F)	0.84 ~ 1.00	1.00 ~ 1.19	1.00 ~ 1.04	0.96 ~ 1.00	0.73 ~ 1.00	1.00 ~ 1.38
^{89}Sr (Type F)	-	-	0.45 ~ 1.00	1.00 ~ 2.22	1.00 ~ 2.41	0.42 ~ 1.00
^{89}Sr (Type S)	-	-	1.00 ~ 5.48	0.18 ~ 1.00	1.00 ~ 6.20	0.16 ~ 1.00
^{90}Sr (Type F)	-	-	0.88 ~ 1.00	1.00 ~ 1.13	1.00 ~ 4.91	0.20 ~ 1.00
^{90}Sr (Type S)	-	-	1.00 ~ 63.37	0.02 ~ 1.00	1.00 ~ 72.59	0.01 ~ 1.00
^{32}P (Type F)	-	-	0.80 ~ 1.00	1.00 ~ 1.26	1.00 ~ 1.19	0.46 ~ 1.00
^{32}P (Type M)	-	-	1.00 ~ 2.85	0.35 ~ 1.00	1.00 ~ 3.11	0.32 ~ 1.00

In the case of ^{137}Cs (Type F) and ^{134}Cs (Type F), the E_{50} ratios remained in the range of 0.96 ~ 1.04 for the urine bioassay, 0.83 ~ 1.21 for the whole body counting and 0.71 ~ 1.40 for the feces bioassay. In the case of ^{90}Sr (Type F) and ^{32}P (Type F), the ratios were close to 1; 0.88 ~ 1.13 and 0.80 ~ 1.26 for the urine assay, respectively. However, the E_{50} ratios were in a wide range of 0.01 ~ 72.59 for ^{90}Sr (Type S), and of 0.06 ~ 16.69 for ^{60}Co (Type S). On the whole larger errors are expected when the feces assay and Type S are applied and smaller errors are expected when the Type F is applied for all the bioassay measurements. Particularly, high potential of unacceptable deviations is observed for Type S; underestimation under ingestion assumption and overestimation under inhalation assumption.

In addition, the feces assay for all the radionuclide except $^{134, 137}$Cs provides underestimates when only ingestion was considered while an inhalation intake exists and overestimates when only an inhalation was considered while ingestion intake exists.

If two methods of bioassay are used for an evaluation of intake, the potential errors caused by a misjudgment of an intake pathway can be reduced. Even though the ratio of inhalation and ingestion intake is not known, intake via each pathway can be estimated by using the following equations which were obtained from equations (2) and (3).

$$I^{inh} = \frac{M_A(t)F_B^{ing}(t) - M_B(t)F_A^{ing}(t)}{F_A^{inh}(t)F_B^{ing}(t) - F_B^{inh}(t)F_A^{ing}(t)} \quad (4)$$

$$I^{ing} = \frac{M_A(t)F_B^{inh}(t) - M_B(t)F_A^{inh}(t)}{F_A^{ing}(t)F_B^{inh}(t) - F_B^{ing}(t)F_A^{inh}(t)} \quad (5)$$

where all of the factors are the same as those used in equation (2) and equation (3). When two successive measurements by one method of bioassay were employed instead of two different methods, $M_A(t)$, $M_B(t)$, $F_A^{inh}(t)$, $F_A^{ing}(t)$, $F_B^{inh}(t)$ and $F_B^{ing}(t)$ in equations (4) and (5) can be replaced with $M(t_1)$, $M(t_2)$, $F^{inh}(t_1)$, $F^{ing}(t_1)$, $F^{inh}(t_2)$ and $F^{ing}(t_2)$, respectively. These replaced factors are defined as the bioassay measurements and the body retention fraction or the daily excretion rate at time t_1 and t_2 days after a single inhalation or ingestion.

By use of equations (4) and (5), each of the intakes by inhalation and ingestion is calculated and then the total E_{50} can be evaluated by equation (1). Ideally, the solutions for I^{inh} and I^{ing} in equations (4) and (5) would give the true fraction of inhalation intake or vice versa according to the quality of data for those factors in the equations. In an actual application, the results by equations (4) and (5) are not necessarily exact because of the counting errors and the systemic errors in the bioassay measurements, but they would be far better than the results by the assumption of a single intake pathway.

IV. Conclusions

The potential errors in the committed effective dose (E_{50}) due to the assumption of a single intake pathway were estimated by using the simulated bioassay measurements of the whole body, urine and feces at 1 day after an inhalation and ingestion of some selected radionuclides; $^{57, 58, 60}$Co, $^{134, 137}$Cs, $^{89, 90}$Sr and ^{32}P. Different absorption Types and various cases of inhalation intake fractions were considered. For inhalation, the particle size was assumed to be AMAD of 5 μm.

The potential errors in E_{50} due to the assumption of a single intake pathway were smaller for the compound of Type F than for the compound of Type M or Type S. The ratios of E_{50} with assumption of a single intake pathway to actual E_{50} were in the range from 0.01 to 72.59 for ^{90}Sr (Type S) and from 0.06 to 16.70 for ^{60}Co (Type S) and varied with the fraction of inhalation intake and the methods of bioassay. Generally larger errors are expected when the feces assay and Type S are applied.

In conclusion, if one assumes only one intake pathway in internal dose assessment for a person involved in a contamination incident, a significant error in the evaluated E_{50} may result. A strategy which employs two methods of bioassay or two successive measurements is proposed to reduce the potential error caused by a misjudgment of an intake pathway.

Acknowledgement

This work was performed under the long-term nuclear research and development program sponsored by Ministry of Science and Technology of Korea.

References

1) ICRP, *Dose Coefficients for Intakes of Radionuclides by Workers*, ICRP Publication 68, International Commission on Radiological Protection, (1994).
2) A. Birchall, N. S. Jarvis, M. S. Peace, A. E. Riddell, and W. P. Battersby, "The IMBA Suite: Integrated Modules for Bioassay Analysis," *Radiat. Prot. Dosim.*, 79[1-4], 107-110 (1998).
3) ICRP, *Individual Monitoring for Internal Exposure of Workers Replacement of ICRP Publication 54*, ICRP Publication 78, International Commission on Radiological Protection, (1997).
4) ICRP, *Human Respiratory Tract Model for Radiological Protection*, ICRP Publication 66, International Commission on Radiological Protection, (1994).
5) ICRP, *Limits for Intakes of Radionuclides by Workers: Part 1*, ICRP Publication 30, International Commission on Radiological Protection, (1979).
6) ICRP, *Age-dependent Doses to Members of the Public from Intake of Radionuclides: Part 2*, ICRP Publication 67, International Commission on Radiological Protection, (1993).
7) ICRP, *Age-dependent Doses to Members of the Public from Intake of Radionuclides: Part 1*, ICRP Publication 56, International Commission on Radiological Protection, (1989).

Journal of NUCLEAR SCIENCE and TECHNOLOGY, Supplement 5, p. 209–212 (June 2008)

Development of the Neutron Calibration Fields using Accelerators at FRS and TIARA of JAEA

Yoshiaki SHIKAZE*, Yoshihiko TANIMURA, Jun SAEGUSA, Masahiro TSUTSUMI, Shigeru SHIMIZU, Michio YOSHIZAWA, and Yasuhiro YAMAGUCHI

Japan Atomic Energy Agency, 2-4 Shirane, Shirakata, Tokai-mura, Ibaraki 319-1195, Japan

The neutron calibration fields using accelerators have been developed at the Facility of Radiation Standards (FRS) of JAEA-Tokai for neutrons below 20 MeV and at Takasaki Ion Accelerators for Advanced Radiation Application (TIARA) of JAEA-Takasaki for those over 20 MeV. At FRS, monoenergetic neutrons are generated by using proton or deuteron beam from a 4 MV Van-de-Graaff (Pelletron) accelerator. Up until the present, developments of the 8, 144, 250, 565 keV, 5.0 and 14.8 MeV fields have been completed. As procedure for the development, measurement of neutron energy spectrum, peak energy and reference fluence, development of monitoring scheme for neutron fluence and establishment of the traceability on neutron fluence to the primary standards were achieved. At TIARA, three neutron fields of 45, 60 and 75 MeV are planned to be established. Quasi-monoenergetic neutrons are generated from ^{7}Li(p,n)^{7}Be reaction by using proton beam from an AVF cyclotron, and led into an irradiation room through a cylindrical collimator, 3 m in thickness. Evaluation of the characteristics of the fields needed for the development as the standard calibration fields is in progress now.

KEYWORDS: neutron calibration field, accelerator, Pelletron, cyclotron, monoenergetic neutron, quasi-monoenergetic neutron, FRS, TIARA

I. Introduction

High energy proton accelerator facilities such as J-PARC have been developed in order to pursue frontier research in particle physics, nuclear technology and so on. To implement the quality radiation protection in such facilities, neutron calibration fields for wide energy range are necessary to evaluate the energy response of neutron monitors and dosemeters.

Although there are some monoenergetic neutron fields for research purposes in Japan, the secondary neutron standard fields traceable to the primary standards had not been constructed in particular for radiation protection purposes. Therefore, such monoenergetic neutron calibration fields below 20 MeV have been developed as the secondary standard fields using a 4 MV Van-de-Graaf accelerator at the Facility of Radiation Standards (FRS) of the Japan Atomic Energy Agency (JAEA)[1,2]. The calibration fields of 8, 144, 250, 565 keV, 5.0 and 14.8 MeV neutrons are available at FRS (**Fig. 1**).

For the neutron fields above 20 MeV, on the other hand, both the standard calibration fields and measurement techniques have not been fully established anywhere. For the development, the quasi-monoenergetic neutron irradiation fields of several tens of MeV at Takasaki Ion Accelerators for Advanced Radiation Application (TIARA) of JAEA[3] can be used. Therefore, the preliminary investigation of the neutron fields at TIARA[4] was started in order to use them as the standard fields together with National Institute of Advanced Industrial Science and Technology (AIST) which was national metrology institute of Japan. Three neutron fields with 45, 60 and 75 MeV peak are planned to be established (**Fig. 1**), considering the international intercomparison of the developed neutron fields with similar energy range. This paper describes development of neutron fields at FRS and TIARA.

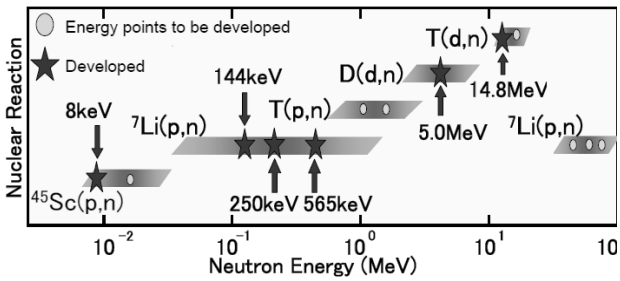

Fig. 1 Neutron energy and nuclear reaction of the calibration fields planned at FRS and TIARA.

II. Monoenergetic Neutron Calibration Fields below 20 MeV at FRS

1. Outline of the Facility at FRS

The 4 MV Van-de-Graaf accelerator is a 4UH-HC Pelletron from National Electrostatics Corp. in USA. It can accelerate protons and deuterons up to 4 MV and the maximum current is 50 μA at target. A cutaway view of the FRS is shown in **Fig. 2**. The accelerator is installed in the basement. The accelerated proton or deuteron beam is bent three times with two 90º vertical magnets and a 6.5º horizontal magnet and transported to an irradiation room at the ground level. The energy of the accelerated particles can be precisely determined using an analyzing magnet and a slit in the vertical beam line. A system with an NMR probe is

*Corresponding Author, Tel. +81-29-282-5637, Fax. +81-29-282-5609, E-mail: shikaze.yoshiaki@jaea.go.jp

adopted to accurately measure the strength of a magnetic field in the analyzing magnet. The dimensions of the irradiation room are 16.5 m (W) × 11.5 m (D) × 12.3 m (H) with an aluminum grating floor at the mid-height of the room. The detectors to be calibrated are set on a calibration table which is remotely controlled from an operation room.

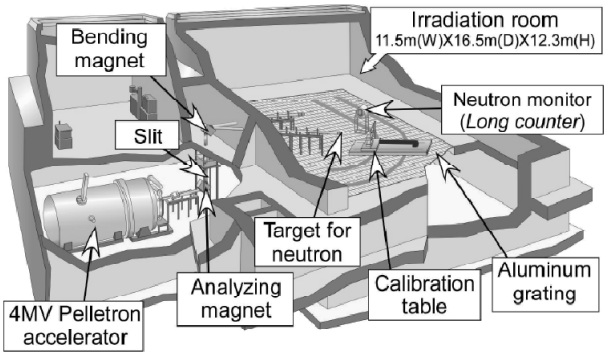

Fig. 2 Cutaway view of FRS from the accelerator to the irradiation room.

Ten energy points between 8 keV and 19 MeV will be available finally after completion and these can cover the energies specified in ISO 8529-1[5]. The nuclear reactions employed for neutron production are the $^{45}Sc(p,n)^{45}Ti$, $^{7}Li(p,n)^{7}Be$, $^{3}H(p,n)^{3}He$, $^{2}H(d,n)^{3}He$ and $^{3}H(d,n)^{4}He$ reactions[6]. A target for neutron production is placed near the center of the room to eliminate the neutrons scattered from the walls.

2. Development of Monoenergetic Neutron calibration Fields of 8, 144, 250, 565 keV, 5.0 and 14.8 MeV

The neutron fields of 8, 144, 250, 565 keV, 5.0 and 14.8 MeV have been developed. For the development, the followings were conducted: the design of targets, the measurements of neutron energies, neutron fluences, the construction of a monitor method for reference fluence and the establishment of traceability to the primary standards.

(1) Target Structure

The target for the $^{45}Sc(p,n)^{45}Ti$ reaction was made by evaporating scandium powder onto a platinum backing disk. The target for the $^{7}Li(p,n)^{7}Be$ reaction is made of thin vacuum-deposited LiF evaporated on a molybdenum backing disk. The gas cell for the $^{2}H(d,n)^{3}He$ reaction consists of a molybdenum foil as an entrance window, a tantalum aperture and a platinum beam stopper which hardly produces unwanted neutrons. The pressure of deuterium gas is regulated to approximately 0.1 MPa. The target for the $^{3}H(d,n)^{4}He$ reaction is made of tritium absorbed in a titanium layer, which is evaporated on a copper backing disk.

(2) Measurement of Neutron Energy

Neutron energies were measured by using an organic liquid scintillation detector (BC501A type; 5.08 cm (L) x 5.08 cm in dia.) except 8 keV and a lithium glass scintillation detector (2 cm (L) x 5.08 cm in dia.) for 8 keV by the time-of-flight (TOF) method. The peak energies of generated neutrons were precisely determined from the flight-time of neutrons between two different positions. The magnetic field strength in the analyzing magnet was adjusted to generate neutrons with demanded energy from the measured neutron energy. These results show that the produced neutrons have a good monochromaticity for the calibration of neutron dosemeters.

(3) Monitor Method for Reference Fluence

Since neutron emission rate from the target of accelerator would vary with time, ISO recommends that a neutron monitor shall be used during the calibration. A Long-Counter (LC) is employed for the neutron monitor to determine the reference neutron fluence at a calibration point because it has a flat response for a wide energy range. The arrangement in the irradiation room is shown in **Fig. 3**. The LC is placed at 2.2 m with an angle of 60º (3.0 m with 90º for 14.8 MeV) to the beam line. The position among several positions available from the arrangement in the room was determined to make the contribution of inscattered neutrons from the devices to be calibrated and their supporting materials small as possible.

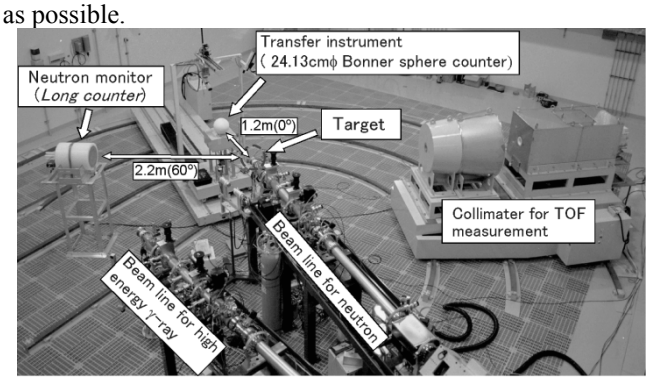

Fig. 3 Overview of the monoenergetic neutron calibration fields

Calibration coefficients K_{LC}, which are used to calculate the reference neutron fluence at a calibration point from the counts of the LC N_{LC}, were determined from the fluence measured by using the detectors mentioned in the following sections[1,2].

(4) Measurement of Neutron Fluence

For precise evaluation of the reference neutron fluence, neutron detectors were developed. For 8 keV field, the lithium glass scintillation detector mentioned before was developed. For 144, 250 and 565 keV fields, a cylindrical proton recoil proportional counter was developed. For 5.0 MeV field, a silicon semi-conductor detector with polyethylene radiator was developed. For 14.8 MeV field, a proton recoil counter telescope was developed. For each of the neutron fields, reference neutron fluence was precisely determined by using these detectors and responses estimated by Monte-Carlo calculation.

(5) Establishment of Traceability

The traceability of the neutron fields produced to the primary standards in Japan, AIST, was established through the calibration coefficient K_{LC} for each of the energies determined by a transfer instrument except 8 and 250 keV neutron fields. A Bonner sphere counter with a 24.1 cm-in-diam. owned by AIST was employed as the transfer

instrument. The counter was calibrated at the monoenergetic standard fields of AIST. The reference neutron fluence was measured with the counter at 1.2 m on the 0º (45º for 14.8 MeV) line as shown in **Fig. 3**. The shadow cone technique was used to eliminate scattered neutrons from the walls and other objects except the target assembly in the room.

(6) Uncertainty of the Calibration Coefficients

The expanded uncertainties of the coefficients K_{LC} were calculated according to the Guide to the expression of Uncertainty in Measurement[7], and estimated to be 5 to 15 % (coverage factor: k = 2) considering the uncertainties on the efficiency of the detectors, the distance from the target to the detectors, the counts of the detectors and the LC, and the fluctuations of the number of neutrons generated per beam current.

(7) Characteristics of the Fields

Table 1 shows the fluence rates and the ambient dose equivalent rates $H^*(10)$ estimated at a maximum beam current. Although the fluence and dose equivalent rates for 8 keV are very low compared with those in the other energy points[1,2], these are sufficient to calibrate many types of neutron survey meters with relatively high sensitivities used for radiation protection.

Table 1 Maximum fluence rates and dose equivalent rates estimated at the position 1 m from the target.

Energy	Maximum Beam Current [μA]	Maximum value at the position 1 m *1 from the target	
		Fluence rate [cm^{-2} s^{-1}]	H*(10) [mSv h^{-1}]
8 keV	50	7×10 *1	2.4×10^{-3} *1
144 keV	50	3×10^3	1.4
250 keV	50	2×10^3	1.4
565 keV	50	6×10^3	7
5.0 MeV	3	7×10^3	10
14.8 MeV	6	3×10^3	6

*1 Position only for 8 keV is 0.5 m from the target.

III. Quasi-monoenergetic Neutron Calibration Fields of Several Tens of MeV at TIARA

1. Outline of the Facility at TIARA

The quasi-monoenergetic neutron fields by using ^{7}Li(p,n)^{7}Be reaction for 40-90 MeV neutrons have been established as the irradiation field at TIARA. **Fig. 4** shows the layout of the quasi-monoenergetic neutron source facility at TIARA. A proton beam from an AVF cyclotron is transported to a ^{7}Li target with thickness corresponding to 2 MeV energy loss. Protons passed through the target are bent by a clearing magnet into a Faraday cup shielded by an iron beam dump. Neutrons are guided to the experimental room through about 3 m thick collimator (inner-diameter of 11 cm) consisting of an iron rotary-shutter and additional polyethylene and iron collimators. Neutron beam obtained in the experimental room, therefore, has low background of neutrons scattered by the materials on the upper side of the beam than the collimators. The dimensions of the experimental room are 11 m (W) × 19 m (D) × 6 m (H). The distance from the ^{7}Li target ranges from 5 to 18 m at on-beam position in the room. As the neutron monitors, the Faraday cup in the beam dump, ^{238}U and ^{232}Th fission chambers placed around the target are used (**Fig. 4**).

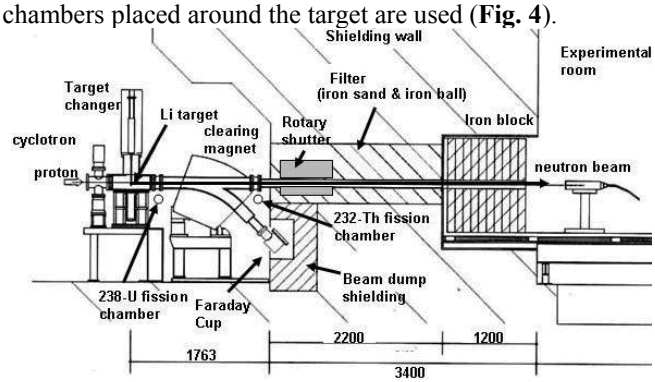

Fig. 4 Schematic view of the quasi-monoenergetic neutron source facility at TIARA of JAEA-Takasaki

2. Evaluation of the Characteristics of the Fields

To develop the neutron calibration field, it is inevitable to evaluate the characteristics of the field. Up until now, beam profile, peak neutron energy, neutron spectra inside and outside the irradiation field were measured. A detector to measure neutron fluence has been developed.

(1) Measurement of Beam Profile

The neutron beam profile was measured in order to investigate spatial distribution and intensity of the irradiation field. The Imaging Plate (IP, FUJI FILM, BAS-SR; for gamma-ray) was set at different positions along the beam line. Since the IP had very low sensitivity to a high energy neutron, high density polyethylene was installed as a converter to measure the recoil protons produced in the converter. Because the IP (BAS-ND) generally used for neutron measurement had high sensitivity only to the thermal neutrons and the response of the IP (BAS-ND) for the scattered neutrons would relatively obscure the response to high energy neutrons of our interest, the IP (BAS-SR) was applied instead of the IP (BAS-ND).

From the results, the following characteristics were confirmed: (a) Irradiation field area is fixed geometrically by the distance from the target and the inner diameter of the collimator exit; (b) The beam intensity within the irradiation field is inversely proportional to the square of the distance from the target.

(2) Measurement of Neutron Spectrum

The peak energy and energy spectrum of neutrons were measured by the TOF method, using the organic liquid scintillation detector (BC501A type; 5.08 cm (L) x 5.08 cm in dia.) set at the different distances from the target. To obtain the neutron flux, the response of the detector was calculated by the SCINFUL-QMD code[8].

For evaluation of the contribution from the scattered neutrons, the same type detector (12.7 cm (L) x 12.7 cm in dia.) was used. The neutron spectra were measured at various positions inside and outside the irradiation field at the same distance from the target. The energy spectra were evaluated from the neutron pulse height spectra by using the

FORIST unfolding code[9] with response functions calculated by the SCINFUL-QMD code.

From the results of the evaluation of the scattered neutrons, the following characteristics were found: (c) There were few differences of the spectral shape between inside and outside the irradiation field for neutrons over 20 MeV; (d) The contribution of the scattered neutrons was estimated to be about 0.5% by extrapolating the measurement results at outside to the center of the irradiation field; (e) From (c) and (d), most of scattered neutrons are attributed to the small-angle-scattered neutrons without energy loss at the collimator.

(3) Development of a Detector for Absolute Measurement of Peak Neutron Fluence

Neutron fluence of peak region is one of the most important parameters of the calibration fields with quasi-monoenergetic spectrum. For absolute measurement of the peak neutron fluence, a proton recoil telescope (PRT) has been developed. The PRT consists of a silicon semi-conductor detector (62 mm in dia., 300 μm in thickness) as Δ-E detector and an organic liquid scintillation detector (7.62 cm (L) x 7.62 cm in dia.) as E detector as shown in **Fig. 5**. In order to shield incident neutrons to the PRT set in the irradiation field on the beam axis, neutron shielding material of brass bar is set on the upper side of the PRT. The PRT measures the recoil protons from the n-p elastic scattering in a polyethylene converter as shown in **Fig. 6.** The influence of protons caused by carbon in the converter is corrected by measurement using a graphite converter. Based on the small uncertainty of the n-p elastic scattering cross-section, an obtained peak neutron fluence is expected to have a small uncertainty. Detection efficiency by calculation and total uncertainty of the fluence will be determined in the near future.

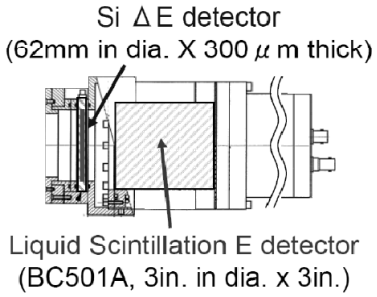

Fig. 5 Schematic view of the proton recoil telescope

IV. Summary

Monoenergetic neutron calibration fields of 8, 144, 250, 565 keV, 5.0 and 14.8 MeV have been developed using the 4 MV Pelletron accelerator at FRS of JAEA. As procedure for the development, neutron energy was measured by the TOF method using a liquid scintillation detector or a lithium glass scintillation detector. A long-counter (LC) is employed as a neutron monitor. The calibration coefficients, K_{LC}, of the LC were obtained from the measurements of the reference fluence using the transfer instrument of the primary standard laboratory (AIST). The traceability to AIST has been established by this calibration for 144, 565 keV, 5.0 and 14.8 MeV fields. The developed fields can be used for calibration of dosemeters, development of new radiation detectors, study on neutron dosimetry, etc.

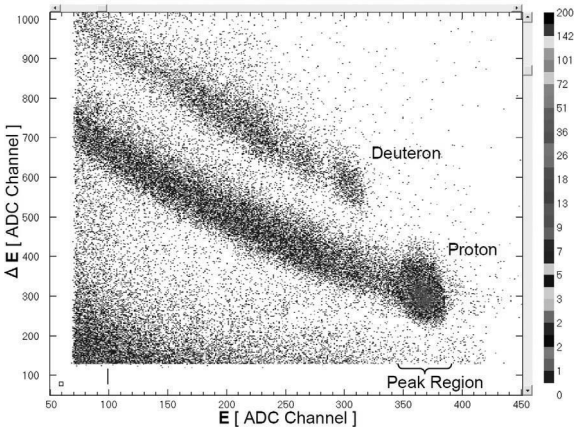

Fig. 6 Energy loss (ΔE) measured by the Si detector v.s. Energy (E) measured by the organic liquid scintillation detector for measurement with polyethylene converter.

For several tens of MeV, quasi-monoenergetic neutron calibration fields at TIARA are being developed now. Three neutron fields with 45, 60 and 75MeV peak are planned to be established, considering the construction of high energy neutron standards and the international intercomparison. The field's characteristics such as beam profile, energy spectrum and influence of scattered neutrons were evaluated. The measurement technique for peak neutron fluence will be established in the near future.

References

1) Y. Tanimura, M. Yoshizawa, J. Saegusa, et al., "Construction of 144, 565 keV and 5.0 MeV monoenergetic neutron calibration fields at JAERI," Radiat. Prot. Dosim., 110[1-4], 85 (2004).
2) Y. Tanimura, J. Saegusa, Y. Shikaze, et al., "Construction of monoenergetic neutron calibration fields using ^{45}Sc(p,n)^{45}Ti reaction at JAEA," Radiat. Prot. Dosim., (in press).
3) M. Baba, Y. Nauchi, T. Iwasaki, et al., "Characterization of a 40-90 MeV ^{7}Li(p,n) neutron source at TIARA using a proton recoil telescope and a TOF method," Nucl. Instrum. Meth., A428, 454 (1999).
4) Y. Shikaze, Y. Tanimura, J. Saegusa, et al., "Investigation of properties of the TIARA neutron beam facility of importance for calibration applications," Radiat. Prot. Dosim., (in press).
5) ISO. "Reference neutron radiations- Part 1: Characteristics and methods of production," ISO 8529-1, (2001).
6) M. Baba, M. Takada, T. Iwasaki, et al., " Development of monoenergetic neutron calibration fields between 8keV and 15MeV," Nucl. Instr. Meth., A376, 115 (1996).
7) ISO, BIPM, IEC, et al., "Guide to the expression of uncertainty in measurement," (1993).
8) D. Satoh, S. Kunieda, Y. Iwamoto, et al., "Development of SCINFUL-QMD code to calculate the neutron detection efficiencies for liquid organic scintillator up to 3 GeV," J. Nucl. Sci. Technol., Suppl. 2, 657 (2002).
9) R.H. Johnson, "A user's manual for COOLC and FORIST," Radiation Shielding Information Centre PNE-75-107, (1975).

Journal of NUCLEAR SCIENCE and TECHNOLOGY, Supplement 5, p. 213–216 (June 2008)

Understanding of the Microdosimetric Quantities Obtained by a TEPC

Si-Young Chang* and Bong-Hwan Kim

Korea Atomic Energy Research Institute, P.O. Box 105 Yuseong, Daejeon 305-600, Korea

A lineal energy, y and a specific energy, z are fundamental microdosimetric quantities for describing a radiation energy deposition event in a microscopic volume simulating a human tissue cell. They can be measured by using a low pressure Tissue Equivalent Proportional Counter (TEPC) with a so-called Bragg-Gray cavity principle. One of the advantages of using a TEPC is that it can directly evaluate a mean quality factor of the neutron in a mixed radiation field from the measured dose-mean lineal energy by applying a quality factor and LET relationship. From this mean quality factor and the absorbed dose estimated in terms of the frequency-mean specific energy, we can further evaluate a neutron dose equivalent for a radiation protection purpose. In this paper were described the results of the lineal and specific energy measurement in the KAERI ^{252}Cf neutron calibration field by a low pressure TEPC system designed and manufactured by the Health Physics Department at KAERI. Mean quality factors and dose equivalents of ^{252}Cf neutron were then evaluated from the measurement results of the lineal and specific energy values

KEYWORDS : TEPC, LET, Lineal energy, Specific energy, Absorbed dose, Quality factor.

I. Introduction

Low pressure Tissue Equivalent Proportional Counters (TEPC) have been widely used in radiation biology studies as well as in radiation protection fields to measure and evaluate a lineal energy and a specific energy of a radiation which are a microscopic analog of an LET and an absorbed dose, respectively.[1] By using a lineal energy, we can easily obtain an absorbed dose and derive a mean quality factor of a radiation to evaluate the dose equivalent in a mixed radiation field.[2),3)]

In this study the lineal energy spectrum and absorbed dose for the KAERI bare ^{252}Cf neutron calibration field have been measured by using a low pressure TEPC system manufactured by the Health Physics Department at KAERI.[4)] Mean quality factors based on the LET and lineal energy have been determined and finally a neutron dose equivalent of the KAERI neutron calibration fields were then evaluated.

II. Materials and Methods

1. KAERI TEPC system

Microdosimetric applications of the TEPCs are based on simulating a microscopic tissue mass by a macroscopic TEPC cavity filled with a TE gas at low pressure under a Bragg-Gray's cavity principle on the charged particle equilibrium.[5)] Considering that the mass stopping power of tissue and TE gas are identical, which is the meaning of the tissue equivalence, one can simulate a tissue cavity diameter by varying the in-filling TE gas pressure into the TEPC chamber.

$$P_g[hPa] = \frac{\rho_t}{\rho_g} \cdot \frac{10^{-4} d_t}{d_g} \cdot 1013.25 \cdot \frac{273+T}{273} \quad (1)$$

where P_g is the in-filling pressure of the TE gas (hPa), ρ_t and ρ_g are the densities of the tissue and the TE gas, d_t and d_g are the diameter of the tissue(㎛) and the TE gas(cm), respectively, and T is a room temperature(℃).

The KAERI TEPC adopts a methane-based TE (MTE) gas produced by the Korea Research Institute of Standards and Science (KRISS). The in-filling pressure of the MTE gas was 17.07 hPa to simulate a tissue cavity diameter of 2 ㎛ at the TEPC chamber cavity, and under this pressure, the mass of the MTE gas was 14.06 mg.[4)]

Table 1 lists the technical design specifications of a KAERI cylinder type TEPC and TE gas.

2. Calibration of the TEPC

KAERI TEPC contains a built-in ^{241}Am calibration alpha source (37 kBq, E_{av} : 5.49 MeV) which deposits alpha energy across the TE gas cavity in the TEPC chamber. The maximum stopping power (S_a) of the ^{241}Am alpha energy at 2 ㎛ of a simulated tissue cavity diameter was calculated by the SPAR code[6)] to be 84.5 keV/㎛, and a maximum pulse height was recorded at the 249th channel of the MCA connected to the TEPC. By this energy calibration process the deposited energy per channel was determined as follows:

$$\varepsilon_i = (84.5 \text{ keV}/\mu\text{m} \times 2\ \mu\text{m})/249 \text{ ch} = 0.679 \text{ keV/ch}$$

3. Measurement of a lineal energy

A lineal energy, y is defined as the quotient of the energy imparted, ε to the matter in a volume from a single energy-deposition event by a mean chord length, $\bar{l}$ in that volume.[2)]

*Corresponding Author, Tel. +82-42-868-2305, Fax. +82-42-868-8609, E-mail: sychang@kaeri.re.kr

$$y = \frac{\varepsilon}{\bar{l}} \quad [\text{keV}/\mu\text{m}] \tag{2}$$

Table 1 Technical specification of the KAERI cylinder type TEPC

TEPC	Remarks
Inner Diameter	**10 cm**
Height	**10 cm**
TE wall thickness	**0.2 cm**
Al container	
Inner Diameter	**12.44 cm**
Thickness	**0.23 cm**
Height	**21.0 cm**
Upper and lower thickness	**1.0 cm**
Contained calibration source	**^{241}Am, ~ 37 kBq**
Central electrode	**50 μm SST 304**
Electricity insulator	**Teflon**
Electricity terminal	**Amphenol 10400**
Gas inlet terminal	**Swagelock DESO type**
Connection sealing	**Torr sealing bonding**
TE gas composition (%)	**CH_4 : CO_2 : N_2 (64.1 : 32.7 : 3.2)**

The lineal energy is a stochastic quantity and is a microscopic analog of the Linear Energy Transfer (LET) which is a non-stochastic quantity. The mean chord length in a spherical cavity with a diameter, d is given as 2d/3.

The lineal energy can be measured by using Eq. (2) with the value of an imparted energy per channel (0.679 keV/ch). Therefore, a lineal energy per channel is

y_i = (0.679 keV/ch) / (2 μm x 2/3) = 0.509 keV/μm/ch.

Therefore, the KAERI TEPC with a 1024 channel MCA can theoretically measure 520 keV/μm at most.

Since a lineal energy is stochastic in nature a probability density of a lineal energy, f(y) has a probability distribution. Therefore the expectation value of the lineal energy distribution described as follows is called a frequency-mean lineal energy, $\bar{y}_F$ and is a non-stochastic quantity.[2)]

$$\bar{y}_F = \int_0^\infty y \cdot f(y)dy \tag{3}$$

The absorbed dose distribution d(y) with respect to a lineal energy distribution can also be considered. The expectation value of the absorbed dose distribution with a lineal energy described as follows is called a dose-mean lineal energy, $\bar{y}_D$ and is a non-stochastic quantity.[2)]

$$\bar{y}_D = \int_0^\infty y \cdot d(y)dy = \frac{1}{\bar{y}_F}\int_0^\infty y^2 \cdot f(y)dy \tag{4}$$

The frequency-mean lineal energy, $\bar{y}_F$ by considering a single-energy deposition event distribution from the MCA counts per channel can be rewritten as follows;

$$\bar{y}_F = \int_0^\infty y \cdot f(y)dy \equiv \frac{1}{n}\sum_i n_i \cdot y_i \tag{5}$$
$$f(y) = n_i / \sum_i n_i$$

where, n_i is the no. of counts of a single-energy deposition event per i^{th} channel, y_i is the lineal energy per i^{th} channel.

Likewise, the dose-mean lineal energy $\bar{y}_D$ can also be obtained from the lineal energy distribution data.

$$\bar{y}_D = \frac{1}{\bar{y}_F}\int_0^\infty y^2 \cdot f(y)dy \equiv \frac{\sum_i n_i \cdot y_i^{\,2}}{\sum_i n_i \cdot y_i} \tag{6}$$

4. Measurement of a specific energy

A specific energy, z is defined as the quotient of the energy imparted, ε by m, where ε is the energy imparted by ionizing radiation to a matter of mass m.[2)]

$$z = \frac{\varepsilon}{m} = \frac{1}{m}\sum_i \varepsilon_i \quad [\text{J/kg, Gy}] \tag{7}$$

Since the specific energy is a stochastic quantity, it is often convenient to use a frequency-mean specific energy of the non-stochastic quantity which can be measured.

$$\bar{z}_F = \frac{\bar{\varepsilon}}{m} = \frac{2d_t}{3m}\sum_i \bar{y}_F \tag{8}$$

A frequency-mean specific energy $\bar{z}_F$ can be also rewritten in the function of frequency distribution of specific energy as follows:

$$\bar{z}_F = \int z \cdot f_1(z)dz \equiv \frac{\sum_i n_i \cdot z_i}{\sum_i n_i} = \frac{z}{n} \tag{9}$$
$$f(z) = n_i / \sum_i n_i$$

where $f_1(z)$ is the probability distribution of a specific energy for a single energy deposition event in a matter of interest and n is a total no. of counts in the MCA attached to the TEPC which are the no. of energy deposition event.

5. Measurement of an absorbed dose

One advantage of the TEPC is that it can directly measure an absorbed dose because it can simulate a microscopic human tissue cavity under a Bragg-Gray cavity principle.

The absorbed dose measurement by a TEPC is done by measuring the energy imparted in a gas cavity of a TEPC as follows:

$$D(Gy) = \frac{d\bar{\varepsilon}}{dm} = \frac{1.602\times10^{-13}}{m_g}\sum_i n_i \cdot \varepsilon_i$$
$$= \frac{1.602\times10^{-13}}{m_g}\cdot\frac{2d_t}{3}\sum_i n_i \cdot y_i \quad (10)$$

where 1.602 x 10^{-13} is a conversion constant (Gy-g/keV), m_g is a mass of the MTE gas and d_t is a tissue cavity diameter(㎛) simulated by the TEPC

6. Evaluation of a neutron mean quality factor

A quality factor, Q of a radiation is usually expressed as a function of the LET as follows: [3,5]

$$\bar{Q} = \frac{1}{D}\int Q(L)\cdot D(L)\cdot dL \quad (11)$$

where D(L) dL is the absorbed dose at 10 mm in the ICRU sphere between L ~ L+dL, respectively.

In 1983, ICRU in its publication 36 suggested a simple equation to derive a mean quality factor of a charged particle based on the report of ICRP/ICRU joint committee on RBE(1963) and the Kellerer and Hahn's study(1972).[2]

$$\bar{Q} = 0.8 + 0.14\bar{y}_D \quad (12)$$

In 1986, ICRU newly proposed an equation in its publication 40 to derive a mean quality factor and a quality factor using the lineal energy which can be readily measured by using a TEPC.[3]

$$\bar{Q} \equiv \frac{1}{D}\int Q(y)\cdot D(y)\cdot dy$$
$$Q(y) = \frac{5510}{y}\left\{1-\exp(-5\times10^{-5}y^2 - 2\times10^{-7}y^3)\right\} \quad (13)$$

where D(y)dy are the absorbed dose at 10 mm in the ICRU sphere between y ~ y+dy, respectively.

In 1990, ICRP in its publication 60[8] recommended a radiation weighting factor, w_R in order to consider both an external and an internal exposure situation to evaluate an equivalent dose. However, ICRP still adopts the mean quality factor concept given in Eq. (11) to derive a radiation weighting factor w_R.[6]

Table 2 shows the relationship between the quality factor and an unrestricted LET(=L).

Table 2 Relationship between Q and LET

L (keV/㎛)	Q(L)
< 10	1
10 ~ 100	0.32 L – 2.2
> 100	300 / $L^{1/2}$

III. Results and discussions

1. Lineal energy and absorbed dose

In order to measure the lineal energy and the absorbed dose, KAERI TEPC was irradiated to neutrons from a bare ^{252}Cf source whose neutron emission rate was 1.507 x 10^8 n/s for 100 seconds at 100 cm distance from the source.[4] The neutron calibration facility of KAERI is a bunker room whose dimensions are 8 m long, 6 m wide and 6 m high, and it is enclosed with 60 cm thick concrete walls and ceiling.

The results of the lineal energy measurement by Eqs. (5) and (6), a frequency-mean specific energy by Eqs. (8) and (9) and an absorbed dose evaluation by Eq. (10) for the KAERI ^{252}Cf calibration neutron field are listed in **Table 3**.

Table 3 Mean lineal energy, mean specific energy and absorbed dose for KAERI ^{252}Cf neutron field

Field	y_F (keV/㎛)	y_D (keV/㎛)	z_F (nGy)	D(=z) (μGy)
n + gamma	15.0	55.8	0.2	8.5
n only	38.8	73.9	0.6	6.2

Fig. 1 and **2** show the lineal energy distribution yf(y) and dose distribution yd(y) of the lineal energy of the KAERI ^{252}Cf calibration neutron field, respectively.

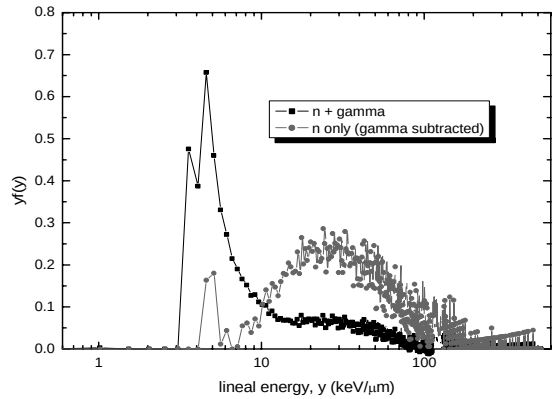

Fig. 1 Microscopic lineal energy distribution of KAERI ^{252}Cf neutron field

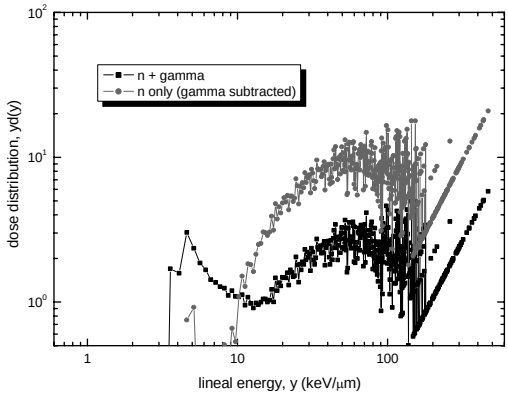

Fig. 2 Microscopic dose distribution of KAERI ^{252}Cf neutron field

2. Mean quality factors and dose equivalents

Neutron mean quality factors for the KAERI ^{252}Cf calibration neutron field were evaluated by Eqs. (11) to (13) and Table 2, and the results are listed in **Table 4** with the radiation weighting factor calculated by the Eq. given in the new ICRP proposal.[8] Neutron dose equivalent has also been obtained by multiplying a neutron mean quality factor to an absorbed dose given in Table 3.

Table 4 shows the mean neutron quality factors and dose equivalents for the KAERI ^{252}Cf neutron field obtained by ICRU-36[2], ICRU-40[3], ICRP-60[7] and ICRP new proposal[8].

In **Fig. 3**, neutron dose equivalent obtained by multiplying different mean quality factors to the neutron absorbed dose are shown.

Table 4 Mean quality factors and dose equivalents for KAERI ^{252}Cf neutron field

Methodologies	$\bar{Q}$	H (μSv)	Remarks
ISO	**11.0**	**-**	**Theoretical value (Ref. 9)**
ICRU-36 ('83)	**11.1**	**68.5**	**Ref. 2)**
ICRU-40('86)	**17.4**	**107.4**	**This study**
ICRP-60 ('90)	**15.7**	**97.1**	**Table 2**
ICRP new proposal ('07)*	**16.9**	**104.5**	**1.0 MeV (Most probable energy)**
	16.5	**102.0**	**2.3 MeV (Mean energy)**

* $\omega_R \equiv \bar{Q} = 5.0 + 17.0\exp[\frac{-\{\ln(2E_n)\}^2}{6}], \quad 1MeV \le E_n \le 50MeV$

The radiation weighting factor values by the ICRP new proposal[8] methodology were simply introduced for the purpose of an intercomparison, because the radiation weighting factor obtained by the equation in the ICRP new proposal is in principle not measurable at all.

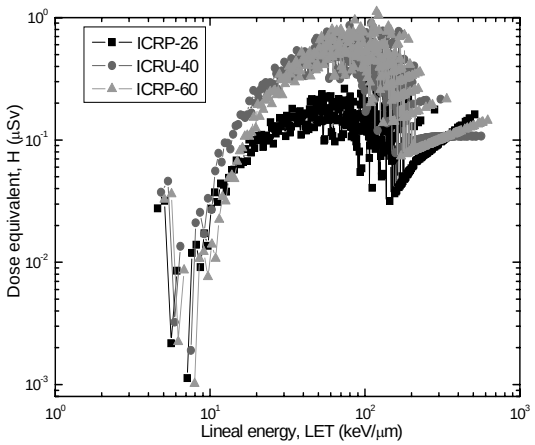

Fig. 3 Distribution of neutron dose equivalents of KAERI ^{252}Cf neutron field

As seen in **Fig. 3**, the neutron dose equivalent value obtained by the ICRP-26 method was lower by 3 times that obtained by the ICRU-40 and ICRP-60 method between 10 to 100 keV/μSv of lineal energy transfer.

IV. Conclusion

From the results of the lineal energy measurement for the KAERI bare ^{252}Cf neutron field, the frequency-mean and dose-mean lineal energy was evaluated to be 15.0 keV/㎛ and 55.8 keV/㎛ for the mixed field, and 38.8 keV/㎛ and 73.9 keV/㎛ for neutron-only field, respectively.

The frequency-mean specific energy was 0.2 nGy for the mixed field and 0.6 nGy for neutron only, respectively, and the absorbed dose was 8.5 μGy for the mixed field and 6.2 μGy for the neutron-only field, respectively. .

The neutron mean quality factor and the dose equivalent obtained by the lineal energy measurement based on the ICRU-40 methodology appeared to be 17.4 and 107.4 μSv, respectively for 100 second of neutron irradiation to the TEPC. These values seemed to be in fair agreement with those by the ICRP-60 method (15.7 and 97.1 μSv) obtained by the Q(L) relationship in Table 2, when considering the difference between the lineal energy(y) and the linear energy transfer(LET) concept.

Therefore the KAERI TEPC can be successfully used in the neutron monitoring and dose measurement in a practical radiation protection purpose by measuring an absorbed dose of neutron as well as evaluating the mean quality factor of neutron from the lineal energy measurement of neutron in the mixed radiation field.

Acknowledgement

This study was the partial product of the national project for long term nuclear energy development supported by the Ministry of Science and Technology of Korea.

References

1) H.H. Rossi and M. Zadier, 'Microdosismtry and Its Application', Springer Verlag, Berlin, Germany (1996)
2) ICRU, .'Microdosimetry', ICRU Report 36, Bethesda, USA (1983)
3) ICRU, 'The Quality Factor in Radiation Protection', ICRU Report 40, Bethesda, USA (1986)
4) S.Y. Chang, et al. 'Technology Development for Evaluation of Operational Quantities in Radiation Protection', KAERI/RR-2358/2002, Korea Atomic Energy Research Institute, (2002)
5) A. J. Waker, 'Principles of Experimental Microdosimetry', Radiat. Prot. Dosim. 61(4) 297-308 (1995)
6) T.W. Armstrong, 'Stopping Power and Range,' ORNL-4869 (1996)
7) ICRP, '1990 Recommendations of the ICRP', ICRP Publication 60 (1991)
8) ICRP, 'Draft Recommendations of the ICRP', ICRP New Proposal (January, 2007)
9) ISO, Neutron reference radiations for calibrating neutron measuring devices used for radiation protection purposes and for determining their response as a function of neutron energy, ISO/DIS 8529 Annex B, International Organization for Standardization (1986)

Journal of NUCLEAR SCIENCE and TECHNOLOGY, Supplement 5, p. 217–220 (June 2008)

An Inter-comparison of the Neutron Calibration Fields by D_2O Moderated ^{252}Cf Source at JAEA and KAERI

Munehiko KOWATARI[1*], Katsutoshi FUJII[1], Masahiro TSUTSUMI[1], Bong-Hwan KIM[2], Ki-Chang LEE[2], Michio YOSHIZAWA[1], and Yasuhiro YAMAGUCHI[1]

[1] *Department of Radiation Protection, Nuclear Science Research Institute, Japan Atomic Energy Agency, Tokai, Ibaraki, Japan*
[2] *Health Physics Department, Korea Atomic Energy Research Institute, Yuseong, Daejeon, Korea*

An inter-comparison of the neutron calibration field of the D_2O moderated ^{252}Cf source was carried out at JAEA and KAERI. Measuring the neutron spectra at KAERI by means of the method employed at JAEA, we attempted to evaluate the basic parameters for the D_2O moderated ^{252}Cf source and validate our method for determination of these parameters. We obtained the differences in the spectrum at each facility and theoretically clarified the effect of the geometries of the source assembly and the dimensions of the irradiation room on the neutron standard field.

KEYWORDS: D_2O moderated ^{252}Cf source, calibration, neutron dosimetry, Bonner sphere

I. Introduction

The reliable calibration should be required for the neutron measuring devices, in order to adequately evaluate the neutron dose rate by measurement. Well defined neutron reference fields can achieve the reliable calibration. It is desirable that the neutron reference field should have an energy spectrum similar to that of which the measurements are to be made. Among radionuclide neutron standard sources recommended by ISO [1)], the D_2O moderated ^{252}Cf neutron source assembly (D_2O-Cf source) has been adopted for the proper calibration of the neutron personal dosemeters2) used at nuclear power reactors. The D2O-Cf source has been installed at various calibration facilities 3-6). At the Korea Atomic Energy Research Institute (KAERI) and the Japan Atomic Energy Agency (JAEA), the D_2O-Cf sources also have been equipped with their own ^{252}Cf neutron source and provided for calibration [7, 8)].

Between the facilities of KAERI and JAEA, There are differences in the dimensions for the D_2O-Cf source assembly and irradiation room. The assessment of the influence of differences on the neutron standard field is essential. We performed the inter-comparison of the characteristics of the neutron standard fields by the D_2O-Cf sources. Measuring the neutron spectra at KAERI by our method employed at JAEA, we verified the basic parameters for D_2O-Cf source and our method. Comparison of the parameters and discussion on the differences in the parameters is made.

II. Material and Methods

1. The neutron Reference Field by D_2O Moderated ^{252}Cf Source Assembly at KAERI and JAEA

In accordance with ISO 8529-1[1)], the D_2O-Cf source consists of the ^{252}Cf source surrounded by the D_2O sphere with a diameter of 30 cm, covered with a Cd shell of thickness approximately 0.1 cm. The basic properties of the calibration field by D_2O-Cf source equipped at KAERI and JAEA are summarized in **Table 1**.

Table 1. The differences of the calibration field by D_2O-Cf source between KAERI and JAEA

	KAERI	JAEA
D_2O sphere		
Inner radius	**161.5 mm**	**150 mm**
SUS wall thickness	**0.80 mm**	**0.50 mm**
Cd shell thickness	**0.5 mm**	**1.0 mm**
^{252}Cf source type	**SR-Cf-100 capsule**	**X1 capsule**
Remarks	**Source loading tube (about 25 mm ^{t})**	**-**
Room dimensions (m^3)	**8 × 6 × 6**	**12.5 × 12.5 × 11.7**

Three major differences can be seen between the source assemblies equipped at KAERI and JAEA: 1) the moderator used at KAERI is larger than that at JAEA; 2) ^{252}Cf source type adopted for the D_2O-Cf source is different each other; 3) the KAERI source assembly is equipped with the stainless steel tube for loading the source from the bottom to the center of the sphere. The neutron source used at KAERI is an encapsulated Savanna River SR-Cf-100 series source and the neutron emission rate, *B*, was determined at National Institute of Standards and Technology (NIST) in the United States. At JAEA, type X1 capsule ^{252}Cf source made by Amersham (now QSA Global Inc.) was adopted and the neutron emission rate was $(1.18\pm 0.022) \times 10^7$ s^{-1} on October 1, 2005, which was determined by the primary standard laboratory, National Institute of Advanced Industrial Science and Technology (AIST) in Japan.

At JAEA, the D2O-Cf source is positioned at the center of a 12.5 × 12.5 × 11.7 m^3 irradiation room using the stainless-steel stand on the zinc plated iron grating floor. At KAERI, the D_2O-Cf source is placed on the center of a bunker room (dimensions: 8 × 6 × 6 m^3) with 60 cm thick concrete wall.

*Corresponding Author, TEL: +81-29-282-5877, FAX: +81-29-282-5609, E-mail : kowatari.munehiko@jaea.go.jp

2. Measurement at KAERI

We measured the neutron spectra from the D_2O-Cf source at each facility, using the Bonner Multi-sphere neutron Spectrometer (BMS) developed by JAEA. The basic parameters for the neutron standard field were derived from the spectrum measurement. The measurement at KAERI was carried out from Feb. 13 to Feb. 16, 2006. The BMS consists of the spherical BF_3 proportional counter with 5.08 cm diameter and surrounding moderators of polyethylene with thicknesses of 1, 2, 4, 8 and 10 cm. The series of the measurements were made as follows:

1) The spectrum of the scatter-free neutron for the D_2O-Cf source was measured at the distance of 150 cm at KAERI, for comparison of the basic parameters, i.e. the ambient-dose-equivalent per fluence, $h^*_{\Phi}(10)$, the personal-dose-equivalent per fluence, $h_{P\Phi}(10,0°)$, and the ratio of the neutron fluence rate of the D_2O-Cf source assembly (φ_{mod}) to that of direct neutrons ($B\ (4\pi L^2)^{-1}$) without the source assembly, β. Here, β is expressed as the following equation, $\beta = \varphi_{mod}\ 4\pi L^2\ B^{-1}$, where L is the given distance. We derived the scatter-free spectral fluence from the net counting rate using the shadow shield method.

2) The response to neutrons in BF_3 counter with the polyethylene moderator (R_{φ}) was determined using the shadow shield and polynomial fitting methods, for the verification of the adaptability of two methods. The BF_3 counter with 8 cm thickness (8 cm^t bonner counter) was selected because of the highest sensitivity and the similar size to the commercial dose equivalent rate meters. The counting rates were measured at the distances of 40, 60, 75, 100, 150 and 200 cm. The shadow cone made of iron and polyethylene was adopted. The dimensions are 50.6 cm long, 32.5 cm and 35.0 cm diameter in the front and rear end, respectively.

3) Spectra including the scattered components by the surroundings were measured at the distance of 150 cm, in order to evaluate the effect to the difference in the shape and the size of the irradiation room. Unfolded neutron spectra were obtained by the JAEA unfolding method using the SAND II code [9]. A set of response functions of the BMS up to 15 MeV was given by Uchita et al. [10]. The ambient and personal dose equivalents per fluence were obtained using fluence-to-dose-equivalent conversion coefficients in the ICRP Publication 74[11].

3. Calculation

The initial guess spectra were estimated by MCNP-4C[12] calculation with the cross section data of the JENDL-3.3 library[13], for obtaining the measured neutron spectra of D_2O-Cf source. Spectra were tallied using a point detector (F5 tally) of MCNP[10]. The moderator assembly was precisely modeled in accordance with the schematic drawing of the assembly construction including the SR-Cf-100 zircalloy-2 capsule. The source region, however, was treated as a void inside of the SR-Cf-100 capsule. As a source spectrum, the spectrum of ^{252}Cf recommended by ISO[1] was adopted. Additional evaluations were made by calculation, concerning the geometry of the source assembly and the effect of the room-size to the scattered component from the surroundings. The effect of the source assembly geometry was evaluated by comparing with the ideal D_2O-Cf sources. For the calculation of neutron spectra including the scattered component, we took into account the concrete-walls, the ceiling and the floor, the aluminum and stainless steel frameworks, the source loading tube, the calibration table, and other peripherals.

III. Results and Discussion

1. Scatter-free Neutron Component for the D_2O Moderated ^{252}Cf Source

Fig. 1 shows the comparison of the scatter-free neutron spectrum measured at KAERI and JAEA. The scatter-free neutron spectra per lethargy were normalized to the total neutron fluence rate. Measured spectrum at KAERI was slightly higher than that obtained at JAEA in the range from 10 keV to 1 MeV. In the energy region lower than 10 keV, the spectrum measured at JAEA was higher than that obtained at KAERI. The difference in the shape of neutron fluence spectra might be caused by the shapes of each D_2O-Cf source assembly.

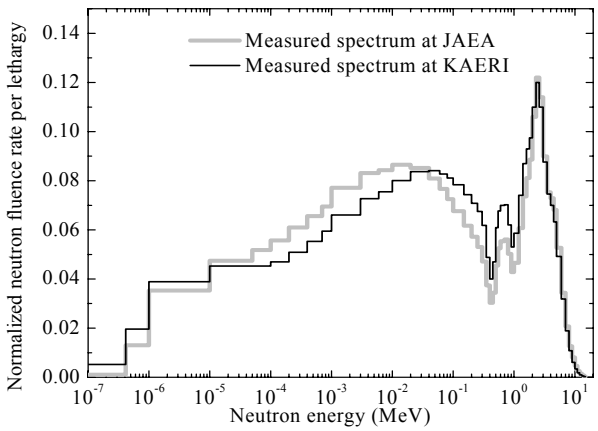

Fig. 1 Comparison of the measured scatter-free neutron spectra for D_2O-Cf source between KAERI and JAEA

The obtained basic parameters for the neutron reference field by D_2O-Cf source are listed in Table 2. The uncertainties in the results at KAERI were: 1) the maximum error of each counting rate for the BMS counter (±0.57%), 2) the relative standard uncertainty associated with the neutron source strength (±2.0%), 3) the uncertainty associated to the response functions (±4.1%), and 4) the uncertainty associated with the unfolding process (±3.0%). The overall uncertainties of 5.5% for the measured results were obtained in accordance with the law of the propagation of the uncertainty. The results obtained at KAERI and JAEA were almost same. The dose equivalents per fluence at KAERI were higher than those at JAEA. This might be also caused by the difference of the spectrum.

Fig. 2 depicts the calculated results of the influence on the scatter-free spectrum by the source geometry. The MCNP calculations show that the spectrum from large size source assembly is lower in the range from 10 keV to 1 MeV, comparing the spectrum calculated from the ISO recommended source assembly[1)]. Oppositely, the spectrum is higher in the same region, assuming the heavy source shell of 25 mm thickness of stainless steel (including SR-Cf-100 source, protection capsule and wall of the source loading tube) in the calculation. Concerning KAERI D_2O-Cf source, the source assembly is larger and has a heavier wall than those recommended by ISO[1)]. As a result of calculation, the shape of the KAERI spectrum could explain the sphere size effect and heavy encapsulation effect. For the case of the KAERI sphere, heavy encapsulation effect seems to be predominant.

Table 2. Results of the basic parameters of the neutron reference field by the D_2O-Cf source

	KAERI	JAEA[8)]	ISO[1)]
$h^*_{\Phi}(10)$ (pSv cm^2)	113 ± 6	110 ± 6	105
$h_{P\Phi}(10,0°)$ (pSv cm^2)	118 ± 6	115 ± 6	110
β	0.881 ± 0.048	0.882 ± 0.007	0.885

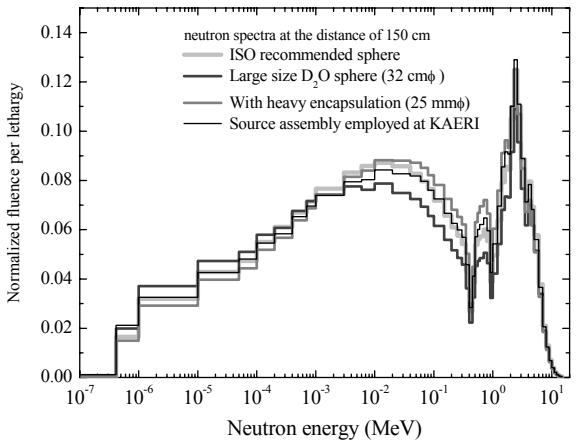

Fig. 2 Comparison of the calculated scatter-free neutron spectra for D_2O-Cf source with different source geometries

2. Response for the 8 cm^t bonner counter

The response to the neutron fluence rate for BF_3 counters with moderator with 8 cm thickness, R_φ, was derived from the counting rate and the fluence rate for the scatter-free neutron of the D_2O-Cf source by the shadow shield method. For the derivation of R_φ by the polynomial fitting method, R_φ was obtained by the least square method using the following empirical expression,

$$\frac{\dot{C}}{\frac{B}{4\pi L^2}} = R_\varphi\left(1 + aL + BL^2\right) \quad (1)$$

where $\dot{C}$ is the counting rate of the BF_3 counter with the polyethylene moderator of 8 cm thickness, L is the distance from the center of the source to the center of the detector (source-to-detector distance), and a and b are free parameters for the least square fitting. Then the series of R_φ obtained by each method were compared.

Table 3 shows the R_φ for the 8 cm^t bonner counter obtained by each facility. The R_φ obtained at KAERI and JAEA are very satisfying. The responses obtained at KAERI were both higher than those at JAEA by each method. This might reflect the difference in shape of the spectrum obtained at each facility. Calculated R_φ at KAERI was estimated to be about 3% larger than that at JAEA, multiplying the response function with the scatter-free component. From the results of the R_φ measurement, the shadow shield and polynomial fitting methods can be both applicable, in the case that the inter-comparison of the response for the neutron measuring devices is to be carried out.

Table 3. The result of R_φ for the BF_3 counter with the polyethylene moderator of 8 cm thickness. (counts n^{-1} cm^2)

	Shadow shield	Polynomial fitting
KAERI	0.80 ± 0.04	0.78 ± 0.02[1]
JAEA	0.76 ± 0.04	0.77 ± 0.02[1]

[1]The uncertainty associated with the least square fitting method using equation (1).

3. Scattered component of the neutron field for the D_2O moderated ^{252}Cf source

Fig. 3 shows the variations of the R_φ to the distance. R_φ increases with increasing the source-to-detector distance. This is because the bonner counter is also sensitive to the scattered neutrons by the surroundings. At the same source-to-detector distance, the R_φ obtained at KAERI is higher than that obtained at JAEA. This could be explained by the difference in the size of the irradiation room.

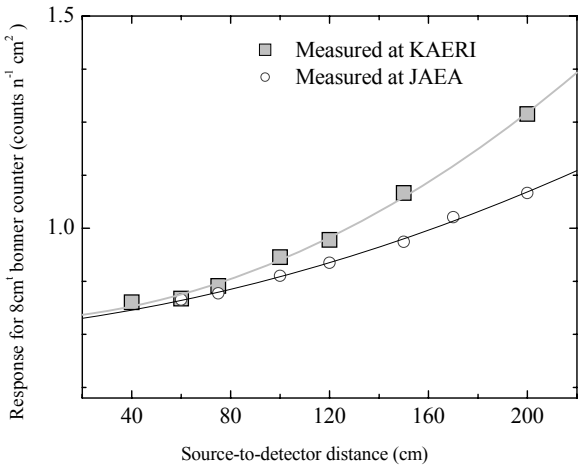

Fig. 3 Variation of the response of the bonner counter as a function of the measurement distance

Fig. 4 shows the calculated neutron spectra of the scatter-free component at the distance of 150 cm. Irradiation room is assumed to consist of the concrete wall, floor and ceiling with 1.0 m thickness. The neutron fluence rate including the

scattered component decreased with increasing the room size. The ratios of the scattered component to the scatter-free component for the D_2O-Cf source indicate the same tendency. As shown in **Fig. 5**, the lower energy neutrons are predominant, as for the scattered neutron component from the surroundings. The measured ratios of the scattered component to the scatter-free neutron fluence rate for the D_2O-Cf source were obtained to be 0.84 for KAERI, and 0.46 for JAEA, respectively. KAERI has smaller irradiation room than JAEA. The counter also has sensitivity to the scattered component as well as the scatter-free component. Consequently, R_φ obtained at KAERI was higher than that at JAEA.

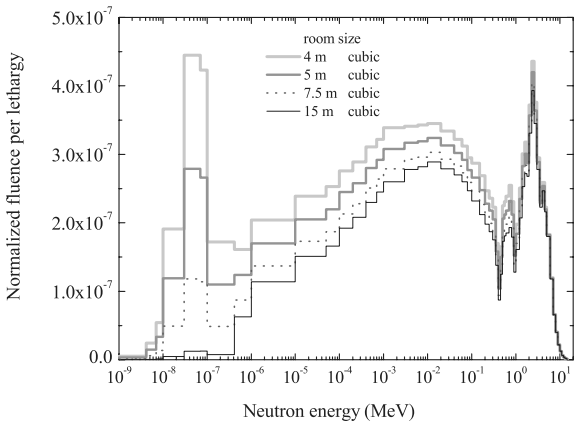

Fig. 4 The variation of the calculated neutron spectra at the distance of 150 cm as a function of the room size

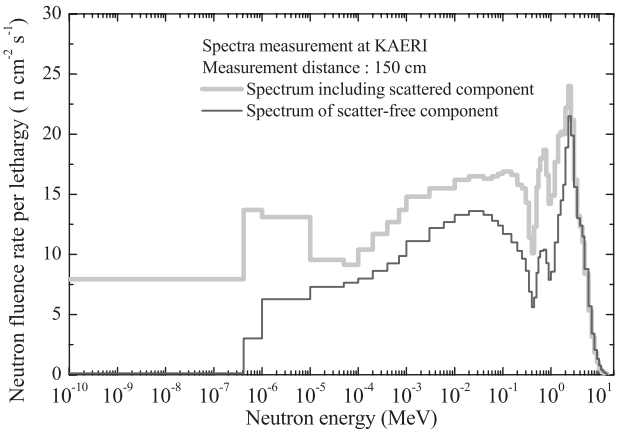

Fig. 5 Comparison of the measured neutron spectrum for the D_2O-Cf source at KAERI

IV. Conclusions

An inter-comparison of the neutron standard field produced by the D_2O-Cf sources was carried out between KAERI and JAEA. We verified that the neutron reference fields for D_2O-Cf source were both well defined at both facilities. The followings were clarified:

1) The derived basic parameters for D_2O-Cf source at each facility were well evaluated, taking the uncertainties into account. Higher values of dose equivalent per fluence obtained **at** KAERI would reflect the difference in the geometry of the source assembly.

2) Using the 8 cm^t bonner counter, almost the same calibration factor could be obtained by the shadow shield and polynomial fitting methods.

Through this inter-comparison, we achieved to evaluate the influence of the difference in the geometry of the source assembly and room dimensions by measurement and calculation.

References

1) International Organization for Standardization (ISO), "Reference neutron radiations – Part 1: Characteristics and methods of production," International Standard ISO 8529-1, (2001).
2) R. B. Schwartz and C. M. Eisenhauer, "The design and Construction of a D_2O-moderated ^{252}Cf Source for Calibrating Neutron Personnel Dosimeters Used at Nuclear Power Reactor," Report to the U.S. Nuclear Regulatory Commission under Interagency Agreement No. NRC-01-78-012, (1979).
3) H. Ing and W. G. Cross, "Spectral and dosimetric characteristics of a D_2O-moderated ^{252}Cf calibration facility," Health. Phys., **46** (1), 97-106 (1984).
4) H. Kluge, W. Rasp and J. B. Hunt, "An Intercomparison of the D_2O-moderated ^{252}Cf reference neutron sources at PTB and NPL," Radiat. Prot. Dosim., **11** (1), 61-63 (1985).
5) S. Jetzke, H. Kluge, R. Hollnagel, et al., "Extended use of a D_2O-moderated ^{252}Cf sources for the calibration of neutron dosemeter," Radiat. Prot. Dosim., **44** (1/4), 131-134 (1992).
6) S. Jetzke and H. Kluge, "Characteristics of the ^{252}Cf neutron fields in the irradiation facility of the PTB," Radiat. Prot. Dosim., **69** (4), 247-256 (1997).
7) B. H. Kim, J. L. Kim, S. Y. Chang, et al., "Characteristics of the KAERI neutron reference fields for the calibration of neutron monitoring instruments," J. Korean Asso. Radiat. Prot. **26** (3), 243-248 (2001).
8) M. Kowatari, K. Fujii, M. Takahashi, et al., **"**Evaluation of the characteristics of the neutron reference field using D_2O-moderated ^{252}Cf source**,**" Radiat. Prot. Dosim., to be published, (2007).
9) W. N. McElroy, S. Berg, T. Crockett et al., "A Computer-automated Iterative Method for Neutron Flux Spectra Determination by Foil Activation," AFWL-TR-67-41, Air Force Weapon Laboratory (1967).
10) Y. Uchita, J. Saegusa, Y. Kajimoto et al., "Characteristics of Thermal Neutron Calibration Fields Using a Graphite Pile," JAERI-Tech **2005-012,** (2005). [in Japanese]
11) International Commission on Radiological Protection, Conversion Coefficients for Use in Radiological Protection against External Radiation, ICRP Publication 74, Ann. ICRP **26**(3/4), Pergamon Press, Oxford, (1996).
12) J. F. Briesmeister, "*MCNP – a general Monte Carlo N-Particle transport cord," Version 4C.* LA-13709-M, Version 4C (Los Alamos, NM: Los Alamos National Laboratory), (2000).
13) K. Shibata, T. Kawano, T. Nakagawa et al., "Japanese Evaluated Nuclear Data Library Version 3 Revision-3: JENDL-3.3," J. Nucl. Sci. Technol., **39** (11), 1125-1136 (2002)

Journal of NUCLEAR SCIENCE and TECHNOLOGY, Supplement 5, p. 221–224 (June 2008)

Dosimetric Radiation Protection Quantities - Impact of the Forthcoming ICRP Recommendations

A. S. PRADHAN*, J.I.LEE, J.L.KIM, and B.H.KIM

Health Physics Department, Korea Atomic Energy Research Institute, P.O. Box 105, Yuseong, Daejeon, Korea

The physical quantities namely fluence, kerma and absorbed dose provide the base for the operational and the protection quantities. The absorbed dose continues to be the fundamental physical quantity for the radiological protection. The most striking feature relating the quantities in the forthcoming recommendations is the updating of the radiation and tissue weighting factors based on the latest available scientific information on radiobiology and the physics of radiation exposure. This is bound to make a significant impact in arriving at the equivalent doses and effective dose. For external exposures of neutrons, the forthcoming recommendations are going to improve the relationship between the operational and protection quantities. The changes in the tissue weighting factors of some tissues / organs, the inclusion of several new tissues / organs for the consideration of tissue weighting factors and the use of the proposed Reference Male and Reference Female voxel phantoms would require new conversion coefficients and dose coefficients for external and internal exposures. The other striking feature appears to be the details of the concepts to ensure that the protections quantities are used for the appropriate and intended purposes only and the misuse is avoided.

KEY WORDS: effective dose, dosimetric quantities, external and internal exposures, neutron dosimetry

I. Introduction

The need for the pragmatic dosimetric quantities for radiation measurements was noted soon after the realization of the harmful effects of radiation following the discovery of X-rays and radioactivity. Early emergence of the units such as "roentgen" and "Radium Equivelent" made a great impact. This was because the available units of flux, fluence and energy exhibited no radiological relevance. Although the fluence which still continues to play a very important role in radiation dosimetry[1] was tried to be used for arriving at the limits for the radiation protection, but with little success. For the protection quantities, the variations in radiosensitivities of different tissue / organs to different types of radiation and also on the age, sex, time of exposure etc. were needed to be considered. Therefore, the efforts at the International Commission on Radiation Units and Measurements (ICRU) and the International Commission on Radiological Protection (ICRP)[2] continued in developing the appropriate dosimetric quantities. For the development of the protection quantities by ICRP, the journey from "rem"[3,4] through "dose equivalent" and "effective dose equivalent" [5] to "equivalent dose" and "effective dose" [6] has been fascinating and the same is true for the operational quantities of ICRU[7]. The development of "effective dose"[6] has made a great impact in providing a single quantity (unified concept) which is additive for external exposures and internal exposures of all types of ionizing radiations. In the forthcoming ICRP recommendation, efforts appear to have been made to further develop the quantities to be used in radiation protection without altering the basic structure and the definitions of the existing quantities which have already proved to be very useful. The most striking features of the forthcoming recommendations[8] appear to be the revised radiation and tissue weighting factors and the details of the concepts for the proper utilization of the protection quantities. It is interesting to evaluate the impact of the forthcoming recommendations on dosimetric quantities.

II. Quantities in Radiation Protection Dosimetry

The prevalent hierarchy of the physical, protection and operational quantities[2] is shown in **Table 1.**

1. Physical Quantities:

The physical quantities are the most basic dosimetric quantities. Fluence and kerma are seen to be the expectation values[9]. However, fluence[1] continues to be widely used in the dosimetry of neutrons and for other particles whereas kerma is widely used for the dosimetry of photons. They provide a base to the measurable operational quantities and are widely used in the external dosimetry. The absorbed dose (D) which is also measurable and well defined at any point of the matter has been considered to have the required scientific rigor of a basic physical quantity needed for the conceptual base of radiological protection. The absorbed dose is the mean of the stochastic distribution of energy deposited in a volume element of a mass and hence does not reflect the random fluctuations because the number of events of the interaction in the tissue being too large. Averaging of absorbed dose over an organ or larger tissue provides a means to correlate it with the radiation detriment from the stochastic effects in all parts of an organ / tissue with sufficient accuracy by using the LNT (linear non-threshold) model of dose response at low doses for the purpose of radiological protection. Thus, the absorbed dose continues to

*Corresponding Author, Email: ambika.s.pradhan@gmail.com

be the fundamental physical quantity for the radiation protection in the forthcoming recommendations of ICRP[8,9] and no significant change is evident.

Table 1 ICRP quantities for radiological protection monitoring purposes[2].

Physical Quantities: 1-Fluence, Φ, 2-Kerma, K, 3-Absorbed dose, D	
Operational Quantities* *(Calculated using Q(L) & validated by phantom measurement and calculations)*	Protection Quantities** *(Calculated using w_R, w_T, and anthropomorphic phantoms)*
1-Ambient dose equivalent, $H^*(10)$	1-Organ absorbed dose, D_T
2-Directional dose equivalent, $H'(0.07,\Omega)$	2-Organ equivalent dose, H_T
3-Personal dose equivalent, $Hp(10)$ & $Hp(0.07)$	3-Effective dose, E

*Related by calibration and calculation to Monitored Quantities: Instrument Responses by using appropriate phantoms.

**Related to Operational Quantities by measurements and calculations using w_R, w_T, and anthropomorphic phantoms.

2. Protection Quantities:

The aim of the protection quantities is to specify the dose limits to ensure that the occurrence of stochastic effects (induction of cancer and heritable effects) are kept below the acceptable levels and the deterministic effects are avoided. The equivalent dose ($H_T = \Sigma_R w_R.D_{TR}$) (where '$w_R$' is the radiation weighting factor which is the same for all organs / tissues and D_{TR} is the averaged dose in the volume of a specified tissue / organ 'T' due to a radiation of type 'R') takes care for the equivalence of the health effects due to the variations in radiation types / ionizing densities through the use of radiation weighting factors w_R **(Table 2).** Though the concept of w_R based on the use data of RBE_{max} is the same as that of Publication 60 (Pub-60)[6] but the values have now been changed. For neutrons of energy less than 1 MeV, a significant reduction in w_R values has been recommended mainly due to the consideration of increased contribution to dose by photons produced by lower energy neutrons incident on the body. The values are also reduced for neutrons of energies above 20 MeV for different reasons mainly due to the consideration of energies of protons. High energy protons behave more like low LET radiation. The reduction in w_R values for protons is mainly for the reasons of considerations of ranges of protons of pragmatic energies[9]. These changes will have far reaching consequences.

Equivalent dose, H_T, will continue to play an important role in the implementation of radiological protection in the situations of extreme partial body / inhomogeneous exposures of tissues and organs, such as exposure by low penetrating radiation and the exposure of extremities, through the special limits for skin / extremity or lens of eye.

Effective dose ($E = \Sigma_T w_T.H_T$) (w_T the tissue weighting factor, the same for all types of radiation) takes care for the equivalence for the variations in the radiosensitivities of different organs / tissues also through the use of tissue weighting factor w_T **(Table 3)**. Though the definition remains the same as that of Pub-60[6] but the concept of risk is now changed to cancer incidences weighted for lethality and life impairment[8] (rather than fatal cancer risk weighted non-fatal cancer, relative life lost for fatal cancer and life impairment for non-fatal cancer in Pub-60) and heritable effects in the two generations only[8] (rather than theoretical equilibrium in Pub-60).

Table 2 ICRP radiation weighting factors, w_R, of Pub-60 (1991) and of the new (2007) recommendations.

Radiation type	New w_R	Old 1991 w_R
Photons	1	1
Electrons and muons	1	1
Protons	2	5 (En >2MeV)
Charged pions	2	-
Alpha particles, heavy ions, and fission fragments	20	20
Neutrons (Eq*)	5 (<10 keV)	
	Continuous function of energy	10 (10 - 100 keV)
		20 (100keV-2MeV)
		10 (2 -20 MeV)
		5 (>20 MeV)

*w_R $= 2.5 + 18.2\, e^{-[\ln(En)]^2/6}$, $En < 1MeV$

$= 5 + 17.0\, e^{-[\ln(2En)]^2/6}$, En 1-50MeV

$= 2.5 + 3.25\, e^{-[\ln(0.04En)]^2/6}$, $En > 50MeV$

Table 3 ICRP tissue weighting factors, w_T, of Pub-26 (1977), Pub-60 (1991) and of the new (2007) recommendations.

Tissue	Pub-26	Pub-60	New
Bone surfaces	0.03	0.01	0.01
Bladder	-	0.05	0.04
Breast	0.15	0.05	0.12
Brain	-	-	0.01
Colon	-	0.12	0.12
Gonads	0.25	0.20	0.08
Liver	-	0.05	0.04
Lungs	0.12	0.12	0.12
Oesophagus	-	0.05	0.04
Red bone marrow	0.12	0.12	0.12
Skin	-	0.01	0.01
Stomach	-	0.12	0.12
Salivary glands	-	-	0.01
Thyroid	0.03	0.06	0.04
Remainder	0.30(5)	0.05(10)	0.12(13/14)

Based on the latest available scientific information on radiobiology of radiation exposure leading to revised risk coefficients, the sex averaged values of tissue weighting factors, w_T, **(Table 3)** have been recommended for all organs and tissues. These are compared with w_T values of earlier ICRP publications. The number of organs / tissue considered for w_T was only 11 ($6+5_{Remainders}$) in the Pub-26 (1977) which

rose to 22 ($12+10_{\text{Remainders}}$) in Pub-60 (1991) and has now (2007) gone up to about 28 ($14+\{13/14\}_{\text{Remainders}}$). A significant increase and decrease in the values of w_T for breast and the gonads, respectively, inclusion of several new organs / tissues, the concept of equal importance (rather than the splitting rule used of Pub-60) to all the 13 tissues under the new remainder with rationalized sex averaging are bound to cause an impact on the calculation of doses. The use of the proposed Reference Male and Reference Female voxel phantoms are also expected to bring out new conversion coefficients and dose coefficients for external and internal exposures. The averaging of absorbed doses for arriving at the effectives doses in the case of external exposures and the use of dosimetric models in the case of internal exposures allows the addition of effective doses in all situations of external and internal exposures.

One of the other attractive features in dealing with the quantities in radiation protection has been the greater emphasis by the Commission (ICRP) on ensuring the proper use of the protection quantities. Among the collective dose quantities, only 'Collective Effective Dose' (with its unit as 'man sievert') is retained with a restriction of summation of doses of individuals incurring doses in a defined dose range of exposures for the limited duration. It is stressed that the collective effective dose is an instrument for optimization, for comparing radiological technologies and protection options and not a tool for epidemiological risk assessment or risk projections. The emphasis in the use of effective dose, in brief, is as follows;-

A)- Renewed emphasis that E and H_T (both having the unit as 'Sv') are relevant only at the lower doses (<100 mSv) of interest in radiation protection (values of w_R are for RBE_{max} at low doses). The main use of E has been emphasized to be for the regulatory compliance of the appropriate dose limits for the workers and the general public through the prospective dose assessment for planning and optimization and / or through the retrospective dose assessment. For higher doses of relevance to tissue reaction, absorbed dose (with its unit as 'Gy') is advised to be used for low LET radiation and in the case of high LET radiation exposures, an appropriate RBE value is recommended to be used and stated along with the mention of the absorbed dose.

B)- It is also emphasized that a value of E does not refer to the actual dose received by any individual and it must not be used for any retrospective assessment of individual risk (which needs detailed information) of stochastic effects from radiation exposure, because E is arrived at by using the highly simplified judgments on w_R and w_T values or estimated on a phantom by using conversion coefficients, dose coefficients and biokinetic and dosimetric models in a reference phantoms representing human body of a Reference Person.

C)- E is not advised to be used for epidemiological evaluations, medical surveillance (risk-benefit assessment or planning the exposure of patients) or treatment.

D)- E has been indicated to have sever limitations in its use for exposures of patients in diagnostic radiology. The use may be limited only for comparing the relative values from different diagnostic procedures in different hospitals and countries or different technologies for the same medical examination, provided the reference patient or patient populations are similar with regard to age and sex.

3. Operational Quantities

The practical need of the measurable operation quantities arose due to the limitation of conceptual nature of the protection quantities, H_T or E, which are not measurable. This is because in practice it is impossible to measure the absorbed doses at all points of all tissues or organs (for averaging) of relevance to protection. The aim of the operational quantities has been to have measurable quantities for the reasonable estimate of protection quantities by avoiding underestimation and too much overestimation. Consequently, a unified concept of operational quantities for all types of radiations leading to direct additivity of the measured values was brought out and was further developed[7] by ICRU. The operational quantities were defined in terms of a receptor, the ICRU sphere for area monitoring and the body for individual monitoring, for both the penetrating and low penetrating radiations. These are ambient dose equivalent $H^*(10)$ and directional dose equivalent $H'(0.07,\Omega)$ for area monitoring and personal doses $Hp(10)$ and $Hp(0.07)$ for individual monitoring. $H^*(10)$ and $Hp(10)$ are used for the assessment of effective dose (E) and the others for the assessment equivalent doses (H_T) to skin and extremities. Use of $Hp(3)$ and $H'(3,\Omega)$ for the estimation of equivalent dose (H_T) to the lens of eye has now been considered to be trivial. Also, the use of terms such as penetrating / strongly penetrating and less / low / weakly penetrating radiation has been discouraged because the extremity doses are caused by both the strongly and weakly penetrating radiation. There appears to be no other significant change in the concept of the operational quantities for the external exposures. The adopted representation of effective dose is $E = Hp(10) + E(50)$, where the $E(50)$ is the committed effective dose from internal exposure. Unlike $Hp(10)$ which is a measured quantity, $E(50)$ is an estimated value from the assessments of intakes by using biokinetic and dosimetric models and dose coefficients. So far no operational quantity has been arrived at for the internal dosimetry.

It may be noted that the term dose equivalent (H) still stays in the definition of the operational quantities for external exposures, which is different than equivalent dose (H_T). H and H_T are different both in the definitions and in the concepts. The dose equivalent (H) is a point quantity (product of absorbed dose 'D' and quality factor 'Q' at a point in tissue). Whereas equivalent dose (H_T) is related to an averaged effect in an organ / tissue for different types of radiation (summation of products of mean absorbed doses of different types of radiation 'D_{TR}' in the volumes of specified tissue / organ and radiation weighting factors 'w_R'). The quality factor (Q) is related to LET of the radiation whereas 'w_R' has been arrived at by the best judgment on the relative biological effectiveness of different radiations. Thus "dose

equivalent" and hence the *Q-L* relationship remains the back bone of the operational quantities for external exposures. Similar to the changes from ICRP-26 to ICRP-60, the new recommendations are also not expected to make a significant impact on the operational quantities for external exposures from X and gamma rays. However, for exposures from neutrons the relationship between the protection and operational quantities is expected to be affected significantly due to the reduction in w_R values for neutrons of energy below 1 MeV. The existing situation of too much underestimation of effective dose by the use *H*(10)* or *Hp(10)* for AP and PA geometry in the neutron energy range from few tens of eV to few tens of keV is expected to improve considerably with the implementation of the new recommendations. The prevalent underestimation of effective dose due to exposures to neutrons is expected to disappear with the use of the revised values of w_R and this will ease the situation for measurement of neutron doses.

III. Conclusions

The definitions and the concepts of the dosimetric radiation protection quantities remain unchanged in the new ICRP recommendations. However, based on the latest available scientific information on radiobiology and physics of radiation exposure, the updating of the radiation and tissue weighting factors for the use in arriving at the equivalent dose and the effective dose will make a significant impact on the quantities. The impact is expected to be very favorable in improving the relationship between operational and the protection quantities in the otherwise complex neutron dosimetry. Widely used X and gamma ray disimetry may not have a significant impact. The changes in tissue weighting factors and the inclusion of consideration of several new tissues / organs and also the use of the proposed Reference Male and Female Voxel phantoms would result in bringing out new conversion coefficients and dose coefficients for external and internal exposures. This will provide an avenue and scope for further research leading to a large number of publications on the relationship between protection and the operational quantities in the coming years.

References

1) R. H. Thomas and J.C. McDonald, 'On fluence and fluency,' Radiat Prot. Dosim 123, 413, 2007.
2) International Commission on Radiological Protection, 'Conversion Coefficient for the use in Radiological Protection against External Radiation', ICRP Publication 74. Annals of ICRP 26 (Pegamon Press, Oxford), 1996.
3) International Commission on Radiological Protection, 'Recommendations of the ICRP,' ICRP Publication 1, (Pegamon Press, Oxford), 1958.
4) International Commission on Radiological Protection, 'Protection against Electromagnetic Radiation above 3 MeV and Electrons, Neutrons and Protons,' ICRP Publication 4, (Pegamon Press, Oxford), 1964.
5) International Commission on Radiological Protection, 'Recommendations of the International Commission on Radiological Protection,' ICRP Publication 26. Annals of ICRP 1 (Pegamon Press, Oxford), 1977.
6) International Commission on Radiological Protection, 'Recommendations of the International Commission on Radiological Protection,' ICRP Publication 60. Annals of ICRP 21 (Pegamon Press, Oxford), 1991.
7) International Commission on Radiation Units and Measurements, 'Quantities and units in radiation protection dosimetry', ICRU Report 51 (Bethesda, MD) 1993.
8) International Commission on Radiological Protection, 'Draft Recommendations of the International Commission on Radiological Protection,' Available on www.icrp.org/ICRP_draft_recommendation.12_january_2007.pdf.
9) International Commission on Radiological Protection, 'Annex B. Basis of dosimetric quantities used in radiological protection' Draft dated 12 February 2007 prepared by the Task Group of Committee 2: Chairman C. Streffer. Available on www.icrp.org/Dosimetry.pdf.`

Journal of NUCLEAR SCIENCE and TECHNOLOGY, Supplement 5, p. 225–228 (June 2008)

Performance of the $H_p(10)$ and $H_p(0.07)$ Measurable Electronic Pocket Dosimeter for Gamma- and Beta-Rays

Masa TAKAHASHI[1*], Masato SEKIGUCHI[1], Hideaki MIYAUCHI[1], Haruo TACHIBANA[1], Michio YOSHIZAWA[1], Toru KATO[2], and Akihito YAMAGUCHI[2]

[1]*Japan Atomic Energy Agency, 2-4 Shirakata-Shirane, Tokai-mura, Ibaraki 319-1195, Japan*
[2]*ALOKA CO., LTD., 6-22-1 Mure, Mitaka-shi, Tokyo 181-8622, Japan*

For individual monitoring for external exposure of workers, electronic dosimeters have been widely used as supplementary dosimeters in nuclear facilities. In this study, an electronic pocket dosimeter for measuring the $H_p(10)$ and $H_p(0.07)$, which was recently developed by Aloka Co., Ltd., has been examined in terms of (1) energy dependences for gamma- and beta-rays and (2) applicability in actual radiation workplaces. For the latter purpose, performance tests were carried out in hot cells of the Reactor Fuel Examination Facility in the Japan Atomic Energy Agency. From the examinations, the followings were found; (1) the energy responses vary within ±20 % in the intended energy range for both radiations. (2) At the actual radiation workplaces, the readings of the dosimeter tend to show slightly higher $H_p(10)$ and lower $H_p(0.07)$ than those of other types of dosimeters, i.e. glass dosimeters and thermoluminescence dosimeters.

KEYWORDS: electronic dosimeter, $H_p(10)$, $H_p(0.07)$, response, Monte Carlo simulation

I. Introduction

In nearly a decade electronic dosimeters have been widely used for individual monitoring for external exposure of workers in nuclear facilities. The electronic dosimeters are quite useful owing to some favorable characteristics, for example, an ability to provide exposure doses in real-time, and the alarm function by which secure radiation protection can be achieved even in high exposure radiation works. In the case of mixed radiation fields with high contaminations, it is often required to measure gamma and beta radiations simultaneously and independently. However, there have been few electronic personal dosimeters which can measure both gamma- and beta-rays.

Recently, the electronic pocket dosimeter, EPD-101, which can measure gamma- and beta-rays simultaneously was developed by Aloka Co., Ltd. in Japan. It is important to investigate characteristics of the EPD-101 before applying it to actual personal dosimetry in gamma and beta mixed workplaces. In the present study, performances of the EPD-101 were examined in standard radiation fields and in actual gamma beta mixed workplaces.

Energy dependences of the EPD-101 for gamma- and beta-rays were obtained in the standard radiation fields. Performance tests of the EPD-101 were conducted at the actual radiation workplaces, in order to compare the dose equivalents measured by the EPD-101 and those by other types of dosimeters, radiophotoluminescence glass dosimeters[1)] (RGD) and thermoluminescence dosimeters[2)] (TLD).

*Corresponding Author, Tel. +81-29-282-5206, Fax. +81-29-282-5962 E-mail:takahashi.masa@jaea.go.jp

II. Materials and methods

1. Electronic pocket dosimeter (EPD-101)

The EPD-101 is designed to measure the personal dose equivalents at a depth of 10 mm ($H_p(10)$) and 0.07 mm ($H_p(0.07)$) for gamma and beta-rays, respectively. In order to distinguish gamma-rays and beta-rays, a detection part of this dosimeter, which is placed behind the entrance window (see **Fig. 1**), consists of two silicon semiconductor detectors and one filter. These are piled in the order of Si-filter-Si and set perpendicular to incident radiations. With the Si-filter-Si configuration, $H_p(10)$ by gamma-rays and $H_p(0.07)$ by beta-rays can be separately estimated by the following steps. (1) If only the first silicon detector senses radiations, those radiations are identified as beta-rays. (2) If radiations penetrate the filter and the second silicon detector senses the radiations, those radiations are identified as gamma-rays. (3) The EPD-101 calculates the dose equivalents, $H_p(10)$ and $H_p(0.07)$, by weighting appropriate factors on the numbers of signals generated by gamma- and beta-rays, respectively.

Fig. 1 $H_p(10)$ and $H_p(0.07)$ measurable electronic pocket dosimeter (EPD-101) manufactured by Aloka Co., Ltd.

The numbers of signals by gamma-rays are obtained by a special circuit with multiple discrimination levels to compensate the energy response. $H_p(0.07)$ by gamma-rays is regarded as equal to $H_p(10)$ by the gamma-rays. The calculated dose equivalents are accumulated into an embedded memory of the EPD-101 and shown on a liquid-crystal display.

2. Experiments on energy dependences

The energy dependences of the responses to gamma- and beta-rays were experimentally investigated in the standard radiation fields at the Facility of Radiation Standards of the Japan Atomic Energy Agency (JAEA).

To obtain the response to gamma-rays, ^{137}Cs and ^{60}Co sources were used. The EPD-101s were irradiated on the ISO water phantom[3] with the dose equivalent, $H_p(10)$, of 1 mSv.

For beta-ray irradiations, three beta sources, ^{147}Pm, ^{204}Tl and ^{90}Sr-^{90}Y were used in conditions with and without energy absorption filters between the source and the EPD-101s. Every source has a circular surface with a diameter of 4.2 cm. The absorption filters, made of polymethylmethacrylate (PMMA), were used for obtaining lower mean beta-ray energies in order to extend the number of energy points. The EPD-101s were irradiated on a PMMA phantom (40×40×1 cm^3). The irradiated dose equivalent, $H_p(0.07)$, was 1 mSv, except for the case of ^{204}Tl with the filter. In the case, the irradiated dose was 0.2 mSv. **Table 1** summarizes the irradiation conditions.

3. Performance tests in actual radiation workplaces

In order to examine the applicability of the EPD-101 in actual radiation workplaces, measured values by the EPD-101s were compared with those by the other two types of dosimeters (the radiophotoluminescence glass dosimeter (RGD) and the thermoluminescence dosimeter (TLD)). The RGD (model GD-450 manufactured by Chiyoda Technol Corporation) and TLD (model UD-808PQ by Panasonic) have been used for the routine monitoring of personal doses in JAEA. These dosimeters have reasonable responses to both gamma- and beta-rays. The three types of dosimeters were worn on each of several radiation workers to measure exposed dose under the same condition.

The measurements were carried out in the hot cells in the Reactor Fuel Examination Facility in JAEA. The cells were contaminated with fission products from the high burn-up nuclear fuels. Major radioactive contaminants, which were thought to be significant for measurements of personal dose, were ^{137}Cs, ^{60}Co, ^{90}Sr-^{90}Y (Maximum beta-ray energy, E_{max}, is 2.3 MeV), ^{144}Ce-^{144}Pr (E_{max}: 3.0 MeV) and ^{106}Ru-^{106}Rh (E_{max}: 3.5 MeV). The beta-ray energy for these sources is considerably high, and hence exposure doses to the high-energy beta-rays, as well as gamma-rays, need to be measured.

4. Monte Carlo simulation

The Monte Carlo simulation was applied to evaluate the energy responses of the EPD-101 to gamma- and beta-rays. The EGS4[4] code, which is the code system for the transport of electrons and photons, was used as the Monte Carlo calculation code. The calculation model of the EPD-101 was constructed as minutely as possible based on the manufacture's specification, although complete structures, especially of the detection part, are not open to the public.

For the gamma-ray calculations, monoenergetic photons were emitted from a point source. As for the beta-ray calculations, electrons were emitted from a circular surface source which was large enough to cover the dosimeter. It was assumed that the radiations impinged on the dosimeter as a unidirectional beam. The data of beta-ray energy spectra were taken from ICRU report 56[5]. The phantom and the absorption filters, which were located between the source and the phantom, were also modeled. In the simulations, deposited energies higher than the discrimination levels of the silicon detectors were tallied. Then the dose equivalents were derived by the same procedure of the EPD-101 described before.

Table 1 Irradiation conditions for measurements of energy dependences

Radionuclide	Radiation	PMMA filter thickness (mm)	Energy (keV)	Dose rate (mSv/h)	Dose (mSv)
^{137}Cs	gamma	–	662	10.0	1.0
^{60}Co	gamma	–	1250[a]	10.0	1.0
^{147}Pm	beta	–	179[b]	21.2	1.0
^{204}Tl	beta	1	427[b]	0.56	0.2
^{204}Tl	beta	–	635[b]	1.32	1.0
^{90}Sr-^{90}Y	beta	6	878[b]	3.04	1.0
^{90}Sr-^{90}Y	beta	4	1250[b]	21.9	1.0
^{90}Sr-^{90}Y	beta	–	1940[b]	7.23	1.0

[a] Effective energy
[b] Residual maximum energy

III. Results and discussion

The energy dependence of the EPD-101 is shown in **Fig. 2** for gamma-rays. Both results by the experiments and the simulations indicate that the differences of the responses between ^{137}Cs and ^{60}Co are approximately 20 %. It is found from the simulations that, above the energy points of ^{137}Cs, the response slightly decreases with increasing the energy since the photon attenuation coefficient decreases with increasing the energy in this range. The energy dependence below 662 keV of ^{137}Cs is good by the response compensation with the multiple discrimination technique.

The energy dependence for beta-rays, as shown in **Fig. 3**, was found to be within ±20 % in the energy range between 500 and 2000 keV. This is fairly good as the electronic pocket dosimeter. Although the response to ^{147}Pm is considerably low due to the loss of energy in the entrance window in front of the detector, the exposures from such low-energy beta-rays would be generally insignificant. In Fig. 3, the response decreases above around 1400 keV because some high-energy beta-particles cannot deposit enough energy above the discrimination levels in the silicon detector due to small energy loss. In order to estimate the reduction in the response to high-energy beta-rays, the response to ^{106}Ru-^{106}Rh (the residual maximum energy: 3.2 MeV) was also calculated by the Monte Carlo simulation. The relative response to ^{106}Ru-^{106}Rh was estimated to be 0.80. Furthermore it was found that some of the high-energy beta-rays could penetrate to the second silicon detector and contributed to indications of $H_p(10)$. The contribution to the $H_p(10)$ indications was estimated to be 8% of those of $H_p(0.07)$ for ^{106}Ru-^{106}Rh.

Fig. 4 and **5** show the indicated $H_p(10)$ and $H_p(0.07)$, respectively, at several radiation works in the hot cells by the three types of dosimeters. The values are the averaged doses over workers in the same radiation works. The measured values by the three dosimeters were roughly comparable. However, in most radiation works, measured $H_p(10)$s by the EPD-101s were higher than those by the other dosimeters. Opposite tendency was found in the case of the $H_p(0.07)$. The higher $H_p(10)$s by the EPD-101s can be explained by the contribution of high-energy beta-rays to the indications of $H_p(10)$ as shown in the simulation results. Main contaminant beta sources such as ^{144}Ce-^{144}Pr and ^{106}Ru-^{106}Rh in the hot cells emitted high-energy beta-rays, which probably contributed to the $H_p(10)$ values. In the case of $H_p(0.07)$, measured $H_p(0.07)$s by the EPD-101s were lower than those by the other dosimeters. This is reasonable from the reduction in the response to the high-energy beta-rays, as shown in Fig. 3.

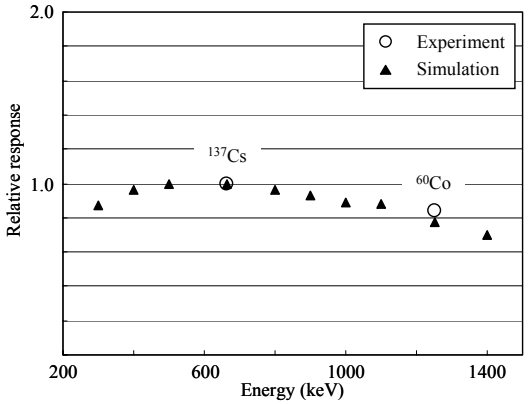

Fig. 2 Energy response for photon. The responses are normalized to ^{137}Cs.

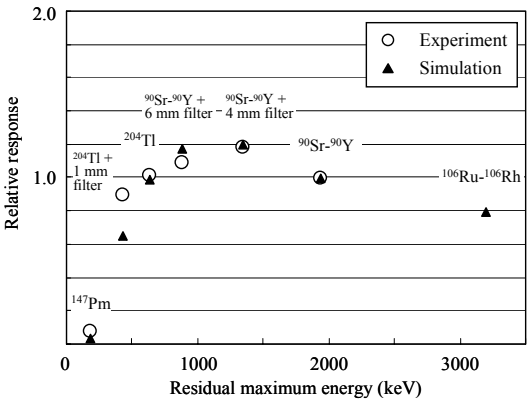

Fig. 3 Energy response for beta-rays. The responses are normalized to ^{90}Sr-^{90}Y.

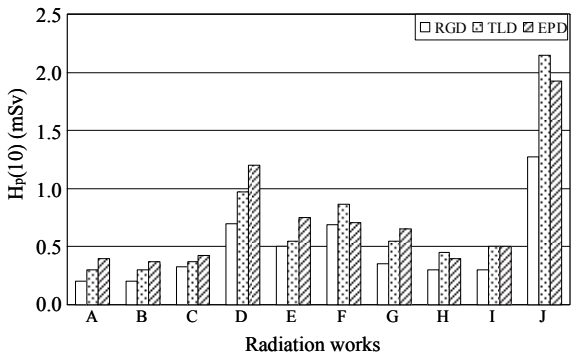

Fig. 4 Comparison of $H_p(10)$ measured by the three types of dosimeters (RGD, TLD and EPD-101) at various radiation works.

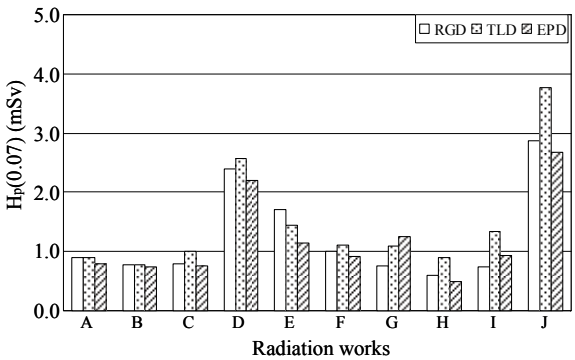

Fig. 5 Comparison of $H_p(0.07)$ measured by the three types of dosimeters (RGD, TLD and EPD-101) at various radiation works.

Furthermore, the response of the EPD-101 has a large angular dependence for beta-rays because a clip exists near the entrance window, as shown in Fig. 1. This also could results in the smaller $H_p(0.07)$ values because beta-rays come from wide directions in the hot cells.

IV. Summary and Conclusions

The EPD-101 is an electronic pocket dosimeter which is able to measure both $H_p(10)$ for gamma-rays and $H_p(0.07)$ for beta-rays. It was found on the energy dependences that the responses to gamma- and beta-rays were within ±20 % relative to ^{137}Cs and ^{90}Sr-^{90}Y, respectively. The responses calculated by the Monte Carlo simulations showed good agreement with those by the experiments. The simulations also showed that the response to high-energy beta-rays decreased but was still -20 % for ^{106}Ru-^{106}Rh.

The comparison measurements were carried out in order to examine the applicability of the EPD-101 in actual radiation workplaces. As a result, the EPD-101 indicated roughly comparable performance to the RGD and the TLD in the contaminated hot cells. This study shows that the EPD-101 is applicable in gamma and beta mixed fields such as the hot cells.

References

1) M. Ito, A. Shiraishi, H. Murakami, "Characteristics of radiophotoluminescent glass dosimeters," JAERI-Tech 2001-048, Japan Atomic Energy Research Institute, (2001), [in Japanese].
2) "TL-budge technical note," NAGASE & Co., Ltd., (1985), [in Japanese].
3) ISO, "X and gamma reference radiation for calibrating dosemeters and doserate meters and for determining their response as a function of photon energy - Part 3: Calibration of area and personal dosemeters and the measurement of their response as a function of energy and angle of incidence, " ISO 4037-3:1999, International Organization for Standardization, (1999).
4) W. R. Nelson, H. Hirayama, D. W. O. Rogers, "The EGS4 code system," SLAC-265, Stanford Linear Accelerator Center, (1985)
5) ICRU, "Dosimetry of external beta rays for radiation protection," ICRU REPORT 56, International Commission on Radiation Units and Measurements, (1997).

Journal of NUCLEAR SCIENCE and TECHNOLOGY, Supplement 5, p. 229–232 (June 2008)

Neutron Spectral Measurement at the Proton Therapy Room of the National Cancer Center of Korea

Bonghwan KIM[1*], Sangeun HAN[2], Jeongwan KWON[2], Sunmi JUN[1], Jongsu KIM[1], Sebyeong LEE[3], and Dongho SHIN[3]

[1]*Korea Atomic Energy Research Institute, P.O Box 105, Yuseong, Daejeon 305-600, Korea*
[2]*Korea Institute of Nuclear Safety, 19, Yuseong,Daejeon 305-338, Korea*
[3]*National Cancer Center, 809, Madu 1-dong, Ilsan, Goyang, Gyeonggi-do 411-769 Korea*

The neutrons, which are mainly induced from a beam modulator and two beam flattening scatters bombarded by high energetic protons inside the gantry of the proton therapy unit of the National Cancer Center (NCC) of Korea, were measured by using the Bonner Sphere (BS) of the Korea Atomic Energy Research Institute (KAERI). Protons were accelerated to 218 MeV using a cyclotron and guided to a gantry for modulating of the beam size and energy. The modulated proton beam irradiated the surface of a water phantom to simulate a condition of a proton therapy. Neutron spectral measurements were performed at two proton therapy rooms with a rotational and a fixed gantry respectively for different beam directions of the proton beam. The fluence average energies were 3.14 and 2.92 MeV at the two measuring positions respectively and there was a significant fraction of low energy neutrons under 0.5 eV. Dose equivalent rates were consistent to within 10% with the survey data measured by a neutron remmeter. Two kinds of neutron spectra were prepared to unfold the BS measurement data and the difference in the unfolding result for the two cases was not big for some dosimetric data.

KEYWORDS: bonner sphere, neutron spectrometry, proton therapy, spectrum unfolding, neutron fluence, LiI(Eu) scintillator

I. Introduction

The Bonner Sphere (BS)[1)] is still playing a crucial role in the neutron spectrometry field for a radiation protection purpose in spite of its poor resolution as a neutron spectrometer. In order to quantify the neutron fields at accelerator facilities, the use of BS also has been preferred for a long time because of its easy operation and its measurement performance over a wide energy range of interest. But there is a limitation for a low detection efficiency for the BS system to a high energy neutron above a few tens of mega-electron volts (MeV). From the nineties the need for a neutron field spectrometry around high energy particle accelerators and in an atmospheric environment at high altitudes has increased and created enhanced BS with high Z materials such as Pb, Fe or Cu which have large (n, xn) cross sections for a high energy neutron[2-4)]. The neutron multiplication process which occurs within a metal shell increases the response for a high energy neutron. The extended BSs of the Korea Atomic Energy Research Institute (KAERI) consisting of an active and a passive system were manufactured and have been implemented to measure several neutron fields at nuclear facilities in Korea[5-7)].

Recently a proton therapy facility which can accelerate a proton to 230 MeV to cure patients with a solid tumor effectively has started operating in Korea. Neutrons are an inevitable contamination during the process of making a proton beam necessary for a medical therapy because all the equipments using high energy particles can produce neutrons resulting from an interaction of them with the surrounding materials or structures[8)].

This paper describes the neutron spectral measurement at the National Cancer Center of Korea (NCC) by using the extended BS of KAERI.

II. Materials and Methods

1. A Proton Therapy Facility and the KAERI's BS

NCC opened a proton therapy facility in Korea in 2005 and it has been operated since the second quarter of 2007. Four irradiation rooms with a rotational or a fixed gantry to each room respectively were prepared for a therapy treatment and a research purpose. Proton beams are accelerated to 218 MeV using a cyclotron and guided to the surface of a water phantom in this measurement after the beam size and energy necessary for a therapy treatment are modulated in the gantry consisting of two scatterers, a range modulator, a snout and bolus as shown in **Fig. 1**[9)].

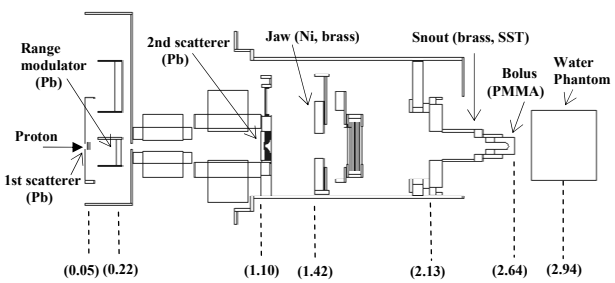

Fig. 1 Conceptual drawing of the gantry to modulate the beam size and energy for a proton therapy. (Numeric values in the parentheses are distances in meter from the entrance point of a proton beam.)

*Corresponding Author, Tel. +82-42-868-8386, Fax. +82-42-868-8609, E-mail: bhkim2@kaeri.re.kr

Proton therapy rooms have a dimension of 13.0 x 15.2 x 2.4 m^3 and are enclosed with 2.2 m thick concrete walls. The access to the therapy room is possible through a maze which is made of 1.2 m thick concrete walls.

KAERI's BS system consists of nine spheres of which six PE spheres have diameters ranging from 5.08 cm to 30.5 cm and three lead-insert spheres with a diameter of 20.3 cm. A 4 mm (dia.) x 4 mm (length) ^{6}LiI(Eu) scintillator is located in the center of the sphere as a neutron detector.

2. Preparation of a *Priori* Information for an Unfolding

Two kinds of neutron spectra as priori information were prepared to unfold the BS measurement data. One was calculated using the MCNPX code (Ver. 2.5)[10] and the other was derived by using analytic functions which can describe one of the neutron fluence spectra at the proton accelerator.

The neutron fluence spectra were calculated by using the MCNPX code for the two cases of the rotational and fixed gantry separately. The direction of the proton beams at the rotational gantry was perpendicular to the axis of a water phantom to the BS while that of the fixed gantry was parallel to the axis facing the BS but 50 cm away from the axis of the proton beams. Due to a difference in the locations of the two gantries in the therapy rooms, separate calculations were carried out to obtain more reasonable neutron spectra. But the physical configuration of two gantries was the same. The nuclear physics mode for neutron production by a proton with an energy over 150 MeV was the Bertini Intranuclear Cascade (INC)[11] model which is one of the models provided in the MCNPX code for high energy particle physics while the LA150 library for the (p,n) reaction was used in case of a proton energy below 150 MeV. Photo-neutron production was not considered in this calculation.

A priori information made by summing several analytical functions representing a thermal (ϕ_{th}), an intermediate (ϕ_{int}) and an evaporation neutron (ϕ_{evap}) including an additional Gaussian distribution (ϕ_G) was as follows[12] ;

ϕ_{th}: $kE^2e^{(-E/a)}$, where k=1.746 x 10^{15} MeV^{-2}, a=23 meV and E in MeV

ϕ_{int}: k[19+(LogE)(1+tanh(5Log(E/a))(1-tanh(5Log(E/b))], where k=0.01, a=0.1 eV, b=4.0 MeV and E in MeV

ϕ_{evap}: $kE^2\ e^{(-E/a)}$, where k=2.16 MeV^{-2}, a=1.85 MeV and E in MeV

ϕ_G: $ke^{[-Log(E/a)]}$, where k=0.05, a=3.0 MeV and E in MeV

A parameter of a in each equation above indicates a peak energy of a thermal, an evaporation neutron and the Gaussian function. The parameters of a and b in the equation of ϕ_{int} mean a start and an end point of the energy of an intermediate neutron function respectively. Each peak position of these spectra obtained by selecting analytical functions is not deterministic but inferential based on the physical characteristics of neutron production and slowing-down when a proton interacts with various materials. Three kinds of neutron fluence spectra prepared as priori information for unfolding are presented in **Fig. 2**.

The energy bin structure of the neutron fluence spectra used as priori information was configured to 10 points per decade from 1 meV to 230 MeV.

3. Spectrum Unfolding and Calibration of the BS System

The measured count rates according to the event of the neutron capture reaction of ^{6}Li(n,α)^{3}H which occurred in the ^{6}LiI(Eu) scintillator were input to the unfolding program, UMG3.1, which uses the maximum entropy method for a deconvolution of the few-channel data such as the BS measurement data[12]. The response function matrix of the KAERI BS system was prepared to fit the structure of the MXD_ FC31 code library. The calibration of the BS system was carried out in the neutron irradiation room at KAERI using an unmoderated ^{252}Cf source by using a polynomial fit method recommended by ISO[13].

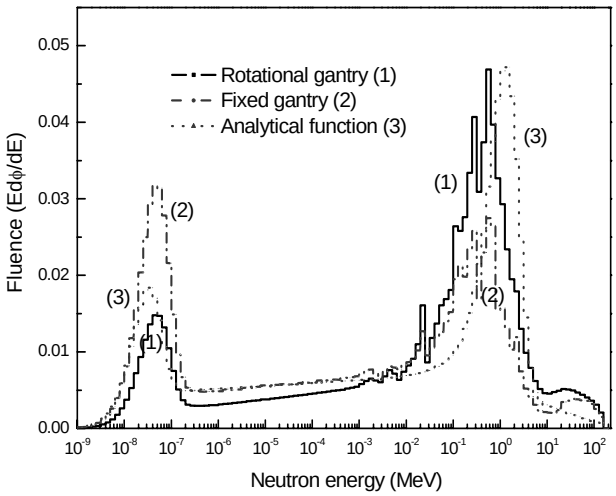

Fig. 2 Comparison of the three kinds of neutron fluence spectra prepared for unfolding. Two spectra, (1) and (2), were calculated to get a priori information at the rotational and fixed gantry room respectively while a spectrum, (3), was made by using analytical functions and was implemented equally at two gantry rooms

4. Neutron Spectral Measurement

Measurements were made at two positions, the fixed and rotational gantry rooms, with the same operation condition ; a proton energy of 218 MeV and a current level of 12 nA were fixed to deliver a proton dose of 1 Gy during an irradiation time of 40 seconds. The distances from the effective center of a water phantom to that of the BS were 2.0 and 2.7 meter for the fixed and rotational gantry rooms respectively. A portable multichannel analyzer, INSPECTOR (Canberra, USA) was used to count the net area under a peak of the energy-deposited spectrum resulting from the (n,α) reaction in the LiI(Eu) scintillator. The statistical uncertainty in each measurement was below 0.6% and the dead time was from 1.4% to 8.6% when the live time was set to 30 seconds. Neutron dose equivalent rates at the measuring positions were monitored by using the commercial neutron survey meter, WENDI-II (Thermo-electron, Germany), which was calibrated by using a ^{252}Cf source at KAERI.

III. Results and Discussion

Low energy neutrons below 0.5 eV were dominant at the fixed gantry room about which were 10% higher when compared with at the rational gantry room because of a geometrical difference of the therapy room and the direction of proton beams facing the BS. But the fraction of the high energy neutrons over 10 MeV was not so different from each other when considering the results of F9C and R9C shown in **Table 1**. The percentiles of the group fluence rates to the total fluence rate are presented in Table 1 and the dosimetric data determined from the unfolded spectra are summarized in **Table 2**.

Table 1 Percentiles of the fluence rates of the four group energies to the total fluence rate

Spect-rum	Percentile to the total fluence rate (%)				Total fluence rate, ϕ_E (s^{-1})
	< 0.5 eV	0.5 eV ~ 10 keV	0.01 ~ 10 MeV	> 10 MeV	
F9A[1)]	27.3	32.3	37.2	2.8	31 191
F6C[2)]	36.2	23.1	36.6	4.1	33 683
F9C[3)]	34.6	24.0	37.3	4.1	34 622
R9A[1)]	21.1	26.5	50.1	2.3	35 819
R6C[2)]	23.3	21.0	49.3	6.4	37 676
R9C[3)]	22.5	22.6	50.6	4.3	36 504

[1)] F9A and R9A : Specrum determined by using the extended BS consisting of nine spheres and the analytical functions as priori information for unfolding at the fixed gantry and at the rotational room respectively.
[2)] F6C and R6C : Specrum determined by using the conventional BS consisting of six polyethylene spheres only and the calculated neutron spectrun as priori information for unfolding at the fixed gantry and the rotational gantry room respectively.
[3)] Character and numeric number have the same meaning as in [1)] and [2)].

Table 2 Summary of the dosimetric data determined by using the unfolded spectra

Spectrum	Average energy (MeV)		h*(10)[4)] (pSv.cm^2)	DE rate ($mSvh^{-1}$)	
	Fluence[2)]	DE[3)]		BS[5)]	SM[6)]
F9A[1)]	2.34	6.29	129	14.4	
F6C[1)]	3.15	8.94	122	14.8	14.3
F9C[1)]	3.14	8.97	122	14.7	
R9A[1)]	1.90	4.17	176	22.7	
R6C[1)]	4.45	8.74	185	25.0	21.4
R9C[1)]	2.92	6.22	180	23.6	

[1)] Characters and numeric numbers have the same notation used in **Table 1**
[2)] Fluence average energy
[3)] Dose equivalent average energy
[4),5)] Fluence to ambient dose equivalent conversion coefficient and dose equivalent were determined using the values presented in ICRP74 for mono-energetic neutrons[14)]
[6)] Neutron survey meter, WENDI-II

The shape of the unfolded spectra with the neutron spectra made by summing the analytical functions are different from those with the calculated neutron spectra due to the peak position of the thermal neutron and the evaporation neutron functions. The peak energy of the thermal and evaporation neutron were 23 meV and 1.85 MeV in analytical functions while the calculated neutron spectra showed a higher peak energy for the thermal neutron and the lower peak energy for the evaporation neutron respectively. Unfolding results using the analytical functions as priori information revealed a little underestimated values for the total fluence, the average energies and the dose equivalent rates except for the fluence to ambient dose equivalent conversion coefficient, h*(10), of the case of the fixed gantry room. There are similar trends for the group fluence percentile and the dosimetric data in the two spectra determined by using the calculated neutron spectra to unfold the measurement data even though the number of detectors was different from each other.

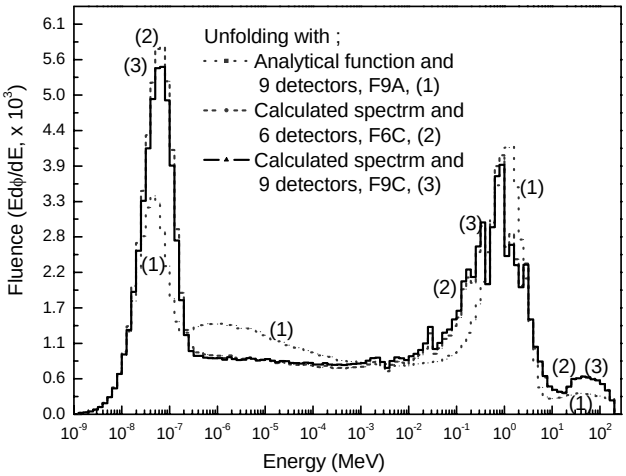

Fig. 3 Neutron fluence spectra determined by using the different unfolding parameters of the priori information and the number of detectors used at the fixed gantry room

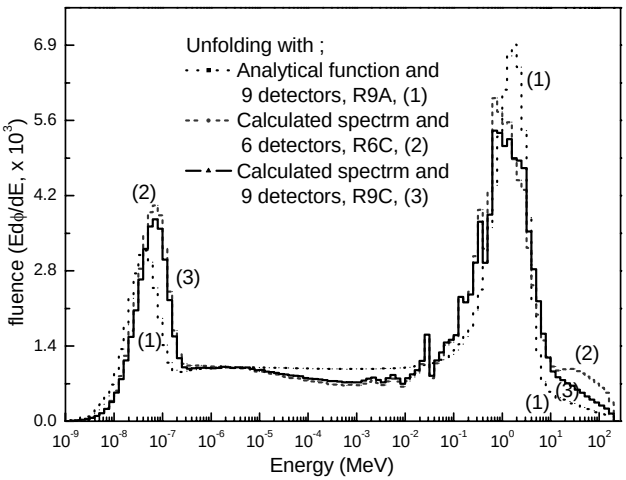

Fig. 4 Neutron fluence spectra determined by using the different unfolding parameters of the priori information and the number of detectors used at the rotational gantry room

The shape of the neutron spectra over the region of the evaporation peak in **Fig. 3** was not consistent with that in **Fig. 4**. Considering the measuring position and the direction of the proton beam it is more probable that the unfolding result by using the data of the nine detectors would be correct. More peaks over the evaporation peak energy were shown in Fig. 3 and in Fig. 4. But the peak of the R6C spectrum shown in Fig. 4 was not realistic because it was not a forwarding beam to the measuring position of the BS and there would be very low probability of the presence of high energy neutron over 20 MeV. On the contrary, the proton beams at the fixed gantry room was forward facing the BS and therefore it was more reasonable that the high energy neutrons were measured clearly at the fixed gantry room. The R9C spectrum in Fig. 4 also supports this by showing that the neutron fluences over the energy of 10 MeV were declined smoothly with an increase of the energy.

It is a merit of an extended BS to measure a neutron of energy over a few tens of MeV because it can detect a high energy neutron more efficiently when compared with the conventional BS made of polyethylene spheres only[5].

Ambient dose equivalent rates calculated from the spectra measured by the BS were about 10% higher than the values monitored by the neutron survey meter, WEBDI-II, at the rotational gantry room. Although the WENDI-II was calibrated with a ^{252}Cf source whose spectrum was not similar to the spectra measured here, it was useful for monitoring the neutron fields inside a proton therapy room.

IV. Conclusion

The fluence average energies of the neutron fields determined by the KAERI BS at the fixed and rotational gantry room of the NCC of Korea were 3.14 and 2.92 MeV respectively and there was a significant fraction of low energy neutrons under 0.5 eV. Dose equivalent rates were consistent to within 10 % with the survey data measured by a neutron remmeter. Two kinds of neutron spectra were prepared to unfold the BS measurement data and the difference in the unfolding result for the two cases was not big for some dosimetric data.

Unfolding measurement data which only have a few points to obtain a unique solution is not easy by using a deterministic process because there is no unique solution in nature and there are many possible solutions. It is a problem of inference to find a better or more reliable one among the many possible solutions after scrutinizing the relationships between the expectations and the observed data. Using the analytic functions to describe a neutron field to be measured is one of the possible methods to come close to a solution spectrum without consuming much time to simulate it.

Acknowledgment

This study was the partial product of the national projects for long term nuclear development supported by the Ministry of Science and Technology of Korea.

References

1) R.L. Bramlett et al., A New Type of Neutron Spectrometer, Nucl. Inst. Meth., 9, 1-12 (1960).
2) B. Wiegel and A.V. Alevra, NEMUS-the PTB Neutron Multi-sphere Spectrometer: Bonner Spheres and More, Nucl. Inst. Meth., A476, 36-41 (2002).
3) P. Goldhagen et al., Measurement of the Energy Spectrum of Cosmic-Ray Induced Neutrons Aboard an ER-2 High Altitude Airplane, Nucl. Inst. Meth., A476, 42-51 (2002).
4) H.H. Hsu, K.R. Alevra and D.G. Vasilik, A New Bonner-Sphere Set for High Energy Neutron Measurement: Monte Carlo Simulation, IEEE Trans. Nucl. Sci. 41[N4], 938-940 (1994).
5) B.H. Kim et al., Measurement of the Neutron spectra Inside and Outside the Taeget Room of the 65 MeV Electron LINAC using an Extended Bonner Sphere, J. Nucl. Sci. Technol. Suppl.4, 176-179 (2004).
6) B.H. Kim et al., Measurement of the Neutron Fluence and Dose Spectra Using an Extended Bonner Sphere and a Tissue-Equivalent Proportional Counter, Radiat. Prot. Dosim. 111[1-4], 717-723 (2004).
7) B.H. Kim et al., Determination of the Neutron Fluence Spectra In the Neutron Therapy Room of KIRAMS, Radiat. Prot. Dosim. Doi:10.1093/rpd/ncm079, 1-6 (2007).
8) National Council on Radiation Protection and Measurement, Radiation Protection for Particle Accelerator Facilities, NCRP-114, 70-112 (2003).
9) S.E. Han, Study of Additional Neutron Dose During Proton Beam Therapeutic Process, Master's Thesis, KAIST (2007).
10) D. B. Pelowitz et al., MCNPX User's Manual version 2.5.0, LA-CP-05-0369, LANL 2005.
11) H.W. Bertini, Low-Energy Intranuclea Calculation, Phys. Rev., 131, 1801-1821 (1963).
12) M. Reginato, B. Wiegel and A. Zimbal, UMG3.1, Unfolding with Maxed and Gravel, PTB, Germany (2002).
13) International Organization for Standardization (ISO): Procedures for calibrating and determining the response of neutron-measuring devices used for radiation protection purposes, International Standard ISO-10647 (1996).
14) International Commission on Radiation Protection (ICRP), Coefficients for use in radiation protection against external radiation. ICRP Publication 74. (Oxford New York: Elsevier Science) (1997).

Journal of NUCLEAR SCIENCE and TECHNOLOGY, Supplement 5, p. 233–236 (June 2008)

Response of ^{6}LiF:Mg,Cu,Si and ^{7}LiF:Mg,Cu,Si TLD Pairs to the Neutrons and Photon Mixtures

J. I. Lee*, A. S. Pradhan, J. L. Kim, B. H. Kim, and K. S. Yim

Health Physics Department, Korea Atomic Energy Research Institute, P.O. Box 105, Yuseong, Daejeon, Korea

Replacement of dopant P by Si in LiF:Mg,Cu,P has provided an improved LiF:Mg,Cu,Si TLD material. Responses of indigenously developed Korean ^{Natural}LiF:Mg,Cu,Si. ^{6}LiF:Mg,Cu,Si and ^{7}LiF:Mg,Cu,Si TLDs to gamma rays and neutrons were evaluated and compared with the commercially available LiF based TLDs. The intrinsic gamma ray sensitivity of ^{Natural}LiF:Mg,Cu,Si was found to be the highest among the studied TLDs. The gamma ray sensitivities of ^{6}LiF:Mg,Cu,Si and ^{7}LiF:Mg,Cu,Si were about 27 and 32 times higher than that of Harshaw LiF:Mg,Ti. The relative neutron sensitivities (ratio of TL/mGy to neutron and gamma rays) of ^{6}LiF TLDs doped with Mg,Cu,P and Mg,Cu,Si were about the same but lower than that of Harshaw ^{6}LiF:Mg,Ti (TLD-600) due to the difference in their LET dependences. The high intrinsic TL sensitivity of ^{6}LiF:Mg,Cu,Si outweighs the higher relative neutron sensitivity of TLD-600. In the testing following ANSI criteria, the performance quotient of the pairs of ^{6}LiF:Mg,Cu,Si / ^{7}LiF:Mg,Cu,Si held in Harshaw neutron TLD badge holders for the dosimetry in the mixed field of neutron and gamma rays was found to be less than 0.1 as against the maximum permitted value of 0.4.

KEY WORDS: TLD, neutron dosimetry, ^{252}Cf neutron fields, $^{6/7}$LiF:Mg,Cu,Si, Albedo dosimetry

I. Introduction

Radiation monitoring is a very important aspect of radiation protection to obtain information of doses in the use radiation sources and radiation generating equipments causing occupational and public exposures. This information is needed in limiting the doses to individuals and in demonstrating the compliance with the legal requirements and with the full system of dose limitation recommended by the International Commission on Radiological Protection (ICRP). Although, both external and internal exposures contribute to occupational exposures, it is the external exposures which are most commonly encountered both at the work places as well as in the environment including at high altitudes and during space flights. It is estimated[1)] that out of 6.5 million persons occupationally exposed to enhanced radiation doses, about 4.6 million are individually monitored the world over by using a radiation detector on the person, generally called monitoring badge. TLD badges based on LiF:Mg,Ti are the most popular among the devices used for personal dosimetry for external radiation. Personal dosimetry for x-rays and gamma and beta radiation is simple and straight forwarded but real challenge lies in the mixed field dosimetry of neutrons and gamma rays in nuclear power plants, accelerators and in other nuclear facilities and also in space flights. Neutrons have much higher biological effectiveness which changes considerably with the change in the energy of neutrons in contrast to gamma and beta radiation.

Most widely used technique for personal dosimetry has been the albedo technique employing pairs of ^{6}LiF (highly sensitivity to thermal neutrons) and ^{7}LiF (insensitive to neutrons) TLDs by using TLD-600 and TLD-700 (Mg & Ti doped ^{6}LiF and ^{7}LiF TLDs) from Harshaw Chemical Co, USA. The major problem has been their low TL sensitivity to gamma rays for measuring low doses. Although, the availability of ^{6}LiF and ^{7}LiF TLDs doped with Mg, Cu, & P have enabled to overcome this problem to some extent, they suffer from the draw backs of a change / reduction in their sensitivities on reuse, limitation of heating not beyond 240˚C and higher residual TL. The dosimetric characteristics of Korean LiF:Mg,Cu,Si TLD[2)] with a gamma ray TL sensitivity 55 times that of LiF:Mg,Ti (TLD-100) demonstrated the availability of a TLD material for a pragmatic replacement of LiF:Mg,Ti in routine personal dosimetry without the hesitations which were associated with the use of LiF:Mg,Cu,P. The next step is obviously to develop LiF:Mg,Cu,Si based TLDs for the dosimetry of mixed fields of neutrons and gamma rays. A curiosity to know whether the method of preparation of ^{Natural}LiF:Mg,Cu,Si can be adopted to prepare ^{7}LiF:Mg,Cu,Si and ^{6}LiF:Mg,Cu,Si having adequate sensitivities, made us to undertake the present work of preparing Korean (KAERI) ^{7}LiF:Mg,Cu,Si and ^{6}LiF:Mg,Cu,Si TLDs. and evaluating their responses.

II. Materials and Methods

High purity ^{6}LiF and ^{7}LiF powders were procured and analyzed to have 90.5±0.2 % of ^{6}Li and 99.97±0.01 % of ^{7}Li, respectively, by using inductive coupled plasma mass spectroscopy (ICPMS). An optimized method of preparation with dopant concentrations of 0.45 mol % of $MgSO_4.7H_2O$, 0.025 mol % of $CuSO_4.5H_2O$ and 0.9 mol % of SiO_2 was adopted. The major features of the new method of preparation were 1- avoidance of use of Na and P dopants in view of the conclusions on our earlier results, 2- use of a method of melting for activation instead of granulation at

*Corresponding Author, E-Mail; jilee@kaeri.re.kr

temperatures below the melting points and 3- adoption of a final dual-step thermal treatment at 300 °C for 10 min followed by 260 °C for 10 min for minimizing the intensity of the high-temperature glow peak responsible for the residual signal. Sintered pellets of thickness 0.8 mm and diameter of 4.5 mm were prepared. For comparison, the commercially available TLDs such as Harshaw ^{Natural}LiF:Mg,Ti (TLD-100), ^{6}LiF:Mg,Ti (TLD-600) and ^{7}LiF:Mg,Ti (TLD-700); Chinese ^{Natural}LiF:Mg,Cu,P (GR-200), ^{6}LiF:Mg,Cu,P (GR-206) and ^{7}LiF:Mg,Cu,P (GR-207) and Polish ^{Natural}LiF:Mg,Cu,P (MCP-N), ^{6}LiF:Mg,Cu,P (MCP-6) and ^{7}LiF:Mg,Cu,P (MCP-7) were procured. For evaluating the neutron responses of the pairs of TLDs (pair of neutron sensitive ^{6}LiF and neutron insensitive ^{7}LiF based TLDs), the Harshaw 8806 neutron TLD badge holders were used. The badge holder had a provision to hold a pair of ^{6}LiF and ^{7}LiF under each of the two different filters, namely an ABS+Cd filter with the mass thickness of 465 mg/cm^2 and an ABS filter with the mass thickness of 300 mg/cm^2. Calibrated ^{137}Cs gamma ray **source** for photons and ^{252}Cf sources held in different moderators for mixed fields of neutrons and gamma rays were used. During exposures to neutron fields, the badges were held on a water phantom of size 30cm x 30 cm x 15 cm whereas for exposures to ^{137}Cs gamma rays, a PMMA phantom of size 30cm x 30 cm x 30 cm was used

III. Results and Discussion

The glow curve structure of LiF:Mg,Cu,Si is similar to that of LiF:Mg,Cu,P **(Fig. 1)** but the sensitivity of the main TL peak was higher by about 10 % and the relative intensities of the lower and higher temperatures TL glow peaks were much smaller. The method of preparation applicable for reproducible batches of ^{Natural}LiF:Mg,Cu,Si did not result in ^{7}LiF:Mg,Cu,Si and ^{6}LiF:Mg,Cu,Si TLDs with the same gamma ray sensitivity. Alterations in the method of preparation at the crucial temperature treatment stage above 800°C were made in view of the differences in the melting points of ^{7}LiF:Mg,Cu,Si and ^{6}LiF:Mg,Cu,Si by a few °C.

Table 1 Relative gamma ray (^{137}Cs) sensitivity (TL/mGy) of different LiF TLDs (Harshaw LiF:Mg,Ti (TLD-100) ribbons=1)

LiF / Make & dopants	^{Natural}LiF	^{6}LiF	^{7}LiF
Harshaw, Mg,Ti	**1.00$_{TLD100}$**	**1.02$_{TLD600}$**	**1.12$_{TLD700}$**
Korea, Mg,Cu,Si	**55.0**	**27.4**	**32.0**
China, Mg,Cu,P	**53.0 $_{GR200}$**	**44.6 $_{GR206}$**	**43.0 $_{GR207}$**
Poland, Mg,Cu,P	**36.0 $_{MCPN}$**	**25.4 $_{MCP6}$**	**32.9 $_{MCP7}$**

The responses of the indigenously prepared TLDs were compared with the commercially available TLDs **(Table 1)**. It may be noted that the intrinsic gamma ray sensitivity of ^{Natural}LiF:Mg,Cu,Si is the highest among the TLDs studied in this work. The sensitivities of ^{6}LiF:Mg,Cu,Si and ^{7}LiF:Mg,Cu,Si are about 27 and 32 times higher than that of TLD-600 and TLD-700, respectively, but lower than that of the Chinese ^{6}LiF:Mg,Cu,P and ^{7}LiF:Mg,Cu,P. This indicates a need for more efforts for improving the gamma ray sensitivities of ^{6}LiF:Mg,Cu,Si and ^{7}LiF:Mg,Cu,Si TLDs.

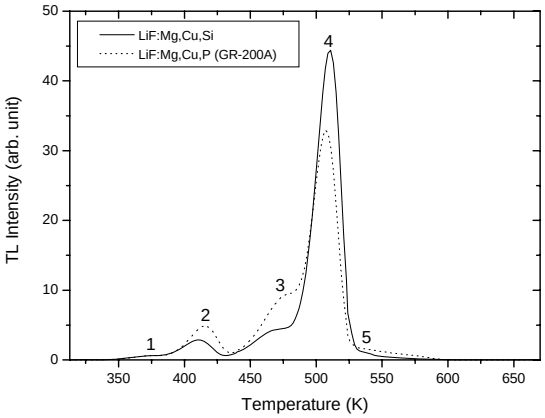

Fig. 1 Comparison of TL glow curves of Korean LiF:Mg,Cu,Si with Chinese LiF:Mg,Cu,P (GR-200A)[2)]

Table 2 Relative responses (TLD-700=1) of different LiF TLDs in mixed field of neutrons (45 mSv) and γ rays (5.58 mSv) of moderated fields of ^{252}Cf neutron sources (in terms of TL equivalent to ^{137}Cs gamma rays)

LiF / Make & dopants	^{7}LiF	^{6}LiF	^{Natural}LiF
Harshaw, Mg,Ti	**1.00$_{TLD700}$**	**25.0$_{TLD600}$**	**8.24$_{TLD100}$**
Korea, Mg,Cu,Si	**1.04**	**10.9**	**3.44**
China, Mg,Cu,P	**1.55$_{GR207}$**	**10.9 $_{GR206}$**	**3.42 $_{GR200}$**
Poland, Mg,Cu,P	**1.08$_{MCP7}$**	**10.2$_{MCP6}$**	**2.58 $_{MCPN}$**

Table 2 shows the relative responses of different LiF based TLDs in a mixed field of neutrons (45 mSv) and gamma rays (5.58 mSv) of moderated fields of ^{252}Cf sources. The relative (relative to the neutron insensitive ^{7}LiF TLD) neutron response of ^{6}LiF TLDs doped with Mg,Cu,P and Mg,Cu,Si were about the same but much lower than that of TLD-600. This was mainly attributed to the enhanced reduction of the responses of Mg,Cu,P and Mg,Cu,Si doped LiF TLDs to higher LET of neutrons[3)]. The LET dependence of LiF:Mg,Cu,Si is similar to that of LiF:Mg,Cu,P as indicated by the similarity in their photon energy dependence[3,4)] but different than that of LiF:Mg,Ti. One of the striking outcome of the present study is that the relative responses of ^{7}LiF:Mg,Cu,Si and ^{7}LiF:Mg,Cu,P (MCP-7) to ^{252}Cf irradiations were found to be the same as that of Harshaw ^{7}LiF:Mg,Ti (TLD-700). This is not in line with the earlier findings[5)] where ^{7}LiF:Mg,Cu,P was predicted to give the lowest response in mixed fields of neutrons and gamma rays due to its much reduced response to neutrons (high LET radiation). The results of inductive coupled plasma mass spectroscopy (ICPMS) show that the depletion of ^{6}Li (^{6}Li responsible for response to neutrons) is much lower (0.03%) in ^{7}LiF used for the preparation of ^{7}LiF:Mg,Cu,Si, than that of the reported depletion (0.007%) in TLD-700. This difference in the depletion of ^{6}Li is attributed to be compensating the impact of LET dependences of ^{6}Li

depleted different LiF TLDs in the neutrons fields of ^{252}Cf sources held in D_2O moderator. Higher response of ^{7}LiF:Mg,Cu,P (GR-207) in the neutron field may be due to ^{6}Li contamination (or lower depletion of ^{6}Li) because a small increase (even at the trace level) in ^{6}Li (high cross-section of 940 barns to thermal neutrons) content increases the neutron response significantly in the fields having thermalized neutrons.

By assuming the response of the Harshaw TLD-700 to be negligible to neutrons and using it for the estimation of gamma rays doses in the mixed fields of neutrons and gamma rays for correcting for the gamma ray content, the relative neutron sensitivities (ratio of TL/mSv to neutrons and TL/mSv gamma rays) of TLD-600, ^{6}LiF:Mg,Cu,Si, GR-206 and MCP-6 were estimated to be 2.96, 1.22, 1.23 and 1.15, respectively for the D_2O moderated fields of ^{252}Cf sources. The values of the relative neutron sensitivities of TLD-100, LiF:Mg,Cu,Si, GR-200 and MCP-N were 0.9, 0.3, 0.3 and 0.24, respectively. Lower values of ^{6}LiF:Mg,Cu,Si, GR-206 and MCP-6 than TLD-600 and also of LiF:Mg,Cu,Si, GR-200 and MCP-N than TLD-100 are due to their reduced relative TL efficiencies to higher LET neutron radiation (mainly n-α reaction).

Table 3 Relative net TL per mSv of neutrons for ^{6}LiF:Mg,Cu,Si / ^{7}LiF:Mg,Cu,Si (Korean TLD pair) and TLD-600 / TLD-700 (Harshaw TLD pair) pairs held in Harshaw neutron TLD badge (on phantom) and exposed in the neutron fields of different average energies from ^{252}Cf sources held in different moderators

Type of neutron field of ^{252}Cf (Average neutron energy)	Harshaw TLD pair	Korean TLD pair
D_2O Moderated (0.43 MeV)	1.00	12.2
D_2O Moderated & Cd Covered (0.53 MeV)	0.74	10.1
Bare (1.84 MeV)	0.10	1.56

Table 3 shows the relative net TL (^{6}LiF TL - ^{7}LiF TL) per mSv of neutron dose for ^{6}LiF:Mg,Cu,Si / ^{7}LiF:Mg,Cu,Si (Korean TLD pair) and TLD-600 / TLD-700 (Harshaw TLD pair) pairs held in the Harshaw neutron TLD badge when irradiated on the phantom in the neutron fields of different average energies. The higher relative neutron response of the TLD-600 **(Table 2)** would result in higher neutron-gamma discrimination for TLD-600 / TLD-700 pair, but the high intrinsic TL sensitivity of ^{7}LiF:Mg,Cu,Si and ^{6}LiF:Mg,Cu,Si **(Table 3)** outweighs this aspect.

Fig. 2 and **3** show the neutron energy dependence of the pairs of ^{6}LiF:Mg,Cu,Si / ^{7}LiF:Mg,Cu,Si (Korean TLD pair) and TLD-600 / TLD-700 (Harshaw TLD pair), respectively. It can be seen that the neutron response of the pair of ^{6}LiF:Mg,Cu,Si / ^{7}LiF:Mg,Cu,Si (Korean TLD) under Cd **(Fig. 2)** to 0.43 MeV average neutron energy (D_2O moderated) is not much different than that to 0.53 MeV average neutron energy (D_2O moderated and Cd covered) whereas for TLD-600 / TLD-700 pair **(Fig. 3)** the response to 0.43 MeV neutrons is significantly higher than to 0.53 MeV neutrons. The difference in the relative neutron responses of the two types of pairs is mainly due to the differences in the responses of ^{6}LiF:Mg,Cu,Si and ^{6}LiF:Mg,Ti (TLD-600). TLD pairs held under Cd filter exhibit reduced neutron energy dependence than those held under ABS plastic. This is because Cd filter cuts off D_2O moderated thermalised neutrons for which ^{6}Li have a very high cross-section.

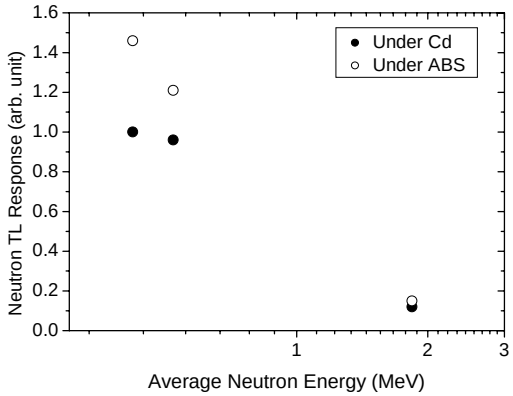

Fig. 2 Relative neutron response (net TL (^{6}LiF - ^{7}LiF) per mSv of neutrons) of ^{6}LiF:Mg,Cu,Si / ^{7}LiF:Mg,Cu,Si pairs held in Harshaw neutron TLD badge versus average neutron energy from ^{252}Cf sources under different moderators

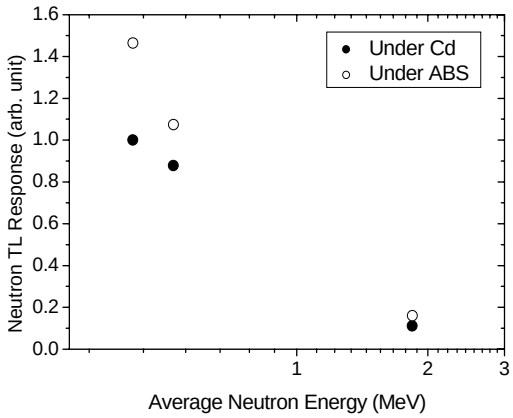

Fig. 3 Relative neutron response (net TL (^{6}LiF - ^{7}LiF) per mSv of neutrons) of TLD-600 / TLD-700 pairs held in Harshaw neutron TLD badge versus average neutron energy from ^{252}Cf sources under different moderators

Table 4 compares the gamma ray doses measured from the readouts of the neutron insensitive TLD-700 (99.993% of ^{7}Li) and ^{7}LiF:Mg,Cu,Si (99.97±0.01 of ^{7}Li) exposed in different neutron fields by using a calibration against ^{137}Cs gamma rays. The doses measured by using TLD-700 and ^{7}LiF:Mg,Cu,Si are about the same. This indicates that the lack of the depletion of ^{6}Li in ^{7}LiF:Mg,Cu,Si is compensated for by its reduced response to high LET radiation.

Table 4 Gamma ray dose content (percent of neutron dose) measured by different neutron insensitive LiF TLDs in different types of mixed fields of neutron and gamma rays from ^{252}Cf sources

Type of neutron insensitive TLD	Measured gamma ray dose content in different ^{252}Cf neutron fields (%)		
	D_2O Mod & Cd Cov	TLD D_2O Mod	Bare
^{7}LiF:Mg,Ti$_{(TLD-700)}$	12.2	10.9	4.3
^{7}LiF:Mg,Cu,Si$_{(Korea)}$	12.2	11.4	4.2

The ^{6}LiF:Mg,Cu,Si / ^{7}LiF:Mg,Cu,Si pairs held in the Harshaw 8806 neutron badge holders were also subjected to ANSI testing protocol for an estimation of the unknown doses of mixtures of neutron and gamma ray exposures. For this, the badges held on the phantoms were exposed to different combinations of doses of ^{137}Cs gamma rays (in the range from 2 to 8 mSv) and neutrons from ^{252}Cf sources in a D_2O moderated and Cd assembly (in the range from 0.9 to 11 mSv) by a member of the testing laboratory and were given to the evaluating authors for an actual estimation of the doses. The types of radiation were disclosed but the doses delivered and the proportion of the neutron and gamma ray doses were not disclosed until the results were submitted by the evaluating authors. The measured and given doses were found to be within 10%. The ANSI performance quotient of the pairs of ^{6}LiF:Mg,Cu,Si / ^{7}LiF:Mg,Cu,Si TLDs was found to be less than 0.1 as against the maximum permitted value of 0.4, thus well within the ANSI limits set for the audit of a quality assurance. This test demonstrated that the ^{6}LiF:Mg,Cu,Si / ^{7}LiF:Mg,Cu,Si pairs can directly replace the TLD-600 / TLD-700 pairs in the Harshaw badge for the use of an estimation of the personal doses encountered by the workers in nuclear facilities, namely nuclear reactors and fuel processing facilities.

IV. Conclusions

Indigenously developed high sensitivity Korean LiF:Mg,Cu,Si TLDs exhibited improved dosimetric characteristics. Korean ^{6}LiF:Mg,Cu,Si / ^{7}LiF:Mg,Cu,Si TLD pair held under Cd filter of the Harshaw 8806 neutron TLD badge exhibited a reduced neutron energy dependence. The ANSI performance quotient of the pairs of ^{6}LiF:Mg,Cu,Si / ^{7}LiF:Mg,Cu,Si TLDs held in the Harshaw 8806 neutron TLD badge holders for the dosimetry in a mixed field of neutron and gamma rays was found to be less than 0.1 as against the maximum permitted value of 0.4. This demonstrated that the ^{6}LiF:Mg,Cu,Si / ^{7}LiF:Mg,Cu,Si pairs can directly replace the TLD-600 / TLD-700 pairs in the Harshaw neutron TLD badge for an estimation of the personal doses encountered by the workers in nuclear facilities, namely nuclear reactors and fuel processing facilities.

Acknowledgement

This work was performed under the long-term nuclear research and development program sponsored by Ministry of Science and Technology of Korea.

References

1) C. WERNLI, External dosimetry : Operational quantities and their measurement. Projection 26 of refresher course RC-3b at 11th International Congress of IRPA, Madrid, Spain, May 23-28, 2004 (http://irpa11.irpa.net/pdfs/RC-3bppt.pdf)
2) J. I. LEE, J. S. YANG, J. L. KIM, A. S. PRADHAN, J. D. LEE, K. S. CHUNG and H. S. CHOE, 'Dosimetric characteristics of LiF:Mg,Cu,Si thermoluminescent materials', Appl. Phys. Lett. 89, 094110, 2006
3) A. S. PRADHAN and R. C. BHATT, 'Thermal neutron response and photon energy dependence on LiF:Mg,Cu,P', Radiat. Prot. Dosim. 27, 185, 1989
4) J. I. LEE, A. S. PRADHAN, J. L. KIM, B. H. KIM and K. S. YIM, 'Role of dopants in LiF TLD materials', Radiat. Meas. Doi:10.1016/j.radmeas.2007.10.040
5) Y. S. HOROWITZ, and B. B. SHACHAR, 'Thermoluminescent LiF:Mg,Cu,P for gamma ray dosimetry in mixed fast neutron-gamma radiation fields'. Radiat. Prot. Dosim. 23, 1988

Journal of NUCLEAR SCIENCE and TECHNOLOGY, Supplement 5, p. 237–240 (June 2008)

Experimental Study of Proton Induced Cross-sections on Natural Cadmium Leading to the Production of ^{111}In Radionuclide

Mayeen U. KHANDAKER[1], Kwangsoo KIM[1], Manwoo LEE[1], Kyung-Sook KIM[1], Young-Seok LEE[2], Young-Sik CHO[3], Young-Ouk LEE[3], and Guinyun KIM[1]*

[1]*Department of Physics, Kyungpook National University,1370 Sankyok-dong, Buk-gu, Daegu 702-701, Korea*
[2]*R & D Division, National Fusion Research Center, Daejeon 305-333, Korea.*
[3]*Nuclear Data Evaluation Lab., Korea Atomic Energy Research Institute, Daejeon 305-600, Korea*

We measured the production cross-sections of ^{111}In induced by proton on the ^{nat}Cd at several proton energies between 4 MeV and 40 MeV by using a stacked-foil activation technique at the MC50 cyclotron of the Korea Institute of Radiological and Medical Sciences. The present results were compared with the earlier reported experimental data and the theoretical calculations by using both the TALYS code and the ALICE-IPPE code. An overall good agreement was found with the recently reported experimental data and the TALYS prediction, as well. Integral yields of ^{111}In were also deduced from the measured cross-sections.

KEYWORDS: ^{nat}Cd+p reactions, 42 MeV proton, stacked-foil activation technique, production cross-section of ^{111}In, integral yield

I. Introduction

Indium (In) is a natural element distributed in a minute quantity (~0.1 μg/g) in earth's crust. The demand of indium and indium containing compounds are increasing rapidly in various industrial, scientific, and medical purposes: decorative coating, bearing, low-melting alloys, glass-sealing alloys, semiconductor research, solar batteries, liquid crystal displays, nuclear reactor control rods, and in nuclear medicine.[1-2)] Recently, indium radioisotopes namely ^{110}In, ^{111}In, ^{113}In, and ^{114m}In are widely used as therapeutic and diagnostic purposes.[3-6)] The important nuclear characteristics for some medically relevant indium radioisotopes are shown in **Table 1.**[7)] Among them, ^{111}In is largely used in diagnostic nuclear medicine due to its suitable half-life ($T_{1/2}$ =2.8 d), abundance of β^--emission and high intense low energy γ-ray emission. It is also used for labeling of cellular blood components and monoclonal antibody, myocardial damage detection, localization of abscess in polyeystic kidney, radiolabeled immunoglobulin therapy, imaging for cancer, and etc. [8-9)]. In addition, a number of clinical investigations are in progress in which antibodies and peptides labeled with ^{111}In are the subject of therapeutic and diagnostic evaluations.[7)] Moreover, the radionuclide ^{111}In plays a great role in time differential perturbed angular correlation studies. Since ^{111}In emits cascade γ-rays (171 and 245 keV) in which the intermediate nuclear level (**Fig. 1**) has a suitable lifetime (84 ns) and significant nuclear quadrupole moment, so it is widely used as a nuclear probe for perturbed angular correlation studies.[10-11)]

In the literature, several studies were carried out with proton, deuteron, alpha, ^{3}He, and ^{12}C beam irradiation on either natural or isotopically enriched Cd, Ag or Sn targets, with the aim of investigating the production cross section of ^{111}In radioisotope.[4,8,12-14)] The use of variable energy proton-cyclotron beams presents remarkable advantages to induce (p, xn) reactions on either natural or isotopically enriched targets with the aim of determining excitation functions and cross-sections. The major and economical production routes of ^{111}In radionuclide with varieties of excitation energy ranges are illustrated in **Table 2**. Among them, protons or deuterons irradiation of cadmium targets is the most easy, convenient, and cheap method for production of ^{111}In radionuclide leading to clinical use. The major aim of this work was to study the production cross-sections of high purity ^{111}In radionuclide from the proton bombardment of natural cadmium (Cd) target using the external beam line of the MC50 cyclotron at the Korea Institute of Radiological and Medical Sciences (KIRAMS).

Table 1 Important nuclear data of medically relevant indium isotopes

Nuclide	Half-life	Decay mode	E_γ (keV)	I_γ (%)	Production method
^{111}In	2.8d	EC to ^{111}Cd	171.2	90.0	^{112}Cd(p,2n)
			245.3	94.0	
^{113m}In	1.66h	IT to ^{113}In	393	64	^{113}Sn(p,2pn)
^{114m}In	49.5d	IT to ^{114}In	190.2	14.7	^{114}Cd(p, n)
		β^- to ^{114}Sn	558.4	4.0	
			725.2	4.0	

II. Experimental Technique

The irradiation technique, the activity determination, and the data evaluation are described in elsewhere.[15)] The well established stacked-foil activation technique combined with high-purity germanium (HPGe) γ-ray spectrometry were employed to determine the production cross-sections of ^{111}In. Stack was prepared using high-purity (99.97%) metallic

*Corresponding Author, E-mail: gnkim@knu.ac.kr

form of natural cadmium foils (50 μm thick) together with 100 μm thick natural copper and aluminum foils where Cu and Al foils were used as beam monitors and energy degraders, respectively. The stacked-foils were irradiated for 0.75 hour by the proton energy of 42.1 MeV with a beam current of about 100 nA from the external beam line of the MC50 cyclotron at the KIRAMS. The beam intensity was kept constant during the irradiation. It was necessary to ensure that equal areas of the monitor and the target foils intercepted the beam. The activity measurements of the irradiated samples were started about 2 hours after the end of the irradiation. Each sample was recounted 4~5 times to avoid disturbance by overlapping gamma-lines from undesired sources and in order to more accurately evaluate the longer-lived radionuclides. The HPGe-detector was coupled with a 4096 multichannel analyzer (MCA) with the associated electronics to determine the photo peak area of the γ-ray spectrum. Interactive peak analysis was done using the program Gamma Vision 5.0 (*EG&G Ortec*).

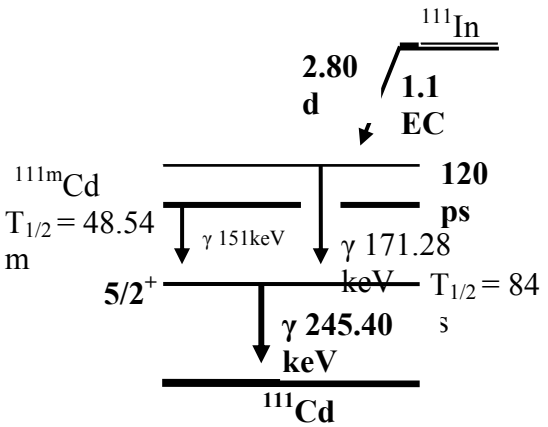

Fig. 1 Partial decay schemes for ^{111}In and ^{111m}Cd nuclides. The half-life of each level is labeled. The 171-245 keV gamma cascade follows the electron capture decay of ^{111}In; the 48.5 minute ^{111m}Cd state decays the 151-245 keV gamma cascade. Both cascades share the same 245 keV ($5/2^+$) ^{111}Cd intermediate nuclear state

The efficiency versus energy curves of the HPGe-detector for the counting distances was determined using the standard point sources, ^{133}Ba, ^{109}Cd, ^{22}Na, ^{60}Co, ^{57}Co, ^{54}Mn, and ^{137}Cs. The proton beam intensity was determined from the measured activities induced in aluminum and copper monitor foils at front of stack using the reactions, ^{27}Al(p,x)^{22,24}Na and ^{nat}Cu(p,x)^{62}Zn, respectively. It was considered the monitor foils were irradiated simultaneously and measured with the same detector and in a comparable geometry as the Cd target. The loss of proton energy along the samples in the stack was calculated by using the computer program SRIM-2003.[16] In order to calculate the cross-sections, the decay data of the ^{111}In were taken from the NUDAT database[17], the threshold energy of the contributing reaction was taken from the Los Alamos National Laboratory.[18] The standard cross-sections for the monitors were taken from internet service.[19]

The production cross-sections of the investigated nuclear reactions were determined from the reaction rates of the radioactive products and the measured beam intensity. In the present experiment, all the errors were considered as independent. The combined uncertainty in each cross-section was estimated by considering the following uncertainties; statistical uncertainty of gamma-ray counting (0.5-10 %), uncertainty in the monitor flux (~7 %) and uncertainty in the efficiency calibration of the detector (~4 %). Consequently, the total uncertainty was obtained according to the error propagation formula. The overall uncertainties of the cross-section measurements were in the range 8-14 %.

Table 2 The Q-values and Coulomb barriers for the reactions leading to the production of ^{111}In radionuclide

Production route	Target abundances (%)	Q-value (MeV)	Effective Coulomb barrier (MeV)
^{111}Cd(p, n)^{111}In	12.75	-1.63	4.11
^{112}Cd(p, 2n)^{111}In	24.07	-11.02	4.10
^{113}Cd(p, 3n) ^{111}In	12.26	-17.56	4.09
^{114}Cd(p, 4n) ^{111}In	28.86	-26.60	4.09
^{110}Cd(d, n) ^{111}In	12.39	3.10	5.09
^{111}Cd(d, 2n) ^{111}In	12.75	-3.85	5.08
^{109}Ag(^{3}He, n) ^{111}In	48.65	6.55	10.92
^{109}Ag(^{4}He, 2n) ^{111}In	48.65	-14.03	10.71
^{112}Sn(p, 2n)^{111}Sb →^{111}Sn→^{111}In	0.95	-17.06	4.27
^{114}Sn(p, 4n)^{111}Sb→^{111}Sn→^{111}In	0.65	-35.10	4.26
^{115}Sn(p, 5n)^{111}Sb→^{111}Sn →^{111}In	0.34	-42.65	4.25
^{116}Sn(p, 6n)^{111}Sb→^{111}Sn →^{111}In	14.24	-52.21	4.24
^{117}Sn(p, 7n)^{111}Sb→^{111}Sn →^{111}In	7.57	-59.15	4.23
^{118}Sn(p, 8n)^{111}Sb→^{111}Sn →^{111}In	24.01	-68.47	4.22
^{110}Cd(^{3}He, 2n) ^{111}Sn →^{111}In	12.39	-5.62	11.13

III. Theoretical Calculations

TALYS is a nuclear-reaction computer program which simulates basically all types of nuclear reactions, in the energy range of 1 keV - 200 MeV. With a few exceptions, the database of this code is based on the Reference Input Parameter Library.[20] In TALYS, the coupled-channel code ECIS-97 [21] is used as a subroutine for all optical model and direct reaction calculations. The default optical-model potentials (OMP) used in TALYS are the local and global parameterizations for neutrons and protons[22] but possible to adjust the parameters on demand. All types of compound nucleus reaction mechanism are included in this code where the calculations are mostly based on the Hauser-Feshbach formalism including the width fluctuation corrections. Several models for the level density are used in this code, which range from phenomenological analytical expressions to tabulated level densities derived from microscopic calculations. For fission, the default model used in this code is based on the Hill-Wheeler expression for the transmission coefficient for one, two, or three barriers. For nucleon reactions, a two-component exciton model with a new form of internal transition rates based on the OMP is implemented, which yields an improved description of pre-equilibrium processes over the whole energy range. The multiple pre-

equilibrium processes are accomplished by keeping track of all successive particle-hole excitations for either proton or neutron. Pre-equilibrium photon emission is taken into account with the model of Akkermans and Gruppelaar.[23] The newly developed Kalbach[24] phenomenological systematics are included in this code for nuclear reaction mechanisms like stripping, pick-up, and knock-out processes, and for the prediction of pre-equilibrium angular distributions. The independent treatment of isomeric state cross-section is the main advantage of this code. The present results of p+^{nat}Cd processes were evaluated using mostly the default values of the code, proper tuning with experimental conditions, and adjustment of some OMP parameters, as well.

IV. Results and Discussion

The production cross-sections of ^{111}In in the interactions of protons with natural Cd are presented in **Table 3** and is shown in **Fig. 2** together with the available literature values[25-28] and theoretical calculations using the newly introduced code TALYS-0.72 version, and also theoretical data taken from the calculations based on the ALICE-IPPE code.[29] The measured cross-sections of ^{111}In radionuclide is a cumulative one, because the activity counting was started after a long cooling time and by this time the short-lived metastable state radionuclide ^{111m}In (7.7 min) decayed completely to the long-lived ^{111}In ground state by IT process. The present results are in good agreement with the measured data reported by Tarkanyi *et al.*[25] and Nortier *et al.*[26] However, the data reported by Zaitseva *et al.*[27] are different form any other measurements. The data calculated by both the TALYS and the ALICE-IPPE code showed good agreement in both the shape and the magnitude with the present measured data. The present results are compared with the deduced normalized values from the IAEA recommended data[28] of the ^{111}Cd(p,n) and the ^{112}Cd(p,2n) reactions up to 20 MeV and the present results show very good agreement.

Table 3 Measured production cross-sections of the ^{111}In radionuclide

E_p (MeV)	σ (mb)	E_p (MeV)	σ (mb)	E_p (MeV)	σ (mb)
39.6	249.4±18.2	27.0	243.0±17.7	12.8	127.6±9.3
37.9	241.8±17.6	26.0	265.1±19.3	11.1	81.5±5.9
36.3	227.8±16.6	23.8	316.2±23.0	9.2	48.6±3.5
34.6	210.9±15.4	22.7	302.5±22.0	6.9	19.6±1.4
32.8	195.0±14.2	20.2	267.4±19.5	4.0	2.3±0.2
30.9	185.5±13.5	17.5	232.7±16.9		
29.0	198.6±14.5	16.2	225.0±16.4		

V. Integral Yield

The integral yield of a radionuclide from a nuclear process was deduced using the measured cross-sections of ^{111}In and the stopping power of ^{nat}Cd over the energy range from threshold upto 40 MeV. It is expressed as MBqμA^{-1}h^{-1}, i.e. for an irradiation at beam current of 1 μA for 1 hour. The present result is shown in **Fig. 3** together with the directly measured thick target yield value reported by Dmitriev and Molin [30] as a function of proton energy and found a very good agreement.

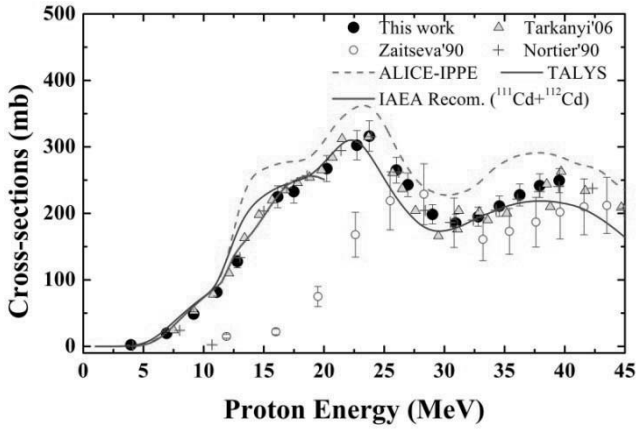

Fig. 2 Excitation function of the ^{nat}Cd(p, x)^{111}In reaction

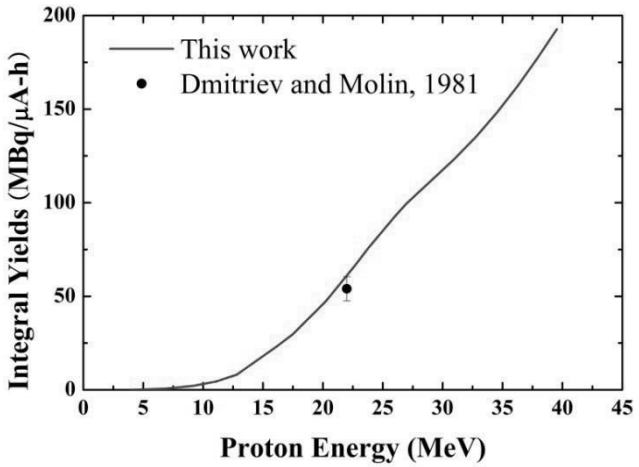

Fig. 3 Integral yields for the production of ^{111}In radionuclide

VI. Conclusions

A new experimental cross-sections data for the production of ^{111}In radionuclide from the proton bombardment on natural cadmium target have been reported in the energy range of 4-40 MeV using the stacked-foil activation technique with an overall uncertainty of about 14%. It is one of the most widely used radionuclide for diagnostic and therapeutic purposes in nuclear medicine. The measured excitation function of this radionuclide will help effectively to optimize the production conditions. The production of ^{111}In through ^{111}Cd(p,n) and ^{112}Cd(p,2n) processes is already recommended by IAEA under Coordinated Research Project (CRP). Hence, the present measured cross sections of ^{111}In from natural cadmium target could be used in validation of the IAEA recommended data. The production of this radionuclide from natural cadmium target is not suitable due to the contamination from other simultaneously produced indium radionuclides in our investigated energy range.

Highly enriched ^{111,112}Cd targets could be used to get the suitable production with minimum impurity level.

Acknowledgement

The author would like to express their sincere thanks to the staffs of the MC50 Cyclotron Laboratories for their cordial help in performing the experiment. This work is partly supported by the Korea Science and Engineering Foundation (KOSEF) through grants provided by the Korean Ministry of Science and Technology (MOST) in 2007 (Project No. M20702000008-07B0200-00810 and M20704000011-7M0400-01110) and by the user program of the Proton Engineering Frontier Project (Project No. M2 02AK010014-07A1101-01419). One of authors (G.N.K.) is partly supported by the Center for High Energy Physics (CHEP), Kyungpook National University through the KOSEF.

References

1) W. Zheng, I. G. Sipes, D. E. Carter, "Determination of Parts-per-Billion Concentrations of Indium in Biological Materials by Electrothermal Atomic Absorption Spectrometry Following Ion Pair Extraction," *Anal. Chem.,* **65,** 2174 (1993).
2) K. Inoue, K. Yoshizuka, S. Yamguchi, "Solvent Extraction of Indium with Trialkylphosphine Oxide from Sulphuric Acid Solutions Containing Choloride," *J. Chem. Engg. Japan,* **27 (6),** 737 (1994).
3) V. Tolmachev, P. Bernhardt, E. F. Aronsson et al., "^{114m}In, a Candidate for Radionuclide Therapy. Low-energy Cyclotron Production and Labelling of DTPA-D-Phe-Octreotide," *Nucl. Medi. Biol*., **27 (2),** 183 (2000).
4) M. L. Thakur, A. D. Nunn, "Cyclotron produced indium-111 for Medical Use," *Int. J. Appl. Radiat. Isot.,* **23 (3),** 139 (1972).
5) W. J. Nieckarz, A. A. Caretto, "Production on ^{111}In and ^{114m}In from the Separated Isotopes of Cadmium Using 70-400 MeV Protons," *Phys. Rev.***, 178 (4),** 1887 (1969).
6) T. Gelford (Supervised by Dr. J. Auria, Simon Fraser University, Burnadby, Britis, Canada), "An Overview of the Radiopharmaceutical Industry", *Nucl. Phys. News*, **14 (3),** 34 (2004).
7) R. E. Weiner, M. L. Thakur, *Chemistry of Galium and Indium Radiopharmaceuticals,* Handbook of Radiopharmaceuticals. Eds. M. Welch, C. S. Redvanly, John Wiley &Sons, p. 363 (2003).
8) M. L. Thakur, *Radiolabelled Blood Cells: Agent for Diagnostic and Kinetics Studies in Applications of Nuclear and Radiochemistry*. Pergamon press, Oxford p. 115 (1982).
9) S. Maji, S. Basu, S. Lahiri, "Alternative separation methods of no-carrier-added ^{111}In produced by heavy ion activation of silver," *Appl. Radiat. Isot.,* **63 (4)**, 513 (2005).
10) D. V. Filossofov, N. A. Lebedev, A. F. Novgorodov et al.," Production, concentration and purification of 111In," *J. Appl. Radiat. Isot.*, **55 (3),** 293 (2001).
11) H. H. Rinneberg, "Application of perturbed agular correlations to chemistry and related areas of solid state physics," *At. Energy Rev.,* **17 (2)**, 477 (1979).
12) L. C. Brown, A. L. Beets, "Cyclotron production of carrier-free indium-111," *Int. J. Appl. Radiat. Isot.,* **23 (2)**, 57 (1972).
13) D. Nayak, S. Lahiri, A. Ramaswami, "Alternative production and separation method of 111In by heavy ion activation of silver," *Indian J. Chem.,* **41 A (11),** 2300 (2002).
14) S. V. Thakare, A. G. C. Nair, S. Chakraborty et al., "Separation of carrier-free ^{111}In formed in the ^{12}C+Rh reaction," *J. Radioanal. Nucl. Chem.*, **242**, 537 (1999).
15) M. S. Uddin et al., "Excitation functions of the proton induced nuclear reactions on ^{nat}Zn up to 40 MeV," *Nucl. Instr. and Meth.,* **B 258**, 313 (2007).
16) J. F. Ziegler, J. P. Biersack, U. Littmark, SRIM 2003 code, Version 96.xx. *The stopping and range of ions in solids.* Pergamon, New York (2003). Available at <http://www.srim.org/>
17) National Nuclear Data Center, information of decay data extracted from the NuDat database, available at <http://www.nndc.bnl.gov/nudat2>
18) Reaction Q-values and thresholds, Los Alamos National Laboratory, T-2 Nuclear Information Service. Available at < http://t2.lanl.gov/data/qtool.html>
19) Monitor cross-section data. Available at < http://www-nds.iaea.org/medical/>
20) Reference Input Parameter Library. Available at <http://www-nds. iaea.org/RIPL-2/>
21) J. Raynal, Notes on ECIS94, CEA Saclay Report No.CEA-N-2772, (1994).
22) A. J. Koning, J. P. Delaroche, "Local and global nucleon optical models from 1 keV to 200 MeV," *Nucl. Phys.* **A713**, 231 (2003).
23) J. M. Akkermans, H. Gruppelaar, "Analysis of continuum gamma-ray emission in precompound-decay reactions," *Phys. Lett.* **B 157**, 95 (1985).
24) C. Kalbach, "Pre-equilibrium reactions with complex particle channels," *Int. Conf. Nucl. Data for Sci. and Tech.* Santa Fe, USA, Sept. 26- Oct. 1, (2004).
25) F. Tarkanyi, B. Kiraly, F. Ditroi et al., "Activation cross-sections on cadmium: Proton induced nuclear reactions up to 80 MeV," *Nucl. Instr. and Meth.,* **B 245**, 379 (2006).
26) F. M. Nortier, S. J. Mills, G. F. Steyn, "Excitation functions and production rates of relevance to the production of ^{111}In by proton bombardment of ^{nat}Cd and ^{nat}In up to 100 MeV," *Appl. Radiat. Isotop.,* **41**, 1201 (1990).
27) N. G. Zaitseva, O. Knotek, A. Kowalew et al., "Excitation functions and yields for ^{111}In production using ^{113,114,} ^{nat}Cd(p,xn)^{111}In reactions with 65 MeV protons," *Appl. Radiat. Isotop.,* **41,** 177 (1990).
28) S. Takacs, F. Tarkanyi, A. Hermanne, "Validation and upgrading of the recommended cross-section data of charged particle reactions: gamma emitter radioisotopes," *Nucl. Instr. and Meth.,* **B 240,** 790 (2005).
29) Yu. N. Shubin, V. P. Lunev, A. Yu. Konobeyev et al., "MENDL-2P, Proton reaction data library for nuclear activation (Medium Energy Nuclear Data Library)," IAEA-NDS-204, (1998).
30) P. P. Dmitriev, G. A. Molin, Radioactive nuclide yields for thick target at 22 MeV proton energy, *Yadernye Konstanty* **44 (5),** 43 (1981).

Journal of NUCLEAR SCIENCE and TECHNOLOGY, Supplement 5, p. 241–244 (June 2008)

Measurement of the Proton-induced Reaction Cross-sections of $^{nat}Zr(p,xn)^{86,87m,87(m+g),88}Y$ up to 40 MeV

M. S. UDDIN[1,2], Mayeen U. KHANDAKER[1], Kwngsoo KIM[1], Manwoo LEE[1], Young-Seok LEE[1,3], and Guinyun KIM[1*]

[1]*Department of Physics, Kyungpook National University,1370 Sankyok-dong, Buk-gu, Daegu 702-701, Korea*
[2]*Institute of Nuclear Science and Technology, Atomic Energy Research Establishment, Savar, GPO Box No.3787, Dhaka-1000, Bangladesh.*
[3]*Material Team, R&D Division, National Fusion Research Center, Dajeon 305-333, Korea*

We measured the production cross-sections of $^{86,87m,87(m+g),88}Y$ radioisotopes for proton-induced reactions on natural zirconium by using a stacked-foil activation technique in the energy range of 4-40 MeV at the MC50 cyclotron of the Korean Institute of Radiological and Medical Sciences. The activation method and the stacked-foil technique using the high-resolution HPGe gamma spectrometry were applied to determine the production cross-sections. The beam current was determined by the monitor reactions $^{nat}Cu(p,x)^{62}Zn$ and $^{27}Al(p,x)^{22,24}Na$. This work reports new data for the above reactions. The results were also compared with ALICE-IPPE model calculations compiled in MENDL-2P file. This experiment is in partial agreement with model calculations. The optimum energy range for the production of ^{86}Y is 40 - 30 MeV. The highest yield of ^{86}Y amounts to 33.37 MBq/μAh over this energy range and the levels of the ^{87}Y, ^{87m}Y and ^{88}Y impurities to 2.3, 26.55 and 0.33 %, respectively at EOB. The $^{nat}Zr(p,x)$ process may be a suitable route for the production of the medically important radioisotope ^{86}Y.

KEYWORDS: natural tungsten, 42 MeV proton, stacked-foil technique, activation method, 186-Re radionuclide, excitation function

I. Introduction

Activation cross-sections of proton-induced nuclear reactions are of interest for several fields; the knowledge of excitation curves is needed for optimization of radioisotope production, wear studies by thin layer activation (TLA) and in general for studies of behavior of materials particle irradiation. The radionuclide ^{90}Y ($T_{1/2}$=64.1 h, I_{β^-}= 100 %, E_{β^-}= 2.3 MeV) is one of the widely used therapeutic nuclides. However, it is not suitable for imaging. A general solution to this problem has been to substitute ^{90}Y by a γ- or β^+-emitting yttrium radioisotope. In a few studies ^{87}Y ($T_{1/2}$= 79.8 h, EC= 99.8 %, E_γ= 388.5 keV (82.1 %) and E_γ= 484.8 keV (89.7 %)) in combination with Single Photon Emission Computed Tomography (SPECT) was used. The positron emitting ^{86}Y ($T_{1/2}$=14.7 h, I_{β^-}= 33 %, E_{β^-}= 1.2 MeV), however, has proved to be more useful because of the possibility of imaging via Positron Emission Tomography (PET).

The database for the proton-induced activation on zirconium (Zr) is rather weak. The present experiment was undertaken to give reliable cross sections for the formation of yttrium radioisotopes via the $^{nat}Zr(p,x)$ processes as a part of our studies on particles induced activation on metals[1)].

II. Experimental Technique

A high-purity (99.98 %) Zr foil (500 μm thick) with a natural isotopic composition (^{90}Zr 51.45%, ^{91}Zr 11.22%, ^{92}Zr 17.15%, ^{94}Zr 17.38% and ^{96}Zr 2.80%) was used as the target for the irradiation. Two stacks with several groups of Cu and Zr were prepared for separate irradiations. Monitor foils of copper (100 μm thick) and aluminum (200 μm thick) with known cross-sections were placed at the front of the stack to determine the beam intensity. Several Cu foils were inserted into the stack to measure the excitation function of the monitor reaction $^{nat}Cu(p,x)^{62}Zn$ to check beam behavior along the stack. The copper foils were also used to degrade the beam energy. These two stacks were irradiated for 18 minutes and for 30 minutes with 42 MeV proton beam of 10 mm diameter at beam current of about 100 nA in the external beam line of the MC50 cyclotron at the Korea Institute of Radiological and Medical Sciences (KIRAMS). The beam intensity was kept constant during the irradiation. It was necessary to ensure that equal areas of the monitor and the target foils intercepted the beam. The irradiation geometry was kept in a position so that the foils received the maximum beam intensity.

III. Data Analysis

A HPGe γ-ray detector (EG&G Ortec.) was used to measure the radioactivity of the residual nuclei in the activated foils without chemical separation. The HPGe-detector was coupled with a 4096 multi-channel analyzer (MCA) with the associated electronics to determine the photo peak area of the γ-ray spectrum and Maestro data acquisition software. The spectrum analysis was done using the program Gamma Vision 5.0 (EG&G Ortec). The source-to-detector distance was kept long enough to assure a low dead time and a point-like geometry. Measurements were started about 5 hours after the end of irradiation, due to the high radiation dose of the short-lived products. Special care was taken to complete decay of shorter-lived parent nuclides in measurements of cross sections for cumulative formation

*Corresponding Author, E-mail: gnkim@knu.ac.kr

of the corresponding longer-lived daughter nuclides. Each sample was recounted 4 times giving several days intervals to avoid disturbance by overlapping γ-lines from undesired sources and in order to find any mistake in data analysis to more accurately evaluate the cross-sections. Measurements were done at 15 cm and 25 cm distances between the sample and the detector to keep dead time within 10 % and to suppress the sum-coincidence effect caused by the coincidental detection of two or more γ-rays in cascade.

The efficiency versus energy curve of the HPGe γ-ray detector for the counting distance was determined using the standard point sources, ^{133}Ba, ^{109}Cd, ^{22}Na, ^{60}Co, ^{57}Co, ^{54}Mn and ^{137}Cs. The proton beam intensity was determined from the measured activities induced in aluminum and copper monitor foils at front of stack using the reactions, ^{27}Al(p,x)^{22,24}Na and ^{nat}Cu(p,x)^{62}Zn[2], respectively. The monitor foils were irradiated simultaneously and measured with the same detector and in a comparable geometry as the zirconium target. The loss of proton flux through the stack was very small and not measurable practically. The beam intensity was considered constant to deduce cross-sections for each foil of the stack. The beam energy loss in foils of the stack was calculated by using the SRIM-2003[3] code.

Table 1 Deacy data for the investigated radionuclide.

Nuclide	Half-life	E_γ (keV)	I_γ (%)	Reactions	Q-value (MeV)
^{86}Y	14.74 h	627.72	32.6	^{90}Zr(p, n α)	-12.69
		1076.6	82.5	^{91}Zr(p, 2nα)	-19.89
		1153.0	30.5	^{92}Zr(p,3nα)	-28.52
^{87m}Y	13.37 h	380.79	78.0	^{90}Zr(p, α)	-0.88
				^{91}Zr(p,nα)	-8.08
				^{92}Zr(p,2nα)	-16.71
				^{94}Zr(p, 4nα)	-31.67
^{87g}Y	79.8 h	388.53	82.0	^{90}Zr(p, α)	-0.88
		484.81	89.7	^{91}Zr(p,nα)	-8.08
				^{92}Zr(p,2nα)	-16.71
				^{94}Zr(p, 4nα)	-31.67
^{88}Y	106.65 d	898.04	93.7	^{90}Zr(p, n2 p)	-19.83
				^{90}Zr(p, pd)	-17.61
				^{91}Zr(p,α)	1.27
				^{91}Zr(p, pt)	-18.54
				^{92}Zr(p, nα)	-7.36
				^{94}Zr(p, 3nα)	-22.32

The γ-ray count rates were converted to decay rates by correcting for the γ-ray intensities and the efficiency of the detector using the well known formula as shown elsewhere[1]. The decay data of the radioactive products were taken from the NUDAT database (*National Nuclear Data Center, information extracted from the NuDat database, http://www.nndc.bnl.gov/nudat2*). The decay data are collected in **Table 1**.

From the decay rates of the radioactive products and the measured beam intensity, the cross-sections of the investigated nuclear reactions were determined using the well known activation formula that has given details in our previous published paper.[1]

The following uncertainties were considered in order to derive the total uncertainty in each cross-section: statistical uncertainty of γ-ray counting (2-5 %), uncertainty in the monitor flux (~5 %) and the uncertainty in efficiency calibration of the gamma ray detector (~4 %). The overall uncertainty in the cross-section measurements is around 8-12 %.

IV. Results and Discussion

The measured cross-sections were obtained from two experiments and found good agreement between them. Our new experimental results are shown in **Fig. 1** together with values given in the earlier investigations and compilations. We present the so-called elemental cross-sections, supposing the targets to be monoisotopic. We discuss the various reactions below.

1. ^{nat}Zr(p,αxn)^{86}Y Process

The activity of the ^{86g}Y was measured by counting 627.72, 1076.63 and 1153.05 keV γ-rays after the complete decay of the 48 minute half-life isomeric state. Therefore, it contains the contribution of ^{86m}Y through internal decay. The ^{86}Y nuclide was produced through the ^{90}Zr(p, nα) (Q = -12.69 MeV), ^{91}Zr(p,2nα) (Q = -19.88 MeV), and ^{92}Zr(p,3nα) (Q = - 28.52 MeV) processes. The decay of ^{86}Zr does not contribute in the investigated energy range. We have obtained new data that are shown in **Fig. 1**. Two data sets were reported by Michel *et al.*[4] and Kondratev *et al.*[5], respectively. A large discrepancy is present between them. The result measured by Michel *et al*. has similar shape, but overestimate the values of this work. The result obtained by the ALICE-IPPE code[6] shows the same overall general behavior as the experimental data both in shape and magnitude.

2. ^{nat}Zr(p,xn)^{87m}Y Process

The isotope ^{87}Y has two isomeric states. The higher energy state ^{87m}Y ($T_{1/2}$ =13.37 h) decays to the ground state ^{87g}Y ($T_{1/2}$ =79.8 h). The measured ^{87m}Y production cross-sections shown in **Fig.1** depict the directly formed contribution and through the decay of ^{87}Zr. In view of Q-values of the possible reactions leading to ^{87}Zr, its contribution to the ^{87m}Y production can be neglected below 30 MeV. No experimental data are reported yet.

3. ^{nat}Zr(p,xn)^{87m,g}Y Process

The cross-sections for the cumulative production of the ground state by the ^{nat}Zr(p,αxn) process and by 98.43 % internal transition decay of the metastable state were measured as shown in **Fig. 1.**

Attention was paid to the complete internal decay of the metastable state to measure cumulative production cross-sections. The measured cross-sections are mainly the sum of cross-sections for the formation of the metastable state and the ground state. As it can be seen in **Fig. 1**, by bombarding the spin/parity = 0 target nuclei with protons the production cross-section for the high spin isomeric state (spin/parity =

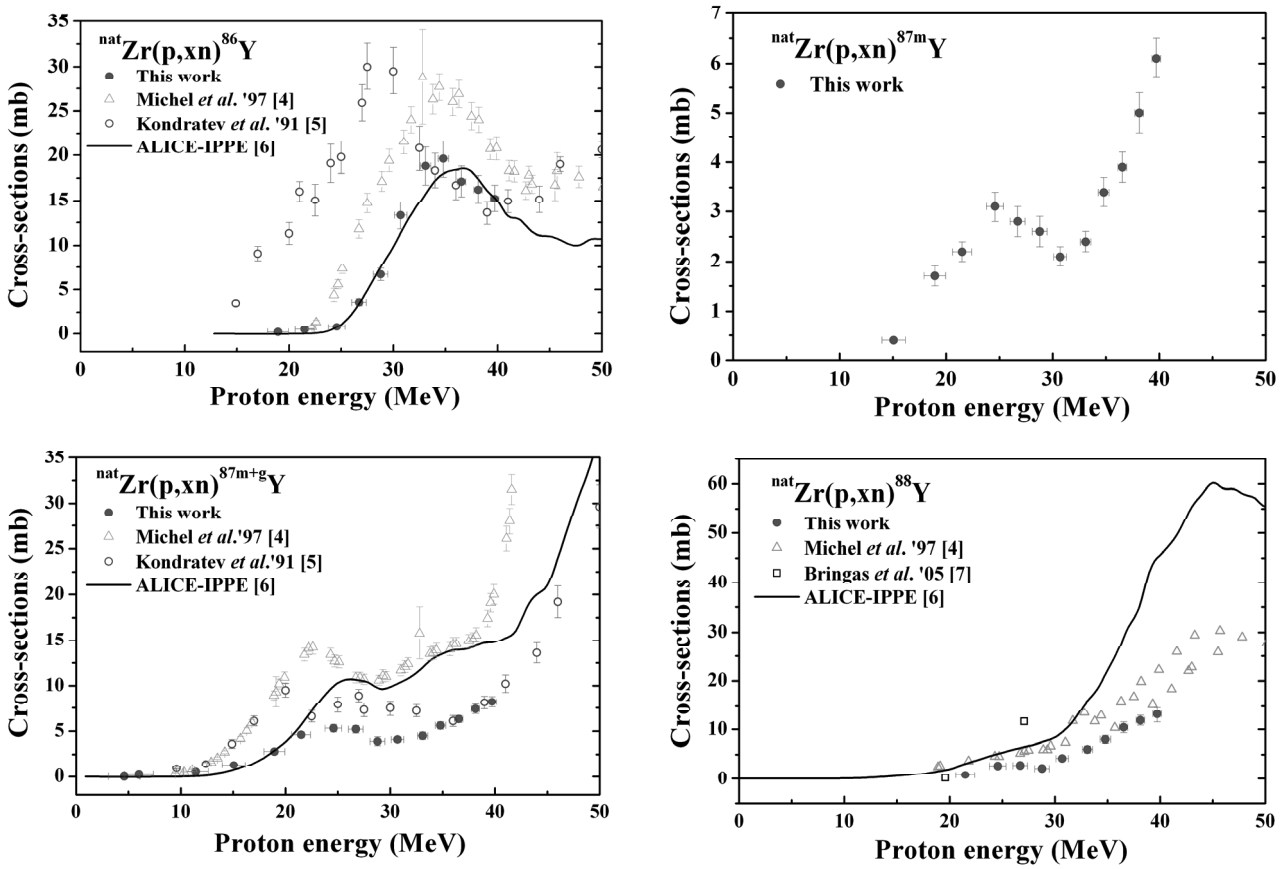

Fig. 1 Excitation function of the $^{nat}Zr(p,xn)^{86,87m,87m+g,88}Y$ reactions.

$9/2^+$) is higher than the one for the lower spin (spin/parity = $½^-$) ground state. The data of Michel *et al.*[4] are appreciably higher than this work. The Kondratev *et al.*[5] data are consistent with this work in higher energy region. The present data are partially consistent with the ALICE-IPPE precompound hybrid model calculation.

4. $^{nat}Zr(p,xn)^{88}Y$ Process

The cross-sections for the formation of ^{88}Y are shown in **Fig. 1.** The nuclide ^{88}Y is produced by the internal transition decay of the short-lived ($T_{1/2}$ = 13.9 ms) ^{88m}Y isomer and the decay of ^{88}Zr. The half-life of ^{88}Zr is 83.4 days. The spectra were measured one day after EOB to minimize the contribution from the decay of ^{88}Zr to the direct production of ^{88}Y. We separated the contribution and observed that the effect of the decay of ^{88}Zr on the ^{88}Y production cross-section is very low and it can be neglected. The experimental data reported by Michel *et al.*[4] are partially consistence with this work. The ALICE-IPPE model calculation shows systematically higher values than this work, because model calculation gives the sum of cross-sections for cumulative zirconium targets.

5. Integral Yields of Yttrium Isotopes

The integral yields of the yttrium radioisotopes at end of bombardment (EOB) formed via the $^{nat}Zr(p,x)$ processes were deduced from the measured excitation function curves as shown in **Fig.1** and the stopping power of ^{nat}Zr. The data were obtained by assuming the beam current as 1 μA and the irradiation time as 1h. The results are shown in **Fig. 2**.

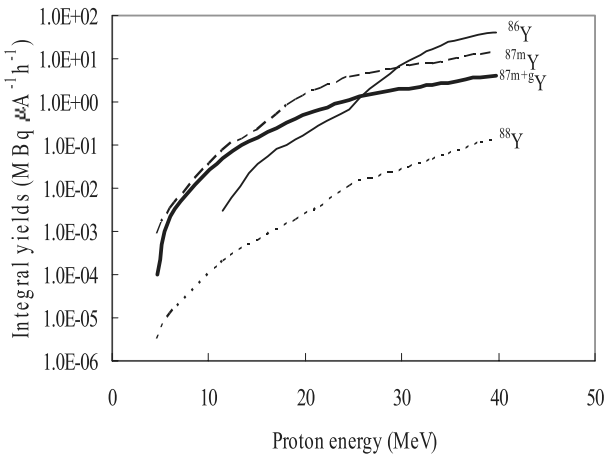

Fig. 2 Integral yields for the formation of the ^{86}Y, ^{87m}Y, $^{87m+g}Y$, and ^{88}Y nuclides

V. Conclusions

Excitation functions for the formation of yttrium radioisotopes from proton induced activation on natural zirconium were measured over the energy range 4 to 40 MeV. We report new data for the formation of these isotopes. Theoretical calculations using the precompound hybrid model code ALICE-IPPE gave results, which are partially consistent with the experimental data. On the basis of the systematic investigations the following conclusion can be drawn:

a) Very few experimental data exist for protons below 40 MeV.
b) The measured nuclear data can be effectively used for selection of optimum production routes.
c) Experimental data like the ones measured in this work could thus play an important role in improving the models and adjusting input parameters.

From the excitation functions and yield curves, the optimum energy range for the production of ^{86}Y is Ep= 40→ 30 MeV. Over this energy range the integrated thick target yield of ^{86}Y amounts to 33.37 MBq/μAh and the levels of the ^{87}Y, ^{87m}Y and ^{88}Y impurities to 2.3, 26.55 and 0.33 %, respectively at EOB. Rosch *et al*.(1993) [8] and Reischl *et al*.(2002) [9] have reported methods for the separation of ^{86}Y from other yttrium isotopes. The ^{nat}Zr(p,x) process can be a suitable route for the production of ^{86}Y by using the medium energy cyclotron. Although the ^{88}Y yield is rather low and increases sharply with increasing of energy, because of its long half-life the radionuclide ^{88}Y ($T_{1/2}$=106.6 d) could be produced with minimum impurities; the shorter-lived ^{87}Y ($T_{1/2}$=79.8 h) and ^{87m}Y ($T_{1/2}$=13.4 h) would decay out completely after about 40 days. Due to the low yield, ^{88}Y is not suitable for TLA. Our data would be useful for the optimization of medical isotopes in the interaction of protons with zirconium target using medium energy cyclotrons and estimation of radiation safety.

Acknowledgements

The author would like to express their sincere thanks to the staffs of the MC50 Cyclotron Laboratories for their cordial help in performing the experiment. This work is partly supported by the Korea Science and Engineering Foundation (KOSEF) through a grant provided by the Korean Ministry of Science and Technology (MOST) in 2007 (Project No. M20702000008-07B0200-00810, M20704000011-7M0400-01110), and by the user program of the Proton Engineering Frontier Project (Project No. M2 02AK010014-07A1101-01419). One of authors (G.N.K.) is partly supported by the Center for High Energy Physics (CHEP), Kyungpook National University, through the KOSEF.

References

1) M. S. Uddin, M. U. Khandaker, K. S. Kim, Y. S. Lee, G. N. Kim, Excitation functions of the proton induced nuclear reactions on ^{nat}Zn up to 40 MeV. Nucl. Inst. and Meth. Phys. Res. B **258** (2007) 313.
2) F. Tarkanyi, S. Takacs, K. Gul, A. Hermanne, M. G. Mustafa, M. Nortier, P. Oblozinsky, S. M. Qaim, B. Scholten, Yu. N. Shubin, Z. Youxiang, IAEA-TECDOC-1211, Beam monitor reactions, Charged Particle Cross-Section Database for Medical Radioisotope Production: Diagnostic Radioisotopes and Monitor Reactions, Co-ordinated Research Project (1995-1999). IAEA, Vienna. Austria, May 2001. Available from <http://www-nds.iaea.org/ medical/>.
3) J. F. Ziegler, J. P. Biersack, U. Littmark, SRIM 2003 code, The stopping and Range of Ions in Solids, Pergamon, New York, 2003.
4) R. Michel, R. Bodemann, H. Busemann et al., Cross sections for the production of residual nuclides by low- and medium-energy protons from the target elements C, N, O, Mg, Al, Si, Ca, Ti, V, Mn, Fe, Co, Ni, Cu, Sr, Y, Zr, Nb, Ba and Au. Nucl. Inst. and Meth. Phys. Res. B **129** (1997) 152.
5) S. N. Kondratev, V. A. Kuzmenko, Yu. N. Lobach, V. S. Prokopenko, V. D. Sklyarenko, V. V. Tokarevskii, Production cross section of radionuclides interaction Zr nuclei with 70 MeV protons. Atomnaya Energiya **71** (1991) 325.
6) Yu. N. Shubin, V. P. Lunev, A.Yu. Konobeyev, A. I. Dityuk, MENDL-2P, Proton reaction data library for nuclear activation (Medium Energy Nuclear Data Library), IAEA-NDS-204 (1998).
7) F. Bringas, M.T. Yamashita, I. D. Goldman, P. R. Pascholati, V. Sciani, Measurement of proton-induced reaction cross sections in Ti, Ni and Zr near the threshold. Proc. Conf. on Nucl. Data for Sci.and Techn., Santa Fe 2004, **2** (2005) 1374.
8) F. Rosch, S. M. Qaim, G. Stocklin, Production of the positron emitting radioisotope ^{86}Y for nuclear medical application. Appl. Radiat. Isot. **44** (1993) 671.
9) G. Reischl, F. Rosch, H. J. Machulla, Electrochemical separation and purification of yttrium-86. Radiochim. Acta **90** (2002) 225.

Journal of NUCLEAR SCIENCE and TECHNOLOGY, Supplement 5, p. 245–248 (June 2008)

Measurements of the Relative Output Factors for Radiosurgical CyberKnife Collimators Using a Glass Rod Dosimeter

Jeong-Eun RAH[1], Ju-Young HONG[1], Sei-Chul YOON[2], Dong-Oh SHIN[3], Hee-Sun KIM[4], and Tae-Suk SUH[1*]

[1]*Department of Biomedical Engineering, The Catholic University of Korea, Seocho-gu, Seoul, Korea*
[2]*Cyberknife Center, Department of Radiation Oncology, Kangnamm St. Mary's Hospital, Seocho-gu, Seoul, Korea*
[3]*Department of Radiation Oncology, Kyung Hee University College of Medicine, Dongdeamun-gu, Seoul, Korea* [4]*Radiation Health Research Institute, Seoul, Korea*

The purpose of this study was to evaluate the accuracy of a glass rod dosimeter (GRD) for relative output factor measurements in the CyberKnife radiosurgery system. The output factors measured with the GRD were compared to those obtained with an ionization chamber, a diode and a Gafchromic film. The GRD was irradiated in a water phantom using an in-house custom designed holder stand. The relative output factors measured with the four dosimeters showed very similar results for collimator diameters larger than 20 mm. The mean value of the output factors of the GRD for the 5 mm collimator was 0.695. The output factor measured with the ionization chamber was approximately 13.7% lower than the corresponding GRD values for the 5 mm collimator. The diode output factors were 3.1% and 1.9% higher than the GRD for the 5 mm and 7.5 mm collimators, respectively. However, the GRD results were in agreement with the measurements obtained with a Gafchromic film for all of the collimator diameters.

KEY WORDS: glass rod dosimeter, cyberknife system, dosimetric properties, relative output factor

I. Introduction

A CyberKnife radiosurgery system can deliver single or several fractions of radiation dose to a well-defined small intracranial or extracranial target with high precision. The CyberKnife system provides circular collimators of 12 different diameters with a ranging from 5 to 60 mm. The relative output factor is defined as the ratio of the dose rate for a given collimator to that of a 60 mm collimator. The accuracy of the relative output factor directly affects the accuracy of dose delivery in radiosurgical treatment. Specifically, a 5 mm collimator output factor is extremely important in dosimetry for the treatment of trigeminal neuralgia. The following dosimeters may be used for output factor measurements in small radiosurgical fields: diode, ionization chamber, diamond detector, thermoluminescent dosimeter (TLD), metal-oxide-semiconductor field effect transistor (MOSFET), radiographic and radiochromic film. Advantages and disadvantages of each dosimeter for small field dosimetry have been discussed in the literature[1-3].

A radiophotoluminescent (RPL) glass rod dosimeter (GRD) system has become commercially available and is being increasingly used for radiosurgery dosimetry. Although the relative output factors of the CyberKnife system using the GRD have been published previously[4-5], data were obtained only in a solid phantom. Basically, the GRD should be irradiated in a water phantom in accordance with the protocol recommended by IAEA TRS-398[7]. This protocol only allows water as the reference phantom material for beam calibration. The purposes of this study are to investigate the effectiveness of the GRD for measuring output factors of the CyberKnife system, and to compare the output factors measured using a GRD with those using an ionization chamber, a diode and a Gafchromic film.

*Corresponding Author, Tel. +82-2-590-2414 Fax. +82-2-532-1779, E-Mail: suhsanta@catholic.ac.kr

II. Materials and Methods

1. GRD system

In this study, the model GD-301 GRD (Asahi Techno Glass Corp., Shizuoka, Japan) and FGD-1000 automatic reader were used. The size of the model GD-301 is 1.5 mm in diameter and 8.5 mm in length, and the sensitive region of measurement for the GRD readout is 1 mm in diameter from the center and 0.6 mm in depth. The weight compositions of the GRD are as follows: 31.55% P, 51.16% O, 6.12% Al, 11.00% Na, and 0.17% Ag[1]. When the silver-activated phosphate glass is exposed to ionizing radiation, stable RPL centers appear in the GRD. Additionally, when a pulsed ultra violet (UV) laser beam also excites the GRD, it emits orange luminescence[4-6]. The amount of luminescence is proportional to the radiation dose that is exposed to the glass. The RPL excited centers are not eliminated by the UV beam excitation and stay at the same states once they are formed. The GRD was annealed (400℃ for 1 h) before it was used for measurement, in order to eliminate the stable RPL center and was then used again. GRD calibration was performed at the national standard laboratory periodically with a dose of 2 Gy to free-air with a ^{137}Cs beam.

2. Dosimetric properties of GRD

Before the measurement of output factor, we evaluated the dosimetric properties of the GRD with respect to reproducibility, linearity, fading, energy dependence and angular dependence, and compared with previously published data. The reproducibility of the GRD was

measured for each of the 50 capsules from the ^{60}Co r-ray beams of an ELDORADO-6 unit. The delivery dose to the GRD was 2 Gy, at a source to surface distance (SSD) of 80 cm, a depth of 5 cm, and a field size of 10 × 10 cm^2 at the phantom surface. The absorbed dose of the ^{60}Co beams was determined by measurement with an NE 2561 ionization chamber connected to a Keithley 6517 electrometer. Reproducibility was determined by an average of one standard deviation of the GRD response.

To determine linearity, the GRD was irradiated with a ^{60}Co r-ray beam at reference conditions with different doses in the range of 0.5–30 Gy.

Long-term fading was determined at normal ambient conditions (temperature ranging from 22 to 26℃, and relative humidity of 50 to 60%) from readings taken over 150 days at 1 week intervals.

The GRD was calibrated in a reference beam generally a ^{137}Cs beam; the energy dependence needs to take into account the difference between the responses in a photon beam or an electron beam of quality and its responses in the reference beam. A dose to water of 2 Gy was given with a photon beam in the energy range of 6, 15 MeV, and electron beams in the range of 6–20 MeV from a Varian CL 2100 linear accelerator. All ionization chamber dosimetry was performed according to the IAEA Code of Practice TRS-398[7].

The angular dependence was measured with a 15 MeV photon beam using a spherical polystyrene phantom. The geometrical center of the GRD was placed at the center of the sphere. With the longitudinal axis of the GRD at the beam isocenter, the responses versus the beam angle could be obtained. The angular dependence of the GRD was measured at 0°, 20°, 40°, 60°, 90°, 110°, 130°, 150°, and 180° by rotating the beam angle.

3. Measurement of output factors for CyberKnife

A 6 MeV x-ray from a third-generation CyberKnife system (Accuracy, Sunnyvale, CA, USA) was used in this study. The collimation of the CyberKnife consists of 12 circular cones consisting of 5, 7.5, 10, 12.5, 15, 20, 25, 30, 35, 40, 50, and 60 mm collimator size. The measured output factor obtained with the GRD was compared with a diode, an ionization chamber, and a Gafchromic film. A p-type silicon diode type 60008 (PTW-Freiburg, Schwarzenbruck, Germany) was used in this study. It has a disc-like shape with a 1 mm^2 surface area and a thickness of 2.5 μm. The ionization chamber (Wellhofer Scanditronix, Schwarzenbruck, Germany, type CC01) has a measuring volume of 0.01 cm^3 with a central electrode made of aluminum. The diode and the ionization chamber were connected to a PTW MULTIDOSE electrometer. With the exception of the film, all measurements were performed in a 60 × 50 × 40 cm^3 water phantom. For output factor measurements, the CyberKnife system was set to give a dose rate of 100 monitor units (MU) min^{-1} corresponding to 1 Gy min^{-1} at a depth of 1.5 cm, with a source to surface distance of 80 cm for the 60 mm collimator.

The GRD was irradiated in a water phantom using a holder stand. The holder consists of a para-methoxy-methamphetamine (PMMA) tube on which a vertical bar has been affixed for the attachment of the GRD at 5 mm from the tube, to minimize absorption and scattering by the holder (**Fig. 1**). The center of the GRD with regard to its diameter was set to be the center of the radiation beam by alignment of the GRD with a laser mounted into the LINAC. Gafchromic MD 55 film (ISP Technologies, Wayne, NJ, USA) measurements were performed with a RW-3 solid water phantom. The films were irradiated with a dose of approximately 300 cGy and were analyzed by the use of commercially available software, OminPro-Accept, in conjunction with a VXR-12 film scanner (Vidar Systems, Herndon, VA, USA).

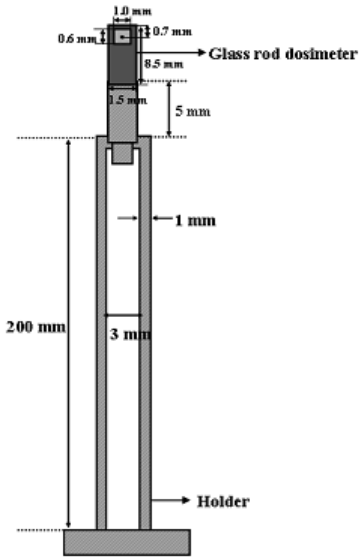

Fig. 1 Schematic diagram of the GRD holder stand designed for this study. The sensitivity of measurement for the GRD readout is 1 mm in diameter from its center and 0.6 mm in depth.

III. Results and Discussion

1. Dosimetric properties of the GRD

For the ^{60}Co beam, the responses of the GRD were found to have a reproducibility of ±0.70% (1SD). The GRD response showed a good linear relationship for doses ranging from 0.5 to 30 Gy, with a correlation coefficient of 0.999. After storage of 150 days, losses in the response of the GRD did not exceed 1.63%. The average energy dependence for photon beams relative to the ^{60}Co r-rays for the GRD was from 0.995 ± 0.004 for a 6 MeV photon beam to 0.988 ± 0.002 for a 15 MeV photon beam. For each electron beam, the responses of the GRD for 6 and 20 MeV were lower by approximately 4.5% and 3.8%, respectively, than the responses for a ^{60}Co r-ray beam. These values are consistent with previously reported data obtained with the same GRD model[2]. It was therefore necessary that the correction factor should be determined and applied for the electron energy

used during assessment of the absorbed dose. The angular dependence results obtained in the GRD are shown in **Fig. 2**. The relative response is normalized to the GRD response of the vertical axis at 0°. The variation of sensitivity for angles ranging from 0° to 180° was within 1.5% for the GRD. **Table 1** summarizes the results of the dosimetric properties of the GRD.

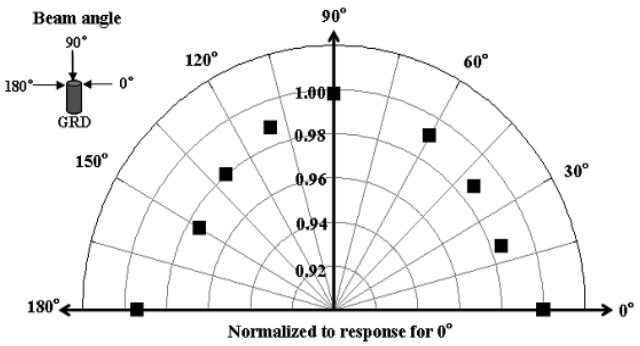

Fig. 2 Angular dependence of the GRD positioned on the center of a spherical polystyrene phantom and irradiated with a 6 MV photon beam. Each point represents a standard deviation of five measurements of the GRD response.

Table 1. Dosimetric properties of GRD

Properties	Specification
Sensitive volume	0.5 mm^3 (r=0.5 mm, h=0.6 mm)
Reproducibility	±0.7% in ^{60}Co beam
Dose linearity	0.999 in 0.5 – 50 Gy
Energy dependence	Photon beam: ≤1.5% Electron beam: ≤4.5%
Angular dependence	≤ 1.3%
Fading	1.63% for 150 days

2. Relative output factors of the CyberKnife system

Fig. 3 shows the relative output factors that were measured as a function of the circular collimator diameters of 5 to 60 mm with the four different dosimetric methods. The mean value of the output factor for the GRD for the 5 mm collimator is 0.695. Each dose point of the GRD is represented by an average of 5 GRD responses and their one standard deviation is within ± 1.0%. For collimator sizes larger than 20 mm, the results measured by the GRD agree with other detectors within approximately 1.0%. It was observed that the difference between the output factor obtained with the GRD and that obtained with the ionization chamber increased rapidly as the collimator diameter decreased. The fact that the ionization chamber had a larger sensitive volume most likely contributed to these differences. The output factor measured with the ionization chamber was approximately 13.7% lower than the corresponding GRD values for the 5 mm collimator. The relative output factors measured with the diode were 3.1% and 1.9% higher than the GRD for the 5 mm and 7.5 mm collimators, respectively. It was not obvious whether the difference was due to the geometric error in diode positioning. The diode also had an angular dependent response, which is due to the asymmetry inherent in the silicon chip. However, the GRD results were in good agreement with the results from the Gafchromic MD-55 film for all of the collimator diameters.

A future study will be attempted to investigate the possibility of using a GRD postal audit program to evaluate the calibration of a stereotactic radiosurgery beam.

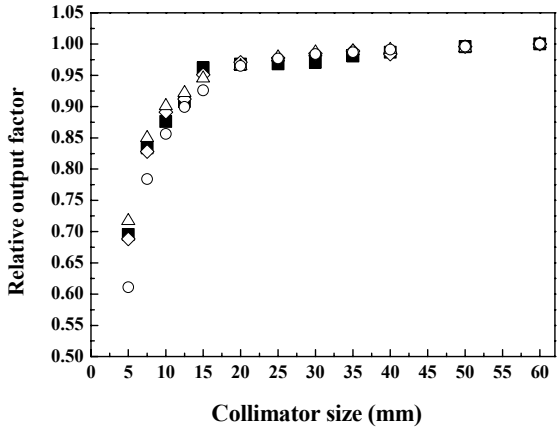

Fig. 3 Comparison of relative output factors measured with the GRD (■), the ionization chamber (○), the diode (△) and the Gafchromic MD-55 film (◇) for collimator diameters 5 to 60 mm. The measured relative output factors are normalized to a 60 mm collimator.

IV. Conclusions

The GRD has good features for a high-energy photon beam in terms of reproducibility, linearity, fading, energy dependence and angular dependence. The energy dependence of the GRD on electron beam was less than 5.0%. Output factors of the CyberKnife obtained by using the GRD were consistent with those obtained by using the other dosimetric methods for collimators larger than 20 mm, and agreed with those obtained by using the Gafchromic MD-55 film for all collimators. The GRD is a useful dosimeter for collimators smaller than 10 mm in diameter.

References

1) C. Fan, W. G. Devanna, L. B. Leybovich, R. G. Kurup, B. J. Hopkins, E. Melian, D. Anderson, G. P. Glasgow, 'Dosimetry of vary-small (5-10 mm) and small (12.5-40 mm) diameter cones and dose verification for radiosurgery with 6 MV x-ray beams,' Stereotact Funct Neurosurg 67,183(1997).
2) P. Francescon, S. Cora, C. Cavedon, P. Scalchi, S. Reccanello, F. Colombo, 'Use of a new type radiochromic film, a new parallel-plate micro chamber, MOSFETS and TLD 800 microcubes in the dosimetry of small beams,' Med Phys 25[4], 503(1998).
3) M. Heydarian, P. W. Hoban, A. H. Beddoe, 'A comparison of dosimetry technique in stereotactic radiosurgery,' Phys Med

Biol 41, 93(1996).
4) F. Araki, T. Ikegami, T. Ishidoya, H.D. Kubo, 'Measurements of Gamma-Knife helmet output factors using a radiophotoluminescent glass rod dosimeter and a diode detector,' Med Phys 30[8], 1976 (2003).
5) F. Araki, N. Moribe, T. Shimonobou, Y. Yamashita, 'Dosimetric properties of radiophotoluminescent glass rod detector in high-energy photon beams for linear accelerator and Cyber-knife,' Med Phys 31[7], 1980 (2004).
6) J. Perks, M. Gao, V. Smith, S. Skubic, S. Goetsch, 'Glass rod detectors for small field, stereotactic radiosurgery dosimetric audit,' Med Phys 32[3], 726 (2005).
7) IAEA, International Atomic Energy Agency. 2000 Absorbed dose determination in external beam radiotherapy: an international code of practice for dosimetry based on standards of absorbed dose to water. Technical Reports Series. TRS-398. IAEA. Vienna. Austria.

Journal of NUCLEAR SCIENCE and TECHNOLOGY, Supplement 5, p. 249–252 (June 2008)

Design of Epithermal Neutron Field Generated by 150-MeV Proton Beam Injections for Boron Neutron Capture Therapy

Ikuo Ohta*, Takenori Matsuura, Nobuhiro Shigyo, and Kenji Ishibashi

Department of Applied Quantum Physics and Nuclear Engineering, Kyushu University, Fukuoka 819-0395, Japan

An epithermal neutron field using a Fixed Field Alternating Gradient (FFAG) accelerator has been studied by Kyushu University to develop epithermal neutron flux monitors. A spallation neutron source was utilized as the neutron generator. Tungsten was chosen as the target material. Iron, aluminum fluoride, and lead were selected for the moderator assembly material for high- and intermediate-energy neutrons and gamma rays, respectively. The Particle and Heavy Ion Transport code System (PHITS) was used to calculate the neutron flux on a water phantom surface and the RBE-weighted dose distributions in the phantom.

KEYWORDS : epithermal neutron, spallation, FFAG accelerator, tungsten, RBE-weighted dose, PHITS

I. Introduction

Boron Neutron Capture Therapy (BNCT) is useful for treating patients with brain tumors while maintaining their quality of life. It is well known that epithermal neutrons are more effective than thermal ones for treating deep-seated brain tumors. It is beneficial to use epithermal neutron beams that have a broad peak within a specific energy range (4 eV – 40 keV)[1]. If epithermal neutrons can be used, craniotomy is unnecessary for brain tumors. A group at Tohoku University proposed a method of generating an epithermal neutron field by moderating the spallation neutrons produced by a high-energy and high-current proton accelerator[1]. Kyushu University has plans to install a Fixed Field Alternating Gradient (FFAG) accelerator[2] at its campus. The FFAG accelerator is compact and supplies intense high energy and protons. There is a photograph of the accelerator[1] in **Fig. 1**. The proton beam energy is up to 150 MeV and the current is a few μA.

It is well known that doses of 22 – 30 Gy-eq[3] are needed to kill a typical brain tumor. To administer this dose within an hour, 5×10^8 n/(cm^{2}sec) neutrons are required. Our purpose was to study moderation systems to create a neutron field by using a proton energy range of 150 MeV and to calculate the dose distribution in a water phantom. The Particle and Heavy Ion Transport code System (PHITS)[4] was used to calculate the neutron flux and dose.

II. Target and Moderator Design

The spallation reaction is used in moderation systems to obtain high energy neutrons. The beam target is made of tungsten because of its high melting point. This is covered by a moderator assembly. The assembly has a rectangular parallelepiped shape. Iron effectively moderates fast neutrons. Aluminum fluoride serves to produce an epithermal neutron field. Lead is used for shielding gamma rays. We studied three types of moderators to obtain an ideal neutron spectrum for tumor therapy.

We simulated the neutron flux by use of the PHITS with the LA-150 evaluated nuclear data library[5]. We used multi-purpose Monte Carlo code that has been used in various fields in nuclear physics, heavy ion therapy, and space radiation shielding. A cylindrical phantom that was 20 cm in diameter and 20 cm long was placed 10 cm from the surface of the moderator perpendicular to the proton beam. The phantom was composed of water. We studied four moderation systems. **Table 1** has a summary of these. We assumed that the proton beam current was 10 μA and adopted boron concentrations in a tumor of 45.5 ppm and 13 ppm[1] in normal tissue.

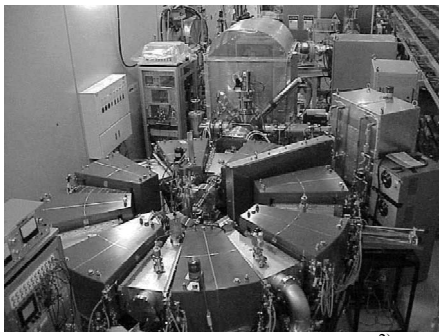

Fig. 1 150 MeV FFAG accelerator[2]

Table 1 Summary of moderation systems.

	Target thickness	Target shape	Reflector
System 1	4 cm	Cylindrocal	N/A
System 2	4 cm	Cylindrocal	lead
System 3	2 cm	Cylindrocal	lead
System 4	2 cm	Three disks	lead

1. Effect of Reflectors

Two types of moderation systems were considered to check what their reflectors would have on the neutron flux. Moderation System 1, which was composed of iron,

*Corresponding author: Tel. +81-92-802-3484, Fax. +81-92-802-3484, E-Mail; ohta@kune2a.nucl.kyushu-u.ac.jp

aluminum fluoride, and lead is outlined in **Fig. 2**. The tungsten target is covered with 30-cm-thick iron, 20-cm-thick aluminum fluoride, and 5-cm-thick lead panels. To obtain a higher neutron flux, iron, aluminum fluoride, and lead were placed only perpendicular to the proton beam. Moderation System 2, which used lead as the reflector is outlined in **Fig. 3**.

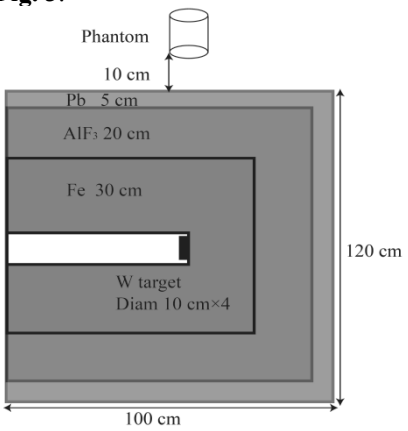

Fig. 2 Schematic of Moderation System 1.

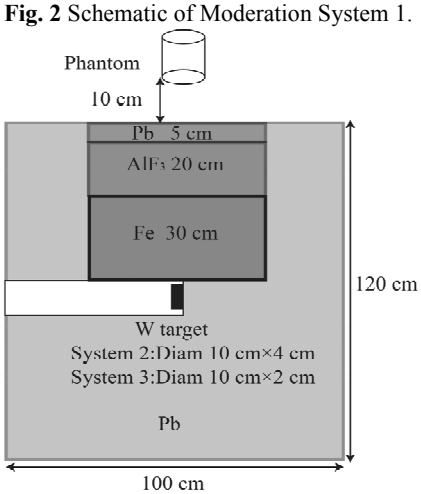

Fig. 3 Schematic of Moderation Systems 2 and 3.

2. Difference in Target Thickness

We calculated the energy deposition of 150-MeV protons in tungsten using PHITS and this is plotted in **Fig. 4**. We can see a tungsten thickness of 2 cm is sufficient to stop 150 MeV protons. The moderation system using 2-cm-thick tungsten is called System 3 and is also outlined in **Fig. 3**.

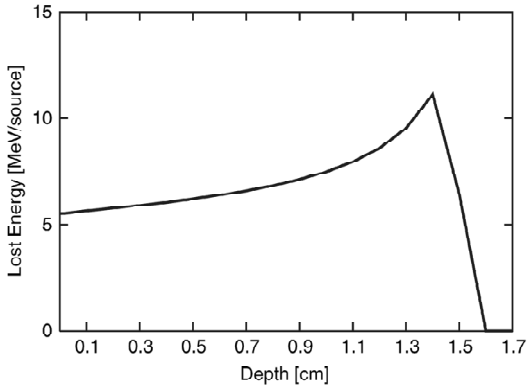

Fig. 4 Energy deposition of 150 MeV-protons in tungsten target.

3. Difference in Target Shapes

The power of a 150-MeV and 10-μA proton beam is 1.5 kW. The target absorbs an energy of 1.3 kW. The rate of increase in temperature is 3.2 ˚C/s. It is therefore necessary to remove heat from the target. The target was divided into three plates to cool it and water was flowed between the gaps as shown in **Fig. 5**. The tungsten target for System 4 is divided into 7-mm disks with 2-mm gaps[8] in **Fig. 5**.

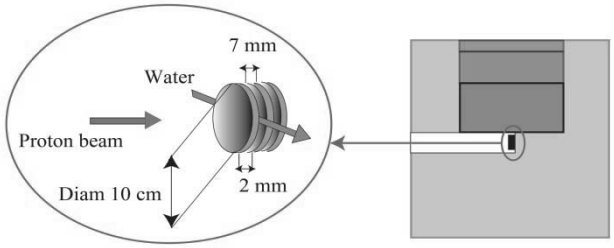

Fig. 5 Schematic of Moderation System 4.

III. Results and Discussion

1. Neutron Fluxes

We calculated the neutron fluxes at the front plane of the phantom. The results are shown in **Figs. 6 - 8**. **Fig. 6** reveals that lead effectively increases the number of neutrons. The neutron flux on the phantom surface in System 2 is twice that in System 1. There is little difference between tungsten and lead in the cross section of the (n,xn) reaction. However, the total cross section of tungsten has many resonance peaks of less than 10 keV. That of lead is constant at about 10 barns below 100 keV. Lead effectively reflects neutrons. **Fig. 7** shows that the thickness of the target does not influence the number of neutrons. We can see that water is ineffective for controlling variations in the number of neutrons in **Fig. 8**. The numbers of neutrons in Systems 3 and 4 are equal to those in System 2.

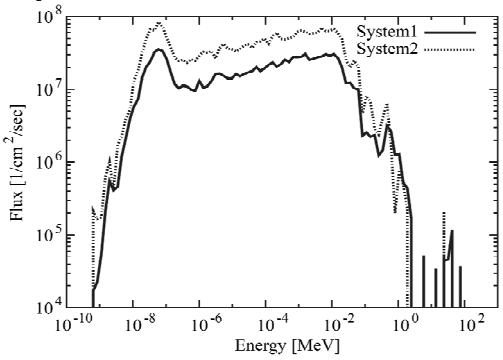

Fig. 6 Neutron spectrum of System 1 and 2 under conditions.

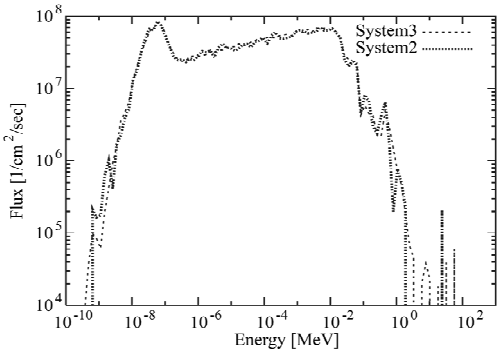

Fig. 7 Neutron spectrum of System 2 and 3 under conditions.

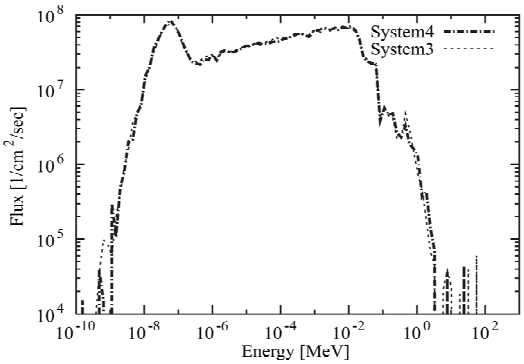

Fig. 8 Neutron spectrum of Systems 3 and 4 under conditions

2. Doses

We calculated the neutron flux at the surface of the phantom using PHITS. The dose distribution in the phantom was estimated by dividing it into 5-mm-thick disks. The RBE-weight dose in a tumor (D_{tumor}) and in normal tissue (D_{normal}) was estimated by[1)]

$$D_{tumor(normal)} = CF_{tumor(normal)} \times D_B + RBE_n \times D_n + RBE_\gamma \times D_\gamma, \quad (1)$$

where D_B, D_n, and D_γ correspond to the absorbed doses from the ^{10}B(n,α) reaction, neutrons, and gamma rays. The absorbed doses are represented by the product of a compound factor[1)] (*CF*) or relative biological effectiveness (*RBE*). The *CF* values for normal tissue and tumors were fixed at 1.3 and 3.8[1)] and the RBE_n and RBE_γ were selected as 3.2 and 1.0[1)], respectively. The D_B value was calculated by the product of the neutron flux and the kerma coefficient proposed by Zamenhof et al.[6)] The D_n and D_γ were calculated using the neutron kerma coefficient for tissue and the photon mass energy absorption coefficient for tissue[7)]. Because the neutron flux of System 2 is twice that of System 1, the therapeutic time for Systems 2 - 4 is half that for System 1. The therapeutic time for System 1 was assumed to be 60 min and for Systems 2 - 4 was assumed to be 30 min to control the maximum dose in normal tissues at below 12.5 Gy-eq[1)].

To compare Systems 2 - 4, we have used the maximum tumor dose (D_{max}) and the advantage depth (*AD*) as Figures-of-Merit (FOM) in this paper. The *AD* was defined as the depth where the tumor depth corresponded to the maximum normal tissue dose.

The irradiation time for System 1 was 60 min, while that for System 2 was 30 min. The dose distributions are plotted in **Fig. 9**. We can see that the dose distribution from System 2 is nearly equal to that from System 1 in **Fig. 9**. System 2 is more beneficial than System 1 in the terms of irradiation time because a shorter irradiation time is not as injurious to patients.

The dose distribution for System 2 is compared with that for System 3 in **Fig. 10**. The D_{max} and the *AD* for Systems 2 and 3 are summarized in **Table 2**. Although the target for System 3 was thinner than that of System 2, the values of D_{max} and *AD* for System 3 were nearly equal to those for System 2. The target thickness for all systems was 2 cm, which is longer than the 150-MeV proton range in tungsten. A target longer than the range does not help to increase the neutron flux at the target position. Water has a smaller impact on the number of neutrons than tungsten because its density is lower. The number of neutrons in System 2 from 4 eV - 40 keV is 1.69×10^9 n/(cm^{2}sec). This is 1.64×10^9 in System 2. The flux difference is 3 %. This causes a dose difference of 4 % in D_{max} between Systems 2 and 3.

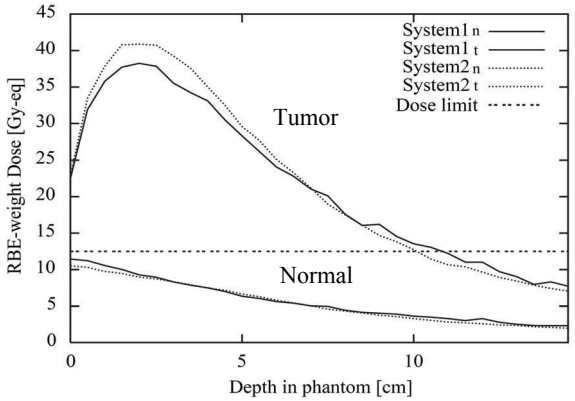

Fig. 9 Dose distributions System 1 and 2 under conditions. Systems 1_t and 1_n mean doses in tumor and normal tissues. Systems 2_t and 2_n mean doses in tumor and normal tissues.

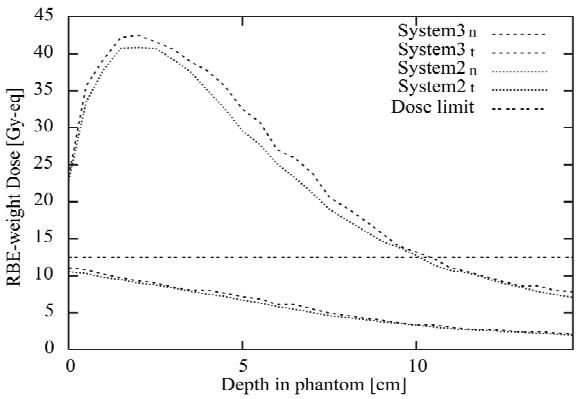

Fig. 10 Dose distributions System 2 and 3 under conditions. Systems 2_t and 2_n mean doses in tumor and normal tissues. Systems 3_t and 3_n mean doses in tumor and normal tissues.

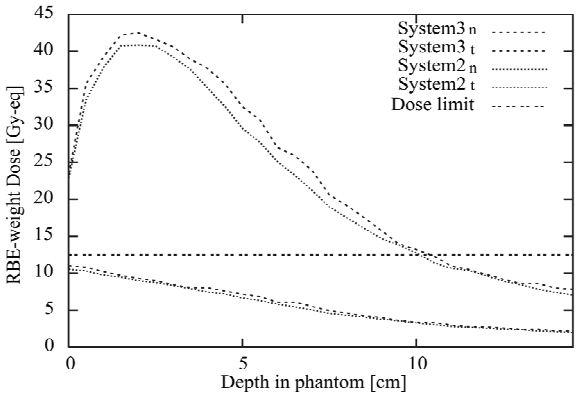

Fig. 11 Dose distributions System 3 and 4 under conditions. Systems 3_t and 3_n mean doses in tumor and normal tissues. Systems 4_t and 4_n mean doses in tumor and normal tissues.

The effects of water at the spallation target on the neutron spectrum and the dose distribution were calculated for

Systems 3 and 4. The dose distribution and the values for D_{max} and AD are shown in **Fig. 11** and **Table 2**. We found that D_{max}, AD, and the therapeutic times for System 4 were 42.2 Gy-eq, 11.3 cm, and 30 min, respectively. However, the values for D_{max}, AD, and the therapeutic times for System 3 were 42.5 Gy-eq, 10.8 cm, and 30 min, respectively. From the viewpoint of removing heat from the target, System 4 is more effective than System 3.

Table 2 Comparison of FOMs for Systems 2, 3, and 4.

	D_{max} [Gy-eq]	AD [cm]	Therapeutic time [min]
System 2	40.9	11.2	30
System 3	42.5	10.8	30
System 4	42.2	11.3	30

IV. Conclusion

Neutron flux generated by the bombardment of a proton beam from a 150 MeV and 10 μA FFAG accelerator was studied for BNCT. Due to practical considerations, iron, aluminum fluoride, and lead were only placed perpendicular to the proton beam and it was more effective to place the lead to adjoin the moderators and the target. The beam target consisted of three tungsten disks and water flowed between the disks to cool the target. This assembly called System 4 is the most suitable for BNCT and neutron monitor studies. Lead effectively gained more neutrons. In addition, water around the beam target had no influence on the neutron flux on the phantom surface. The values for D_{max}, AD, and the therapeutic times were 42.2 Gy-eq, 11.3 cm, and 30 min in System 4.

Reference

1) D. L. Bleuel et al., "Designing of accelerator-based epithermal neutron beam for boron neutron capture therapy," Med. Phys., 25, 1725-1734 (1998).
2) S. Machida. et al., "Status of 150 MeV FFAG synchrotron", Proc Particle Accelerator Conference, Portland (2003).
3) Current Statues of Neutron Capture Therapy, IAEA TECDOC 1223 (2001).
4) H. Iwase. et al., "Development of General –purpose Particle and Heavy Ion Transport Monte Carlo code", J. Nucl. Sci. Technol., 39, 1142-1151 (2002).
5) M. B. Chadwick. et al., "Cross-section evaluations to 150 MeV for accelerator-driven system and implementation in MCNPX," Nucl. Sci. Eng., 131, 293-328 (1999).
6) R. G.Zamennhof. et al., "Boron neutron capture therapy for treatment of cerebral gliomas.1 The theoretical evaluation of the efficiency of various neutron beam," Med. Phys., 2, 46-60 (1975).
7) "Photon, Electron, Proton and Neutron Interaction Data for Body Tissues," ICRU Report No.46, Int. Conf. on Radiat. Units and Meas. (1992).
8) N. Takenaka. et al., "Thermal hydraulic design and decay heat removal of solid target for a spallation neutron source," J. Nucl. Materials., 343, 169-177 (2005).

Journal of NUCLEAR SCIENCE and TECHNOLOGY, Supplement 5, p. 253–255 (June 2008)

Design of the Online Integral Dose Monitor System for BESIII EMC

Hui Gong[1*], Lei Hou[1], Guanghua Gong[1], Beibei Shao[1], Yuxiong Li[2], and Jin Li[3]

[1]*Department of Engineering Physics, Tsinghua University, Beijing 100084, P.R.China,*
[2]*NSRL, University of Science and Technology of China, Hefei, 230029, P.R.China*
[3]*Institute of High Energy Physics, CAS, Beijing, 100039, P.R.China*

High beam current of BEPCII leads to high radiation background around the interaction point where the Electro-Magnetic Calorimeter (EMC), a key sub-detector of BESIII, is located. The performance of EMC degrades due to accumulated exposure to the high radiation background. In order to monitor the integral dose deposited in the EMC, an online integral dose monitor system has been developed according to the study on 400nm IMPL RadFET. This system consists of 72 RadFETs located around EMC. A microcontroller based DAQ box can readout all the RadFET information and send to computers via an Ethernet interface. The detail of this system and the BEPC testing result are presented in this paper.

KEY WORDS: BESIII, electro-magnetic calorimeter, dose monitor, RadFET

I. Introduction

To achieve the precision measurements of charm physics and search for new particles and phenomena, the Beijing electron-positron collider (BEPC) and its detector, the Beijing Spectrometer (BESII), are upgraded to BPECII and BESIII. BEPCII is a double-ring collider within the existing BEPC tunnel. The designed luminosity of BEPCII is $10^{33}cm^{-2}s^{-1}$ with beam energy of 1.89GeV, which is about two orders of magnitudes higher than BEPC and results in a much stronger radiation background. The performance of BESIII sub-detectors need to be greatly improved for higher event rate and better resolution.

Electro-Magnetic Calorimeter (EMC) is the most expensive and heaviest sub-detector of BESIII, which consists of more than 6000 CsI crystals and can measure precisely energies and positions of electrons and photons. According to the physics requirement of BESIII, the energy and position resolutions of EMC should be about $\sqrt{(2.3\%)^2/E+(1\%)^2}$ and $6mm/\sqrt{E}$, where E is the energy of electrons or photons in the unit of *GeV*.

However, the performance of EMC degrades due to accumulated exposure to radiation field[1)]. This will seriously affect the energy and position resolutions. Tests show that the light yield of CsI Crystals decreases measurably at exposures as low as 1 Gy. On the other hand, Monte Carlo simulation shows that the maximum integral dose deposited in EMC in one year is about 2.3 Gy. This means that the performance of EMC may be affected by the radiation background of BEPCII. Therefore the integral dose deposited in EMC should be monitored to correct EMC data.

The room where the dosimeters can be installed is very small. The total size of one dosimeter and its front end electronics should be less than $30\times15\times8mm^3$. Once the dosimeters are installed, it is difficult to take them out for the purpose of offline measurement. So a small and online dosimeter should be chosen in the design of dose monitor system. Some available passive dosimeters (such as TLD and alanine dosimeter) obviously don't meet the design requirement because they aren't online readout dosimeters. Some active dosimeters (such as plastic scintillators) aren't the best choice either due to dead time problem, size problem and so on. RadFET dosimeter is chosen at last because it has advantages such as extremely small size, immediate online readout and low price.

Since the radiation deposited in various parts of EMC is different according to Monte Carlo simulation, a total of 72 RadFETs are employed in the dose monitor system and distributed around EMC.

II. RadFET Dosimeter

RadFETs are p-channel Metal Oxide Semiconductor Field Effect Transistors (MOSFETs)[2)]. Its sensitive region is the gate region with lots of hole traps. When the RadFET is exposed to ionizing radiation, electron-hole pairs are generated inside the device. A certain number of the generated carriers recombine immediately after generation. As those which do not recombine drift under the electric field, some holes get trapped and this causes the positive charge within the sensitive region to increase. As a result, the threshold voltage of the RadFET increases as a function of dose.

As shown in **Fig. 1**, the threshold voltage V_T can be measured between the source and drain by applying a constant current to the RadFET. The shift of the threshold voltage ΔV_T is gotten by subtracting initial pre-irradiation V_{T0} from the current V_T.

The sensitivity of RadFET depends on gate bias voltage, which decides the electric field in gate region. In general, the

*Corresponding Author, Tel. +86-10-62782026, Fax. +86-10-62782026, E-Mail: gonghui02@mails.tsinghua.edu.cn

sensitivity under positive bias voltage is higher than under zero bias voltage.

RadFET is inherently non-linear because of the way RadFET works. Thus its response curve, ΔV_T as a function of dose under a given gate bias voltage, should be calibrated by using of a γ-ray source with energy around 1 MeV.

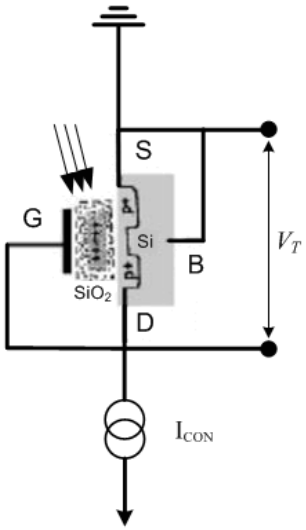

Fig. 1 RadFET threshold voltage measurement circuit.

The RadFET we used is 400nm implanted gate oxide RadFET from NMRC (here referred to as 400nm IMPL RadFET) [3]. Each RadFET chip contains 4 sensors differing in size, two of them with a W/L (Width/Length) ratio of 300/50, the other two with a ration of 690/15. The gate oxide of both types is 400nm thick, grown in dry oxygen and annealed in nitrogen at about 1000ºC. Boron implantation is done through the oxide to reduce the initial pre-irradiation threshold voltage thus increase the dynamic measurement range.

By using of ^{60}Co source, the performance of this RadFET was studied with different gate bias voltages (positive and zero bias voltage) under three different dose rates (8.91, 3 and 0.5 cGy/min). The response curves of this RadFET measured at different dose rates are a little different, which is known as dose rate dependency. The threshold voltage will slowly decrease after the irradiation, and this phenomenon is called as fading. The RadFET sensors irradiated under zero gate bias voltage have much lower dose rate dependency, fading and sensitivity than those under positive gate bias voltage. 300/50 sensors have a little lower fading but higher sensitivity than 690/15 sensors.

Both dose rate dependency and fading are disadvantages of RadFET, which can affect the dose measurement accuracy. According to the study result, two 300/50 sensors with zero gate bias voltage are used for BESIII EMC dose monitor.

III. Design of the System

The whole system can be divided into two parts: front end electronics and readout electronics as **Fig. 2** shows.

Front end electronics consists of 80 front end boards including 8 spares. To be radiation hard, every front end board contains only one RadFET chip and one radiation-hard resistive temperature sensor, YSI55036. Two 300/50 sensors in each RadFET chip are connected to readout electronics via 20-meter cables. The temperature will be used to correct the threshold voltage of the corresponding RadFET chip.

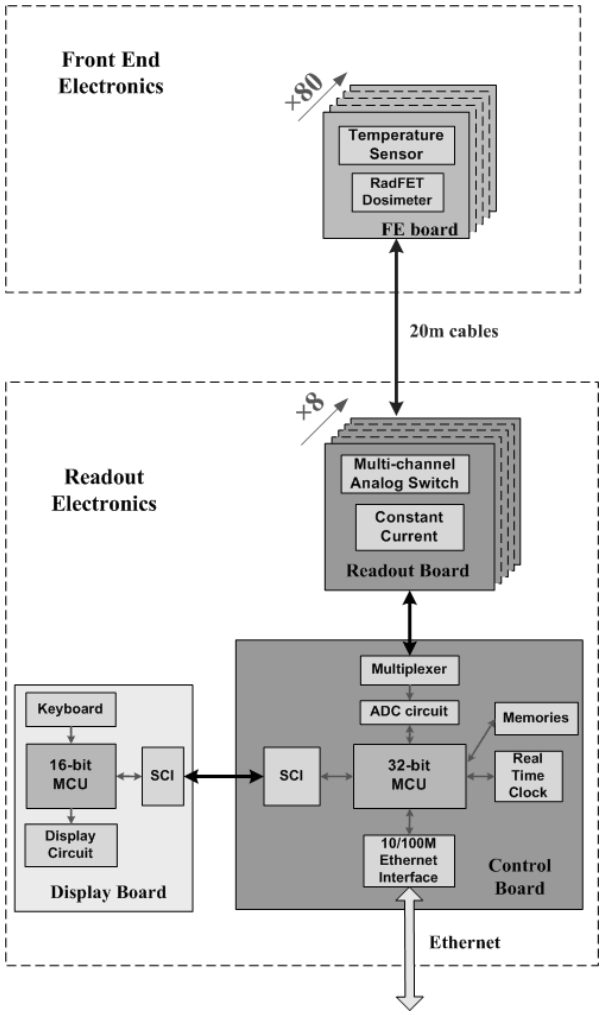

Fig. 2 Block diagram of the system.

Readout electronics consists of 8 readout boards, one control board and one display board. All of them are installed as modules inside a 3U crate as **Fig. 3** shows.

The readout board contains a current source and some multi-channel analog switches. The current source provides 10μA and 50μA constant currents, which can be applied to each RadFET sensor and temperature sensor respectively under the control of analog switches.

The control board contains an 8-input multiplexer, an ADC circuit, a 32-bit microcontroller (MCU), a SDRAM memory, a NandFLASH memory and a 10/100Mbps Ethernet interface etc. The output of a certain readout board can be selected by the multiplexer, and then sampled by the ADC circuit, which can measure a voltage between 0 and 12V with a resolution of 1mV. The 32-bit MCU we used is Freescale ColdFire MCF5282[4], which runs uClinux

embedded operation system with the support of SDRAM memory to ensure the system stability. The MCU calculates the dose absorbed by each RadFET chip according to the data sampled by the ADC circuit. Then the calculated dose is saved into the NandFlash memory on the board and waits for users to read via the Ethernet interface. The calculated dose is also sent to the display board via a serial communication interface (SCI).

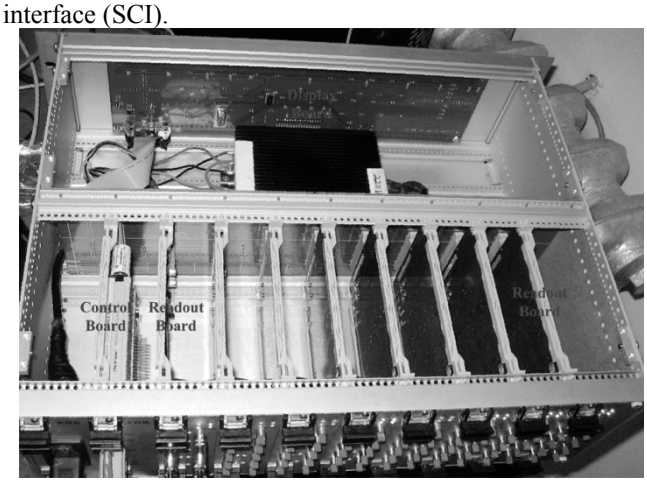

Fig. 3 Readout electronics.

The display board consists of a 16-bit MCU (Freescale MC9S12D64) [5], a keypad circuit and a display circuit. It shows the dose received from the control board.

IV. Performance of the System

The system performance has been verified with BEPC test beam, which has the most similar radiation field with BEPCII. The test beam is produced by BEPC linear accelerator and controlled by bending magnets. A single RadFET chip was used at this experiment. The threshold voltages of both 300/50 sensors inside the RadFET chip were constantly read out in an interval of 5 minutes during the experiment. The agreement between two sensors is found to be good (within 2%) by comparing the experimental data of two sensors.

The average dose can be calculated from the threshold voltages of the two sensors according to the response curve calibrated by using of ^{60}Co source. The integral dose as a function of time is shown in **Fig. 4**. In this figure, the beam state as a function of time is also given, while 1 is used to indicate beam is on.

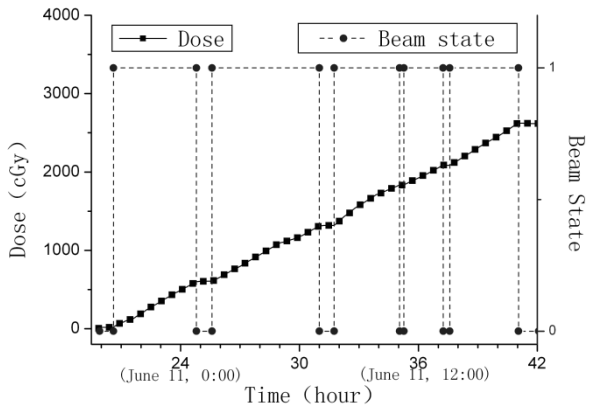

Fig. 4 The integral dose curve and beam state curve.

As shown in **Fig. 4**, the value of integral dose increases nearly linearly when beam is on and remains constant when beam is off. The fade phenomenon on integral dose can be observed when beam is off by further analysis. But the fading rate is rather small (within 0.5%) and acceptable. So even in the high energy environment, the fade of the 300/50 sensors inside the RadFET chip isn't evident, which is what we expect to see.

In addition, the average dose rate, which is about 2.5cGy/min when beam is on, can be calculated from the integral dose curve.

V. Conclusions

The online integral dose monitor system has been built for BESIII EMC based on the study on 400nm IMPL RadFET. It is proved to work well at BEPC test beam. Its future measurement on BESIII will be important for EMC data correction.

References

1) M. A. H. Chowdhury et al., 'Thermal annealing and optical darkening effects in CsI(Tl) crystals,' Nucl. Instr. and Meth. A432(1999) 138-146.
2) A. Holmes-Siedle and L. Adams, 'RadFET: A Review of the Use of Metal-Oxide-Silicon Devices as Integrating Dosimeters. Radiat,' Phys. Chem., vol. 22, pp. 235-244, 1986.
3) Jaksic, A., Ristic, G., Pejovic, M., Mohammadzadeh, A. and Lane, W., 'Characterisation of radiation of radiation response of 400 nm implanted gate oxide RadFET,' In: Proceedings of 23rd International Conference on Microelectronics (MEIL2002), Vol. 2, 15–17 May, (Yugoslavia: Nis) pp. 727–730 (2002).
4) Freescale Semiconductor, 'MCF5282 ColdFire Microcontroller User's Manual,' http://www.freescale.com. Nov, 2004.
5) Freescale Semiconductor, 'MC9S12DJ64 Device User Guide,' http://www. freescale.com. Sep, 2004.

Journal of NUCLEAR SCIENCE and TECHNOLOGY, Supplement 5, p. 256–259 (June 2008)

Energy Correction Factors for Silicon Semiconductor Dosimeter in Adult-male Phantom for Accurate Measurement of Organ Doses

Chan Hyeong KIM[1*], Sungkoo CHO[1], Sang Hyoun CHOI[2], and Jong Kyung KIM[1]

[1]*Department of Nuclear Engineering, Hanyang University, Seoul, Korea*
[2]*Department of Radiation Oncology, Inha University, Incheon, Korea*

Metal oxide semiconductor field effect transistor (MOSFET) dosimeters are used to measure radiation dose in various medical applications and radiation safety. The advantage of the MOSFET dosimeter is that it is very small and provides practically real-time reading. However, given the fact that it is made mainly of silicon and epoxy, which are not ideally tissue equivalent, the MOSFET dosimeter shows some energy dependence for low-energy photons and will overestimate the energy deposition or absorbed dose in tissue when it is used in a phantom, due to the existence of scattered low-energy photons in the phantom. The present study determined, by Monte Carlo simulations with MCNPX, the relative response of the MOSFET dosimeter to the tissue dose, and thereby the energy correction factors, at various dosimeter locations in the ATOM adult-male phantom, in order to be able to accurately measure organ and tissue doses. The calculated values of relative response were 1.0-1.2 and 1.0-1.1 for 0.662 MeV and 1.25 MeV photons, respectively, which shows that if we do not use appropriate correction factors, the measurement of an organ dose could be overestimated by 10-20%, depending on the measurement condition. The result in study also shows that the energy correction factors are not very sensitive to the detailed energy spectrum of the photon field, and that the energy correction factors determined from the 0.662 MeV and 1.25 MeV photons can be used in the radiation fields in nuclear power plants without significant errors.

KEYWORDS: MOSFET dosimeter, energy dependence, physical phantom, Monte Carlo, dosimetry

I. Introduction

It is very difficult and time consuming to measure effective dose[1)]. Measurement of effective dose usually involves several hundreds of thermo-luminescence dosimeter (TLD) chips and a RANDO-type physical phantom to measure the equivalent doses to various organs and tissues in the human body. To measure this effective dose very quickly, i.e., on a practically real-time basis, a measurement system, called Effective Dose Measurement System (EDMS), is under development at Hanyang University in Korea. The EDMS uses 32 high-sensitivity Metal Oxide Semiconductor Field Effect Transistor (MOSFET) dosimeters[2)] in the ATOM adult-male phantom[3)] to measure organ and tissue doses.

The MOSFET dosimeter is used because it is very small and provides practically real-time reading[2)]. However, given the fact that it is made mainly of silicon and epoxy, it shows energy dependence for low-energy photons[4,5)] and will overestimate the energy deposition or absorbed dose due to the existence of scattered low-energy photons in the phantom. The objective of this study was to determine, by Monte Carlo simulations with Monte Carlo N-Particle Transport Code System (MCNPX)[6)], the relative response (to tissue dose) of the MOSFET dosimeter, and thereby the energy correction factors, at various dosimeter locations in the ATOM adult-male phantom, in order to be able to accurately measure organ and tissue doses.

*Corresponding Author, Tel: +82-2-2220-0513, Fax: +82-2-2220-4059, E-mail: chkim@hanyang.ac.kr

II. Methods

1. High-sensitivity MOSFET dosimeter

MOSFET dosimeter is used to measure radiation dose in various medical applications and radiation safety[7,8)]. The high-sensitivity MOSFET dosimeters (Model 1002RD, Thomson and Nielson Electronics, Ltd., Ottawa, Canada)[2)] investigated in this study are a 1 mm^2 area and 0.25 mm thick silicon chip covered with a 0.85 mm thick epoxy bulb. The silicon chip includes two MOSFET devices, each of which has an active area of 0.2 mm × 0.2 mm and an active thickness of 1 μm. The silicon chip and epoxy bulb are affixed at the end of a very thin and flexible polyamide laminate cable. Wang et al., who investigated the energy and angular dependence of the high-sensitivity MOSFET dosimeter, reported that it shows an angular dependence of less than 8% for the photon energies of 80 keV, 300 keV, and 1.25 MeV[9)]. They also reported that the energy dependence of the MOSFET dosimeter becomes significant if the photon energy is less than 100 keV, due to the domination of the photoelectric effect for low-energy photons.

2. ATOM Adult-male Phantom

The ATOM adult-male phantom (Model 701-D, CIRS, Norfolk, Virginia, U.S.A.)[3)] considered in this study represents an adult male of 173 cm and 73 kg. The phantom is composed of four types of artificial material — soft tissue, lung, average bone, and brain — in 25 mm thick slices. The slices have 1.5 cm × 1.5 cm grid holes for dosimeter placement. The artificial material simulates real tissues within an absorbed-dose error margin of 1-3% for the photon

energy range of 30 keV to 20 MeV[10]. The manufacturer provides detailed data on the density and composition of the artificial materials[3]. **Fig. 1** shows the ATOM adult-male phantom wired with 32 high-sensitivity MOSFET dosimeters to measure organ and tissue doses.

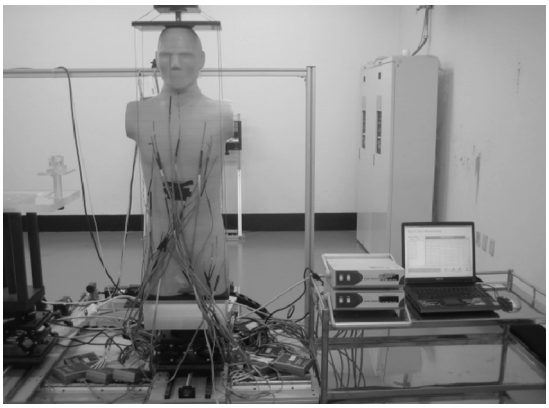

Fig. 1 ATOM adult-male phantom wired with 32 high-sensitivity MOSFET dosimeters to measure organ and tissue doses

3. Voxel Model and Monte Carlo simulation

A computational model (a tomographic voxel model) was constructed based on the CT image data for the ATOM adult-male phantom. The voxel resolution of the model was 0.457 × 0.457 × 0.45 cm^3. The size of the voxel array was 102 × 102 × 216 (= 2,247,264), corresponding to 46.6 cm, 46.6 cm, and 97.2 cm, respectively. The computational model was then implemented into the Monte Carlo radiation transport simulation code (MCNPX^{TM}2.4.0) and used to calculate the detailed energy spectrum of the photon field at the MOSFET dosimeter locations in the phantom. **Fig. 2** shows the computational model as implemented into MCNPX.

Fig. 2 Computational model of the ATOM adult-male phantom as implemented in the MCNPX code

The energy spectrum of the photon fluence at each dosimeter location in the phantom was determined using MCNPX's F4 tally, which calculates volume-averaged photon fluence by track-length estimation[6]. The number of source particles simulated for each case was 5×10^7, and the resulting statistical errors were insignificant (< 1-2%) for most of the cases, never exceeding 5%. Thirty-two dosimeter locations were calculated in this study so as to cover all of the major organs and tissues in the human body. For each dosimeter location, six photon beam directions and two MOSFET dosimeter directions were calculated.

4. Calculation of Energy Correction Factors

The relative responses (to tissue dose) of the MOSFET dosimeter were calculated with reference to the energy spectrum of the photon field at a dosimeter location and the pre-determined energy dependence of the MOSFET dosimeter[9]. The energy correction factors of the MOSFET dosimeter were calculated by taking inverse of the median value of the relative responses calculated for the irradiation conditions considered in this study. The relative responses and energy correction factors were calculated for 0.662 MeV and 1.25 MeV monoenergetic photons representing ^{137}Cs (and ^{58}Co) and ^{60}Co, respectively. The energy correction factors of the MOSFET dosimeter were determined also for the energy spectrum in a steam generator channel head of a nuclear power plant, and the results were compared with the energy correction factors previously determined for the 0.662 MeV and 1.25 MeV monoenergetic photons in order to evaluate the sensitivity of those correction factors to the energy spectrum of the photon field.

III. Results and Discussion

The relative response of the MOSFET dosimeter was calculated by the convolution of the energy spectrum of the photon field at a given dosimeter location and the pre-determined energy and angular dependence of the MOSFET dosimeter. **Fig. 3** shows the energy spectrum and relative response of the MOSFET dosimeter at a dosimeter location in the liver for the 0.662 MeV monoenergetic photon beam for six orthogonal beam directions: antero-posterior (AP), postero-anterior (PA), right lateral (RLAT), left lateral (LLAT), overhead (OH), and underfoot (UF).

The results show that the major fraction of the photons at the dosimeter location has energies greater than 100 keV for all of the cases considered in this study. The results for the other dosimeter locations did not differ significantly. The energy spectrum for the 1.25 MeV monoenergetic photon beam was even harder. The results suggest that the overestimation of the MOSFET dosimeter in the phantom is not very large. For the given case illustrated in Fig. 3, the relative responses of the MOSFET dosimeter were within in the range of 1.03-1.14 considering all of the irradiation directions and dosimeter directions. A careful investigation of the results also revealed that the relative response of the MOSFET dosimeter increased with the thickness of the tissue between the photon source and the dosimeter location, due to the increase in the number of the low-energy scattered photons.

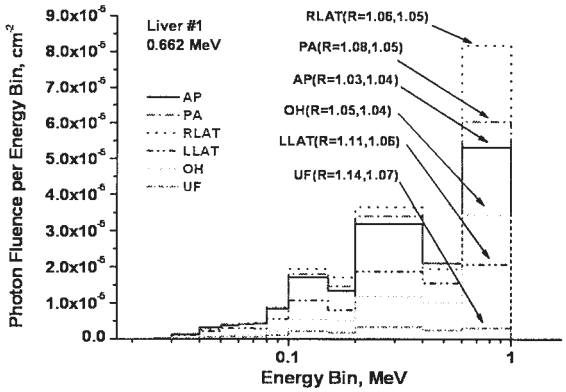

Fig. 3 Energy spectrum and relative response of the high-sensitivity MOSFET dosimeter at a dosimeter location in the liver for the 0.662 MeV monoenergetic photon beam for antero-posterior (AP), postero-anterior (PA), right lateral (RLAT), left lateral (LLAT), overhead (OH), and underfoot (UF).

Fig. 4 shows the distributions of the relative response (R) values of the MOSFET dosimeter for the 0.662 MeV and 1.25 MeV monoenergetic photons, considering all of the dosimeter locations in the phantom, all of the photon beam directions, and all of the dosimeter directions. The relative response values were within the range of 1.0-1.2 and 1.0-1.1 for 0.662 MeV and 1.25 MeV, respectively. The results show that if we do not correct for the MOSFET dosimeter's energy dependence, it might overestimate an organ dose by up to 10-20%.

The energy correction factors were calculated based on the relative response (R) values of the MOSFET dosimeter for six orthogonal photon beam directions, two MOSFET dosimeter directions, and two photon energies (i.e., 0.662 MeV and 1.25 MeV). Therefore, a total of 24 relative response values were used to calculate an energy correction factor. The energy correction factor for a dosimeter location was calculated by taking the inverse of the median value of these 24 relative response values. The energy correction factors for the 32 dosimeter locations in the ATOM adult-male phantom were calculated within the 0.89-0.97 range.

The energy correction factors were also calculated for the energy spectrum in a steam generator channel head within a Korean nuclear power plant[11], and the results were compared with the energy correction factors determined for the 0.662 MeV and 1.25 MeV monoenergetic photons. The inside of the steam generator channel head is heavily contaminated by activation products including ^{60}Co, ^{58}Co, ^{54}Mn, ^{51}Cr, and ^{59}Fe. Currently, ~95% of the radiation field in a steam generator channel head is formed by ^{60}Co and ^{58}Co, and the other activation products also emit high-energy photons within the range of 300-1,300 keV. There also exist scattered photons and characteristic X-rays from the wall, which are mostly within the range of 100-300 keV.

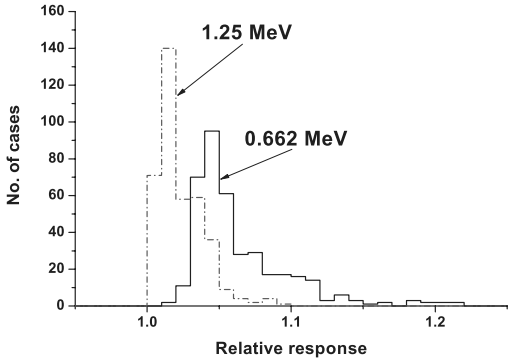

Fig. 4 Distributions of the relative response (R) values of the high-sensitivity MODFET dosimeters in the ATOM adult-male phantom for 0.662 MeV and 1.25 MeV photons

Fig. 5 shows the distribution of the differences of the energy correction factors, between 0.66 and 1.25 MeV monoenergetic photons and the energy spectrum inside of the steam generator channel head, for the 32 dosimeter locations in the ATOM adult-male phantom. The differences were very small (i.e., < 1.5%) in most of the cases, which shows that the energy correction factors are not very sensitive to the detailed energy spectrum of the photon field, and therefore that the energy correction factors determined from 0.662 MeV and 1.25 MeV photons can be used in various radiation fields in nuclear power plants without incurring significant errors.

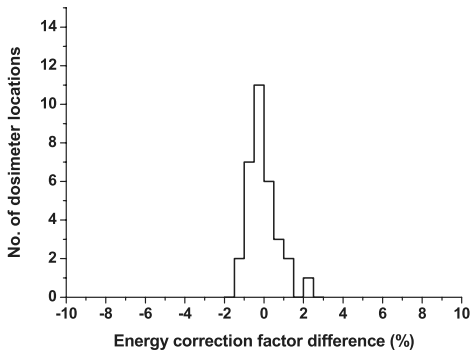

Fig. 5 Difference of energy correction factors for the 32 dosimeter locations in the ATOM adult-male phantom

V. Conclusions

This study determined, by Monte Carlo simulations with MCNPX, the relative responses of the high-sensitivity MOSFET dosimeter, and thereby the energy correction factors, at various dosimeter locations in the ATOM adult-male phantom. The relative responses were calculated as 1.0-1.2 and 1.0-1.1 for 0.662 MeV and 1.25 MeV photons, respectively. This result shows that if we do not use appropriate correction factors, the measurement of an organ dose by a high-sensitivity MOSFET dosimeter could be overestimated by 10-20%, depending on the measurement condition. The calculated energy correction factors were

within the range of 0.89-0.97. These factors were calculated also for the energy spectrum in the steam generator channel head of a nuclear power plant, and were found to be very close to those calculated for the 0.662 MeV and 1.25 MeV monoenergetic photons. This shows that the energy correction factors are not very sensitive to the detailed energy spectrum of the photon field, and that the energy correction factors determined from the 0.662 MeV and 1.25 MeV photons can be used in various radiation fields in nuclear power plants without incurring significant errors.

Acknowledgement

This work was supported by the Korean Ministry of Science and Technology through ERC (RII-2000-067-03002-0), BAERI (M20508050003-05B0805-00310), and the Korea Institute of Nuclear Safety (KINS).

References

1) ICRP, Recommendations of the International Commission of Radiological Protection, Pergamon Press, 21[1-3], 23 (1990).
2) Thomson & Nielsen Electronics Ltd., MOSFET Autosense^{TM} Operator's Manual, Thomson & Nielsen Electronics Ltd., Ottawa (2002).
3) CIRS Tissue Simulation Technology, ATOM Adult Male Phantom: Model Number 701-C, CIRS, Virginia (2003).
4) M. Soubra, J. Cygler, G. Mackay, "Evaluation of a dual bias dual metal oxide-silicon semiconductor field effect transistor detector as radiation dosimeter," Med. Phys., 21[4], 567 (1994).
5) D. J. Gladstone, L. M. Chin, "Automated data collection and analysis system for MOSFET radiation detector," Med. Phys., 18[3], 542 (1991).
6) L. S. Waters, et el., MCNPX User's Manual, Version 2.4.0, LA-UR-02-2607, Los Alamos National Laboratory (2002).
7) J. J. DeMarco, C. H. Cagnon, et al., "A Monte Carlo based method to estimate radiation dose from multidetector CT (MDCT): cylindrical and anthropomorphic phantoms," Phy. Med. Biol., 50, 3989 (2005).
8) R. Ramaseshan, K. S. Kohli, et al., "Performance characteristics of a micro MOSFET as an in vivo dosimeter in radiation therapy," Phys. Med. Biol., 49, 4031 (2004).
9) B. Wang, X. G. Xu, C. H. Kim, "Monte Carlo study of MOSFET dosimeter characteristics: dose dependence on photon energy, direction and dosimeter composition," Rad. Prot. Dosi., 113[1], 40 (2005).
10) ICRU, Tissue substitutes in radiation dosimetry and measurement, ICRU Report 44, International Commission on Radiation Units and Measurements, Behesda, MD (1989).
11) S. Cho, S. H. Choi, et al., "Monte Carlo study of MOSFET dosimeter dose correction factors considering energy spectrum of radiation field in a steam generator channel head," J. Korean Asso. Radiat. Prot., 31[4], 165 (2006).

Journal of NUCLEAR SCIENCE and TECHNOLOGY, Supplement 5, p. 260–263 (June 2008)

TLD Postal Dose Quality Audit Intercomparison for Megavolts Photon Beam of Radiotherapy Centers in Bangladesh

Md. Shakilur RAHMAN[1,2], Guinyun KIM[1*], A.F.M. Mizaur RAHMAN[2], M. Shamsuzzaman[2], Zahangir ALAM[3], and Rashid un NABI[4]

[1]*Department of Physics, Kyungpook National University, 1370 Sakyuk-Dong, Buk-Gu, Daegu 702-701, Korea*
[2]*Institute of Nuclear Science & Technology, Atomic Energy Research Establishment, Ganakbari, Savar, GPO Box. 3787, Dhaka.1000, Bangladesh*
[3]*Oncology Department, Delta Medical Center, Mirpur, Dhaka, Bangladesh*
[4]*Dept. of Radiation Oncology, National Institute of Cancer Research and Hospital, Dhaka, Bangladesh*

A postal dose intercomparison program based on the thermo-luminescence dosimeter (TLD) was carried in order to investigate and reduce uncertainties involved in the measurement of absorbed dose, and to improve the accuracy of dose measurement at different radiotherapy centers in Bangladesh. The intercomparison program was organized by the Secondary Standard Dosimetry Laboratory (SSDL) with the assistance of the IAEA/WHO postal dose intercomparison network. A set of three TLDs (encapsulated LiF powder) including a control was sent to the participating radiotherapy centers for irradiation with 2 Gy of absorbed dose to water. The measurements were made for ^{60}Co and megavolts X-ray beam. Thirteen beams in total were checked. Deviation of ±5% between stated and evaluated dose was considered to be acceptable for ^{60}Co and 6MV X-ray beam. The result of ^{60}Co beam of two centers exceeds the acceptance limit. The maximum deviation was -8.6% with an uncertainty of 1.8% i.e., the ratio of intercomparison dose to locally measured dose was 1.09. We discussed the immediate and corrective action to minimize the discrepancies. For ten ^{60}Co beam measurements, a mean valued of the ratio of intercomparison dose to locally stated dose was 0.988 with a standard deviation of 0.031. The importance of a proper ongoing quality assurance program is essential in maintaining the consistency and the uniformity of absorbed dose measurement for the precision dose delivery to the patient.

KEYWORDS: intercomparison, absorbed dose, TLD, radiotherapy, SSDL, IAEA, ^{60}Co, high energy x-ray beam, dosimetry protocol, SSD

I. Introduction

Maximum control of tumors with minimum of complications to the normal tissues depends on various factors especially on the accuracy of absorbed dose. The demands on precision in radiotherapy dosimetry and treatment delivery are determined by the steepness of the relevant clinical dose-effect curves, both for tumor control and for normal tissue complications. Clinical data consideration lead to generally agreed recommendations on the required accuracy in clinical dosimetry for radical curative being given in ICRU report-24 (1976) for at least accuracy of ±5 % in the delivery of absorbed dose to the target volume of the treatment tumor[1-2]. Brahme[3] also proposed a tolerance value of accuracy in dose delivery of ±3.5 % at one standard deviation level. Mijnheer *et al.*[4] has proposed ±3 % by considering limiting uncertainties for acceptable increase in normal tissue complication risk. This includes patient data acquisition, treatment planning, and the delivery of prescribed dose to the patient. Therefore, accuracy of each contributing stage must be better than a tolerance value of accuracy in order to achieve these overall requirements. It is suggested that more than 10 % of 2,500,000 patients who are treated by around 6000-7000 tele therapy units (^{60}Co and megavolts X-rays) yearly receive more than 20 % different doses from the prescribed doses[5]. This could be concluded that at least 250,000 patients annually receive poor radiotherapy through lack of proper equipment, personnel skill or training etc. This consideration [Bleehan 1991, AAPM 1994, Thwaites *et al.* 1995] supports to make it necessary to establish a comprehensive quality assurance system at local level in each centre[6-8]. Dosimetry intercomparison is designed to establish the accuracy and the precision of dosimetry at given level in the dosimetry chain and to assess consistency between the centers. It also acts as an audit that can reveal the presence of error. Whilst audit system can employ mailed TLD or site visit using ionization chambers. There are 10 radiotherapy facilities (equipped with ^{60}Co unit and electron linac) operating at the present time in Bangladesh serving a population of 140 million. Eight centers are equipped with ^{60}Co gamma beams. The other two centers are equipped with 6 MV linac and ^{60}Co gamma beam. Five other new linacs are under installation. The rapidly increasing number of radiotherapy units in Bangladesh has brought out its necessity and interest in the local radiotherapy community to harmonize and compare consistency of dose delivery amongst the center and to establish greater confidence in dose delivery. A number of quality assurance programm[9-14] or a mixture of the program are followed. Some previous dosimetric quality audit program was conducted in Bangladesh but no data yet been published. Rahman[15] emphasized the necessity for a study

*Corresponding Author, Tel.: +82-53-950-5320, Fax: +82-53-955-5356, E-mail address: gnkim@knu.ac.kr

of TLD quality audit program in Bangladesh hospitals in order to ensure better accuracy of dose delivery to the patient.

Recognizing the better accuracy of consistent dosimetry, a number of dosimetry protocols and codes of practices[16-23] are recommended by international organization. Protocols used for the determination of absorbed dose also differ from center to center in Bangladesh. The Secondary Standard Dosimetry Laboratory (SSDL) in Bangladesh as a member of the IAEA/WHO SSDL network has conducted this program with help of the IAEA. This study is the first time in Bangladesh that covers all radiotherapy centers and units.

II. Experimental Procedure

Nine radiotherapy centers, which have twelve ^{60}Co-units and one 6 MV X-ray beam, have participated in this study. Dosimetry protocols for the absorbed dose differ from center to center. Four different dosimetry protocols TRS-277[19], TRS-381[20], TRS-398[21] and TG-51[23] were used for this study. A set of three TLDs, one of them is a control (capsulated LiF powder), was sent for the irradiation with 2 Gy of absorbed dose to water. A special instruction was given to the hospital for the absorbed dose to water measurement by their used protocol and detailed explanation of used factor along with data presented in **Table 1**. A special type of holder feasible to set with the IAEA standard phantom size of 30×30×30cm^3 and some water tank made of perspex sheath was used in this study. The irradiations were carried at a depth of 10 cm for a field size of 10×10 cm^2 at source to surface distance (SSD) 80 cm or 100 cm. The dose for irradiation is fixed at 2 Gy of absorbed dose to water because this value is approximately equal dose to the patient at each fractionation of treatment. A set of TLD irradiation holder made of perspex which supports for the irradiation of TLDs by geometry of horizontal and vertical set up. The deviations Δ of reported and measured absorbed dose for each participant were calculated according to the formula recommended by the IAEA TRS-277[19]

$$\Delta = \frac{D_P - \overline{D}}{\overline{D}},$$

where, $\overline{D}$ is the absorbed dose determination by the TLD system (IAEA) and D_P is the reported dose by the participant.

The IAEA TLD system[24] consists of a PCL3 TLD automatic reader (Fimel, France) for the measurements of TL dosimeters. The PCL3 reader provides fast readings of a large number of TLD samples with a reproducibility of 0.3±0.5 %. Four readings per TL capsule are made.

The TL dosimeters are polyethylene capsules of 20 mm inner length and 3 mm inner diameter, filled with approximately 155 mg of TLD powder. The TL material used is a virgin lithium fluoride powder, LiF:Mg,Ti, type TLD-100 (Harshaw). The TL powder is annealed before it is used for dose measurements in order to optimize the LiF characteristics. The annealing is performed at 400 °C for 1 hour followed by fast cooling and subsequent annealing at 80 °C for 24 hours. Since the dosimetric characteristics of the LiF powder are closely related to its grain size and homogeneity, the powder is sifted after annealing to eliminate the smallest grains (below 80 μm). In order to determine the absorbed dose to water (D_w) from the reading of TL dosimeters, a calibration of the TLD system is performed. Several correction factors such as holder correction factor 1.01±0.003 and non linearity correction factor 1.00 for 2 Gy dose. The fading correction factor is applied by $f_{fad} = e^{-0.0004(t_{RD}-t_{PD})}$, where t_{RD} and t_{PD} are the time delays between the starting time t_0 and the time of read out for the reference and participant dosimeter, respectively.

The TLD response per unit of absorbed dose to water is determined by irradiating in a ^{60}Co beam. A set of TLDs to different doses used under the standard configuration (field size 10×10 cm^2 at 1 m from the source, at a depth in the water of 5 g·cm^2). The combined relative standard uncertainty u_C of the determination of the D_w from TLD measurements has two components: (i) the uncertainty of the calibration of the TLD system from the determination of the D_w using an ion chamber and (ii) the uncertainty in the TLD procedure itself. The latter includes the uncertainty of the process of reading the TLD (corrected for daily fluctuations of the reader) and the uncertainties of the individual coefficients and correction factors mentioned above. The relative standard uncertainty of the TLD procedure (ii) is estimated to be 1.7%. The uncertainty in the calibration of the TLD system (i) arises mainly from the uncertainty of the determination of the absorbed dose in reference conditions from the ionization chamber measurements. This increases the combined relative standard uncertainty of the entire TLD process u_C from 1.7% to 2.3%. It should be noticed, however, that when the same dosimetry protocol is used at a hospital to determine the dose given to the TLD, most of its contribution in uncertainty of D_w cancels out.

III. Results and Discussion

A total number of twelve ^{60}Co and one 6MV X-ray beams quality audit is performed by TLD technique. **Table 1** shows the present selected data gathered from the centers concerning their radiotherapy units, dosimetry system and ambient dose to water determination for ^{60}Co and high energy X-ray beams. During the evaluation of TLDs, for each capsule, the mean reading and standard error of the mean standard deviation were determined. The deviations Δ of the quoted absorbed dose from the average measured were within ±5% for 10 participants out of twelve for ^{60}Co beam. For two units, a large discrepancies of the stated to evaluated dose (-6.7% and -8.6%) have been observed. These cases are thoroughly studied by SSDL personnel by on-site visit. The reasons of these discrepancies are so far detected and have taken step in minimizing error. The average ratio of measured mean dose (TLD system) and hospital stated dose of ten units (^{60}Co), which lies within acceptance limit were 0.99 with a standard deviation of 1.00 %.

Table 1 Data of ^{60}Co and high energy X-ray beams in Bangladesh

Radiotherapy Center No.	1	2	3-8	9-10	11	12	13
Radiotherapy Unit (No.1-12 ^{60}Co, No.13 linac)	Alcyon II	Cirus	FYC-260	Elite-80	Elite-100	ATC C-9	Mevatron 7445 6MV linac
Electrometer	PTW Unidos	PTW Unidos	Capintec/PTW Unidos	Capintec	Capintec	PTW Unidos	PTW Unidos
Ionization chamber	N31003	N23323	TW30013	IC-70	IC-10	TW31013	N23323
Protocol	TG-51	TG-51	TRS-277&398	TRS-277	TRS-398	TRS-398	TRS-398
D_{max} rate in cGy/min	180.847	170.85	162.37	196.09	103.74	53.98	98.19Gy/100MU
Deviation	5.0%	1.2%	-8.6% to 0.1%	-3.3% to 3.5 %	-4.9%	-0.4%	0.6%

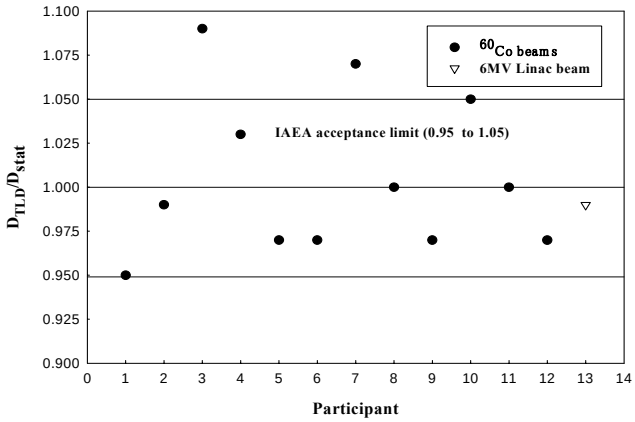

Fig. 1 The ratio of measured dose (D_{TLD}) and stated dose (D_{stat}) of the participant

Table 2 Results of a few recent TLD photon beam intercomparisons for the mean ratio of measured and stated dose

Reference	Study	Number of Beam	Mean	Standard deviation
Hanson *et al.*[25], 1993	Europe	357	1.007	0.040
Dutriex *et al.*[26],1994	EC	125	0.970	0.095
Huntley *et al.*[27], 1994	Australia	30	0.993	0.033
Izewska *et al.*[28], 1995	Poland	22	1.004	0.038
Nisbet *et al.*[29], 1998	Ireland	13	1.002	0.012
Rassiah *et al.*[30], 2004	Malaysia	12	1.027	0.031
Izewska *et al.*[31],2006	IAEA '00-'03	706	1.007	0.037
Present work , 2007	Bangladesh	13	1.004	0.043

Fig. 1 shows the dose ratio of measured and stated for all participated centers. Eleven among thirteen units were within the ICRU acceptance limit. The deviation Δ for high energy X-ray (6 MV linac) was 0.6 % with a standard deviation of 0.014 % which lies within the ICRU acceptance limit. The intercomparison has been designed to identify the reasons for the differences in doses determined in the intercomparison and the locally stated. A few recent the intercomparison for recent TLD photon beam was listed in Table 2. The deviation might be arisen, first, due to different dosimetry protocol used by the participants. The uncertainty of dose measurement of various codes of practice for the determination of absorbed dose to water for photon beams typically agrees within 2 % among hospitals[32]. Secondly, correction of air density (pressure and temperature) might be the great cause because most of the clinics used uncalibrated barometers and thermometers. It is observed that both the ^{60}Co units which exceed the limits of variations of stated and measured doses are FYC-260 type. Practically this type of machine is mechanically unstable. First, large iso-centric deviation is observed in both the units and secondly, error in SSD between ion-chamber measurement and in TLD irradiation is reported. We also observed a deviation of K_{tp} (the correction factor for pressure and temperature) from standard measurement. It is noted here that the chambers and the electrometers of the participated centers are calibrated from the Secondary Standard Dosimetry Laboratory (SSDL), Bangladesh, which is a part of IAEA/WHO SSDL network. The SSDL is traceable to the National Physical Laboratory (NPL), UK and Physikalisch-Technischen Bundesanstalt (PTB), Germany.

IV. Conclusions

The main object of TLD audit programme is to ensure that the radiation doses delivered to patient is the same as the prescribed dose with high accuracy. The programme is made successive with assistance of the IAEA and with the cooperation by local radiotherapy centers. The TLD intercomparison study has been made it possible to test the consistency of ^{60}Co gamma and mega voltage X-ray beam at the radiotherapy centers in Bangladesh. A conclusive verification of absorbed dose actually delivered to patients during radiation treatment can be performed in vivo dosimetry which is under consideration. The mean ratio of measured dose to locally stated dose was 1.004 standard deviation of 0.043. Two ^{60}Co photon beams lay outside the intercomparison tolerance level ±5%. The reason of discrepancies is determined and correction is made by on-site visit by SSDL personnel. The intercomparison performed is a successful step from the point of view in improving the dosimetry situations in hospitals. It has given confidence in the basic of clinical delivery of dose in radiotherapy treatment and consistency of dosimetry at different radiotherapy centers in Bangladesh. TLD system is the convenient way to check radiotherapy dsoimetry other than ion chamber dosimetry. A regular monitoring system

need to maintain for the consistency and in improving quality of radiotherapy dosimetry by TLD technique could be emphasize and harmonizing dsoimetry in radiotherapy centers in all over the world.

Acknowledgement

The authors wish to express their sincere thanks to Dr. Ahmed Meghzifene, SSDL Officer and Dr. J. Izewska, TLD Officer of the Dosimetry and Medical Radiation Physics Section (DMRP) of the IAEA. We also honestly thank Dr. Sabine Danker and all other staffs of DMRP of the IAEA for their helpful cooperation in making the efforts successful. The authors would like to thank the medical physicists at various centers in participating and contributing to this study. This work is partly supported by the Korea Science and Engineering Foundation (KOSEF) through a grant provided by the Korean Ministry of Science & Technology (MOST) in 2007 (Project No. M2 07B0900-10810).

References

1) ICRU, "Determination of absorbed dose in patient irradiated by means of X or gamma rays in radiotherapy procedures" , Report-24, Bethesda, MD: ICRU (1976).
2) A. Brahme, "Accuracy requirements and quality assurance of external beam therapy with photon and electron", Acta. Oncol. Suppl. 1 (1988).
3) A. Brahme, "Dosimetric precision requirements in radiation therapy," Acta. Radiol.Oncol. 23, 379-91 (1984).
4) B. Mijnheer *et al.*, "What degree of accuracy is required and can be achieved in photon and neutron therapy?" Radiotherapy. Oncol. 8, 237–52 (1987).
5) SSDL Newsletter No. 31, Report on the fifth meeting of the SSDL Scientific Committee (SSC), Vienna 23-27 Nov. (1992).
6) N. Bleehan, "Quality assurance in radiotherapy", Report of standing committee on cancer, Department of Health, London (1991).
7) AAPM, "Comprehensive QA for radiation oncology: report of AAPM Task Group 40," Med. Phys. 12, 581–618 (1994).
8) D. I. Thwaites, P. Scalliet, J. W. Leer and J. Overgaard, "Quality assurance in radiotherapy (European Society for Therapeutic Radiology and Oncology advisory report to the Commission of the European Union for the 'Europe against Cancer Programme')," Radiother. Oncol. 35, 61–73 (1995).
9) G. J. Kutcher et al., "Comprehensive QA for radiation Oncology: Report of AAPM Radiation Therapy Committee Task Group 40," Med. Phys. 21 (4): 581-619 (1994).
10) WHO, "Quality assurance in radiotherapy", World Health Organization, Geneva, Switzerland (1988).
11) NCRP, "Dosimetry of X-ray and gamma-ray beams for radiation therapy in the energy range 10 keV to 50 MeV," National Council on Radiation Protection and Measurements (NCRP), Report 69, Bethesda (1981).
12) IEC, "Safety of medical electrical equipment, part 2: particular requirements for medical electron accelerators in the range of l-50 MeV," International Electrotechnical Commission. IEC Publication, Geneva, 601-2-L (1990).
13) ICRU, Prescribing, Recording and Reporting Photon Beam Therapy. Report No. 50, ICRU, Washington (1993).
14) IAEA, "Design and implementation of a radiotherapy programme: Clinical, Medical Physics, Radiation Protection and safety aspects," IAEA-TECDOC-1040 (1988)
15) M.S. Rahman, "International intercomparison program for ^{60}Co teletherapy level dosimetry: SSDL Bangladesh," Nucl. Sci. & Applications Vol. 14 (2), (2005).
16) HPA, "Revised code of practice for the dosimetry of 2 to 35MV x-ray, and of caesium-137 and cobalt-60 gamma ray beams," Phys. Med. Biol. 28, 1097-104 (1983).
17) AAPM, "A protocol for the determination of absorbed dose from high-energy photon and electron beams," Task Group No. 21, Med. Phys. 10, 741–771 (1983).
18) AAPM, " The calibration and use of plane parallel ionisation chambers for dosimetry of electron beams: an extension of the 1983 AAPM protocol," Report of AAPM Radiation Therapy Committee Task Group No. 39. Med. Phys. 21: 1251–1260 (1994).
19) IAEA, "Absorbed dose determination in photon and electron beams: An International Code of Practice," Technical Report Series No. 277. IAEA, Vienna (1987).
20) IAEA, "The use of plane parallel ionization chambers in high energy electron and photon beams: An International Code of Practice," Technical Report Series No. 381. IAEA, Vienna (1997).
21) IAEA, "Absorbed dose determination in external beam radiotherapy, An International Code of Practice," Technical Report Series No. 398, Vienna (2000).
22) ICRU, "Determination of absorbed dose in a patient irradiated by beams of x- or gamma rays in radiotherapy procedures," ICRU Report No. 24. ICRU, Bethesda, MD (1976).
23) P. R. Almond *et al*., "AAPM's TG-51 protocol for clinical reference dosimetry of high-energy photon and electron beam," Med. Phys 26 1847-1870 (1999).
24) J. Izewska, P. Andreo, "The IAEA/WHO TLD postal programme for radiotherapy hospitals," Radiation Oncology 54, 65-72 (2000).
25) U. Hanson *et al*., "Mailed TL dosimetry for machine output check and clinical application in the EORTC radiotheraphy group," Radiother. Oncol. 29, 85-90 (1993).
26) A. Dutreix et al., "Quality control of radiotherapy centers in Europe: beam calibration," Radiother. Oncol. 32, 256-264 (1994).
27) R. B. Huntley et al., "IAEA/WHO TLD radiotherapy dosimetry intercomparison for Australia. Measurement Assurance in Dosimetry," Proc. of a Symposium, Vienna, 24-27 May 1993, IAEA-SM-330/70, 177-190 (1994).
28) J. Izewska *et al*., "TLD postal dose intercomparison for megavoltage units in Poland," Radiother. Oncol. 36, 143-152 (1995).
29) A. Nisbet *et al*., "A dosimetric intercomparison of kilovoltage X-rays, megavoltage photons and electrons in the Republic of Ireland," Radiother. Oncol. 48, 95-101 (1998).
30) P. Rassiah *et al*., "A thermoluminescence dosimetry postal dose inter-comparison of radiation therapy centers in Malaysia," Australian Physical & Engineering Sciences in Medicine, 27, 25-29 (2004).
31) J. Izewska et al., "Postal dose audits for radiotherapy centers in Latin America and the Caribbean: trends in 1969-2003," Rev. Panam Salud Publica. 20, 161-172 (2006).
32) J. Izewska *et al*., "Quality audit for radiotherapy: a perspective of dosimetry practices at hospitals in developing countries," Radiation Oncology 69, 91-97 (2003).

Journal of NUCLEAR SCIENCE and TECHNOLOGY, Supplement 5, p. 264–267 (June 2008)

Influence of the PMMA Slab and ISO Water Phantom in Calibrating Personal Dosimeter in the Energy Range of 36-662 keV

Md. Shakilur RAHMAN[1,3], Guinyun KIM[1*], Norio TSUJIMURA[2], Tadayoshi YOSHIDA[2], Katsu KANAI [2], and Osamu KURIHARA[2]

[1]*Department of Physics, Kyungpook National University, 1370 Sakyuk-Dong, Buk-Gu, Daegu 702-701, Korea*
[2]*Radiation Protection Division, Japan Atomic Energy Agency (JAEA), 4-33 Muramatsu, Tokai-mura, Naka-gun, Ibaraki-ken, 319-1194, Japan*
[3]*Institute of Nuclear Science & Technology, Atomic Energy Research Establishment, Ganakbari, Savar, GPO Box. 3787, Dhaka.1000, Bangladesh*

Personnel dosimeter calibration for the determination of operational quantities used in individual monitoring requires placement on a phantom that provides a reasonable approximation to the backscatter properties of the part of the body on which it is worn. The personal dose equivalent Hp(d) is defined in the human body which is not a measurable quantity. The reference International Commission on Radiation Units and Measurements (ICRU) tissue is not readily available; hence a phantom of alternative must be used for calibration. The well recognized polymethyl-methacrylate (PMMA) slab phantom of size 30 × 30 × 15 cm^3 are still being used in calibrating personal dosimeters. The International Organization for Standardization (ISO)-4037(3) has proposed another phantom of the same size as ICRU, which is named as ISO water phantom. In the present study, calibrated X-ray fields are characterized for National Institute of Advanced Industrial Science and Technology (AIST) middle beam spectrum series by which the influence of these proposed phantoms has been studied by the thermoluminescence dosimetry (TLD) technique. Discrepancies of responses within 8% have been observed at lower energies up to 42 keV. There is a very good agreement in responses is observed for ISO water slab and PMMA slab phantom for photon energies above 42keV. Experimentally obtained correction factors for AIST radiation qualities of M50 and M60 for PMMA slab to ISO water phantom is proposed. Measured backscatter factor results from PMMA to ISO water-filled phantoms over the photon energy range 36 to 662 keV are reported. This shows that the new ISO water phantom is a better substitute of ICRU tissue phantom than the PMMA slab.

KEYWORDS: individual monitoring, PMMA, phantom, ICRU sphere, ISO, IAEA, X-ray beam, backscattering factor, AIST middle beam spectrum

I. Introduction

Dosimetric concepts and the definition of dose quantities for use in radiation protection were defined by the International Commission on Radiological Protection (ICRP) and International Commission on Radiation Units and Measurements (ICRU). The operational dosimetric quantity recommended for individual monitoring is the personal dose equivalent Hp(d)[1-3], which would exist on a phantom approximately in human body. From this concept, the calibration of personal dosimeter should be carried out on a suitable phantom surface as recommended by different international organizations related to the radiation protection standard.

The extent to which phantom composition affects dosimeter response was measured with a widely used personnel thermoluminescence dosimeter (TLD) system. The calibration phantom should provide a backscatter contribution similar to that of the part of the body where the dosimeter is worn. In several times, different phantoms recommended for and later were rejected due to raised difficulties. In 1992, the ICRU-47[4] gave a list of five different phantoms that were being used by several laboratories, which is considered to be enough within the accepted overall uncertainty in most radiation protection measurement of 30%. In this recommendation, calibration of personal dosimeter should be carried out on a polymethyl-methacrylate (PPMA) slab phantom of size 30 × 30 × 15 cm^3. Recent recommended phantom proposed by the International Organization for Standardization (ISO) in its report ISO-4037(3)[5] is named as the ISO water phantom of same dimension, which is represented as the human torso with regard to backscattering of the incident radiation. For calibration, this definition is extended to include a phantom having the composition of ICRU tissue and the same size and shape as the calibration phantom (30 × 30 × 15 cm^3, ICRU four element tissue phantom)[6]. However, since ICRU tissue is not readily available, a phantom of alternative composition must be specified. Calculated and measured photon backscatter results for the ICRU tissue phantom and calibration phantoms have been reported[7-8]. Traub *et al.*[8] reported that measurements with the ionization chamber indicated that the influence of phantom composition on dosimeter response to backscatter is less than calculated values. The extent to which phantom composition affects dosimeter response was measured with a widely used personnel TLD system. Kramar *et al.*[9] studies of the PMMA rectangular phantom indicated that photon energies in the range from about 10-500 keV, the backscatter factor could be 8 % high relative to ICRU tissue. Nelson and Chilton[10], for

*Corresponding Author, Tel.: +82-53-950-5320, Fax: +82-53-955-5356, E-mail Address: gnkim@knu.ac.kr

instance, have calculated dose equivalents in plastic and ICRU tissue equivalent semi-infinite slab phantoms for photon energies range 10-150 keV. Backscatter factor and tissue kerma at the phantom surface have been published by Bartlett *et al.*[11] for photon energies of 15-662 keV for an ICRU tissue equivalent cube phantom and PMMA slab. Grosswendt[12] and Bohm and Grosswendt[13] reported that conversion coefficients of a PMMA slab or a cube tissue material are not exactly known and can be approximately calculated from the other data. Conversion coefficients from air kerma to dose equivalent quantities were defined by using different phantoms for routine calibration service. There is still lack of experimental data. The main problem associated with a phantom differing from the ICRU sphere is that different types of dosimeters will respond to different extends to the fraction of dose equivalent phantom specific correction factor for which, with the acceptable uncertainties are independent of the type of dosimeters.

The aim of the present work is the characterization of calibrated X-ray beam for the National Institute of Advanced Industrial Science and Technology (AIST) middle beam qualities and an experimental investigation of the influence of ISO water phantom and PMMA slab phantom by the TLD technique in the energy range of 36 - 662 keV.

II. Materials and Experimental Methods

1. Characterization of Calibrated X-ray Beam

X-rays are widely used at different types of nuclear facilities for the convenient use of different radiation qualities. The use of X-ray facilities for precise irradiation requires an exact knowledge of the radiation field. A bipolar high-resolution industrial X-ray unit Pantak HF320C # 0202-7573, which has a tube potential of 5-320 kV that continuously adjustable in 0.01 kV increment with an accuracy of ±1 % and the tube current of 0.5-30 mA with adjustable increment of 0.1 mA that installed at Japan Atomic Energy Agency (JAEA), was used in this study. The stability and the ripple of the X-ray generator are tested for constant tube potential (kV) varying with the tube current (mA) and for constant tube current with varying tube voltage and are found to be good agreement with each other. To obtain the required radiation qualities as per the recommendation by AIST, the half value layer (HVL) is measured by the combination of an electrometer and ionization chamber of model DMR-201, Sl No. 17R1103 for the recommended filter combination by AIST. The effective energy is then obtained by extrapolating the 1st HVL for AIST reference beam quality and compared with ISO narrow beam spectrum series. The obtained effective energy is then compared with an established empirical formula which is obtained by the interpolation value from Hubble mass attenuation coefficients;

$$E = 76.48 \cdot t^{0.336} + 2.54 \cdot t^{2.01} \quad , t=1^{st} \text{HVL for Al in mm.} \qquad (1)$$

$$E = 76.48 \cdot t^{0.365} + 2.543 \cdot t^{2.00} \quad , t=1\text{st HVL for Cu in mm.} \qquad (2)$$

Fig. 1 shows the experimental values of HVL for Cu as a function of photon energy for AIST recommended filter combinations.

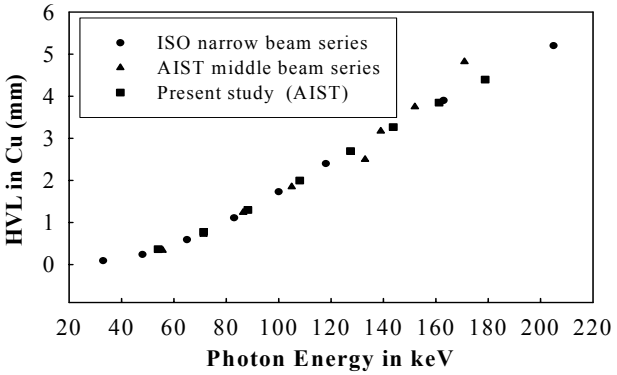

Fig. 1 HVL for Cu in mm

The conversion coefficients[14] (Sv/Gy) from air kerma to personal dose equivalent $H_P(10)$ and $H_P(0.07)$ is then calculated from ISO photon energy for operational dose qualities as shown in **Fig. 2.**

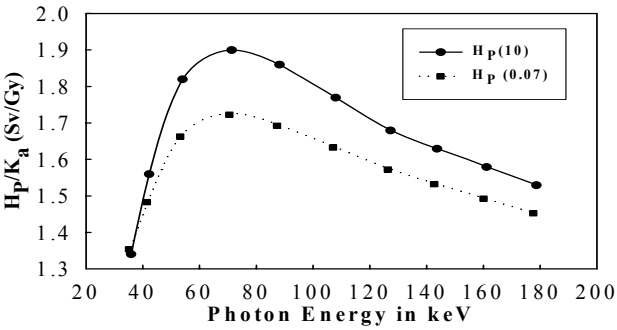

Fig. 2 Conversion coefficients from air kerma to personal dose equivalent

2. Thermoluminescence Dosimeter

Panasonic type TLD card of model UD-808P and holder were used in this study. Each card contains four elements; the element #1, 2, and 4 are $^7Li_2{}^{11}B_4O_7$(Cu) and the element #3 is $CaSO_4$ (Tm). The $^7Li_2{}^{11}B_4O_7$(Cu) phosphor is made from enriched isotope ^{7}Li and ^{11}B. This element is almost no sensitive to neutron. It responds to γ-, X-, and beta-rays. $CaSO_4$ (Tm) is a phosphor activated by Tm has the effective atomic number 15.3, which is not equivalent to soft tissue. This element is used to measure low dose γ- and X-rays with a metal shield, since it is highly sensitive to them. Position 1, 2 and 4 consists of $^7Li_2{}^{11}B_4O_7$(Cu) phosphor TLD with a thickness of 14, 61 and 160 mg/cm^2 respectively. The hunger filtrations of these positions are 3 (mylar), 3 (mylar) and 840 (plastic) mg/cm^2. Position 1 & 2 are used for skin dose measurement which are sensitive to beta-gamma radiation whereas position 4 is used to measure whole body gamma dose. The position 3 of the TLD card is composed of $CaSO_4$ (Tm) with a thickness of 160 mg/cm^2 corresponds to the holder of 840 mg/cm^2 plastic material as a filter. This position is used for low energy photon dose. An automatic

TLD reader of model Panasonic UD-7100P which is designed to measure with high speed and good reproducibility was used to read out the TLD card after exposure.

3. Experimental Procedure

TLD irradiations were performed with the same size ($30\times30\times15$ cm^3) of PMMA and ISO water-filled phantoms. The water phantom was a PMMA shell with a removable top to facilitate filling. The wall thickness is 10 mm except for the front face, which is 2.5 mm to minimize the effects of the PMMA. The front wall exhibited some deformation (outward bowing) due to the water pressure inside the phantom. The phantoms were placed on the irradiation bench of the X-ray unit at a distance of 2.5 m from the beam focus and perpendicular to the beam axis. To mark the geometric centre of the phantom and to measure the distance between the focus and the entrance phantom wall, a laser beam was used who's central axis has coincided with that of the X-ray beam. Dosimeters are held to the surface using double sided stick paper on the front surface. When calibrating, four TLD holders were placed on the front face. The irradiation is performed by using 11 kinds of photon beams as stated in **Table 1**.

Table 1 Dose equivalent CF for PMMA to ICRU tissue

Radiation Quality	Energy in keV	Conversion Coefficients (Sv/Gy)		K'_P
		Hp(10)	Hp(0.07)	
M50	**35.94**	**1.34**	**1.36**	**0.925**
M60	**42.28**	**1.56**	**1.49**	**0.924**
M75	**54.03**	**1.82**	**1.67**	**0.929**
M100	**71.37**	**1.90**	**1.73**	**0.935**
M125	**88.27**	**1.86**	**1.70**	**0.947**
M150	**108.06**	**1.77**	**1.64**	**0.957**
M175	**127.46**	**1.68**	**1.58**	**0.961**
M200	**143.8**	**1.63**	**1.54**	**0.964**
M225	**161.28**	**1.58**	**1.50**	**0.969**
M250	**178.84**	**1.53**	**1.46**	**0.972**
Cs-137	**662**	**1.21**	**---**	**0.981**

4. Correction Factor for PMMA Slab Phantom

A correction factor (K'_P) for backscattering difference in a PMMA and ICRU tissue equivalent phantom was introduced when calibrating TLDs, where K'_P was calculated by

$$K'_P = \frac{B_m^{ICRU}}{B_m^{PMMA}} = \frac{(K_m)_{ICRU}}{(K_m)_{PMMA}} = \frac{(K_{ICRU})_{ICRU}}{(K_{ICRU})_{PMMA}} \quad (3)$$

B_m^{ν} is the backscattering factor at a given radiation on a phantom material m, in a media ν and $(K_m)_\nu$ is the kerma in a media m on the surface of a semi-infinite phantom of material ν. The values of K'_P is calculated for the monoenergetic photon beam using the Grosswendt data[14] as the ratio of dose equivalent in the two phantoms. When TLDs were irradiated on the PMMA phantom, the calibration factor for the TL dosimeters, N, on PMMA phantom was defined as

$$N_{TLD}^{PMMA} = \frac{H_P(10)\cdot K_a}{K'_P.M} \quad (4)$$

The expression used for the measurement of calibration factor, N, on ISO phantom is

$$N_{TLD}^{ISO} = \frac{H_P(10)\cdot K_a}{M}, \quad (5)$$

where, H_P is the conversion coefficient from air kerma to the dose equivalent. M is the corrected dosimeter reading in arbitrary units and K_a is the air kerma free in air, in the point of test, when there is no phantom. Hence, the response, R_{PMMA} and R_{ISO} of the TL dosimeters was calculated by the ratio of measured and reference values.

III. Results and Discussion

The influence of ISO water phantom and PMMA slab phantom on Panasonic type of TLD cards UD-808 is verified at different photon energies. The response and correction factor obtained in this study for these two types of phantom is presented in **Table 2**. The measuring uncertainty of TLDs associated with the different calibration factors are 3.43 % for N_{PMMA} and 2.89 % for N_{ISO}. K'_P uncertainty was 1.50 %[14] and the uncertainty for air kerma reference measurement was 1.16 %. For TLDs, the mean value of ratio of response between PMMA and ISO phantom in the energy range of 35.94 keV to 662 keV was 1.01 ± 0.04 with measuring uncertainty of 3.59 %. This result indicates in general a good agreement within uncertainties between the two calibrations. **Fig. 3** shows the response of TLDs on PMMA and ISO phantom at different photon energies. It is observed that at lower energies, backscattering factor (BSF) dominates due to PMMA material which leads higher response. The tendency of response apparently turned to the opposite in the range from 143.8 to 178.84 keV. This tendency depends on the energy of photon and its qualities. It is found that the ratio of responses of PMMA slab (K'_P applied) and ISO water phantom varies from 0.97 to 1.09. It is also seen that at energy above 42 keV the response on PMMA and ISO water phantom meets a good agreement in radiation protection practice. The experimental result in **Table 2** shows that the relative BSF value of PMMA to ISO water slab phantom lies in the range between 1.00 and 1.17. The discrepancies of BSF values were found to be within 8 % compared to MCNP generated BSF values[8].

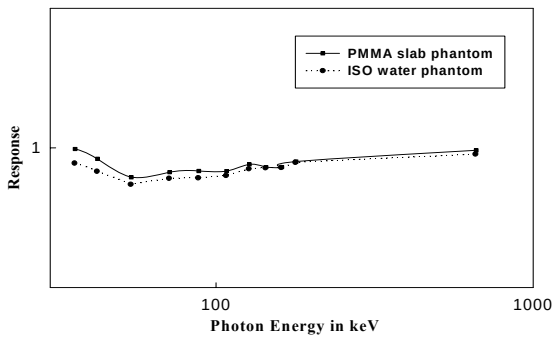

Fig. 3 Response of TLDs on two different phantoms

The peak deviations of BSF values are 7.7 % and -5.2 % at 35.94 keV and 42.28 keV, respectively. Above 42 keV the values meets a very good agreement with the MCNP data. However, the result found in this study shows a satisfactory agreement with other calculated and measured values by different author Traub *et al.*[8], Schauer *et al.*[15], and Grosswendt[16] above 42 keV.

Table 2 Response ratio of TLDs on PMMA slab (K'_P applied) and ISO water phantom and PMMA BSF to ISO phantom

Radiation quality	Photon energy in keV	TLD response R_{PMMA}	TLD response R_{ISO}	R_{PMMA}/R_{ISO}	Relative BSF for PMMA to ISO	MCNP generated BSF[8]
M50	**35.94**	**0.914**	**0.842**	**1.09**	**1.17**	**1.08**
M60	**42.28**	**0.815**	**0.766**	**1.06**	**1.15**	**1.09**
M75	**54.03**	**0.663**	**0.659**	**1.01**	**1.08**	**1.08**
M100	**71.37**	**0.707**	**0.706**	**1.00**	**1.07**	**1.07**
M125	**88.27**	**0.726**	**0.710**	**1.02**	**1.08**	**1.05**
M150	**108.06**	**0.733**	**0.729**	**1.01**	**1.05**	**1.04**
M175	**127.46**	**0.796**	**0.788**	**1.01**	**1.05**	**1.04**
M200	**143.8**	**0.773**	**0.797**	**0.97**	**1.01**	**1.03**
M225	**161.28**	**0.777**	**0.800**	**0.97**	**1.00**	**1.03**
M250	**178.84**	**0.831**	**0.849**	**0.98**	**1.01**	**1.02**
Cs-137	**662**	**0.954**	**0.934**	**1.02**	**1.04**	**1.01**

IV. Conclusions

The result shows that TLD response with PMMA and ISO phantom observed is not significant in radiation protection practices but at lower energy some discrepancies are reported. PMMA slab phantom has a larger BSF value at lower energy indicates that correction factor need to be apply while using this phantom for personal dosimeter calibration. As the correction factor (K'_P) of PMMA to ICRU tissue is applied, the ratio of response between two phantoms are good in agreement It is observed that at higher energy i.e., 143 keV or above, the BSF between PMMA slab and ISO water phantom is not significant in the radiation protection view point. However, the backscatter measurements between two different phantoms reported in this study indicates that differences are small and considered to be insignificant. The result obtained could be applied to the calibration of individual TL dosimeter when using PMMA phantom. The ICRU recommendation to use a PMMA slab in order to achieve uniformity in calibration procedures is also supported by these results.

Acknowledgement

The author would like to express their sincere thanks to the staffs of the radiation protection division, JAEA (Former JNC) for their cordial help in performing the experiment. This work is partly supported by the Korea Science and Engineering Foundation (KOSEF) through a grant provided by the Korean Ministry of Science & Technology (MOST) in 2007 (Project No. M2 07B0900-10810).

References

1) ICRU, “Determination of Dose equivalents resulting from external sources”, ICRU report 39, Bethesda, Maryland (1985).
2) ICRP, "Conversion coefficients for use in radiological protection against external radiation", ICRP Publication 74, Annals of the ICRP Vol. 26 no. 3-4. Pergamon Press, Oxford (1996).
3) IAEA, "Calibration of radiation protection monitoring instruments", Safety Report Series-16, IAEA, Vienna (1999).
4) ICRU, "Measurements of dose equivalents from external photon and electron radiation", ICRU Report 47, Bethesda, Maryland (1992).
5) ISO, "X-ray and gamma reference radiations for calibrating dosimeters & dose rate meters and for determining their response as a function of photon energy, Part-3", ISO 4037-3, Geneva (1999).
6) NVLAP, "National Voluntary Laboratory Accreditation Program bulletin," Dosimetry, Vol. II, No 1., January (1995).
7) HPS, "Personnel Dosimetry Performance—Criteria for Testing" McLean, Virginia, ANSI/HPS N13 11: Health Physics Society (1993).
8) R. J. Traub, J.C. McDonald, and M.K. Murphy, "Determination of photon backscatter from several calibration phantoms". Radiat. Prot. Dosim. 74, 13–20 (1997).
9) H. M. Kramer, J. Böhm, W. J. Iles and I. M. G. Thompson, "On the current status of an ISO working document on the calibration and type Testing of radiation protection dosimeters for photons," Radiat. Prot. Dosim. 54, 267-272 (1994).
10) R. F. Nelson, and A. B. Chilton, "low-energy photon dose deposition in tissue slab and spherical phantoms". Report NUREG/CR-3425 (Washington, DC;US NRC (1983).
11) D. T. Bartlett, P. J. Dimbylow, and T. M. Francis, "Calculated backscatter from phantoms for photon dosimeter calibration," Radiat. Prot. Dosim. 32, 123-125 (1990).
12) B. Grosswendt, "Conversion factors for the IAEA cube phantom for external photon irradiation," Radiat. Prot. Dosim. 29, 177-182 (1989).
13) J. Bohm and B. Grosswendt, "10 years of intercomparison measurements of dosimeter systems for the individual monitoring of photon and beta radiation- retrospective view, new data and perspective". PTB-mitt. 99, 107-118 (1989).
14) B. Grosswendt, "The angular dependence and irradiation geometry factor for the dose equivalent for photons in slab phantom of tissue equivalent material and PMMA," Radiat. Prot. Dosim. 35, 221-235 (1991).
15) D. A. Schauer, J. R. Cassata, and J. J. King, Radiat. Prot. Dosim. 88, 319-321 (2000).
16) B. Grosswendt, "Conversion coefficients for calibrating individual photon dosimeter in terms of dose equivalents defined in an ICRU tissue cube and PMMA slabs," Radiat. Prot. Dosim.32, 219-231 (1990).

Journal of NUCLEAR SCIENCE and TECHNOLOGY, Supplement 5, p. 268–270 (June 2008)

Evaluation of Self-Absorbed Doses for the Kidneys of a Voxel Mouse

Sakae KINASE*, Masa TAKAHASHI, and Kimiaki SAITO

Japan Atomic Energy Agency, 2-4 Shirane, Shirakata, Tokai-mura, Naka-gun, Ibaraki 319-1195, Japan

Kidney dosimetry in mice is of considerable significance in preclinical studies of new radiopharmaceuticals. There has been a gradual accumulation of kidney dosimetry data in mouse studies. However, a comprehensive understanding of the kidney dosimetry is still lacking. To conduct reliable kidney dosimetry, there exists a need to evaluate self-absorbed fractions (self-AFs) for sophisticated models of the kidneys. In the present study, self-AFs for photons and electrons in the kidneys of a voxel mouse were evaluated using Monte Carlo simulations. The sources were assumed to be monoenergetic in the energy range 10 keV-4 MeV, and be uniformly distributed in the kidneys. The self-AFs for the kidneys of the voxel mouse were compared with those for voxel humans. In addition, self-S values (μGy/MBq·s) for ^{18}F and ^{90}Y of potential interest in the kidney dosimetry were assessed using the self-AFs. It was found that the photon self-AFs for the voxel mouse are significantly smaller than those for the voxel humans and that the electron self-AFs for the voxel mouse are consistent with those for the voxel humans in the energy range 10 - 100 keV, followed by a sharp fall. The self-S values for the voxel mouse were found to be much larger than those for the voxel humans.

KEYWORDS: mouse, kidney, dosimetry, AF, S value, voxel, Monte Carlo simulation, interspecies scaling

I. Introduction

Small animal dosimetry is indispensable for developing new radiopharmaceuticals for use in nuclear medicine diagnosis or treatment. The dosimetry should be made as exactly as possible since the dose-response relationships in the animals such as mice would be translated to those in humans. In particular, kidney dosimetry in mice is of considerable significance from the viewpoint of kidney toxicity. Various studies have been conducted on the kidney dosimetry in mouse studies[1-7]. The point-kernel convolution method[1-3] and the Monte Carlo method[4-7] were applied to the kidney dose evaluations. A stylized mouse phantom[1-4] using ellipsoids, spheroids and cylinders was offered to evaluate absorbed fractions (AFs) -the fraction of energy emitted as a specified radiation type in the source organ is absorbed in the target organ- and S values (μGy/MBq·s) - mean absorbed dose to a target organ per unit cumulated activity in the source organ- for the kidneys. Recently voxel mouse phantoms[5-7] based on computed tomography (CT) and magnetic resonance imaging (MRI) data were offered to improve these evaluations. However, to our knowledge, there have been few efforts to evaluate kidney dosimetry data using both voxel mouse and Monte Carlo method. To conduct reliable kidney dosimetry, it is necessary to evaluate self-AFs and self-S values for a voxel model of the kidneys using Monte Carlo simulations.

It was the objective of the present study to provide data relevant to the kidney dosimetry in a voxel mouse using Monte Carlo simulations. Self-AFs for photons and electrons in the kidneys of a voxel mouse were evaluated and were compared with those for voxel humans, in order to discuss the interspecies scaling. In addition, self-S values for ^{18}F and ^{90}Y of potential interest in the kidney dosimetry were assessed using the self-AFs.

*Corresponding Author, E-mail:kinase.sakae@jaea.go.jp

II. Materials and Methods

1. Voxel Phantoms

Three voxel phantoms were used: the male mouse "Digimouse" [8], the adult male human "Otoko" [9], the adult female human "Onago" [10]. Digimouse was constructed from co-registered micro-CT and colour cryosection data of a normal nude male mouse. The voxel mouse was developed at the University of Southern California. The voxel size is $0.1\times0.1\times0.1$ mm^3. The Otoko and Onago phantoms were constructed from CT data of real Japanese human bodies. The voxel humans were developed at the Japan Atomic Energy Agency. The voxel size is $0.98\times0.98\times10.0$ mm^3. The masses of the kidneys for the phantoms are shown in **Table 1**. It can be seen, that there are differences between the kidney masses of the Digimouse, Otoko and Onago phantoms.

Table 1 Comparison of the kidney masses for the Digimouse, Otoko and Onago phantoms

Phantoms	Kidney (kg)
Digimouse	**5.1×10^{-4}**
Otoko	**2.7×10^{-1}**
Onago	**2.6×10^{-1}**

2. Absorbed fractions

Self-AFs for photons and electrons in the kidneys were evaluated for Digimouse, Otoko and Onago phantoms using the Monte Carlo code, EGS4[11], in conjunction with an EGS4 user code, UCSAF[12]. In the EGS4-UCSAF code, the radiation transport of electrons, positrons and photons in the phantoms was simulated, and correlations between primary and secondary particles are included. In the present study, the source of the photons and electrons were assumed to be

monoenergetic in the energy range from 10 keV to 4 MeV and uniformly distributed in the kidneys. Photon and electron histories were run at numbers sufficient to reduce statistical uncertainties below 5%. The cutoff energy was set to 1 keV for both the photons and electrons. The Parameter Reduced Electron-Step Transport Algorithm (PRESTA) [13] to improve the electron transport in the low-energy region was used. The cross-section data for photons were taken from PHOTX[14,15] and the data for electrons are taken from ICRU report 37[16]. No variance reduction technique was used.

3. S values

Self-S values for the kidneys were calculated for Digimouse, Otoko and Onago phantoms using the results of the self-AFs for both photons and electrons. The nuclides considered were ^{18}F and ^{90}Y of potential interest in the kidney dosimetry. **Table 2** shows the maximum and mean energies for ^{18}F and ^{90}Y. The self-AFs were converted into the self-S values considering the masses of the kidneys and the decay modes of the radionuclides. The self-AFs for electron were used for beta particle components. The self-AF for photon with energy 511 keV was used for two annihilation photons from ^{18}F. The decay mode for ^{18}F was assumed to consist only of the main branching since a few percentages branching for the decay mode would be insignificant for the self-S value evaluation. The beta spectra for ^{18}F and ^{90}Y were extracted from DECDC[17].

Table 2 Maximum E_{max} and mean E_{mean} energies for ^{18}F and ^{90}Y

Nuclides	E_{max} (MeV)	E_{mean} (MeV)
^{18}F	0.634	0.250
^{90}Y	2.281	0.934

III. Results and discussion

1. Absorbed Fractions

Fig. 1 shows the self-AFs for photons in the kidneys of the Digimouse, Otoko and Onago phantoms in the energy range from 10 keV to 4 MeV. The self-AFs decrease with an increase in photon energy on the whole. From a comparison with the results it can be stated that the self-AFs for the Digimouse phantom are close to those for the Otoko and Onago phantom in the low-energy region, but the large deviations are exhibited in the high-energy region. The self-AFs for the Digimouse phantom are significantly smaller than those for the Otoko and Onago phantoms. This is due to the different shape and size of the kidneys. Since the mean free path of the photon with low-energy is not large compared with the size of the kidney in the Digimouse phantom, low-energy photons could not be considered "pure" penetrating for the dosimetry. This fact means that the interspecies scaling is no longer simple.

The self-AFs for electrons in the kidneys of the Digimouse are shown in **Fig. 2**. The self-AF for the Digimouse is almost unity in the electron energy range from 10 keV to 100 keV, followed by a sharp fall. This result indicates that electrons with energies above 100 keV should be treated as penetrating radiation for the kidney dosimetry in mice. For the kidneys in small animals such as mice, all electrons are not always absorbed within the kidneys that emit them. **Fig. 2** also shows that the electron self-AFs for the Digimouse are inconsistent with those for the Otoko and Onago phantoms in the higher energy region. The apparent inconsistency is attributable to the different size of the kidneys.

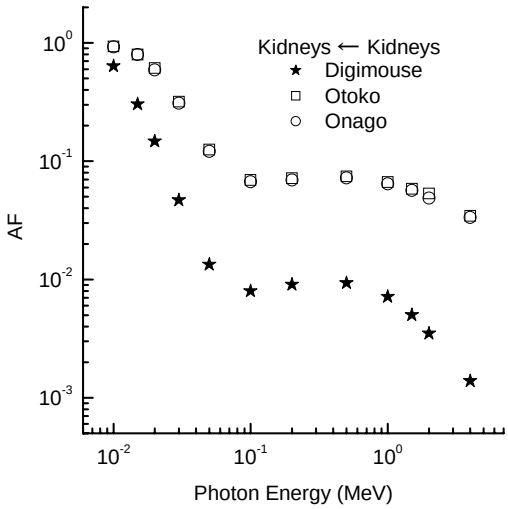

Fig. 1 Self-AFs in the kidneys for the Digimouse, Otoko and Onago phantoms in the photon energy 10 keV-4MeV.

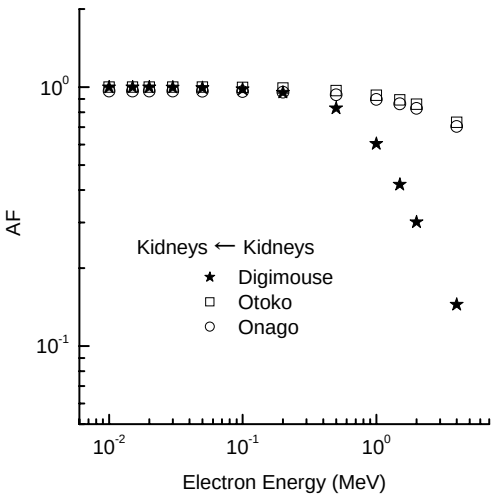

Fig. 2 Self-AFs in the kidneys for the Digimouse, Otoko and Onago phantoms in the electron energy 10 keV-4MeV.

2. S Values

Fig. 3 shows the self-S values for the kidneys of the Digimouse, Otoko and Onago phantoms, for ^{18}F and ^{90}Y. It can be seen that, as expected, the self-S values for the Digimouse phantom are much larger than those for the Otoko and Onago phantoms. For ^{18}F, the self-S value for the Digimouse phantom is 380 times as large as that for the Otoko phantom. This is, as already known, due to the different masses of the organs. In the figure, the self-S values for the Digimouse phantom on linear basis using the

multiplicative factor (linear mass scaling) against the Otoko phantom are also shown. The corrected self-S value for ^{18}F is 0.7 times as small as that for the Otoko phantom. It would appear that linear mass scaling is not necessarily appropriate.

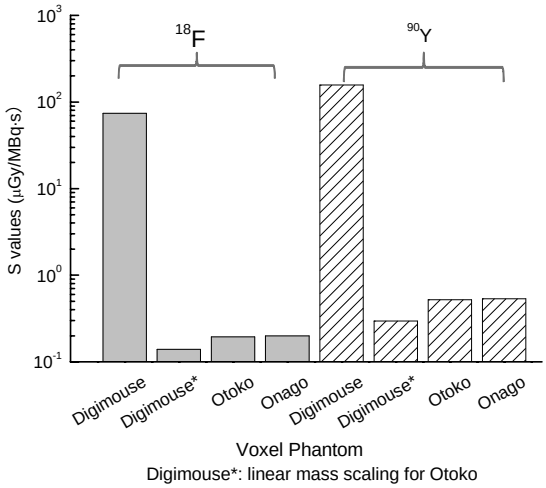

Fig. 3 Self-S values for ^{18}F and ^{90}Y in the kidneys of the Digimouse, Otoko and Onago phantoms, respectively.

IV. Conclusions

The self-AFs for photons and electrons in the kidneys of a voxel mouse and two voxel humans were evaluated using Monte Carlo simulations in the energy range from 10 keV to 4 MeV. Furthermore, the self-S values for ^{18}F and ^{90}Y in the kidneys of the voxel phantoms were evaluated using the obtained self-AFs. It was found that the photon self-AFs for the voxel mouse are significantly smaller than those for the voxel humans and that the electron self-AFs for the voxel mouse are inconsistent with those for the voxel humans in the high-energy region above 100 keV. The self-S values for the voxel mouse were found to be much larger than those for the voxel humans. The results confirm the conventional wisdom that there seems to be no scaling procedure which is approximately correct for all energies of particles and masses of organs as MIRD Pamphlet No.11 stated[18].

Acknowledgments

We wish to express our sincere thanks to Dr. Dogdas and Prof. Leahy for allowing us to use the Digimouse.

References

1) T. E. Hui, D. R. Fisher, J. A. Kuhn, L. E. Williams, C. Nourigat, C. C. Badger, B. G. Beatty and J. D. Beatty, A mouse model for calculating cross-organ beta-doses from yttrium-90-labeled immunoconjugates. *Cancer* 73, 951-957 (1994).
2) A. A. Flynn, A. J. Green, R. B. Pedley, G. M. Boxer, R. Boden and R. H. J. Begent, A mouse model for calculating the absorbed beta-particle dose from ^{131}I- and ^{90}Y-labeled immunoconjugates, including a method for dealing with heterogeneity in kidney and tumor. *Radiat. Res.* 156, 28-35 (2001).
3) K. S. Kolbert, T. Watson, C. Matei, S. Xu, J. A. Koutcher and G. Sgouros, Murine S factors for liver, spleen, and kidney, *J. Nucl. Med*. 44, 784-791 (2003).
4) C. Hindorf, M. Ljungberg and S-E. Strand, Evaluation of parameters influencing S values in mouse dosimetry. *J. Nucl. Med*. 45, 1960-1965 (2004).
5) M. G. Stabin, T. E. Peterson, G. E. Holburn and M. A. Emmons, Voxel-based mouse and rat models for internal dose calculations, *J. Nucl. Med*. 47, 655-659 (2006).
6) A. Bitar, A. Lisbona, P. Thedrez, C. S. Maurel, D. L. Forestier, J. Barbet and M. Bardies, A voxel-based mouse for internal dose calculations using Monte Carlo simulations (MCNP). *Phys. Med. Biol.* 52, 1013-1025 (2007).
7) R. Taschereau and A. F. Chatziioannou, Monte Calro simulations of absorbed dose in a mouse phantom from 18-flurorine compounds. *Med. Phys*. 34, 1026-1036 (2007).
8) B. Dogdas, D. Stout, A. F. Chatziioannou and R. M. Leahy, Digimouse: a 3D whole body mouse atlas from CT and cryosection data. *Phys. Med. Biol.* 52, 577-587 (2007).
9) K. Saito, A. Wittmann, S. Koga, Y. Ida, T. Kamei, J. Funabiki and M. Zankl, Construction of a Computed Tomographic Phantom for a Japanese Male Adult and Dose Calculation System, *Radiat. Environ. Biophys*. **40**, 69-76 (2001).
10) K. Saito, S. Koga, Y. Ida, T. Kamei and J. Funabiki, Construction of a voxel phantom based on CT data for a Japanese female adult and its use for calculation of organ doses from external electrons. *Jpn. J. Health Phys*. (in press).
11) W. R. Nelson, H. Hirayama and D. W. O. Rogers, The EGS4 Code System, SLAC-265 (1985).
12) S. Kinase, M. Zankl, J. Kuwabara, K. Sato, H. Noguchi, J. Funabiki and K. Saito, Evaluation of Specific Absorbed Fractions in Voxel Phantoms using Monte Carlo Simulation, *Radiat. Prot. Dosim*. **105 (1-4)**, 557-563 (2003)
13) A. F. Bielajew and I. Kawrakow, The EGS4/PRESTA-II electron transport algorithm: Tests of electron step-size stability, Proceedings of the XII'th Conference on the Use of Computers in Radiotherapy 153-154 (Madison, WI:Medical Physics Publishing) (1997).
14) RSIC. DLC-136/PHOTX Photon Interaction Cross Section Library (contributed by National Institute of Standards and Technology) (1989).
15) Y. Sakamoto, Photon Cross Section Data PHOTX for PEGS4, KEK Proceedings 93-15, 77-82 (in Japanese).
16) ICRU. Stopping Powers for Electrons and Positrons. ICRU Report 37 (Bethesda, MD, USA: ICRU) (1984).
17) A. Endo, Y. Yamaguchi and K. Eckerman, Nuclear decay data for dosimetry calculation revised data of ICRP Publ.38. JAERI 1347 (2005).
18) W. S. Snyder, M. R. Ford, G. G. Warner and S. B. Watson, "S," absorbed dose per unit cumulated activity for selected radionuclides and organs, MIRD Pamphlet No.11 (New York, NY:Society of Nuclear Medicine) (1975).

Journal of NUCLEAR SCIENCE and TECHNOLOGY, Supplement 5, p. 271–274 (June 2008)

Simulation of the Mammography X-ray Spectrum

Chul-Young YI*, Kook Jin CHUN, Suck-Ho HAH, and Hyun-Moon KIM

Health Metrology Group, Korea Research Institute of Standards and Science, Doryong-Dong 1, Yuseong-Gu, Daejeon 305-340, Korea

The X-ray spectra from a dual track mammography X-ray tube were calculated by means of Monte Carlo method using PENELOPE. The simulation geometry was modeled realistically. The variation of the calculated spectral shapes with the anode material, tube voltage and inherent filtration was investigated. Comparison of our results with other experimental and theoretical works was made. Detailed procedure of the simulation was described.

KEYWORDS: Monte Carlo simulation, mammography X-ray, energy spectrum, PENELOPE, bremsstrahlung spectrum, low-energy X-ray, electron impact ionization

I. Introduction

The X-rays are widely used in various fields of medicine, industry, research and academy. Mostly, the X-rays are generated from the conventional X-ray tube in which the accelerated electrons are incident on the target and emit bremsstralung photons along the passage. The characteristic X-rays are also created due to the electron impact ionization and the atomic shell ionization by bremsstrahlung photons. Resultantly, the X-ray energy is distributed to the maximum energy and accompanied by a series of the sharp peaks of the characteristic X-rays.

The evaluation of the X-ray energy distribution is a matter of importance in X-ray dosimetry. Some authors measured the X-ray energy spectrum using the Compton spectrometer.[1-3] The diffraction spectrometer was employed to measure the X-ray energy distribution.[4,5] In the measurement of the mammography X-rays, the CdZnTe spectrometers have been introduced recently.[6-8] In any case, special devices are required to measure X-ray energy spectrum with reasonable accuracy.

In the meantime, Birch and Marshall, Boon, Tucker *et al*., and Blough *et al*. predicted the X-ray energy spectra using the semi-empirical model.[9-12] Many authors had recourse to the Monte Carlo method in estimating the X-ray spectra.[13-17] The semi-empirical models give the fast result but have limitations in application[18]. With the computing power greatly enhanced these days, the Monte Carlo simulation is becoming more practical.

In the present study, the mammography X-ray spectra were obtained by means of Monte Carlo simulation using PENELOPE 2003[19,20]. The results were compared with other calculated and measured spectra. The details of the calculation were also described and discussed.

II. Method

1. Simulation Geometry

The materials and dimensions of the dual target mammography tube were modeled as specified by the manufacturer. The target materials were selected to either molybdenum or rhodium during simulation. The target angle to the beam axis was 10 degree with the focal spot size of 0.3 mm. The diameter of the target disk was 70 mm. The window was made of beryllium with the thickness of 0.69 mm.

The simulation geometry is shown in **Fig. 1**. The reference point to record the photon spectrum was placed at a distance of 1.0 m from the focal spot.

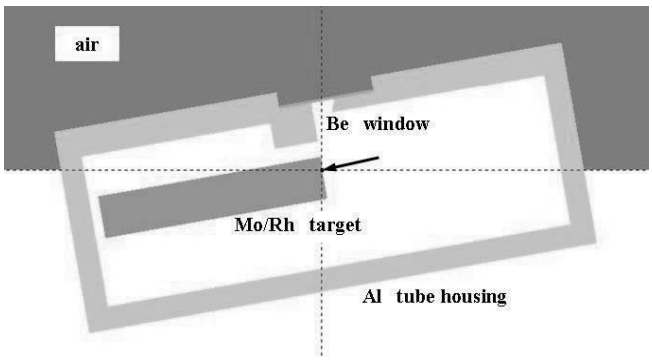

Fig. 1 The geometry modeled for the simulation of the mammography X-ray spectrum. The arrow marks the incident direction of the electron.

2. Simulation Procedure

In PENELOPE[19], the electron history consists of a chronological succession of events, which can be either hard events, artificial events (hinges) or other relevant stages of the particle history such as interface crossing and absorption. The trajectory of the electron between a pair of successive events is straight and referred to as a "segment". The term "step" is denoted to designate the portion of a track between two hard events, which consists of two segments and a hinge. The step length s to be traveled to the following hard event is sample as

$$s = -\ln \xi / \Sigma_h \quad (1)$$

where ξ is the random number in the range 0 – 1 and Σ_h the inverse mean free path for the hard events. When

*Corresponding Author, Tel. +82-42-868-5370, Fax. +82-42-868-5671, e-mail; cyyi@kriss.re.kr

$s > s_{\max}$, truncate the step by setting $s = s_{\max}$ with $s_{\max}$ being the maximum step length.

The kind of the hard event is selected according to the point probability

$$p_i = \sigma_i / \sigma_T \quad (2)$$

where σ_i stands for the interaction cross-section of the hard elastic scattering, the hard inelastic collision, the hard bremsstrahlung, the ionization of the inner shells and the delta ray interaction, and σ_T is the total interaction cross-section.

Since the radiation yields remain within a few tenths of a percent for the low-energy electron, calculation of the bremsstrahlung energy spectrum may be unacceptably time-consuming. To speed-up the calculation in the present study, additional events of the bremsstrahlung and the electron impact ionization were forced to occur after any hard interaction, in which the energy and direction of the electron were unaltered but those of the photon resulting from the additional events was determined as normal bremsstrahlung and electron impact ionization processes. The additional events were weighted by the bremsstrahlung and the electron impact ionization probabilities, respectively, for the incident electron.

The energy, direction and position of the photons generated in the passage of the electron were saved in memory and later they were used to obtain the mammography X-ray spectrum at the reference distance of 1.0 m from the focal spot in the target.

3. CdTe spectroscopy

The mammography X-ray energy spectra were measured with a 3×3×1 mm CdTe diode detector mounted on the thermoelectric cooler. On the cooler are the input FET feedback components to the charge sensitive preamp. The internal components are known to be kept at approximately -30 ºC and monitored by a temperature sensitive integrated circuit. The detector has a 250 μm Be window.

During the measurement, the detector surface was fixed at a distance of 1.0 m from the X-ray focal spot. To reduce the photon fluence rates incident on the detector, the tungsten collimator with the aperture diameter of 100 μm was used.

III. Results

The photon energy spectra created in the target are given in **Figs. 2** and **3**. The energy of the electron incident on the target was in the range from 20 to 35 keV. As expected from the bremsstrahlung event, the energy spectrum distributed continuously to the energy of the incident electron. The sharp peaks appeared in the figures were the characteristic X-rays mainly due to the electron impact ionization.

In **Fig. 4**, the photon energy spectra of the Mo target on the reference plane are presented as a function of the energy of the incident electron. As shown in the figure, the number of the low-energy photons decreased drastically because of the relatively large attenuation coefficients of the low-energy photons in the target, beryllium window and air.

The mean energy of the X-ray spectrum was evaluated as follows

$$E_{mean} = \frac{\int_0^{E_{\max}} \Phi_E \; E \; dE}{\int_0^{E_{\max}} \Phi_E \; dE} \quad (3)$$

where E_{mean} is the mean energy, $E_{\max}$ the maximum energy of the X-ray, Φ_E the derivative of the photon fluence $\Phi(E)$ of the photon with energy E with respect to the energies between E and $E + dE$.

Most of the mammography units are operated with the additional filtration using either Mo or Rh sheets. The thickness of the Mo added filter is typically 0.03 mm. The filtered X-ray spectra obtained from the simulation are given in **Figs. 5, 6** and **7** with the experimental and theoretical spectra.

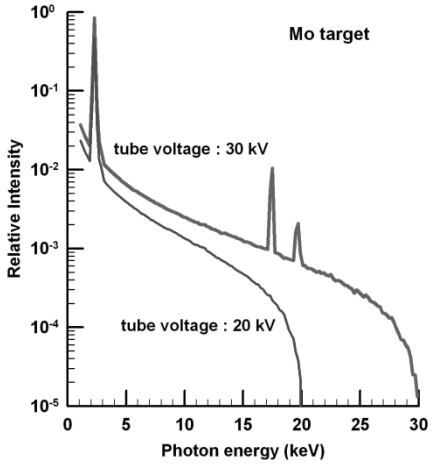

Fig. 2 Photon energy spectra created in the Mo target.

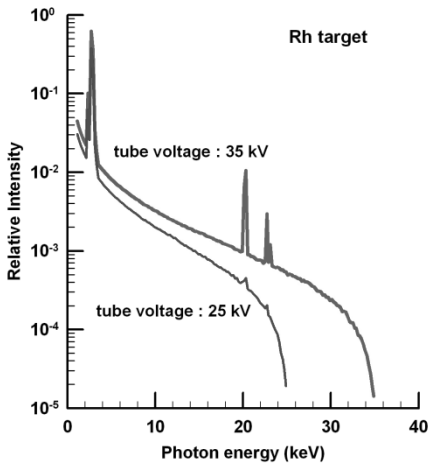

Fig. 3 Photon energy spectra created in the Rh target.

The deviation of the simulated spectrum from that measured by Miyajima and Imagawa[21] using the CdZnTe detector in Fig. 5 might come mainly from the difference of the target material. The target material of the mammography unit Miyajima and Imagawa[21] used was a compound of Mo and W. Due to the greater bremsstrahlung cross section of W atom, the number of X-rays generated in the target would be

increased but at the same time the increased self-absorption by the W atoms would reduce the low energy intensity. The geometrical difference of the measurement layout may aggravate the discrepancy further. It should be noted that the CdZnTe detector was placed at a distance of 38 cm from the focal spot. [21)]

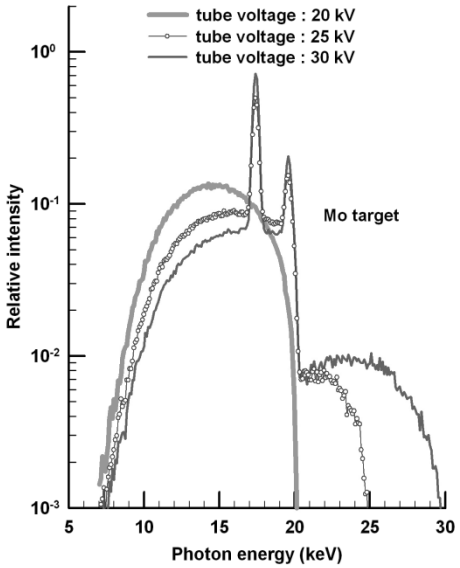

Fig. 4 Spectral variation of the mammography X-rays on the reference plane at a distance of 1.0 m from the focal spot of the Mo target.

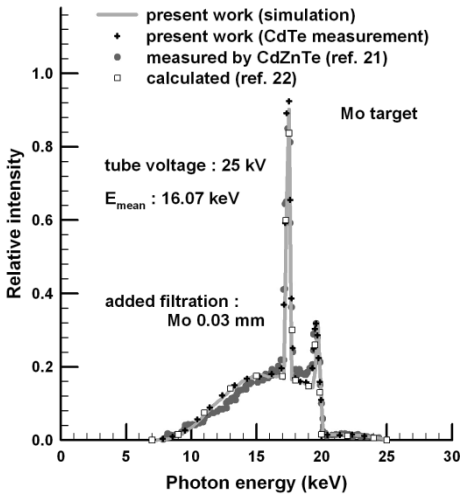

Fig. 5 Comparison of the simulated spectrum with the experimental and theoretical work.

Our measurement results by the CdTe detector agreed well with those simulated, which means that the spectral distortion of the CdTe detector was minor for the photon with energy ranged from 20 to 30 keV as found earlier by Matsumoto *et al.*[7)] for their CdZnTe detector.

The 17.5 keV characteristic X-ray intensity of the present work for the tube voltage of 30 kV were higher than those of others as shown in Fig. 6 but the mean energies of our mammography spectra agreed well within 2 % with other theoretical work,[22)] which were based on the semi-empirical model.[9)] In this theoretical scheme, the un-attenuated X-ray spectrum was deduced from the empirically modified differential bremsstrahlung cross section and the linear attenuation correction was made to the un-attenuated spectrum using the photon cross section data library of XCOM.[23)] For the Mo target, the X-ray spectrum can be produced with the tube potential ranged from 25 to 32 kV and target angles from 9 to 23 degree.

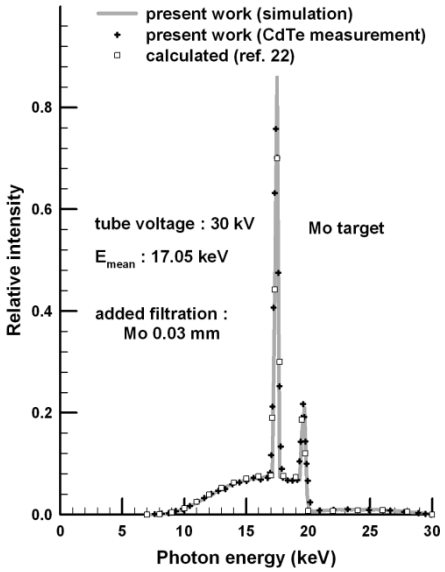

Fig. 6 Comparison of the simulated spectrum with the experimental and theoretical work (continued).

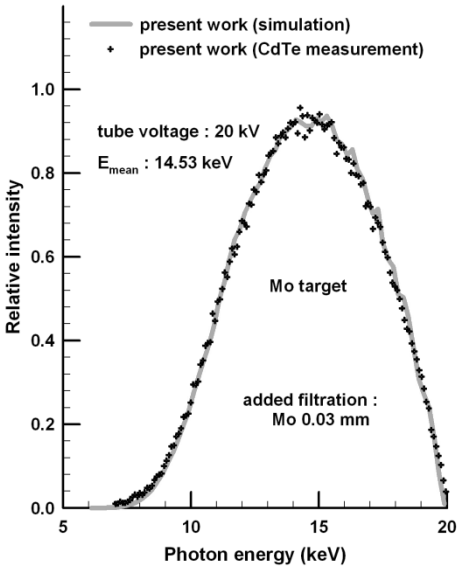

Fig. 7 Comparison of the simulated spectrum with that measured by the CdTe detector.

IV. Conclusion

In the present study, the energy distributions of the mammography X-rays were calculated using a Monte Carlo code PENELOPE 2003. To calculate the spectrum more efficiently, the events of the bremsstrahlung and the electron impact ionization were forced to accompany any hard interaction. The energy and direction of the electron were unaltered after the additional events. All the information

such as the energy, direction and space coordinates of the photons were saved in memory and later they were used to obtain the mammography X-ray spectrum at the reference distance of 1.0 m from the focal spot in the target.

The simulated spectra were in good agreement with other experimental and theoretical results. The average energies of the calculated mammography spectra agreed well with those of IPEM report 78 within a few percent. It was confirmed in the present study that the simulation routines for the mammography X-ray spectrum was successfully setup with PENELOPE package.

Acknowledgement

This work was supported in part by the research fund for the development of the nuclear energy granted by the Ministry of Science and Technology (MOST) and in part by the research fund granted by the Korea Food and Drug Administration (KFDA).

References

1) M. Yaffe, K. W. Talor, H. E. Johns, "Spectroscopy of diagnostic X-rays by a Compton-scatter method," *Med. Phys.*, **3**, 328 (1976).
2) G. Matscheko, R. Ribberfors, "A Generalized Algorithm for Spectral Reconstruction in Compton Spectroscopy with Corrections for Coherent Scattering," *Phys. Med. Biol.*, **34**, 835 (1989).
3) G. A. Carlsson, K. F. Berggren, C. A. Carlsson *et al.*, "The Compton Spectrometer," *Int. J. Quantum Chem.*, **35**, 721 (1989).
4) L. T. Hudson, R. D. Deslattes, A. Henins *et al.*, "A Curved Crystal Spectrometer for Energy Calibration and Spectral Characterization of Mammographic X-ray Sources," *Med. Phys.*, **23**, 1659 (1996).
5) J. M. Boone, T. Yu, A. Seibert, "Mammography Spectrum Measurement Using an X-ray Diffraction Device," *Phys. Med. Biol.*, **43**, 2569 (1998).
6) E. Di. Castro, R. Pani, R. Pellegrini *et al.*, "The Use of Cadmium Telluride Detectors for the Qualitative Analysis of Diagnostic X-ray Spectra," *Phys. Med. Biol.*, **29**, 1117-1131 (1984).
7) M. Matsumoto, A. Yamamoto, I. Honda *et al.*, "Direct Measurement of Mammographic X-ray Spectra Using a CdZnTe Detector," *Med. Phys.*, **27**, 1490 (2000).
8) S. Miyajima, K. Imagawa, "CdZnTe Detector in Mammographic X-ray Spectroscopy," *Phys. Med. Biol.*, **47**, 3959 (2002).
9) R. Birch, M. Marshall, "Computation of bremsstrahlung x-ray spectra and comparison with spectra measured with a Ge(Li) detector," *Phys. Med. Biol.*, **24**, 505 (1979).
10) J. M. Boone, "The three parameter equivalent spectra as an index of beam quality," *Med. Phys.*, **15**, 304 (1988).
11) D. M. Tucker, G. T. Barnes, D. P. Chakraborty, "Semiempirical model for generating tungsten target x-ray spectra," *Med. Phys.*, **18**, 211 (1991).
12) M. M. Blough, R. G. Waggener, W. H. Payne *et al.*, "Calculated mammographic spectra confirmed with attenuation curves for molybdenum, rhodium, and tungsten target," *Med. Phys.*, **25**, 1605 (1998).
13) R. N. Kulkarni, S. J. Supe, "Monte Carlo calculations of mammographic x-ray spectra," *Phys. Med. Biol.*, **29**, 185 (1984).
14) E. Acosta, X. Liovet, E. Coleoni *et al.*, "Monte Carlo simulation of x-ray emission by kilovolt electron bombardment," *J. Appl. Phys.*, **83**, 6038 (1998).
15) M. Bhat, J. Pattison, G. Bibbo *et al.*, "Off-axis x-ray spectra: a comparison of Monte Carlo simulated and computed x-ray spectra with measured spectra," *Med. Phys.*, **26**, 303 (1999).
16) X. Liovet, L. Sorbier, C. S. Campos *et al.*, "Monte Carlo simulation of x-ray spectra generated by kilo-electron-volt electrons," *J. Appl. Phys.*, **93**(7), 3844 (2003).
17) M. R. Ay, M. Shahriari, S. Sarkar *et al.*, "Monte Carlo simulation of x-ray spectra in diagnostic radiology and mammography using MCNP4C," *Phys. Med. Biol.*, **49**, 4897 (2004).
18) P. Meyer, E. Buffard, L. Mertz *et al.*, "Evaluation of the use of six diagnostic X-ray spectra computer codes," *Brit. J. Radiol.*, **77**, 224 (2004).
19) F. Salvat, J. M. Fernández-Varea, J. Sempau, *PENELOPE – A Code System for Monte Carlo Simulation of Electron and Photon Transport*, Workshop Proceedings, OECD Nuclear Energy Agency, France (2003).
20) J. Sempau, J. M. Fernández-Varea, E. Acosta *et al.*, "Experimental benchmarks of the Monte Carlo code PENELOPE," *Nucl. Instr. Meth. Phys. Res. B*, **207**, 107 (2003).
21) S. Miyajima, K. Imagawa, "CdZnTe detector in mammographic x-ray spectroscopy," *Phys. Med. Biol.*, **47**, 3959 (2002).
22) K. Cranley, B. J. Gilmore, G. W. A. Fogarty *et al.*, *Catalogue of diagnostic X-ray spectra and other data* (CD-Rom Edition 1997) (electronic version prepared by D. Sutton), IPEM Report 78, York: The Institute of Physics and Engineering in Medicine (IPEM) (1997).
23) M. J. Berger and J. H. Hubbell, *XCOM: Photon Cross Sections on a Personal Computer*, NBSIR 87-3597, National Bureau of Standards, Maryland (1987).

Journal of NUCLEAR SCIENCE and TECHNOLOGY, Supplement 5, p. 275–277 (June 2008)

Evaluation of Commercial Grade Ferrous Ammonium Sulfate as Potential Dosimeter for Technological Irradiations

J. Manuel JUAREZ-CALDERON, Sergio RAMOS-BERNAL, and Alicia NEGRON-MENDOZA*

Instituto de Ciencias Nucleares, Universidad Nacional Autónoma de México (UNAM), A.P. 70-543, México, D.F. México

In this work, we have studied the behavior of crystalline ferrous ammonium sulfate (FAS) under gamma irradiation. The doses studied ranged from 33.5 to 270 kGy. The purpose of this study is to explain the setup, measurement, and reporting procedures for using FAS as a dosimeter.

The results obtained in the present study show that this salt very easily gave reproducible results, a linear response, as well as, simple sample preparation and reading. The irradiation temperature and dose rate in the response of the iron salt were found to have slight influence. Any storage time up to 18 months resulted in a 36% decrease in the response. The variation in the response obtained for short periods of storage is negligible for this application. Due to the properties of the FAS system also can be use as transfer dosismeter.

KEYWORDS: Dosimetry, ferric ion, high dose, low temperature, ferrous ion, gamma irradiation, ferrous sulfate

I. Introduction

Many industrial applications utilizing ionizing radiation are now well established, as in food preservation, sterilization, the killing of fungi and microorganisms, the irradiation of semiconductors and electrical supplies. Such uses cover a large dose range from few grays (Gy) to over 10^6-10^7 Gy[1,2]. For these purposes, a reliable dosimetry method is fundamental to the quality assurance of the irradiated products.

Several high-dose dosimeters are adequate for radiation processing measurement purposes up to 15 kGy. However, for higher doses, almost all dosimetric systems present some disadvantages in their use, while the demand for proper dosimetry systems remains high[3]. Routine dosimeters are devices that are used on a daily basis to measure the radiation environment at gamma irradiation facilities. These dosimetric systems need to be easy to use, capable of rapid measurement, and cost-effective.

Such dosimeters must also be calibrated against primary or reference standard dosimeters[2]. Reference standard dosimeters are of high metrological quality and represent the highest quality dosimeters that are available for use in irradiation facilities. The optimal dosimeter will fulfill the traditional requirements of precision, dose-rate independence, and post-irradiation stability[4].

This study was based upon the radiation-induced decomposition of crystalline ferrous ammonium sulfate and ferrous sulfate in an underlying study by Johnson[5]. The products of the radiolysis were ferric ion, sulfite ion, and molecular hydrogen. Both the chemical effects and these products were analyzed by dissolving the solid in deaerated water.

*Corresponding Author, Tel.: 5255-56224674, Fax.: +5255-56162233, E-mail: negron@nucleares.unam.mx

We carried out a detailed study of ferrous ammonium sulfate in poly-crystal powder form, testing its possible use for very high dose dosimetry purposes. Basic properties, such as dose response and post-irradiation storage effect, were studied and the results are reported in this paper. This compound was irradiated under dose and dose rates conditions comparable to those used in the sterilization protocol at Instituto de Ciencias Nucleares (ICN), UNAM, as part of a program to evaluate dosimetry for the irradiation of commercial products.

II. Methodology

1. Chemicals and Sample Preparation

Poly-crystalline ferrous ammonium sulfate (FAS) in powder form was used in the present work as a hexahydrated salt ($Fe\ (NH_4)_2(SO_4)_2 \cdot 6H_2O$) 97 % purity without further purification.

Two types of samples were prepared: 1) a powder form within a glass flask and 2) a weighted amount in gelatin capsules.

2. Irradiation

The irradiations were performed at ICN-UNAM, in a cobalt-60 Gammabeam 651PT facility (Nordion Inc., Canada) with a nominal 2.96 x 10^{15} Bq (80, 000 Ci) activity. The absorbed doses were measured by using a ferrous sulfate-cupric sulfate dosimeter as a reference standard[6]. This dosimeter is a variation of the Fricke dosimeter with a higher upper limit of the dose. Dose rates at the samples location were 50.5. Gy/min at 295 K (room temperature) and 46 Gy/min at 77 K (liquid nitrogen). Other dose rate intervals tested were 159-239 Gy/min. Irradiation doses ranged from 33.5 to 270 kGy. Each set of three samples or capsules containing FAS and ferrous sulfate-cupric sulfate dosimeter solutions were irradiated at different dose rates and doses.

The irradiation of samples at different temperatures was conducted in a special device designed to maintain a precise temperature. The irradiation temperature region examined ranged from 77 K to 325 K, and used different cooling and heating systems: liquid nitrogen (77 K), and a cooling-heating liquid (Dynalene HC-50) for 263, 273, 295, 313 and 325 K. Three sets of samples were irradiated in glass flasks at a fixed position for each dose.

3. UV-Analysis

The irradiated ferrous ammonium sulfate was analyzed by preparing a solution of 2 x 10^{-3} M in 0.8 N sulfuric acid. The contents of the capsules were dissolved in 10 ml of an acid solution. The change of valence was measured spectrometrically at 304 nm. The analysis was conducted in a Carry 100 spectrophotometer. The temperature of the sample holder was in the range of 22-23 C. The molar extinction coefficient for ferric ion was 2160 $M^{-1}cm^{-1}$ at 22 C. The doses were based on the ferrous sulfate-cupric sulfate dosimeter at 22 C, under the assumption that 0.66 ferric ions are formed by each 100 eV absorbed in an air-saturated solution[6,7].

III. Results and Discussion

1. Dose Effect

Upon irradiation, the color of the salt changed from pale blue to dark yellow, indicating the oxidation of the ferrous ion. The radiochemical yield of ferric ion was calculated and found to be 0.0146 ± 0.00084 molecules per 100 eV, a value making it possible to use this salt for large doses.

A linear response was found between optical density and the dose (from 33.5 to 270 kGy), as shown in **Fig. 1.** Detailed investigations were carried out in the dose range of 6-270 kGy. The reproducibility of the measurement was better than ± 10 %, although somewhat larger variations were observed at lower doses. In relation to use of this salt for dose control in goods irradiated within our facilities, specifically in the range 6-12 kGy the results are satisfactory. The results were the same in gelatin capsules or in glass flasks.

The advantages of FES dosimeter is the stability of its response, its reproducibility, and linear behavior in the dose range studied, and it is made with commercial reagents.

The main disadvantage of the system is its poor response for doses lower than 5 kGy. The dose rate had no significant effect upon the response of the dosimeter between 159-239 Gy/min. The dose calculation can be made as follows:

$$D = \frac{N\Delta OD}{\varepsilon l \rho (1000) f G_{Fe3+}}$$

Where,
D in Gy
N = Avogadro's number
ΔOD optical density is at 304 nm
ρ Density of the solution, 1.024 g /mL
ε Molar extinction coefficient, 2160 L/mol• cm
l Cell length 1 cm
f conversion factor=6.24E15 eV/g•Gy

G_{Fe}^{3+} solid = 0.0146 ± 0.00084 molecules/100 eV

Taking into account 1kGy=1000 Gy, the equation for calculating the dose in kGy is:

$$D \approx 300\, OD \qquad (2)$$

2. Temperature Dependence

The effect of temperature variation within the 77 to 295 K range was measured (**Fig. 1**) a small temperature dependence during irradiation was found. The values obtained for samples irradiated at room temperature (295 K) are slightly higher in relation to those irradiated at 77 K probably due to the mobility of the intermediate species formed by irradiation, and because the diffusion of gases, like oxygen, in the frozen solid is slow.

3. Post-Irradiation Stability of Response

The post-irradiation storage effect was also measured (**Fig. 2**). The response of the dosimeter was measured for storage periods of 332 and 548 days, and correlated with a 20 and 36 % decrease in the response respectively. The samples were stored in the dark. For shorter periods, the variation in the response was found to be negligible for this application. For this reason, this system can be used as transfer dosimeter between different laboratories. Transfer dosimeters are stable systems suitable for mailing and upon analysis show a reproducible signal.

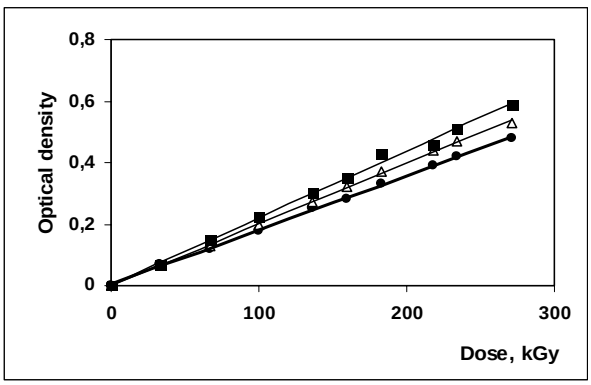

Fig. 1 The absorbance of ferric ion as a function of the dose. The irradiation temperatures were: ■ 295 K, Δ 263 K and ●77 K.

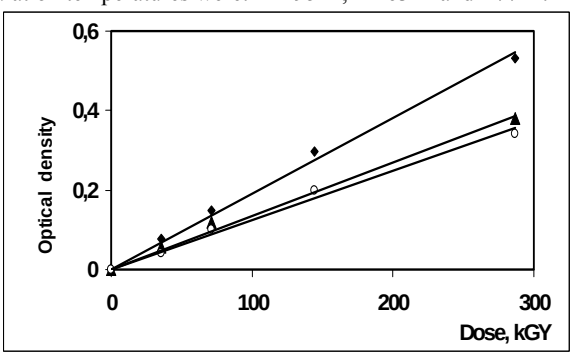

Fig. 2 The stability of the response of irradiated ferrous ammonium sulfate during post-irradiation storage in the dark and at room temperature. ♦ t=0, ▲ t=332 days, ○ t=548 days.

IV. Conclusions

Based upon the above discussions, we have found that ferrous ammonium sulfate (FAS) in powder form can be

used on a relatively wide range of applied doses. The use of commercial FAS as a routine dosimeter in a gamma irradiation facility has numerous advantages. It is very reproducible; it is also cost-effective and commercially available in large reproducible commercial batches, the analytical procedure for its determination is simple. Further, it has little temperature dependence and good stability toward environmental conditions. The stability of the response during post irradiation storage at the dark is good. The responses of irradiated samples 548 days of storage under ordinary conditions of humidity and temperature decrease about 36% and, for short periods of storage the change of the response is negligible. We have concluded that this salt may be used in many radiation-processing applications, and as transfer dosimeter.

Acknowledgement

This work was performed under the research program sponsored by UNAM, Grant DGAPA Grant IN223406-3. The authors thank C. Camargo, F. García, A. Vázquez, and S. Ham for their technical assistance. The authors are very gratefully with the reviewers for their valuable suggestion to our manuscript.

References

1) A. Wieser and D.F. Regulla, "Ultra high level dosimetry by ESR spectroscopy of crystalline quartz and fused silicate," Rad. Prot. Dosimetry, 34, 91, 1990.
2) B. L.Gupta, R.M. Bhat, G.R. Narayan, and S.R. Nilekani, "Chemical dosimetry techniques for various applications under different geometries," *Rad. Phys. Chem*., 59, 81, 2000.
3) ISO/ASTM E1261-94, "Guide for selection and calibration dosimetry systems for radiation processing," American Society for Testing and Materials, PA., USA, 1994.
4) W.L. McLaughlin, A.W Boyd, K.H Chadwick, J.C McDonald, and A. Miller, "Dosimetry for radiation processing," Taylor and Francis, 1989.
5) E.R., Johnson, "The radiation induced decomposition of ferrous ammonium sulfate," J. Phys. Chem., 78, 5196, 1956.
6) W.L. Mclaughlin, "Topics in radiation dosimetry", Instituto de Física, UNAM, Vol. 4 (2), México, 1981.
7) J.H O´Donnell and D.F. Sangster, "Principles of Radiation Chemistry," American Elsevier Publishing Company, United States, 1970.

Journal of NUCLEAR SCIENCE and TECHNOLOGY, Supplement 5, p. 278–281 (June 2008)

Establishment of Filtered X-ray Reference Radiation Based on ISO4037-1:1996 in CIRP

ZHANG Qingli*, HAN Minchen, HUANG Yawen, WEI Yingjing, and NIU Qiang

China Institute for Radiation Protection, Taiyuan, Shanxi, 030006, CHINA

According to the recommendations of ISO4037-1:1996, we have established the filtered x-ray reference radiation of low air kerma rate series (10 reference radiations), narrow spectrum series (13 reference radiations), wide spectrum series (7 reference radiations) and high air kerma rate series (8 reference radiations) in CIRP. The relevant calibration facilities, such as ISO water phantom, are also built for calibration practice. An Yxlon MG325 is used as x-ray generator. Totally 38 reference radiations are produced with tube voltage range from 15 kV to 300 kV. The characteristics, such as HVL (half value layer), for these reference radiations are investigated. They are well consistent with the recommendations of ISO and can be used for the calibration of dose & doserate meters for radiation protection purpose.

KEYWORDS: filtered x-ray radiation, half value layer

I. Introduction

In order to perform the calibration of dosimeters and doserate meters, and to determine their energy response, series of reference radiation fields with wide range of energy and doserate are needed. For the harmonization of standards in different countries, International Organization for Standardization (ISO) has revised ISO4037:1979 and published the ISO4037-1:1996[1)], ISO4037-2:1997[2)], ISO4037-3:1999[3)]. In this series of standards, 8 keV to 100 keV fluorescence x radiation, 7 keV to 250 keV continuous filtered x-ray radiation, 600 keV to 1.3 MeV gamma radiation, 4 MeV to 9 MeV gamma radiation are recommended for these purposes. The filtered x-ray radiations, totally 41 beam qualities, consist of low air-kerma rate series, narrow spectrum series, wide spectrum series and high air-kerma rate series with different spectrum resolution.

It is very important to establish the series of reference radiation based upon the recommendations of ISO4037-1: 1996 at China Institute for Radiation Protection (CIRP) that it is one of the five members of IAEA/WHO SSDL network in China. We have established the filtered x-ray reference radiations of low air kerma rate series, narrow series, wide series and high air kerma rate series, and made the measurement of beam qualities and uniformity of radiation field. The inverse square law has also been verified.

II. Production of X-ray Reference Radiations

The calibration facilities to produce the filtered x-ray reference radiation are shown in **Fig.1**. They consist of a x-ray unit, a main power stabilizer, a beam collimator and shutter, a additional filtration wheel selector, calibration cart & rail, ISO water slab phantom, ISO water pillar phantom, ISO PMMA rod phantom, a thermometer, a hygrometer, a barometer, 3 laser positioning units, a closed circuit television unit with controlled camera and monitor, safety interlock unit and main control console. The main computer on the console can control the moving of beam shutter and the moving of calibration table along X-Y-Z axis. Also the calibration table can rotate 360° around Z axis. The accuracy of positioning is less than 0.5 mm.

1. Outline and Specification of X-ray Generator

An Yxlon MG325 is used as x-ray generator. It consists of ±160 kV high-voltage generator, power unit, range selector, temperature compensation unit, control unit, x-ray tube and cooler. The model of x-ray tube is YTU/320-D03, a metal-ceramic tube with dual focus spot 3.0 mm/5.5 mm. The target of the tube is made of tungsten. It is reflection type target with the target angle of 21º and emergent beam angle of 40º. Its output window is made of beryllium with the thickness of 3mm. The tube potential & current can be set by the thumbwheel on control unit with step of 0.2 kV & 0.01 mA. The adjustment range of high voltage is 15 kV-320 kV and the accuracy of high voltage is ±1% of demand value ± 0.2 kV. The adjustment range of tube current is 0-22.5 mA and the accuracy of tube current is ±0.2% of demand value ± 0.01 mA. With compensation unit, the temperature drift of high voltage and tube current can reach to 30 ppm/℃. The range selector is used to extend the tube current from 22.5 mA to 45 mA.

2. Additional Filtration

The total filtration consists of inherent filtration and additional filtration. Inherent filtration is caused by the various elements, such as output window, oil and so on. For the production of reference radiation series, the series of combinations of tube potential and additional filtration are recommended by ISO. Additional filters consist of the metal plates with different thickness of aluminum, copper, tin and

*Corresponding Author, Tel.: +86-351-2203461, Fax.: +86-351-7020407, E-Mail: zhangqing_li@sina.com

lead with the purity not less than 99.9%. Correspond to the four series of reference radiation, the 38 combinations of additional filter are mounted on a rotary wheel which can be controlled by main computer in CIRP.

Fig. 1 The Photo of Filtered X-ray Calibration Facilities

III. Characteristics of X-ray Reference Radiation

According to the ISO recommendations, we have built the filtered reference radiations of low air kerma rate series, narrow spectrum series, wide spectrum series and high air kerma rate series. In general, the beam qualities are used to describe the characteristics of these reference radiations. The beam qualities of reference radiation consist of tube voltage, first & second half value layer (HVL), homogeneity, uniformity of radiation field, and so on.

For the measurement of beam qualities of these filtered x-ray radiations with energy range from 10 keV to 250 keV, we used ionization chamber PTW M23361 (30 ml), PTW M2337 (1000 ml) and PTW M23332 (0.6 ml) and PTW DI4/DL4 dosimeter. These chambers are traced to national standard at National Institute of Metrology, China.

For the measurement of 1st & 2nd HVL, we use a number of aluminum and copper foil absorbers, which can be set in a desired thickness. The purity of these absorbers is not less than 99.9%. By measuring attenuation curve for different reference radiations with these aluminum and copper absorbers and the above mentioned ionization chambers, we can obtain the 1st & 2nd HVL of these reference radiations.

The 1st & 2nd HVL of these reference radiations are listed in **Table 1**, together with the homogeneity and relevant recommended values of ISO4037-1:1996.

The homogeneity of these reference radiations, 1st HVL /2nd HVL, ranges from 0.88 to 1.00 for narrow series, from 0.85 to 0.97 for wide series and from 0.64 to 0.84 for high air kerma rate series. In ISO4037-1:1996, the values of recommended homogeneity are from 0.75 to 1.0 for narrow series, from 0.67 to 0.98 for wide series and from 0.64 to 0.86 for high air kerma rate series.

By comparing the HVL of reference radiations of CIRP with ISO, it can be seen that the most of our measurement HVL are well consistent with the ISO recommendations, except for some points, such as L30, H20, H30. The reason for these dissimilarities is the difference of inherent filtration between CIRP and ISO x-ray generators. The inherent filtration of 1 mm beryllium is required for 30 kV & below reference radiations of narrow spectrum series and low air kerma rate series in ISO4037-1:1996. Whereas the window of our x-ray tube YTU/320-D03 is made of 3 mm beryllium. The inherent filtration of 4 mm beryllium is required for 100 kV & below of high air kerma rate series in ISO4037-1:1996. The inherent filtrations for all others are required 4mm aluminum at 60 kV. So MG325 and YTU/320-D03 can not meet the requirements of ISO for production of low energy reference radiations. And more about filtration, the additional filters that we have used to produce reference radiations cannot be made exactly same with the recommendations for some kVs. It is difficult to construct the filters with thickness same as ISO recommendations, especially when the thickness is small.

It can be seen that the HVL are larger than the one of ISO4037-1:1996 for reference radiations with tube voltage above 200 kV. Beside the total filtration, the difference of irradiation geometry between CIRP and ISO can also result in the deviation of HVL from ISO recommendation. According to E.D. Trout[4] who made the detail investigation on the variation of HVL with diameter of irradiated filter, with focal-filter and focal-chamber distances, the more detail investigation will be done.

With ionization chamber PTW M23332, we check the uniformity of radiation field at the distance of 3 meters. The variation of doserate is less than 5% which can meet the requirement of ISO.

The inverse square law of doserate has been verified and the variation is less than 4% within the distance of 5 meters between focal spot and ionization chamber after the correction of air absorption.

IV. Conclusions

We have established of x-ray reference radiations based upon the recommendations of ISO4037-1:1996 for low air kerma rate series (10 reference radiations), narrow series (13 reference radiations), wide series (7 reference radiations) and high air kerma rate series (8 reference radiations). The investigation of the characteristics of the reference radiations shows that these reference radiations are well consistent with

Table 1: The Comparison of Some Beam Qualities between ISO and CIRP for Reference Radiation Series

Reference Radiation Series	Tube Voltage kV	1st HVL (mmCu)		2nd HVL (mmCu)		Homogeneity	
		ISO	CIRP	ISO	CIRP	ISO	CIRP
Low air kerma rate series (10)	L20	0.42 Al	0.42 Al				
	L30	1.46 Al	1.58 Al				
	L35	2.20 Al	2.21 Al				
	L55	0.25	0.24				
	L70	0.49	0.47				
	L100	1.24	1.22				
	L125	2.04	2.02				
	L170	3.47	3.45				
	L210	4.54	4.61				
	L240	5.26	5.29				
Narrow spectrum series (13)	N15	0.14 Al	0.15 Al	0.16 Al	0.17 Al	0.88	0.88
	N20	0.32 Al	0.36 Al	0.37 Al	0.38 Al	0.86	0.95
	N25	0.66 Al	0.66 Al	0.73 Al	0.71 Al	0.90	0.93
	N30	1.15 Al	1.14 Al	1.30 Al	1.25 Al	0.88	0.91
	N40	0.084	0.086	0.091	0.095	0.92	0.91
	N60	0.24	0.24	0.26	0.26	0.92	0.92
	N80	0.58	0.59	0.62	0.64	0.94	0.92
	N100	1.11	1.12	1.17	1.16	0.95	0.97
	N120	1.71	1.71	1.77	1.77	0.97	0.97
	N150	2.36	2.42	2.47	2.49	0.96	0.97
	N200	3.99	4.06	4.05	4.12	0.99	0.99
	N250	5.19	5.20	5.23	5.35	0.99	0.97
	N300	6.12	6.25	6.15	6.24	1.00	1.00
Wide spectrum series (7)	W60	0.18	0.19	0.21	0.22	0.86	0.86
	W 80	0.35	0.35	0.44	0.44	0.80	0.80
	W 110	0.96	0.96	1.11	1.13	0.86	0.85
	W 150	1.86	1.88	2.10	2.12	0.89	0.89
	W 200	3.08	3.12	3.31	3.40	0.93	0.92
	W 250	4.22	4.32	4.40	4.51	0.96	0.96
	W 300	5.20	5.24	5.34	5.39	0.97	0.97
High air kerma rate series (8)	H 20	0.12 Al	0.14 Al	0.16 Al	0.20 Al	0.75	0.72
	H 30	0.38 Al	0.44 Al	0.60 Al	0.68 Al	0.63	0.65
	H 60	2.42 Al	2.45 Al	3.25 Al	3.24 Al	0.74	0.76
	H 100	0.30	0.30	0.47	0.47	0.64	0.64
	H 200	1.70	1.71	2.40	2.43	0.71	0.70
	H 250	2.47	2.56	3.29	3.38	0.75	0.76
	H 280	3.37	3.43	3.99	4.10	0.84	0.84
	H 300	3.40	3.47	4.15	4.23	0.82	0.82

Note：The fixed filtration is 3 mm Be (ISO:1 mm Be) for 30kV & below of narrow spectrum series and low air kerma rate series. The fixed filtration is 3 mm Be (ISO:4 mm Be) for 100 kV & below of high air kerma rate series. The others are 4 mm Al

the recommendations of ISO, except for some low energy radiations and they can be used for the calibration of dosimeter for the radiation protection purpose.

The difference of HVL between CIRP and ISO may be attributed to the difference of total filtration. It is unavoidable for small total filtrations.

The investigation on the energy spectrums of these reference radiations will be done in the near future.

Acknowledgment

Thanks to Prof. Chen Huili who has helped in the measurements of the characteristics of x-ray reference radiation.

References

1) International Organization for Standardization, “X and gamma reference radiation for calibrating dosemeters and doserate meters and for determining their response as a function of photon energy Part1: Radiation characteristics and production methods, ” ISO4037-1:1996, (1996)
2) International Organization for Standardization, “X and gamma

reference radiation for calibrating dosemeters and doserate meters and for determining their response as a function of photon energy Part2: Dosimetry for radiation protection over the energy ranges from 8 keV to 1.3 MeV and 4 MeV to 9 MeV," ISO4037-2:1997, (1997)
3) International Organization for Standardization, "X and gamma reference radiation for calibrating dosemeters and doserate meters and for determining their response as a function of photon energy Part3: Calibration of area and personal dosemeters and the measurement of their response as a function of energy and angle of incidence," ISO4037-3:1999, (1999)
4) Trout,E.D., et al, "Determination of Half-Value Layer," Am. J. Roentgenology .84[4], p.729-740, (1960)

Journal of NUCLEAR SCIENCE and TECHNOLOGY, Supplement 5, p. 282–285 (June 2008)

Alpha Contamination Monitoring Instrument Based on LRAD Technique for Complex Surface Monitoring

Xianguo Tuo, Zhe Li*, Keliang Mu, and Xiangyang Li

Chengdu University of Technology, Si Chuan, China，610059

Traditional alpha contamination monitors have a low detection efficiency, and can miss contamination on less accessible surfaces, uneven surfaces and piping inner surfaces etc. New measuring equipment with alarming system designed to be used to solve these problems is discussed in this paper. This system uses Long-Range Alpha Detection (LRAD) technology, which monitors alpha contamination by measuring the ionization in ambient air formed by alpha particles. The whole monitor system contains an iron chamber detector, a high quality MCU system, and adopts ∑-△ signal processing technology. It is designed to be used primarily in the field and in the laboratory measurements. The monitor is battery-powered and can operate continuously for up to ten hours. The test result indicates that the available detect length L is more than 2m, the relative detect efficiency η is better than 40%. This kind of alpha surface contamination monitor has been well used at some radiation site and has been proven to meet the needs.

KEYWORDS: LRAD technology, uneven surface alpha contamination, ion chamber

I. Introduction

It is essential to monitor the surface contaminations at some radioactive labor site or laboratory. Alpha surface contamination monitor is needed in any plant or building that is being decommissioned or transferred, and radiation medicine or other radioactive measure fields. However, traditional alpha detectors are designed to detect alpha particles directly and these particles must be passed slowly within about several millimeters or centimeters of an alpha source to operate effectively and they are severely limited by the relatively short range of alpha particles in air. These methods face a high difficulty and have low alpha collection efficiency, and can miss contamination on less accessible surfaces, uneven surfaces and piping inner surfaces etc[4]. In order to solve these inconveniences, a new alpha surface contamination monitor device based on Long-Range Alpha Detector (LRAD) technique[3,4]was used in the study.

The LRAD technology was developed at Los Alamos National Laboratories (LANL) and has been demonstrated to be a highly sensitive method of measuring alpha activity[6]. The LRAD technology is based on monitoring the ionization created by alpha interactions with ambient air, rather than the alpha particle itself. The primary mechanism for alpha particle energy loss in the ambient air (and other gases) is ion pair production. Alpha particles interact with ambient air (an alpha particle loses about 35 eV per ion pair produced) producing ionization in the air at the rate of about 30000 ion pairs per MeV of alpha energy[1,3]. These charges can be transported by a fan effectively, which is used to drive the air from the potential polluted surfaces, and to transport the air current into an ion collector located up several meters away from the initial decay. The charge collected on a sense grid by the moving air can produce electric current with the effect of external electric field. The intensity of this electric current has a direct proportion with the activity of alpha particles, which is each Bq can produce several femtoamp (10^{-15} amperes) current, so that care must be taken.

Using the LRAD technique, contamination can be detected, even small cracks and comers can be effectively monitored if air passes over them, in any location into which air can penetrate, then ions produced can be detected directly[2]. Therefore, they are better able to monitor less accessible surfaces, uneven surfaces, piping inner surfaces and can be operated at a much greater distance from alpha source than traditional alpha detectors. Furthermore, because LRAD detectors remain stationary during monitoring, they are less subject to operator error than traditional alpha detectors.

An ionization chamber with the kind of small volume and portability is placed in the alpha contamination monitor to measure its gross alpha activity. The whole device which is motivated by lithium batteries can be recognized as a portable alpha surface contamination detector. This battery-powered monitor is designed to measure alpha activity quickly, easily, and accurately in the field. It can monitor the radioactive material collected on inner surfaces of pipes with small diameter or other uneven surfaces without any damage (eg. Incise of the long pipe into some small segments or sections just to meet the need of hand-holding detect), and it also can monitor the activity timely, effectively and safely.

II. Construction

The alpha contamination monitor is in a standard case of dimensions of 34 cm × 24 cm × 14.5 cm. The system is fundamentally made up of an air-pipe, a fan, an ionization chamber, an I-V converter, a signal acquisition and

*Corresponding Author, Tel. +86-28-8407-7936, E-Mail: lizhe3017@163.com, NSFC No.: 40574059, MOST FUND: 2006JG2002500

processing system, an electrical source (Li-batteries and DC-DC) and a charger. **Fig. 1** shows the principle of this system, that is, the contaminated air driven by the fan (The maximum velocity is 10000 rotations per minute.) is transported into the ionization chamber through air pipe and ionization current is produced. The low current is converted into voltage signals which can be easily measured by I-V convertor and then voltage signals are inputted into A/D convertor in the signal processing module, with a core MCU in it. The final result will be displayed by LCD.

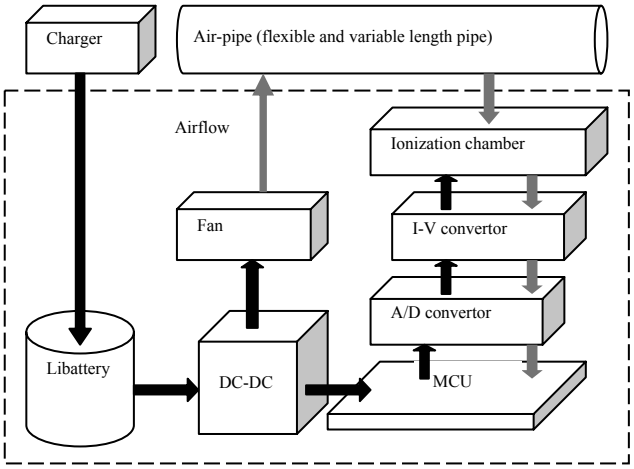

Fig. 1 Architecture of the system

The main detection component is an ion chamber of 18 cm × 11 cm× 6.6 cm with two brass plates as the electronics pole fastened by four polyethylene columniations. The leakage current from the chamber is less than 10^{-14}A under NTP condition and the chamber's work voltage is 100 V. When high-voltage added, low electric current is formed by the gas containing alpha particles which are taken out through the pipe. There are two holes with the diameter of 4 cm on each side of the ionization chamber to connect the fan box and the air-in pipe. **Fig. 2** shows the structure of the ionization chamber.

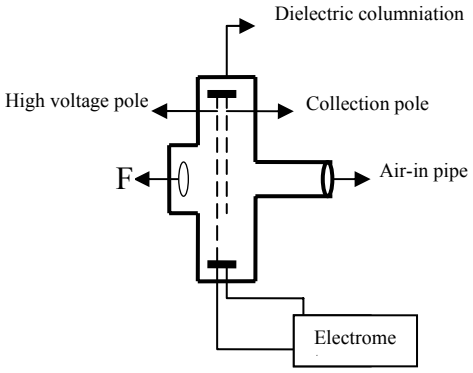

Fig. 2 Framework of pumping ionization chamber

The signal collection and transaction cell is MCU (89C52) as a core component. Voltage signals enter into the 16 bits A/D convertor by using $\sum-\triangle$ technique[5)] to achieve an accurate convert without an error code. Samplings are carried every one minute and the result is displayed on the LCD screen.

The portable monitor is also with some characters such as high capacity, low power，small volume, and intelligent operation etc. It can swiftly show the correct result on the spot. The system is powered by Li-battery which can support continuously for up to eight hours on a full charge. The attached charger can supply power to Li-battery and other devices respectively. The alpha contamination monitor has some other functions, for example, people can set the alarm level as they need in advance. Users can achieve their demanding orders or parameters via key-board buttons input, which can make the users feel convenient when using it. The measurement results are displayed clearly on the LCD screen, which can also be saved by using a software that permits file transfers with other computers through a serial port (RS232).

III. Surveys and Results

Some surveys about the alpha surface contamination monitor have been achieved，and the results are showed as follows.

1. Background Surveying

A background measurement assures the accuracy and sensitivity of the system by measuring the background ionization of the environment surrounding the system. Both environmental conditions and internal contamination of the instrument may contribute to the background result.

The device must be warmed up for 15-30 minutes in advance, and then set the survey time of 60s, 120s, 300s, and 900s separately. Five times measurements in each survey time should be taken to get the average value.

The result is showed in **Table 1**.

Table 1 Background measurement (V)

Time (s) / Trials	60	120	300	900
I	0.0008	0.0009	0.0010	0.0009
II	0.0008	0.0008	0.0008	0.0008
III	0.0007	0.0009	0.0009	0.0007
IV	0.0008	0.0009	0.0010	0.0007
V	0.0008	0.0008	0.0008	0.0008

2. Survey of Standard Alpha Source

Chose ten standard alpha sources (^{239}Pu), 1.443×10^3 dpm、2.731×10^3 dpm 、 6.688×10^3 dpm 、 1.095×10^4 dpm 、 2.369×10^4 dpm 、 2.540×10^4 dpm 、 3.416×10^4 dpm 、 2.007×10^5 dpm、2.412×10^5 dpm and 3.005×10^5 dpm for each. Each radioactive source was located in a sample enclosure (aluminum box) with an air inlet filter to provide standardization of the system (Following measurements are using the same structure). Data collection time was one minute per source. The distance between each source and detector was keep accurately with 10 cm in 10 times determination for each source. Average results showed in

Table 2 indicate that the coefficient of linearity correlation is 0.997. **Fig. 3** shows the result of the linearity measurement.

3. Detection Efficiency

As is known to all, the detection efficiency is one of the most important indexes of each device, and survey result will be strictly affected by inaccurate or low detection efficiency. The alpha surface contamination monitor's detection efficiency was evaluated under the condition of changing the distance between the source and the detector. Each measure time was set T=60 seconds under normal temperature. Measurement was taken by changing the distance length L between source and detector. In the test, suppose the detect efficiency is 1 when the detect length L is 9.5 cm. Other measurement's detect efficiencies are compared with it and given out the instrument's detect efficiencies at different lengths. The data in **Table 3** was obtained from a 7.6×10^4 dpm ^{239}Pu standard source, and demonstrates that the whole system's detect efficiency is better than 50% when the length is 200 cm.

Table 2 Survey results

Source intensity A(dpm)	Survey value (Mean value) A0 (dpm)	A/ A0	A/A0 Mean value
0			1.342
1.431×102	1.70×102	0.842	
4.998×102	3.12×102	1.602	
1.443×103	1.00×103	1.443	
2.731×103	2.10×103	1.300	
6.688×103	5.10×103	1.311	
1.095×104	8.20×103	1.335	
2.369×104	1.820×104	1.302	
3.416×104	2.480×104	1.377	
2.007×105	1.449×105	1.385	
2.412×105	1.679×105	1.437	
3.005×105	2.1047×105	1.428	

Note: A: Source intensity, A_0: Survey value.
Convert coefficient in this system is 1000.

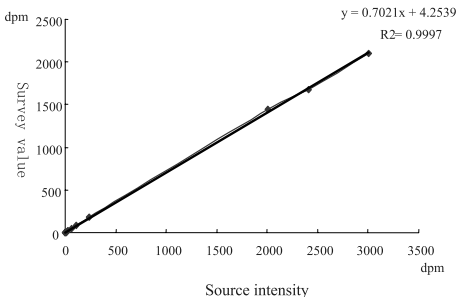

Fig. 3 The linearity of instrument measurement

All measurement results can show that the linearity correlation is 0.997, the background is lower than 0.001 V, and the detection efficiency is still better than 50% when L is 2 m. In addition the alpha surface contamination monitor has better detection sensitivity as it can measure even a low level of femtoamp (10^{-15} A) current. Furthermore, users can choose an appropriate η and examine it according to theirs needs.

Table 3 The influence of distance (L) to measurement response

L (cm)	V_{avg} (V)	η (%)
9.5	0.06414	100.00
16.0	0.06096	95.04
22.5	0.05782	90.15
29.0	0.05472	85.31
35.5	0.05404	84.25
42.0	0.05308	82.76
70.0	0.04644	72.40
102.0	0.04302	67.07
134.0	0.04082	63.64
166.0	0.03916	61.05
200.0	0.03430	53.48

4. Measurement of Different Source Intensities in Different Lengths

Four different radioactive source intensities were tested in three tracts with different lengths. Measurement results showed in **Table 4** were simulated by using the MATLAB 7.0 software, and the simulation result can be well used to meet users' needs as it has done in some experiment site. Units of source intensity, length, and measure voltage are dpm, cm, and mV respectively.

Table 4 Measurement results of different source intensities in different lengths

Source intensity (dpm) / Length (cm)	1.32×10^2	6.75×10^2	1.10×10^4	1.07×10^5
40	0.58	1.00	11.5	100.56
70	0.26	0.52	9.83	93.86
100	0.26	0.70	11.76	103.4

IV. Conclusion

With dimensions of 34 cm × 24 cm × 14.5 cm, the battery-operated alpha surface contamination monitor provides an easily fieldable unit for accurate alpha monitoring at uneven surfaces and piping inner surfaces. It can reduce the possibility of mistakes made by operators as it just measures the ambient air, and also it can reduce the possibility of contamination loss as long as in any location into which air can penetrate. Normal operation of the alpha surface contamination monitor has been designed to be readily used by personnel and to meet their needs.

The alpha surface contamination monitor with series special structures (such as different particulate filters or sample enclosure) can be well used to measure the activity of alpha particles in block of long tube inner surfaces without any destruction, and it has a good application foreground in the field of the decommission of nuclear facility.

References

1) C.R. Whitley, J.A. Bounds, and P.A.Steadman, 'A Portable Swipe Monitor for Alpha Contamination,' IEEE TRANSACTIONS ON NUCLEAR SCIENCE, VOL. 45, NO. 3, JUNE 1998.
2) D. W. MacArthur, K. S. Allander, J. A. Bounds, M. M. Catlett, R. W. Caress, and D. A. Rutherford, 'Alpha Contamination Monitoring of Surfaces, Objects, and Enclosed Areas,' IEEE TRANSACTIONS ON NUCLEAR SCIENCE, VOL. 40,N O. 4, AUGUST 1993.
3) D. W. MacArthur, K. S. Allander, J. A. Bounds, M. M. Catlett, and J. L. McAtee, 'Long-Range Alpha Detector (LRAD) for Contamination Monitoring,' IEEE TRANSACTIONS ON NUCLEAR SCIENCE, VOL. 39. NO. 4, 1992.
4) J. D. Johnson , K. S. Allander, J. A. Bounds, S. E. Garner, J. P. Johnson, D. W. MacArthur, L. L. Sprouse and S. G. Walters, 'Long-range alpha detector sample monitoring,' Los Alamos National Laboratory, Los Alamos, NM 87545, USA Available online 29 October 2002.
5) GAO Song, CHENG Yi, TUO Xianguo, MU Keliang, LI Xiangyang, CHEN Mingxiu, LENG Huimin,' Development of alpha surface contamination meter based on embedded module,' NUCLEAR TECHNIQUES, Vo1. 29, No. 6 June 2006.
6) K.S.Allander, D.W.MacArthur, J.A.Bounds, R.W.Caress, M.M.Catlett, J.P.Johnson, J.D.Johoson, and D.A.Rutherford, 'Long-Range Alpha Detector (LRAD) Technology Applied to ER and D&D Problems,' Los Alamos National Laboratory, Augusta, Georgia, October 25-27,1993.

Journal of NUCLEAR SCIENCE and TECHNOLOGY, Supplement 5, p. 286–289 (June 2008)

Calibration of Spherical Neutron Measuring Devices with a ^{252}Cf Source in the Neutron Calibration Room of the KAERI

Sun-Mee JUN[1,2*], Bong-Hwan KIM[1], Jang-Lyul KIM[1], and Jai Ki LEE[2]

[1]*KAERI, Dukjin-dong, Yuseong-gu, Daejeon, Korea*
[2]*Hanyang University, Haengdang-dong, Seongdong-gu, Seoul, Korea*

ISO recommends that the neutron scattering correction procedures, such as the shadow-cone method, the polynomial fit method and the semi-empirical method, be used for a calibration of neutron measuring devices. This study compared three methods using the Bonner Multisphere Spectrometer (BMS) and neutron survey meters based on a ^{252}Cf source in the neutron calibration room of the Korea Atomic Energy Research Institute (KAERI). As for the results, the average correction factors and calibration factors of the shadow-cone method compared with the semi-empirical method using the BMS and neutron survey meters. The results were consistent to within ± 0.7 % and ± 2.6 % respectively. These averaged values for the three methods by the BMS and the neutron survey meters were then varied within ± 5 %, respectively. It is then noted that the results based on the BMS and the neutron survey meters agreed well with each other. From the results, it is suggested that the semi-empirical method be useful for the neutron calibration room of the KAERI.

KEYWORDS: Shadow-cone method, Polynomial fit method, Semi-empirical method, ISO 8529, Neutron scattering correction

I. Introduction

In general, neutron measuring devices used in radiation protection work for measuring a neutron field have to be calibrated before any reliance can be placed upon their obtained readings. Proper calibration procedures require that an instruments reading should be corrected for all possible effects that may influence it, including a neutron scattering by air, and the neutrons reflected by the walls, floor and ceiling of a calibration room. Room scattering corrections are dependent on a specific neutron source type, detector type, calibration distance, and calibration room configuration.

ISO (the International Organization for Standardization) recommends that the following procedures such as the shadow-cone method, the polynomial fit method and the semi-empirical method, should be applied for a calibration of neutron measuring devices[1)]. These methods are applied to the analyses of measurement data, to elucidate the scattering component and to obtain the free-field response. Free-field response is the response coming directly from the neutron source, in the absence of any scattered one.

Based on the three methods referred in the preceding paragraph, we compared these procedures by determining the detector response of the Bonner Multisphere Spectrometer (BMS) and the neutron survey meters using a ^{252}Cf source in the neutron calibration room of the Korea Atomic Energy Research Institute (KAERI).

II. Materials and Method

1. Irradiation facility and Neutron detector

The neutron calibration room of KAERI is a bunker room whose dimensions are 7.9 m long, 5.5 m wide and 5.8 m high, and it is enclosed with 60 cm thick concrete walls and a ceiling. The calibration source was a ^{252}Cf that was placed at the center of the room and moved from storage to a calibration position of a height of 2.9 m at the time of irradiation.

The BMS was consisted of the followings: (1) 5 polyethylene (PE) spheres with diameters of 7.62 cm (3″), 12.7 cm (5″), 20.32 cm (8″), 25.4 cm (10″) and 30.48 cm (12″), (2) 3 spheres inserting a lead sphere into the PE spheres (P3L5P8, P4L6P8 and P5L6P8; P:PE, L:lead, Numbers:OD (Outer diameter in inch) as illustrated in **Fig.1**, and (3) a ^{6}LiI(Eu) scintillation detector.

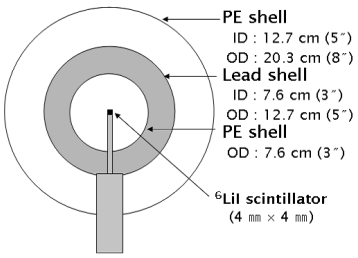

Fig. 1 Diagram of the P3L5P8 sphere

Measurements were carried out at 12 different separation distances from source center to detector center ranging from 40 cm to 150 cm, with increment of 10 cm. Shadow-cone used to shield the detector from the direct source beam was made of two parts: a 20 cm long part made of iron and a 30 cm long part made of PE. Two cones was used by the shadow-cone method according to the size of the PE sphere in this experiment. One was tested in the range of 2.54 cm to

*Corresponding Author, Tel.: +82-42-868-2013, Fax.: +82-2-42-868-8609, E-Mail; ex-smjun89@kaeri.re.kr

12.7 cm, the other in the range of 12.7 cm to 30.48 cm. Measurements using a shadow-cone were performed at 10 cm from the source center to the front end of the shadow-cone, and at 100 cm or 110 cm from source center to detector center.

An experiment was performed for the commercially available neutron dose-equivalent meters of six types; E600/NRD (Eberline, USA), Ludlum 12-4 (Ludlum, USA), LB123/LB6411 (Berthold, Germany), FT40G-X/FHT752 (Thermo, USA), NG-2AS1(NRC, USA) and 190N/RP-N (Victoreen, Austria). Diameter of the detectors was ranged from 21 to 25 cm.

2. Calibration of the detectors

To measure the free-field response for the detectors, the inevitable neutron-scattering effects, including a neutron scattering by air and by the walls, floor and ceiling of a calibration room, must be corrected. This scattering correction was made by use of the following measurement method.

The shadow-cone method depends strongly upon the design of a shadow-cone and upon its position relative to the source-detector geometry. If $M_T(d)$ and $M_S(d)$ are the detector readings obtained without and with the shadow-cone placed between the source and the detector, then

$$[M_T(d) - M_S(d)]F_A(d) = \frac{BF(\theta)\varepsilon}{4\pi d^2} \quad (1)$$

where d is the distance between the center of the source and the reference point, $F_A(d)$ is the air-attenuation factor, B is the neutron source strength, $F(\theta)$ is the source anisotropy correction factor, ε is the detector response. The source anisotropy factor was evaluated through a Monte Carlo simulation and determined to be 1.057 in the calibration room of the KAERI[2]. For the neutron spectrum emitted by a ^{252}Cf source, the averaged linear attenuation coefficient of air, $F_A(d)$, is recommended by ISO 8529-2[1].

The polynomial fit model proposed by Hunt[3] is independent of all scattering effects, and should be applicable to all spherical devices in any sized calibration room. The measurement response at a source-to-detector center distance of d cm, $M_T(d)$, after corrections of the inverse square law ($4\pi d^2$) and the geometry factor, $F_G(d)$, can be fitted to a second-order polynomial function of d with the least squares technique[4].

$$\frac{M_T(d)4\pi d^2}{F_G(d)} = BF(\theta)\varepsilon(1 + Ad + Rd^2) \quad (2)$$

From the fitting, the neutron source-detector characteristic constant, K, is related to the neutron emission rate B and the detector response, by the following equation, $K = BF(\theta)\varepsilon/4\pi$, and then the air scattering factor, A, and the room scattering factor, R, components can be obtained, and the response, ε, can be derived.

Semi-empirical method proposed by Eisenhauer et al.[5] is based on the assumption that an air-scatter component is very small when compared with a room-scatter component, and the room-scattered neutrons are uniformly distributed throughout a room. The measurement data was corrected first for an air scattering using the calculated correction factors.

$$\frac{M_T(d)4\pi d^2}{F_G(d)(1 + Ad)} = BF(\theta)\varepsilon(1 + Rd^2) \quad (3)$$

The air scattering factor, A, is 1.4 of a fluence and 1.2 of a neutron dose-equivalent ratemeter for the ISO-recommended ^{252}Cf source[1]. The semi-empirical method agreed well with the measured reading in the rooms of a small and an intermediate size (about 6 m cube)[6].

III. Results and Discussion

1. Calibration of the BMS

The measured data of the BMS was applied to different types of the methods recommended by ISO. **Table 1** shows the results obtained with the scattering correction methods for the BMS. The data applicable to the shadow-cone method were fitted to Eq. (1). The measured count rates were fitted to polynomial fit method given by Eq. (2) and semi-empirical one given by Eq. (3). The measured response of the BMS, ε, was calculated using the neutron source-detector characteristic constant, K, together with corrected source emission rates. The results of measured responses vary within about 8 % between these three different scattering correction methods, although the polynomial fit method gives the lowest values among them.

The calculated response showed by Kim et al.[7] was obtained using the MCNPX code[8]. This calculated response is generally used only as the relative response of the detector in the absence of any scattered radiation. The purpose of the BMS calibration was to compare the calculated response with the measured response, so that a response correction factor for each detector can be applied to correct the absolute sensitivity. The ratio of the measured and calculated responses gave the sensitivity correction factor for each detector.

The correction factors for the shadow-cone, the polynomial fit, and the semi-empirical methods are presented in **Table 2**. The average correction factors based on the shadow-cone method are compared with those based on the polynomial fit and the semi-empirical methods. The results are consistent within ± 6.5 % and ± 0.7 %, respectively. From the comparison, a good agreement was presented between the shadow-cone and semi-empirical method. According to Hunt[3], the variation of the averaged calibration factors using the applied calibration methods of the spherical devices should be consistent within ± 3 % for the NPL (National Physical Laboratory, UK) calibration room. It is shown in **Table 2** that the average variation of the correction factors is within ± 4.1 %.

Table 1 Measurement data of the BMS applied the shadow-cone, the polynomial fit and the semi-empirical methods

Bonner spheres	scatter-corrected count rate (s^{-1})			direct neutron (cm^{-2} s^{-1})		measured response (cm^2)			calculated response (cm^2)
	shadow-cone	polynomial fit[3)]	semi-empirical	shadow-cone[1)]	polynomial fit & semi-empirical[2)]	shadow-cone	polynomial fit	semi-empirical	
3″	17.68	34.64	37.77	326	680	5.42×10^{-2}	5.10×10^{-2}	5.56×10^{-2}	6.21×10^{-2}
5″	60.50	119.41	127.03	326	680	1.86×10^{-1}	1.76×10^{-1}	1.87×10^{-1}	1.98×10^{-1}
8″	69.70	134.58	146.02	326	680	2.14×10^{-1}	1.98×10^{-1}	2.15×10^{-1}	2.44×10^{-1}
10″	53.89	106.21	110.19	326	680	1.66×10^{-1}	1.56×10^{-1}	1.62×10^{-1}	1.61×10^{-1}
12″	37.02	74.21	77.81	326	680	1.14×10^{-1}	1.09×10^{-1}	1.15×10^{-1}	1.04×10^{-1}
P3L5P8	63.89	122.74	128.24	324	679	1.97×10^{-1}	1.81×10^{-1}	1.89×10^{-1}	2.25×10^{-1}
P4L6P8	67.16	132.03	137.31	324	679	2.07×10^{-1}	1.94×10^{-1}	2.02×10^{-1}	2.33×10^{-1}
P5L6P8	73.06	143.43	151.11	324	679	2.25×10^{-1}	2.11×10^{-1}	2.23×10^{-1}	2.48×10^{-1}

1) Direct neutron was calculated at the distance of 110 cm from the source on data of 23 ~ 31 Mar. 2006.
2) Direct neutron was calculated at the distance of 100 cm from the source on data of 24 ~ 27 Feb. 2004.

Table 2 The correction factors for BMS applied the shadow-cone, the polynomial fit and the semi-empirical methods

Bonner spheres	Correction Factor		
	shadow-cone	polynomial fit	semi-empirical
3″	**1.146 ± 0.084**	**1.219 ± 0.089**	**1.118 ± 0.091**
5″	**1.069 ± 0.084**	**1.130 ± 0.093**	**1.062 ± 0.094**
8″	**1.140 ± 0.083**	**1.230 ± 0.088**	**1.134 ± 0.093**
10″	**0.977 ± 0.084**	**1.033 ± 0.087**	**0.996 ± 0.086**
12″	**0.919 ± 0.085**	**0.955 ± 0.089**	**0.911 ± 0.086**
P3L5P8	**1.141 ± 0.085**	**1.244 ± 0.087**	**1.191 ± 0.085**
P4L6P8	**1.124 ± 0.084**	**1.198 ± 0.086**	**1.152 ± 0.086**
P5L6P8	**1.099 ± 0.084**	**1.173 ± 0.085**	**1.113 ± 0.087**

2. Calibration of the neutron dose-equivalent meters

A calibration of the neutron dose-equivalent meters was applied for the spherical type such as E600/NRD, Ludlum 12-4 and LB123/LB6411, and the cylindrical one such as FT40G-X/ FHT752, NG-2AS1 and 190N/RP-N. For spherical types, the effective point of measurement was at the geometrical center. For cylindrical types, the effective point of measurement was at the intersection of the cylindrical axis and the line from the source.

Based on the measurement data and the three methods of the calibration, the reading-corrected response, the free-field response and calibration factors obtained from these survey meters are presented in **Table 3**. The average calibration factors based on the shadow-cone method were compared with those based on the polynomial fit and semi-empirical methods. The results are consistent within ± 6.6 % and ± 2.6 %, respectively. The average value of calibration factors for these methods is about ± 3.1 %. The results are very similar to the results of the BMS. As shown by Eisenhauer[7)], the semi-empirical method agreed well in small and intermediate size rooms. It is suggested that the semi-empirical method will be useful for the neutron calibration room of the KAERI.

3. Scattering Corrections

The scattering correction terms of the polynomial fit and the semi-empirical method are given in **Tables 4** and **5,** respectively. From **Tables 4** and **5**, the parameters K, A and R of the polynomial fit method are determined by using the least squares technique.

Table 3 The Measurement data and calibration factors for neutron survey meters applied the shadow-cone, the polynomial fit and the semi-empirical methods

Survey meter	Reading-corrected response[1)] ($\mu Sv\ h^{-1}$)			Free-field response [2)] ($\mu Sv\ h^{-1}$)		Calibration Factor (CF)		
	Shadow-cone	Polynomial fit	Semi-empirical	Shadow-cone	Polynomial fit & Semi-empirical	Shadow-cone	Polynomial fit	Semi-empirical
E600/NRD	411.5	374.9	396.5	401	403	0.974 ± 0.084	1.076 ± 0.089	1.017 ± 0.090
12-4	464.9	442.8	449.8	401	406	0.863 ± 0.129	0.926 ± 0.113	0.902 ± 0.114
LB6411	442.8	391.2	423.4	395	395	0.892 ± 0.082	1.010 ± 0.084	0.933 ± 0.086
FHT752	447.2	418.8	448.5	401	405	0.897 ± 0.081	0.968 ± 0.082	0.904 ± 0.086
NG-2AS1	450.6	449.8	452.8	401	405	0.890 ± 0.081	0.901 ± 0.093	0.895 ± 0.095
190N/RP-N	423.2	421.0	419.3	395	395	0.934 ± 0.093	0.939 ± 0.086	0.942 ± 0.087

1) Reading-corrected response was measured and corrected for the scattering factor at the distance of 100 cm from the source on data of 14. May. ~ 20. Jun. 2007.
2) Free-field response was calculated at the distance of 100 cm from the source on data of 14. May. ~ 20. Jun. 2007.

Table 4 The scattering correction terms of the polynomial fit and the semi-empirical method using the BMS

Bonner spheres	Polynomial fit $K(1+Ad+Rd^2)$	Semi-empirical $K(1+Rd^2)$
3″	$435.3(1+0.22d+0.74d^2)$	$37.96(1+0.78d^2)$
5″	$1500.6(1+0.16d+0.24d^2)$	$127.9(1+0.30d^2)$
8″	$1691.1(1+0.21d+0.05d^2)$	$147.9(1+0.14d^2)$
10″	$1334.7(1+0.10d+0.09d^2)$	$111.9(1+0.123d^2)$
12″	$932.6(1+0.10d+0.05d^2)$	$78.95(1+0.08d^2)$
P3L5P8	$1542.4(1+0.11d+0.16d^2)$	$129.5(1+0.20d^2)$
P4L6P8	$1542.4(1+0.13d+0.15d^2)$	$140.2(1+0.20d^2)$
P5L6P8	$1542.4(1+0.13d+0.12d^2)$	$152.3(1+0.17d^2)$

Table 5 The scattering correction terms of the polynomial fit and the semi-empirical method using the neutron survey meters

Detector	Polynomial fit $K(1+Ad+Rd^2)$	Semi-empirical $K(1+Rd^2)$
E600/NRD	$4710.9(1+0.17d+0.04d^2)$	$401.2(1+0.13d^2)$
12-4	$5564.3(1+0.07d+0.09d^2)$	$455.2(1+0.13d^2)$
LB6411	$4915.9(1+0.23d+0.02d^2)$	$428.6(1+0.13d^2)$
FHT752	$5262.8(1+0.20d+0.02d^2)$	$453.8(1+0.12d^2)$
NG-2AS1	$5652.7(1+0.04d+0.10d^2)$	$458.2(1+0.13d^2)$
190N/RP-N	$5290.6(1+0.02d+0.05d^2)$	$423.6(1+0.07d^2)$

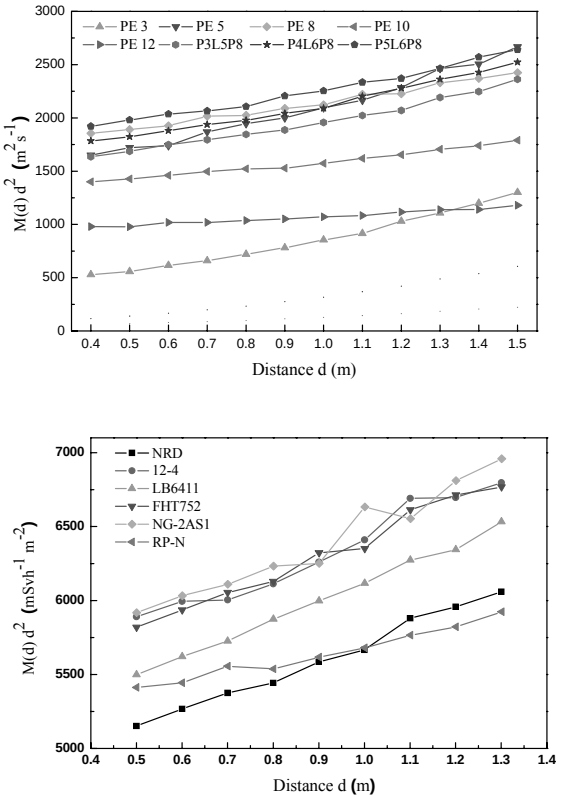

Fig. 2 Plotting for polynomial fit method using the BMS and the neutron survey meters

The semi-empirical method assumed that an air scatter, A, was very small when compared with a room scatter, R. Therefore, A is a constant calculated for the neutrons scattered by air, parameters K and R determined by the least squares techniques. **Fig. 2** shows the scattering correction data obtained with the polynomial fit method using the BMS or the neutron survey meters and a ^{252}Cf neutron source.

IV. Conclusion

ISO recommends that the following procedures such as the shadow-cone method, the polynomial fit method and the semi-empirical method, should be applied for a calibration of neutron measuring devices. This study compared the correction factors and calibration factors of three methods using the Bonner Multisphere Spectrometer (BMS) and neutron survey meters based on a ^{252}Cf source in a neutron calibration room of the KAERI. As for the results, the average correction factors derived from the shadow-cone method using the BMS were consistent within ± 6.5 % and ± 0.7 % for the polynomial fit and the semi-empirical methods, respectively. While the average calibration factors derived from them using the neutron survey meters were consistent within ± 6.6 % and ± 2.6 % for the above two methods. These averaged values for the three methods were then varied within ± 4.1 % and ± 3.1 % for the BMS and the neutron survey meters, respectively. It is suggested that the semi-empirical method be useful for the neutron calibration room of the KAERI.

References

1) ISO, 'Reference Neutron Radiations-Part 2 : Calibration Fundamentals of Radiation Protection Devices related to the Basic Quantities Characterizing the Radiation Field,' ISO 8529-2, 2000.
2) KAERI, 'Quantification of Neutron Fields at the Neutron Therapy Room of KCCH Using a Bonner Sphere,' KAERI/RR-2442, 2003.
3) J.B. HUNT, 'The Calibration of Neutron Sensitive Spherical Devices,' Radiatiaon Protection Dosimetry 8(4), 239, 1990.
4) J.C. LIU et al., 'Neutron Spectral Measurements at ORNL,' Radiation Protection Dosimetry 30(3). 169, 1990.
5) C.M. EISENHAUER et al., 'Calibration Techniques for Neutron Personal dosimetry,' Radiation Protection Dosimetry 10(1-4) 43, 1985.
6) IAEA, 'Guidelines on Calibration of Neutron Measuring Devices,' IAEA Technical Reports Series 285, 1988.
7) B.H. KIM et al., 'Measurement of the Neutron Spectra Inside and Outside the target Room of the 65 MeV Electron LINAC using an Extended Bonner Sphere,' Journal of Nuclear Science and Technology Supplement 4. 176, 2004.
8) L.S. Waters Ed., 'MCNPXTM User's Manual, Version 2.1.5', TPO-E83-G-UG-00001 Rev.0 Nov.14, 1999.

Journal of NUCLEAR SCIENCE and TECHNOLOGY, Supplement 5, p. 290–293 (June 2008)

Frozen Solutions of Fricke Dosimeter

Alejandro RAMOS[1], Sergio RAMOS-BERNAL[2], Diego FRIAS[3], F. Guillermo MOSQUEIRA[4] and Alicia NEGRON-MENDOZA[2]*

[1]*Facultad de Ciencias, Universidad Nacional Autónoma de México (UNAM), C.U. México, D.F. México*
[2] *Instituto de Ciencias Nucleares, Universidad Nacional Autónoma de México (UNAM), C.U. México, D.F. México*
[3]*Universidad Estatual de Santa Cruz, Santa Cruz, Brazil.*
[4] *Dirección General de Divulgación de la Ciencia, Universidad Nacional Autónoma de México, UNAM*

Commercial product irradiation using ionizing radiation has provided a method to safely treat products in a variety of ways. Temperature is a very important factor when determining the absorbed dose of the product. However, most irradiation complexes apply dosimetric knowledge and calculations in a temperature range above water-freeze temperature to products that could be at a much lower temperature. This could lead to systematic errors in the irradiation procedures and to health issues.

In this paper, we study the response of the Fricke dosimeter as a function of the irradiation temperature. The temperatures studied were: 77 K (liquid nitrogen), 198 K (dry ice as powder), 263 K, 298 K (room temperature), 306 K and 328 K.

The results obtained show that the change in valence of iron (II) as a function of the dose was linear for frozen solutions. There is a change of the slope in the doses-response curve that shows the effect of the irradiation temperature. This suggests that a temperature correction should be considered for low-temperature irradiation. This led to the conclusion that the Fricke dosimeter can be used as a dosimeter for low-temperature, and up to 600 Gy.

An attempt has been made to theoretically model the chemical response of the Fricke dosimeter and results agreed with the experimental values fairly well.

KEYWORDS: Fricke dosimetry, iron salts, low temperature, gamma irradiation, ferric sulfate, frozen solution doimetry

I. Introduction

Nowadays, the commercial irradiation of products has been widely assimilated, and it is applied to products in diverse physical states. In fact, it is often applied to products at different temperatures, and with complete disregard to the problems that could arise from this practice.

The irradiation of frozen food[1)] is a clear example of this, since it is a well-documented practice, particularly considering the case of marinade chicken and seafood[2)]. Another common practice is to irradiate medical implants that are to be transported from one place to another, in order for them to survive a longer time with a reduced risk of contamination. Medical implants, as well as seafood, are also sometimes kept at temperatures lower than water-freeze temperature (i.e. solid carbon dioxide). It is this practice that motivated this research.

In this work we study the response of the Fricke dosimeter in frozen solutions as a function of the irradiation temperature. The temperatures studied were: 77 K (liquid nitrogen), 198 K (solid carbon dioxide), 263 K, 298 K (room temperature), 306 K, and 328 K

1. Chemical Dosimeters:

In a chemical dosimeter, the radiation dose is determined by the chemical change produced in a given medium. The response is obtained by a quantifiable reaction result (*G* product).

It is usually stated that the response of chemical dosimeters should be: 1) proportionate to the radiation dose in the dose interval used, 2) independent of the dose rate, 3) independent of the energy and radiation LET, 4) reproducible, and 5) independent of the temperature.

Although the existence of a small temperature coefficient for radiolytic products is often mentioned, very little effort has been put into characterizing commonly used dosimeters in a wide range of temperatures and, accordingly, physical states.

The Fricke dosimeter is one of the most widely used since it is precise within 0.1% with gamma rays. It is often used for a linear dose range of 40 to 400 Gy. Its dosimetry is based on the oxidation of ferrous ions (Fe^{2+}) to ferric ions (Fe^{3+}) in the presence of oxygen and under the influence of ionizing radiation[3)].

The Fricke solution has to be protected from light, since it can cause oxidation of the ferrous ion. Calculations on the amount of formed ions are in accordance to the following equation:

$$F.I. = \frac{(O.D_i - O.D_b)}{\varepsilon b} \qquad (1)$$

Where $O.D_i$ and $O.D_f$ are the optical densities of the irradiated and non-irradiated dosimeter, εb is the molar

*Corresponding Author, Tel.: 525556224674, E-mail: negron@nucleares.unam.mx

extinction coefficient for ferric ions, and *b* is the irradiation cell thickness.

II. Methodology

1. Sample Preparation and Irradiation

Irradiation of the dosimeter samples was carried out at Cobalt 60 source (Gammabeam 651 PT) located at the Instituto de Ciencias Nucleares of the Universidad Nacional Autónoma de Mexico (UNAM). The dose rate was 10 Gy per minute.

The chemical components were of the highest quality (Baker Analyzed, Merck and Sigma Chemical Company), in order to reduce the possibility of error in the measurements. Water based dosimeters are very sensitive to impurities that can be oxidized or reduced. To avoid impurities, triple-distilled water was used[4].

The treatment of the glassware was taken into account. The cleaning process followed standard procedures in radiation chemistry[4].

Several cryogenic substances were used to lower the dosimeter's temperature: 1) liquid nitrogen, 2) solid carbon dioxide, 3) water-ice with salt, and 4) water-ice. A thermal bath was used to raise the temperatures of the dosimeter to 303 K and 326 K.

2. Fricke Dosimeter

In the making of the solution the following recipe[3] was used for a total of 500 cc of triple distilled water: 0.20 g of $FeSO_4O$-H_2O, 0.03 g of $NaCl$, 11 cc of H_2SO_4 (95.5-96.5% pure).

Ferric ion production was made by the measurement of the optical density value by UV spectrophotometry using a "Cary 100" instrument. Measurements were taken once the samples had reached room temperature and almost immediately after irradiation.

III. Results and Discussion

1. Basis of the Theoretical Model

The developed model considers the complex chemical reaction kinetics of the phenomena, represented by the set of differential equations that describe the ferrous sulfate radiolysis in a water-based solution.[3]

A two-dimensional matrix containing the reaction equations was created. The program identifies the species involved, as well as their rate constants, initial conditions, and where the species came from. Every line of the matrix contains the reactant for which its derivative is to be computing: *Xi (t)* is the molar concentration for each *i* species (*i* = 1, 2,..., 10) at time *t*, k_j is the reaction rate constant. This constant relates to the species *i* and *j*, f_i is the source term, which contains the production of the *i* species due to radiolysis, and it is a linear function of the intensity of the radiation dose. The equation (1) describes the mass-balance in the sample (which has a direct impact on the f_i factors). The first contribution to consider in the equation is the production due to all the reactions between species *n* and *m* of the samples, which yields the production of the *i* species. The second term of the equation shows the depletion of the *i* species due to the reactions that takes place with any other *j* species in the sample. This matrix is used by a subroutine computing the right hand side of the differential equation system and the Jacobian matrix for the system.

$$\frac{dX_i(t)}{dt} = \sum_{n,m} k_{n,m} x_n(t) \cdot x_m(t) - \sum_j k_{i,j} x_i(t) \cdot x_j(t) + f_i(I_d) \qquad (2)$$

Two factors are present in the mass balancing process: 1) the reaction mechanism and, 2) the program's integration process. Equation (1) represents the relation between the existing species and the quantities in which they are present, and the ferric ion yield after irradiation.

2. Reaction Mechanism

The Theoretical Model previously presented is based in the reaction mechanism that takes place after irradiation of the Fricke dosimeter. The model solves a differential equation based on the different reactions that take place during and after the irradiation of the Fricke dosimeter. These reactions are presented in a time ordered fashion, as given by their rate constants. The considered reactions are

$$H_2O \rightarrow H^{\bullet}, eq^-_{aq}, {}^{\bullet}OH, H_2, H_2O_2, H_3O^+$$

$$H^{\bullet} + O_2 \xrightarrow{k_1} HO_2^{\bullet}$$

$$eq^-_{aq} + H_3O^+ \xrightarrow{k_2} H^{\bullet}$$

$$Fe^{2+} + {}^{\bullet}OH \xrightarrow{k_3} Fe^{3+} + OH^-$$

$$Fe^{2+} + H_2O_2 \xrightarrow{k_4} Fe^{3+} + {}^{\bullet}OH + OH^-$$

$$Fe^{2+} + HO_2^{\bullet} \xrightarrow{k_5} Fe^{3+} + HO_2^-$$

$$HO_2^- + H^+ \xrightarrow{k_6} H_2O_2$$

$$H_2O_2 \xrightarrow{k_7} HO_2^- + H^+$$

The rate constant values are:

$$k_1 \approx 2 * 10^{10} M^{-1} \sec^{-1}, pK_{HO_2^{\bullet}} = 4.4$$

$$k_2 \approx 2.3 * 10^{10} M^{-1} \sec^{-1}, pK_{H^{\bullet}} = 9.7$$

$$k_3 \approx 3 * 10^{8} M^{-1} \sec^{-1}, pK_{OH} = 11.9$$

$$k_4 \approx 50 M^{-1} \sec^{-1}$$

$$k_5 \approx 7.3 * 10^{5} M^{-1} \sec^{-1}$$

$$k_6 \approx 7.3 * 10^{5} M^{-1} \sec^{-1}$$

$$k_7 \approx 10^{5} M^{-1} \sec^{-1}$$

3. Experimental and Theoretical Correlation

Fig. 1 shows the comparative change of the ferric ion formed at different irradiation temperatures. The graphs are presented as their optical density value vs. irradiation dose for three different temperatures: 1) room temperature, 2)

solid carbon dioxide and 3) liquid nitrogen. A very clear change of slope is present when the temperature of irradiation is higher. A higher dispersion of the data is also found as the temperature is raised. The graph response for all three temperatures was linear.

Fig. 1 displays both the experimental values found for the three temperatures mentioned, and it show the tendency lines that the theoretical model, developed for this research, threw as a result.

The validation of the theoretical model is given by the agreement between the experimental results at room temperature (298 K) and the values predicted by it. The correlation between the experimental and the theoretical results is extraordinary with correlation coefficients very close to the unity (i.e. $R^2 = 0.9919$, $R^2 = 0.9932$, $R^2 = 0.9852$).

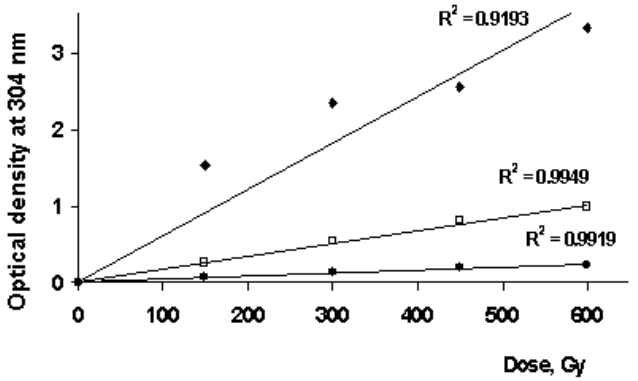

Fig. 1 Doses–response graphs for the Fricke dosimeter at different irradiation temperatures. Symbols represent the experimental data and the lines the theoretical results. ● liquid nitrogen temperature, □ solid carbon dioxide temperature, ◆ room temperature (298 K).

The dependence of the optical density for samples irradiated at the same doses but at four different temperatures near room temperature: 263 K, 273 K, 306 K, and 332 K was linear in all cases, at least for this irradiation dose interval (0 to 600 Gy).

There was dispersion of the experimental results for temperatures near 273 K, but all the samples followed the same trend, and the change in slope is small for this group of temperatures. The highest dispersion is found for water-freeze temperature. This could be related to the fact that at these temperatures solid and liquid phases coincide

In **Fig. 2** we can see more clearly the oxidation behavior of the ferrous ion with respect to the temperature. The graph shows the optical density vs. temperature of irradiation for a single irradiation dose of 600 Gy. This condition was chosen because it is the upper boundary of the linear behavior of the dosimeter. Three different temperatures are used in this graph: liquid nitrogen, solid carbon dioxide and water-freeze temperatures. A much higher dose absorbance is shown for higher temperatures. An exponential relation is depicted by the graph with a correlation coefficient of 0.9974.

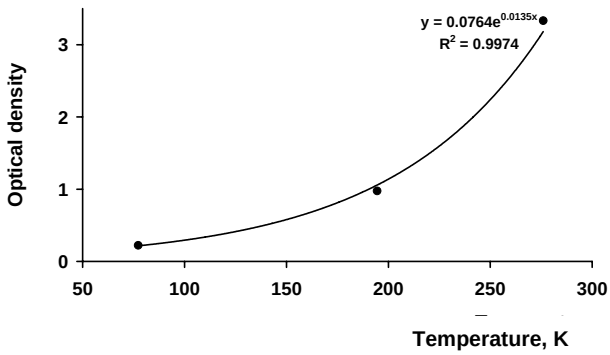

Fig. 2 Change of optical density as function of the irradiation temperature at the same dose (600 Gy).

IV. Conclusions

A definite and clear dependence of the absorbed dose to the temperature was observed for the Fricke dosimeter. In particular, for temperatures within the interval of 77 K to room temperature, a clear change of slope in the absorbance vs. dose graph was found. This means that the energy dose absorbed in the dosimeter is less while at these conditions. A plausible explanation of this phenomenon is that at low temperatures the mobility of the free radicals, and therefore their ability to recombine, is considerably reduced.

The high dispersion found on the experimental data of irradiation near water-ice temperature could be due to the non-homogeneity of the solution, and again, the free radical mobility.

On the other hand, the response of Fricke dosimeter to irradiation is linear up until the point of the dosimeter's saturation. In this work it was found that the interval of linear response was amplified when the temperature of irradiation was lower. This sheds new light upon the use of the Fricke dosimeter for commercial purposes. It also makes very clear that more care needs to be put in the product-irradiation industry, to provide newer and more efficient methods of product treatment in order to reduce the risk of contamination.

Finally, the correlation between experimental and theoretical values was extraordinarily high, and it shows that the basic mechanisms of the oxidation of the Fricke dosimeter are well understood.

Acknowledgements

This work was partially supported by DGAPA Grant IN223406-3. The authors would like to thank C. Camargo, F. García, and S. Ham for their technical assistance. The authors are very gratefully with the reviewers for their valuable suggestion to our manuscript.

References

1) M.L. Lacroix, M. Jobin, S. Hamel, V. Stahl, M. Gagnon and C. De Couvercelle. Effects of 3 and 7 kGy Gamma irradiation doses on odor and flavor of fresh chicken breast". Microbiologie-Aliments-Nutricion. 9, 375-379, 1991.
2) B.L.Gupta; R. Bhat, M.; G.R. Narayan; S.R.

Nilehani,"Chemical dosimetry techniques for various applications under different geometries". Radiation Physics and Chemistry. 59, no.1, pp 81-90, 1991.
3) C.K. Ross, N.V. Klassen, K.R. Short, G.D. Smith, A direct comparison of water calorimetry and Fricke dosimetry. Phys. Med. Biol. 34, 23–42, 1989.
4) J.W.T. Spinks., R.J. Woods, "Introduction to Radiation Chemistry", Ed. John Wiley and Sons, Inc. USA, pp. 475, 1964.

Journal of NUCLEAR SCIENCE and TECHNOLOGY, Supplement 5, p. 294–297 (June 2008)

The Determination of Neutron Dose for Accelerator-Produced Neutrons by Using a Bonner Sphere Spectrometer

Jungho KIM*, Hyeonseo PARK, and Kil-Oung CHOI

Korea Research Institute of Standards and Science, Daejoen 305-340, Korea

The spectral fluences of the neutrons from the $^{18}O(p,n)^{18}F$ reaction were measured at Korea Institute of Radiological & Medical Sciences MC-50 cyclotron. Neutrons were measured with the Bonner sphere spectrometer of Korea Research Institute of Standards and Science. The neutron spectral fluences including the scattered neutrons were evaluated by unfolding together with the initial guess spectrum. The variation of the spectral fluence and the ambient dose equivalent rates were investigated by changing thermal-, intermediate-, and high-energy ratios of the initial guess spectrum. The results show that the spectral fluences and the ambient dose equivalent rates are stable within 2% even though the initial guess spectrum is highly changed. Therefore, if the spectral shape of the initial guess spectrum is chosen properly for the measurement, the spectral fluence of the accelerator-produced neutron can be determined by the unfolding process

KEYWORDS: $^{18}O(p,n)^{18}F$ reaction, Bonner sphere spectrometer, neutron spectral fluence, ambient dose equivalent, initial guess spectrum, unfolding process

I. Introduction

Studies on the characteristics of the accelerator-produced neutrons become important these days as the number of accelerators is increasing like medical cyclotrons used for a high-yield of an indicator substance Fluorine-18 in the positron emission tomography. For the safe and effective operation of the accelerators, it is highly recommended to measure the neutron spectral fluence and to evaluate the ambient dose equivalent during the operation. However, the measurement of the accelerator-produced neutrons has some difficulties due to the high dose rate for the very short time period and the high electromagnetic noise level.

The ambient dose equivalent, $H^*(10)$ can be determined as follows,

$$H^*(10) = \int_{E_{\min}}^{E_{\max}} h^*(10,E) \cdot \Phi_E(E), \qquad (1)$$

where $\Phi_E(E)$ is the neutron fluence and $h^*(10,E)$ is the neutron fluence-to-ambient dose equivalent conversion coefficient. Because $h^*(10,E)$ varies about 100 times higher as the dynamic energy range of the neutron expands from thermal to several tens of MeV[1], the best way to determine the neutron dose is to measure the spectral fluence of neutron.

The neutrons are produced in the target during the accelerator operation. Some neutrons undergo scattering from the accelerator equipments, the walls, and the ceiling in the accelerator room and become thermal neutrons through moderation. Therefore, both the direct neutrons from the target and the scattered neutrons should be measured to determine the scatter-free neutron fluence spectrum by subtracting the scattered from the direct component.

Bonner sphere spectrometer[2] (BSS) is the one of the best devices to measure the neutron spectral fluence for the neutron dose determination. BSS is composed of the thermal neutron detector and polyethylene spheres which are used to moderate fast neutrons to thermal neutrons. The thermal neutron detector is installed in the center of the Bonner sphere and measures the moderated neutrons. The polyethylene sphere is called Bonner sphere. Several Bonner spheres with different diameters are used to measure the large dynamic range of neutron energies from thermal to several tens of MeV.

Korea Research Institute of Standards and Science has 10 PTB-designed Bonner spheres[3] made of high-density polyethylene and ^{3}He spherical proportional counters (SP9, Centronic) which are detectors for thermal neutron measurement. The diameters of each Bonner sphere is 7.62 cm, 8.89 cm, 10.16 cm, 11.43 cm, 12.70 cm, 15.24 cm, 17.78 cm, 20.32 cm, 25.40 cm, and 30.48 cm, respectively. The density and diameter of each Bonner sphere are measured precisely and the response functions of BSS are calculated by the MCNP4C[4] simulation. Finally, the response functions are calibrated and confirmed with a well-specified ^{252}Cf neutron source[5].

II. Experiment

The measurements of neutrons from the $^{18}O(p,n)^{18}F$ reaction were performed at Korea Institute of Radiological & Medical Sciences MC-50 cyclotron[6]. The incident proton energy was 30 MeV and degraded to 21.3 MeV after passing through a 2 mm-thick Al degrader. Water with enriched ^{18}O contained in a 22 mm vial was used for a ^{18}O target. Typical proton beam current was 10.5 nA. Because the neutron count rates depend on both the response of Bonner sphere and the

*Corresponding Author, Tel.: +82-42-878-5788, Fax.: +82-42-868-5671, E-Mail; jungho@kriss.re.kr

beam current, it is very important to measure the fluctuation of the beam current.

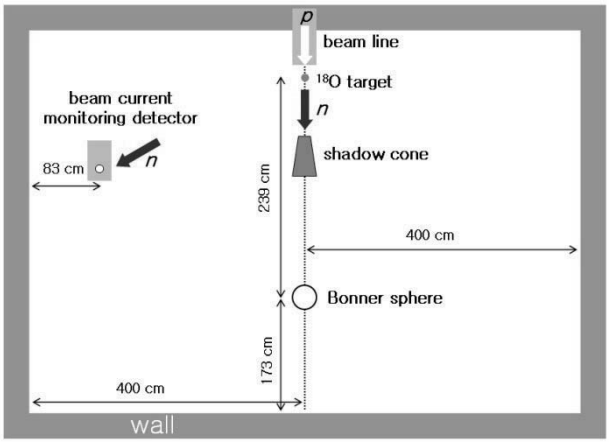

Fig. 1 Schematic view of the experimental setup (top view)

The fluctuation of the beam current during the neutron count rate measurement was monitored with a SP9 ^{3}He proportional counter enclosed in the polyethylene box. The fluctuations of the neutron numbers are proportional to those of the beam currents. The largest beam current variation was about 20% during the measurements.

The measurements were performed at 239 cm from the target with the bare SP9, the SP9 with 1 mm-thick Cd plate, and 10 Bonner spheres as shown in **Fig. 1**. In order to measure the scattered neutrons, shadow cones were installed at 45 cm from the target to block direct neutrons towards Bonner sphere. Shadow cones are composed of iron and polyethylene and the size of a shadow cone and the distance from the target were chosen to fully block the direct neutrons for the each measurement. The measurements were performed with and without shadow cones for each Bonner sphere.

The signals of SP9 ^{3}He proportional counter were converted to ADC channels and recorded with a MCA module. The background events from γ-ray or noise were subtracted to the neutron events.

III. Results

1. Neutron count rates

Neutron count rates of Bonner spheres are presented in **Fig. 2**, where diameters 2.54 cm and 5.08 cm denote the bare SP9 and SP9 with 1 mm-thick Cd plate, respectively. The circles and squares are the count rates without shadow cones (Total) and with shadow cones (S.C.), respectively. The beam current fluctuations were monitored at the same time during the measurements and the neutron count rates were corrected and normalized according to the fluctuations. Open and closed figures in **Fig. 2** denote the neutron count rates before and after normalization of the beam currents, respectively. The queer protrusion of the neutron count rates before normalization of the beam currents disappears in both the measurements and the neutron count rates vary smoothly as the diameter of Bonner sphere increases.

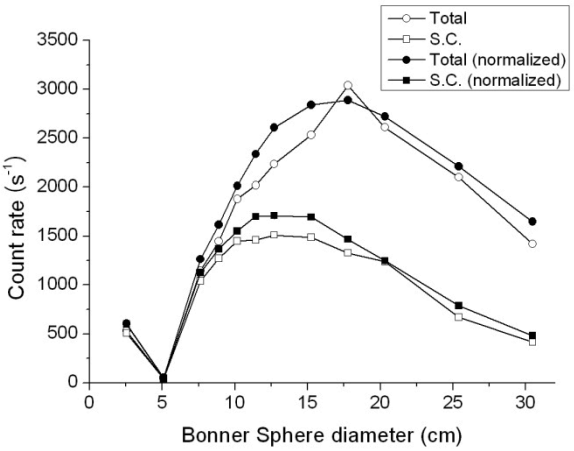

Fig. 2 Neutron count rates of Bonner spheres with (square) and without (circle) shadow cones before and after beam current fluctuation correction. The details are written on the text.

From the neutron count rates, the neutron spectral fluence can be extracted by unfolding procedure. Before unfolding process, a neutron energy spectrum called the initial guess spectrum should be provided as an input of the unfolding. The initial guess spectrum was modeled as the sum of three spectra in thermal-, intermediate-, and high-energy regions, as shown in **Fig. 3**. The parameters of each spectrum were estimated using the statistical estimation based on the Bayesian inference package, WinBUGS[7] code. With the optimized initial guess spectrum, the spectral fluence of the neutron was extracted with the MAXED[8] code of UMG package developed for unfolding process at PTB.

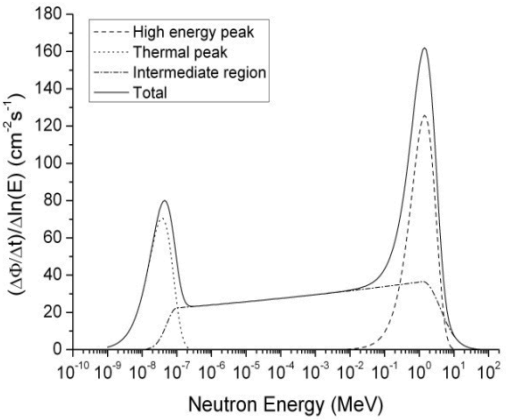

Fig. 3 The model of the initial guess spectrum used for unfolding. It was modeled as the sum of three spectra in thermal-, intermediate-, and high-energy regions.

Table 1 Summary of neutron spectral fluence and ambient dose equivalent for several energy divisions. "Scattered" denotes the scattered neutrons measured with shadow cones and "Total" denotes the all neutrons measured without shadow cones. "Scatter-free" denotes the scatter-free neutrons from the target. See the text in detail.

Neutron energy	Fluence rate ($s^{-1}cm^{-2}$)			Ambient dose equivalent rate (μSvh^{-1})		
	Total	Scattered	Scatter-free	Total	Scattered	Scatter-free
< 0.5 eV	210 (6%)	202 (5%)	7.9 (188 %)	8.64 (6%)	8.25 (5%)	0.4 (160 %)
0.5 eV – 10 keV	277 (4%)	274 (3%)	2.7 (500 %)	10.1 (4%)	9.81 (3%)	0.24 (190 %)
10 keV – 100 keV	72.9 (7%)	81.8 (6%)	-8.9 (73%)	9.1 (7%)	10.2 (7%)	-1.1 (87%)
100 keV – 2 MeV	472 (5%)	290 (3%)	182 (12%)	614 (5%)	346 (3%)	268 (12%)
2 MeV – 5 MeV	381 (7%)	74.0 (7%)	307 (8%)	564 (7%)	110 (7%)	454 (9%)
> 5 MeV	181 (7%)	29.5 (7%)	151 (9%)	272 (7%)	48 (7%)	224 (9%)
Total	1610 (1%)	957 (1%)	652 (2%)	1500 (2%)	539 (2%)	961 (3%)

2. Spectral fluence and ambient dose equivalent rates

Fig. 4 shows the neutron spectral fluence for total, scattered, and direct neutrons from the $^{18}O(p,n)^{18}F$ reaction for several energy divisions. The spectra are represented as lethargy plots. The direct spectral fluence was estimated by subtracting the scattered spectral fluence from the total spectral fluence. Because the incident protons lose their energies and stop in the thick target, the neutrons with the wide spread of the energy are produced above threshold energy of the $^{18}O(p,n)^{18}F$ reaction. The mean energies are 1.97, 0.95, and 3.55 MeV for total, scattered, and direct spectra, respectively. It is clearly shown in the figure that only the scattered neutrons contribute the fluence below 100 keV because the total and the scattered spectral fluences are almost same below 100 keV. The fraction of the scattered neutrons below 100 keV is about 35% for the total measurement and about 60% for the measurement with shadow cones. The large fraction of the scattered neutrons in the measurement represents the fact that it is hard to neglect the scattering effects at the interesting point to measure the spectral fluence in the accelerator room of small size.

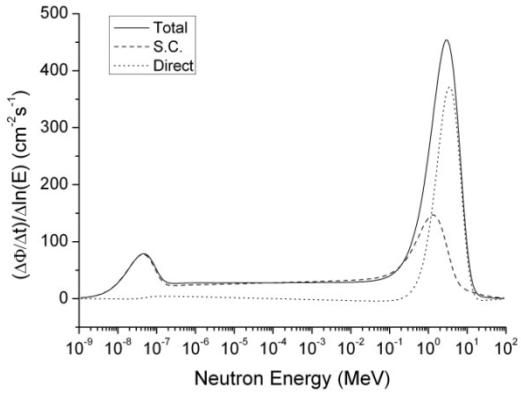

Fig. 4 Neutron spectral fluences for total, scattered, and direct neutrons from $^{18}O(p,n)^{18}F$ reaction.

The ambient dose equivalent rate was determined by the neutron spectral fluence and the neutron fluence-to-ambient dose equivalent conversion coefficient, $h^*(10,E)$ from the ICRP74 recommendation[1]. In **Table 1**, the neutron spectral fluences and the ambient dose equivalent rates for several energy divisions are summarized. The numbers in parentheses are the uncertainties (k=1). The dose-weighted mean energies are 3.18, 2.59, and 3.72 MeV for total, scattered, and direct spectra, respectively. Because $h^*(10,E)$ of the scattered neutrons below 100 keV is about 1/30 to that of the fast neutrons above 1 MeV, the characteristics of the ambient dose equivalent rate are much different to those of the spectral fluence. The fraction of the neutrons below 100 keV for the ambient dose equivalent rates is about 2~3% which is much reduced compared to the fraction 35% for the spectral fluence rates. The fractions of both the neutron spectral fluences and the ambient dose equivalent rates are also summarized for several energy divisions.

Table 2 Summary of the neutron fractions for several energy divisions. "S" denotes the scattered neutrons measured with shadow cones and "T" denotes the all neutrons measured without shadow cones. "SF" denotes the scatter-free neutrons from the target. See the text in detail.

Neutron energy	Fluence rate ($s^{-1}cm^{-2}$)			Ambient dose equivalent rate (μSvh^{-1})		
	T	S	SF	T	S	SF
< 0.5 eV	13	21	1.2	0.6	1.5	0
0.5 eV – 10 keV	17	29	0.4	0.7	1.8	0
10 keV – 100 keV	4.5	8.5	-1.4	0.6	1.9	0
100 keV – 2 MeV	9.3	30.3	27.9	40.9	64.2	27.9
2 MeV – 5 MeV	23.7	7.7	47.1	37.6	20.4	47.2
> 5 MeV	11.2	3.1	23.2	18.1	8.9	23.3
Total	100	100	100	100	100	100

IV. Conclusions

In this study, the spectral fluences of the neutrons from the $^{18}O(p,n)^{18}F$ reaction were measured with the Bonner sphere spectrometer at Korea Institute of Radiological & Medical Sciences MC-50 cyclotron. The spectral fluences of the total and the scattered neutrons showed that the spectral fluence and the ambient dose equivalent are stable within 2% even though the initial guess spectrum of unfolding is highly changed. The fraction of the scattered neutrons in this work was 35% in the neutron spectral fluence, which represents that the effects of the scattered neutrons are not negligible for the application using neutron beams.

Active detectors like ^{3}He proportional counters easily malfunction when neutron production rate is very high due

to a high-current operation. For the study of the accelerator-produced neutrons in such a case, the neutron spectral fluence should be performed using the passive detector measurement like gold-foil activation. In the near future, the measurement with gold-foil activation will be performed and compared with the results of Bonner sphere spectrometer.

Acknowledgement

This work was performed under the long-term nuclear research and development program sponsored by Ministry of Science and Technology of Korea.

References

1) ICRP 74, Annals of the ICRP 26 (1996) No. 3/4.
2) A. V. Alevra and D. J. Thomas, 'Neutron Spectrometry in mixed fields: Multisphere spectrometer', Rad. Prot. Dosim. Vol. 107, pp37-72, 2003.
3) B. Wiegel, A. V. Alevra, 'NEMUS-the PTB neutron Multisphere Spectrometer: Bonner Spheres and more', Nucl. Instrum. Meth. A447, pp36-41, 2002.
4) J. F. Briesmeister, Ed., 'MCNP-A General Monte Carlo N-Particle Transport Code Version 4C.' LA-13709-M, Los Alamos National Laboratory, 2000.
5) Hyeonseo Park, Jungho Kim, and Kil-Oung Choi, "Neutron Calibration Facility with Radioactive Neutron Sources at KRISS", Rad. Prot. Dosim., in print, 2007.
6) J. H. Kim, H. Bhang, and J. H. Ha, et al, 'A Measurement of Monoenergetic Neutrons from $^{9}Be(p,n)^{9}B$', Jour. Kor. Phys. Soc. 32, 462, 1998
7) Marcel Reginatto, Paul Goldhagen, Sonja Neumann, 'Spectrum unfolding, sensitivity analysis and propagation of uncertainties with the maximum entropy deconvolution code MAXED', Nucl. Instrum. Meth. A476, pp242-246, 2002.
8) The BUGS Project : WINBUGS http://www.mrc-bsu.cam.ac.uk/wiinbugs/contents.stml.

Journal of NUCLEAR SCIENCE and TECHNOLOGY, Supplement 5, p. 298–301 (June 2008)

Neutron Spectrum Measurement at the Workplace of Nuclear Power Plant with Bonner Sphere Spectrometer

Hyeonseo PARK[1*], Jungho KIM[1], and Kil-Oung CHOI[1]

[1] *Korea Research Institute of Standards and Science, Daejeon, 305-340, Korea*

With BSS system, the neutron spectral fluences at the workplace of nuclear power plant at Wolsong were measured. The 9 points at the 4th and 5th floor of the reactor building were selected for the spectrum measurement, where the radiation workers access for the ordinary check of the operation. The spectra show the distribution from the thermal to several MeV, which are composed of the original fission spectrum, scattered fast neutrons and thermal neutrons. The spectral shapes for the places at the same floor are similar to each other. Although the number of data points is limited, we may determine the standard neutron spectrum for each floor and this would help improving the uncertainties of neutron doses. For the comparison, we measured the neutron ambient dose with neutron survey meter (EG&G Ortec, LB6411) and personal dose with TLD on PMMA phantom.

KEYWORDS: bonner sphere spectrometer (BSS), workplace field, nuclear power plant, neutron spectral fluence, neutron dose

I. Introduction

The determination of neutron dose is quite difficult because of the wide spread of the neutron energy from thermal to several tens of MeV and the strong dependence of the biological influence on the neutron energy. Most of the neutron dosimeters show different responses depending on the neutron energy distribution and one should be careful if his/her neutron dosimeter is properly chosen and/or calibrated considering the energy distribution of the interesting places. The information of the neutron energy spectrum can give the most accurate dosimetric quantities and may provide the tools to evaluate the reliability of the dosimetric devices.

One of the best ways to determine the neutron dose is to measure the neutron energy spectra at the interesting point. If one knows the energy spectra, $\Phi_E(E)$, he can determine the ambient dose equivalent H*(10) due to neutrons using the fluence-to-ambient dose equivalent-conversion coefficient, h*(10,E)[1)], according to the formula:

$$H^*(10) = \int_{E_{\min}}^{E_{\max}} h^*(10,E)\cdot\Phi_E(E). \quad (1)$$

The Korea Research Institute of Standards and Science (KRISS) recently set up the Bonner Sphere Spectrometer (BSS) system[2)], which is one of the best and most widely used devices for the measurement of neutron energy spectra. It could measure the neutron energy spectra from the thermal region to the several tens of MeV at the same time.

Fig. 1 shows the KRISS Bonner sphere system, which is composed of 10 polyethylene spheres of KB030 (diameter: 7.62 cm), 035 (8.89), 040 (10.16), 045 (11.43), 050 (12.70), 060 (15.24), 070 (17.78), 080 (20.32), 100 (25.40), and 120 (30.48), and 010 (bare SP9, Centronic : He-3 spherical proportional counter) as a thermal neutron detector. KRISS BSS is PTB-designed[3)] and produced by Centronic. The response functions are calibrated very carefully with MCNP4C[4)] and calibrated/confirmed with well specified ^{252}Cf neutron source[5)].

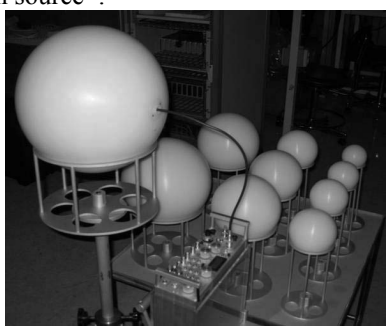

Fig. 1 KRISS Bonner Sphere System

II. Measurement

The series of the measurements of the neutron spectral fluence were performed at the workplace field inside reactor building at the Nuclear Power Plant of Wolsong Site. The reactor is CANDU-type PHWR (Pressurized Heavy Water Reactor). For this type of reactor, the fuel exchange was done during the ordinary operation continuously. The measurement should be performed during the day when the fuel exchange is not planned, in order to avoid the effect of the direct exposure of neutrons from the spent fuel. The time period when the spent fuel was exposed was just several minutes, but it could spoil the whole spectrum measurement which should be taken for several hours. The points where the radiation workers entered frequently for the ordinary work, were selected for the measurement. **Fig. 2** shows the points for the spectrum measurements. The 3 points on the 4th floor of reactor building are near the steam generator but just beside the wall (R406-4A, 4B and R405-4C). On the 5th floor, one point is at the center of the floor (R501-5A) and

*Corresponding Author, Tel. +82-42-868-5703, Fax. +82-42-868-5671, E-Mail; hyeonseo@kriss.re.kr

another one is near the steam generator but just beside the wall (R501-5B). The remaining 4 points are around the steam generators (R501-5C, D, E, F).

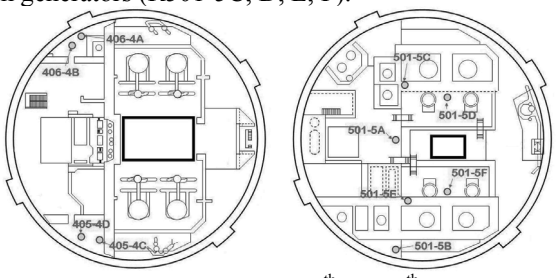

Fig. 2 The schematic view of the 4th and 5th floor of Wolsong Nuclear Power Plant. The filled circles labeled with room numbers indicate the points where the neutron spectra were measured.

At each point, the count rates for one bare He-3 counters and 9 Bonner Spheres (except for KB120 sphere) were measured. The count rate measurements were done till the total count exceeded 100,000. The whole count rate measurement for each point took about 4-5 hours. After finishing count rate measurement for the whole set, the measurement with the survey meter, Berthold LB6411 (EG&G Ortec) and the measurement with TLD (Panasonic UD-802AT) installed on PMMA phantom (40cm x 40cm x 15cm) were performed at the exactly same position for the comparison. **Fig. 3** shows the typical count rate spectrum measured at R501-5B.

Fig. 3 Count rate for each Bonner Sphere measured at the 5th floor, R501-5B position. The label of X-axis represents for KRISS Bonner Sphere ID (KB010 to KB100). KB035, 045 were omitted because it was too busy.

To extract the neutron spectral fluence from the count rate, the spectrum unfolding should be performed. The MAXED code[6] of UMG package was used for the spectrum unfolding. The initial spectrum for the input of unfolding procedure was estimated using WinBUGS code, which is the package for the statistical estimation based on the Bayesian inference[7].

III. Results

1. Neutron spectral fluence

Fig. 4 shows the neutron spectral fluence for each point measured by KRISS BSS. **Fig. 4-a**, **4-b**, and **4-c** represent the neutron spectral fluences measured at the 4th floor. The fractions of thermal neutrons are different for each measured position. However, the spectral shapes of the fast neutron part are similar to each other. In addition, R406-4A and R405-4C (**Figs. 4-a** and **4-c**) are located symmetrically from the point of view of steam generator and the results show very similar spectral shapes of two points including thermal neutron fractions. R406-4B was located a bit farther from the steam generator compared to other two points and the spectrum shows more thermal neutron fraction.

Fig. 4-d to **4-i** show the neutron spectral fluences measured at the 5th floor. Among 6 spectra, 5 spectra of **Figs. 4-d**, **4-f**, **4-g**, **4-h**, and **4-i** show very similar spectral shapes. The locations of these measurements are around the steam generator. **Fig. 4-e** shows different spectral shape from the other spectra in the 5th floor. The spectrum of R501-5B (**Fig. 4-e**) shows similar shape with the spectra of the 4th floor. This is because the location of R501-5B is almost same with the location of R405-4C except for the floor. That is, the relative location to the steam generator and the wall of reactor building is same for both measurement positions. This makes the similar spectral shape for neutrons.

Table 1 shows the neutron fluences at each measurement. The neutron fluences are changed from 50 $n \cdot cm^{-2} \cdot s^{-1}$ to 1000 $n \cdot cm^{-2} \cdot s^{-1}$ depending on the measurement position. As discussed before, the spectral shape of each position is similar with each other but the absolute fluence or the amount of neutrons is different depending on the position, especially due to the distance from the steam generator. The fractions of the thermal neutrons for each measurement were also estimated and the thermal neutron fraction is bigger when the measurement was performed near the wall.

Table 1 also shows the mean energy of the spectrum and also dose-weighted mean energy. The differences between the mean energy and the mean energy weighted by dose are due to the different thermal neutron contaminations in the spectra.

2. Neutron dose equivalent

The neutron dose equivalent was determined by the neutron spectral fluence, $\Phi_E(E)$, and the neutron fluence-to-ambient dose equivalent-conversion coefficient, h*(10,E). **Table 2** shows the neutron dose equivalent determined from the neutron spectral fluence applying ICRP74. The dose determined in this way should be most accurate because the dependence of the quality factor on the neutron energy is fully considered.

The survey meter measurements were carried out just after the spectrum measurement at the exactly same position and the results are shown in the table, labeled with "LB6411." The survey meter used is calibrated with standard ^{252}Cf source at KRISS. The measured value with LB6411 shows very good agreement with the true value, which is determined with the energy spectrum.

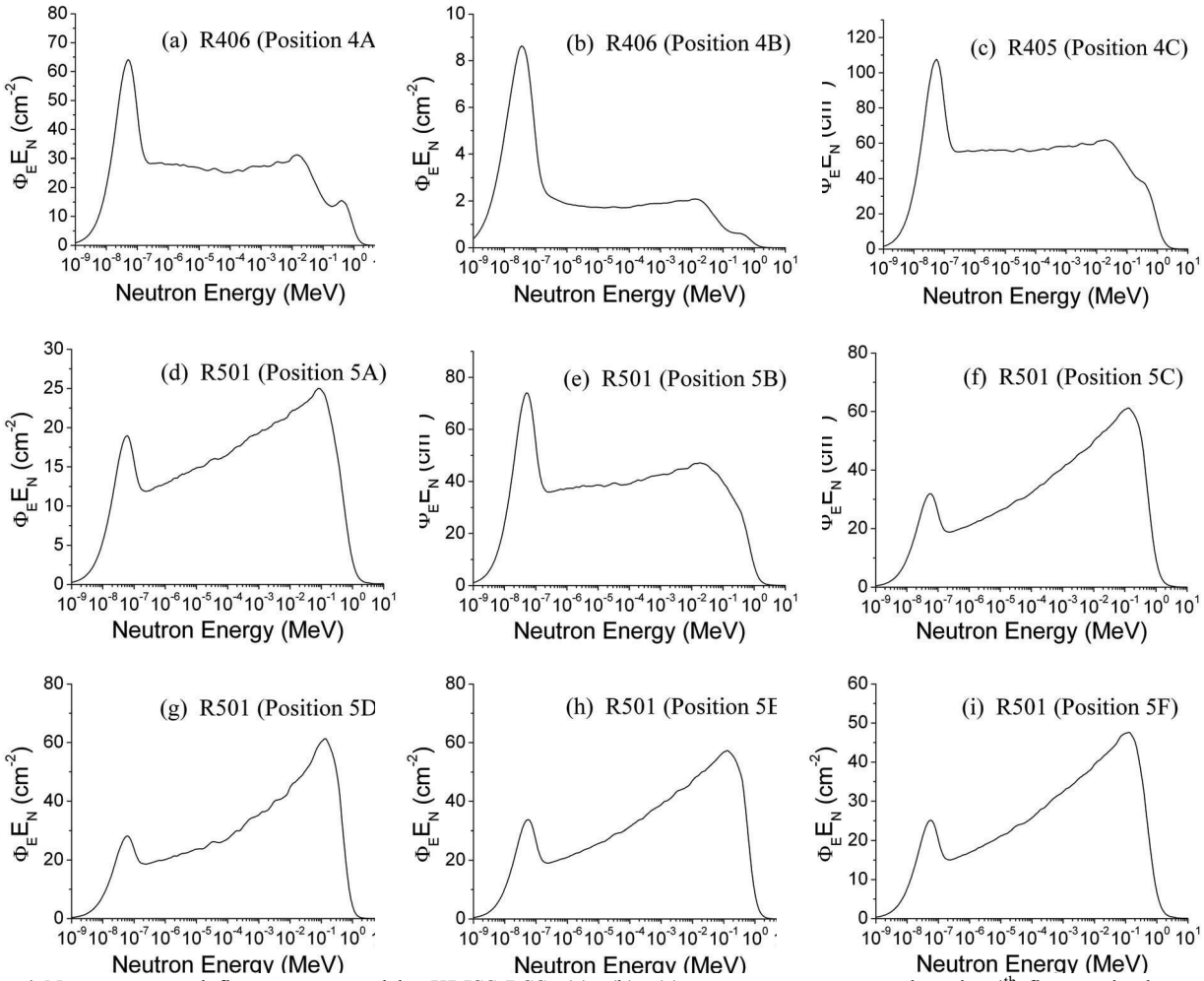

Fig. 4 Neutron spectral fluence measured by KRISS-BSS. (a), (b), (c) were spectra measured at the 4th floor and others are measured at the 5th floor. The details are written on the text.

Even though neutron survey meter measurement was done with LB6411 only, the expected reading of several types of neutron survey meters could be estimated using the neutron spectral fluence and the known response of the neutron survey meter. This was performed for the survey meters from LEAKE (Leake Spherical remmeter, 95/0075), Eberline (Eberline NRD), and Studsvik (Studsvik 2202D). The response functions of these survey meters were taken from IAEA technical note.[8] **Table 2** shows the estimated reading for those survey meters. LEAKE and Eberline show about 2 times higher dose than the true value. Studsvik shows good agreement with the true value.

This study shows that LB6411 and Studsvik 2202D are adequate survey meter for the workplaces at Wolsong site.

TLD measurement with PMMA phantom was also performed for several points. The reading from TLD shows about 3~5 times higher value than the expected reading and the amount of the overestimation increases as the thermal neutron fraction increases. It means that the thermal neutron at the field affects the TLD reading and one should consider the effect of thermal neutrons seriously.

IV. Conclusions

In this study, the neutron spectral fluences were measured with Bonner Sphere Spectrometer system at the workplaces of reactor building at Wolsong Site of Nuclear Power Plant. The 3 points at the 4th floor and 6 points at the 5th floor were measured. The total fluences were changing, depending on the measured positions and the distances from the steam generator which would be the source of neutrons. However, the spectral shapes of the neutron field were not much different from each other. Especially, the spectral shapes of the neutron fields at the middle part of the reactor building are very similar with each other. The spectral shapes measured beside the wall were very similar with each other, too.

This suggests that one or two "typical" neutron spectra could be evaluated for the workplaces and that it would help to give the better calibration procedure for the neutron survey instruments and/or to determine more accurate neutron dose.

The measurement with the various type of neutron survey meters were also performed in reality or simulated. At

Wolsong Site, LB6411 and Studsvik survey meter give the good estimates of the neutron dose. TLD is also tested and it gives quite big overestimation and the reading from TLD can give only ON/OFF signature for neutrons, not give the real dose for neutrons.

The neutron spectrum measurement at the workplace field should be continued for the whole reactors and it will make the neutron dosimetry at NPP more reliable and the radiation work safer.

Acknowledgement

This work was performed under the long-term nuclear research and development program sponsored by Ministry of Science and Technology of Korea. The authors would like to give special thanks to Mr. Lee, Seung-Soo and other staff members of Wolsong site of KNHP for their supports for the measurement. Also, authors want to appreciate to Mr. Seo, Jang-Soo, Mr. Won, Yoo-Ho, Mr. Son Joong-Kwon of NETEC for their efforts and help during the co-works for the measurement.

References

1) ICRP 74, Annals of the ICRP 26 (1996) No. 3/4.
2) A. V. Alevra and D. J. Thomas, "Neutron Spectrometry in mixed fields: Multisphere spectrometer", Rad. Prot. Dosim. Vol. 107, pp37-72, 2003.
3) B. Wiegel, A. V. Alevra, "NEMUS-the PTB neutron Multisphere Spectrometer: Bonner Spheres and more", Nucl. Instrum. Meth. A447, pp36-41, 2002.
4) J. F. Briesmeister, Ed., "MCNP-A General Monte Carlo N-Particle Transport Code Version 4C." LA-13709-M, Los Alamos National Laboratory, 2000.
5) Hyeonseo Park, Jungho Kim, and Kil-Oung Choi, "Neutron Calibration Facility with Radioactive Neutron Sources at KRISS", Rad. Prot. Dosim., in print, 2007.
6) Marcel Reginatto, Paul Goldhagen, Sonja Neumann, "Spectrum unfolding, sensitivity analysis and propagation of uncertainties with the maximum entropy deconvolution code MAXED", Nucl. Instrum. Meth. A476, pp242-246, 2002.
7) The BUGS Project : winbugs http://www.mrc-bsu.cam.ac.uk/wiinbugs/contents.stml.
8) "Compendium of Neutron Spectra and Detector Responses for Radiation Protection Purposes", Technical Reports Series No. 403, IAEA, VIENNA, 2001.

Table 1 Summary of neutron spectral fluence measurement. The mean energy is weighted by neutron fluence. The mean energy with asterisk is weighted by the neutron dose. Thermal neutrons were defined to be the neutrons of $E_n < 0.5$ eV.

	Fluence $n/cm^2/s$	Mean Energy (keV)	Mean Energy* (keV)	Thermal neutron Fraction
4A	538	29	299	33 %
4B	48.7	14	184	33 %
4C	1090	39	348	28 %
5A	313	71	579	18 %
5B	778	41	360	27 %
5C	652	64	336	15 %
5D	585	57	272	14 %
5E	633	61	317	16 %
5F	511	63	359	15 %

Table 2 Neutron dose equivalent determined with the spectral fluence applying ICRP74. The measured values with Berthold LB6411 were compared. The value for the other survey meters, LEAKE remmeter, Eberline NRD, Studsvik 2202D are estimated values using the calculated response.

	ICRP 74 μSv/h	LB 6411 μSv/h	LEAKE (μSv/h) Estim	Eberline (μSv/h) Estim	Studsvik (μSv/h) Estim
4A	52.5	51.2	111	121	48.2
4B	3.2	-	7.5	7.8	2.9
4C	125	122	249	274	113.6
5A	43.4	49.2	83.6	95.3	39.2
5B	88.4	87.2	179	199	80.4
5C	115	109	201	228	99.7
5D	99.1	91.2	177	202	85.9
5E	110	-	193	218	95
5F	85.1	-	154	175	75

Journal of NUCLEAR SCIENCE and TECHNOLOGY, Supplement 5, p. 302–305 (June 2008)

A Novel Method of 3-Dimensional Radiotherapy for Head-and-Neck Cancer Treatment

Yong Nam KIM, Chang Geol LEE*, Kyoungkeun JEONG, Joo Young KIM, and Jinsil SEONG

Yonsei University, 134 Shinchon-dong, Seodaemun-gu, Seoul 120-791, Korea

This study intends to develop a novel method to resolve the problem of extreme dose inhomogeneity in the photon-electron abutting fields in the 3DCRT (3-Dimensinal Conformal Radiation Therapy) for head-and-neck cancer. Firstly, the conventional method using bilateral irradiation of photon and electron beam is reviewed, concerning the inhomogeneity of dose distribution, i.e., the root cause of a hot and a cold spot. Second, based on the root causes in the conventional plan, an alternative method is developed using oblique irradiation of photon and electron beam. Finally, a comparative analysis between both plans is performed to assess feasibility of the new method. From the results of qualitative comparison, it is shown that that the new method can reduce dramatically the maximum dose inside the irradiation fields for all the target region. The volume fractions of hot regions receiving higher dose than the prescribed dose are also significantly decreased. It is also noted that the new method does not give rise to increase in dose to spinal cord. The obtained results suggest that the new method using oblique irradiation of both photon and electron beam can reduce significantly improve the dose inhomogeneity inside radiation field for treatment of head and neck cancer.

KEYWORDS: radiation therapy, 3DCRT, head-and-neck cancer, dose inhomogeneity, photon-electron abutting fields

I. Introduction

In the conventional method of 3DCRT (3-Dimensinal Conformal Radiation Therapy) for head-and-neck cancer treatment, 4-6 MV X-rays in a laterally opposed setup are used to treat the gross disease and the primary tumor. In this treatment, a major planning issue is to limit the dose to spinal cord below the tolerance dose. The margins of the photon fields are then moved anteriorly to exclude the irradiation to spinal cord before tolerance dose is exceeded. In order to boost the dose to the cervical nodes overlying the spinal cord, enface electron fields are "hot-matched" on skin with the posterior edges of the respective ipsilateral photon fields irradiating the primary tumor.

When an electron field is abutted at the surface with a photon field, the traditional method using bilateral field gives rise to an extreme inhomogeneity of dose distribution with both very hot and very cold regions[1,2,3]. When we consider clinically only tumor doses of primary concern regardless of dose to normal tissues, the hot spots can be accepted, depending on their magnitude, extent, and location. However, an extreme inhomogeneity inside the radiation field is generally undesirable. An overdose to normal tissues around a target region or an underdosage in the tumor may be problematic.

This study intends to suggest a novel approach to improve the dose distribution inside the photon-electron abutting fields for head-and-neck cancer treatment. The patient with supraglottic cancer, previously treated with the conventional method in Yonsei University Medical Center, is considered in this study. Firstly, the conventional method using bilateral fields is reviewed, concerning the inhomogeneity of dose distribution, i.e., the root cause of a hot and a cold spot. Based on the root causes in the conventional plan, an alternative method is developed using oblique fields. A comparative analysis between the conventional and the alternative plan is performed concerning coverage and homogeneity of the dose distribution within the target volume, and the sparing of the organs at risk. All the treatment plans are made using a commercial three-dimensional treatment planning system (Pinnacle^{3TM} Version 6.2b, Philips Medical Systems, Milpitas, CA, USA).

II. Development of a Novel Method

1. Conventional Method Using Bilateral Fields

The beam configuration and treatment setup using bilateral fields on the planning system is illustrated in **Fig. 1** and **Fig. 2**. In the conventional method, 6 MV photon beams are irradiated bilaterally from the left side and the right. In order to prevent spinal cord from irradiation, the right jaw in the left photon field is closed to the edge of spinal cord adjacent to the target volume, as shown in **Fig. 1** and **2 (a).** For the same reason, the lead block is set up with the sufficient margin to prevent the dose to spinal cord cause by setup error and the penumbra of photon field. In order to give dose to the part of right lower neck node overlying spinal cord, excluded from the photon field, 6MeV electron beam is irradiated from the ipsilateral direction. As shown in **Fig. 2 (b)**, the lead block is precisely adjusted to match the borders of blocks adjacent to the right lower neck node in the photon and electron fields.

*Corresponding Author, Tel.: +82-2-2019-3152, Fax.: +82-2-3463-7441, E-Mail : cglee1023@yuhs.ac

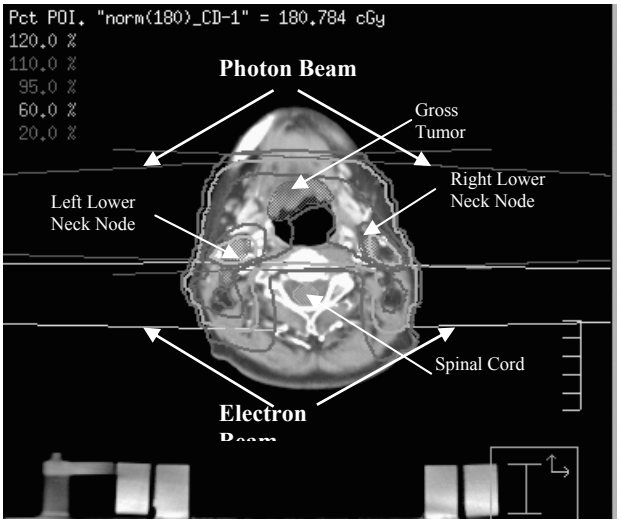

Fig. 1 Beam configurations and isodose distributions in the conventional method 3

2. Rationale for a New Approach

The dose to be delivered is prescribed in terms of point dose to a certain point for prescription. In both region using photon fields and electron fields, the point dose of 180 cGy is prescribed. In **Fig. 1**, it is shown that the conventional method gives rise to extreme hot region more than 120% of prescribed dose in the abutting region of photon and electron fields. **Fig. 3** shows the independent contribution of each field of photon and electron to dose to target volume. It should be noted that isodose line above 110 cGy goes beyond the edge of electron field in **Fig. 3 (b).** In other words, the extreme inhomogeneity is caused by electron dose contribution.

It should be also noted the isodose line of very small dose, 20 cGy, in the photon field is sharply cut in the border line. Here, we can consider an alternative method to reduce extreme inhomogeneity:

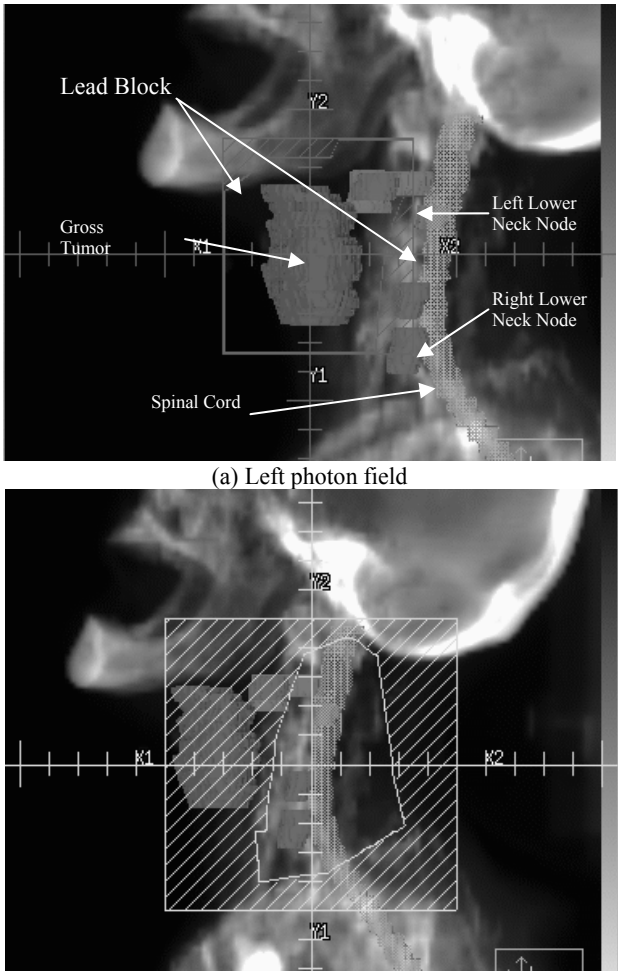

(a) Left photon field

(b) Left electron field

Fig. 2 Treatment setup using lead block in the conventional method

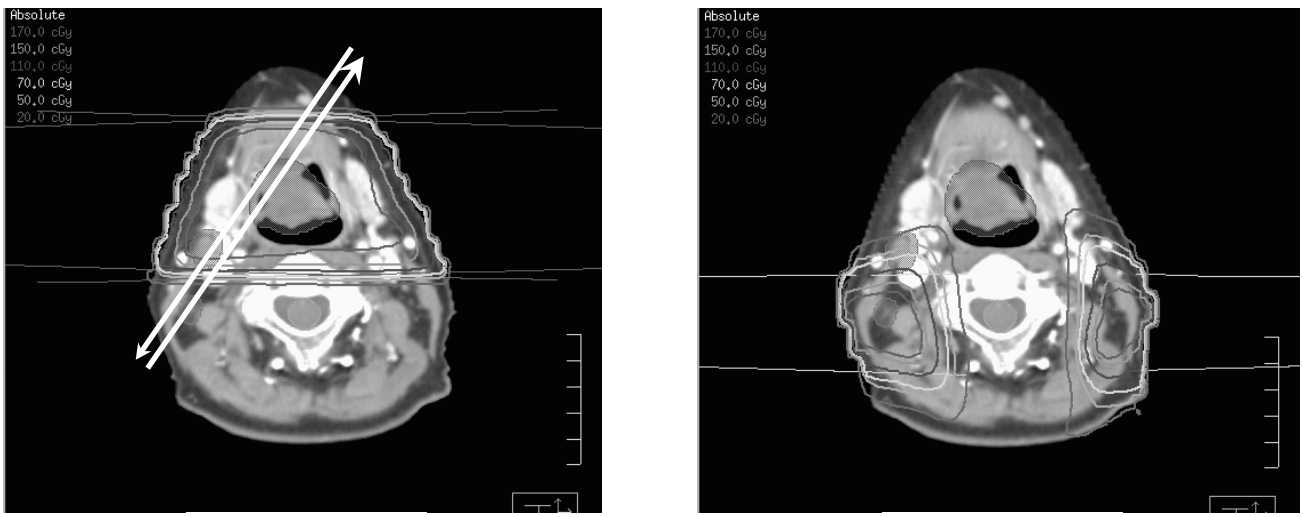

(a) Photon fields (b) Electron fields

Fig. 3 Independent dose contributions by photon and electron field in the conventional method

The root cause for inhomogeneity is electron dose contribution.

If and only if we decrease the electron dose contribution to lower neck node, dose inhomogeneity can be reduced.

The photon field can not give any contribution to dose to lower neck node.

In order to decrease the electron dose contribution to lower neck node, we consider an oblique irradiation of photon beam which passes through the entire lower neck node in the direction of the white arrow in **Fig. 3 (a)**.

3. The Novel Method Using Oblique Fields

Fig. 4 shows the beam configuration in conjunction with isodose curves in the new method. The treatment set up is shown in **Fig. 5**. To deliver dose to primary gross tumor two photon beams is irradiated in the posterior-oblique direction. As shown in **Fig. 5 (a)**, the left sided photon field covers the whole left lower neck node as well as the primary gross tumor. Additionally, 9 MeV electron beam is irradiated in the anterior-oblique direction to boost the dose to the left lower neck node. The lead blocks are adjusted carefully to cover all the target volumes and to escape overlapping of the both field of photon and electron beam. Similarly, two fields of photon and electron beam in the right side are set up. Dose deliveries by each field are adjusted to meet the clinical prescription, 180 cGy, for all the target volumes. The oblique irradiation setup can decrease the contribution of electron dose to the lower neck node to 70 cGy (40% of the prescribed dose), because the photon beam is overlapped in the neck node to deliver 60% of the prescribed dose, 110 cGy.

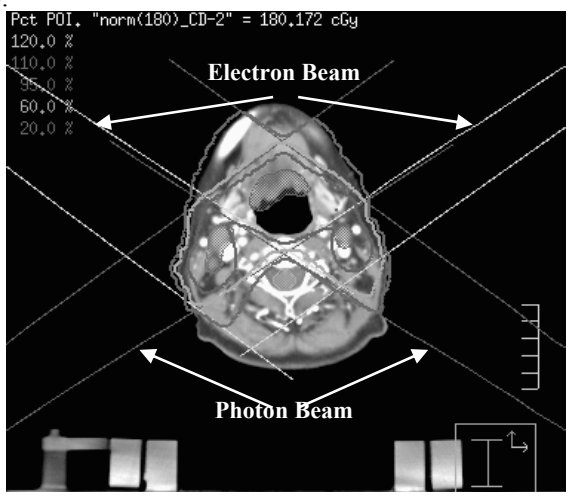

Fig. 4 Beam configurations and isodose distributions in the new method

III. Comparative Evaluation of the Novel Method

From the comparison the isodose curves between **Fig. 2** and **4**, it can be noticed that the isodose line of 120% in the lateral irradiation is spread out inward to the photon fields. However, not only 120% line but also 110% line disappears in the oblique irradiation. This indicates that the oblique irradiation can remove or reduce hot regions in the abutting regions without formation of any cold region.

The dose statistics data are compared in **Table 1**. In the case of lateral irradiation, the hot regions of primary gross disease receiving 107% of prescribed dose are spread over the 38.9% of volume. However, the oblique irradiation can reduce dramatically the volume fraction of V107% to 5.3%. Concerning the lower neck lymph nodes, the lateral irradiation increases the maximum dose more than 250 cGy in both the right and the left neck node. Their volume fractions are considerably large, as shown in the column of V115%. On the other hand, the hot region in the case of oblique irradiation is removed clearly; the values of V115% are zero in both neck nodes.

In **Fig. 6**, the dose volume histograms (DVH) are compared. The improvement of dose homogeneity in the target region, especially the lower neck node, is noticed clearly. The DVH for spinal cord is slightly higher in the case of oblique irradiation. However, it should be also noted that the difference is not significant between each other. This difference can be reduced by adjusting the margin for blocking the spinal cord. This indicates that the oblique irradiation does not give rise to increase in the dose to spinal cords.

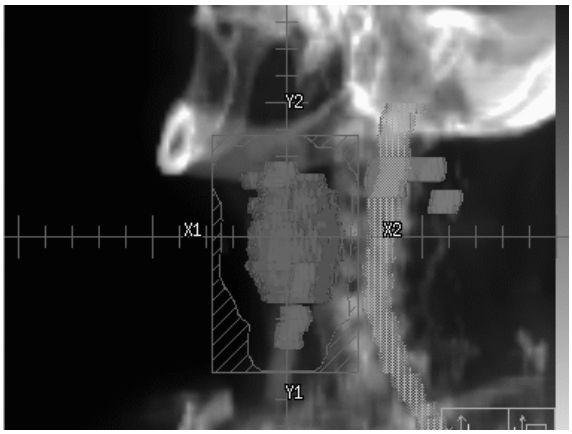

(a) Left posterior photon field

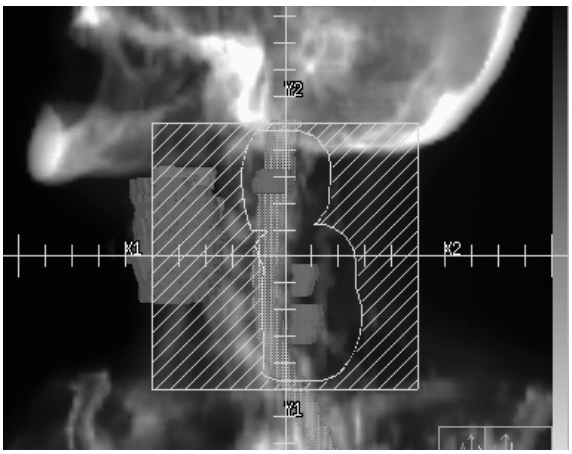

(b) Left anterior electron field

Fig. 5 Treatment setup using lead block in the new method

Table 1. Comparison of dose statistics between the conventional and the new method

Target	D_min [cGy]	D_mean [cGy]	D_max [cGy]	V95%[a)] [%]	V107% [%]	V115% [%]
			Lateral irradiation (conventional method)			
Primary Gross Tumor	170.8	190.5	216.1	99.9	38.9	1.6
Left Lower Neck Node	121.8	199.9	252.1	86.6	66.5	43.1
Right Lower Neck Node	134.1	214.9	262.2	93.0	79.2	66.2
			Oblique irradiation (new method)			
Primary Gross Tumor	171.1	186.7	196.9	99.9	5.3	0.0
Left Lower Neck Node	120.8	182.4	196.4	88.5	8.9	0.0
Right Lower Neck Node	157.1	184.4	193.2	94.3	4.9	0.0

[a)] V95% denotes the fraction of target volumes receiving more than 95% of the prescribed dose.

IV. Conclusions

The obtained results in this study suggest that the extreme inhomogeneity of dose distribution in the region of photon-electron abutting fields for treatment of head and neck cancer can be resolved by employing oblique irradiation of both photon and electron beams.

References

1) C. Sum, C. W. Cheng, D. S. Shin, et. al., "Dose profiles in the region of abutting photon and electron fields in the irradiation of head and neck cancer tumors," Medical Dosimetry, 23, 5(1998).
2) F. M. Khan, The Physics of Radiation Therapy, 3rd Edition, Lippincott Williams & Wilkins, Philadelphia, 328 (2003).
3) T. W. Johnson and F. M. Khan, "Dosimetric effects of a abutting fields and photon fields in the treatment of head and neck cancer," Int. J. of Radiation Oncology, Biology, and Physics, 28, 741(1994).

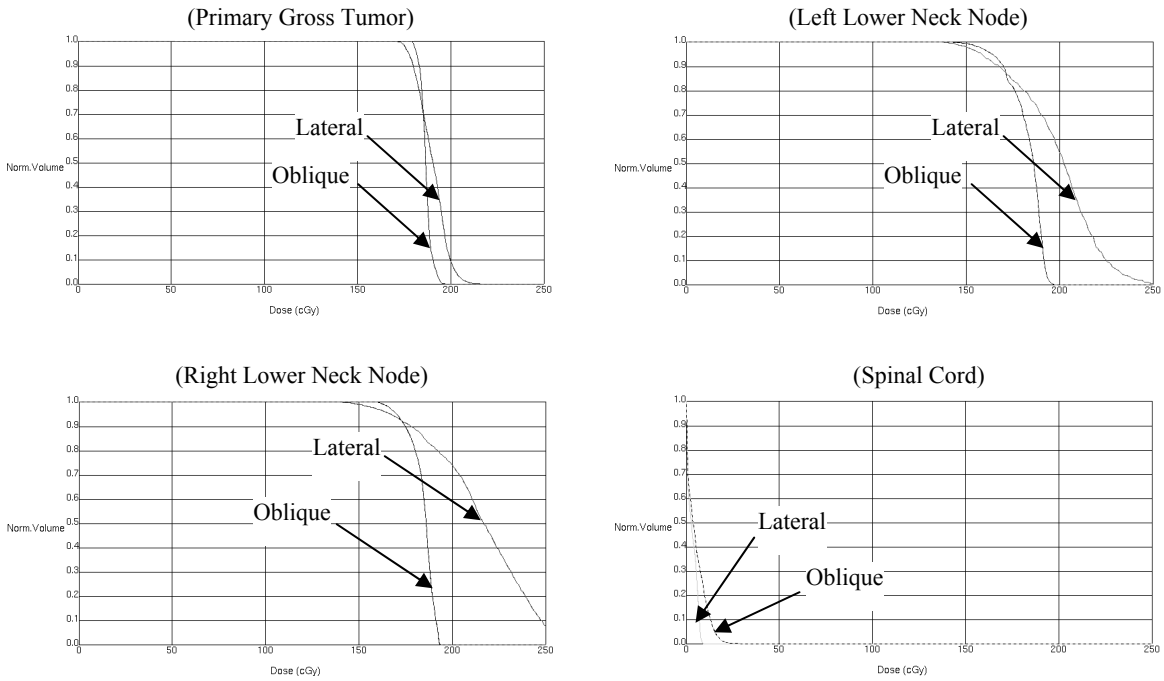

Fig. 6 Dose-volume histograms

Journal of NUCLEAR SCIENCE and TECHNOLOGY, Supplement 5, p. 306–308 (June 2008)

ATOM-MIRD Hybrid Voxel Model for Monte Carlo Calculations of Organ Doses: A Complement to a Physical Phantom

Sungkoo CHO[1], Sang Hyoun CHOI[3], Chul-Young YI[2], and Chan Hyeong KIM[1*]

[1]*Department of Nuclear Engineering, Hanyang University, Seoul, Korea*
[2]*Korea Research Institute of Standard and Science, Daejeon, Korea*
[3]*Department of Radiation Oncology, Inha University, Incheon, Korea*

In this study, a hybrid voxel model was constructed by combining the voxel model of the ATOM adult male phantom with the organ models of the MIRD5 mathematical phantom. The organ models of the mathematical phantom were successfully transferred to the hybrid model, replicating the sizes of the organs within a 3% difference. Consequently, a total of 14 main radiosensitive organs were defined in the hybrid model. The developed model was implemented into a Monte Carlo particle transport simulation code, MCNPX, and used to calculate the organ doses, which were then compared with the TLD measured values.

KEYWORDS: voxel model, hybrid, ATOM phantom, MIRD5 mathematical phantom, Monte Carlo, organ dose calculations

I. Introduction

Humanoid phantoms such as Anderson Rando and ATOM family phantoms are used in medical research and radiation protection community to determine radiation dose in the human body[1-3]. These physical phantoms, however, cannot be used directly to measure the organ doses, simply because organs are not defined in these phantoms. Some researchers have used anatomical atlas and patient CT images to define organs in the Rando phantom, but the sizes of the defined organs were significantly different from the ICRP reference data[4-7]. Very recently, in an effort to define the organs of reference sizes, the organ models of the MIRD5 mathematical phantom[8] were defined in the ATOM adult male phantom (physical phantom) and used to measure organ doses and effective doses[9,10]. In this context, the objective of the present study was to develop a computational model that combines the voxel model of the ATOM adult male phantom (Model 701-C, Norfolk, Virginia, U.S.A) with the organ models of the MIRD5 mathematical phantom in order to complement the physical phantom of the ATOM adult male phantom with organs.

II. Methods

The ATOM adult male phantom (**Fig. 1**), which represents an adult male of 173 cm and 73 kg, has only three internal organs, which are bone, lungs, and brain. The phantom is made of tissue equivalent materials, the photon attenuation coefficients of these materials being very close to those of real tissues for a wide range of photon energies (0.03 - 20 MeV)[11].

The hybrid voxel model was constructed by combining the voxel model of the ATOM adult male phantom with the organ models of the MIRD5 mathematical phantom (**Fig. 2**). The voxel model of the ATOM adult male phantom was constructed, first, by scanning the phantom with a CT scanner (Model: Siemens SOMATOM Sensation 16). A total of 639 transversal CT images were taken at 1.5 mm intervals, and the images were then segmented for air, bone, lung, and soft tissue to construct the voxel model of the ATOM adult male phantom. Axial plane images of the MIRD5 mathematical phantom were obtained at the same intervals (= 1.5 mm). The hybrid model was completed by combining the transversal CT images of the ATOM adult male phantom and the axial plane images of the MIRD5 mathematical phantom.

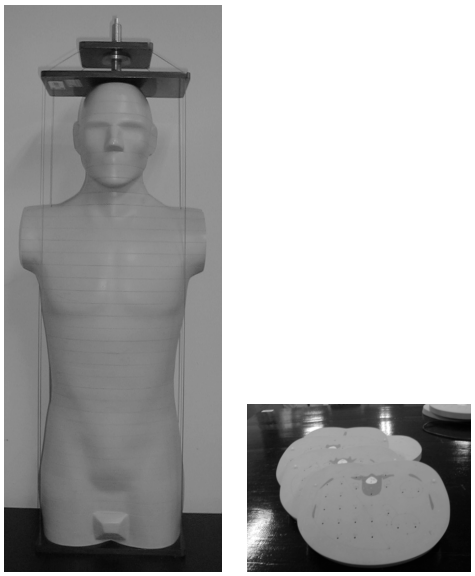

Fig. 1 ATOM adult male phantom (Model 701-C, Norfolk, Virginia, U.S.A)

The constructed hybrid voxel model was then ported to a Monte Carlo particle transport simulation code, MCNPX[12],

***Corresponding Author, Tel: +82-2-2220-0513; Fax: +82-2-2220-4059, E-mail: chkim@hanyang.ac.kr

to calculate organ doses for the organs defined in the hybrid model. In the present study, an organ dose was defined as an organ-averaged absorbed dose. The organ doses, however, were not determined as defined, but rather determined from a collection of point-wise absorbed dose values. This approach was necessary because the measurement of the organ doses had to be done with a limited number of TLD rods. A total of 36 point-wise absorbed dose values were calculated to determine the organ doses to the 14 radiosensitive organs in the phantom. To calculate the point-wise absorbed dose values, *F4 tally, an energy fluence tally based on track-length estimation, was used[12]. A total of 10^9 histories were simulated for each calculation, and the resulting statistical errors were always less than 1%.

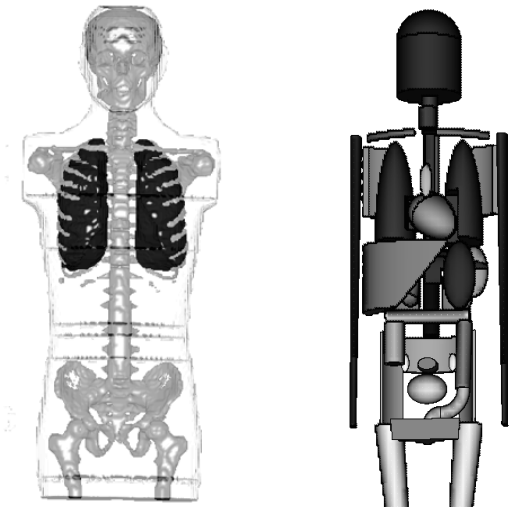

Fig. 2 Voxel model of ATOM adult male phantom and organ models of MIRD5 mathematical phantom

Fig. 3 GR-200 TLD rods and Harshaw model 3500 TLD reader used in the measurement

To measure the point-wise absorbed dose values, GR-200 thermo-luminescence dosimeter (TLD) rods (LiF:Mg,Cu,P, 1 mm in diameter and 6 mm in length) and a Harshaw 3500 TLD reading system (**Fig. 3**) were used. Four TLD rods were employed for each of the 38 dosimeter locations in the ATOM adult male phantom. The calibration factors of the TLD rods were determined with ^{60}Co. In the calibration, the TLD rods were placed on a 6.5 cm-thick polystyrene phantom and covered with 1 cm-thick bolus material to achieve the charged particle equilibrium (CPE) condition at the dosimeter locations. Only the TLD rods exhibiting thermo-luminescence output within 8% of deviation (from the average value for all of the TLD rods) were selected for use. The calibration factors were determined by repeating the same calibration process five times.

III. Results and Discussion

Fig. 4 shows the hybrid voxel model developed in this study. The organs of the MIRD5 mathematical model were successfully transferred to the hybrid model, replicating the sizes of the organs within a 3% difference. Consequently, a total of 14 radiosensitive organs were defined in the hybrid model. The hybrid model is composed of a 256 x 256 x 649 voxel array, and the voxel resolution is 1.8 mm x 1.8 mm x 1.5 mm.

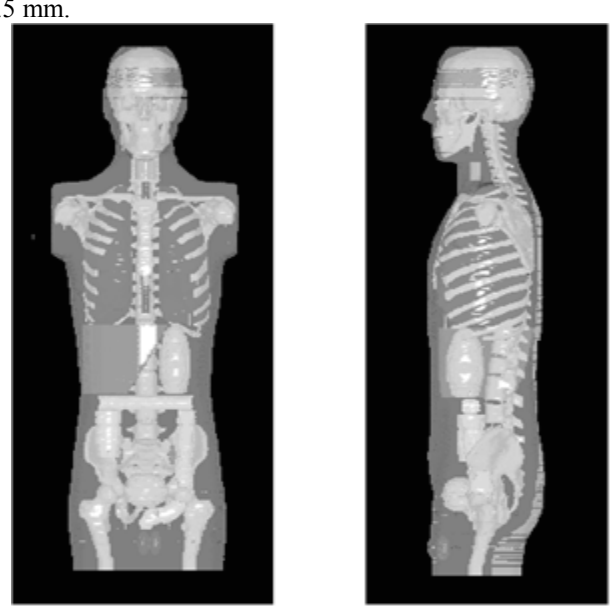

Fig. 4 Hybrid voxel model developed in this study

Fig. 5 compares the organ doses measured by the TLD rods (dark gray) and calculated by the Monte Carlo simulation with the hybrid voxel model constructed in this study (bright gray) for the anterior-posterior (AP) irradiation geometry of ^{137}Cs and ^{60}Co. The results show that the hybrid voxel model produces reasonable dose values for the organs defined in the model. The minor differences seem to have resulted from the fact that the measurement environment in the simulation study was not precisely modeled.

IV. Conclusions

In this study, a hybrid voxel model was constructed by combining the voxel model of the ATOM adult male phantom with the organ models of the MIRD5 mathematical phantom. A total of 14 radiosensitive organs are defined in the model. The developed model was used to calculate the organ doses, which were then compared with the TLD measured values. Our results show that the developed model produces very reasonable dose values for the organs defined in the model. We believe that the complementary pair of the ATOM adult male phantom (a physical phantom with the organs defined inside) and the hybrid voxel model, a

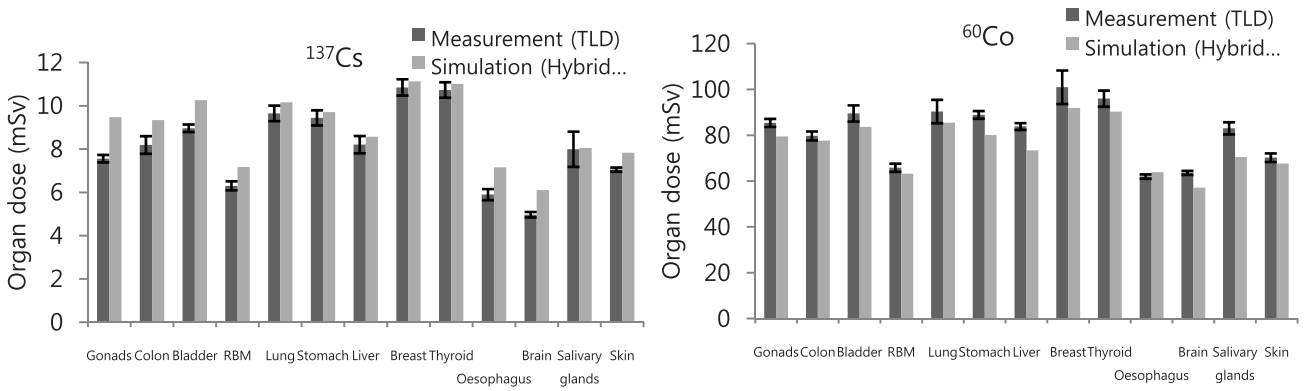

Fig. 5 Comparison of organ doses which are measured by TLD rods (dark gray) and calculated by Monte Carlo simulation with hybrid voxel model constructed in this study (bright gray) for anterior-posterior (AP) irradiation geometry of ^{137}Cs and ^{60}Co

computational model developed in this study, will provide a unique opportunity to measure and calculate organ doses at the same time.

Acknowledgement

This work was supported by the Korean Ministry of Science and Technology through ERC (RII-2000-067-03002-0), BAERI (M20508050003-05B0805-00310), and the Korea Institute of Nuclear Safety (KINS).

References

1) P. C. Shrimpton, B. F. Wall, E. S. Fisher, "The tissue-equivalence of the Alderson Rando anthropomorphic phantom for x-rays of diagnostic qualities," Phys. Med. Biol., 26[1], 133 (1981).
2) M. Mazonakis, J. Damilakis, et al., "Brain radiotherapy during pregnancy: an analysis of conceptus dose using anthropomorphic phantoms," Br. J. Radiol., 72[855], 274 (1999).
3) J. J. DeMarco, C. H. Cagnon, et al., "A Monte Carlo based method to estimate radiation dose from multidetector CT (MDCT): cylindrical and anthropomorphic phantoms," Phys. Med. Biol., 50[17], 3989 (2005).
4) W. Huda, G. A. Sandison, "Estimation of mean organ doses in diagnostic radiology from Rando phantom measurements," Health Phys., 47[3], 463 (1984).
5) R. L. Mini, P. Vock, et al., "Radiation exposure of patients who undergo CT of the trunk," Radiology, 195[2], 557 (1995).
6) M. Wyatt, C. Corredor, et al., "Comparison of treatment planning dose calculations with measurements and Monte Carlo calculations in a Rando phantom," Rad. Prot. Dosi., 116[14], 461 (2005).
7) V. Y. Golikov, V. V. Nikitin, "Estimation of the mean organ Doses and the effective dose equivalent from Rando phantom measurements," Health Phys., 56[1], 111 (1989).
8) M. Cristy and K. F. Eckerman, Specific Absorbed Fractions of Energy at Various Ages from Internal Photon Sources. ORNL/TM-8381, Oak Ridge National Laboratory (1987).
9) K. W. Jang, C. S. Lee, et al., "Evaluation of patient dose from computed tomography using TLD measurement," Journal of Radiation Protection Bulletin, 25, 64 (2005)
10) S. Cho, K. S. Seo, et al., "Primary study for the calibration and the measurement of real-time effective dose measurement system," Proceeding of Autumn Conference and International Symposium Korean Association for Radiation Protection, Gurye, Korea, Nov. 3-4, p.74 (2005).
11) D. R. White, C. Constantinou, Progress in Medical Radiation Physics, Vol.1, Plenum Press, New York, 133 (1982).
12) L. S. Waters, et al., MCNPX User's Manual, Version 2.4.0, LA-UR-02-2607, Los Alamos National Laboratory (2002).

Journal of NUCLEAR SCIENCE and TECHNOLOGY, Supplement 5, p. 309–312 (June 2008)

Organ Absorbed Doses and Effective Doses to the Patient and the Medical Staff in Interventional Radiology Calculated from Voxel Phantom

Sang-hyun PARK[1*], Choonsik LEE[2], and Jai-ki LEE[1]

[1]*Department of Nuclear Engineering, Hanyang University, Haengdang-dong, Sungdong-ku, Seoul, Korea*
[2]*Department of Nuclear and Radiological Engineering, University of Florida, Florida, USA*

In this study, organ absorbed doses and effective doses to patient and medical staff during interventional radiological procedures were estimated using voxel phantom, Korean Typical Man-2 (KTMAN-2). Four projections of cardiac catheterization were simulated for dose calculation by Monte Carlo technique. The parameters of x-ray source and exposure conditions were obtained from literature data. Calculated doses were normalized to dose area product (DAP). The effective doses per DAP of patient were between 0.1 and 0.5 mSv Gy^{-1} cm^{-2}. The results were compared with those derived from stylized phantom. KTMAN-2 received up to 105 % higher effective doses than stylized phantom. The dose differences were mainly caused by more realistic internal topology of KTMAN-2 compared to stylized phantom. For postero-anterior projection, organ absorbed dose per DAP to patient and cardiologist were calculated simultaneously. Absorbed doses per DAP of adipose tissue, lens, muscle, skin and thyroids of cardiologist were up to 0.01 mGy Gy^{-1} cm^{-2}. Doses to adipose tissue, muscle and skin within hand or neck would be much higher than calculated values. The results of this study showed that voxel phantoms are more suitable for dose assessment of lying patients undergoing the interventional radiology.

KEYWORDS: cardiac catheterization, doses, Monte Carlo, voxel phantom

I. Introduction

Since the late 1960s, interventional radiology techniques have been utilized for the diagnostic and treatment purposes and increased significantly up to now[1]. Fluoroscopically-guided interventional radiology techniques have been preferred as alternatives to surgical procedures because of a decreased burden to the patient and social profits led by short term recovery of patient[1]. Although the partial of body is exposed to radiation, prolonged fluoroscopy time leads to high patient dose. Medical staffs have the probability of radiation injuries to the hands or lens. There have been several studies to assess radiation risk of patient and medical staff during interventional procedures. The International Commission of Radiological Protection (ICRP) publication 85 provides a brief summary of dose assessment of patient and medical staff in several interventional procedures[1]. According to the publication, in some interventional radiology procedures, skin doses to patients reach to those from some radiation cancer therapy fractions[1]. Lens injuries of medical staffs were reported too[1]. Therefore, to ensure the safety of the interventional procedure, accurate dose assessment of a patient and a medical staff should be performed.

Absorbed dose to organ or tissue and its weighted sum effective dose have been commonly used to estimate the overall risk of patients from radiation exposure[2]. Because organ doses cannot be measured directly, Monte Carlo simulation coupled with computational human phantom is the well-known way to estimate absorbed dose to organ with good accuracy. Stylized human phantoms have been used to calculate organ dose of patient from interventional procedures. Stern et al. estimated absorbed doses in selected tissues for fluoroscopic and cineangiographic examinations of the coronary arteries of adults using a male and a female stylized phantoms[3]. Vetter et al. estimated effective dose from uterine artery embolization using stylized phantom[4]. Schultz et al. calculated radiation dose to paediatric patients and cardiologist during cardiac catheterization using one of the paediatric phantoms designed at the Oak Ridge National Laboratory (ORNL)[5),6)]. However, because of the intrinsic limitation of three dimensional mathematical equations used to describe human anatomy in stylized phantoms, they have a drawback in representing real human anatomy. Voxel phantoms have been developed to satisfy the demand to represent the human anatomy more realistically[7]. Recently Bozkurt et al. estimated equivalent dose to organs of the patient and the physician in cardiac catheterization using voxel phantom, VIP-man[8]. However, there was not enough dose assessment data derived from voxel phantoms for interventional procedure.

In this study, absorbed doses to organs and effective doses of the patient and the cardiologist during cardiac catheterization were calculated by Monte Carlo simulation. Voxel phantom representing Korean adult male was employed to obtain dose assessment data for non-Caucasian. Calculated doses for the patient were compared with those derived from ORNL adult phantom.

*Corresponding Author, Tel No: +82-2-2220-1843, Fax No: +82-2-2296-3690, Email: sanghyunpark01@gmail.com

II. Materials and Methods

1. Mathematical Phantoms Used in Dose Calculation

Voxel phantom, Korean Typical Man-2 (KTMAN-2) was employed to calculate radiation dose[9]. KTMAN-2 was constructed based on whole body computed tomography (CT) images of a healthy male volunteer (height: 172cm, weight 68 kg). A total of 29 organs and tissues and 19 skeletal sites were segmented via image manipulation techniques. KTMAN-2 consists of 300×150×344 voxels with a voxel resolution of 2×2×5 mm^3. Organ masses within KTMAN-2 showed differences within 40 % of Asian and ICRP reference values except the gall bladder, pancreas and testes[9].

ORNL adult phantom was adopted to calculate radiation dose and to compare with results from KTMAN-2[6]. Body dimension and organ masses within ORNL adult phantom was based on the Reference man data of ICRP Publication 23[10].

2. Energy Spectra and Projections of X-ray

Three combinations of peak tube potential and aluminum filtration were obtained which were 60 kVp/3.5mm Al filtration, 90 kVp/4mm Al filtration and 120 kVp/4.3mm Al filtration from reported data by Stern et al[3]. The energy spectra corresponding to these peak tube potential and filtration were generated using spectrum generation software, SPEC 78[11]. In this study, antero-posterior (AP), postero-anterior (PA), left anterior oblique (LAO), and right anterior oblique (RAO) projections were simulated. Direction and position information of the x-ray beam and field sizes at mid-plane of heart were obtained from the reported data by Hart et al[12]. Field sizes at center (mid-plane) of the heart were 12 × 12 cm^2 for AP and PA projections and 14 × 14 cm^2 for lateral oblique projections, respectively. All obliques lie in a transverse plane and form a 45 degree angle with the AP/PA axis[12].

3. Monte Carlo Simulation Using MCNPX Code

A general purposed Monte Carlo code, MCNPX version 2.5.0[13] was employed to simulate the x-ray source and calculate dose distribution within computational phantom. X-ray tube was expressed as a point source which emits photon particles into restricted solid angles. The range of photon emission angle was determined by the source to heart distance and heart area. Because photons were emitted as cone beams, the circular cross section photon beam was reduced to a rectangle using collimation. Generated x-ray spectra were imported into MCNPX using source information card and a source probability card. The absorbed doses in organs (except red bone marrow) of KTMAN-2 were calculated using the tally type 6 (flagged with an asterisk) of MCNPX. To assess the absorbed dose to red bone marrow (RBM), absorbed dose per unit fluence referred to as dose-response functions (DRF) for the active marrow of each trabecular bone of the adult were utilized[14]. Through the MCNPX calculation, average fluences over each bone site were calculated using tally type 4 and multiplied by DRF. These values of all bone sites were summed up to obtain the absorbed dose to RBM. Effective doses of all projections were calculated using the organ weighting factor provided in ICRP publication 60[2]. For all simulations, 5×10^7 photon histories were used to obtain enough statistical precision. Organ doses with over 10% error were not reported in this study. Calculated absorbed doses in organs were normalized to DAP to provide the DAP-to-dose conversion coefficients. In this study, DAP for each projection was calculated as the absorbed dose in air averaged over the beam area at 15 cm from the focus, multiplied by the beam area at this distance[15].

For PA projection, organ absorbed dose per DAP to patient and cardiologist were calculated simultaneously. In the simulation, voxel phantom representing the patient lay as supine position at origin. Using 'Like m But' feature and 'TRCL' (cell transformation) card of MCNPX[13], coordinated transformed voxel phantom representing the cardiologist was reproduced at right hand side of the phantom representing the patient. Reproduced phantom was standing 15 cm away from about the waist level of the phantom representing patient. **Fig. 1** shows geometrical setting of two voxel phantoms in MCNPX calculation.

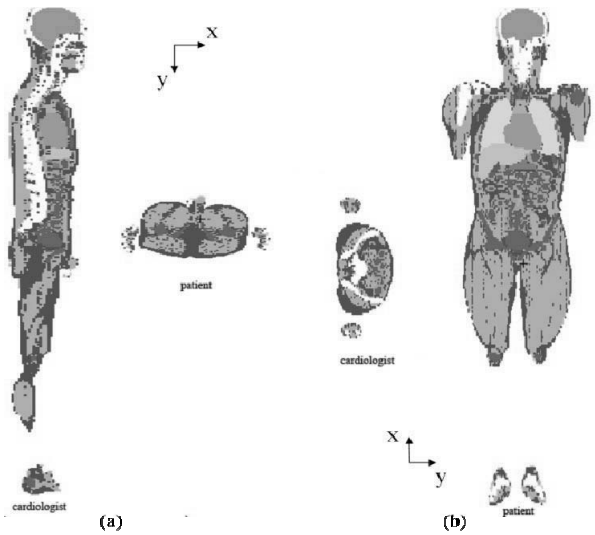

Fig. 1 Geometry of the exposure conditions of cardiologist and patient. Left (a) is the side view of cardiologist. Right (b) is the axial view of cardiologist.

III. Results and Discussions

1. Radiation Doses for Patient

The absorbed doses per DAP of heart and organs near to the heart and effective doses per DAP calculated from KTMAN-2 and ORNL adult phantom are listed in **Table 1**. The two phantoms received higher effective doses at oblique projections. KTMAN-2 received higher effective dose than ORNL adult phantom for all projections. In the AP projection where 60 kVp peak tube potential was simulated, effective dose of KTMAN-2 was 105 % higher than that of ORNL adult phantom. In this case, the absorbed dose to lungs of KTMAN-2 was 332 % higher than that of ORNL

Table 1. Absorbed doses per DAP (mGy $Gy^{-1}cm^{-2}$) of organs near to the heart and abdominal organs and effective doses per DAP (mSv $Gy^{-1}cm^{-2}$) calculated from KTMAN-2 and ORNL adult.

	60 kVp, 3.5 mm Al		90 kVp, 4.0 mm Al		120 kVp, 4.3 mm Al	
Organs	KTMAN-2	ORNL adult	KTMAN-2	ORNL adult	KTMAN-2	ORNL adult
AP projection						
Colon*	-	-	0.08	-	0.10	-
Esophagus	0.32	0.24	0.71	0.52	1.00	0.72
Liver	0.20	0.14	0.40	0.27	0.52	0.35
Lung	0.58	0.13	0.94	0.28	1.18	0.37
Stomach wall	0.21	0.08	0.46	0.18	0.59	0.24
Effective dose	0.17	0.08	0.26	0.17	0.36	0.23
PA projection						
Colon	-	-	0.04	-	0.06	-
Esophagus	0.33	0.24	0.78	0.63	1.14	0.93
Liver	0.07	0.04	0.18	0.11	0.27	0.17
Lung	0.45	0.17	0.81	0.32	1.04	0.42
Stomach wall	0.11	0.03	0.25	0.09	0.35	0.12
Effective dose	0.11	0.08	0.22	0.18	0.30	0.29
LAO projection						
Colon	-	-	0.04	-	0.07	-
Esophagus	0.29	0.29	0.74	0.65	1.07	0.93
Liver	0.32	0.12	0.63	0.24	0.85	0.32
Lung	0.89	0.48	1.50	0.73	1.89	0.90
Stomach wall	0.08	0.02	0.22	0.07	0.34	0.11
Effective dose	0.17	0.12	0.33	0.24	0.44	0.34
RAO projection						
Colon	-	-	0.07	-	0.10	-
Esophagus	0.77	0.30	1.43	0.62	1.88	0.84
Liver	0.08	0.03	0.21	0.09	0.31	0.14
Lung	0.76	0.67	1.32	0.96	1.69	1.12
Stomach wall	0.24	0.06	0.50	0.14	0.69	0.18

adult. For all projections, absorbed doses per DAP of esophagus and lungs of KTMAN-2 were higher than those of ORNL adult. **Fig. 2** shows the axial cross-sectional images of KTMAN-2 and ORNL adult phantom at the level of heart. For KTMAN-2, esophagus and lungs are relatively closer to the heart than those of ORNL adult phantom. Because of intrinsic limitation of mathematical equations of ORNL phantom, it is impossible to represent inter-organ overlapping in stylized phantom.

Doses to abdominal organs, such as colon, liver and stomach, of KTMAN-2 were higher than those of ORNL adult. Volunteer's supine position during image data acquisition for the construction of KTMAN-2 causes the compression of the thorax by abdominal organs[7]. Therefore, the distances from heart to abdominal organs were reduced so that these organs received more scattered radiation than

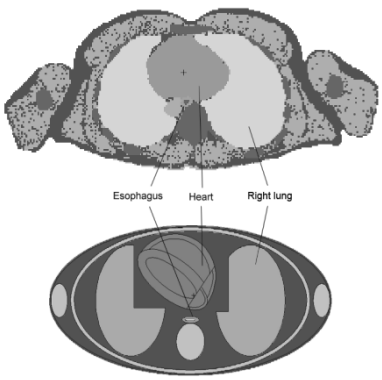

Fig. 2 Axial images at the position of heart centroids within the KTMAN-2 (top) and ORNL adult (bottom).

those of ORNL adult. This result suggested that internal topology of lying patient undergoing the interventional

radiology procedure was more reflected in voxel phantom rather than stylized phantom.

2. Radiation Doses for Cardiologist

The absorbed doses per DAP of adipose tissue, lens, muscle, skin and thyroids of cardiologist are listed in **Table 2**. Doses to adipose tissue, lens and muscle were averaged to whole body. The doses to these tissues within neck or hands were much higher than averaged whole body value. Absorbed doses of other organs were not available due to large statistical errors of Monte Carlo simulation.

Table 2. Absorbed doses per DAP (mGy $Gy^{-1}cm^{-2}$) of selected organs of cardiologist calculated using KTMAN-2

Organs	60 kVp, 3.5 mm Al	90 kVp, 4 mm Al	120 kVp, 4.3 mm Al
Adipose tissue	0.0019	0.0026	0.0033
Lens	0.0060	0.0082	0.0102
Muscle	0.0026	0.0036	0.0043
Skin	0.0059	0.0064	0.0069
Thyroids	0.0059	0.0069	0.0080

IV. Conclusion

Organ absorbed doses and effective doses per DAP from heart AP, PA, LAO, and RAO projections of cardiac catheterization were calculated by employing Korean voxel phantom, KTMAN-2. At oblique projections, effective doses per DAP of patient, calculated using KTMAN-2 and ORNL adult phantom, were higher than AP/PA projections. For all projections, KTMAN-2 received higher effective doses per DAP than ORNL adult phantom. Realistic position of organs near to the heart and shift of abdominal organs caused KTMAN-2 received higher effective doses than ORNL adult phantom. For PA projections, absorbed doses per DAP of adipose tissue, lens, muscle, skin and thyroids of cardiologist were calculated simultaneously.

KTMAN-2 represented the human anatomy more realistically than stylized phantoms in terms of interventional radiology dosimetry in this study. Moreover this phantom provided supine position of patient undergoing interventional radiology procedures. The results from Korean voxel phantom, KTMAN-2 provided dose assessment data of non-Caucasian individuals from cardiac catheterization. The organ absorbed doses per DAP and effective doses per DAP provided by the current study would be useful for purposes of radiological protection in practical procedures.

References

1) International Commission on Radiological Protection, Avoidance of radiation injuries from medical interventional procedures, ICRP Publication 85, International Commission on Radiological Protection (2000).
2) International Commission on Radiological Protection, 1990 recommendations of the International Commission on Radiological Protection, ICRP Publication 60, International Commission on Radiological Protection (1991).
3) S. H. Stern, M. Rosenstein, L. Renaud, M. Zankl, Handbook of selected tissue doses for fluoroscopic and cineangiographic examination of the coronary arteries, HHS Publication FDA 95-8288, Food and Drug Administration (1995).
4) S. Vetter, F. W. Schultz, E. P. Strecker, and J. Zoetelief, "Patient radiation exposure in uterine artery embolization of leiomyomata: calculation of organ doses and effective dose," Eur Radiol., 14, 842 (2004).
5) F. W. Schultz, J. Geleijns, F. M. Spoelstra, and J. Zoetelief, "Monte Carlo calculations for assessment of radiation dose to patients with congenital heart defects and to staff during cardiac catheterizations," Br. J. Radiol., 76, 638 (2003).
6) K. F. Eckerman, M. Cristy, J. C. Ryman, "The ORNL mathematical phantom series," http://homer.ornl.gov/VLab/mird2.pdf. December (1996).
7) M. Caon, "Voxel-based computational models of real human anatomy: a review," Radiat. Environ. Biophys., 42, 229 (2004).
8) A.Bozkurt, D. Bor, "Simultaneous determination of equivalent dose to organs and tissues of the patient and of the physician in interventional radiology using the Monte Carlo method," Phys. Med. Biol., 52, 317 (2007).
9) C. Lee, C. Lee, S. H. Park, and J. K. Lee, "Development of the two Korean adult tomographic computational phantoms for organ dosimetry," Med. Phys., 33, 380 (2006).
10) International Commission on Radiological Protection, Report of the task group on Reference man, ICRP Publication 23, International Commission on Radiological Protection (1975).
11) K. Cranley, B. J Gilmore, G. W. A. Fogarty, and L. Desponds, Catalogue of Diagnostic X-ray Spectra and Other data, IPEM Report No 78, Institute of Physics and Engineering in Medicine (IPEM), (1997).
12) D.Hart, D .G. Jones, and B. F. Wall, Estimation of effective dose in diagnostic radiology from entrance surface dose and dose-area product measurements, NRPB-R262, National Radiological Protection Board, (1994).
13) D. B. Pelowitz, MCNPXTM User's manual version 2.5.0, LA-UR-05-0369, (2005).
14) M. Cristy, and K. F. Eckerman, Specific absorbed fractions of energy at various ages from internal photon sources. I. Methods, ORNL/TM-8381/V1, Oak Ridge National Laboratory (1987).
15) International Commission on Radiation Units and Measurements, Patient dosimetry for X rays used in medical imaging, ICRU Report 74, International Commission on Radiation Units and Measurements (2005).

Journal of NUCLEAR SCIENCE and TECHNOLOGY, Supplement 5, p. 313–316 (June 2008)

Beta-Ray Dose Assessment from Skin Contamination Using a Point Kernel Method

Sang-hyun PARK*, Bo-yeol CHOI, and Jai-ki LEE

Hanyang University, Haengdang-dong, Seongdong-gu, Seoul, Korea

In this study, a point kernel method to calculate beta-ray dose rate from skin contamination was introduced. The beta-ray doses rates were computed by performing numerical integration of the radial dose distribution around an isotropic point source of monoenergetic electrons called as point kernel. In this study, in-house code, based on MATLAB version 7.0.4 was developed to perform a numerical integration. The code generated dose distributions for beta-ray emitters from interpolated point kernel, and beta-ray dose rates from skin contamination were calculated by numerical integration. Generated dose distributions for selected beta-ray emitters agreed with those calculated by Cross et al within 20 %, except at a longer distance where there are differences up to more than 100 %. For a point source, calculated beta-ray doses were agreed well with those derived from Monte Carlo simulation. For a disk source, the differences were up to 17 % at a deep region. Point kernel method underestimated beta-ray doses than Monte Carlo simulation. The code will be improved to deal with a three-dimensional source, shielding by cover material, air gap and contribution of photon to skin dose. For the sake of user's convenience, the code will be equipped with graphic user interface.

KEYWORDS: point kernel method, beta-ray, skin, MATLAB, Monte Carlo simulation

I. Introduction

The skin can often receive the highest absorbed dose from an external radiation since it is the most superficial organ of the body[1]. There are two categories of the main biological effects induced by ionizing radiations: 1. early and late deterministic effects, 2. stochastic effects (cancer induction). The most important factors influencing these effects are the dose, dose rate, type of radiation, area of skin exposed and the skin thickness. Different types of radiation exhibit different values of radiobiological effectiveness and more importantly have different penetrating powers. The International Commission on Radiological Protection (ICRP) proposed skin dose limit as 0.5 Gy averaged over 1 cm^2 area[2], while National Council on Radiation Protection and Measurements (NCRP) suggested 0.5 Gy averaged over 10 cm^2 areas as skin dose limit[3]. Because skin dose is inversely proportional to area, dose limit of the ICRP was more conservative than that of NCRP. There are several types of deterministic effects such as erythema, moist desquamation, dermal necrosis, dermal atrophy and damage to the deep vasculature, and these are occurred in the depth between 150 and 1500 μm[1]. The basal layer of the epidermis (between 20 and 100 μm in a man) has been chosen as the target cells which play a dominant role in the induction of skin cancer. For general radiation protection purposes the ICRP and NCRP assumed a nominal skin thickness of 7 mg cm^{-2}, which corresponds to a physical depth of 70 μm[3, 4]. Since the annual skin dose limit is based on the limitation of deterministic effects, a more appropriate depth would be greater than 70 μm. The use of a nominal skin depth of 7 mg cm^{-2} may be more suitable for the estimation of cancer risk and the assessment of the contribution to effective dose which is made by skin exposure.

The skin is potentially at risk from weak penetrating radiations such as beta particles or low energy X-rays[5]. Actually the exposure of the skin from beta emitting small radioactive sources known as “hot particles” has been important in radiological protection[6]. Many researchers have employed point kernel methods to calculate skin dose from skin contamination by beta emitting nuclides. This has been done by integrating, over the contaminated area, the radial dose distributions for isotropic point beta ray sources[7]. Thus, the radial dose distribution around an isotropic point source of electrons or beta rays is the basis for this method. This dose distribution was called a point kernel and calculated from various empirical and analytical approximations[8] or by solving a simplified form of the transport equation[9]. However, due to approximate empirical expressions and neglecting statistical fluctuations in energy losses, these methods gave less accurate dose distributions[10]. Researchers employed Monte Carlo techniques to get the more accurate dose distribution from monoenergetic electrons in an infinite water medium[10, 11]. They chose water instead of skin or tissue because it is well defined material for Monte Carlo simulation and has similar density with skin.

Because point kernel method gives quick results and is relatively easy to use, point kernel method has been employed to estimate the dose assessment in a variety of practical problems including skin contamination. In this study, beta-ray dose from skin contamination was calculated using point kernel method. Radial dose distribution for monoenergetic electron source obtained from Monte Carlo simulation was employed. Two kinds of skin contaminations from a point source and a disk source were considered. To calculate beta-ray dose, in-house code was developed. Dose distributions for beta-ray emitters were compared with other

*Corresponding Author, Tel. +82-2-2220-1843, Fax. +82-2-2296-3690, Email: sanghyunpark01@gmail.com

point kernel methods and beta-ray doses were compared with those calculated from Monte Carlo simulation.

II. Materials and Methods

1. Radial Dose Distributions Around Isotropic Point Sources of Monoenergetic Electrons

Radial dose distributions for monoenergetic electrons are in the form of scaled, dimensionless values $j(r/r_E, E)$, given by

$$j(r/r_E, E) = 4\pi\rho r^2 J(r,E) r_E / E \quad (1)$$

where r is the radial distance, r_E is the continuous slowing-down approximation (CSDA) range at energy E, ρ is the density of the medium, and $J(r, E)$ is the dose at radius r. To get the $j(r/r_E, E)$, $J(r, E)$ should be simulated using Monte Carlo code systems such as ETRAN, ITS and EGS[12]. In this study, $j(r/r_E, E)$ derived from ETRAN code by Berger and Seltzer was used[11]. They calculated $j(r/r_E, E)$ for electrons of 27 energy levels at intervals of 0.025 in r/r_E. **Fig. 1** shows scaled and dimensionless dose $j(r/r_E, E)$ given by Berger and Seltzer.

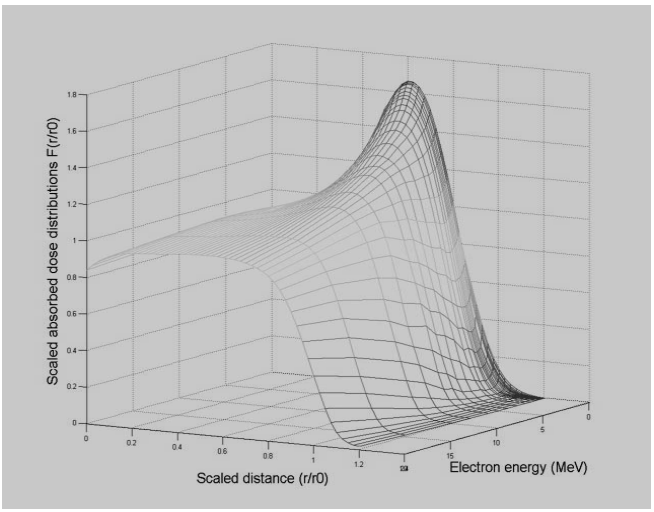

Fig. 1 Three-dimensional meshed grid image of scaled, dimensionless dose distribution $j(r/r_E, E)$ calculated by Berger and Seltzer.

2. Radial Dose Distributions for Beta-ray Emitters

The dose at distance r (cm) per disintegration of beta-ray emitting nuclide having a normalized spectrum of $N(E)$ beta particles per MeV is

$$J(r) = \frac{n}{4\pi\rho r^2} \int_0^{E_{max}} N(E)\, j(r/r_E, E) \left(\frac{E}{r_E}\right) dE \quad (2)$$

where E_{max} is the maximum energy of the spectrum and n is the number of betas emitted per disintegration. Since the $j(r/r_E, E)$ vanished at energies where r exceeds ~1.20 r_E, the lower limit of the integral was replaced by the energy corresponding to distance r/1.20. Normalized spectrum of $N(E)$ was obtained from ICRP publication 38[13]. In this study, the dose contributions from monoenergetic internal conversion or Auger electrons were not added to dose distributions for beta-ray emitters.

3. In-House Code for Beta-ray Dose Calculation

In this study, in-house code, based on the language of technical computing, MATLAB version 7.0.4, was developed to calculate beta-ray dose from skin contamination[14]. First of all, our code calculates normalized spectrum $N(E)$ of the specific nuclide from data based on ICRP publication 38. The values of r_E and $j(r/r_E, E)$ according to the beta energies of nuclide are generated by cubic spline interpolation. These interpolated values are stored as vector (1 by n or n by 1 matrix). Using the feature of element-by-element operation of MATLAB, numerical integration of interpolated r_E, $j(r/r_E, E)$ and $N(E)$ are performed and $J(r)$ at given radius is calculated.

Our code is able to deal with point and disk sources. For a disk source, 8 radially equidistant points on the source are chosen. One of these circles defined by a radial dose point is chosen, subdivided into eight source points at equiangular locations. Therefore, totally 64 (=8×8) source points are assigned on the disk. Numerical integration of dose distributions is performed on the dose points in the dose area at the skin depth level. 60 dose points are chosen with identical radial interval[15]. **Fig. 2** shows the schematic diagram of source points and dose points assigned.

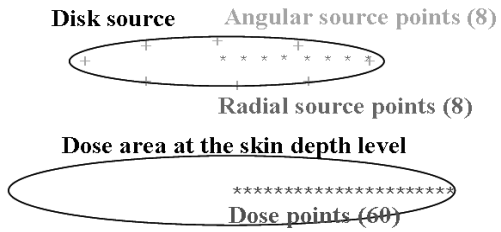

Fig. 2 Schematic diagram of assignment of dose points and source points.

For a disk source, the dose rate at a dose point is calculated as

$$\dot{D}(d) = 2\pi \int_0^R A_{disk} J(r')\, r'\, dr' \quad (3)$$

where, A_{disk} is the activity of disk source. Dose rates at all 60 dose points were averaged over an area in the skin using the equation

$$D_{avg} = \frac{2\pi \int_0^R \dot{D}(d')\, d'\, dd'}{\pi R^2} \quad (4)$$

Dose from skin contamination is specific to an air-tissue (air-water) boundary problem. However, since $j(r/r_E, E)$ is calculated in the infinite water, calculated dose using $j(r/r_E, E)$ includes backscattering from material (water) behind the

source and would overestimate skin doses. Backscattering factor provided by Cross et al was included in the code[16].

4. Monte Carlo Simulation using MCNPX

Calculated beta-ray doses were compared with those derived from Monte Carlo simulation. A general purposed Monte Carlo code, MCNPX version 2.5.0[17] was employed to simulate skin contamination and to calculate beta-ray dose distribution in the skin. Beta particles were emitted isotropically from point or disk sources. Spectra of beta particles per MeV were imported into MCNPX using source information (SIn) card and source probability (SPn) card. Beta-ray dose at the skin depth level was calculated using the tally type 2 of MCNPX. This tally records flux averaged over a surface (particles per cm^2). Total stopping power (MeV cm^2 g^{-1}) was utilized[18]. These values were imported into MCNPX using dose energy and dose function (DE/DF) card. Through the MCNPX calculation, average electron fluences over dose area were calculated and multiplied by total stopping power. In this study, ITS-style algorithm was employed for more accurate simulation of electron within water. MCNPX provides ITS (Integrated Tiger Series)-style electron energy indexing algorithm. ITS-style algorithm uses the data from the group whose boundary is closet to the energy of the electron at the beginning of the step[19]. Jeraj et al reported that the results using the ITS-style algorithm were closer to the experiment data for water[19].

III. Results and Discussion

1. Comparison of Dose Distributions for Beta-ray Emitters

Fig. 3 shows the calculated radial dose rate distributions in infinite water for C-14, Co-60, and Sr-90. The dose rate in nGy h^{-1} Bq^{-1} was given by multiplying by 567.7. At short distances, there were the large variations of $J(r)$ due to the inverse square law. A square of radial distance (r^2) was multiplied to $J(r)$ to remove the large variations at short distances. Calculated dose rate distributions were compared with reported data by Cross et al[16]. In most cases, $r^2J(r)$ values of this study showed differences within 20 % of data reported by Cross et al. As radial distance was increased, $r^2J(r)$ values of this study were larger than those of Cross et al. For Co-60, at 0.075 cm radial distance, $r^2J(r)$ of this study was 107 % higher than that of Cross et al. Cross et al. employed $j(r/r_E, E)$ calculated from ACCEPT code[16]. These data were smaller than those of Berger and Seltzer[11], which were calculated using ETRAN code, at a longer radial distance. Also, $J(r)$ values of Cross et al were derived using cubic Lagrange interpolation[16]. As stated above, cubic spline interpolation was used in this study. Discrepancies of dose distribution of monoenergetic electron and interpolation methods would cause the difference of dose distribution of beta-ray emitters.

2. Calculated Skin Dose from Skin Contamination by Beta-ray Emitters.

Dose rate at 70 μm skin depth, averaged over 1.0 cm^2, from Co-60 contamination as point type (1.0 μCi activity) and disk type (1.0 μCi cm^{-2} activity) were listed in **Table 1**. The area of disk source was assigned as 100 cm^2. In all cases, the results from point kernel method (this study) and Monte Carlo simulation (MCNPX) were agreed well. In this study, gamma dose distribution of Co-60 was not considered.

Table 1. Comparison of calculated beta-ray dose rates (mGy h^{-1}) for Co-60 point source (with 1μCi activity) and area disk source (with 1μCi cm^{-2} activity over 100 cm^2).

Source	This study	MCNPX	Difference (%)
Point	37.70	34.82	8
Disk	37.80	37.97	1

Fig. 4 showed dose distributions at various skin depths averaged over 0.01 cm^2 from disk type Y-90 source (radius=1.0 cm). For all cases, dose distributions from MCNPX calculation were larger than those of this study. At 400 μm depth, the dose rate of this study was 17 % lower than that of MCNPX. This result showed that point kernel method would give underestimated dose rate, especially at a deep region.

VI. Conclusions

In this study, radial dose distributions for beta-ray emitters in an infinite water medium were calculated. In-house code, based on MATLAB version 7.0.4, was developed to calculate radial dose distributions for beta-ray emitters and beta-ray dose from skin contamination. Dose

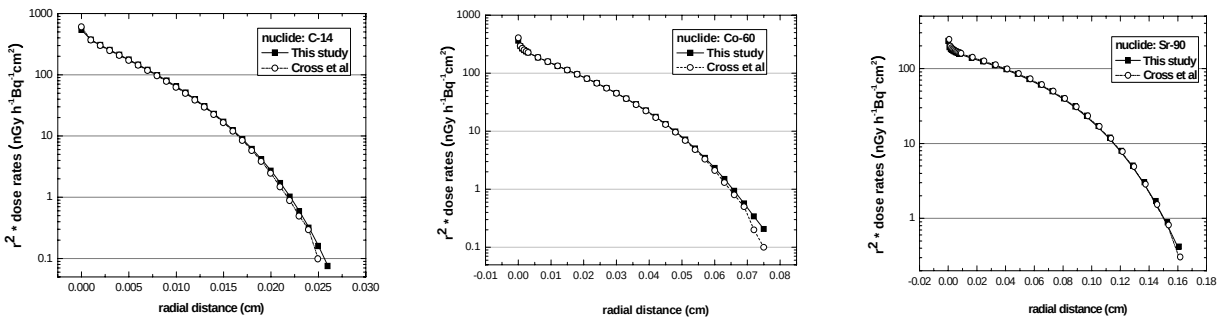

Fig. 3 Comparison of beta-ray dose rate distributions, $r^2J(r)$, around C-14, Co-60, and Sr-90 point source in water.

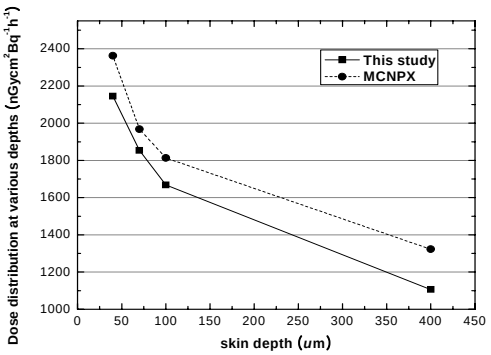

Fig. 4 Comparison of dose distribution for Y-90 disk source from 40 to 400 μm.

calculation was performed by numerical integration using interpolated values. Dose distributions for beta-ray emitters of this study were agreed well with other reported data derived from point kernel method. Calculated skin doses were compared with those derived from MCNPX calculation. For disk type contamination, point kernel method would underestimate skin dose than MCNPX.

In the present, we are performing the project to develop skin dose calculation code based on point kernel method. The code introduced this study will be improved to be able to deal with three-dimensional source, shielding by cover material, air gap between source and skin, and contribution of photon to skin dose. Also the code will be equipped with graphic user interface for user's convenience.

Acknowledgement

This work was supported by the KOREA HYDRO & NUCLEAR POWER (KHNP) Co. Ltd.

References

1) M. W. Charles., "The skin in radiological protection-Recent advances and residual unresolved issues," Radiat. Prot. Dosim., 109[4], 323-330 (2004).
2) International Commission on Radiological Protection, 1990 recommendations of the International Commission on Radiological Protection, ICRP Publication 60, International Commission on Radiological Protection (1991).
3) National Council on Radiation Protection and Measurements, Biological effects and exposure limits for "hot particles", NCRP Report No. 130, National Council on Radiation Protection and Measurements (1999).
4) International Commission on Radiological Protection, The biological basis for skin dose limitation, ICRP Publication 59, International Commission on Radiological Protection (1991).
5) M. W. Charles., "Skin, eye, and testis: Current exposure problems and recent advances in radiobiology," J. Soc. Radiol. Prot., 6[2], 69-81 (1986).
6) P. J. Darley, M. W. Charles, I. E. Othman, A. Sh. Al-Aydarous and A. J. Mill., "Origins and dosimetry of 'Hot particles' from nuclear plant operation," Radiat. Prot. Dosim., 92, 131-137 (2000).
7) W. G. Cross, N. O. Freedman, and P. Y. Wong., "Beta ray dose distributions from skin contamination," Radiat. Prot. Dosim., 40[3], 149-168 (1992).
8) R. Loevinger., "The dosimetry o beta sources in tissue: The point source dose function," Radiol.,66, 55-62 (1956).
9) L. V. Spencer, "Theory of electron penetration," Phys. Rev., 98, 1597-1615 (1955).
10) W. G. Cross, N. O. Freedman, and P. Y. Wong., "Beta-ray dose distributions from point sources in an infinite water medium," Health Phys. 63[2], 160-171 (1992).
11) R. E. Faw, J. K. Shultis., Radiological Assessment: Source and Exposures, PTR Prentice-Hall, New Jersey, 335-337 (1993).
12) T. M. Jenkins, W. R. Nelson, A. Rindi., Monte Carlo Transport of Electrons and Photons, Plenum Press, New York, 153-344 (1988).
13) International Commission on Radiological Protection, Radionuclide Transformations: Energy and Intensity of Emissions, ICRP Publication 38, International Commission on Radiological Protection (1981)
14) MATLAB® The Language of Technical Computing. Getting Started with MATLAB® Version 7. The MathWorks, Inc. (2004).
15) J. S. Durham., VARSKIN 3: A Computer Code for Assessing Skin Dose From Skin Dose Contamination, NUREG/CR-6918, U.S. Nuclear Regulatory Commission (2006).
16) W. G. Cross, N.O. Freedman, and P. Y. Wong., Tables of beta-ray dose distributions in water, AECL-10521, Atomic Energy of Canada Ltd. (1992).
17) D. B. Pelowitz., MCNPX™ User's manual version 2.5.0, LA-UR-05-0369, (2005).
18) http://physics.nist.gov/PhysRefData/Star/Text/ contents.html
19) R. Jeraj, P. Keall, P. Ostwald., "Comparisons between MCNP, EGS4 and experiment for clinical electron beams," Phys. Med. Biol. 44, 705-717 (1998).

Journal of NUCLEAR SCIENCE and TECHNOLOGY, Supplement 5, p. 317–320 (June 2008)

Response Characteristics of a Cylindrical Ionization Chamber to the Low- and Medium-Energy X-ray Beams

Chul-Young YI*, Kook Jin CHUN, Suck-Ho HAH, and Hyun-Moon KIM

Health Metrology Group, Korea Research Institute of Standards and Science, Doryong-Dong 1, Yusung-Gu, Daejeon 305-340, Korea

The response of a cylindrical NE2571 ionization chamber to the low- and medium-energy X-ray beams was simulated using a Monte Carlo code PENELOPE. The simulation geometry of the cylindrical chamber was modeled as specified by the manufacturer. The ratio of the air kerma to the cavity dose of the chamber was calculated as a function of photon energy for the broad parallel beam incident normally to the cylindrical axis of the chamber. Results were compared with other experimental and theoretical works

KEYWORDS: ionization chamber response, Monte Carlo simulation, medium-energy X-ray, PENELOPE, calibration factor, air kerma, NE2571, cylindrical ion chamber

I. Introduction

The ionization chamber response varies with the energy of the incident photon since the contribution of the attenuation and scatter in the wall material of the chamber is dependent on the energy of the incident photon. Many authors calculated the ionization chamber response using Monte Carlo codes[1-7].

Most of the authors focused on the evaluation of the ionization chamber response to relatively high-energy photons such as ^{60}Co gamma-rays. Using the code EGSnrc[4], Seuntjens *et al.* calculated the air kerma response of the ionization chamber in low- and medium-energy photon beams. They reported that the calculated responses were in good agreement within 0.7 % for X-rays with the mean energies greater than 160 keV.

In the present study, the air kerma calibration factors of a cylindrical ionization chamber NE2571 for the low- and medium-energy X-ray beams were calculated by means of Monte Carlo simulation using PENELOPE[8,9]. We compared the calculated responses with measurements and the consistency of the calculation was also investigated.

II. Method

1. Simulation Geometry

The materials and dimensions of the NE2571 ionization chamber were modeled realistically considering the specification given by the manufacturer. The inner diameter of the chamber was 6.3 mm and the wall thickness was 0.36 mm. The electrode was 20.6 mm long with the diameter of 1.0 mm. The electrode was aluminum and the chamber wall was graphite. The sensitive volume of the chamber was 0.69 cm^3. The conic end of the chamber was approximated as a cylinder with the same volume. It was assumed that the broad parallel beam was incident normally to the central axis of the chamber. The simulation geometry is shown in **Fig. 1**.

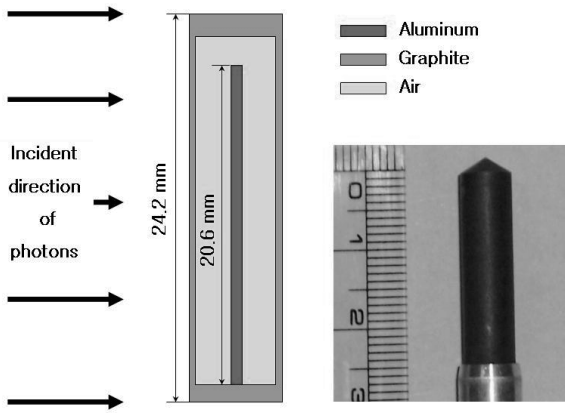

Fig. 1 NE2571 chamber and simulation geometry.

2. Calculation Accuracy

It is well-known that PENELOPE[8,9] is accurate and efficient, especially in dealing with electron transport. The accuracy of the cavity dose simulated by a code depends on the internal transport parameters of the code and can be investigated using the formalism of Kawrakow[3]. We followed the procedures of Yi *et al.*[6] in the accuracy evaluation of the cavity dose simulated using PENELOPE for the NE2571 chamber modeled in the present study but the re-entrance technique used by Yi *et al.* was switched off since it might perturb the electron fluence at the medium interface.

Assuming that the materials of cavity gas and the chamber wall is the same and an ionization chamber is placed in the unattenuated and unscattered photon fields, the cavity dose can be given by[3]

$$D_{cav} = \Psi \left(\frac{\mu_{en}}{\rho} \right)_{wall} \qquad (1)$$

where D_{cav} is the cavity dose, Ψ the photon energy fluence and $(\mu_{en}/\rho)_{wall}$ the mass energy absorption coefficients of the chamber wall material. If we rule out any bremsstrahlung events and the creation of the characteristic

*Corresponding Author, Tel No: +82-42-868-5370, Fax No: +82-42-868-5671, E-mail: cyyi@kriss.re.kr

X-rays in the chamber wall then the mass energy absorption coefficients equal to the mass energy transfer coefficients. In the case, from Eq. (1) we have

$$D_{cav} = \Psi\left(\frac{\mu_{tr}}{\rho}\right)_{wall} \quad (2)$$

where $(\mu_{tr}/\rho)_{air}$ is the mass energy transfer coefficients of the chamber wall marerial. Using PENELOPE, Yi *et al*. calculated the mass energy transfer coefficients with the uncertainty of 0.01 %.[6] We can evaluate the simulation accuracy by comparing the simulated cavity dose with the right-hand side of Eq. (2).

3. Calculated Quantities

The air kerma calibration factor of an ionization chamber in the photon field was given by

$$N_K = \frac{K_{air}}{D_{cav}} \quad (3)$$

where N_K is the calibration factor and K_{air} is the air kerma of the photon field. The air kerma can be calculated from the photon energy fluence as follows[10]

$$K_{air} = \Psi\left(\frac{\mu_{tr}}{\rho}\right)_{air} \quad (4)$$

where $(\mu_{tr}/\rho)_{air}$ is the mass energy transfer coefficients of air.

To speed-up the calculation of the cavity dose, we used the uniform interaction technique[6]. Skin model[5] was also employed. The thickness of the skin was determined from the continuous slowing-down approximation range of the electron. The thickness of inner-most skin formed in the chamber wall was 2 μm. The skin surrounded the chamber cavity in which the cut-off energy of the electron was set to 0.1 keV. When the electron reached the cut-off energy, it was assumed to be absorbed with losing all its energy in the spot where it was. Another skin for the electron cut-off energy of 10 keV was modeled outside the inner-most skin in the chamber wall with thickness of 0.1 mm. In the outer shell of the chamber wall, the cut-off energy was 100 keV.

The energy of the bremsstrahlung generated in the medium by the electron is distributed continuously to the maximum energy of the incident electron. In general, the characteristic X-rays are also emitted from the target material when the energetic electron is incident on the target. The X-ray energy spectrum, therefore, will vary with the energy of the incident electron, target material and filtration.

We focused mainly on those X-rays suggested in ISO 4037[11] where the characteristics and production method of the reference X-rays for calibrating protection-level dosemeters and dose rate meters at air kerma rates are described. The maximum energy of the X-ray ranged from 10 keV to 300 keV. The air kerma calibration factor of the X-ray was obtained by

$$\overline{N}_K = \frac{\int_0^{E_{\max}} \Phi_E \; N_K(E) \; dE}{\int_0^{E_{\max}} \Phi_E \; dE} \quad (5)$$

where $E_{\max}$ is the maximum energy of the X-ray, $N_K(E)$ the air kerma calibration factor of the ionization chamber for the photon with energy E, Φ_E the derivative of the photon fluence $\Phi(E)$ of the photon with energy E with respect to the energies between E and $E + dE$.

III. Results and Discussion

1. Calculation Accuracy

The accuracy of the cavity dose calculated using PENELOPE was evaluated for the NE2571 cylindrical ionization chamber modeled in the present paper and the results are given in **Fig. 2**. The statistical uncertainty of the simulated cavity was 0.1 % (1 standard deviation). As shown in the figure, the cavity dose calculated for the photon energy in the range 10 keV to 1.25 MeV was accurate within 0.2 % to the values expected from the internal interaction cross-sections of PENELOPE. For the calculation of 1.25 MeV photon, the 3.87 mm-thick build-up cap was added to the chamber. On average, the ratio of the cavity dose to the right-hand side of Eq. (2) was 0.9999 ± 0.0017.

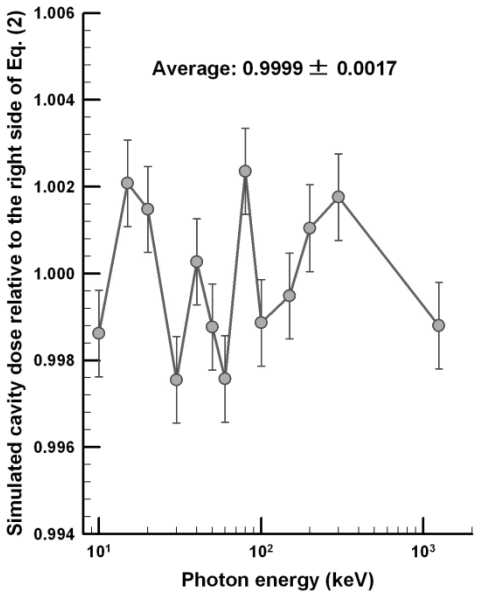

Fig. 2 Calculation accuracy of the cavity dose of the NE2571 ionization chamber. The statistical uncertainty is 0.1 % (1 standard deviation).

2. Air Kerma Calibration Factors

The air kerma calibration factors of the NE2571 ionization chamber for the mono-energetic photons were presented relative to that of the 1.25 MeV ^{60}Co gamma-ray in **Fig. 3**. The calibration factors were calculated with the statistical uncertainty less than 0.1 % (1 standard deviation). The number of the simulation histories was about 500 millions for the photons with the energies less than 100 keV above which the histories decreased with the increase of the photon energy. The calculation time ranged 4 to 7 hours in the IBM compatible PC with 3.4 GHz Pentium D CPU.

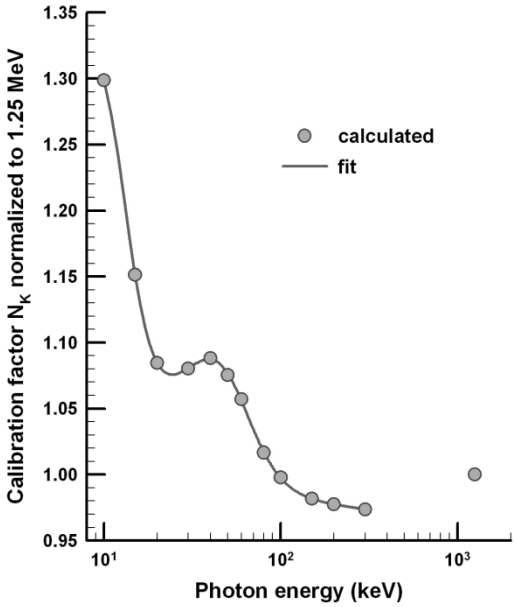

Fig. 3 Calculated air kerma calibration factors for the mono-energetic photons. The values were normalized to that of 1.25 MeV ^{60}Co gamma-ray. The statistical uncertainty was 0.1 % (1 standard deviation).

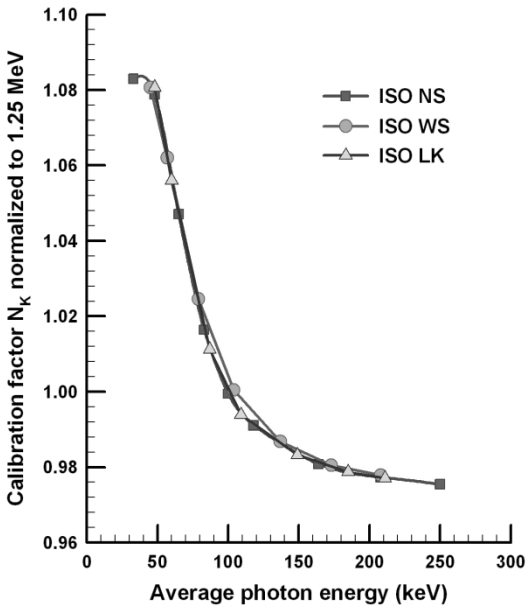

Fig. 4 Calculated air kerma calibration factors for the medium energy X-ray beams. ISO NS stands for the narrow-spectrum series specified in ISO4037[11], ISO WS the wide-spectrum series, ISO LK the low air kerma rate series, respectively.

The calibration factors were fitted with a commercially available curve fit program callecd TableCurve 2D v4. The fit curve is shown in **Fig. 3**. the maximum deviation of the fit from the data points was less than 0.15 %. The X-ray energy spectra of the ISO4037 beam qualities were taken from the X-ray spectrum catalogue compiled by Birch *et al.*.[12] Substituting the air kerma calibration factors for the mono-energetic photons to Eq. (5), we obtained those for the X-rays.

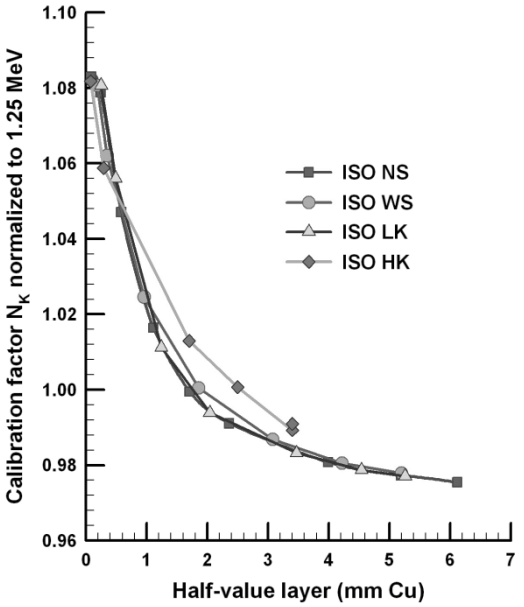

Fig. 5 Calculated air kerma calibration factors given as a function of half-value layer. ISO HK means the high air kerma rate series. Refer to **Fig. 4** for other legends.

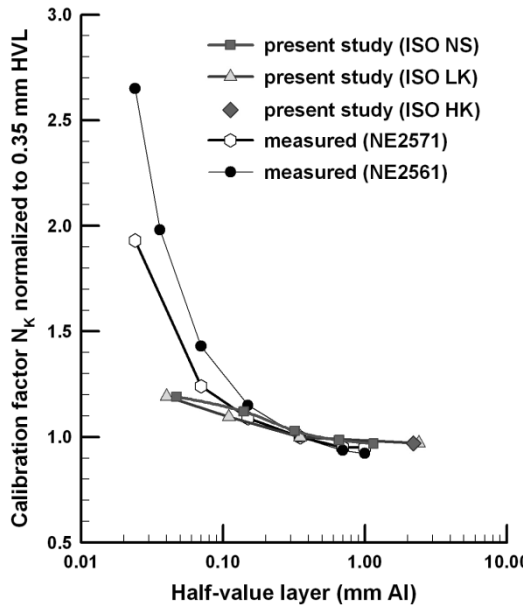

Fig. 6 Comparison of the calculated air kerma calibration factors with measurements[13]. The values were normalized to the half-value layer of 0.35 mm Al.

In **Figs. 4** and **5**, the calibration factors for the medium energy X-rays are given. In the figures, ISO NS means the narrow-spectrum series specified in ISO4037, ISO WS is the wide-spectrum series, ISO LK the low air kerma rate series and ISO HK the high air kerma rate series, respectively. The the calibration factors varied slightly within ± 5 % when the average energies of the X-rays were between 50 to 250 keV or in other words when the half-value layers of the X-rays were between 0.04 and 6.15 mm Cu.

In **Fig. 6**, The calculated air kerma calibration factors for the low-energy X-rays were compared with the measured

values.[13] As confirmed in the figure, the calculated factors were in good agreement within a few percent when the half-value layers were lager than 0.1 mm Al. But the measured calibration factors were higher than the calculated values when the half-value layers are less than 0.1 mm Al. The deviation became worse with decrease of the half-value layer. This tendency was also reported by Seuntjens *et al.*.[4]

The discrepancy might come from the uncertain knowledge of the low energy tail of the X-ray spectrum. Due to the low energy tail, the chamber response can drop abruptly, i.e., increase the calibration factor while the simulated cavity response is less affected. Detailed discussions on the discrepancy between the measured and simulated chamber response to the X-rays were given in Ref. 4. Other factors such as the impurities in the chamber, the chamber-to-chamber difference of material and dimension, and the uncertainty of the photoelectric effect cross section data will cause errors in the calculated chamber response. The geometrical difference between the measurement and simulation may increase the discrepancy in part.

IV. Conclusions

In the present study, we calculated the air kerma calibration factors of the NE2571 cylindrical ionization chamber for the X-rays incident normally on the cylindrical axis of the chamber by means of the Monte Carlo simulation using PENELOPE. The calculated cavity dose approached to the expected value from the internal cross sections of PENELOPE with a ratio of 0.9999 $\pm$ 0.0017 for the photons from 10 keV to 1.25 MeV.

The variation of the calculated calibration factors were about 5 % when the average energies of the X-rays were between 50 to 250 keV (or when the half-value layers of the X-rays were between 0.04 and 6.15 mm Cu). The calculated calibration factors for the low-energy X-rays were agreed within a few percent when the half-value layers were lager than 0.1 mm Al but below which the measured calibration factors became higher.

Acknowledgement

This work was supported in part by the research fund for the development of the nuclear energy granted by the Ministry of Science and Technology (MOST) and in part by the research fund granted by the Korea Food and Drug Administration (KFDA).

References

1) C-M. Ma, A. E. Nahum, "Monte Carlo calculated stem effect corrections for NE2561 and NE2571 chambers in medium energy X-ray beams," Phys. Med. Biol., 40, 63 (1995).
2) H. Tölli, A. F. Bielajew, O. Mattsson, et al., "Fluence non-uniformity effects in air kerma determination around brachytherapy sources," Phys. Med. Biol., 42, 1310 (1997).
3) I. Kawrakow, "Accurate condensed-history Monte Carlo simulation of electron transport: II. Application to ion chamber response simulation," Med. Phys., 27, 499 (2000).
4) J. P. Seuntjens, I. Kawrakow, J. Borg, et al., "Calculated and measured Air-kerma Response of Ionization Chambers in Low and Medium Energy Photon Beams, Proc. Int. Workshop on Accurate Radiation Dosimetry, J. P. Seuntjens and P. N. Mobit (eds), AAPM Proceedings Series 13, Med. Phys. Publishing, 69 (2002).
5) D. T. Burns, "Calculation of kwall for ^{60}Co air-kerma standards using PENELOPE," Comité consultatif des rayonnements ionisants (CCRI) working document CCRI(I)/03-40 (2003).
6) C-Y. Yi, S-H. Hah, M. S. Yeom, "Monte Carlo calculation of the ionization chamber response to ^{60}Co beam using PENELOPE," Med. Phys., 33(5), 1213 (2006).
7) M. D. S. Seneviratne, M. I. Reinhard, C. Baldock, "The energy response of a T.P.A. Mk-II ionization chamber using GEANT4 Monte Carlo simulation," Phys. Med. Biol., 52(13), 3837 (2007).
8) F. Salvat, J. M. Fernández-Varea, J. Sempau, PENELOPE – A Code System for Monte Carlo Simulation of Electron and Photon Transport, Workshop Proceedings, OECD Nuclear Energy Agency, France (2003).
9) J. Sempau, J. M. Fernández-Varea, E. Acosta et al., "Experimental benchmarks of the Monte Carlo code PENELOPE," Nucl. Instr. Meth. Phys. Res. B, 207, 107 (2003).
10) F. H. Attix, Introduction to Radiological Physics and Radiation Dosimetry, John Wiley & Sons, New York, 22 (1986).
11) International Organization for Standardization(ISO), X and gamma reference radiation for calibrating dose meters and dose rate meters and for determining their response as a function of photon energy, ISO 4037 (1996).
12) R. Birch, M. Marshall, G. M. Adran, Catalogue of Spectral Data for Diagnostic X-rays, The Hospital Physicists' Association, London (1979).
13) N. E. Ipe, K. E. Rosser, C. J. Moretti et al., "Air kerma calibration factors and chamber correction values for PTW soft x-ray, NACP and Roos ionization chambers at very low x-ray energies," *Phys. Med. Biol.*, 46, 2107 (2001).

Journal of NUCLEAR SCIENCE and TECHNOLOGY, Supplement 5, p. 321–324 (June 2008)

Development of a Reference Korean Voxel Model by Adjusting the Size of the Organs and Tissues

Jong Hwi JEONG[1], Sang Hyoun CHOI[2], Sungkoo CHO[1], Choon-Sik LEE[3], Kun-Woo Cho[4], and Chan Hyeong KIM[1*]

[1]*Department of Nuclear Engineering, Hanyang University, Seoul, Korea*
[2]*Department of radiation Oncology, College of Medicine, Inha University, Incheon, Korea*
[3]*Department of Nuclear Engineering, University of Florida, Gainesville, Florida, U.S.A*
[4]*Korea Institute of Nuclear Safety, Daejeon, Korea*

The objective of this study was to adjust the height, weight, and organ and tissue sizes of a Korean voxel model in order to construct a Reference Korean voxel model. The adjustment of the height and skeletal mass was achieved by scaling the voxel dimensions. The sizes of the organs and tissues were adjusted to the Reference Korean data by adding or removing voxels on the surface. The adjusted voxel model is 171 cm in height, 68 kg in weight, which exactly matches the Reference Korean data. The size of the voxels (= voxel resolution) is 1.981 mm x 1.981 mm x 2.0854 mm. The organ and tissue masses of the adjusted model also are in a good agreement with the Reference Korean data; the differences are less than 7% for most of the organs and tissues. The unadjusted and adjusted voxel models were ported to the MCNPX Monte Carlo particle transport simulation code to calculate the equivalent doses to the organs and tissues and the effective doses. The calculated values were then compared in order to quantify the effect of the adjustment.

KEYWORDS: voxel model, Reference Korean, Monte Carlo simulation

I. Introduction

The International Commission on Radiological Protection (ICRP) has decided to use the tomographic voxel models to calculate the dose quantities for radiation protection[1)]. The adopted voxel models are believed to faithfully represent Caucasians, considering that they were adjusted to the reference data of ICRP Publication 89[2)], but do not necessarily represent the average radiation workers in Korea, because there exist differences between the races in height, weight, and even in the sizes and topologies of the body's organs and tissues.

Recently a high-quality voxel model of an adult male was constructed in Korea using the serially-sectioned anatomical images of a cadaver. Although the model is based on the cadaver of a Korean adult male, it cannot represent the average Korean workers, because the height and weight of the cadaver (164 cm, 55 kg) differ from the Reference Korean data (171 cm, 68 kg)[3)].

The objective of the present study was to adjust the voxel model for height, weight, and organ and tissue sizes to construct a Reference Korean voxel model. The unadjusted and adjusted models were ported to the MCNPX Monte Carlo particle transport simulation code[4)], and the equivalent doses to the organs and tissues and the effective doses were calculated in order to observe the effect of the adjustment on the dose calculations.

*Corresponding Author, Tel No: +82-2-2220-0513; Fax No: +82-2-2220-4057; E-mail: chkim@hanyang.ac.kr

II. Methods

1. Unadjusted Model

The Ajou University School of Medicine has conducted a national research project, the Visible Korean Human (VKH), by which were acquired very valuable, serially-sectioned color images from a cadaver of a Korean adult male (164 cm and 55 kg)[5)]. Very recently, in the course of developing a Korean voxel model, a total of 30 organs and tissues were very precisely and accurately segmented. The voxel resolution of the model is 1.875 x 1.875 x 2 mm^3. In the present study, the model was adjusted to the Reference Korean data following the procedure recently followed by Zankl et al. in developing the ICRP reference models[6)].

2. Adjustment of Height and Skeletal Mass

The adjustment of the height and skeletal mass was achieved by scaling the voxel dimensions. The height of the model (164 cm) was adjusted to the height of the Reference Korean (171 cm) simply by increasing the voxel size from 2 mm to 2.0854 mm in the z direction.

Due to the absence of the total skeletal mass in the Reference Korean data, it was calculated based on the method suggested by Clays et al.[7)], at 9.6 kg. The skeletal mass of the model was then adjusted to that value (9.6 kg) by adjusting the size of the voxels in the x-y-plane direction, increasing them from 1.875 mm x 1.875 mm to 1.981 mm x 1.981 mm.

3. Adjustment of Organs Masses and Body Weight

The sizes of the organs and tissues were adjusted to the Reference Korean data by using the Inner Grow and Outer Grow functions of Photoshop7.0™. The sizes of the organs

that were larger than those in the Reference Korean data were adjusted by erosion, and the eroded regions were filled with adipose tissue. The sizes of some organs (the thymus, small intestine, heart wall, adrenal, and prostate) were smaller than those in the Reference Korean data, and so those smaller organs were enlarged by adding pixels onto their surfaces. Appropriately, the increased regions did not overlap with any of the other organ regions.

The Reference Asian data[8] were used for the prostate, bladder, adrenals, colon, and small intestines, for which the Reference Korean data were not available. The eye lenses were not adjusted, because they are not sufficiently large. The skin was defined as one voxel layer on the surface of the model. The remaining volume in the model was filled with adipose tissue.

Table 1 Comparison of organ and tissue masses

Organ	Mass (g)			Diff. (%)
	Unadjusted model	Adjusted model	Reference Korean	
Bone	9607	9607	9649 [a]	-0.4%
Liver	2259[b]	1474	1438	2.5%
Lung	1505	1156	1123	2.9%
Brain	1962	1620	1522	6.4%
Kidney	447	359	338	6.2%
Spleen	1135[b]	177	170	4.1%
Stomach	195	141	140	0.7%
Pancreas	127	126	130 [c]	-3.1%
Thymus	32	39	40	-2.5%
Gonads	28	28	29	-3.4%
Eyes	21	21	20	5.0%
Lens	0.51	0.51 [d]	0.4	27.5%
Muscle	23300	23300	25000	-6.8%
Bladder	45	42	40 [c]	5.0%
Colon	410	343	330[c]	3.9%
Small intestine	294	602	590[c]	2.0%
Oesophagus	40	40	40	0.0%
Adrenal	10	14	14[c]	0.0%
Skin	4260	4260 [e]	2400	77.5%
Extrathoracic tissue	73	73	-	-
Thyroid	21	15	15	0.0%
Red bone marrow	1068	1068	1000	6.8%
Prostate	6	12	12[c]	0.0%
Blood	254	254	-	-
Salivary gland	87	87	82	6.1%
Gall bladder	26	13	13	0.0%
Oral mucosa	21	21	-	-
Heart wall	422	391	380	2.9%
Breast	23.3	23.3	22	5.9%
Adipose tissue	20950.2[f]	23400.2	11000	112.7%

[a] The mass of the skeletal system was calculated based on ICRP-70 (1994).
[b] The liver and spleen are large because the cadaver had pneumonia and leukemia.
[c] The Reference Asian data were used for the organs and tissues for which the Reference Korean data are not available.
[d] It was impossible to adjust some of the small organs due the limitation of the voxel resolution.
[e] The skin was defined as one voxel layer on the surface of the model.
[f] All of the undefined organs and the eroded regions were filled with adipose tissue.

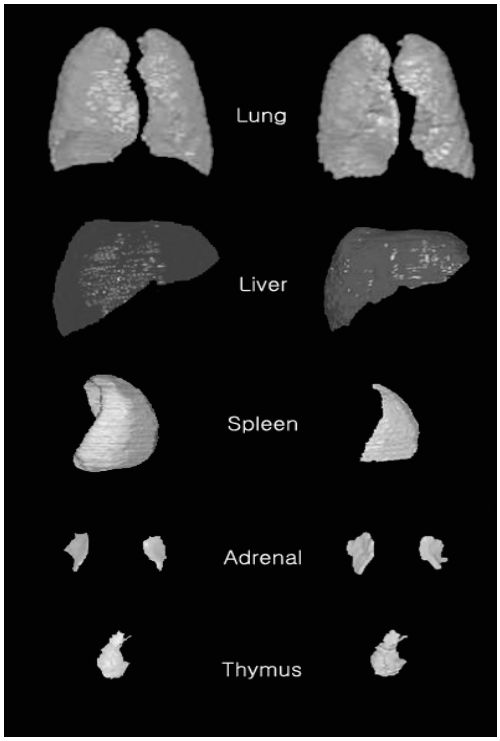

Unadjusted Adjusted

Fig. 1 3D views of unadjusted and adjusted organs

After the adjustment of the height, skeletal mass, and the organ and tissue sizes, the weight of the model was 67.8 kg, 0.2 kg less than the weight of the Reference Korean (68 kg). The weight of the model was adjusted by adding 0.2 kg of adipose tissue on the surface of the legs.

Finally, the organ and tissue masses of the model were adjusted to the Reference Korean data, most of them within 7%. **Fig. 1** shows 3D views of some of the organs, before and after adjustment. The masses of the organs and tissues are compared in **Table 1** for the unadjusted model, the adjusted model, and the Reference Korean.

4. Monte Carlo Simulations

The unadjusted and adjusted voxel models were ported to a Monte Carlo particle transport simulation code, MCNPX, for the calculation of the organ and tissue doses and thereby the effective doses. The organ- and tissue-averaged absorbed doses and effective doses were calculated per unit air kerma. The considered irradiation geometries were broad parallel photon beams of anterior-posterior (AP), posterior-anterior (PA), left lateral (LLAT), and right lateral (RLAT) with photon energies of 0.015 - 10 MeV. The statistical errors for the organ and tissue doses were less than 5% for all of the cases considered in this study except for 0.015 MeV, for which the statistical errors were as large as 100%.

III. Results and Discussion

The adjusted voxel model is 171 cm in height and 68 kg in weight. The size of the voxels (voxel resolution) is 1.981 x 1.981 x 2.0854 mm^3. The size of the voxel array is 247 x 141 x 850 (29,602,950) in the x, y, and z directions, which

corresponds to 489.307 mm, 279.321 mm, and 1,772.59 mm, respectively. Three-dimensional views of the adjusted model are shown **Fig. 2**.

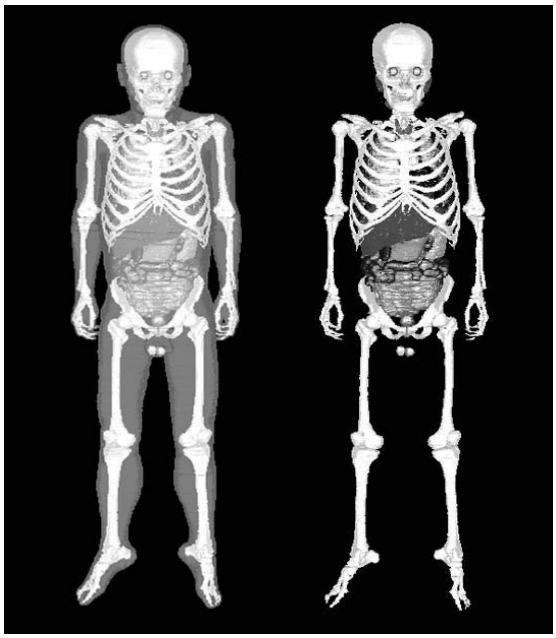

Fig. 2 Adjusted model

This study calculated the organ and tissue doses and the effective doses using both the unadjusted and adjusted models. The calculated values were then compared in order to quantify the effect of the adjustment. In general, the differences were not so large (< a few %), except for the spleen and prostate. The largest difference was 51% for the spleen (RLAT, 0.03 MeV). For the spleen, however, the differences were significant only for the RLAT geometry, as the differences for the other irradiation geometries were mostly less than a few %. Note that the size of the spleen was reduced by a factor of 6. The differences were also large for the prostate, even though the size of the prostate was adjusted by only 20%. By contrast, the differences were very small for the liver, which was reduced by as much as 38% in the adjustment. The effective dose differences were very small, less than 3-4% in most cases. **Fig. 3** compares the organ doses and effective doses for both the unadjusted and adjusted models.

IV. Conclusions

In this study a Korean voxel model has been adjusted for its height, weight, and organ and tissue sizes in order to construct a Reference Korean voxel model. It is believed that the adjusted model can represent the average Korean workers more reasonably, considering the facts that (1) the original image data were taken from a Korean male, (2) the quality of the original images was very high (color images of 0.2 mm x 0.2 mm resolution), and (3) the model was adjusted to the Reference Korean data. The adjusted model can be used to calculate the dose conversion coefficients for Korean workers in the future.

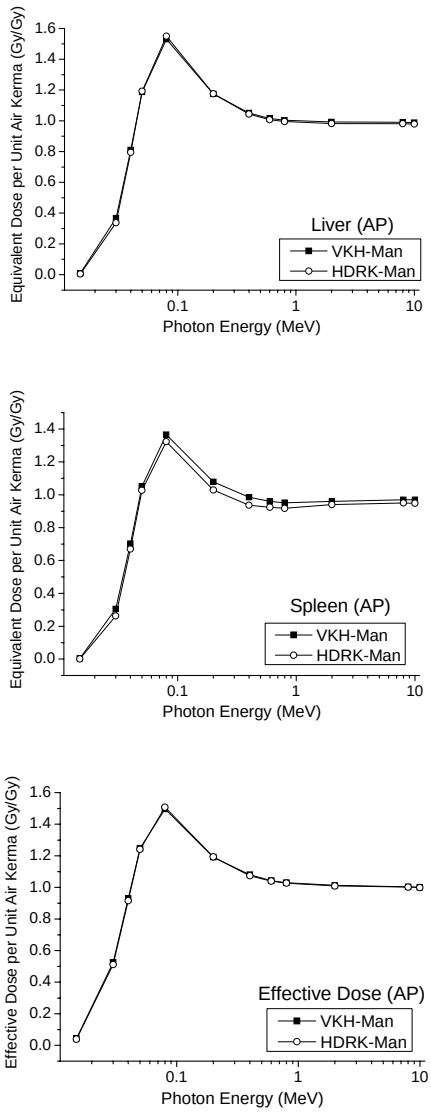

Fig. 3 Comparison of organ doses and effective doses for unadjusted and adjusted models

Acknowledgement

This work was supported by the Korean Ministry of Science and Technology through ERC (RII-2000-067-03002-0), BAERI (M20508050003-05B0805-00310), and the Korea Institute of Nuclear Safety (KINS).

References

1) H. Schlattl, M. Zankl and N. Petoussi-Henss, "Organ dose conversion coefficients for voxel models of the Reference male and female from idealized photon exposures," Phys. Med. Biol. 52, 2123 (2007).
2) International Commission on Radiological Protection, Basic Anatomical and physiological Data for use in Radiological Protection: Reference Values, ICRP Publication 89, Pergamon Press, Oxford (2003).
3) S. Park, J. Lee, J. I. Kim, Y. J. Lee, Y. K. Lim, C. S. Kim and C. Lee, "In vivo organ mass of Korean adults obtained fron whole-body magnetic resonance data," Rad. Prot. Dosi. doi:10.1093/rpd/nci340 (2005).

4) D. B. Pelowitz, Ed, MCNPX User's Manual Version 2.5.0, NM: Los Alamos National Laboratory, Los Alamos, LA-CP-05-0369 (2005).
5) J. S. Park, M. S. Chung, J. Y. Kim, H. S. Park, "Visible Korean Human: Another trial for making serially sectioned images," Medical Imaging 4681[3], 171 (2002).
6) M. Zankl, J. Becker, U. Fill, N. Petoussi-Henss, KF. Eckerman, "GSF male and female adult voxel models representing ICRP Reference Man - The present status", American Nuclear Society, The Monte Carlo Method (2005)
7) International Commission on Radiological Protection, Basic Anatomical and physiological Data for use in Radiological Protection: The Skeleton, ICRP Publication 70, Pergamon Press, Oxford (1994).
8) International Atomic Energy Agency, Compilation of anatomical, physiological and metabolic characteristics for a Reference Asian Man. IAEA-TECDOC-1005, Vienna: IAEA (1998).

Journal of NUCLEAR SCIENCE and TECHNOLOGY, Supplement 5, p. 325–328 (June 2008)

Dose Rate Simulation of a Panoramic Gamma Irradiator using the MCNPX Code and Comparison with Measurements

Yong Ho KIM and Jae Woo PARK*

Applied Radiological Science Research Institute
Cheju National University, 1 Ara-dong, Jeju-si, Jeju-do , Korea

Monte Carlo simulation has been carried out to determine the dose rate distribution inside the Co-60 irradiation cell of Cheju National University, Korea using the MCNPX code. The panoramic gamma irradiator loaded with an initial activity of 400TBq (10,807Ci) has an activity of 270TBq (7,280Ci) at time of this study. Calculated are the circumferential dose rate distribution around the source rod, the dose rate distribution as a function of the distance from the source, and vertical dose rate distribution along the source rod. Also calculated is the dose rate behind a lead shield. The calculated results are compared with the measured data obtained with a Farmer type ionization chamber and MOSFET dosimeters. The simulated results agree within acceptable ranges with the measured data obtained with the ionization chamber. There exist considerable deviations between the simulated result and measured data obtained with the MOSFET dosimeters. This deviation seems to result from the imprecision of the MOSFET dosimeters in some dose ranges.

KEYWORDS: panoramic gamma irradiator, Monte Carlo simulation, dose rate distribution, Farmer's type ionization chamber, MOSFET dosimeter

I. Introduction

A panoramic gamma irradiator is useful in circumstances where multiple samples need to be simultaneously irradiated. Two panoramic research irradiators with moderately high radioactivity are currently in operation in Korea, and one is operated by Applied Radiological Science Research Institute (ARSRI), Cheju National University. The whole irradiation facility was designed and constructed by a domestic company. It was loaded with an MDS Nordion standard ^{60}Co source (C188) with an initial activity of 400TBq (10,800Ci) as of February 19, 2004. The irradiator was intended to be used for various research purposes. It has been primarily used for irradiating plants and biological samples such as cultured cells and mice. Until now, the dose rates at specified points have been determined only by measurements. The measuring efforts can be saved or the accuracy of the measured data can be checked if a computation model is available, which can calculate the radiation dose at an arbitrary point inside the irradiation room.

A number of computer codes have been used to calculate the radiation dose distribution for gamma irradiators[1-4]. These include QAD, FUDGE, EGS4 and MCNP. Of these MCNP code has been most widely used due to its accuracy, advanced graphic features and simplicity of geometric modeling. MXNPX is a superset of MCNP with some extended capabilities. We have used MCNPX code[5] to determine the air kerma rate distribution at equidistant points on a circular line around the source rod, and at points on a radial line differently distant form the source. The accuracy of the computation modeling is evaluated by comparing the computed results with the measured data provided that the measuring device functions correctly.

*Corresponding Author, Tel No: +82-64-754-3645, Fax No: +82-64-757-9276, E-Mail: jwpark@cheju.ac.kr

II. Description of the Irradiator

The ARSRI gamma irradiator consists of a plug-type source holder which contains the ^{60}Co source rod of about 1cm diameter and 40cm length, the lead shield container and the motor-driven source driving system which is located outside the irradiation cell. The source holder is normally plugged into the shield container which is placed below the floor of the irradiation cell. For irradiation, samples are placed at predetermined positions and then the source holder is pulled out of the shield container by a steel cable connecting the source holder and source driving system. The source holder is constrained to move only vertically along the guide tube. When irradiation is finished, the source holder is automatically inserted into the shield container by timer setting. There are 3 annular lead shields which can be used to reduce the dose rate by surrounding one by one the source guide tube. Hence, the total dose delivered to the samples can be controlled either by irradiation time, distance to the source or the annular lead shields.

Fig. 1 shows the horizontal view of the irradiation facility. The irradiation cell is a rectangular parallelepiped space with a dimension of 320 x 420 x 27cm^3(W x L x H). The source is positioned at the center on the width (W) and shifted 60cm from the center toward the wall on the length (L). An aluminum irradiation stand is installed 20cm above the floor. The ^{60}Co source rod has a cylindrical shape with a dimension of 1.1cm diameter and 40.6cm length. The source holder is made of a stainless steel pipe with the inner and outer diameters of 1.61cm and 2.17cm, respectively. The source holder is jointed to a cylindrical lead shield which

functions as the lid of the source container. The source holder and lead shield run inside the guide tube made of a stainless pipe with the inner and outer diameters of 10.83cm and 11.43cm, respectively. Fully withdrawn, the center of the source rod is positioned 35 cm above the irradiation stand with its lower end 15cm above it. At time of this study the initial activity of the source has decreased to 270TBq (7,280Ci).

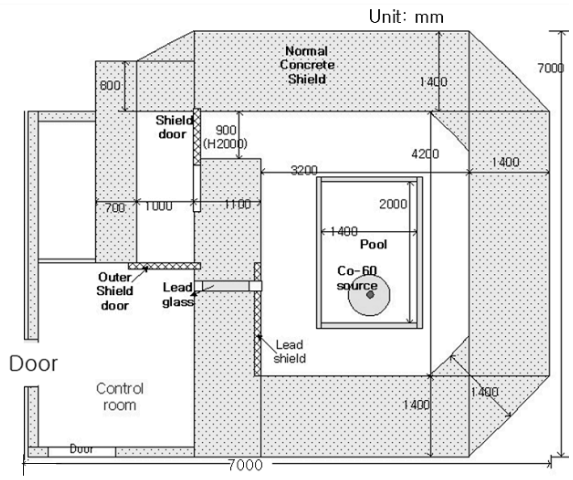

Fig. 1 Horizontal view of the irradiation facility.

III. Methods of MCNPX Simulation

We have conducted MCNPX simulations to calculate the air kerma dose for 4 cases. The first case is the circumferential dose distribution around the source. Simulation results are obtained at 8 points equidistant (1m) from the source rod on the mid plane. **Fig. 2** shows the 8 radial directions on which the circumferential dose distribution is computed. The geometric model of the irradiation cell is shown in **Fig. 3**. The second case is the horizontal dose distribution as a function of the distance from the source along the radial line B.

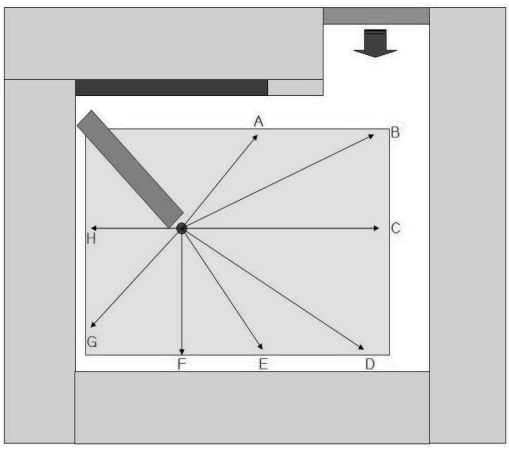

Fig. 2 Radial directions on which the circumferential dose distribution are calculated.

The third case is the vertical dose distribution as a function of the height from the irradiation stand. We have also performed extensive computations to obtain the dose distributions when the annular lead shields are used. Due to limitation of the space, we omit presenting the simulation results here. Instead, we considered a case in which a simple lead shield was placed between the source and the detector. The shield was prepared by stacking 4 lead blocks. **Fig. 4** shows the geometric model for the case with a lead shield.

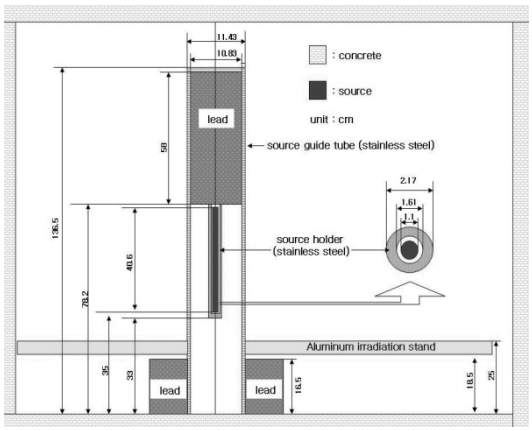

Fig. 3 Geometric model of the irradiation cell for MCNPX simulation.

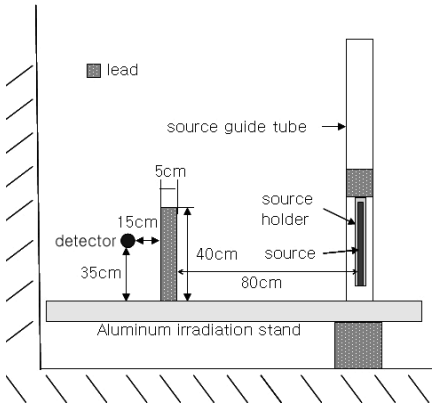

Fig. 4 Geometric model for dose calculation with a lead shield.

In MCNPX simulation, there are several distinct ways of obtaining the air kerma dose. These can be accomplished by specifying an appropriate F tally card in the input data. We tested three tally options: F4, F5 and F6. With F4 tally option, the sensitive volume of the dosimeter is represented by a cell and the air kerma dose is calculated from the photon flux averaged over the cell, multiplied by the particle energy and the mass energy absorption coefficient of the air. With F5 tally option, the dosimeter is represented by a point and the air kerma is calculated from the photon flux at the point. With F6 tally option, the dosimeter is represented by a cell, and the air kerma is directly calculated from the energy deposited in the cell. Appropriate conversion constant can be given by a tally multiplier which is specified in FM card. We neglected to track the secondary electrons generated by gamma ray interactions with air atoms since otherwise it took too much computation time. This implies that the energy transferred to an electron is completely dissipated at the point the electron is generated. Hence all of the energy

transferred to a secondary electron generated in the dosimeter cell contributes to the air kerma dose.

IV. Dose Rate Measurement

In order to evaluate the accuracy of the computation model, we compare the calculated and measured air kerma doses. Two types of dosimeters are used: a Farmer-type ion chamber with a volume of 0.6cc (Cardinal Health model 30-351) and a MOSFET dosimeter system (Thompson and Nelson Co. model TN-1002RD). The radial and circumferential dose distributions are measured with the ion chamber while the vertical dose distribution is measured with the MOSFET dosimeters. The MOSFET dosimeter system is convenient for simultaneous measurement at multiple points. The air kerma dose by the ion chamber is expressed as:

$$J_s = k_Q \cdot k_D \cdot N_k \cdot M \quad (Gy) \qquad (1)$$

where

k_Q = radiation quality correction (1 for ^{60}Co)
k_D = correction for air density change
N_k = calibration factor for air kerma dose(Gy/nC)
M = measured amount of ionization (nC)

The ion chamber was calibrated for the measurement of air kerma dose at Korea Food and Drug Administration and the calibration factor was given as $N_k = 4.928\times10^{-2}$ Gy/nC. Measurement of the radial dose distribution starts at 20cm from the source with an increment of 20cm. Measuring time at each point is three minutes. Since the ion chamber is a free air type, correction for the ambient temperature and pressure with respect to the calibrated reference values (22 ^{o}C and 760mmHg) is made.

The MOSFET dosimeter system consists of 4 bias voltage supply modules, a voltage reader, MOSFET dosimeters and a laptop PC. 5 MOSFET dosimeters are connected to each module and a total of 20 dosimeters are connected to the reader. The dosimeters are attached on a PVC pipe with 5cm interval and the pipe is vertically erected at 1m from the source on C line in **Fig. 2**. Voltage signals from the reader are fed through an RS232 cable into the laptop PC outside the irradiation cell. Air kerma dose at each point is automatically calculated by multiplying the measured voltage drop from the beginning to the end of the measurement by the calibration factor of the corresponding dosimeter. Twenty dose data are simultaneously obtained by one measurement. The measuring time is 2 minutes. The dosimeters were calibrated at Korea Research Institute of Standards and Science for the measurement of air kerma dose and the calibration factors were stored in the laptop PC.

V. Computation Results and Comparison with Measured Data

In order to achieve the relative error below 0.5% in the MCXPX simulation, the number of particle history was adjusted in the range 10^8~10^9. The actual dose rate was obtained by multiplying the calculated dose by the source activity. **Table 1** compares the measured and calculated dose rates as a function of distance from the source as obtained with different tally options.

Table 1 Calculated air kerma dose rate as a function of distance from the source with different tally options.

Distance (cm)	Measured (Gy/h)	MCNPX Calculation (Gy/h)		
		F4	F5	F6
20	1233.2	1298.6	13121.3	1285.1
40	400.6	407.6	408.7	403.5
60	191.2	191.0	194.4	189.1
80	115.5	111.2	113.6	110.0
100	75.0	73.8	74.7	72.5
120	52.2	52.9	53.0	52.1
140	39.6	39.1	39.7	38.7
160	31.0	31.4	30.9	31.0
180	23.6	24.5	24.8	24.0
200	21.0	20.1	20.4	20.1

It is found that F5 tally option, which calculates the dose from the photon flux at the dosimeter point, results in the largest dose and F6 tally option, which calculates the dose from the energy deposited in the dosimeter volume, gives the smallest dose. Compared with the measured data, it seems difficult to conclude any one tally option will give more accurate results than the others. In higher dose region near the source (20cm and 40cm), the calculated result shows higher values than the measured data, while in the lower dose region(80cm~200cm) the calculated values are generally lower than the measured data. This pattern is more certain with F6 tally option than with other tally options. With F6 tally option, the deviation from the measured data lies below 5%.

Fig. 5 shows the circumferential dose distribution 1m distant from the source. The calculated result was obtained with F6 tally option and the ion chamber was used for the measurement. Though the irradiation cell itself has an asymmetric structure, the calculated result shows almost symmetric dose distribution. This implies that the scattered gamma rays have very little effect on the calculated dose. The measured dose distribution shows a relatively lower value on the H direction, which we can not accounted for. Since there is some gap between the source rod and the source holder, the source may not be at the center of the source holder. Or the source holder may not be aligned along the centerline of the guide tube. In MCNPX simulation, we assumed that the source rod and holder are exactly aligned along the centerline.

Table 2 shows the dose rates calculated and measured behind a lead shield. This problem was intended to see the capability of the computation model to accurately simulate a thick lead shield. The calculated dose differs from the measured by 3.3%, which is within acceptable error limit.

Fig. 6 shows the vertical dose distribution as a function of the height from the irradiation stand at 1m from the source. The dose rate was compared from the lower end position

(15cm) of the source to 110cm. The center of the source rod locates at 35cm and its top locates at 55cm. Both of the measured and calculated dose distributions show slightly asymmetric patterns with generally higher values in the lower half. This may have resulted from scattered gamma rays from the irradiation stand and the irradiation room floor. The simulation result agrees relatively well with the measured data around the source length region, while the deviation increases as the height increases. The MOSFET measured data show an irregular pattern in the upper region. Considering that there is no geometric irregularity in the irradiation room and the vertical alignment of the source rod and holder, these deviations seem to result from imprecision of the MOSFET dosimeters in some dose ranges.

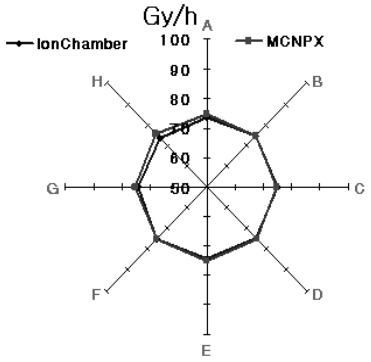

Fig. 5 The circumferential dose rate distribution around the source 1m from the source.

Table 2 Dose rate calculated at a point behind a lead shield of 5cm thickness.

	Measured data	Calculated result	Deviation (%)
Dose rate (Gy/h)	7.15	7.39	3.3

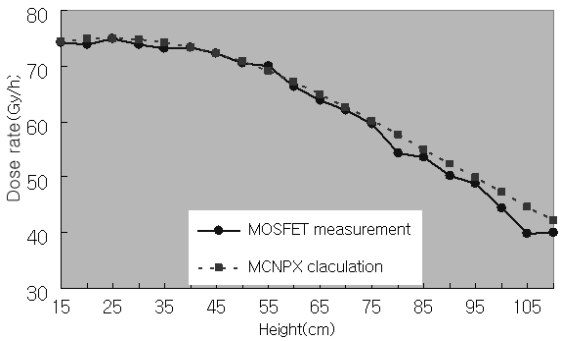

Fig. 6 The vertical dose rate distribution as function of the height from the irradiation stand.

VI. Conclusion

MCNPX simulation has been performed to compute the dose distribution inside the panoramic gamma irradiation facility of Cheju National University, Korea. The simulation includes the radial dose distribution as a function of distance from the source, the equidistant circumferential dose distribution around the source, the vertical dose distribution along the source rod, and the dose behind a thick lead shield. Three different F tally options are tested for the air kerma dose calculation. The calculated results are compared with the measured data obtained with a Farmer-type ionization chamber and a MODFET dosimeter system.

The simulated results agree within acceptable ranges with the measured data obtained with the ionization chamber. Use of different F tally options results in slightly different values. It seems difficult to conclude which tally option is more adequate than the others. Considerable deviation exists between the simulated results and measured data obtained with the MOSFET dosimeters. This deviation seems to result from the imprecision of the MOSFET dosimeters in some dose ranges.

Acknowledgement

This work was performed under the program of Basic Atomic Energy Research Institute (BAERI), which is a part of Nuclear R&D Programs sponsored by Korea Ministry of Science and Technology.

References

1) C. Oliveira, J. Salgado, A. Ferro de Carvalho, “Dose Rate Determinations in the Portuguese Gamma Irradiation Facility: Monte Carlo Simulations and Measurements, Radiation Physics and Chemistry, Vol. 58, pp 279-285, 2000.
2) G.R. Raisali and M. Sohrabpour, “Application of EGS4 Computer Code for Determination of Gamma ray Spectrum and Dose Rate Distribution in Gammcell 220”, Radial. Phys. Chem. Vol. 42, Nos 4-6, pp 799-805, 1995.
3) G. PllqA-VILLALPANDO* and D. P. SLOAN, “Dose Distribution Studies of A Gamma Industrial Irradiator Using A PC Code 1” Radiat. Phys. Chem. Vol. 52, Nos I 6. pp. 563 567, 1998.
4) G. Pina-Villalpando and D. P. Sloan, “ Use of Computer Code for Dose Distribution Studies in A ^{60}Co Industrial Irradiator”, Radial. Phys. Chem. Vol. 46, No. 4-6, pp. 1385-1389, 1995.
5) Denise B.Pelowitz, “MCNPXTM-USER'S MANUAL” version 2.5.0, 2005.